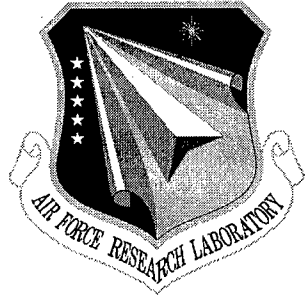


AFRL-SN-RS-TR-1999-86

Final Technical Report

April 1999



PROCEEDINGS OF THE 1998 ANTENNA APPLICATIONS SYMPOSIUM

University of Massachusetts

Daniel H. Schaubert, et al

APPROVED FOR PUBLIC RELEASE; DISTRIBUTION UNLIMITED.

19990622 155

AIR FORCE RESEARCH LABORATORY
SENSORS DIRECTORATE
ROME RESEARCH SITE
ROME, NEW YORK

DTIC QUALITY INSPECTED 4

This report has been reviewed by the Air Force Research Laboratory, Information Directorate, Public Affairs Office (IFOIPA) and is releasable to the National Technical Information Service (NTIS). At NTIS it will be releasable to the general public, including foreign nations.

AFRL-SN-RS-TR-1999-86 has been reviewed and is approved for publication.

APPROVED: *Zachary O. White*

ZACHARY O. WHITE
Project Engineer

FOR THE DIRECTOR:

Robert V. McGahan

ROBERT V. McGAHAN, Technical Advisor
Electromagnetics Technology Division
Sensors Directorate

If your address has changed or if you wish to be removed from the Air Force Research Laboratory Rome Research Site mailing list, or if the addressee is no longer employed by your organization, please notify AFRL/SNHA, 31 Grenier Street, Hanscom AFB MA 01731-3010. This will assist us in maintaining a current mailing list.

Do not return copies of this report unless contractual obligations or notices on a specific document require that it be returned.

REPORT DOCUMENTATION PAGE			Form Approved OMB No. 0704-0188
<p>Public reporting burden for this collection of information is estimated to average 1 hour per response, including the time for reviewing instructions, searching existing data sources, gathering and maintaining the data needed, and completing and reviewing the collection of information. Send comments regarding this burden estimate or any other aspect of this collection of information, including suggestions for reducing this burden, to Washington Headquarters Services, Directorate for Information Operations and Reports, 1215 Jefferson Davis Highway, Suite 1204, Arlington, VA 22202-4302, and to the Office of Management and Budget, Paperwork Reduction Project (0704-0188), Washington, DC 20503.</p>			
1. AGENCY USE ONLY (Leave blank)	2. REPORT DATE	3. REPORT TYPE AND DATES COVERED	Final Jan 98 - Dec 98
4. TITLE AND SUBTITLE		PROCEEDINGS OF THE 1998 ANTENNA APPLICATION SYMPOSIUM	
6. AUTHOR(S)		Daniel H. Schaubert, et al	
7. PERFORMING ORGANIZATION NAME(S) AND ADDRESS(ES)		8. PERFORMING ORGANIZATION REPORT NUMBER	
University of Massachusetts Department of Electrical & Computer Engineering Amherst MA 01003		N/A	
9. SPONSORING/MONITORING AGENCY NAME(S) AND ADDRESS(ES)		10. SPONSORING/MONITORING AGENCY REPORT NUMBER	
Air Force Research Laboratory/SNHA 31 Grenier Street Hanscom AFB MA 01731-3010		AFRL-SN-RS-TR-1999-86	
11. SUPPLEMENTARY NOTES			
Air Force Research Laboratory Project Engineer: Zachary O. White/SNHA/(781) 377-3191			
12a. DISTRIBUTION AVAILABILITY STATEMENT		12b. DISTRIBUTION CODE	
Approved for public release; distribution unlimited.			
13. ABSTRACT (Maximum 200 words) The Proceedings of the 1998 Antenna Applications Symposium is a collection of state-of-the-art papers relating to phased array antennas, multibeam antennas, satellite antennas, microstrip antennas, reflector antennas, HF, VHF, UHF and various other antennas.			
14. SUBJECT TERMS			15. NUMBER OF PAGES
Antennas, Satellite Antennas, Broadband Antennas, Microstrip, Reflector, HF, VHF, UHF, Multibeam Antenna, Array Antennas			360
16. PRICE CODE			
17. SECURITY CLASSIFICATION OF REPORT	18. SECURITY CLASSIFICATION OF THIS PAGE	19. SECURITY CLASSIFICATION OF ABSTRACT	20. LIMITATION OF ABSTRACT
UNCLASSIFIED	UNCLASSIFIED	UNCLASSIFIED	UL

TABLE OF CONTENTS
FOR
1998 ANTENNA APPLICATIONS SYMPOSIUM

I. ANTENNA SYSTEMS

Keynote Address Antennas for Industry and Government in the Next Century <i>Warran Stutzman, Virginia Tech</i> <i>Blacksburg, VA</i>	1
Concealed AM/FM Antenna on the Rear Side Glass of a Mini-Van <i>Andrew Adrian, Visteon Automotive Systems</i> <i>Dearborn, MI</i>	13
DAB Multiband Glass Antenna <i>S. Miyahara and Jun Yamaguchi, Visteon Automotive Systems</i> <i>Kanagawa, Japan</i> <i>Naoki, Shibata, Harada Industry Company, Ltd</i> <i>Tokyo, Japan</i>	43
A Novel Aperture-Coupled Microstrip Antenna Array Fed By A Dielectric Guide <i>David Li and Robert Knox, Epsilon Lambda Electronic Corporation</i> <i>Geneva, IL</i>	63
A Low-Profile Luneberg Lens Airborne GBS Antenna <i>Mark E. Rayner, Datron/Transco, Inc.</i> <i>Simi Valley, CA</i>	86

II. PHOTONICS AND SPACE ANTENNAS

Experiments on an Optically Controlled 2-D Scanning Antenna <i>George W. Webb, Stephen C. Rose, Mario S. Sanchez, J. Martin Osterwalder</i> Innova Laboratories, Inc. San Diego, CA	99
True Time Delay with Binary Time Delay Control For Large Arrays <i>Stuart A. Collins, Jr., Betty Lise Anderson, Craig Liddle</i> Ohio State University Columbus, OH	113
EHF Optical Nuller <i>R. A. Brown, P. A. Schulz, S. R. Henion</i> MIT Lincoln Laboratory Lexington, MA	127
SAC-C Satellite Antennas <i>Valentin Trainotti, Norberto Dalmas Di Giovanni, Juan Skora, Diego A. Schweitzer</i> CITEFA Buenos Aires, Argentina	135
An Array Antenna Space Experiment Using Transmit/Receive Antenna Module (TRAM) Technology <i>Hugh Southall, Hanscom AFB, MA William Kornrumpf, GE Corporate R&D, Schenectady, NY Jim Staggs, Fred Jonas, Nichols Research Yolanda King, Kirkland AFB</i>	160
Design of an Active Antenna Using the Series Feedback Oscillator <i>Byoung woo Park, Jeong se Han, Kyung soo Jin, Bierng Chearl Ahn Chungbuk National University, Korea Young chang Cho, ACE Electronic Technology Company, Korea</i>	172

III. ADVANCED ARRAY TECHNIQUES

Characteristics of Dielectric Multilayer Filters Incorporating A Resonant Grating	184
<i>T. R. Holzheimer, Raytheon Systems, Greenville, TX</i>	
<i>S. Tibuleac, P. P. Young, R. Magnusson</i>	
University of Texas at Arlington, Arlington, TX	
Electrically Small, Efficient, Wide-Band, Low-Noise Antenna Elements	214
<i>George Skahill, NTL Technologies, Inc., Greenlawn, NY</i>	
<i>Ronald M. Rudish, John Piero, AIL Systems, Inc., Deer Park, NY</i>	
Traveling Wave Slotted Array Antenna Employing Asymmetric Ridge Waveguide	232
<i>H. Shnitkin, D. Collier, J. Dickstein</i>	
Northrop Grumman Corp., Baltimore, MD	
Limited Scan Phased Array Antenna	255
<i>Richard R. Kinsey</i>	
Sensis Corporation, DeWitt, NY	
Distributed MEMS True-Time Delay Phase Shifters	270
<i>N. S. Barker, G. M. Rebeiz</i>	
University of Michigan	
Ann Arbor, MI	

IV. SHORT COURSE ON NUMERICAL METHODS

Fast Algorithms in CEM and Overview

Weng Chew

University of Illinois

Fast Illinois Solver Code

Jiming Song

University of Illinois

Fast Time Domain Integral Equation Solvers

Eric Michielssen

University of Illinois

Finite Element Method and FFT Base Method in CEM

Jianming Jin

University of Illinois

Finite Methods in CEM

Andreas Cangellaris

University of Illinois

Application of CEM to Circuits Problems

Jose Schutt-Aine

University of Illinois

V. MEASUREMENTS/PROCESSING

The Multilevel Fast Multipole Algorithm for Analyzing Electromagnetic Radiation from Complex Surfaces-Wire Structures <i>Hsueh-Yung Chao, Jiming Song, Eric Michielssen, Weng Cho Chew</i> University of Illinois at Urbana-Champaign, Urbana, IL	282
An Electronic "On Aircraft" Boresight Correction Procedure for Single Axis Scanned Phased Array Antennas <i>Gary L. Kosanovic, Benjamin R. Meyers, David P. Parrish, Richard S. White, Kurt G. Ramsey</i> Northrop Grumman, Baltimore, MD	295
Low-Cost Portable Near-Field Antenna Measurement System <i>David P. Woollen, Jeffrey M. Snow, Allen R. Tillerson, George Leaf</i> Naval Surface Warfare Center, Crane, IN <i>William Slowey</i> , Technology Service Corporation, Bloomington, IN	301
Ultra-Wideband Coherent Processing <i>K. M. Cuomo, J. E. Piou, J. T. Mayhan</i> MIT Lincoln Laboratory, Lexington, MA	306
Impact of Frequency Dependent Mutual Coupling and Channel Mismatch on Closed Loop Digital Adaptive Nulling Antenna Performance <i>K. A. Falcone, Ilir F. Progr</i> Mayflower Communications Company, Inc., Billerica, MA <i>P. Olson, K. Beam</i> U. S. Army CECOM, Fort Monmouth, NJ	333

ANTENNAS FOR INDUSTRY AND GOVERNMENT IN THE NEXT CENTURY

Warren Stutzman, Director
Antenna Group
Electrical and Computer Engineering Department
Virginia Tech
Blacksburg, VA 24061-0111

Abstract: The challenges to the antenna designer in the 21st century will be to integrate antennas into systems to meet a broad range of requirements. The first century of antenna development has primarily focused on the antenna as a separate and distinct device. But two things have changed the landscape of antenna design. First, the specifications on antennas have become increasingly more challenging. Reduced allocated volume and increased bandwidth are examples. Second, system functions are being integrated at the platform level and antenna functions are also expected to be integrated. For these two reasons, antenna design at the system level will emerge in the next century. This paper discusses the antennas required to accomplish this.

1. The Past

The foundations of electromagnetics introduced during the 19th century were put into practice in the 20th century. Radio engineers met the demand for wireless communication services using low frequencies and large antennas. With the development of high frequency sources, came new antennas. The development pace increased dramatically during World War II to support critical defense communication needs. In addition, radar became a key technological weapon in the war and lead to many antenna innovations. The post war economic boom fueled the innovation rate even further. As the century closes, we find an environment of reduced regulations on many communication services that will add even more to the development pace of wireless systems. This is not limited to the developed regions of the world. In fact, the so-called third world nations are experiencing the most rapid growth in communication infrastructure.

Electromagnetics applications that require antennas extend far beyond communications and radar to more recent applications such as passive remote sensing and industrial uses. Communication traffic began with broadcast voice

and expanded to point-to-point voice and video. Voice and video applications were followed by data services and messaging. [1,2] Industrial applications for communications are also popular, such as remote control. For example, radio-link garage door openers have been used for many years. Most recently, position location applications have exploded with the availability of worldwide coverage offered with, for example, the Global Positioning Satellite service. [1] At the beginning of the 20th century, radio communications was the only application for electromagnetics and was referred to as wireless. Interestingly, as the century closes the term wireless has returned to popular use. However, wireless now includes many of the electromagnetics applications mentioned above.

This century has witnessed expansion of the arena for wireless. The initial applications were deployed on land and at sea. This expanded to air and eventually to deep space. Thus, all corners of the universe have been explored by electromagnetics in this century. In contrast, physical exploration of the globe required many centuries and we have visited only a few nearby locations in space.

This tremendous development pace for wireless in the 20th century was made possible by antennas. For example, earth-space communications requires combined space and ground segment antenna gains of up to 80 dB and more. Without high gain antennas, the signals would be hopelessly lost in noise. In addition to long distance communications and sensing, antennas also enable frequency reuse by using patterns with different angular coverage and using different polarizations.

2. The Present

Although it is risky to form any conclusions about the state of a technology in relation to possible future development, it appears that all types of antennas were invented in the 20th century or shortly before. This statement depends on how antenna "type" is defined. The four antenna types discussed here are summarized in Table 1. [3] This division of antenna types is based on fundamental operation of antennas but also aligns closely to major performance specifications. That is, small, low gain antennas are usually electrically small. Narrow band, but impedance matched, antennas with simple geometries are usually resonant. Antennas with wide bandwidth are a special class of antennas. High gain is achieved using aperture antennas. It is likely that the categorization in Table 1 will also apply through the next century. This, of course, does not mean that the pace of innovation will slow any. To illustrate for resonant antennas, the half-wave dipole antenna appeared early in the century and the microstrip antenna was invented late in the century.

Table 1
Types of Antenna Elements

Antenna Type	Properties	Examples
Electrically Small	Very low directivity Low input resistance High input reactance Low radiation efficiency	Short dipole Small loop
Resonant	Low to moderate gain Real input impedance Narrow bandwidth	Half-wave dipole Microstrip patch
Broadband	Low to moderate gain Constant gain with frequency Real input impedance Wide bandwidth	Spiral LPDA
Aperture	High gain Gain increases with frequency Moderate bandwidth	Horns Reflectors

Antennas can also be divided by geometric continuity. Much as signals are either analog or digital, antennas are either continuous or discrete. Of course, discrete antennas are referred to as array antennas and are a collection of continuous antennas interconnected by a feed network. The feed network can be as simple as transmission lines of fixed lengths connecting each element through a combiner or can include active devices such as controllable phase shifters and amplifiers. A fully distributed feed network with signal control at each element provides the most flexibility. Fueled by military phased array applications, there were many advances in transmit/receive (T/R) modules for use in fully (or partially) distributed arrays, including MMIC devices. It was expected that these developments would stimulate widespread deployment of arrays outside the defense community. However, this has not happened due to cost issues. Today, the costs of conventional phased arrays are limited by phased shifter or T/R module costs. Affordable phased arrays are emerging, but in a new way – using digital beam-forming (DBF) techniques.

Commercial applications within recent years have provided both economic opportunity as well as technical challenges to the antenna world. This includes all possible antenna platforms from spacecraft to vehicles to personal. This is driven

by the demand for go-anywhere communications that wireline communications cannot provide. Included at the user level is maritime, land mobile, and personal communications. The user wants connectivity regardless of his/her location. Thus, the key to wireless communications is coverage. This, in turn, requires adequate signal power, which depends greatly upon antenna efficiency and gain at the user terminals and base stations.

3. The Future

The next century will certainly be one of active research, development, and production of antennas for government and industry. Although world tension has eased significantly since the early part of this century, military organizations continue to have need for communications and sensing. While the expansion of weapons systems has slowed, intelligence gathering and trafficking of data for military purposes has not. Much of this is in the RF portion of the spectrum and places new demands on antennas.

At the same time, commercial applications in communications, sensing, position location, messaging, etc. continue to challenge the antenna designer. Advances in technologies associated with signal processing, RF components, and batteries will stimulate more innovative applications in wireless that will, in turn, require new antennas. The three areas where activity in research and operational systems will certainly occur in the next century are listed in Table 2. These areas are discussed further in this section.

3.1 Size-Reduced Antennas

One of the biggest demands in the commercial world is for size-reduced antennas for personal communications. Technological advances in electronics have lead to a continual decrease in the overall size of radios such as handheld wireless telephones. The expectation is that antenna sizes will continue to reduce as well. However, fundamental physics limitations prevent significant reduction of the size of antennas as devices. Progress is limited because in many applications bandwidths on the order of 10% are required to cover allocated frequency bands and size reduction is obtained at the expense of bandwidth. The antenna engineer's challenges are made more difficult by comparisons to other technological advances. In the computer field, for example, the performance of memory chips has doubled in a time interval of 18 to 24 months since the 1960s (Moore's Law). Thus, expectations are often imposed on engineers to make dramatic reductions in antenna volume. However, continuous and significant size reduction of antennas is not possible using conventional approaches.

Table 2
Areas of Antenna Activity in the Future

- Size-Reduced Antennas
 - Device innovations
 - Integrated designs
 - Ground plane or portions of the antenna shared with other portions of the system
- Materials
 - Dielectric material loading
 - Magnetic material loading
 - Superconducting
- Smart Antennas
 - Base Station
 - Handheld
- Multifunctional Antennas
 - Handheld antennas
 - Voice, data, position location applications
 - Wideband multifunctional arrays for various platforms

The key to achieving additional progress is to view the antenna not as separate device, but as integrated into the system. The antenna of tomorrow must be designed along with the entire communications unit. For example, a physically small handheld radio can have an effective antenna only if the entire layout of the radio is considered in the design phase. It is no longer acceptable to merely reduce the specified antenna volume and let the antenna engineer worry about finding an antenna that fits in the volume. An electrically small antenna leads to currents being driven out onto the radio, which dramatically affects performance. Thus, the entire radio must be considered in the antenna design. In addition, surrounding environmental conditions must be examined as well. For instance, the human operator greatly influences the operation of handheld radio antennas.

Proper design and evaluation of size-reduced antennas must include simulation of the entire system (such as a handheld radio with an operator present). Many techniques have been developed in the past few decades that permit such simulation. Even more advances will be made in the next century together with greater computing power to support numerical calculations.

At the same time there is room for progress in the size reduction of many conventional antennas. For example, the helix antenna is an extremely popular antenna, providing moderate gain and bandwidth along with circular polarization and low cost. Conventional helix design requires that the circumference of the helix be near a wavelength. However, by adding interior stubs to the turns, the physical size (both the diameter and length) can be reduced. This stub loaded helix antenna shown in Figure 1 operates very similar to a conventional helix, but occupies with only 25% of the volume. [4] Considerable research has been performed on this antenna under sponsorship of Astron Corp. One prototype stub loaded helix antenna designed for operation at 3.6 GHz is shown in Table 3 compared to a conventional helix antenna. The measured pattern of the stub loaded helix shown in Fig. 2 is that normally obtained from a conventional helix. The gain as a function of frequency is plotted in Fig. 3. Some performance compromise occurs in bandwidth, usually being limited by polarization performance. However, the bandwidth for most applications is 20% or greater, which is usually more than adequate. The volume is only 25% that of a conventional helix, making the stub loaded helix an ideal choice at VHF and UHF frequencies.

Another area of investigation will be that of material loading for size reduction. Dielectric, magnetic, or both dielectric and magnetic materials can be used in the antenna structure to lower the operating frequency. The challenge is to do this without unacceptable penalties in bandwidth and efficiency. New low loss materials will be an area of active research. Superconducting materials may also find acceptance in some aspects of antenna implementation.

3.2 Smart Antennas

In order to provide adequate coverage and capacity in communication systems, it is often necessary to include intelligence in the antenna system. Most such work has been performed with base stations during reception to overcome the low power of the uplink from the user. A smart base station in its simplest form is a switched beam array. The array is fed with a beam-forming network such as a Butler matrix, forming separate beams that cover portions of angular space. For example, a 90° sector can be covered with four 22.5° beams as shown

in Fig. 4. Computing power is used to process the received signals and to decide how to assign users to beams; typically, the beam with the strongest received signal for a given channel is selected.

Table 3

Example of a Size-Reduced Antenna – The Stub Loaded Helix

	Stub Loaded Helix (Fig. 1)	Conventional Helix
Center frequency	3.6 GHz ($\lambda_c=8.3$ cm)	3.6 GHz
Number of turns, N	10	10
Diameter, D	1.9 cm ($0.23\lambda_c$)	2.6 cm ($0.32\lambda_c$)
Length, L	8.4 cm ($1\lambda_c$)	19.2 cm ($2.3\lambda_c$)
Pitch angle, α	8°	13°
Volume ($\pi D^2 L/4$)	23.8 cm ³	102 cm ³
Gain	13 dBi	13 dBi
Gain Bandwidth	25% (3.2-4.0 GHz)	>30%
Polarization bandwidth (3 dB)	20% (3.3-4.0 GHz)	>30%

Smart antennas can also employ adaptive algorithms. Generally, the two main purposes are to track the users with a beam and to place nulls on interferers. Adaptive antenna arrays have been used on military applications for quite sometime. In the next century, they will find their way into commercial systems in ways that are cost effective and yield robust performance.

Future uses for smart antennas will include transmit base stations and terminals. Especially challenging is the handheld radio in the presence of severe multipath and blockage of the line of sight path by objects. Although there is very little space on a handheld radio, it turns out that considerable reliability improvement can be realized using spatial diversity with two separate antennas on

the radio. Processing can be simple switched diversity or adaptive beam steering and null steering. In addition to space diversity, polarization and pattern diversity are also very promising.

3.3 Multifunctional Antennas

With the increase in wireless services will come an increase in the number of functions for a single antenna. This will occur in all levels of systems, ranging from handheld radios to battleships. On the handheld level, multifunctional antennas are needed for multimode radios. Today dual mode radios are being manufactured for use with both satellite and terrestrial communications. Usually this is a single antenna structure with ports for, say, PCS terrestrial communications and for L-band Big LEO satellite communications. In the future, more functions will be incorporated such as position location (e.g. GPS).

Many platforms are so loaded with antennas that performance is greatly degraded due to mutual coupling with other antennas. Military ships and planes are the most prominent examples. However, with broad expansion by regulatory agencies in the available frequency bands, there will be many applications for multiple frequency band operation in a single terminal. Multiband antennas often cannot be realized with aperture antennas such as reflectors. In addition, reflectors are rather deep structures that are readily visible and are heavy. Arrays offer a low profile solution. Arrays also can be phase scanned, avoiding the mechanical scanning of an aperture antenna.

Wideband arrays, however, present design challenges. For conventional fixed grid arrays, the electrical spacing between the elements changes with frequency, which strongly influences array performance. For example, suppose a $0.4\lambda_L$ element spacing is used at low end of the operating frequency range f_L ; $\lambda_L = c/f_L$. For an octave of bandwidth, the electrical element spacing will be $0.8\lambda_U$ at the upper end of the frequency band, f_U . Spacings this large limit the phase scanning ability of the array because wide spacings introduce grating lobes during scan. For wider bandwidths, the problem is worse and the array may be useless. Thus, innovation solutions are needed and will be investigated in the next century. New array architectures are needed. An example of a dual-band, dual-polarized planar array is shown in Fig. 5. Two sizes of elements (represented as bow-ties in the figure) are used, the large ones are used for the low frequency band and the smaller ones for the high frequency band. Interweaving them permits sharing of the same aperture for the two bands. Each element location has separate crossed bow-ties for full polarization capability or polarization diversity. Array designs that reduce part count, and thus cost and weight, will be of prime importance. In

addition to array architectures, element design and feed networks must be found. In particular, low cost components, including phase shifters, must be found.

4. Conclusions

This century has seen most of the electromagnetic spectrum used for many applications. The next century will see more of the spectrum utilized. Essential to full and efficient use of the RF spectrum are high performance, affordable antennas. New applications for wireless will emerge. New antenna designs, of course, will be required to support them. Some of the major antenna areas that are certain to be active in the next century were outlined in Section 3 and Table 2.

Of course, there are many associated technical areas that will grow synergistically with antenna technology. The most prominent one is numerical techniques. Evaluation of integrated systems and complex material environments require extensive computational power.

5. References

- [1] W.L. Stutzman and C.B. Dietrich, Jr., "Moving beyond wireless voice systems," *Scientific American*, vol. 278, pp.92-93, April 1998.
- [2] Warren L. Stutzman and Carl Dietrich, "Wireless Monitoring and Position Location," *Advancing Microelectronics*, vol. 25, pp. 29-32, June 1998.
- [3] W.L. Stutzman and G.A. Thiele, *Antenna Theory and Design*, second edition, pp 10-11, New York: John Wiley, 1998.
- [4] R.M. Barts and W.L. Stutzman, "A Reduced Size Helical Antenna", *IEEE Ant. & Prop. Soc. Symp.* (Montreal), pp. 1588-1591, July 1997

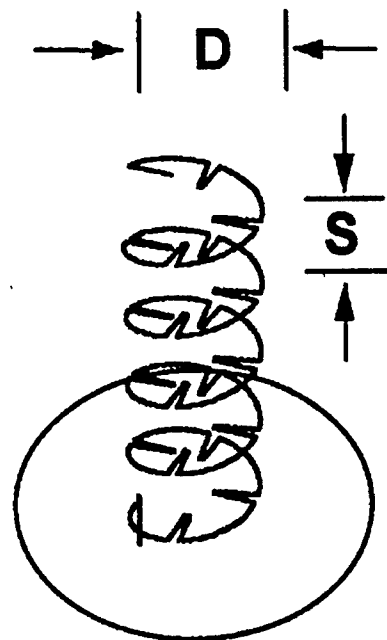


Figure 1 The stub loaded helix antenna as an illustration of a size-reduced antenna. It performs similar to a conventional helix antenna, but with a 75% volume reduction.

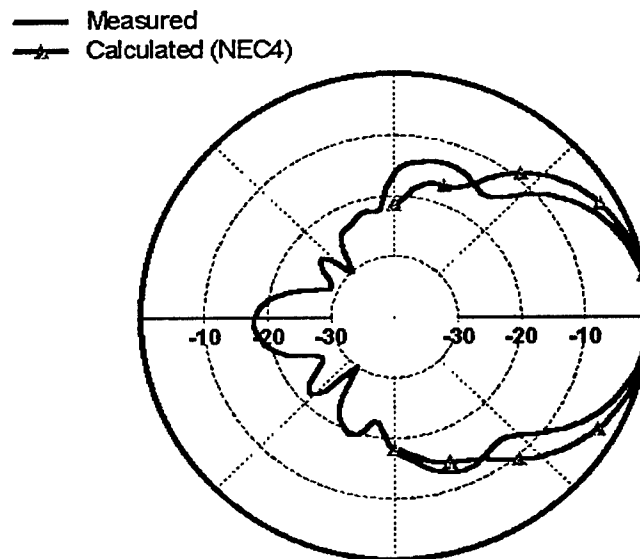


Figure 2 Measured and computed patterns for a 10-turn stub loaded helix antenna.

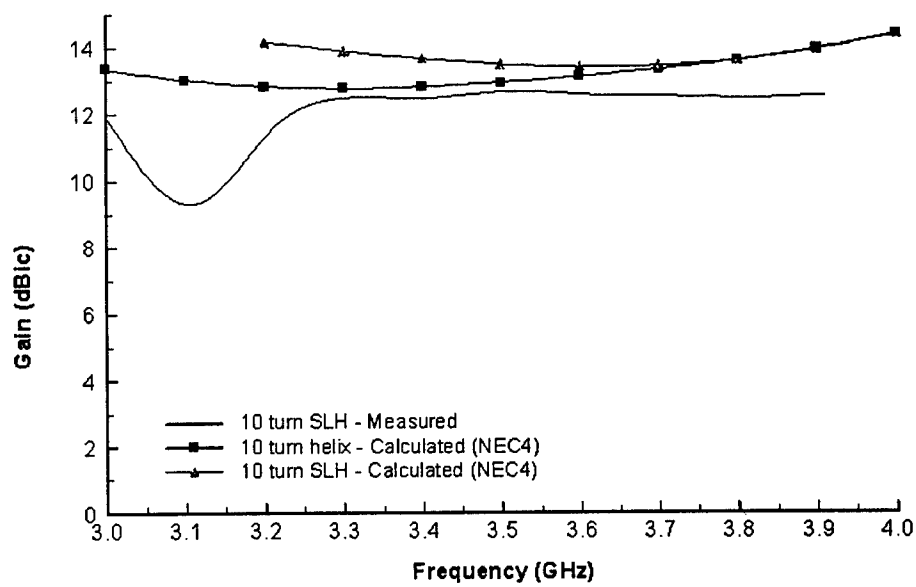


Figure 3 Measured and computed gain for a 20 turn stub loaded helix antenna of Figure 1 compared to a conventional 10-turn helix antenna.

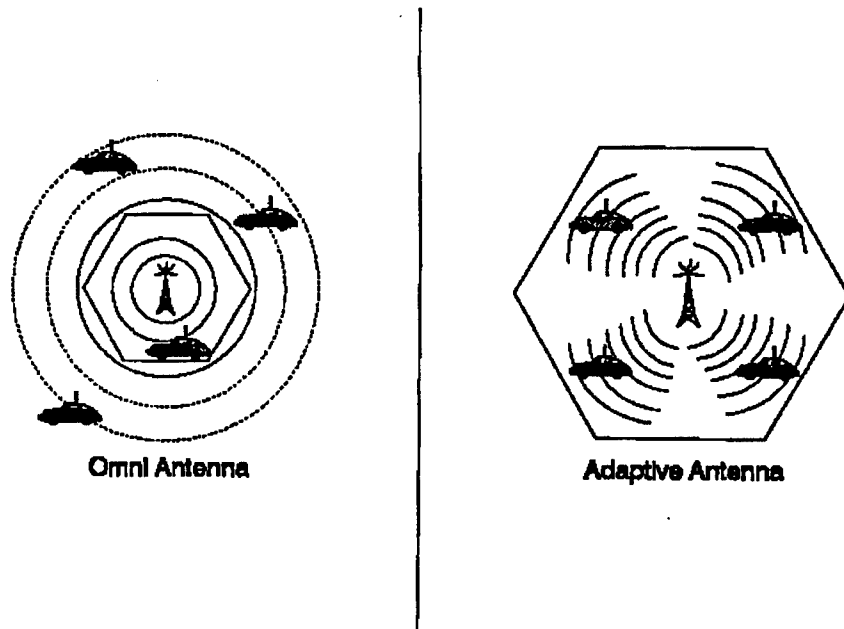


Figure 4 Illustration of smart antenna coverage compared to omnidirectional antenna coverage.

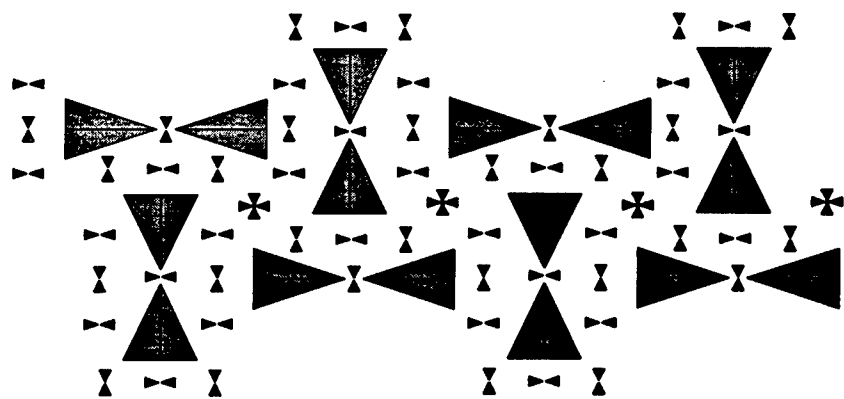


Figure 5 Illustration of a dual-band, dual-polarized array antenna for use as a multifunctional antenna.

CONCEALED AM/FM ANTENNA ON THE REAR SIDE GLASS OF A MINI-VAN

Andrew Adrian
Visteon Automotive Systems

Abstract

Automotive antenna applications are quickly becoming more and more concealed. Typical for many years was the use of a quarter wave mast (tuned for VHF FM broadcasts), vertically mounted on the sheet metal of a vehicle. This antenna topology also did double duty on Medium and Long Wave AM broadcasts. Fixed mast antennas are seen as a detraction from the vehicle styling design as well as a nuisance due to wind noise and damage during car washing. Attempts have been made to provide retractable (electric or manual) antenna masts so as not to be visible when not in use, however reliability, durability, and user satisfaction with these type of products have been poor. Due to the above drivers, there has been a resurgence in the use of concealed automotive antennas for reception of broadcast radio in the last four years. Typically, these antennas have been located on the vehicle glass. In recent history, concealed antennas have employed some sort of electronic module (passive and/or active) remotely packaged from the radio to achieve the level of reception performance required in today's automotive radio market place. Here a mini-van antenna system that does not require a remotely located electronic antenna module and has a receiving element screened on the rear side glass of the vehicle is described.

1.0 DESIGN REQUIREMENTS

The antenna, radio, and the rest of the vehicle in any reception system must perform in concert with each other to provide reception performance for the vehicle occupant(s) that is as good as a reception system using an external fixed or

retractable mast. Additionally, as a vehicle reception system gets redesigned it must perform as good or better than its predecessor and its best competition in the same vehicle class. These are the basic and unbreakable ground rules for success in the mobile radio reception marketplace.

These basic requirements were applied to the design of a concealed antenna system for a mini-van such as the typical vehicles illustrated in Figure 1. A similar design can also be applied to sport utility vehicles (Figure 2.)

2.0 FIXED MAST SYSTEM TOPOLOGY

Typical fixed mast systems consist of an Antenna Mast Assembly that screws into an Antenna Base Mounting. This is the monopole portion of the system. The Antenna Base Mounting mounts to the vehicle fender or cowl. Its function is to mechanically support and align the Antenna Mast Assembly as well as provide a means of grounding the antenna system to the vehicle sheet metal. A Coaxial Cable Assembly (or Assemblies) connects the Antenna Base Mounting to the Receiver. Figure 3. captures the components of this architecture. This system receives desired broadcast signals as well as undesired radiated and conducted electrical emissions from the vehicle.



(a)

(b)



(c)

(d)

Figure 1. Typical Mini-Vans. (a) Ford Winstar, (b) Mercury Villager, (c) Dodge Caravan, and the (d) Chevrolet Astrovan.



(a)

(b)



(c)

Figure 2. Typical Sport Utility Vehicles. (a) Ford Explorer, (b) Dodge Grand Cherokee (c) Chevrolet Blazer.

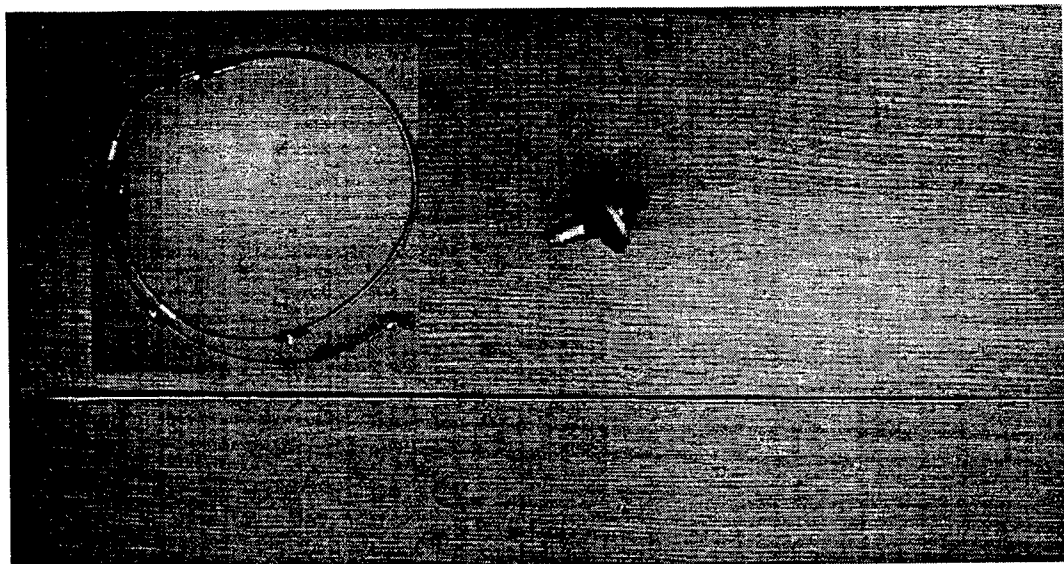


Figure 3. Fixed Mast Reception System.

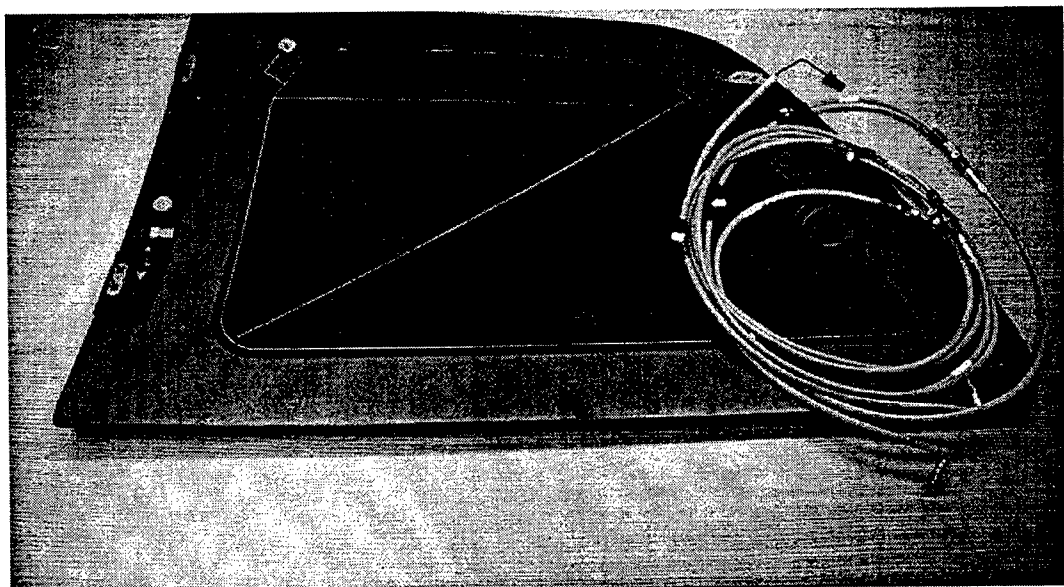


Figure 4. Concealed Antenna Reception System.

3.0 CONCEALED ANTENNA SYSTEM TOPOLOGY

The Rear Side Glass System that is described herein utilizes a conducted screen print on the quarter glass as the AM/FM antenna element. The conductive screen print involves the same technology that is utilized to produce electric defrosters on rear windows. A Coaxial Cable Assembly (or Assemblies) that is grounded to the vehicle sheet metal at the antenna element feed conducts the radio frequency signal to the Receiver. As a result, all of the system components are located interior to the vehicle, greatly enhancing long term durability and reliability. These items are pictured in Figure 4. As with the fixed mast system, the concealed system also receives desired broadcast signals as well as undesired radiated and conducted electrical emissions from the vehicle. However the overall noise level of the concealed system, in this case, is typically lower than that of the fixed mast system due to its location in the vehicle. This allows for additional degrees of freedom in the system design.

4.0 CONCEALED ANTENNA SYSTEM RECEIVING ELEMENT

Figure 5. depicts the antenna element design. It is fed near the forward upper corner of the window opening. The element is tuned for maximum FM reception capability. Effort is also made to maximize area over the window opening which the antenna element occupies to maximize received AM signal strength without

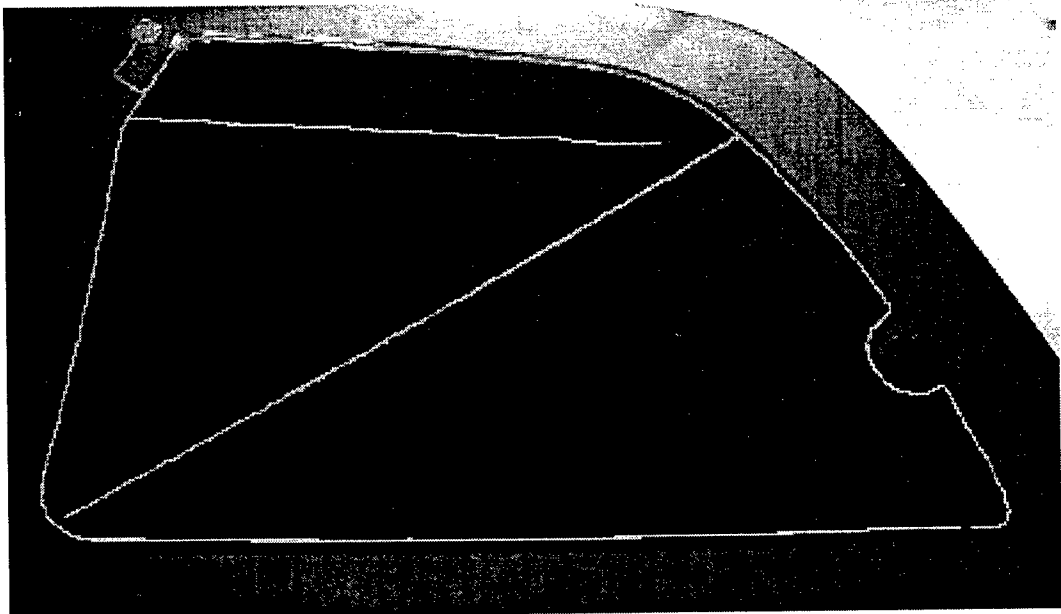


Figure 5. Concealed Antenna System Receiving Element.

compromising FM performance. In order to additionally maximize AM response, distributed parallel capacitance to the vehicle sheet metal is minimized.

The coaxial cable that feeds the antenna has its shield grounded to the vehicle sheet metal next to the feed point of the antenna element. Shielding of the coaxial cable ends at the vehicle sheet metal while the center conductor is extended to the antenna feed point. The length of the unshielded center conductor is kept to a minimum in order to control its placement and repeatability of the antenna element performance for high volume production.

5.0 SYSTEM PERFORMANCE PARAMETERS AND ISSUES

In order to meet the reception requirements, the gain of the concealed system needs to match the gain of the fixed mast system so that such items as seek/stop performance are consistent from old model to new model. The sensitivity of the concealed antenna reception system also needs to equal or outperform the that of the fixed mast antenna reception system.

As a result, the major parameter that needs to be examined is gain (into the receiver load) for both AM and FM. However this is not the only parameter that is examined. FM Band gain of the concealed antenna element subsystem (antenna on glass with coaxial cable) as compared to the fixed mast system gain is illustrated in Figure 6. As you can see for comparable polarizations, it in itself is deficient compared to the fixed mast. However, this architecture has two significant items going for it. First, FM Broadcast Band receivers have become good enough that the system is atmospheric noise limited. Second, the vehicle noise floor further limits performance.

Nothing can be done about the first item, however, it serves as a reminder that there is excess gain and signal available with the fixed mast antenna reception system. Consequently, the level of element gain that is required to meet the

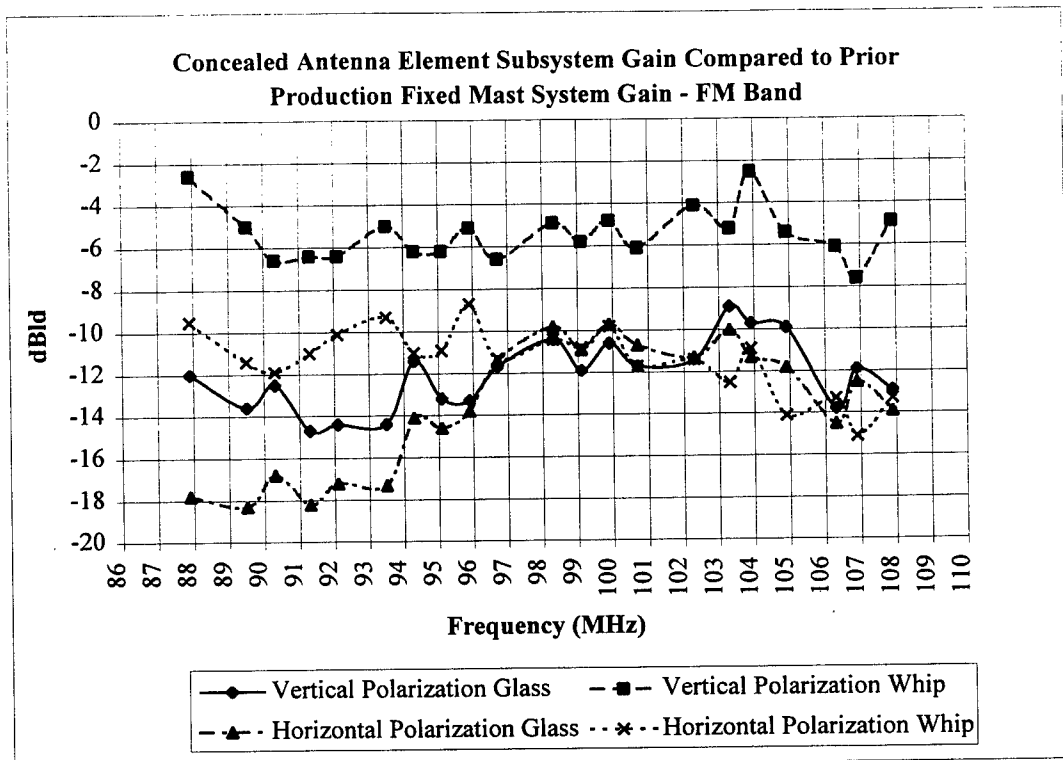


Figure 6. Concealed antenna element subsystem gain (dBd) versus frequency for the FM Band into a 108Ω load compared to the prior production fixed mast system.

requirements for reception performance is not as great as what the fixed mast system provides.

The vehicle noise floor can be affected and provides an advantage. Noise power at the location of the fixed mast antenna is typically greater than the noise power

at the concealed antenna element (quarter glass) primarily due to engine related emissions. It is also easier (less costly) to reduce the noise power at the concealed antenna element than it is to reduce it at the fixed mast. In other words, the noise temperature of the concealed antenna element is lower than the noise temperature of the fixed mast. The difference in noise power is great enough such that overcoming the difference in antenna system gain without giving up system sensitivity can be achieved by adding gain to the receiver front end. Once the receiver front end is modified, the effective gain of the antenna system improves by 5 dB as illustrated in Figure 7. This also establishes the same seek stop levels for the concealed system as exists in the fixed mast system for the same quality (signal-to-noise ratio) signal.

The final proof is in the evaluation of vehicle system fading performance at a point away from the transmitter. This involves comparative jury evaluations per customer usage profiles of the concealed antenna reception system to ensure that performance compared to the fixed mast reception system is equal or better on FM. Unfortunately, an objective test for FM weak signal reception is not available.

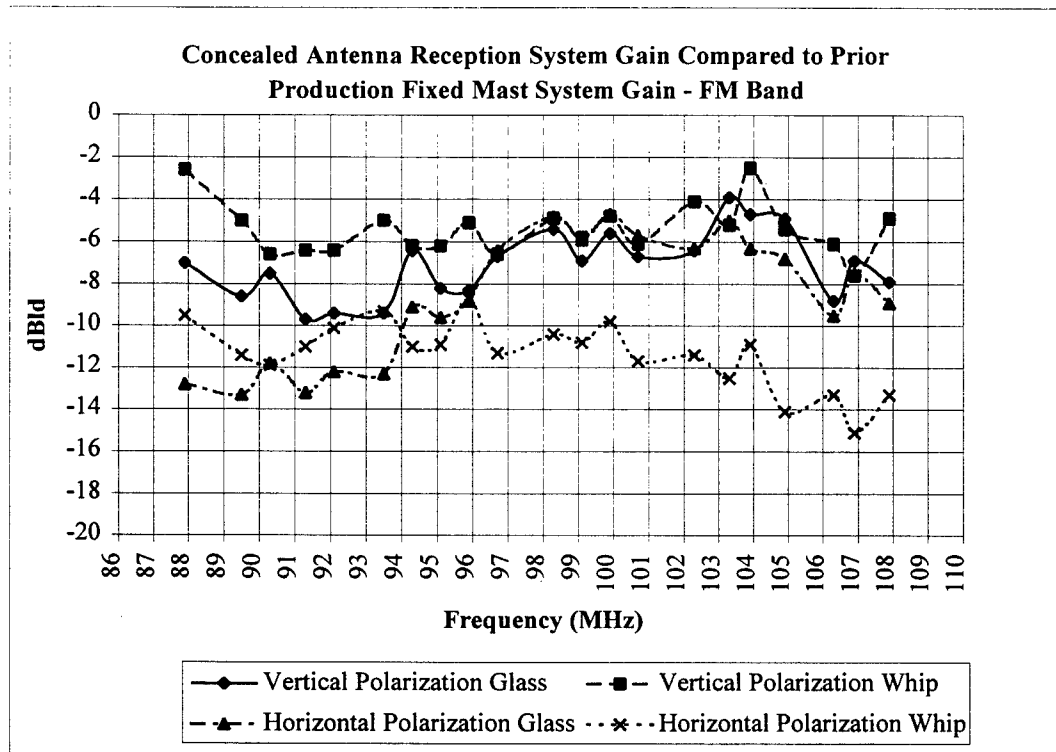


Figure 7. Concealed antenna reception system gain (dBd) versus frequency for the FM Band into a 108Ω load compared to the prior production fixed mast system.

The AM side of this system has similar issues. The terminal antenna factor of the concealed antenna element (without the antenna cables) is illustrated in Figure 8. When the same result at the end of the antenna cables where they are plugged into the receiver is compared to the antenna factor of a typical fixed whip, one can see that the concealed antenna system is deficient in the AM Band compared a fixed

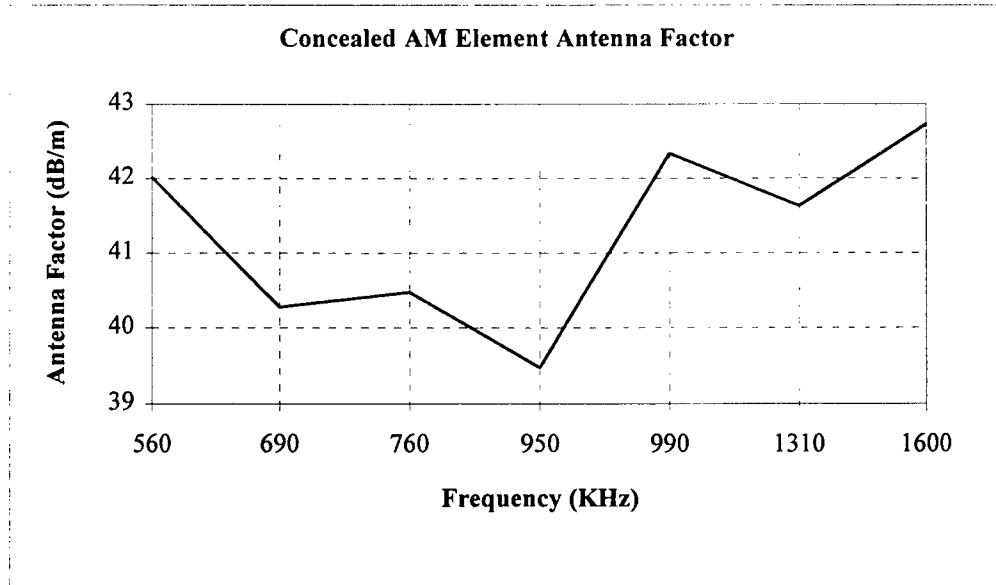


Figure 8. Concealed antenna element AM antenna factor (V/m/V). The measurement represents the antenna factor of the antenna element into a $1\text{M}\Omega$ load.

mast system (Figure 9.) This is due to the excessive parallel capacitance to sheet metal that the concealed antenna element exhibits, and the longer length of the concealed antenna system cable. This disparity can be overcome using one of two major methods. The antenna element can be matched with circuit elements at the glass (including active as well as passive components.) This has the advantage of significantly reducing the mismatch due to the cable by transforming the element impedance to a lower capacitance or perhaps even eliminating it all together if an active device is used to drive the coax. Of course with the use of active devices

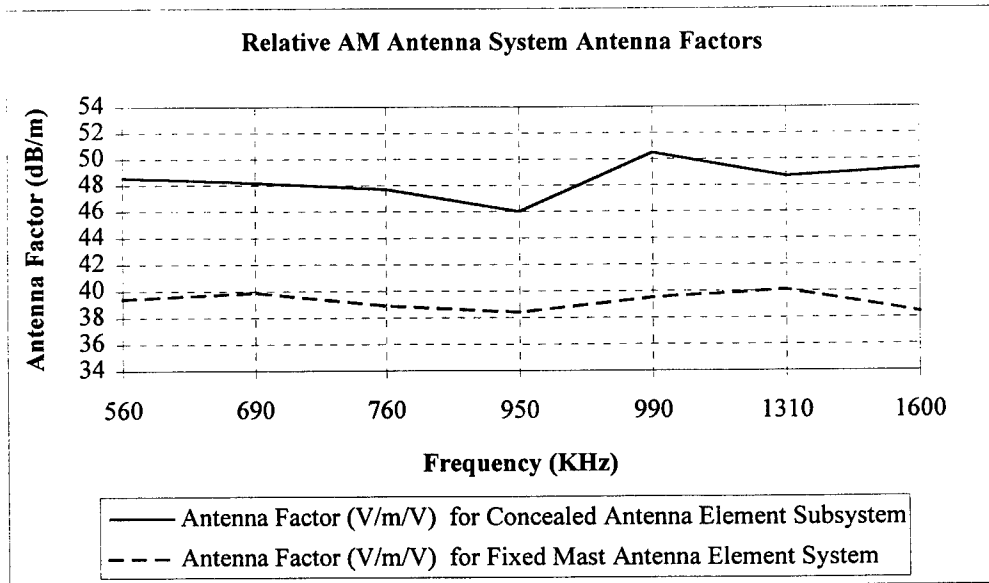


Figure 9. Relative AM Band antenna factors (V/m/V) of the concealed antenna system and a typical fixed mast antenna system into a $1\text{M}\Omega$ load.

one has to be careful of nonlinearities that could reduce the dynamic range of the entire reception system. Alternatively, as with the FM portion of the system, the noise floor can be reduced to improve the signal-to-noise performance of the system and gain can be added to the receiver in order to preserve the number and quality of the radio seek stops. By taking the second approach, the need for an additional electronic module is eliminated. This becomes possible because the AM sensitivity of any vehicle reception system is always limited by on board vehicle generated noise. By reducing the noise, an extra part in the antenna system is not needed. The result of this is illustrated in Figure 10. which depicts

the vehicle reception sensitivity of concealed and fixed mast antenna reception systems. Further confirmation is obtained in the evaluation of vehicle system fading performance at a point away from the transmitter. Again, this involves comparative jury evaluations per customer usage profiles of the concealed antenna reception system to ensure that performance compared to the fixed mast reception system is equal or better on AM as well as FM.

6.0 CONCLUSION

The architecture of a concealed, moduleless AM/FM broadcast reception system for a mini-van has been presented. System trade offs and issues were reviewed and a best value system has been architected.

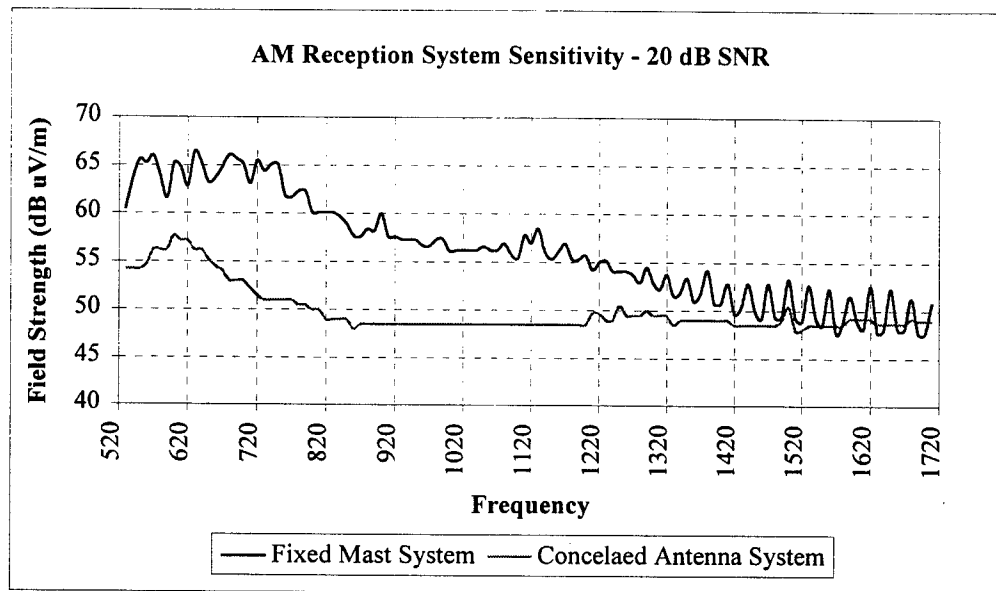


Figure 10. AM band vehicle sensitivity of the concealed and fixed mast reception systems.

The author would like to acknowledge Dennis R. Mullins for his technical contributions and Joseph M. Huk for the high quality photographs that he took in support of this paper and presentation.

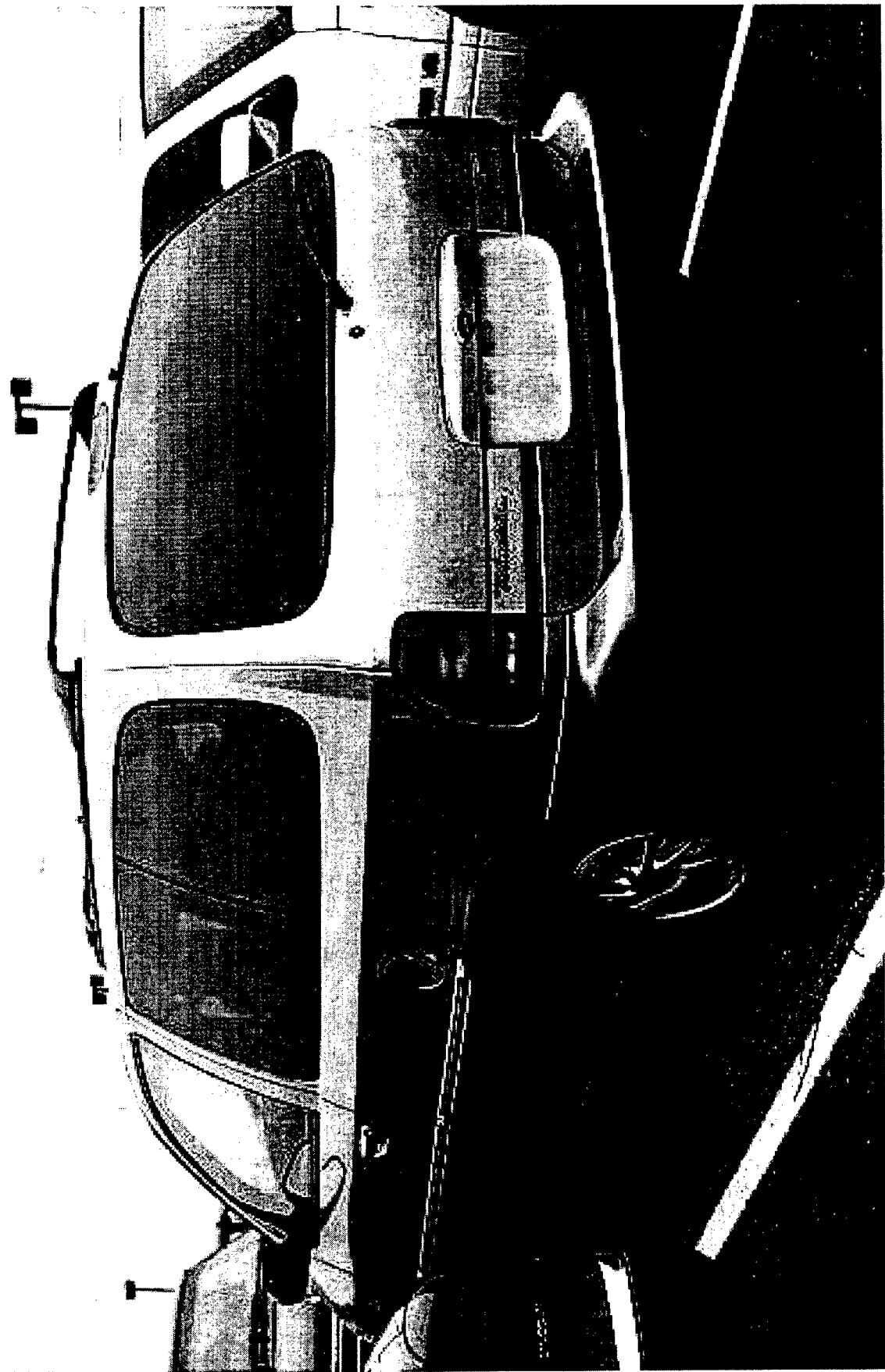


Figure 1a.



Figure 1b.

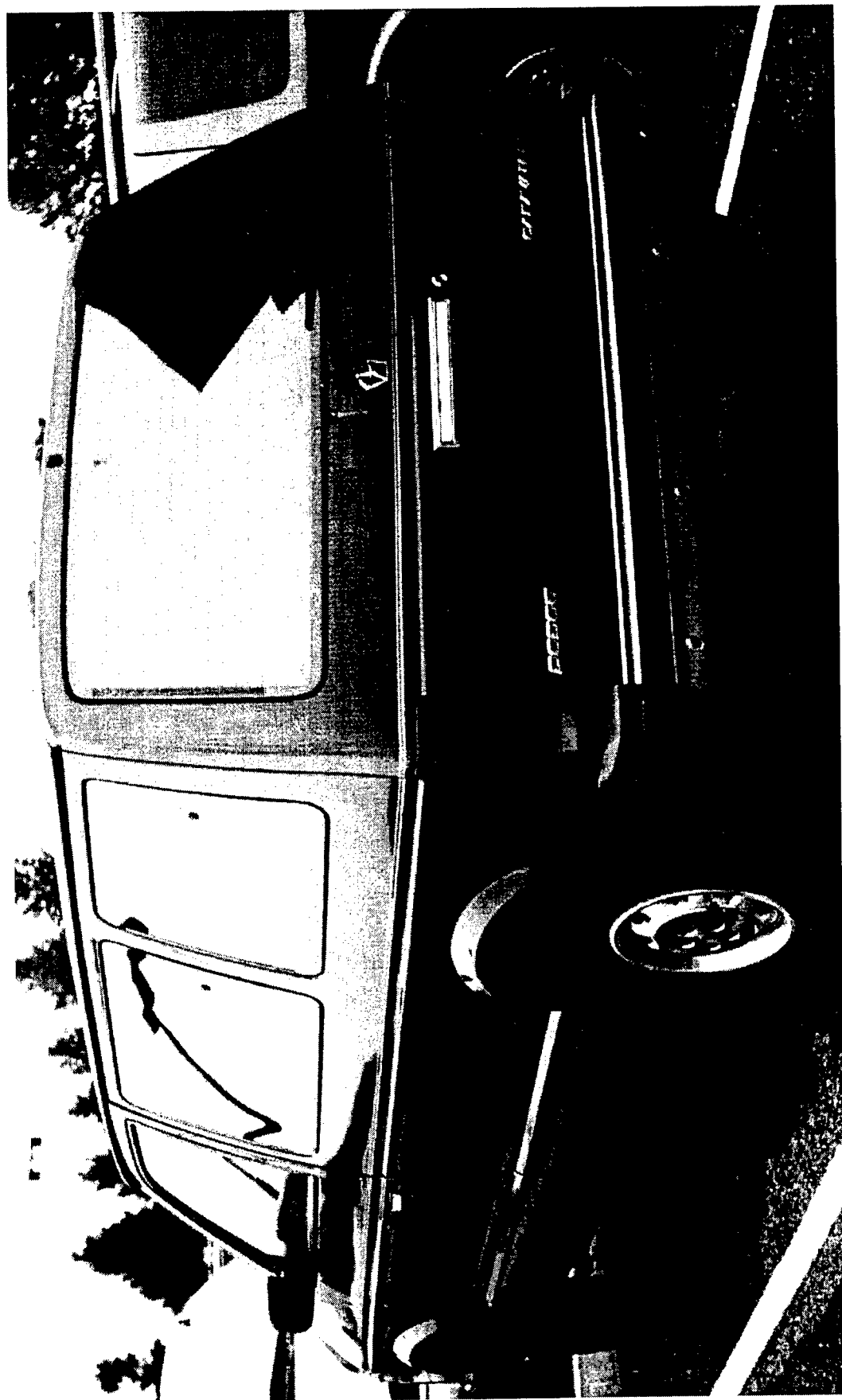


Figure 1c.

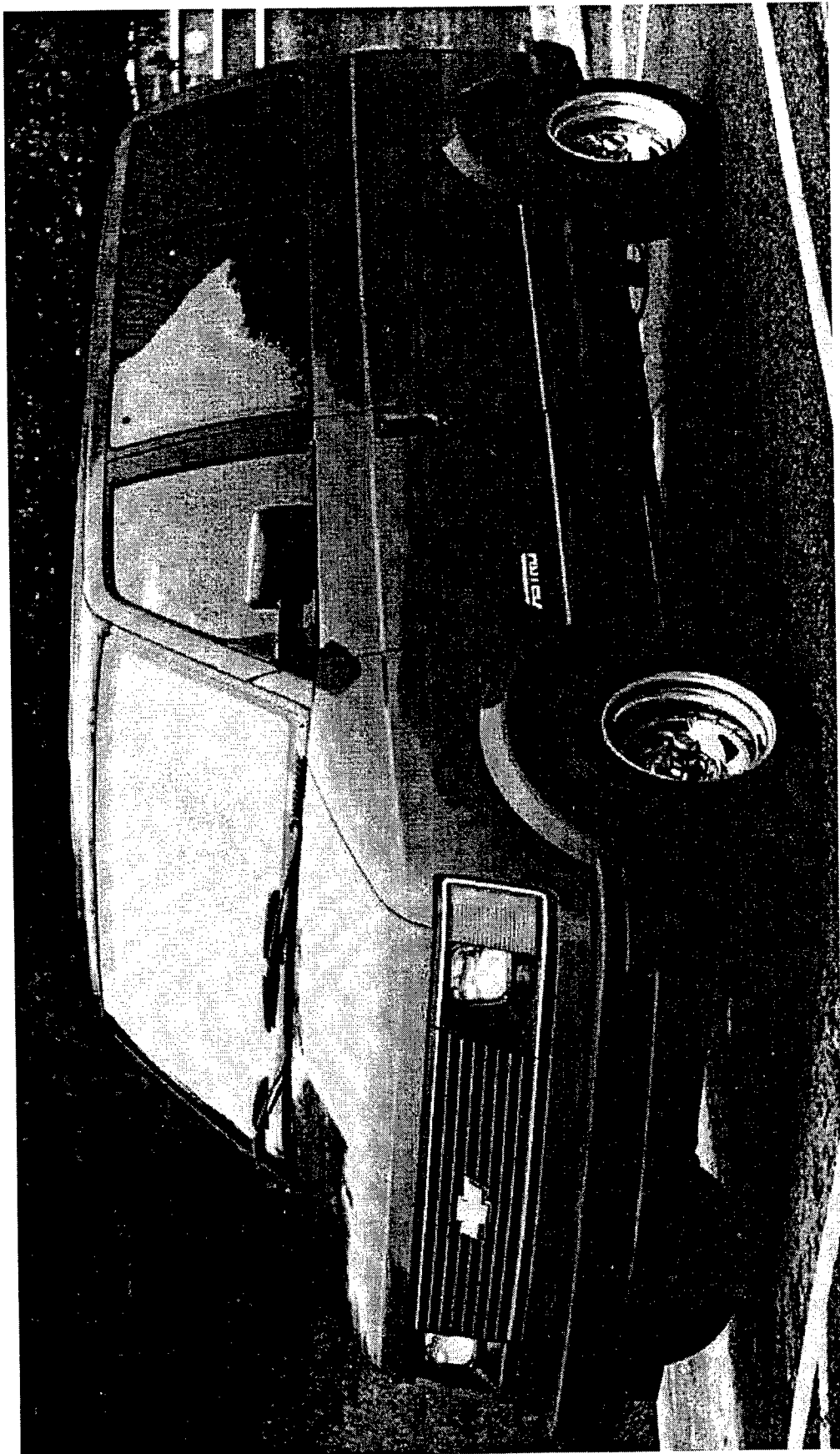


Figure 1d.

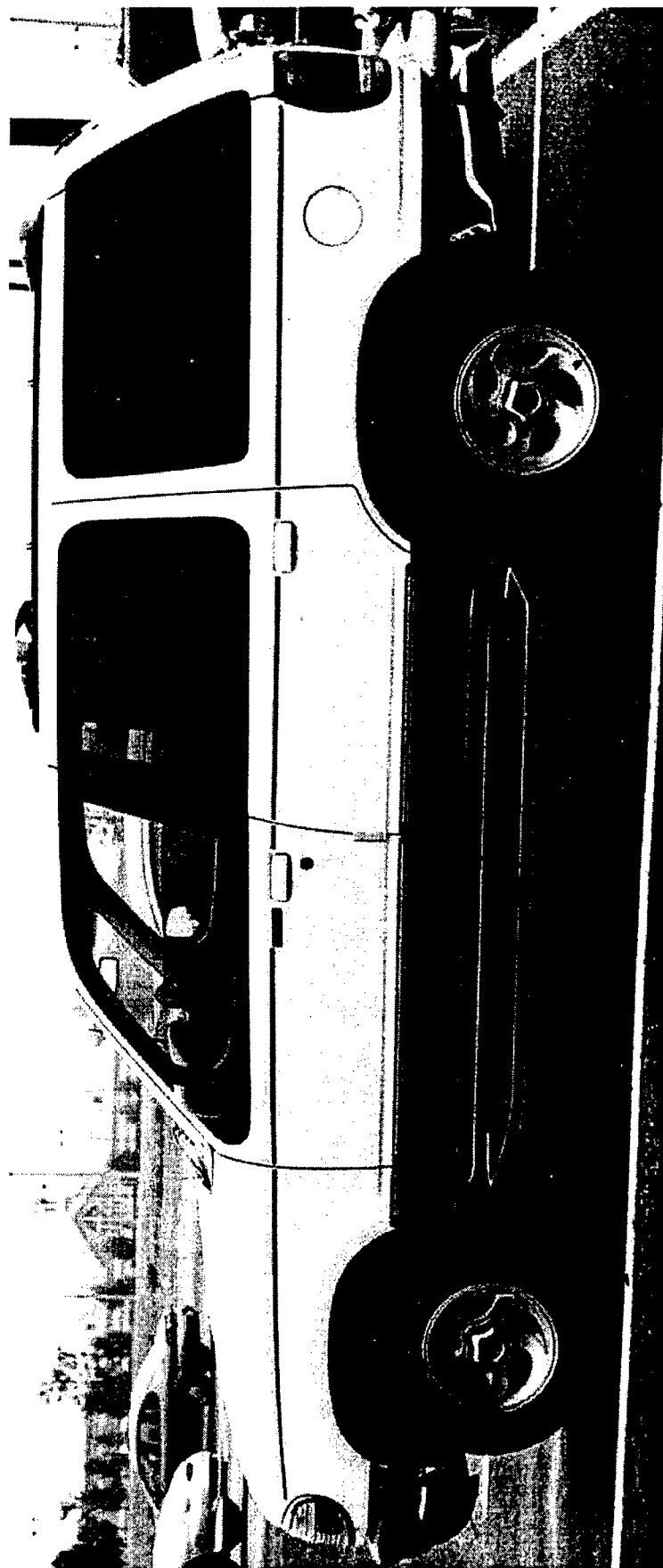


Figure 2a.

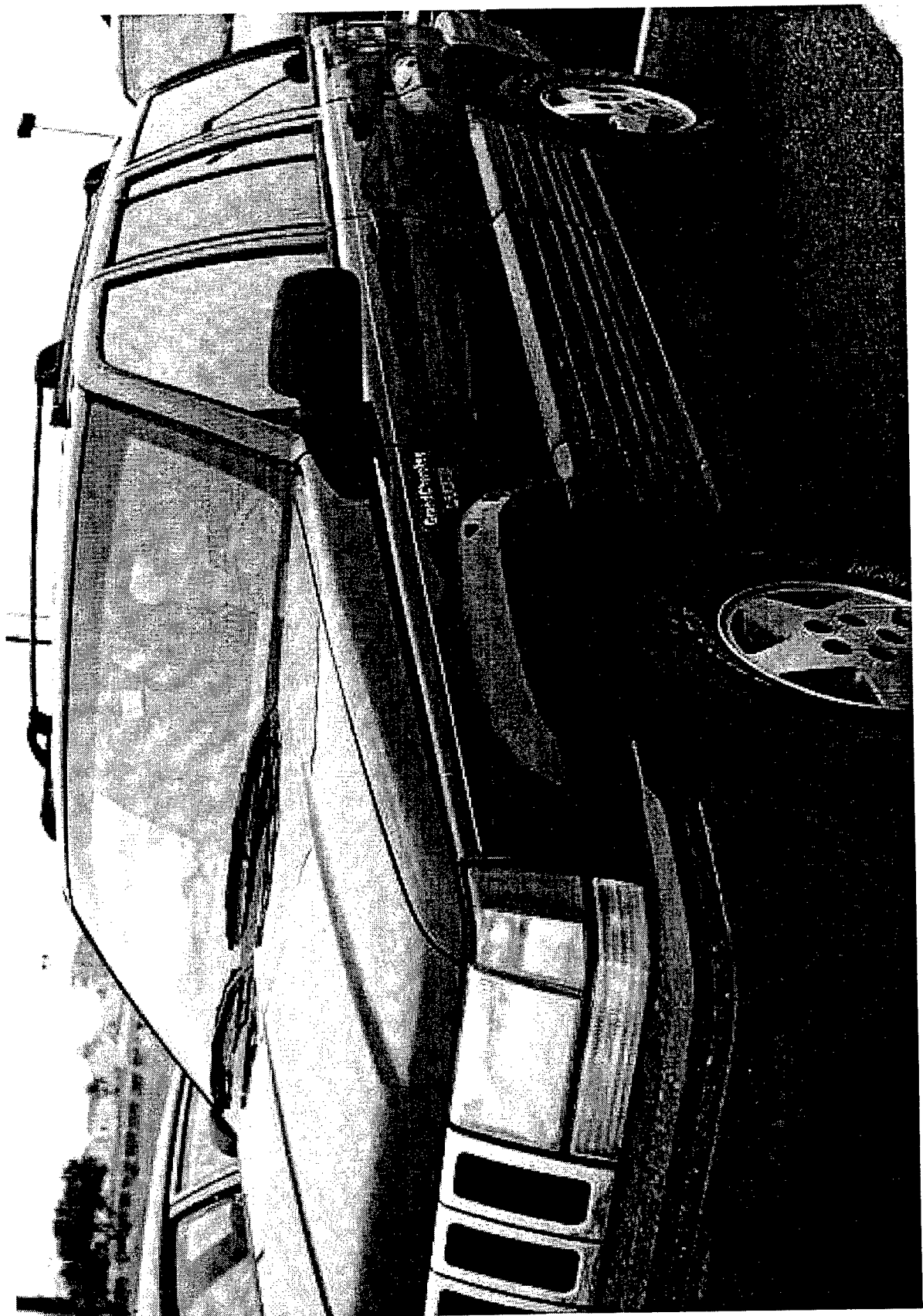


Figure 2b.

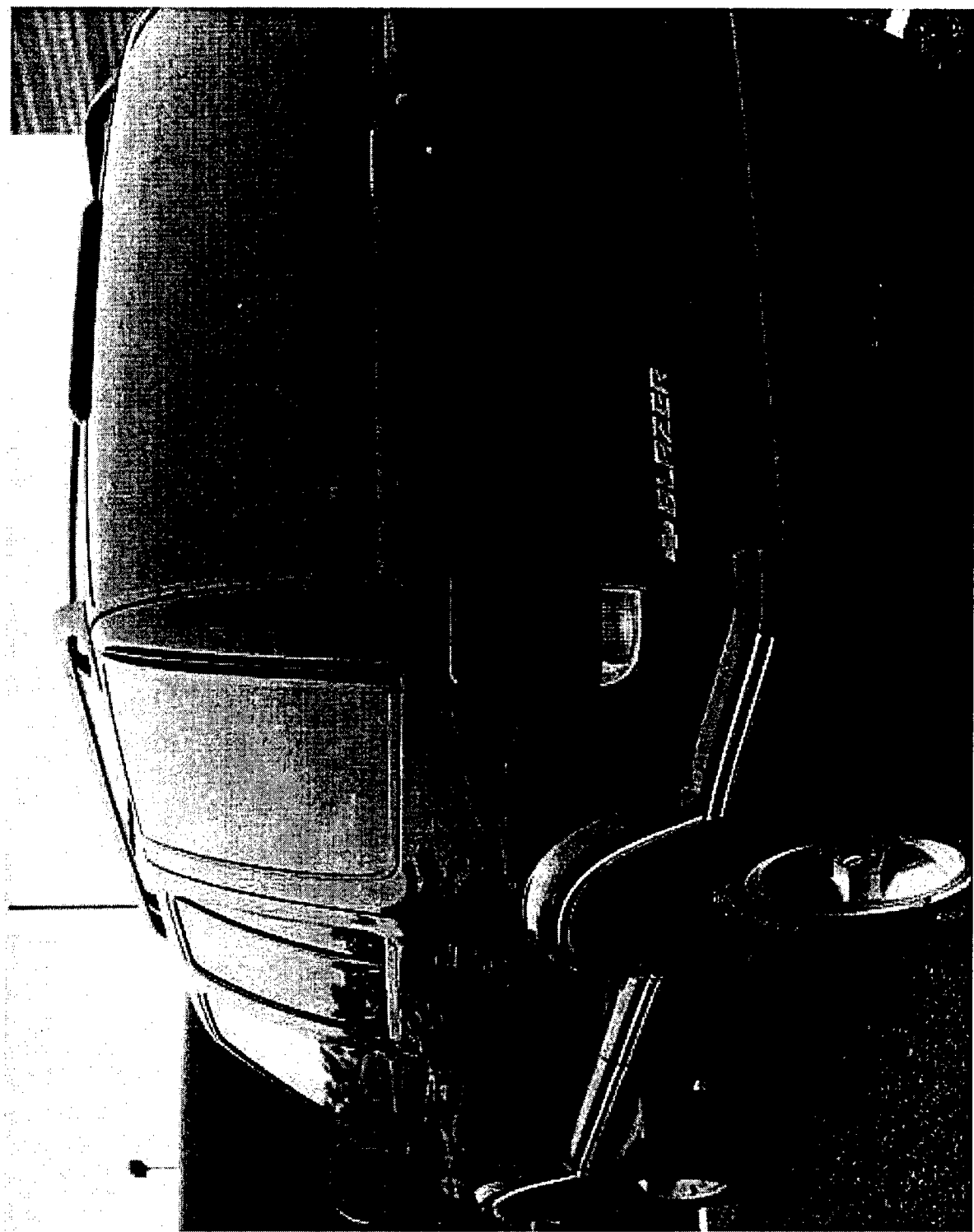


Figure 2c.

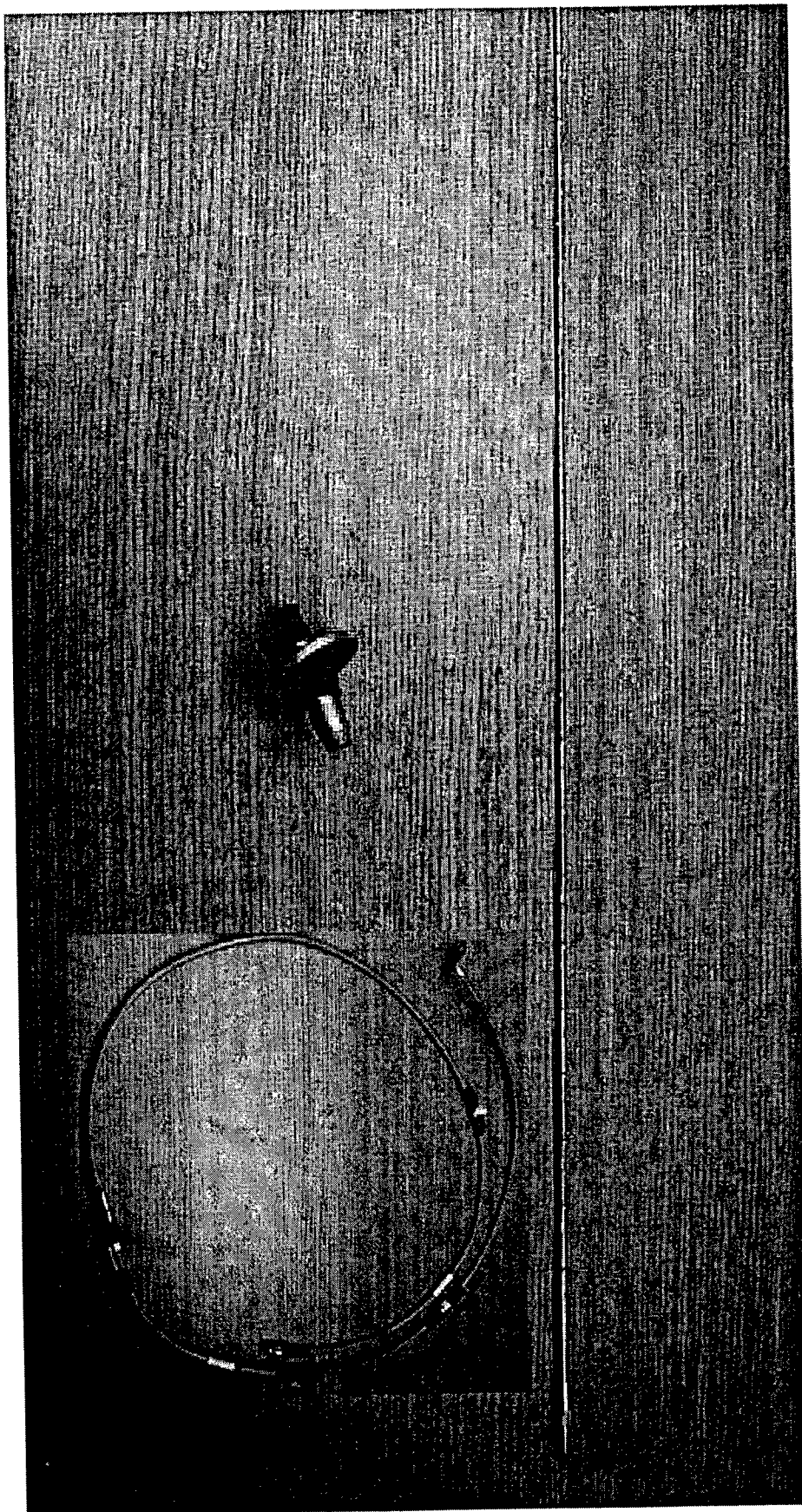


Figure 3.

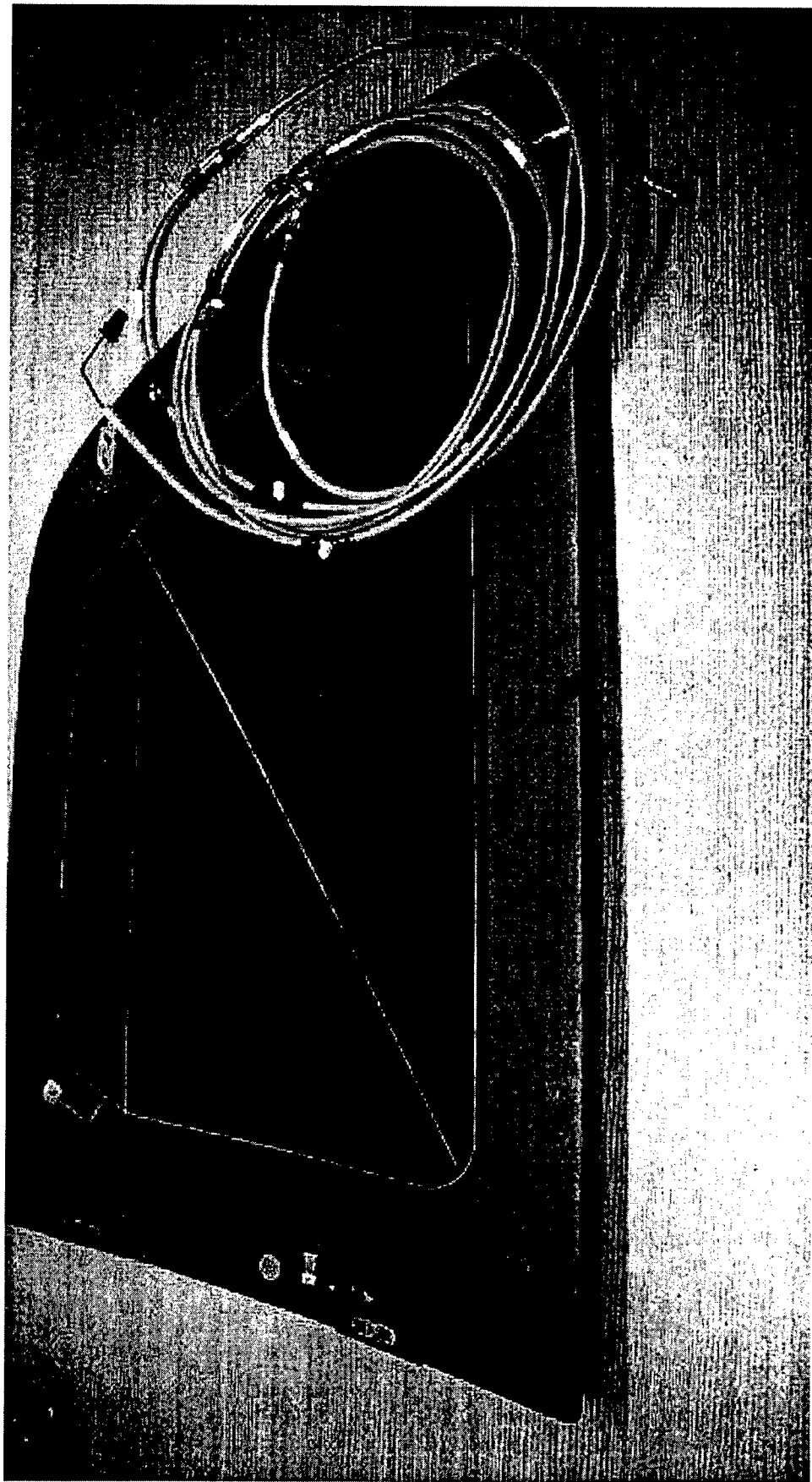


Figure 4.

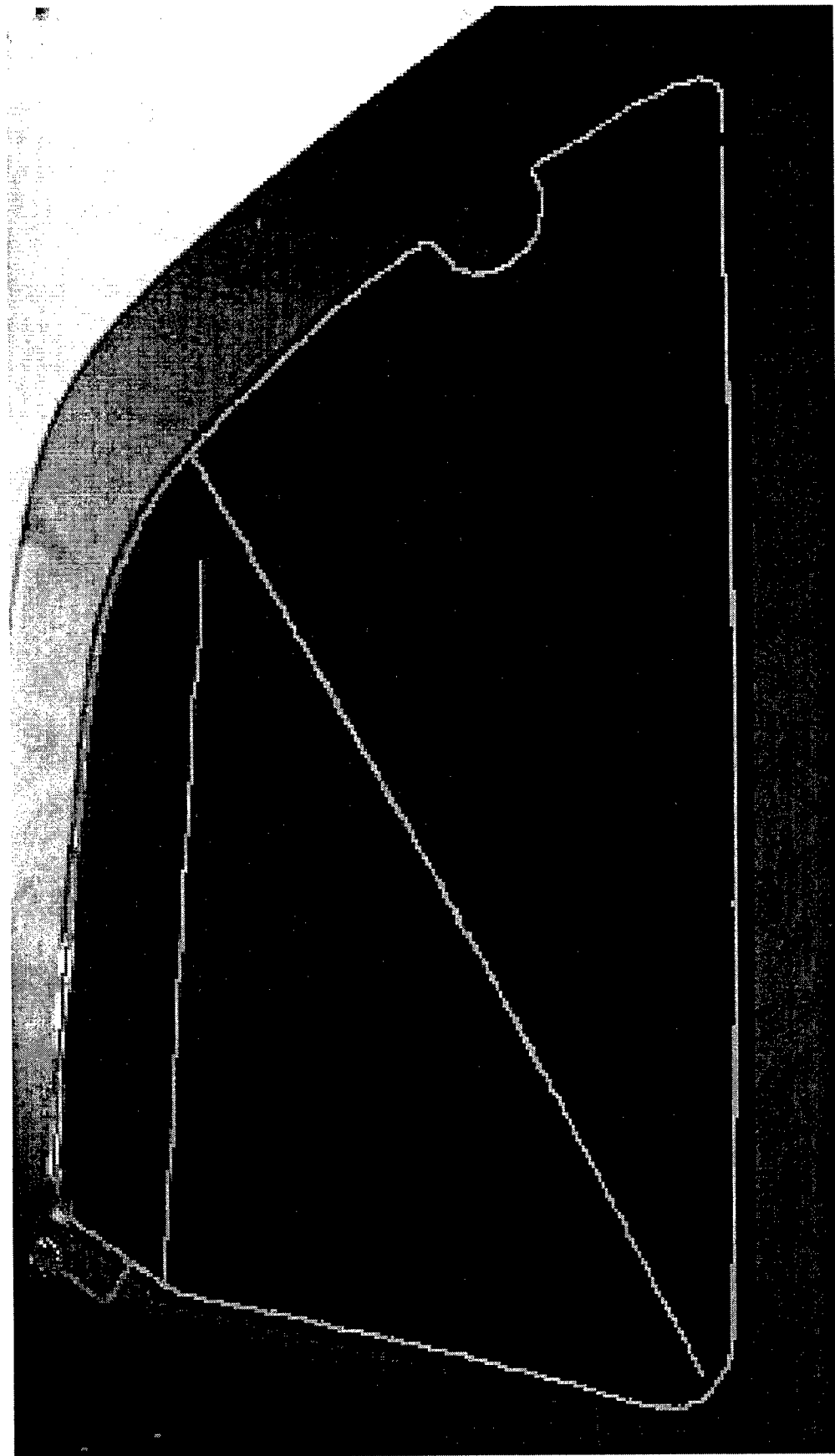


Figure 5.

**Concealed Antenna Element Subsystem Gain Compared to Prior
Production Fixed Mast System Gain - FM Band**

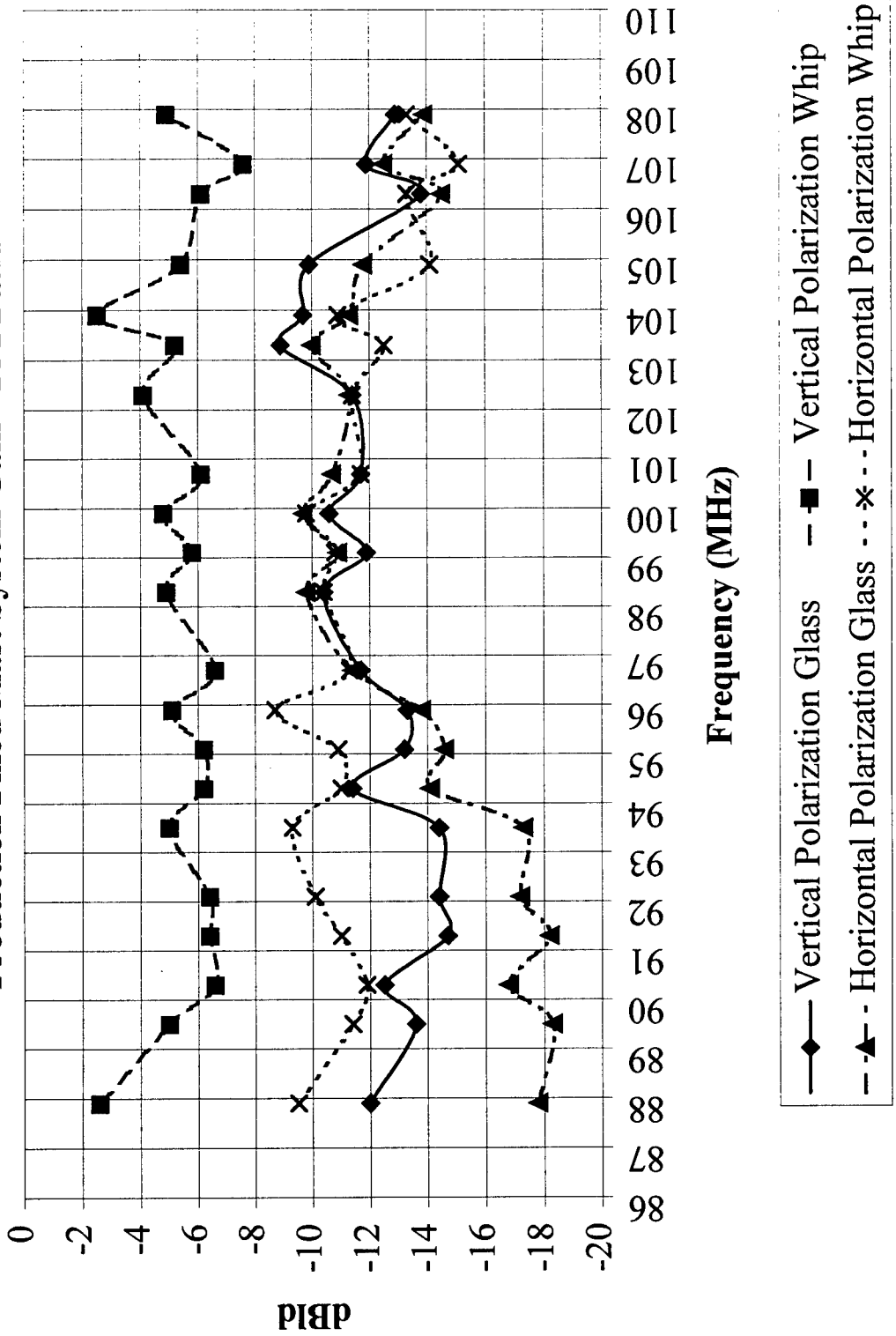


Figure 6.

**Concealed Antenna Reception System Gain Compared to Prior
Production Fixed Mast System Gain - FM Band**

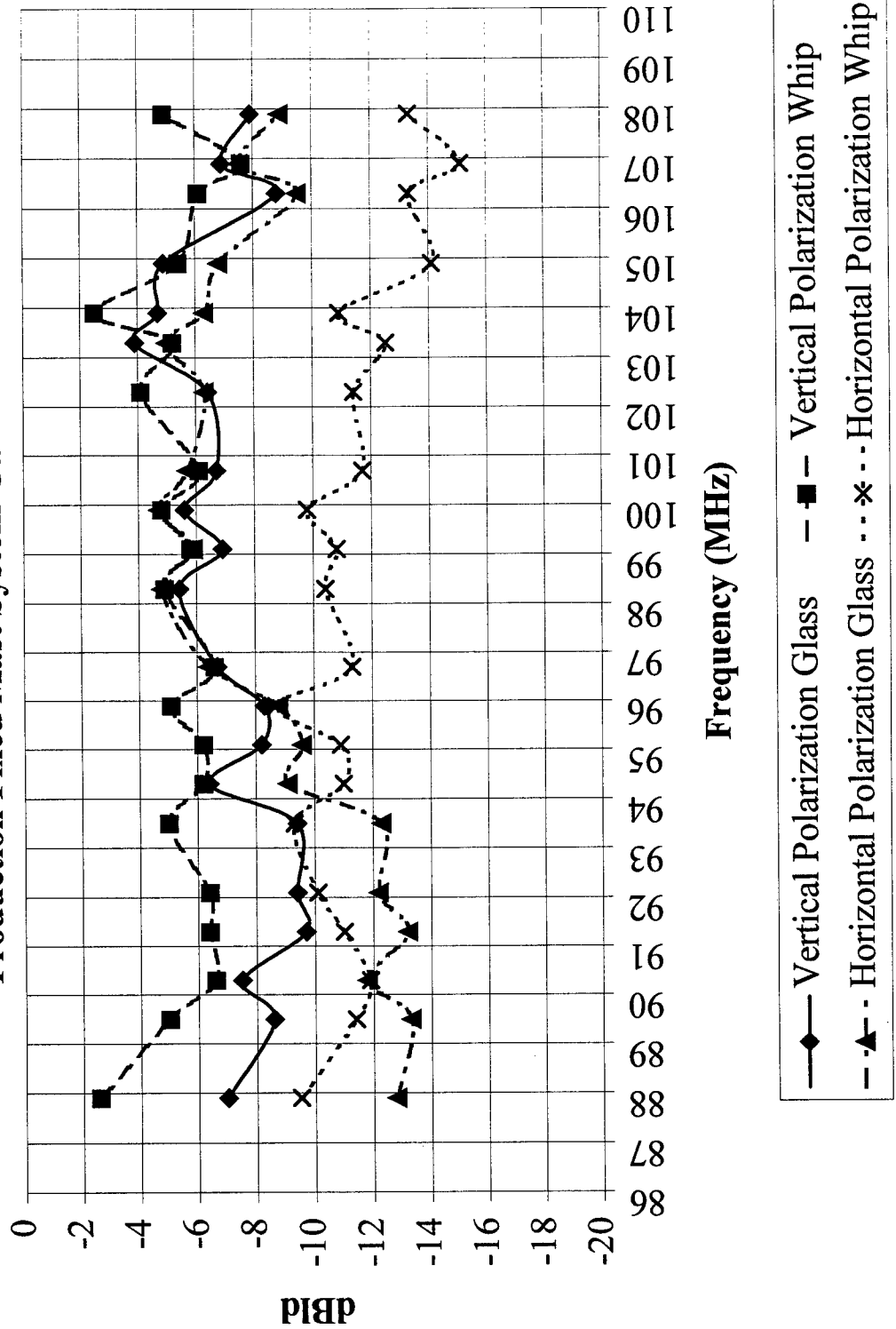


Figure 7.

Concealed AM Element Antenna Factor

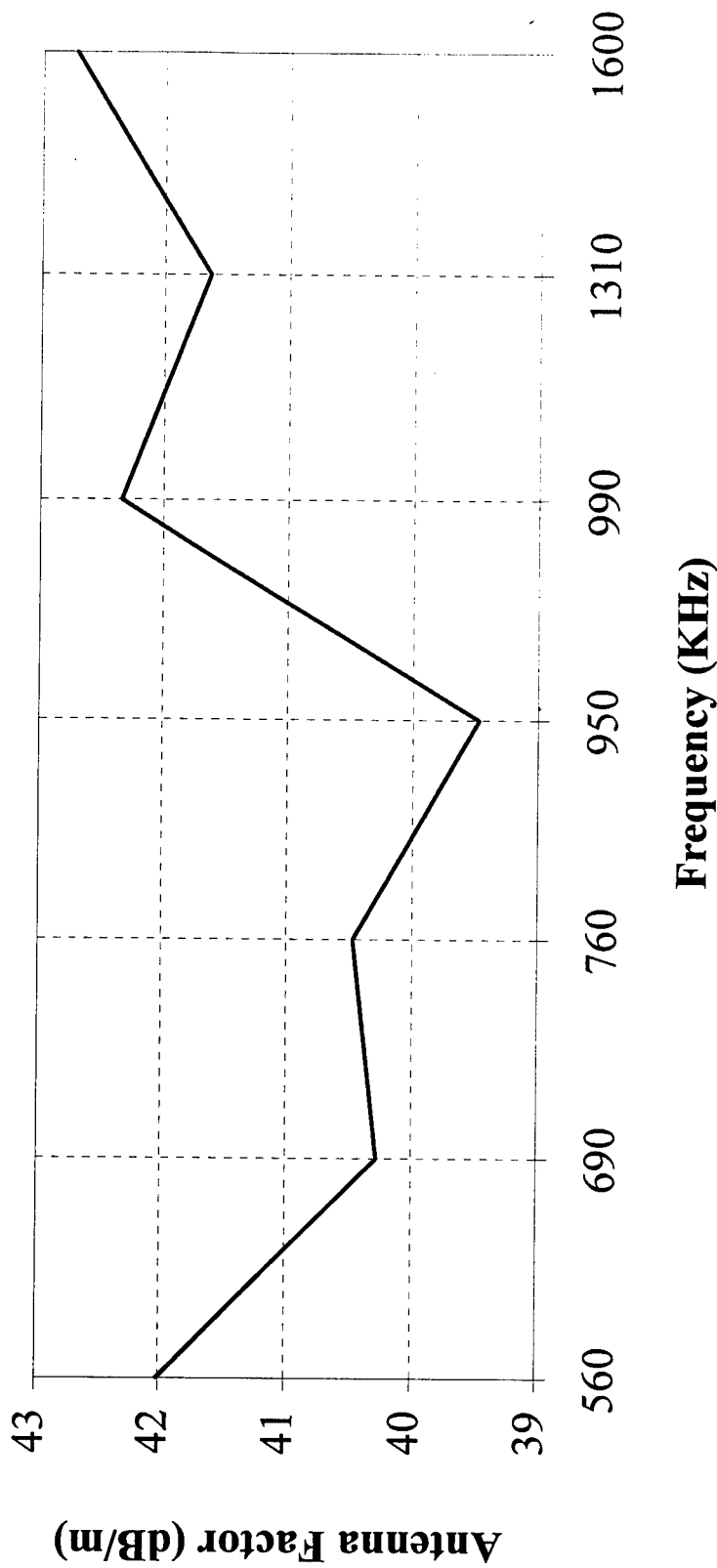


Figure 8.

Relative AM Antenna System Antenna Factors

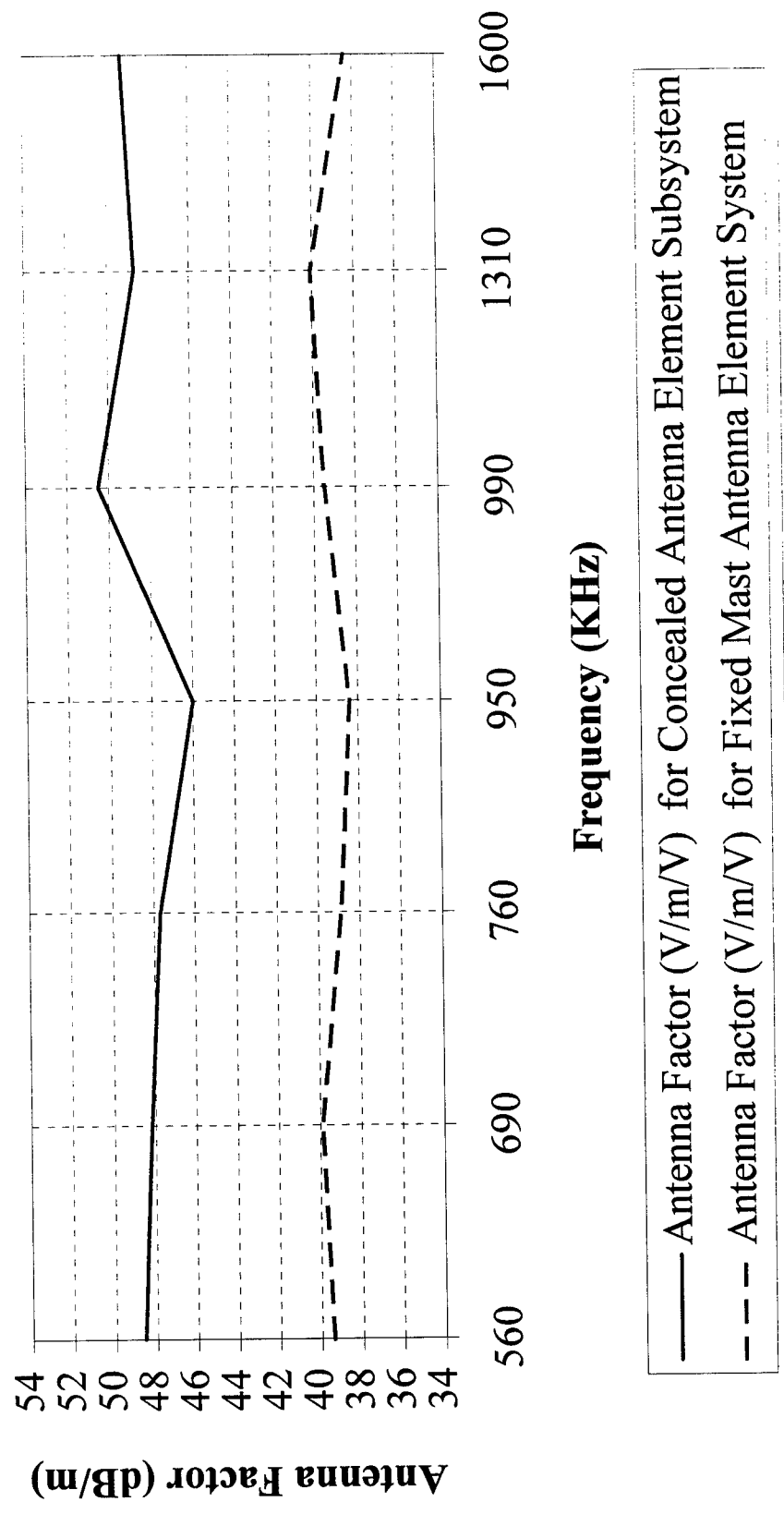


Figure 9.

AM Reception System Sensitivity - 20 dB SNR

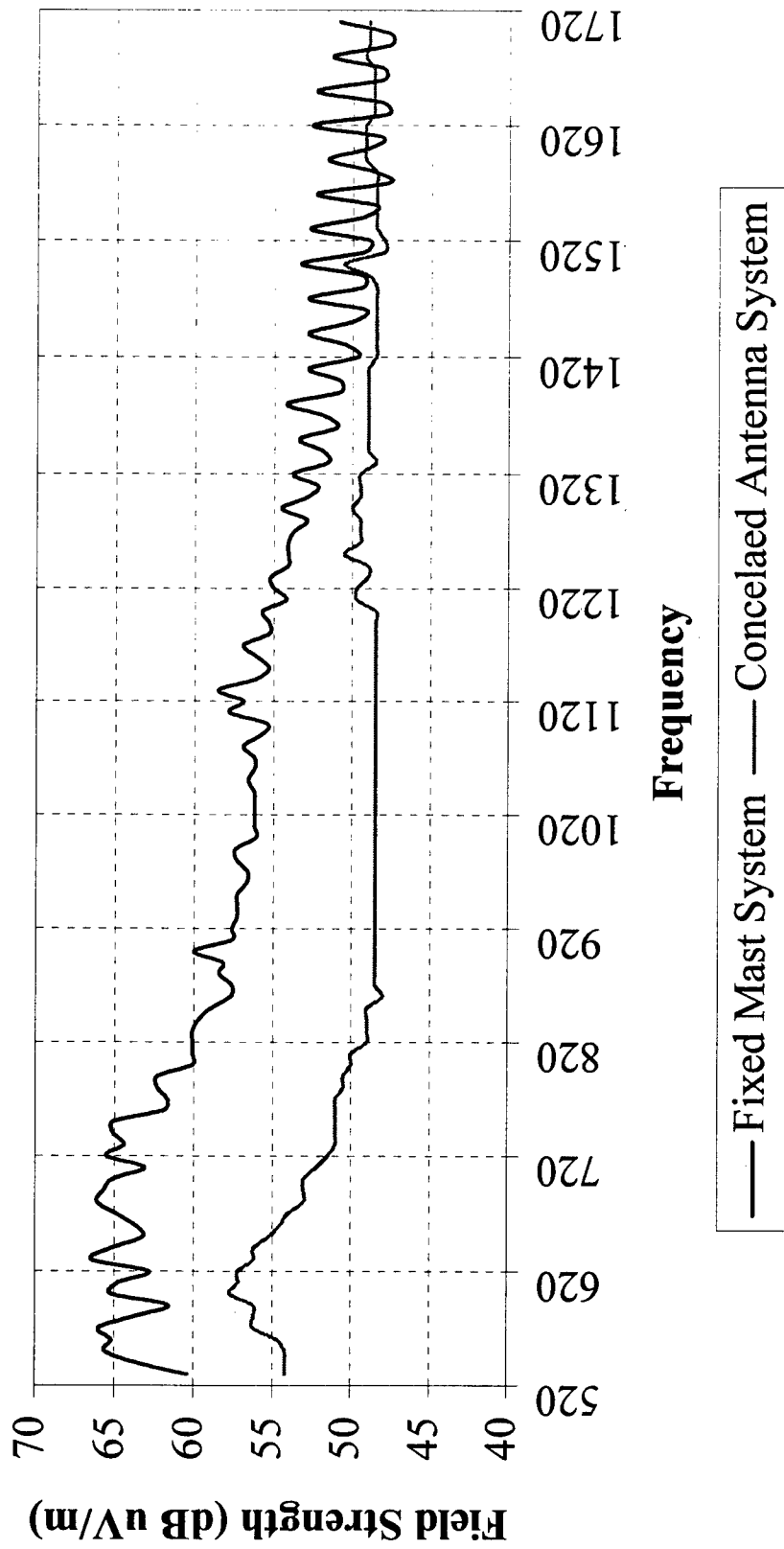


Figure 10.

DAB MULTIBAND GLASS ANTENNA

Shunji Miyahara and Jun Yamaguchi

Visteon Asia-Pacific Laboratory,

Visteon Automotive Systems

4-25-2 Kitayamada, Tsuzuki-ku, Yokohama-shi,
Kanagawa 224-0021, Japan

Naoki Shibata

Harada Industry Co., Ltd.

17/13, 4-chome, Minamiohi, Shinagawa-ku,
Tokyo 140-0013, Japan

Abstract: A new type of antenna, installed on the rear glass of a vehicle, to receive both Band III and L band was proposed. This antenna consists of a rectangular loop, inductance elements inserted in the loop and a monopole connected to the edge of the loop. It works, through the use of the elements, both as a one-wavelength loop antenna for Band III and a half-wave dipole for L band. This antenna is (1) conformal and (2) compatible with the defogger heater grid lines. The prototype of this antenna was fabricated and compared with a commercially-available whip-type multiband antenna (monopole antenna) for both bands. For the vertical polarization, the gain of this antenna was lower than that of the whip-type antenna by about 3 dB for band III, but higher than or equal to for L band. For the horizontal polarization, the gain of this antenna was higher than or equal to that of the whip-type antenna for both bands.

1. Introduction

Digital Audio Broadcasting, DAB, is the most advanced fundamental radio technology since the introduction of FM stereo radio. DAB provides near CD sound quality and interference-free signal, and also can transmit text, data and picture. Since BBC initiated experimental DAB broadcasting in 1995, Germany, France, Switzerland, Canada, etc. followed it [1,2]. As a first step to automobile application, in-car receivers will be launched in England in the summer of 1998.

In DAB, three frequency bands (Band I, III and L band) are allocated. In Europe, the selection of the two bands, Band III and L band, depends on each country or area, and a multiband antenna, which can receive both of them, is expected to be developed especially for a vehicle receiving the terrestrial broadcasting. For such purpose, several whip-type multiband antennas are developed and have already become commercially-available. Those antennas, however, are not conformal (protrusive), do not look good, and these facts become their drawback from the vehicle application point of view [3]. Therefore we have started the development of a new multiband antenna, which is conformal and also applicable to a vehicle [4]. This antenna has the following features. 1) Can receive both band III and L band, 2) be conformal and good-looking since it is installed in the surface of the rear glass of a vehicle, and 3) compatible with the defogger grid lines in the glass. Here the concept of this antenna, design for basic structure, fabrication of prototype and the results of the open site test are described.

2. Concept of a multiband antenna

2.1 Specification

Before the development, the goal specification for the multiband antenna was determined so that it should be no protrusion and less impact to vehicle design as shown in Table 1.

Table 1 Goal specification of a multiband antenna

Items	Specification
- Installation position	Above the defogger on the surface of the rear glass
- Frequency	Band III (216 ~ 237 MHz) and L band (1452 ~ 1492 MHz)
- Gain	Better or equal to commercially-available whip-type multiband antennas for vertical polarization of terrestrial broadcasting.

2.2 Concept

The problems in realizing this multiband antenna are 1) that there is extreme difference of wavelengths, 1300 mm (Band III, λ_1) and 200 mm (L band, λ_2), and 2) that the vertical length (about 150 mm) of the area above the defogger is too short for the conventional band III antenna to receive the vertical polarization

waves. One solution to the problems is the combination of rectangular loop and dipole antennas as shown in Fig.1. In the loop, there are two coils (inductance elements), which work as short for Band III and as high impedance (open) for L band. The one-wavelength loop antenna of λ_1 and the half-wave dipole of λ_2 can be realized above the defogger. This antenna is installed as shown in Fig.2. For the higher gain for the vertical polarization wave of Band III, the feeding point is set at the top of the vertical part of the loop so that the current peaks exist in the vertical part of the loop. Therefore by this setting, the higher gain is expected even though the length of the part is much shorter the wavelength. This shortness also makes this antenna compatible with the defogger.

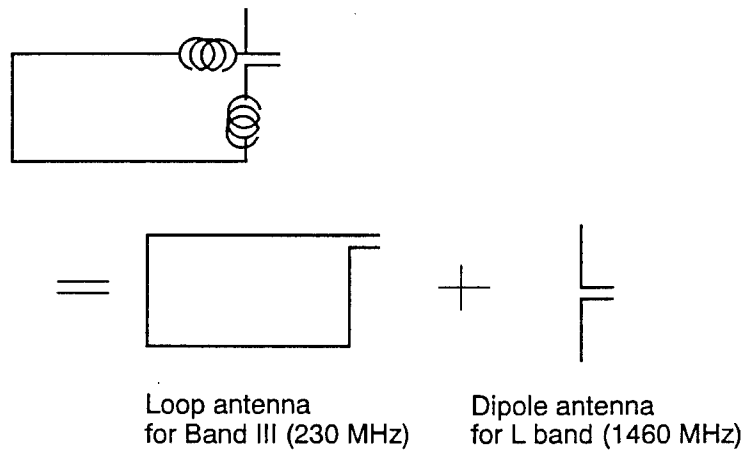


Fig.1. Concept of the loop and dipole antenna.

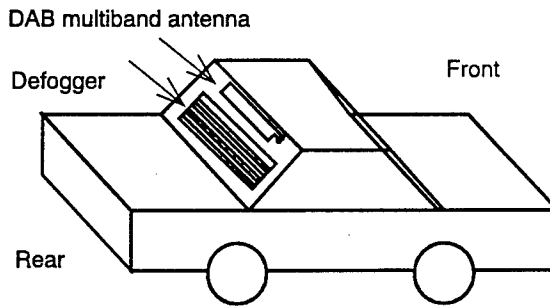


Fig.2. Multiband antenna in the rear glass of a vehicle.

3. Design for basic structure

3.1 Loop antenna structure design

Since the dipole for L band can be expected to have reasonable performance, we made the analysis of the loop antenna by the moment method simulator, NEC-2 [5], in order to determine the basic structure. Three kinds of antennas shown in Fig.3 were investigated on the basis of the vehicle model shown in Fig.4. The model has metallic roof, trunk lid, and floor plate. The relative permittivity of the glass was assumed to be one. The results are shown in Table 2. The case (c) was the best from the impedance and gain points of view.

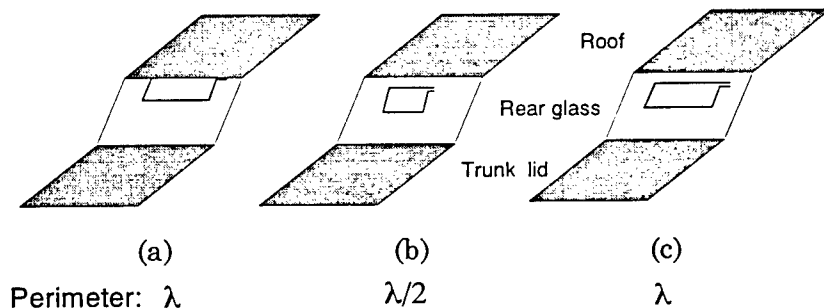


Fig.3. Loop antennas.

Length of vertical part on one side: 0.073λ . λ is wavelength.

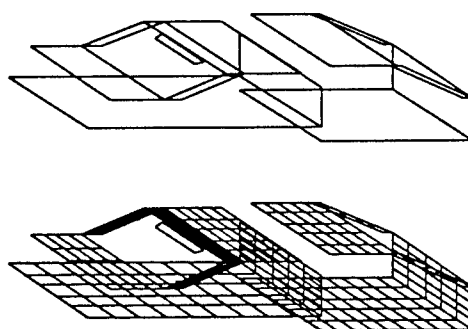


Fig.4. Model and grid for simulation.

Condition: free space (no dielectric), frequency: 210 MHz, glass area: 1200 x 700 mm, tilted angle of antenna: 32 degrees, and source position: at the upper right part of the loop.

Table 2 Comparison of loop antennas

Items	(a)	(b)	(c)
Perimeter	λ	$\lambda/2$	λ
Impedance (Ohm)	188.	28000.	8.8
- j 8500.	+ j 46000.	- j 98.	
Gain for vertical polarization in horizontal plane (dBi)	-14	-3	+3

For the one-wavelength loop antenna corresponding to Fig.3(c), the relation between the maximum gain for the vertical polarization in the horizontal plane and the ratio of the length of the vertical part on one side to that of the perimeter was also investigated. The results are shown in Fig.5. The antenna always had the maximum gain at the rear direction and the peak was obtained when the ratio was 0.05. It was found that the length should be chosen between 0.05 and 0.1 λ .

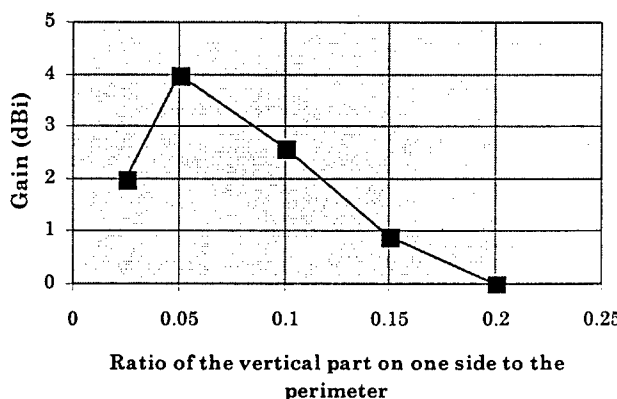


Fig.5. Gain for the vertical polarization in the horizontal plane and the vertical length for one-wavelength loop antenna (simulation).

3.2 Inductance elements

The specification of inductance is investigated. From (c) in Table 2, the impedance of the inductance was determined around 100 Ohm to cancel the reactance of the loop antenna at Band III. As the structure of the inductance, the

coil was selected as shown in Fig.6. This has 43 nH, and the reactances were corresponding to 56 and 390 Ohm at 210 and 1460 MHz, respectively. At Band III, the impedance, $j56$ Ohm, might be judged to be near enough to $j100$ Ohm at the stage of determining the basic structure by considering that the loop has two inductances. At L band, it is expected to work as high impedance. By using this coil, the structure of the multiband antenna (dip-loop antenna) was made on flat glass as shown in Fig.7, and the current distribution was measured at 1460 MHz by using the miniature loop antenna [6]. The amplitude of the current was 10 dB difference between the both side of the coil. This means that the coil worked as high impedance.

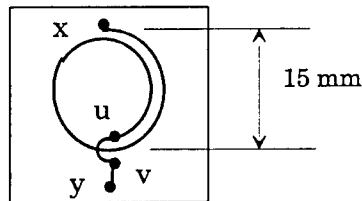


Fig.6. Structure of the inductance element.
The part between 'u' and 'v' is a bridge.

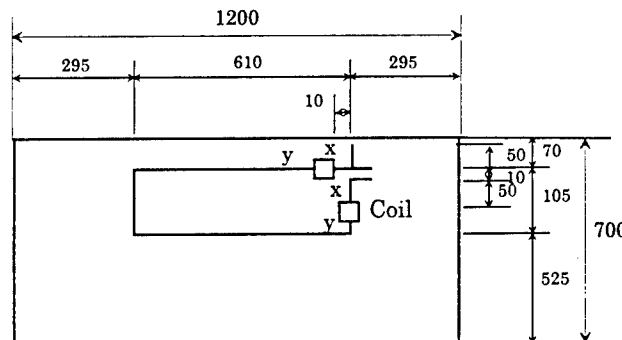


Fig.7. Dip-loop antenna structure.
Thickness of flat glass: 4 mm.
Feeding point is at the top-right.

4. Fabrication of prototype antenna and open site test

Since the design of the basic structure was completed, the dip-loop antenna was fabricated, and installed on the loading platform of a truck. At an open site, the impedance of the antenna and antenna pattern are measured. For comparison, the pattern of commercially available whip-type multiband antennas is also measured.

4.1 Prototype dip-loop antennas

The antennas used in this measurements are shown Fig.8. The wavelength reduction owing to the dielectric of the glass was considered. The reduction rate was experimentally determined. A simple loop antenna for Band III on the same glass was made and the rate was determined by measuring resonant frequency. The rate was about 0.7 for the flat glass of 4 mm thickness. This rate was used for Band III. In order to investigate the bandwidth, a dip-loop antenna using a 5-mm width Cu tape is fabricated as well as that using the 1-mm tape.

The height of the dipole in the dip-loop antenna was determined to be longer than the half-wave length of the L band by 1.3 times. The reduction rate for the dipole in L band was about 0.5.

The installation of the antennas are shown in Fig.9.

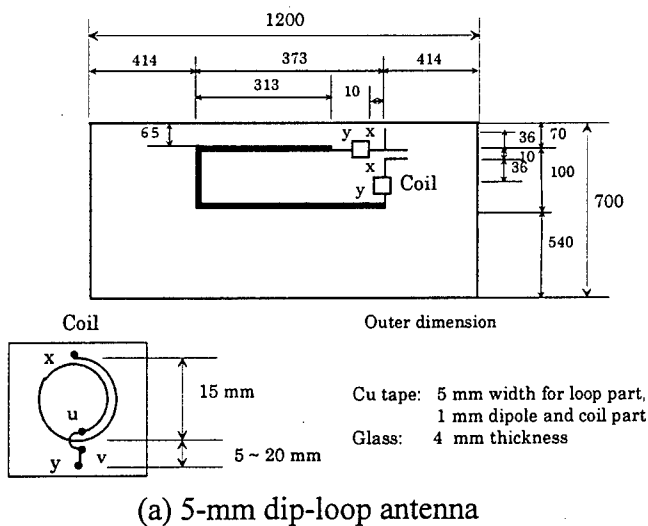
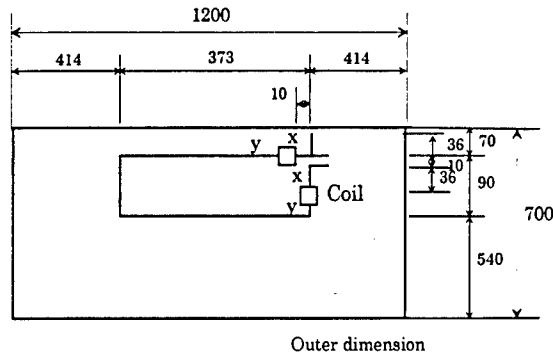


Fig.8. Dip-loop antennas.



(b) 1-mm dip-loop antenna

Fig.8. (Cont.) Dip-loop antennas.

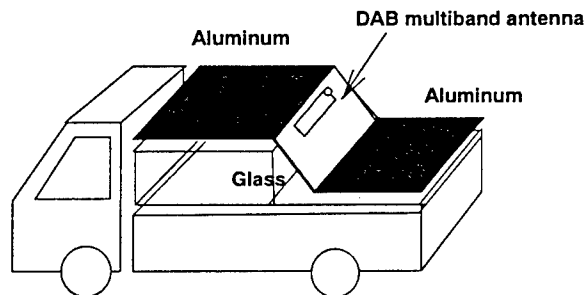
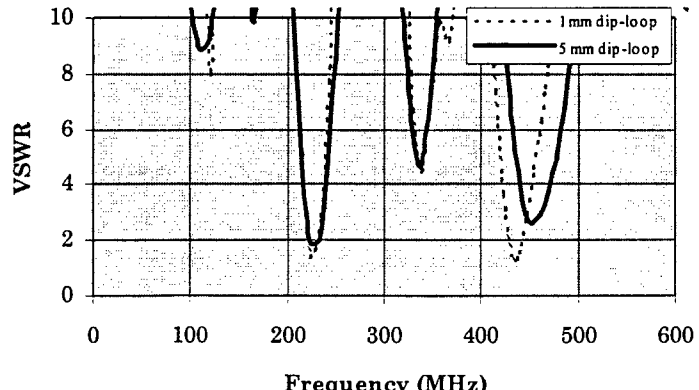


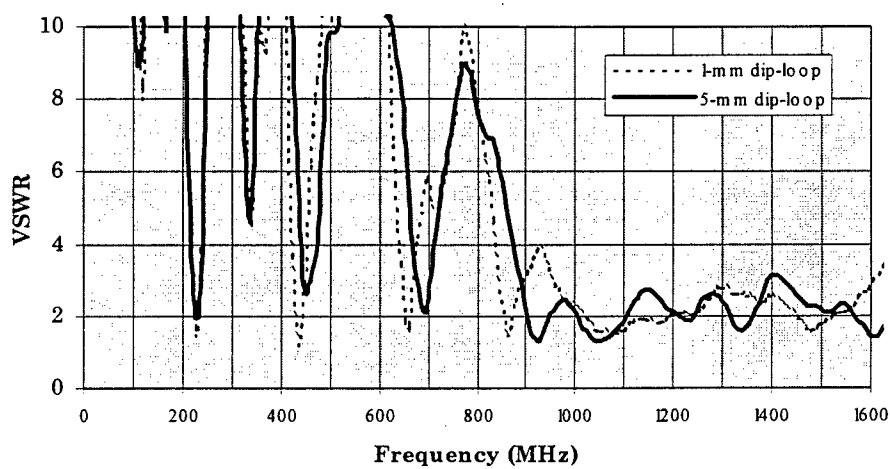
Fig.9. Vehicle rear part model. (Truck: Toyota Lite Ace.)

4.2 Impedance measurement

The impedance was measured by a network analyzer, HP8714B. The results are shown in Fig.10. There was a resonance around 240 MHz and a low VSWR of 2 was realized around 1460 MHz. The bandwidth at Band III is shown in Table 3. The 5-mm dip-loop antenna had 23 MHz bandwidth. This satisfied the target bandwidth, 20 MHz, but the 1-mm dip-loop antenna did not.



(a) Near Band III



(b) Across Band III and L band

Fig.10. VSWR of dip-loop antennas.

Band III: 216 - 237 MHz, L band: 1452 - 1492 MHz.

Table 3 Measured bandwidth of dip-loop antennas

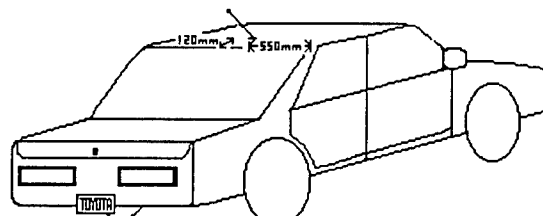
Antenna or target	Bandwidth at Band III *)
(a) 5-mm dip-loop antenna	23 MHz
(b) 1-mm dip-loop antenna	18 MHz
Target	20 MHz

*) Range, in which VSWR is lower than 4.

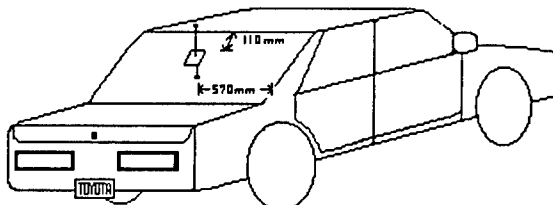
4.3 Antenna pattern measurement

4.3.1 Conditions

The receiving patterns of the dip-loop antennas, shown in Fig.8, were measured as well as commercial multiband whip-type antennas at an open site. The commercial antennas, which are passive, are shown in Fig.11. The site is shown in Photo 1. The equipment and measuring conditions are shown in Table 4 and 5, respectively.



(c) X antenna



(d) Y antenna

Fig.11. Commercial whip-type multiband antennas.
Vehicle: Toyota Vista.



Photo 1. Open site.

Table 4 Equipment of the open site

Items	Specification
Antennas	
- Transmitting antenna on pedestal	EMCO Model 3142 Biconilog antenna
- Antenna on the turn table	Dip-loop, commercial multiband and standard dipole antenna
Measuring system	
- Spectrum analyzer	Advantest TR4172
- Amplifier	HP 8447D

Table 5 Measuring conditions at open site

Items	Specification
- Distance between the turn table and pedestal for an antenna	20 m
- Rotation of the turn table	Clockwise for top view, 0 - 360 degrees by 5 degree step
	17 dBm. And 16 dB amplification
- Power of RF	(for only L band)
- Frequency	230, 1460 MHz
- Polarization of transmitting antenna	vertical and horizontal polarization

4.3.2 Results of antenna pattern measurement

The receiving patterns are shown in Fig.12 and 13. In Fig.12, the dip-loop antenna was compared with the commercial antennas. In Fig.13, the different dip-loop antennas, in which the 1- and 5-mm width Cu tapes are used, were compared. And also the patterns for the 5-mm dip-loop were measured twice for more validity and compared in the figure by expressing (a) and (a'). These patterns are normalized by half-wave dipole antennas. And the cable loss is compensated. The average antenna gain is shown in Table 6 and Fig.14. The results were as follows:

- 1) For the vertical polarization and 230 MHz: The 5-mm dip-loop antenna had lower gain than that of the commercial whip-type monopole and dipole antennas by 3 dB and 7 dB on the average, respectively. Among the dip-loop antennas, their patterns were similar, and there was not clear gain difference between the 5-mm and 1-mm dip-loop antennas.
- 2) For the vertical polarization and 1460 MHz: All the patterns showed serrated ones. The dip-loop antennas had smoother pattern than the commercial antennas. On average, the gain of the 5-mm dip-loop antenna was higher than or equal to that of the commercial ones.
- 3) For the horizontal polarization and 230 MHz: On average, the 5-mm dip-loop antenna had the same gain as the commercial monopole antenna, and higher gain than the commercial dipole antenna by more than 3 dB.
- 4) For the horizontal polarization and 1460 MHz: On average, the 5-mm dip-loop antenna had higher gain than the commercial ones by more than 2 dB.

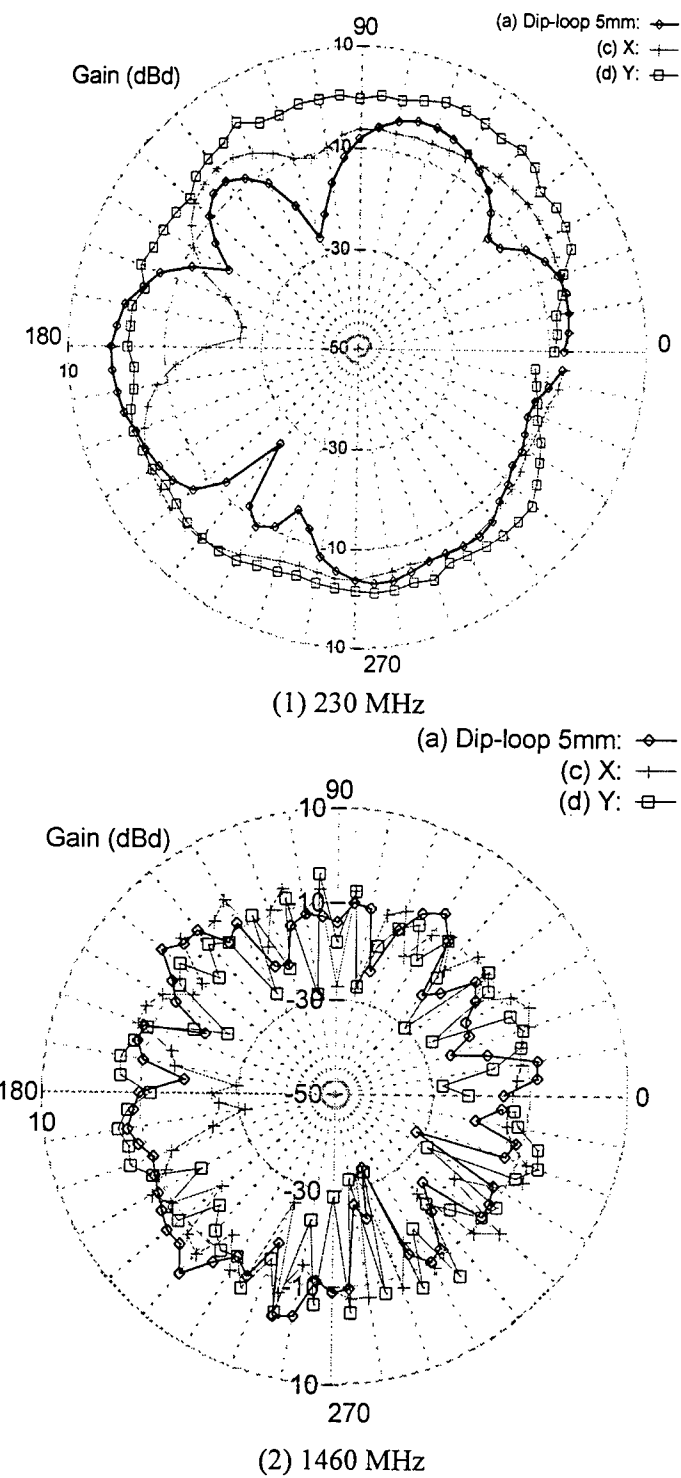


Fig.12. Measured receiving pattern.
 Vertical polarization. Cable loss is compensated.

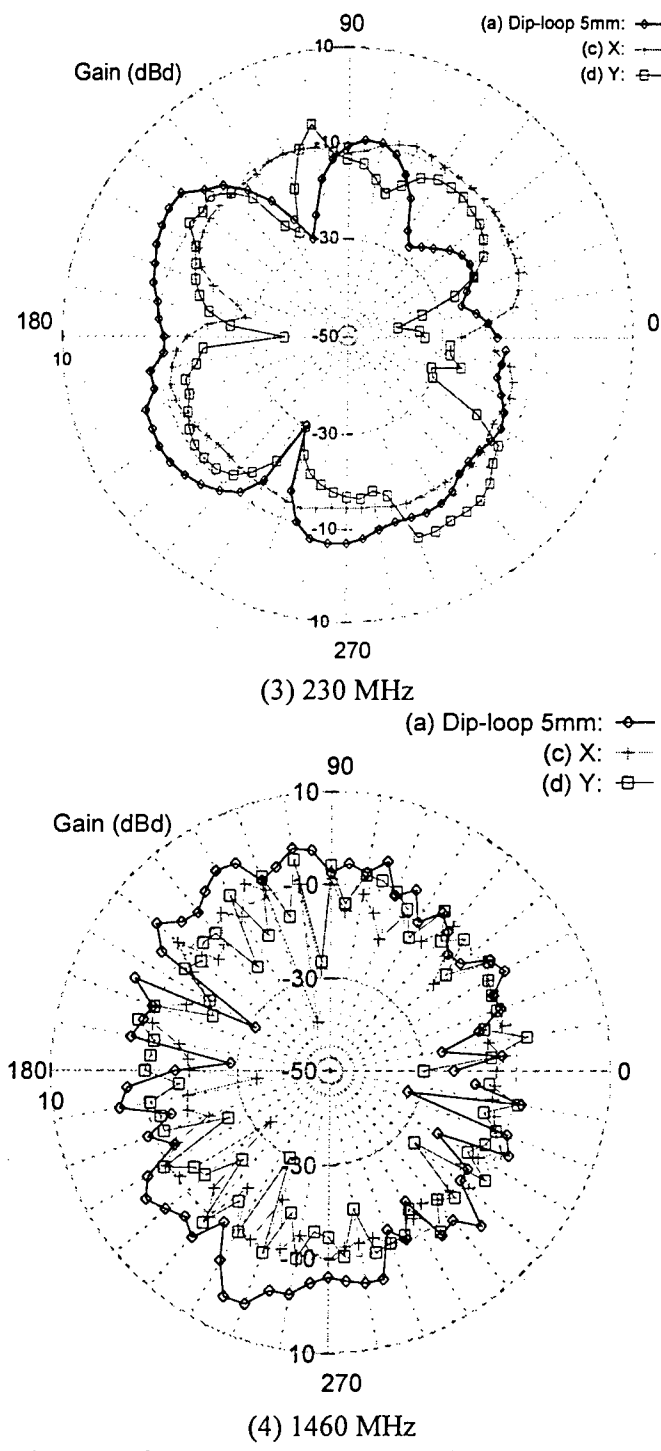


Fig.12 (Cont.): Measured receiving pattern.

Horizontal polarization. Cable loss is compensated.

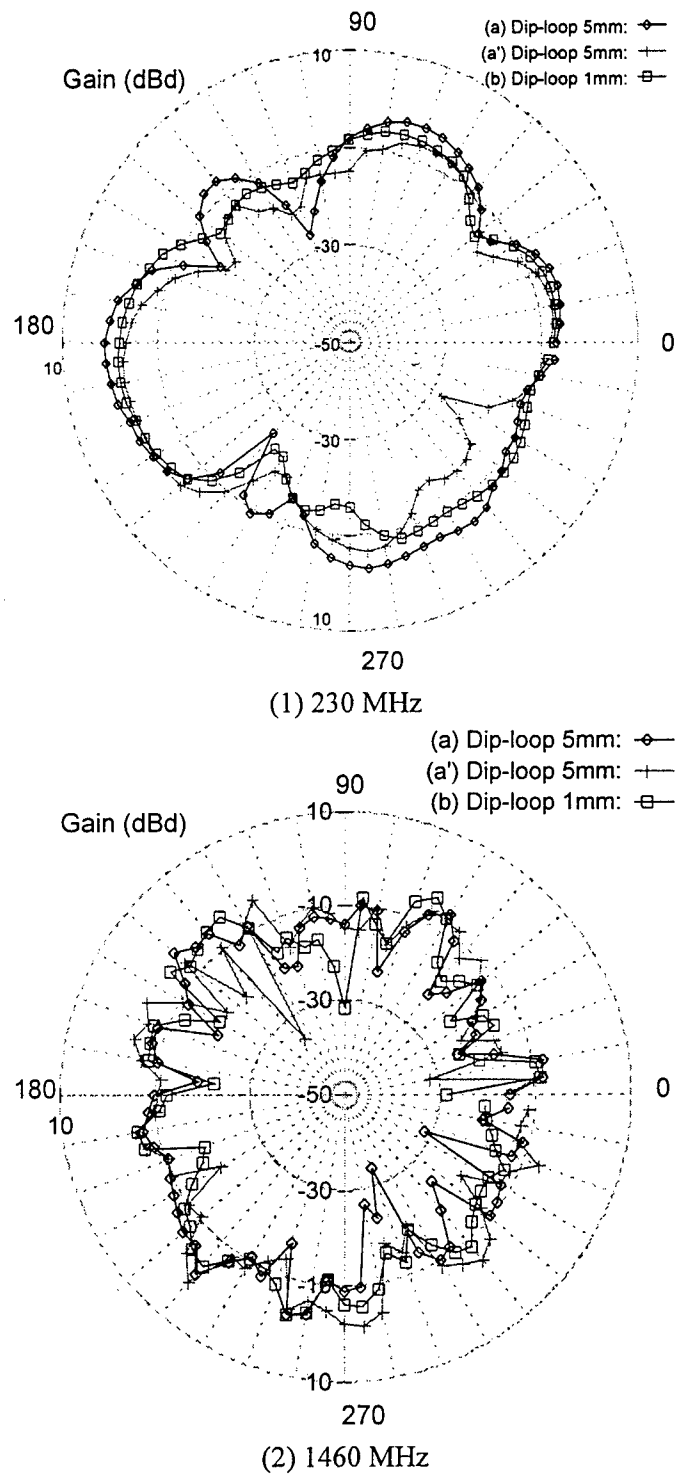


Fig.13. Measured receiving pattern for the dip-loop antennas.
 Vertical polarization. Cable loss is compensated.

Table 6 Average gain of dip-loop and commercial antennas

	(a) 5-mm dip-loop	(a') 5-mm dip-loop	(b) 1-mm dip-loop	(c) X	(d) Y
230 MHz, vertical	-8.0	-11.6	-9.6	-6.8	-2.3
1460 MHz, vertical	-12.8	-11.3	-12.6	-12.7	-13.7
230 MHz, horizontal	-13.5	-10.7	-17.9	-13.5	-17.1
1460 MHz, horizontal	-8.4	-10.9	-9.8	-14.5	-13.5

Unit: dBd. Average: geometric mean regarding azimuth angle.
Cable loss is compensated.

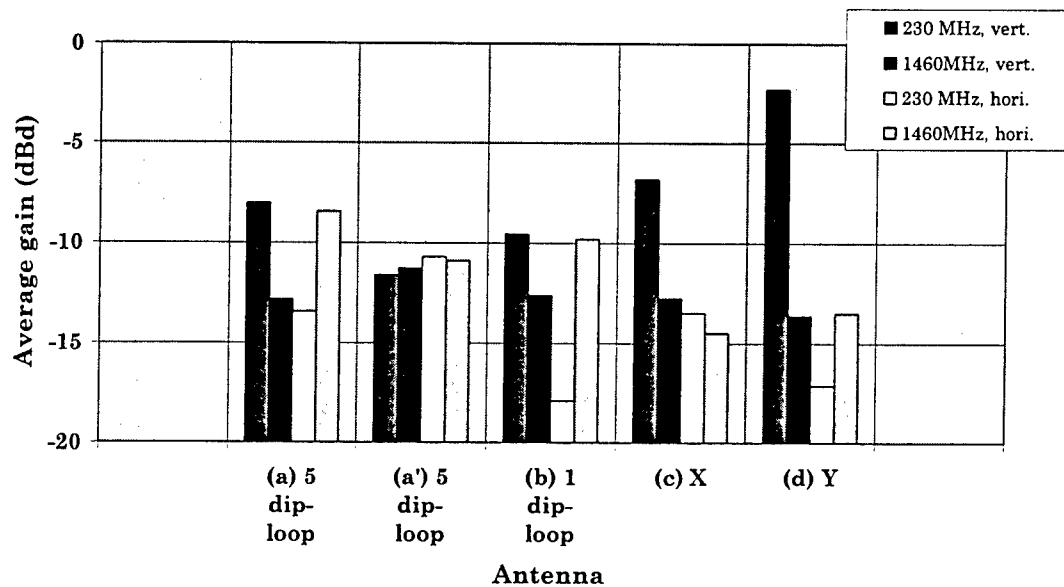


Fig.14. Average gain of dip-loop and commercial antennas.
Average: geometric mean regarding azimuth angle. Cable loss is compensated.

5. Discussion

The gain of the dip-loop antenna at Band III and the operation mode at L band are discussed here.

5.1 Gain at Band III and for the vertical polarization

The operation mode at Band III in the dip-loop antenna is considered. From Fig.10 (a), the resonance was observed at about 230 and 460 MHz. It seems to correspond to the dominant (one-wavelength) and second harmonic (two-wavelength) modes, respectively. This fact may indicate that this antenna works in the dominant mode at Band III.

The current distribution was measured by the miniature loop antenna [6]. The minimum of the current existed near the middle of both the horizontal parts of the loop. (Since it was easier to find the minimum than the maximum along the loop, the minimum was identified through the distribution measurement.) This means that the current might have its maximum at both the vertical parts of the loop and that the current at the vertical parts was in phase. This fact corresponds to the current distribution in the simulation shown in Fig.4 and 5.

From the above two facts, the fabricated antenna worked as designed. But the gain of the antenna was lower than that of the commercial monopole antenna by 3 dB as shown in Fig.12 (a). The measured and simulated patterns for the vertical polarization are shown in Fig.15. They have a comparable gain. This tells that the dip-loop has shown the intrinsic performance and that it needs the remarkable change of the structure of the dip-loop for much higher gain.

5.2 Operation mode at 1460 MHz and for the vertical polarization

The dip-loop and commercial antennas had the same gain for the vertical polarization. One of the reason for that is that the dip-loop antennas did not have clear resonance at this frequency as shown in Fig.10 (b). (This needs more detailed analysis.) In the reception test prior to the antenna pattern measurement, the dip-loop antenna with the vertical dipole part had higher gain than with the horizontal-vertical dipole (refer to Fig.16). This might suggest that the upper part of the vertical dipole was working and that the length adjustment of the upper part may contribute to improve the gain.

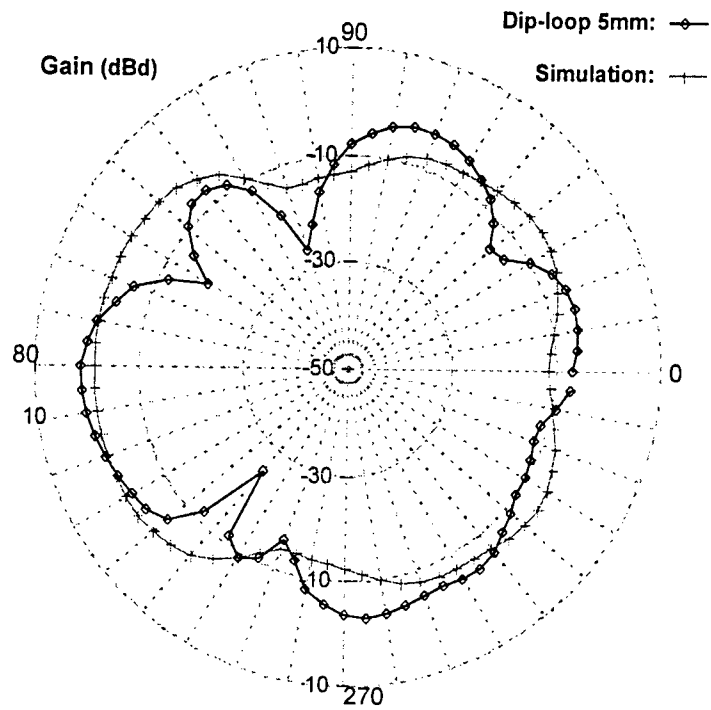
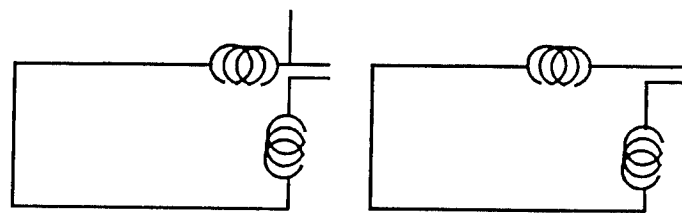


Fig.15. Comparison between measured and simulated antenna patterns for the vertical polarization in the horizontal plane.

Dip_loop 5mm: Measured pattern at 230 MHz. The antenna shape and installation are shown in Fig.8(a) and 9. The cable loss is compensated. Simulation: Simulation result for the simple loop, having no inductance elements. The grid is the same as that of Fig.4. Frequency is 230 MHz. The perimeter of the loop is one wavelength and the ratio of the vertical part on one side to the perimeter is 0.097.



(a) Vertical dipole (b) Horizontal-vertical dipole

Fig.16. Dipole structures for L band.

6. Conclusions

We have been developing an DAB multiband glass antenna (Band III, 230 MHz; L band, 1460 MHz), which consists of dipole and loop antennas. It is conformal and compatible with the defogger grid lines in the rear glass of a vehicle. The prototype of the antenna was fabricated, installed on the loading platform of a truck, and compared with commercial whip-type multiband antennas on a vehicle regarding antenna pattern at the open site. The results are as follows.

1) At band III, the prototype antenna (5-mm dip-loop antenna) had enough bandwidth (23 MHz).

2) For the vertical polarization, which is more important than the horizontal one: At 230 MHz, the 5-mm dip-loop antenna had lower gain than that of the commercial whip-type monopole and dipole antennas by 3 dB and 7 dB on the average, respectively.

At 1460 MHz, all the patterns showed serrated ones. The dip-loop antennas had smoother pattern than that of the commercial antennas. On average, the gain of the 5-mm dip-loop antenna was higher than or equal to that of the commercial ones.

3) For the horizontal polarization:

At 230 MHz, on average, the 5-mm dip-loop antenna had the same gain as the commercial monopole antenna, and higher gain than the commercial dipole antenna by more than 3 dB.

At 1460 MHz, the antenna had higher gain than the commercial ones by more than 2 dB.

The performance of the prototype antenna surpassed that of the commercial products except the vertical polarization of 230 MHz. We will improve the gain and proceed to the development of the peripheral devices (extension line between the connector and feeding point, and one layer coil) in order to make the dip-loop antenna more practical.

Acknowledgment

The authors would like to thank Mr. M. Saitoh, Harada Co., Ltd. and Dr. N. Lazarov, Visteon Automotive Systems, for many useful technical discussions.

Reference

- [1] T. Takenohara, "Practical of DAB", *Broadcast Engineering*, Vol.49-3, pp.76/83, 1996.
- [2] K. Yamauchi, "DAB Receiver and the Present Situation Canada", *Broadcast Engineering*, Vol.49-3, pp.84/87, 1996.
- [3] J. L. McComas, M. A. Kady and B. J. Warren, "Manufacturing DAB automobile receivers", *1st International Symposium on DAB-1992 proceedings*, pp.235/244, 1992.
- [4] S. Miyahara and N. Shibata, "DAB Multiband Glass Antenna", *SAE 981144*, 1998.
- [5] G. J. Burke and A. J. Poggio, Numerical Electromagnetics Code (NEC-2), Lawrence Livermore National Laboratory, 1981.
- [6] H. Whiteside and R. King, "The loop antenna as a probe", *IRE Trans. Antennas & Propag.*, AP-12, 3, pp.291, May 1964.

A Novel Aperture-Coupled Microstrip Antenna Array Fed By A Dielectric Guide

David D. Li and Robert M. Knox
Epsilon Lambda Electronic Corp.
427 Stevens Street
Geneva, IL 60134

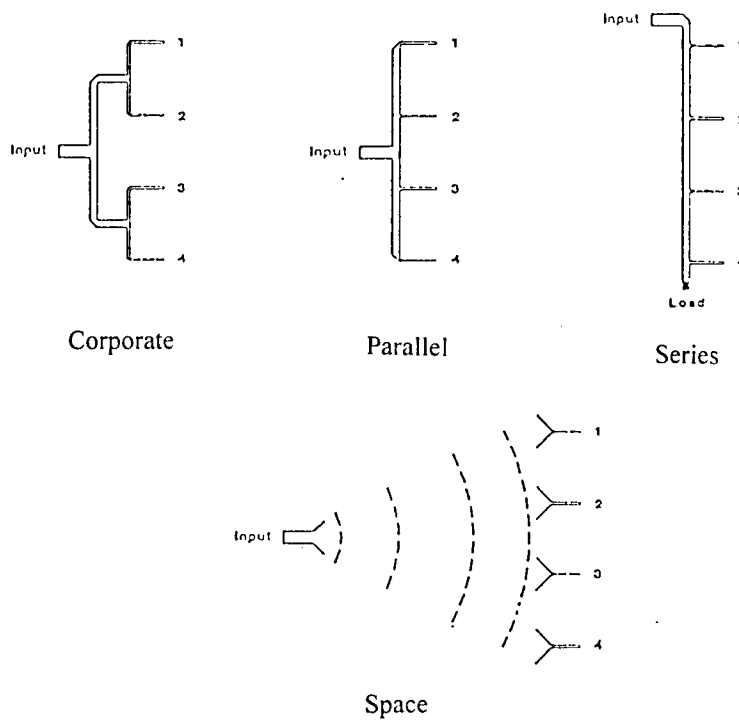
Abstract -- An aperture-coupled microstrip antenna array fed by a dielectric guide was studied. The study focused on applications for Ka-band satellite communication systems as well as W-band automobile forward looking radar. A unique combination of aperture-coupled patch arrays, a dielectric waveguide feed line and a mechanically variable phase shifter applied to the dielectric feed line has demonstrated the feasibility of this novel structure as a scanning antenna at millimeter wave frequencies. This structure is projected to have lower losses, higher gain, and lower cost than existing technology. A simplified analysis of the coupling between the dielectric guide and microstrip line was developed to facilitate the antenna design. A 4 x 6 element microstrip patch antenna array fed by the dielectric guide at Ka-band was designed based on this analysis and an antenna array synthesis. There was a good agreement between the theoretical and experimental results. A scanning angle of approximately 30 degrees was demonstrated. Both an electromechanical and a rotating CAM shaft approach were investigated in order to obtain a cost-effective, mechanically adjusted phase shifter.

1. INTODUCTION

Many systems require high output powers and large antennas with very directive radiation patterns. In application such as communication links, radar and astronomy, the antennas may function as transmitters, receivers, or both simultaneously. To produce these pencil beams, large reflector antennas have

been used extensively. Instead of reflectors, large planar arrays which consist of several hundred to several thousand antennas can also provide narrow, high-gain pencil beams. They may be arranged in one, two or three dimensions. Large antenna arrays are not as bulky as comparable reflector antenna, but they often require complicated feeding networks.

Feed networks which distribute energy to each radiator in a patch type phased array antenna include corporate, parallel, series and space fed arrays as shown in Fig. 1. Feed networks increase complexity, cost and losses in an array



in Fig. 1. Various feed structures used for antenna arrays.

aperture but they add flexibility over a conventional reflector type system. Since one has access to each radiator, electronic methods can be employed for beam steering. Feed networks can be integrated with amplifiers and phase-shifters to provide both beamwidth flexibility and electronic steering capability. Electronic beam steering can be achieved using frequency scanning, beam switching, time delay or phase delay [1-6]. Electronic steering allows beam manipulations in tens

of nanoseconds using compact, mechanically-rigid structures. Due to the increase in complexity from the additional components there is some loss in gain and pattern deterioration at large scan angles. Conventional electronic phase-shifters include solid-state and ferrite phase-shifters. Although faster than conventional mechanical gimbals, electronic beam steering is far more expensive than mechanical beam pointing approaches. When cost is the primary driver of the system design, phased arrays are typically ruled out. Mechanical gimbals are commonly used to point the antenna beam over several axes. For a radar, the motor positions are correlated to return signals for tracking. A communication link, on the other hand, finds the peak in received signal strength. Mechanical beam pointing methods are relatively inexpensive when compared to electronic beam steering. Also the antenna performance is not compromised throughout the scan. However, they can be large, bulky and slow. What is studied in this paper is a low-loss, low-cost approach to a phased array antenna. Of the various feed networks, series-fed arrays provide a relatively simple and efficient approach to a large aperture for modest bandwidths. So the question becomes how to provide a good progressive phase-shift along a linear array without using expensive electronic components.

A new method for achieving a microstrip antenna phased array fed by a dielectric guide feed line (for fixed frequency) is described in this paper. The method involves mechanical displacement of an imaging plane (conducting plate) which changes the guide wavelength of the propagating mode in the dielectric waveguide. The change in phase between the feed points of the phased array causes angular scanning in one plane of the phased array.

2. FEED STRUCTURE

For a linear array of antennas spaced φ electrical degrees apart, the progressive phase-shift ($\Delta\phi$) which will steer the array beam ϕ_o degrees away from boresight is given by

$$\phi_o = \sin^{-1} \left(\frac{\Delta\phi}{\varphi} \right) = \sin^{-1} \left(\Delta\phi \frac{\lambda}{2\pi d} \right) \quad (1)$$

where d is the physical separation between antennas at the wavelength operation (λ). For a given spacing, the maximum one-sided beam angle allowed ($\phi_{o,max}$) depends on the maximum phase progression per element ($\Delta\phi_{max}$). Re-arranging equation (1), the required phase progression ($\Delta\phi$) between antennas needed to steer a beam (ϕ_o) degrees away from boresight is given by

$$\Delta\phi = \frac{2\pi d}{\lambda} \sin(\phi_o) \quad (2)$$

As shown in Figure 2, we propose to use the following low-loss dielectric guides for the feedline.

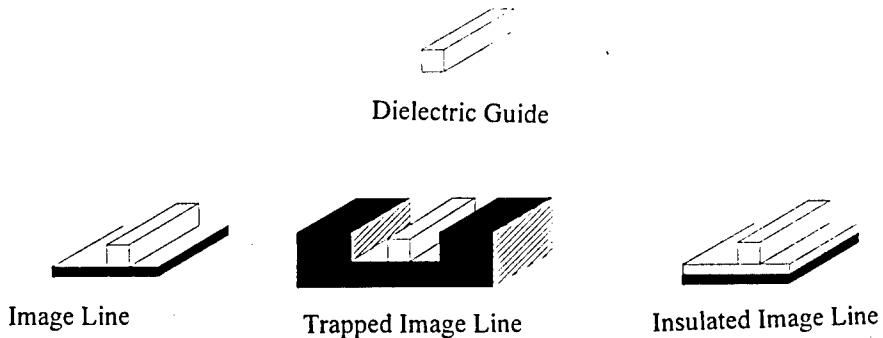


Fig. 2. Various dielectric guide configurations.

In order to keep the entire feed network away from the radiating patch antennas an aperture coupled configuration has been designed and verified at X-, Ka- and W-band. This approach not only isolates the feed network from the antennas but also provides design flexibility for wider operating bandwidth. To keep feedline losses to a minimum, the dielectric guide used is alumina. The series feed network is well suited for the ceramic guides chosen. Since the dielectric guide is an open structure, the electric and magnetic fields can be used to manipulate the guiding properties of the transmission line. Figure 3 shows a mechanical scheme used to change the guided wavelength of the dielectric guide essentially providing an electrical phase-shift along the line. The relative phase-shift for the dielectric guide is given by the following relation

$$\Delta\phi = \text{Length} \cdot [k_z(g_2) - k_z(g_1)]. \quad (3)$$

where g_1 and g_2 are the minimum and maximum gap spacings g between the reflecting plate and the dielectric guide as shown in Fig. 3. The gap affects the propagation constant of the transmission line thereby providing the electrical phase shift.

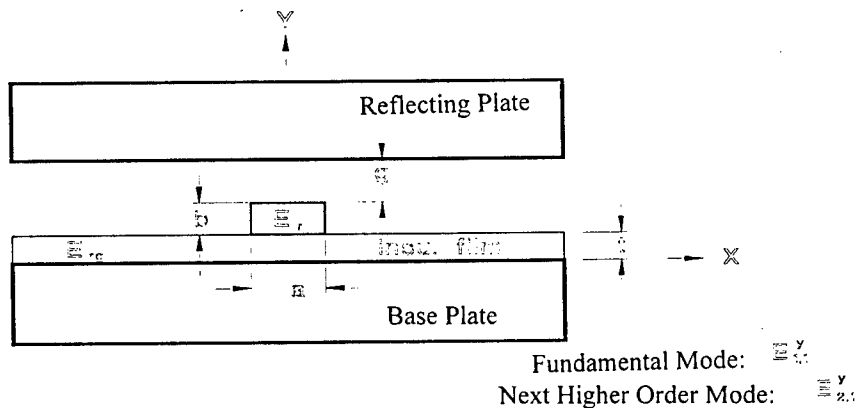


Fig. 3. Electromechanical phase-shifter.

The configuration of Fig. 3, for large gap g is the insular dielectric waveguide. As the insulating dielectric film layer approaches zero thickness, the structure is the dielectric image waveguide. The phase change of the dielectric image line due to the movement of the reflecting plate is investigated theoretically by using the full wave analysis method. Figure 4 shows the numerical results of the propagation constant in the Ka-band dielectric guide for different gap spacings at 28.0 GHz. The propagation constant is found to increase 12.8% at 28.0 GHz when the gap distance g decreases from 10.0 mm to 1.3 mm, which corresponds to a 46 degree phase change at 28 GHz in one dielectric wavelength.

The mechanical phase-shifter has been demonstrated at Ka-band and W-band with good results. The measured phase-shift at Ka-band is plotted in Figure 5. As shown most of the phase-shifting occurs for gaps below 20 mils.

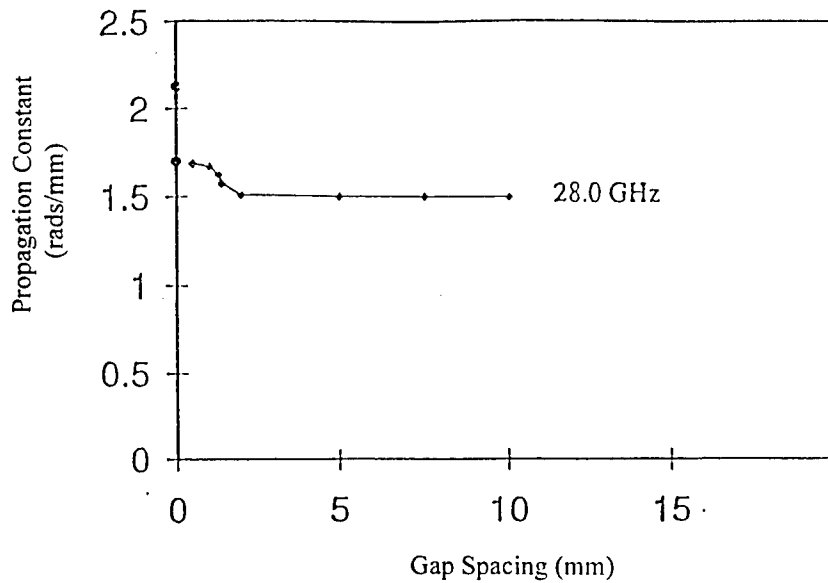


Fig. 4 The propagation constant at Ka-band.

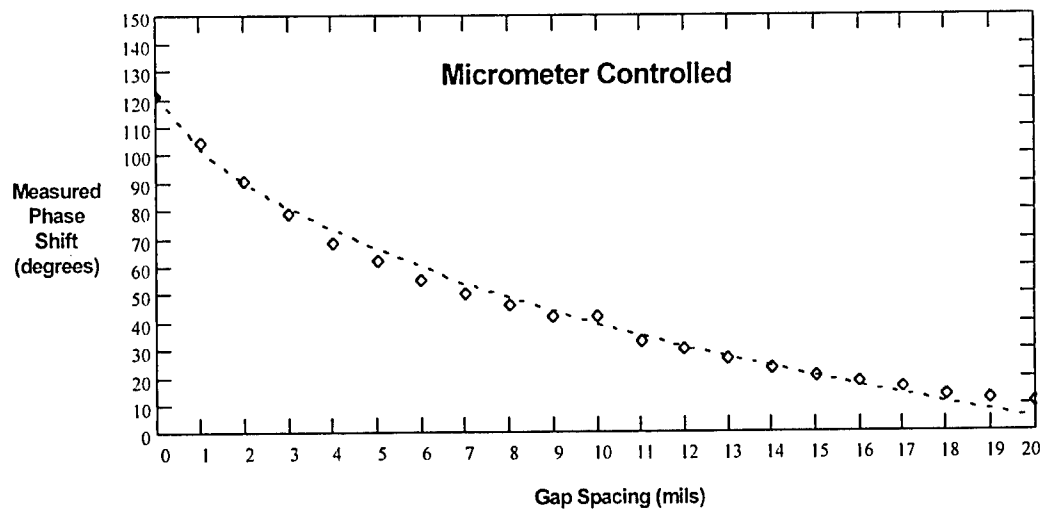


Fig. 5. Phase-shifter measurements at Ka-band.

The next step is to use this single element phase-shifter in a configuration which can provide a progressive phase-shift across an array of radiating elements. The concept was tested at X-band using a five element linear array of dielectric fed aperture coupled microstrip patch antennas as shown in Figure 6. A voice coil was used to move the top plate a total of 0.160" and provide beam steering capability. A simple driver circuit was used to provide current to the coil which has a peak force of 10 lb. The total stroke is +/- 0.1". An electronic sensor was placed within the housing to provide accurate position of the top plate. The top plate has been moved throughout its range at a rate of 30 Hz. This corresponds to a beam steering speed of 1200 degrees per second. Higher speeds are possible if the load on the coil is reduced.

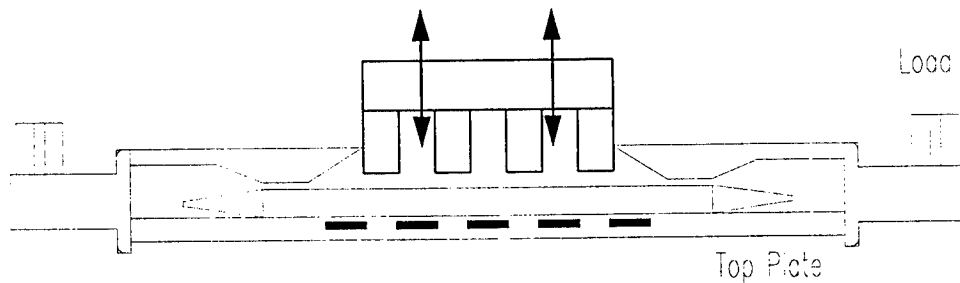


Fig. 6. Five element X-band phased-array.

A rotating cam approach as shown in Figure 7 could also be used as the actuator. Stepper motors are used to rotate the Cams which induce a phase shift across the linear aperture. Faster motors can be used along with shaft encoders to quickly scan the beam of the linear array.

As our measurements show, this beam steering approach has the potential of providing relatively good beam steering performance at an incredible low cost. The phase shift problem of the scanning antenna array has been changed from an expensive electronic system to a low cost electromechanical method. The control voltages have been reduced from N voltages for an $1 \times N$ electronic phased array to a single control voltage for the electromechanical approach. The method can be adapted to beam steering in both planes for an $N \times M$ phased array with only two control voltages required, one for the X plane and one for the Y plane.

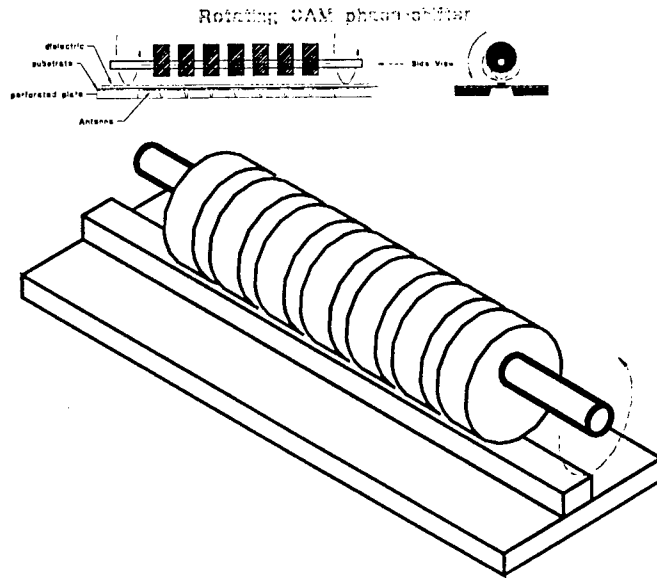


Fig. 7. Rotating cam beam steering approach.

To feed the energy from the rectangular waveguide to the dielectric guide, a transition between the rectangular waveguide and the dielectric guide is required. A three section transition was proposed and demonstrated with good results by Dydyk [7]. A modified design is used in the test to get a better insertion loss in the experiment. A 4-inch long alumina dielectric guide was properly tapered at both ends in E-plane for efficient launching electromagnetic field into a standard Ka-band metal waveguide. The width, height and relative dielectric constant of the dielectric guide are 2.54 mm, 1.27 mm and 10.5 respectively. The ground plane is polished aluminum. At 28 GHz the measured insertion loss characteristics of the 4-inch long dielectric guide main feed line with two launchers is 0.9 dB. The loss includes two back to back transitions and the section of dielectric guide. Considering the tapered ends of the dielectric guide as part of launchers and assuming a per launcher loss of 0.3 dB, the main feed line loss of 0.9 dB is in good agreement with the calculated dielectric line loss of 0.1 dB/in at this frequency. The assumed launcher efficiency of 0.3 dB is based on the experience with various investigations of alumina dielectric guide at millimeter wave length. The return loss of the transition is less than -15 dB at the operating frequencies.

3. DIELECTRIC GUIDE TO MICROSTRIP COUPLING

The proposed dielectric image line to microstrip line aperture coupling geometry consists of a microstrip line deposited on the top of the ground plane of dielectric image line. Fig. 8 shows the geometry of the proposed transition. The microstrip line is orthogonal in space with respect to the dielectric image line. The coupling is achieved through a rectangular slot etched on the ground plane. The coupling slot is oriented perpendicularly to the microstrip line. It is known that the fundamental mode of the microstrip line is a quasi-TEM mode, while the dielectric image line can support E_{11}^z and E_{11}^y modes of propagation. This implies that two fundamental modes corresponding to the E_{11}^z and E_{11}^y modes can propagate in the same range of frequencies simultaneously. However, the presence of the PEC plane and the configuration of the waveguide to dielectric image line launcher resolves this degeneracy. Therefore, single mode operation is obtained over a considerable range of frequencies. The magnetic field of the E_{11}^z mode is parallel to the interface. Both magnetic fields of the quasi-TEM mode in the microstrip and the E_{11}^z mode in the dielectric image line are well matched at the coupling aperture. The operating frequency range is expected to be dependent on the cross-section dimensions of alumina image line, which will be chosen to get the optimized phase shift by changing the gap spacing.

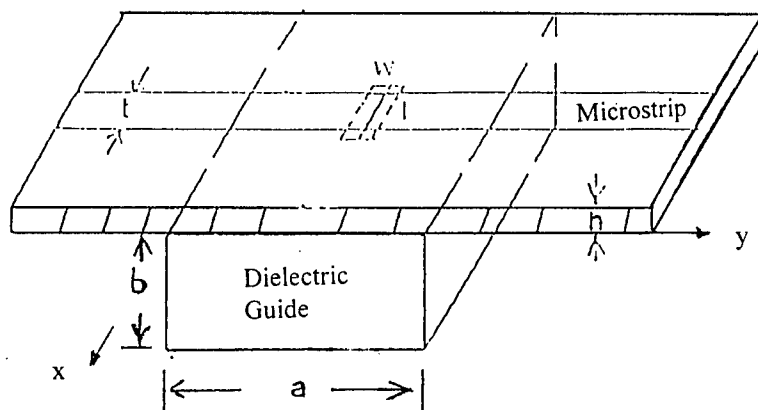


Fig. 8 Coupling model of dielectric guide and microstrip.

The electric and magnetic fields of both guides are formulated in terms of the modal field vector \mathbf{e} , \mathbf{h} , as well as the modal voltage V and current I , respectively. The orthogonal modal vectors \mathbf{e} and \mathbf{h} satisfy the normalization condition,

$$\iint e \cdot e ds = \iint h \cdot h ds = 1 \quad (4)$$

It is known that E_{11}^z mode of the dielectric image line cannot be expressed in a simple form of the modal vector because of the composite dielectric-air geometry. To obtain a concise analytical formulation, an equivalent waveguide concept is introduced. This concept is based on the field profile of the E_{11}^z mode, which is similar to the TE_{10} mode bounded by a rectangular metallic enclosure. To begin with, the modal functions for the dielectric image line with a perfect reflect plane can be written in the same way as the dominant TE_{10} mode of the rectangular waveguide with an appropriately efficient dielectric constant. This is done by

$$e_1 = \sqrt{\frac{2}{ab}} \hat{a}_z \sin \frac{\pi y}{a} e^{-j\beta_{11}x} \quad (5)$$

$$h_1 = \sqrt{\frac{2}{ab}} \left[j \frac{\pi}{\beta_{11}a} \hat{a}_x \cos \frac{\pi y}{a} - \hat{a}_y \sin \frac{\pi y}{a} \right] e^{-j\beta_{11}x} \quad (6)$$

in which β_{11} refers to the propagation constant of the E_{11}^z mode, and a and b are the width and height of dielectric guide respectively.

The normalized modal vectors for the microstrip line can also be obtained from the equivalence of the microstrip line to a parallel plate waveguide model, which is well documented in [8]. Thus

$$e_2 = \hat{a}_z \sqrt{\frac{1}{Dh}} e^{-j\beta y} \quad (7)$$

$$h_2 = \hat{a}_x \sqrt{\frac{1}{Dh}} e^{-j\beta y} \quad (8)$$

in which D is the effective width of the parallel plate, and h is the height of microstrip line. Note that the length of the aperture slot does not affect the equivalent waveguide model since the coupling between the microstrip and the dielectric guide is determined separately by the small aperture coupling theory. The modeling error comes basically from the intrinsic accuracy of the coupling theory. Generally speaking, a smaller geometry of the coupling aperture yields better modeling accuracy.

The small aperture in the common wall between dielectric guide and microstrip line can be replaced by its equivalent electric and magnetic dipoles. The equivalent electric and magnetic dipole moments P and M, respectively, are given by [9]

$$P = -\alpha_e n n \cdot E_n \quad (9)$$

$$M = -\hat{\alpha}_m \cdot H_t \quad (10)$$

where E_n and H_n are normal electric and tangential magnetic fields in the primary guide at the aperture. α_e is the electric polarizability of the aperture, and α_m is the dyadic magnetic polarizability of the aperture.

The amplitude of the modal voltage induced in the microstrip line due to the electric dipole and magnetic dipole that is located at the center of dielectric guide is given by

$$V_e^+ = V_e^- = \frac{j\omega\epsilon\alpha_e}{2y_0} \sqrt{\frac{2}{abDh}} \quad (11)$$

$$V_m^+ = V_m^- = 0 \quad (12)$$

and the expression for coupling is obtained as

$$C^+(dB) = 10 \log_{10} \left(\frac{P_2^+}{P_1^-} \right) = 10 \log_{10} \left[\frac{2}{abDh} \left(\frac{\omega\epsilon\alpha_e}{2\sqrt{y_{10}y_0}} \right)^2 \right] \quad (13)$$

where P_1 and P_2 are the power carried by dielectric guide and microstrip line respectively, y_{10} and y_0 are the characteristic wave admittance of the dielectric guide and microstrip line respectively.

The analysis was implemented in a computer code to calculate the characteristic of the coupling factor from the dielectric image line to the microstrip line. Figure 9 shows the theoretical coupling factor between dielectric guide and microstrip line at 28 GHz. The geometrical parameters are: dielectric guide width $a=2.54$ mm, dielectric guide height $b=1.27$ mm, dielectric constant of the dielectric guide $\epsilon_r=10.5$, microstrip width $d=0.76$ mm, microstrip substrate thickness $h=0.254$ mm and dielectric constant of microstrip substrate $\epsilon_m=2.2$. And

the horizontal coordinate axis is the slot length of the coupling aperture, w is the width of the slot. It appears that the coupling factor increases with the increasing of the size of the coupling slot.

A test fixture with two waveguide-to-dielectric image line launchers at one side and two microstrip-to-waveguide launchers at another side, which can be used to test the coupling between dielectric image line and microstrip line is designed and fabricated. The coupling level between the dielectric guide and the microstrip line is measured. We can find a fairly good agreement between the experimental and theoretical results.

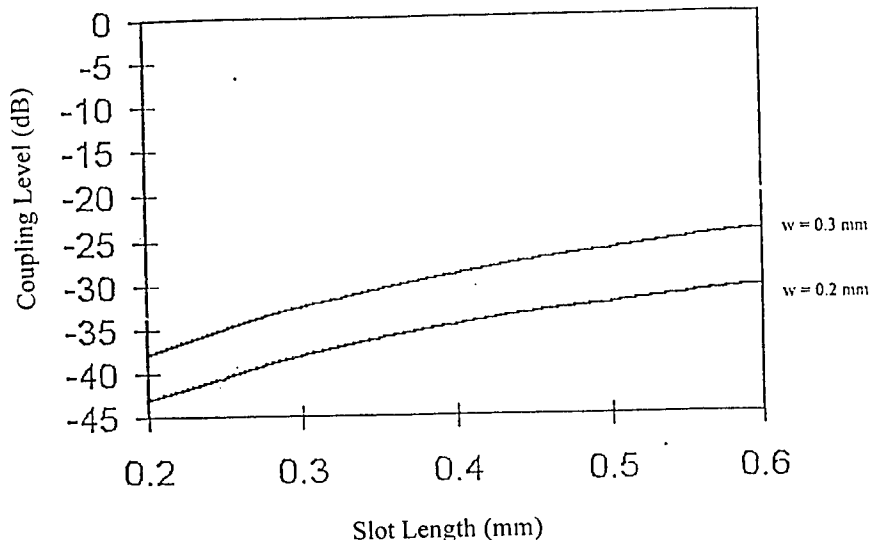


Fig. 9 Theoretical coupling factor at Ka-band.

4. SCANNING ARRAY DESIGN APPROACH

The aperture coupled microstrip antenna array fed by dielectric guide is studied on the basis of the analysis of dielectric guide, microstrip antenna, microstrip to dielectric guide coupling and waveguide to dielectric guide transition.

The microstrip patch antenna array is designed at 28 GHz. The width of the patch is 4.2 mm and the length of the patch is 3.4 mm. The feed line impedance is 100Ω and its length is $\lambda_g/4$. Fig. 10 shows the calculated impedance of the patch with the $\lambda_g/4$ feed line in the Smith Chart. The sweep frequency is from 27 GHz to 29 GHz. The reference input impedance is 100Ω . It is noticed that the patch antenna with the $\lambda_g/4$ feed line is matched very well to 50Ω input impedance at 28GHz.

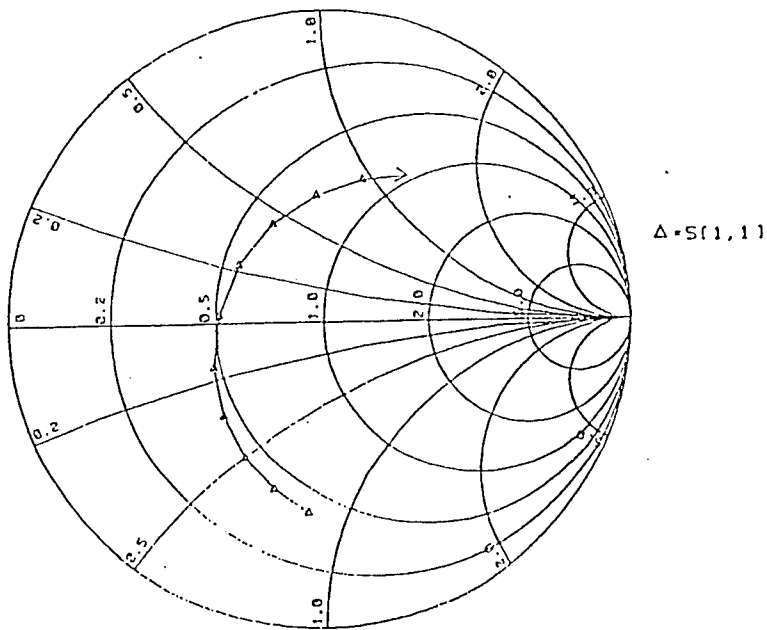


Fig. 10. Patch impedance with the feed line.

To get a required H-plane radiation pattern, the Chebychev amplitude distribution is used in the linear antenna array design. To get the required current distribution, the microstrip feed network is optimized by matching the impedance at each junction. The aperture size of each coupling slot of the Ka-band 4 x 6 microstrip antenna array fed by the dielectric waveguide was calculated by using the small aperture coupling theory to get the required current distribution. The propagation constant of the dielectric guide at 28 GHz was calculated by using the

method described in section 2. The distance between each linear antenna array was determined to get a broadside radiation pattern. The distance between each antenna patch in elevation direction was determined by keeping one waveguide wavelength in the microstrip feed line. The microstrip antenna patch size was calculated so that it can resonate at the given frequency.

Figure 11 shows the drawing of the 4×6 antenna array with its feed network. Figure 12 shows the return loss at junction A and Fig. 13 shows the return loss at junction B. It is noticed that the return losses at these two points are very low at center frequency.

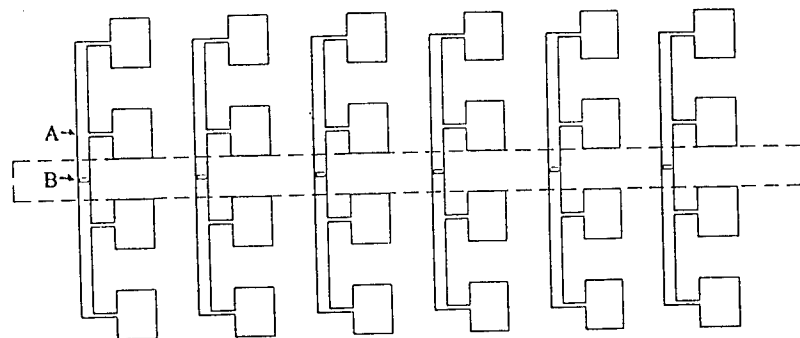


Fig. 11. Drawing of the 4×6 antenna array with feed network

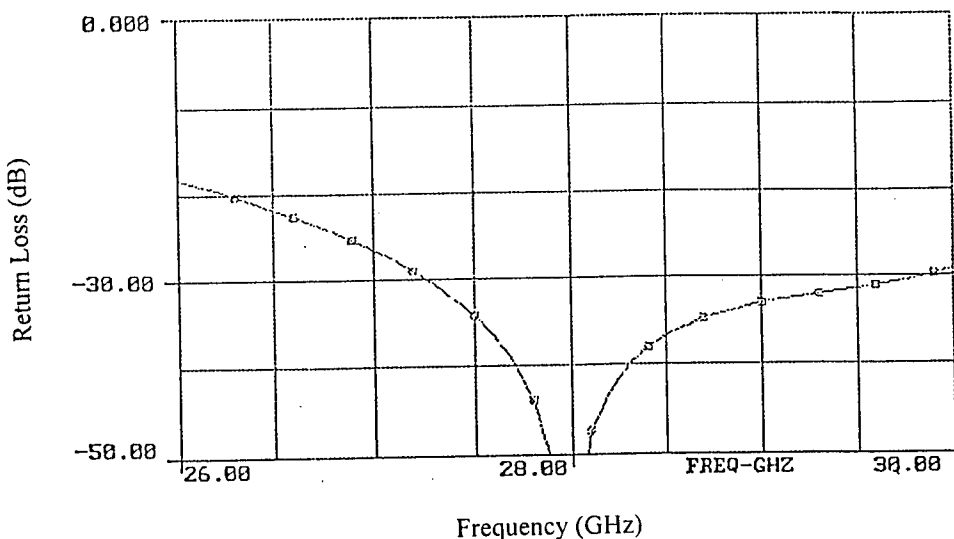


Fig. 12. Return loss at junction A

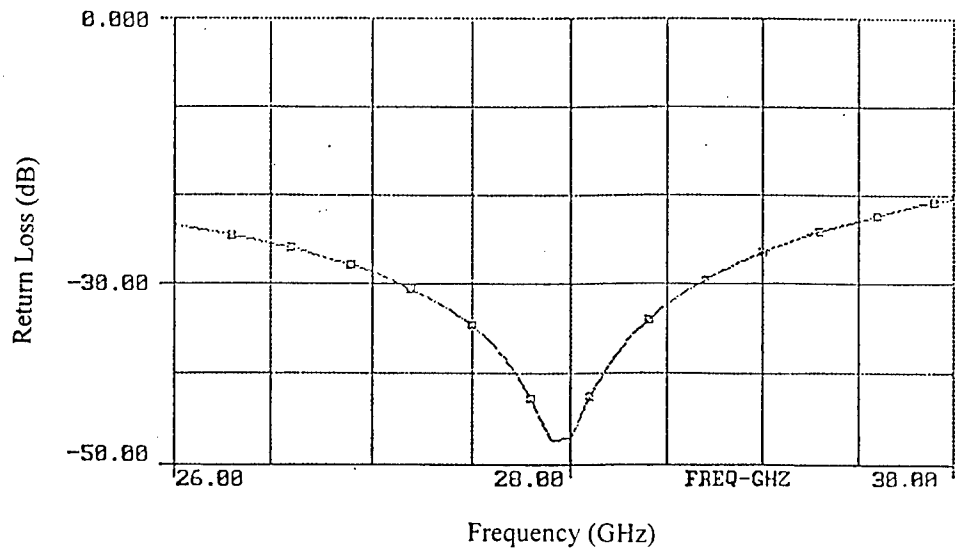


Fig. 13. Return loss at junction B

Figure 14 shows the theoretical E-plane radiation pattern. The calculated beam width at E-plane is 9.5° . Figure 15 shows the H-plane radiation pattern. The theoretical beam width at H-plane is 19.5° .

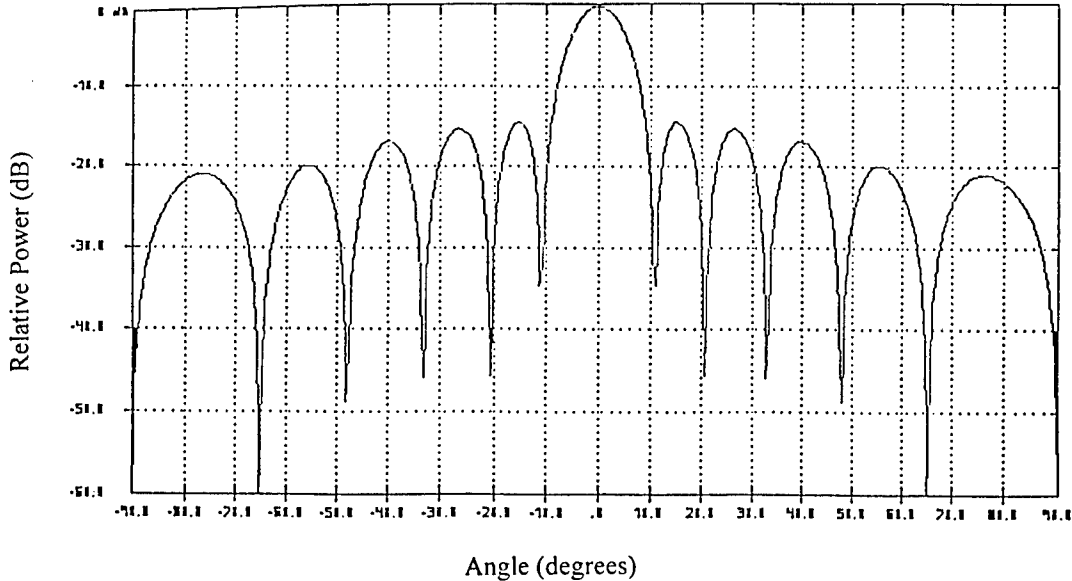


Fig. 14. Theoretical E-plane radiation pattern.

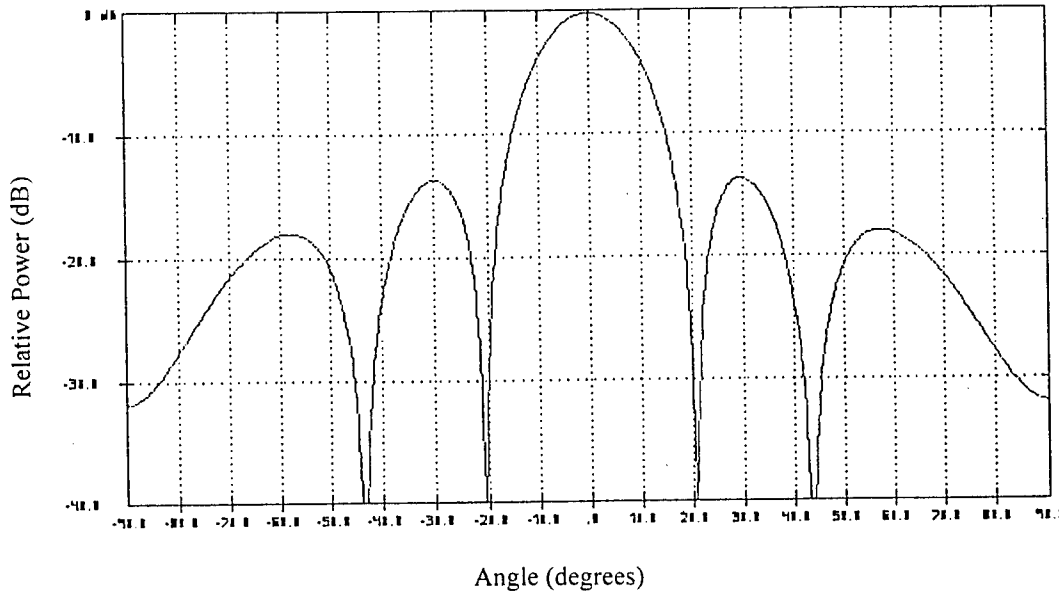


Fig. 15. Theoretical H-plane radiation pattern.

Figure 16 and 17 show the simulation results of the E-plane radiation pattern when the phase shift between each linear antenna array is 80 degree and 120 degree respectively. It is noticed that the grating lobe of the small antenna array appears with the increasing of the shifted phase in the main dielectric feed line.

The 4 x 6 microstrip antenna array fed by the dielectric guide was assembled by carefully aligning the dielectric guide on the antenna base plate. The dielectric guide was glued on the antenna ground plane. The microstrip antenna substrate was clipped between the base plate and the launchers. A 80 mm x 60 mm window was opened on the base plate. Then some absorbing material was put around the edges of the window to reduce the reflection and diffraction. The adjustable reflecting back plate was designed by using two movable screws in the middle of the plate and four fixed screws with tension springs at the corners of the plate. By tuning the two movable screws, the distance between the dielectric guide and the back plate can be changed smoothly.

The return loss of the microstrip antenna array fed by the dielectric guide is measured by using the network analyzer. Figure 18 shows the measured return loss when the distance between the dielectric guide and the conducting back plate is 2 mil. Figure 19 shows the measured return loss when the distance between the

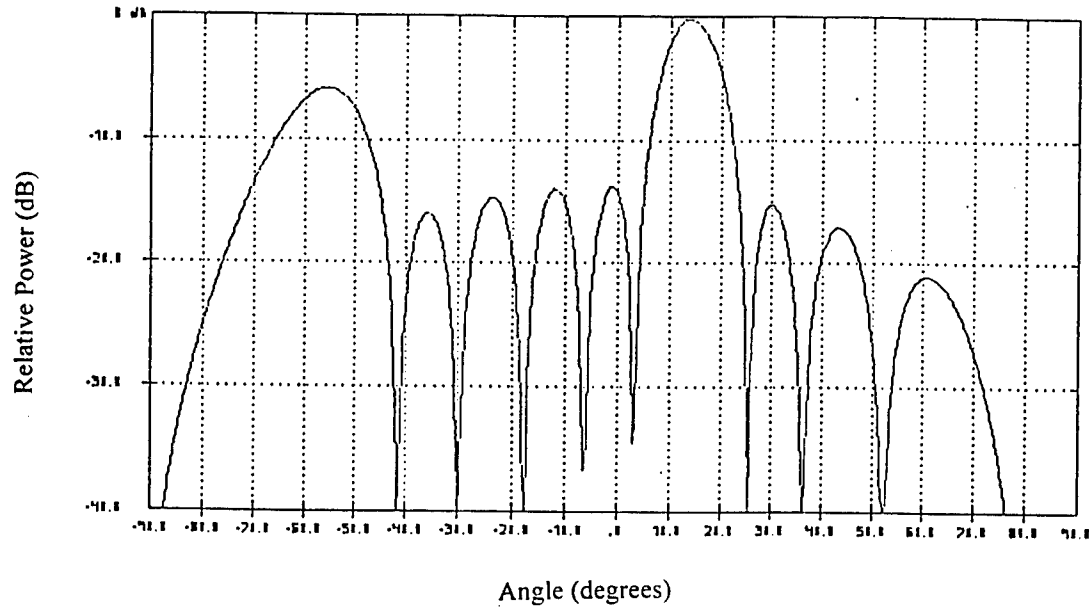


Fig. 16. E-plane radiation pattern with 80 degree phase shift.

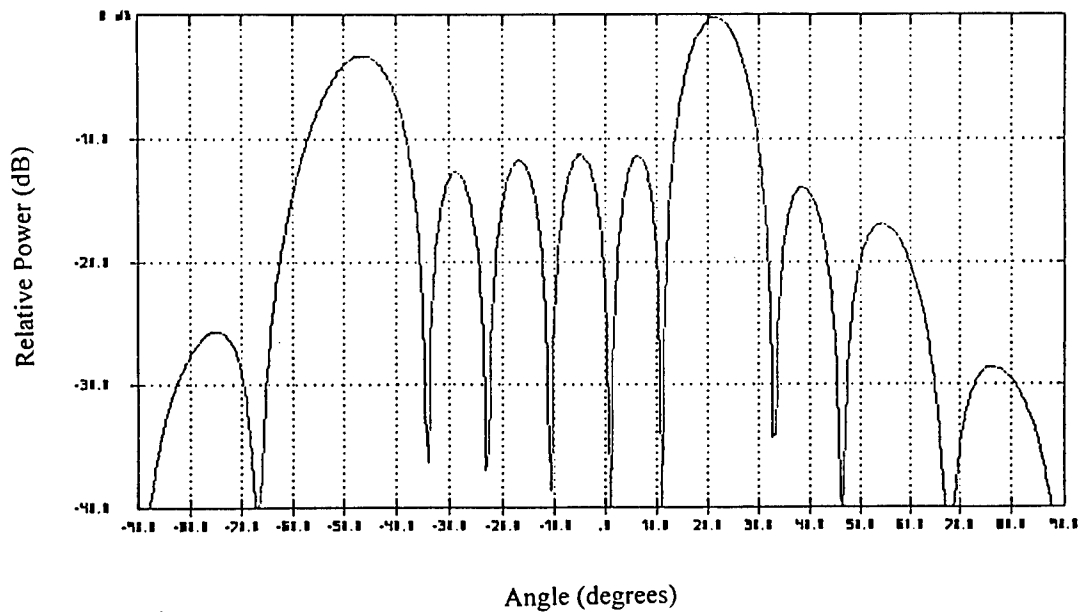


Fig. 17. E-plane radiation pattern with 120 degree phase shift.

dielectric guide and the conducting back plate is 300 mil. Figure 20 shows the measured E-plane radiation patterns when the conducting back plate are 2 mil and 300 mil away from the dielectric guide. It is shown that the main beam of the antenna array steered about 30 degrees. It is noticed that a higher grating lobe appeared when the phase shift in the main feed line is larger. This phenomenon is also predicted by the theoretical results in Fig. 16 and Fig. 17. Figure 21 shows the measured H-plane radiation pattern. The H-plane side lobe is about -10.5 dB and the 3-dB beam width is 15 degrees.

Compared with the theoretical results in Fig. 14 and Fig. 15, the side lobe level in both E-plane and H-plane is about 3 ~ 5 dB higher than the theoretical results due to the etching tolerance of the microstrip antenna and the alignment tolerance of the coupling slots and the dielectric guide. It is also noticed that when the distance between the dielectric guide and the conducting plate is changed, the beam width of the main beam is also changed. This is reasonable since the propagation constant is different with the position change of the conducting plate, the amount of power coupled to each linear array is also different.

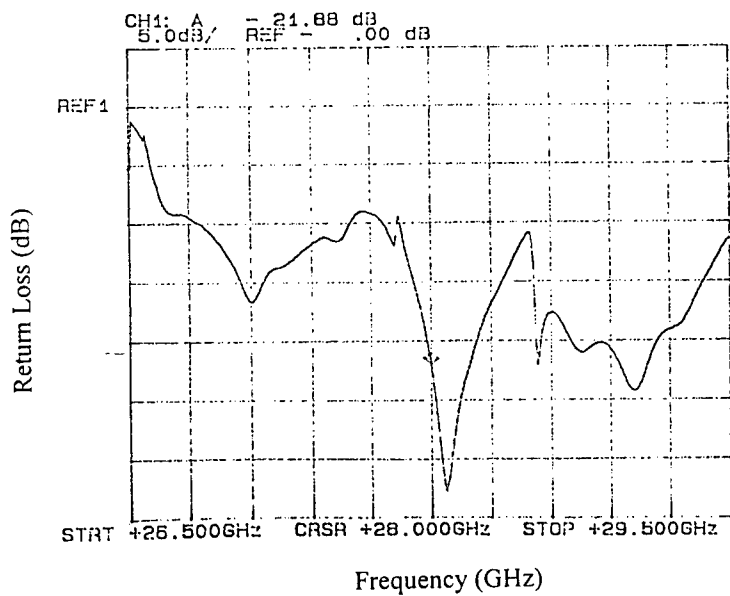


Fig. 18. Measured return loss of the antenna array (d=2 mil).

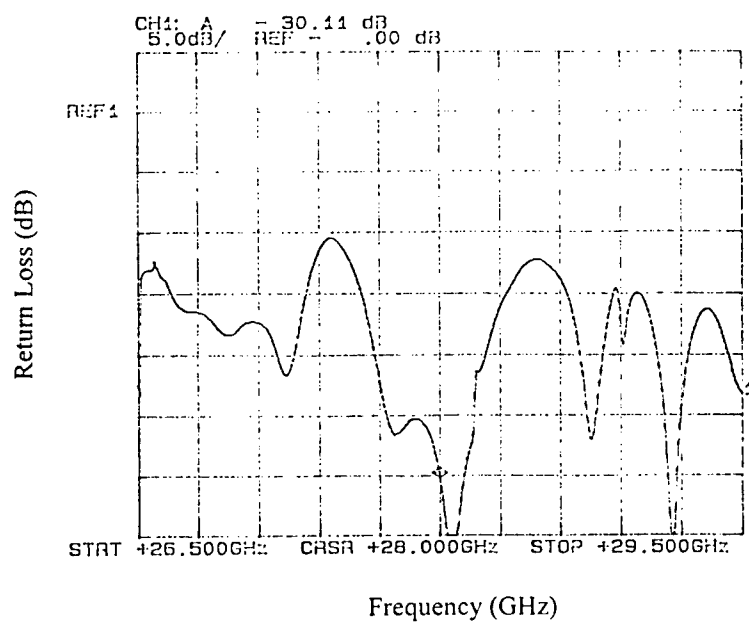


Fig. 19. Measured return loss of the antenna array (d=300 mil).

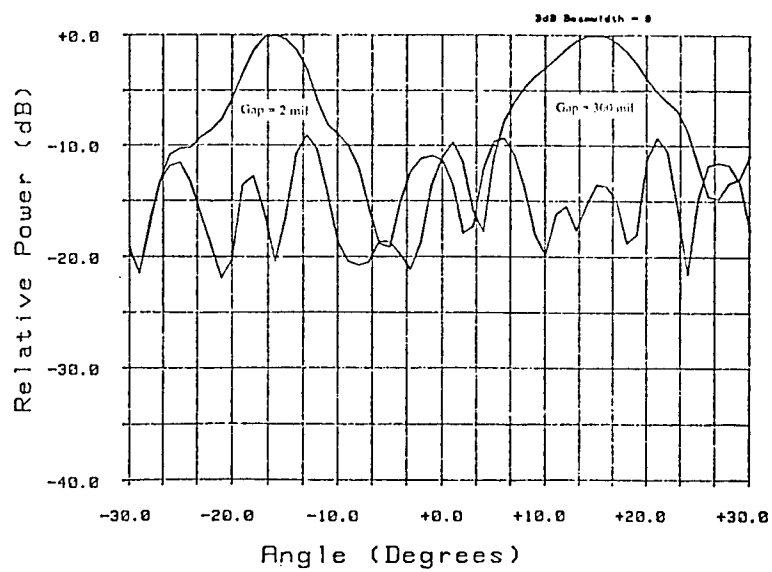


Fig. 20. Measured E-plane radiation pattern (d=2 mil and d=300 mil).

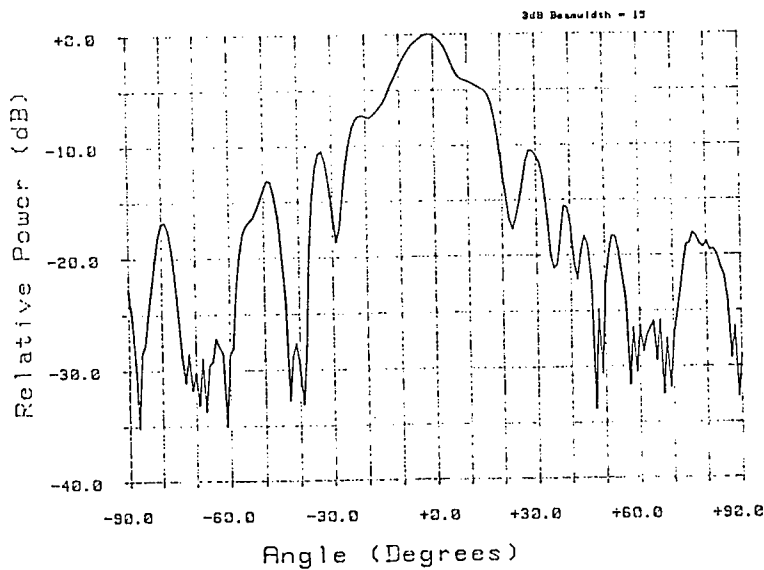


Fig. 21. Measured H-plane radiation pattern.

5. CONCLUSION

The scanning mechanism of a Ka-band 4 x 6 microstrip antenna array fed by the dielectric waveguide has been successfully demonstrated and the scanning angle of the antenna array is measured. This investigation of the aperture coupled microstrip antenna array fed by dielectric guide has demonstrated the feasibility of this novel structure as an scanning antenna at millimeter wave frequencies. The unique combination of aperture coupled patch arrays, a dielectric waveguide feed line and a mechanically variable phase shifter applied to the dielectric feed line is studied. This structure is projected to have lower losses, higher gain and lower cost than existing technology.

This study focuses on single plane scanning because it is a logical first step toward two plane scanning. The technique developed will be capable of extension to two plane scanning in the future, if successful in the single plane applications. The focus is also on a near term commercial application so that the emerging technology can be brought to maturity and low cost because of market demand. The two promising commercial opportunities, Ku band satellite

communications and the W band forward looking radar, are both very attractive for commercialization in the near future.

From the evaluation and selection of the baseline mechanical positioning technologies, we noticed that piezo-electric phase-shifter could not be found for the range of motion and load requirements in the current application. Voice coils are a less expensive method and they are relative small and provide large displacements for a load. A rotating CAM shaft approach provides another more compact and even more cost effective mechanical adjustment method for the conducting wall.

For a practical application in a radar system, several issues still need to be solved, such as the side lobe level, main lobe beam width changing with the position of the reflecting plate and the coupling aperture matching problem. Further investigation may be carried out to optimize the impedance matching of the dielectric guide to the slot aperture and to the microstrip linear array.

ACKNOWLEDGMENT

Portion of this work was sponsored by the NASA Lewis Research Center, Cleveland, Ohio and the Air Force Research Laboratory, Hanscom AFB, MA.

REFERENCES

- [1] S. Sanzgiri, et al, "Active Subarray Module Development for Ka Band Satellite Communication Systems", p. 860, IEEE reference 0-7803-2009-3/94.
- [2] J. Navarro, "Active Inverted stripline Circular Patch Antennas for Spatial Power Combining", *IEEE Transactions on Microwave Theory and Techniques*, v41, no. 10, October 1993, p 1856.
- [3] R. York and R. Compton, "Mode locked Oscillator Arrays", *IEEE Microwave Guided Wave Letters*, v1, pp. 215-218, Aug. 1991.
- [4] R. York and R. Compton, "Experimental Observation and Simulation of Mode Locking Phenomena in Coupled Oscillator Arrays", *J. App. Phys.*, v71, no. 6, 15 March 1992.
- [5] R. York and R. Compton, "Coupled Oscillator Arrays for Millimeter Wave Power Combining and Mode Locking", *1992 IEEE MTTs Digest*, pp. 429-432.
- [6] J. A. Navarro and K. Chang, "Integrated Active Antennas and Spatial Power Combining", John Wiley and Sons, Inc., New York, 1996.

- [7] M. Dydyk, "Image line: A promising medium for EHF circuits," *Microwaves*, vol. 20, pp. 71-80, Apr. 1981.
- [8] R. F. Harrington, *Time Harmonic Electromagnetic Fields*. New York: MaGraw Hill, 1961.
- [9] R. E. Collin, *Field Theory of Guided Waves*. New York: MacGraw Hill, 1960.

A LOW-PROFILE LUNEBERG LENS AIRBORNE GBS ANTENNA

Mark E. Rayner

Datron/Transco Inc.

200 W. Los Angeles Ave.

Simi Valley, CA 93065

805.579.2955

mrayner@dtsi.com

ABSTRACT

Satellite receiving antenna installations on airborne platforms, shipboard, motor vehicles, dwellings, etc., are often required to be flush mounted to a mounting surface. If the antenna is to be attached to the surface of an aircraft, the profile must be sufficiently small to prevent intolerable drag and air stream turbulence. In addition to this low-profile requirement, the antenna must have excellent wide-angle scanning performance, and good gain properties over the full range of motion. This can be realized by either scanning the beam mechanically, electrically, or as a combination of both. This paper describes a low-profile GBS antenna solution capable of satisfying these requirements and producing a wide-angle mechanical scanning beam with relatively constant antenna gain over the scanned coverage area.

1.0 INTRODUCTION

Current interest in the Armed Forces' use of Global Broadcast Service (GBS) communications system has stimulated the ongoing need for a low-profile airborne antenna system. To that end Datron is currently under contract to design, develop, and deliver one prototype GBS Receive Only (R/O) antenna system to the US Air Force Research Laboratory, Information Connectivity Branch (AFRL/IFGC). The GBS R/O antenna system is essentially a scaled version of the commercial patented Datron/Transco DBS-2400 airborne antenna system which is a Ku-Band receive only antenna designed to provide live Direct Broadcast Satellite (DBS) service for commercial and general aviation (see figure 1). The GBS antenna system is 32" in diameter by 6" tall and can easily fit into a radome that protrudes no more than 6.5" above the aircraft. The current plan is for prototype evaluation to occur aboard a Wright Patterson C-135 aircraft during the fourth quarter of 1998. The GBS version will have a G/T > 10 dB/K; is circularly polarized and able to scan from 10° to 90° in elevation and 360 degrees continuously in azimuth.

The GBS R/O antenna system consists of four hemispherical "Luneberg" lenses mounted on a 32" diameter conducting ground plane illuminated by four dual linearly polarized broadband feed horns. The four horns are phase combined through a coaxial transmission line combiner and amplified by 2 LNAs. The Horizontal (H) and Vertical (V) components are fed to a 0/90 Hybrid to produce Left Hand Circular Polarization (LHCP) and Right Hand Circular Polarization (RHCP). Output from this device is in turn fed into a transfer switch and then into a single channel rotary joint. The output runs into the communications processing equipment. The antenna ground plane is mounted on bearings and is rotated using low cost stepper motors. The 4 horn feed array is pivoted above the Luneberg Lens' using a stepper motor. A self contained servo control system (see figure 2) uses an Integrated Avionics Encoder (IAE) provided by AFRL that generates pointing commands to position the antenna to receive from a satellite

sending the GBS signals. The entire antenna assembly is mounted on the top surface of the airplane's fuselage and enclosed in a protective radome. Interface connections to control and communications equipment is provided via three, 1" diameter penetrations in the fuselage.

Details of the major components of this antenna system will be discussed first, followed by a brief description of the measured performance of the dual polarized GBS antenna, and concluded with a brief description of what takes place on the next phase.

2.0 HEMISPHERICAL LENS ON GROUNDPLANE

A low profile requirement forces medium gain and high gain antenna (> 20 dBi) to have an approximately rectangular, or elliptical radiating aperture with a width-to-height ratio greater than about four. Considering only those antennas whose beam is scanned mechanically in azimuth and elevation, it was assumed that planar and phased array antennas, and elliptically shaped reflector antennas, either cost much more, are less reliable, or have greater height than a hemispherical lens antenna as described here. An expansion of this reasoning and detailed evaluation of these types of antennas resulted in choosing a lens to obtain a low profile antenna.

A Luneberg lens is commonly used in wide angle scanning applications such as radar reflectors for targets, drones, etc. In the most basic form they exist as a sphere of low-loss dielectric material. The index of refraction or relative dielectric constant ϵ_r , varies with distance r from the center of the sphere. For a classical Luneberg lens, ϵ_r has a value of one at the outer surface of the sphere and two at its center. Specifically (1),

$$\epsilon_r = 2 - \left(\frac{2r}{D} \right)^2 \quad (1)$$

Where D is the lens diameter. Usually, the desired variation in ϵ_r is approximated by N concentric spherical shells, each with a value of ϵ_m equal to the desired value of ϵ_r near the center of the shell. The refraction property of the lens can be represented by the ray paths traveled by energy radiated by the illuminator, as shown in figure 3. These paths are those of a cross-section of the sphere and they show that all rays pass through the lens and form a plane wavefront propagating in the direction diametrically opposite the illuminator. That is, with respect to a reference line, the central ray makes an angle θ on entering the lens and $-\theta$ on exiting the lens. Since the lens has spherical symmetry, the illuminator can be scanned over 4π steradians and the radiation properties, gain, beamwidth, and sidelobes will not vary regardless of location on the illuminator, or where the beam points. This property is extremely useful to the wide-angle scanning antenna.

When a Hemispherical Luneberg Lens (HLL) antenna is mounted on a ground plane, the ray paths are reflected at the surface of the ground plane. At the reflector's surface, the rays follow paths in accordance with Snell's law: the angle of incidence, ϕ_i is equal to the angle of reflection ϕ_r , as shown in figure 4. For classical planar arrays, or reflector antennas, the antenna aperture's effective vertical dimension must be less than h , the maximum allowable protrusion of the

antenna above the ground plane. Thus for low beam direction angles, θ , measured from the ground plane, the vertical dimension of a classical planar array, or reflector antenna, cannot exceed h . By comparison, the vertical dimension of the HLL antenna's aperture is always $2h$ – it is inherently twice as large as the maximum allowable vertical height of a planar array, or reflector antenna. The inherently larger aperture of a HLL results in antenna gain up to twice that of a conventional array antenna, or reflector antenna, with the same aperture height, h , above the ground plane.

3.0 FEED HORNS

Exciting the Luneberg lens' are four, open circuited circular waveguide feed horns. Figure 5 shows details of the feed horns mounted on the single machined channel coaxial combiner. Each horn measures 0.8" in diameter, and has single horizontal and single vertical probes that excite the cavity. The probes are oriented orthogonally from each other, with the entire feed horn being perpendicular in orientation to the lens. Each horn is spaced approximately 0.55" from the surface of the lens – the last dielectric shell being air with a constant of 1.0, the actual focal distance is dependent on the phase center of the horn. The broadband feed horn is a scaled version of the feed used successfully for both the commercial DBS-2100 and DBS-2400 airborne antenna systems.

4.0 COMBINING NETWORK

The final combining network, which collects input power, consists of low loss machined channel coaxial line and waveguide. Each horn has a vertical (V) and horizontal (H) port. It takes two steps to combine four like-polarization ports into a single port. The first step is to use two 2-to-1 combiners. Integrated coaxial lines are used in connecting two vertical ports to the combiner module. The second step is connecting the two 2-to-1 combiners together again using a waveguide T-section to generate either a vertical or a horizontal output. The waveguide combiner uses a machined channel coaxial combining circuit for the first 2-to-1 combination, and standard WR42 waveguide with a typical insertion loss level of 0.1 dB/ft at 20 GHz for the last combination. Care is taken in this combining circuit to ensure phase matching between the four hemispheres is optimized otherwise performance will be degraded. Typical phase matching is to better than 10 degrees on both the H and V channels.

After phase combining, the H and V components are amplified via high gain, Low Noise Amplifiers (LNAs). Each amplifier has a gain of 45 dB, and noise figure of better than 1.5 dB.

The output ports of the two LNAs are connected to a 90 degree hybrid coupler (polarizer) to convert the linear polarization into LHC and RHC Polarization.

5.0 MEASURED PERFORMANCE

The GBS antenna system was evaluated for performance on the Datron range for patterns, gains, and polarization isolation across frequency, elevation angle, and polarization. The testing utilized a far field test setup as shown in figure 6. Figure 7 presents a composite pattern graph showing the measured patterns at 20°, 40°, 60°, 80° and 90° elevation cuts. Gain varies by about 2 dB from 10° to 90° in elevation, this can be attributed to two things; at the higher elevation angle blockage comes into play from the feed-stick itself, reducing some of the effective

aperture. Second, at lower elevation angles the loss in gain is due to the use of a finite ground plane that is not large enough to produce the required image, and scattering effect at the edge of the ground plane. Sidelobe level peaks at approximately -16 dBp. Figure 8 shows the antenna gain performance across elevation angles from 10° to 90° , and from 19.2 GHz to 21.2 GHz in frequency. The gain varies by up to 2 dB across elevation for any specific frequency, notice the dip out of gain at 80 degrees for all three frequencies (attributed above to the blockage effect). Notice also the difference in gain between the 19.2 GHz and 21.2 GHz is approximately 1 dB, about what one would expect from the difference in wavelength. This leads us to conclude the HLL suffers from no unusual frequency dependent effects, and is inherently broadband enough to handle wideband GBS downlinks, or spread spectrum Milstar downlinks.

Figure 9 presents the polarization isolation level across elevation angle from 10° to 90° , and from 19.2 GHz to 21.2 GHz in frequency. The Figure 10 and 11 present the cross polarization isolation levels, and calculated axial ratio performance vs. elevation angle for the frequency range from 19.2 GHz to 21.2 GHz. The HLL exhibits extremely good cross-polarization performance across the band.

Based on the tested gain of the antenna, and measured component values through the rest of the resistive circuit pre and post LNAs, an antenna system G/T has been computed. Figure 13 provides a spreadsheet calculation of GBS antenna system G/T. Resistive losses in front of the LNA are a combination of measurement and engineering estimate. Spillover is conservatively estimated to be 0.3 dB, and the blockage effects of the elevation motor, combined with any ground plane interference is estimated at 0.5 dB. Resistive loss in the combining circuit is very low but measured at 0.6 dB for the combination of the machined channel coax line, and WR42 waveguide. The LNAs have gains of better than 45 dB to ensure setting of the system noise temperature. After amplification, approximately 5.3 dB of loss is measured through the hybrid, cables, transfer switch, rotary joint, and bulkhead connector. This loss has negligible effect on system noise temperature, having been set by the LNAs. Calculation of the overall system G/T yields a conservative 10 dB/K, which assumes a receiver noise figure of 12 dB and an integrated sky temperature of 23 K.

6.0 MISCELLANEOUS

The antenna system layout is shown in figure 12 and emphasizes the major components of the Datron GBS antenna. The antenna is mounted on bearings and driven by a large diameter ring gear. The azimuth motor is mounted on the ground plane, behind the lens to preclude blockage. The elevation motor is mounted to the front of the lens but out of direct Line Of Sight (LOS) to the satellite at most elevation angles. This motor moves the feed stick about bearing mounted support arms. Worst case blockage is calculated to be 0.36 dB at 10 degrees elevation. Stepper motors are used for both axes, and have proven very effective from our experience on the DBS airborne product line. The antenna is accurately close loop pointed via the Integrated Avionics Encoder (IAE) provided by AFRL. The IAE obtains high dynamic inertial coordinates (pitch, roll, and yaw) from the aircraft Inertial Reference System (IRS) and process other navigation information and satellite ephemeris to provide pointing commands to the antenna. An outer tracking loop is closed around this inner loop to eliminate long term drifts, bias, or any other mis-pointing induced by the IAE, IRS, or aircraft. Power estimates are to be derived from the on-board receiver.

7.0 WHAT'S NEXT

Demonstrations will take place in January of 1999 for the receive only GBS antenna system. The satellite to be used for this demonstration is UFO-8, which contains a Ka-Band communications payload. Installation will be on a C-135, which will be provided by the Air Force Flight Test Center out of Wright Patterson Air Force Base. To perform the demonstration a radome must be designed. Datron/Transco is currently in the process of developing the radome. The radome will be 60" wide by 70" long by 9" tall to accommodate the antenna from Phase II. Datron/Transco is currently examining several different materials and comparing structural vs. RF properties at 20 GHz and 44 GHz for the Radome.

Phase II is to bring full duplex operation to the HLL design. Datron/Transco is partially funded by AFRL for a 20/44 GHz antenna system much like the above mentioned antenna system. We have increased the lens size from 7" in diameter to 8" in diameter, which will increase the gain by about 1 dB. Current design studies and trades taking place are lens shell design, dual feed vs. broadband feed design, combiner architecture, and diplexer filter. All these factors will be optimized to provide an antenna that maximizes EIRP and G/T performance. The goal is to fly a demonstration of this antenna system on the same aircraft by the end of 1999.

8.0 SUMMARY

This paper has described the Datron/Transco R/O antenna system currently being built for AFRL. It has been shown that the antenna gain remains fairly constant over elevation travel range, and the gain over frequency varied primarily with the wavelength. It was also shown that the polarization isolation is very good and remains constant over full travel range and frequency. The G/T analysis showed better than 10 dB/K when taking into account the measured gain of the antenna, and measured/estimated losses, and noise temperatures of the receive system. The calculated G/T compares quite favorably with the design goal set fourth by AFRL over 2 years ago.

9.0 ACKNOWLEDGEMENTS

Datron/Transco would like to acknowledge the expertise and efforts of Leon J. Ricardi of Creative Engineering who remains an invaluable source of information and ideas. Datron/Transco also appreciates the continued support and guidance provided by Paul J. Oleski at AFRL/IFGC, without their support none of this would have been possible.

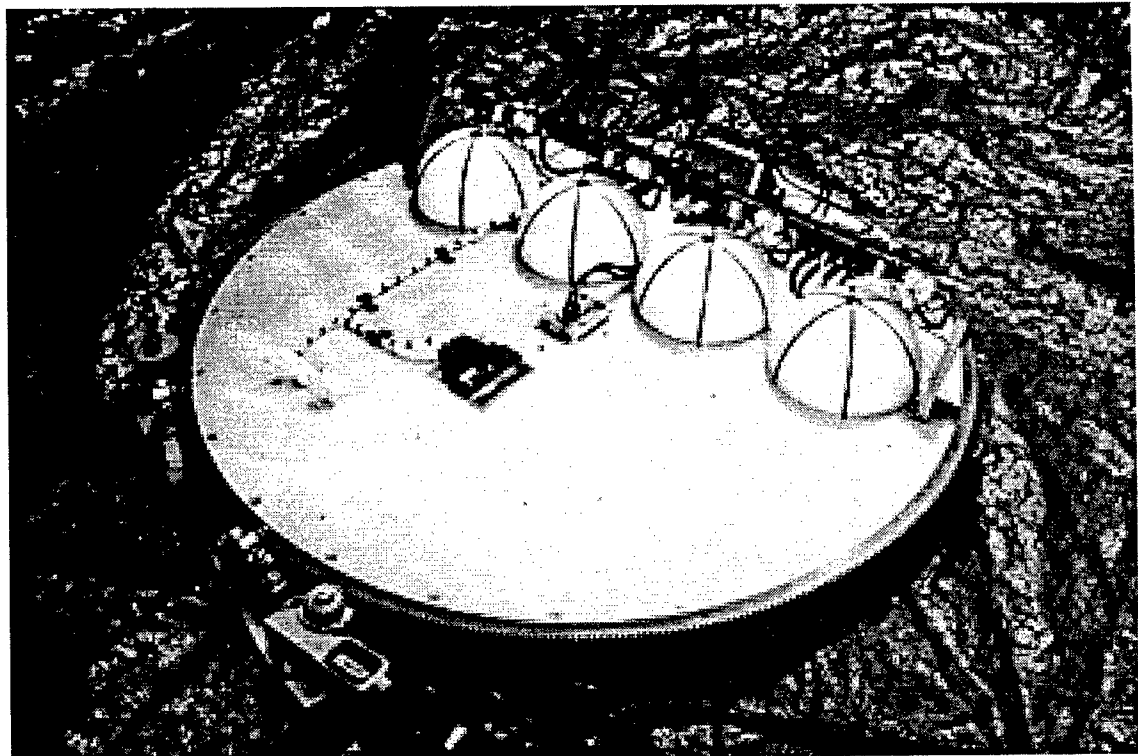


Figure 1, DBS-2400 Four hemisphere Luneberg lens. (US Patent # 5,781,163)

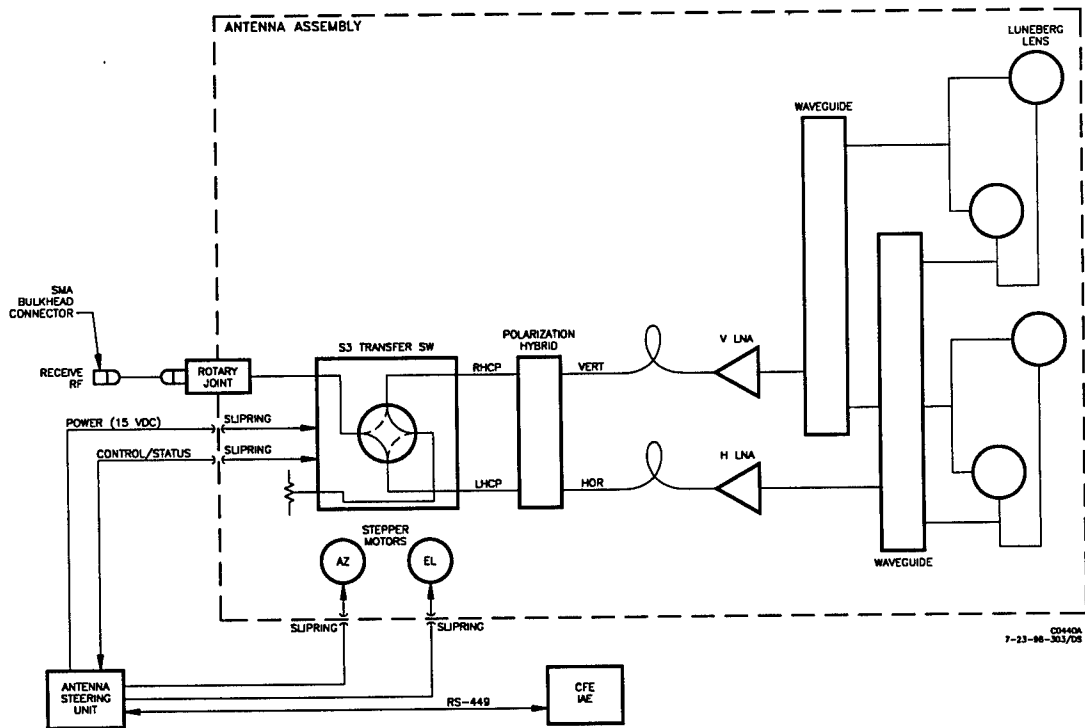


Figure 2 GBS Antenna System Block Diagram

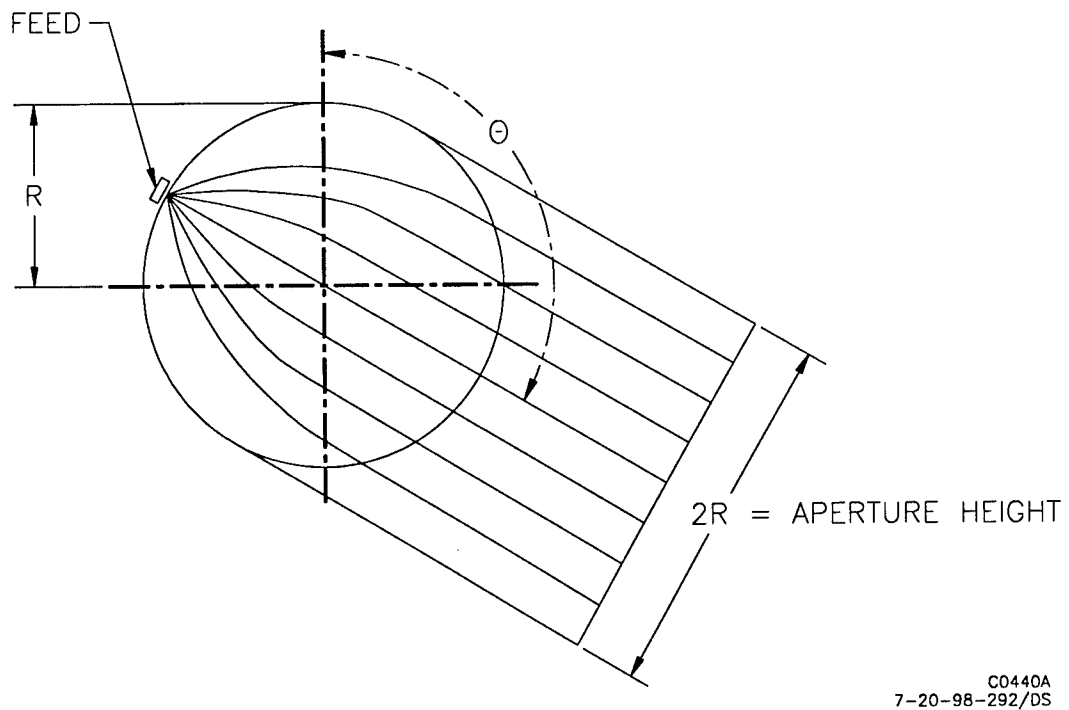


Figure 3 Ray Geometry for Luneberg lens sphere.

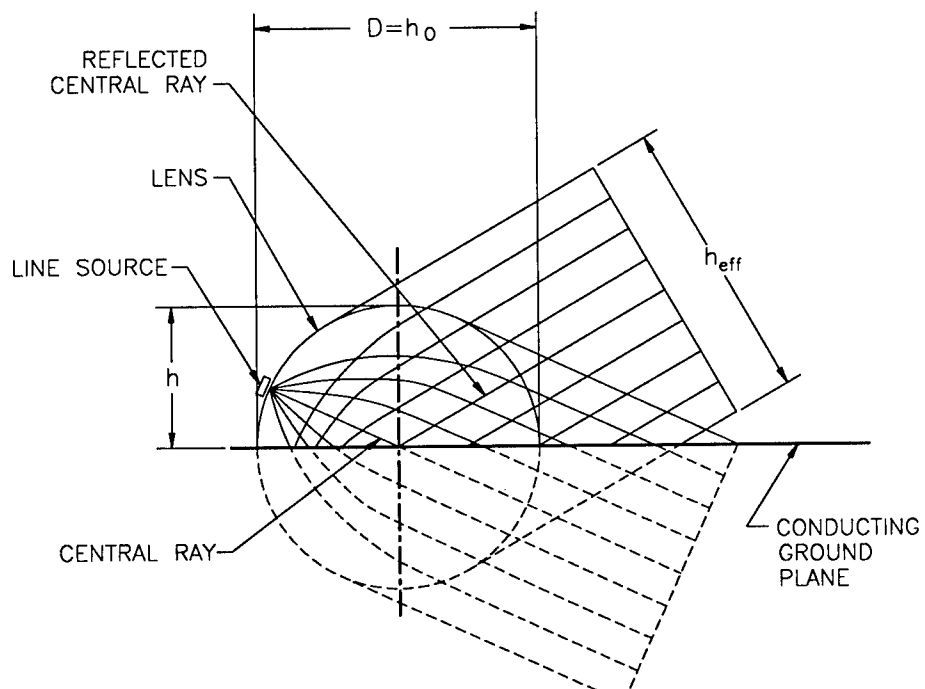


Figure 4 Ray Geometry for a Hemispherical Lens Design

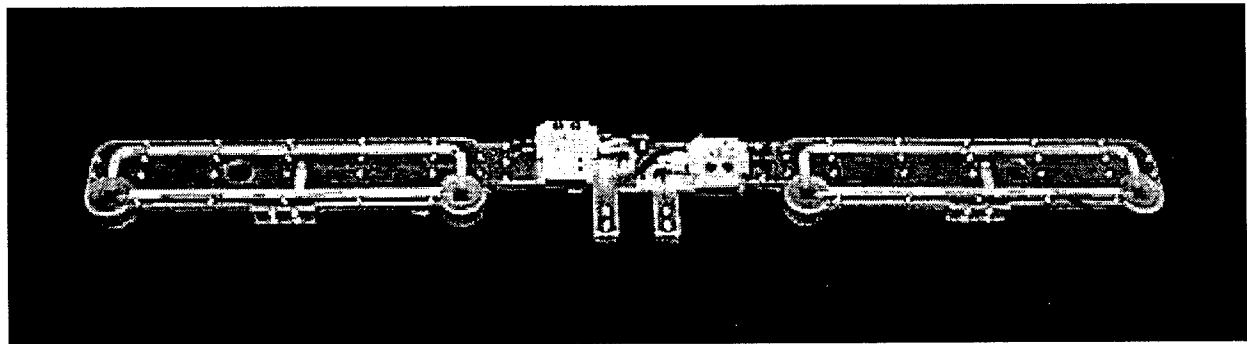


Figure 5 GBS Antenna System Feed Stick Assembly

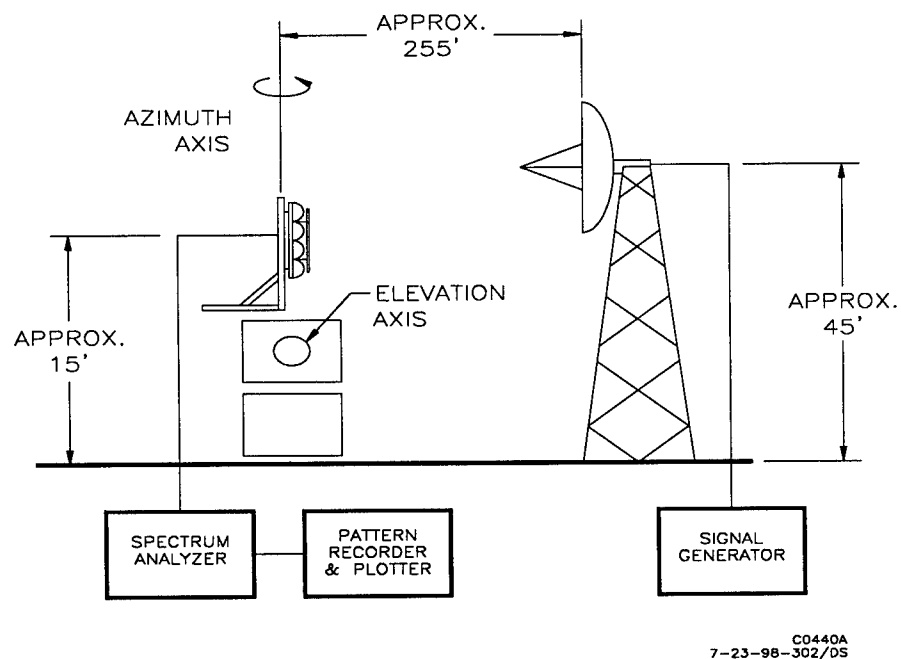


Figure 6 Field Test Setup for Measuring Antenna Patterns

FILENAME: GBS.024, GBS.023, GBS.026, GBS.027, GBS.028
FREQ: 20.200 GHz, 20.20, 20.20, 20.20, 20.20
POLARIZATION: LINEAR
B = 0.00 Degrees

03/17/98 14:47:12
PLOT: Channel 1
Data:

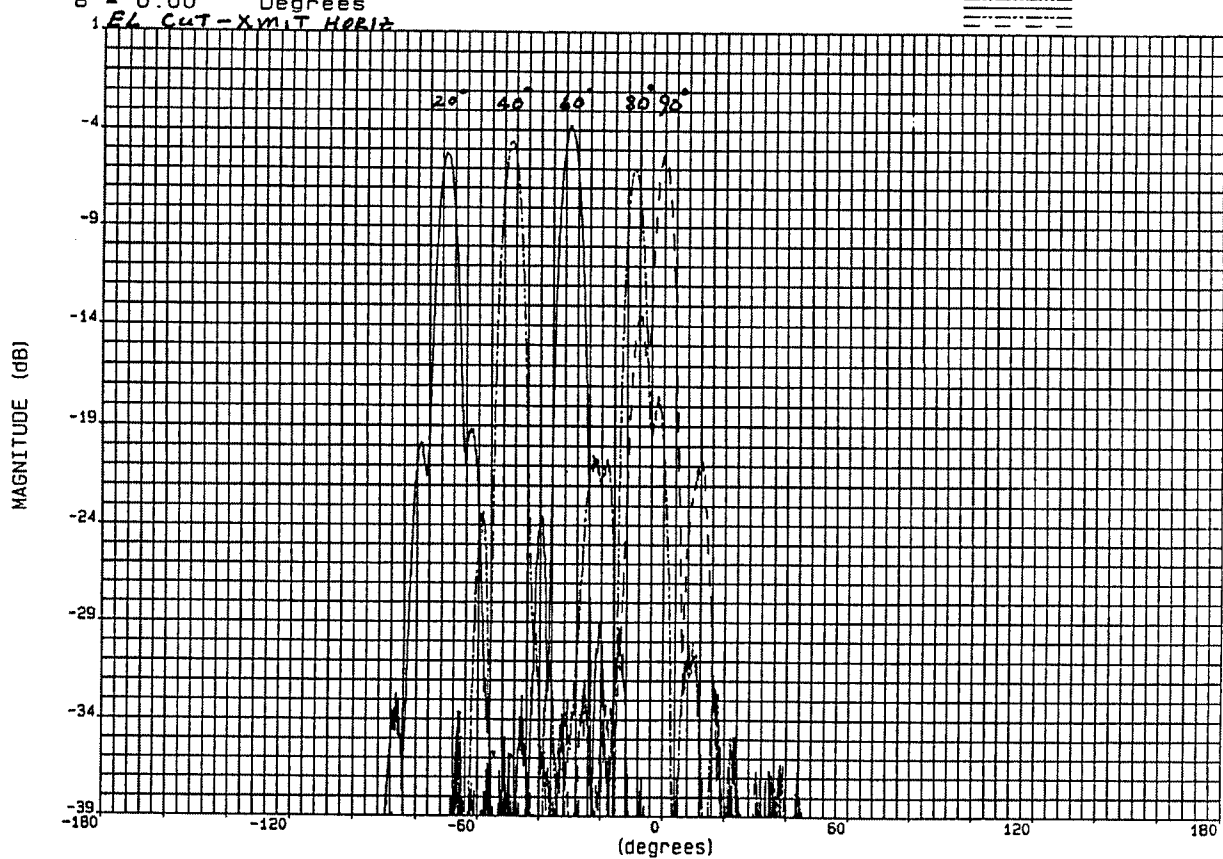


Figure 7 Composite Antenna Patterns for Elevation Cuts from 20° to 90° .

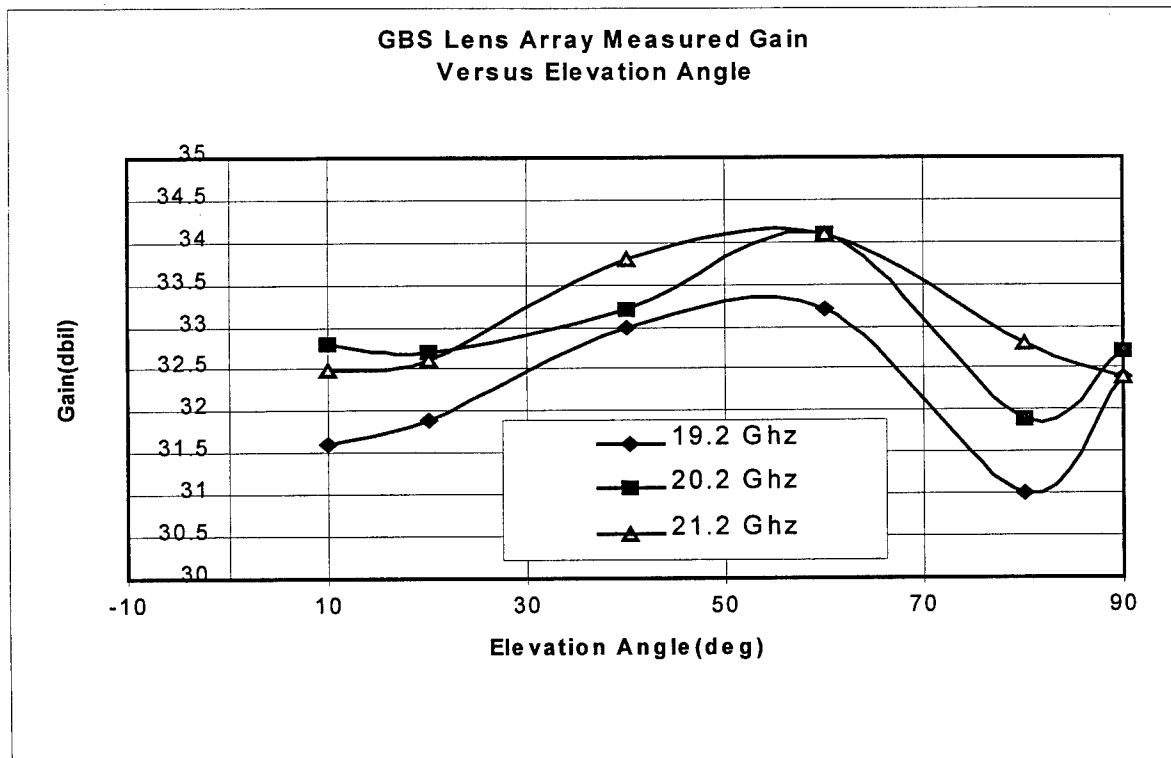


Figure 8 Antenna Gain Performance vs. Elevation Angles and Frequency.

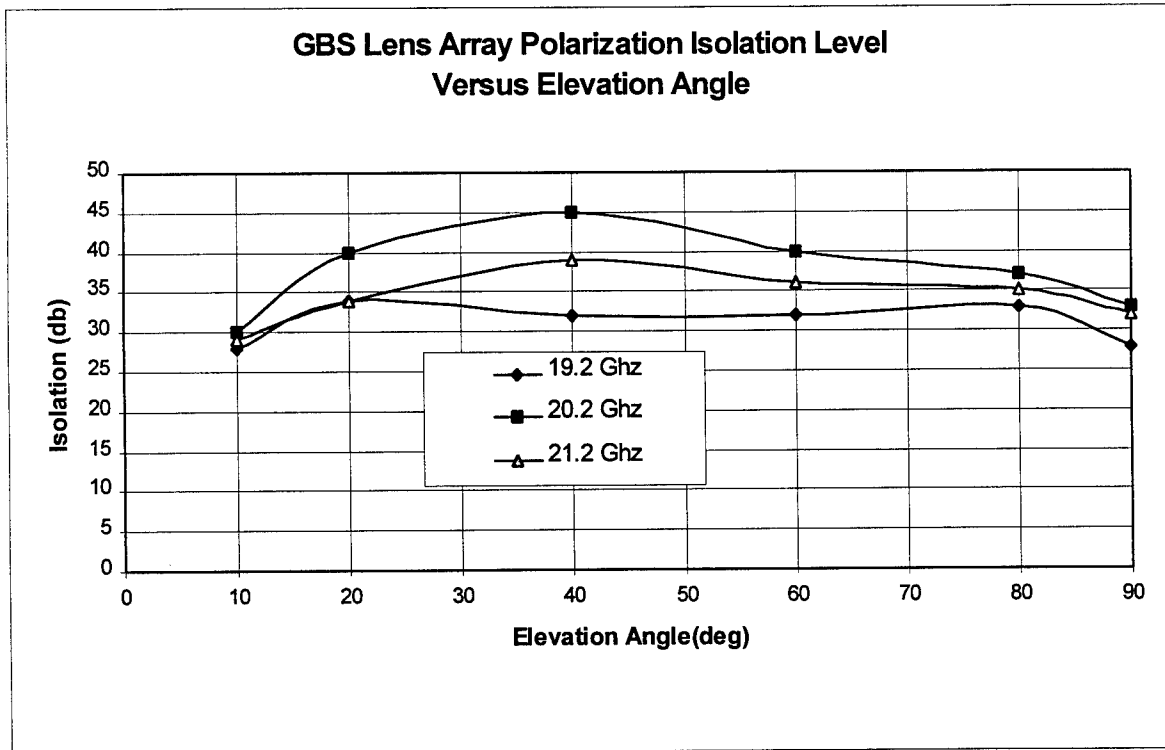


Figure 9 Antenna Polarization Isolation Level vs. Elevation Angles and Frequency.

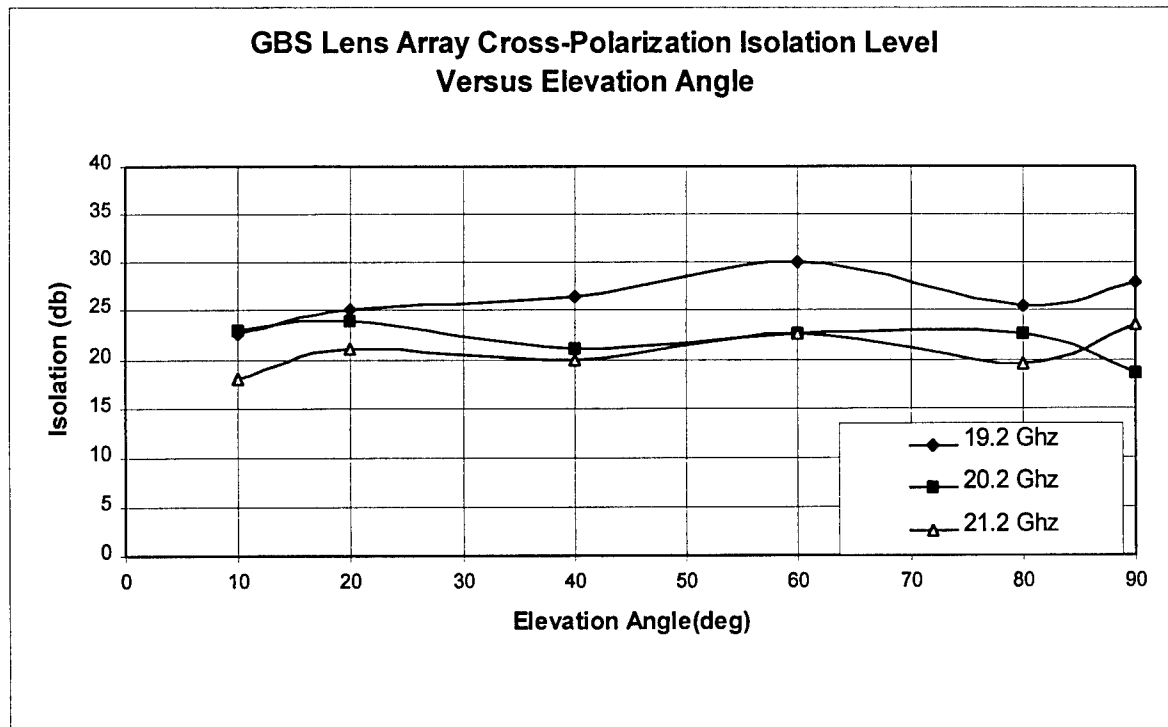


Figure 10 Antenna Cross-Polarization Isolation Level vs Elevation Angles and Frequency.

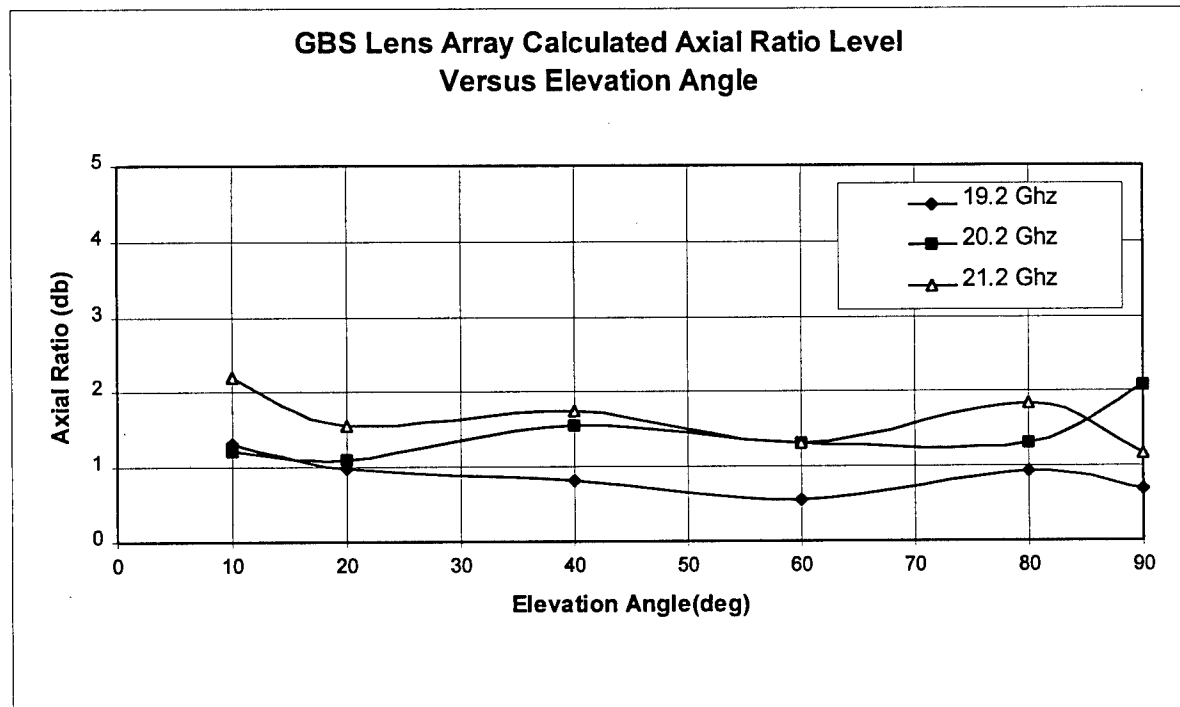


Figure 11 Antenna Axial Ratio Level vs. Elevation Angles and Frequency.

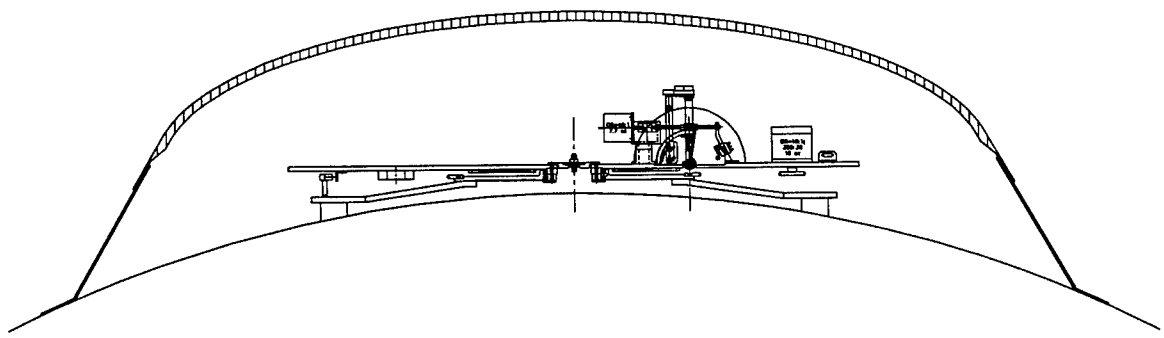


Figure 12 Antenna Mechanical Layout.

FREQUENCY (MHz)	AMBIENT TEMP (K)	ANTENNA EFF (%)	ANTENNA BEAMWIDTH (°)
21200.0	290.0	70.0	2.89

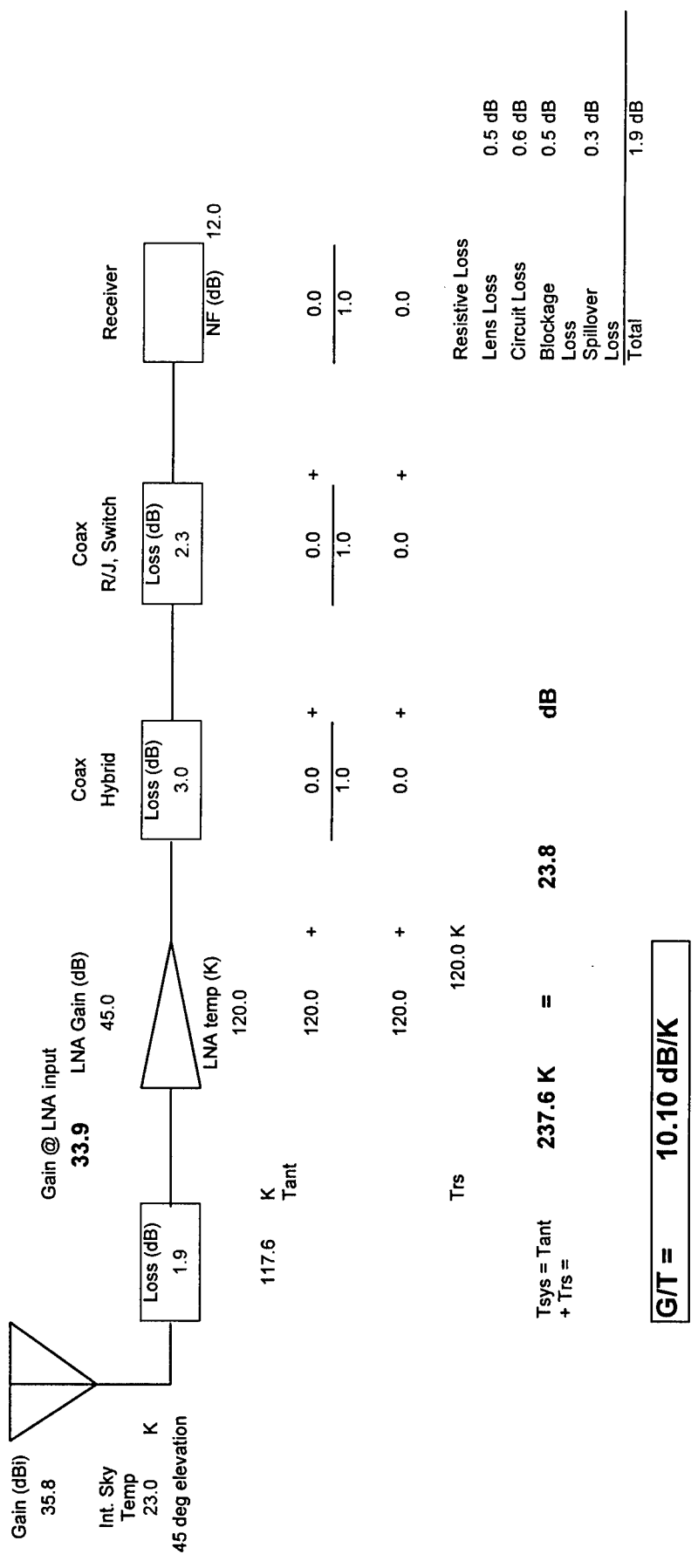


Figure 13

GBS Antenna System Gain over Temperature Spreadsheet.

Experiments on an Optically Controlled 2-D Scanning Antenna¹

George W. Webb, Stephen C. Rose, Mario S. Sanchez, and J. Martin Osterwalder

Innova Laboratories, Inc.
11199-L Sorrento Valley Road
San Diego, CA 92121-1334
Tel: (619) 452-8760
Fax: (619) 452-0478
e-mail: innova@connectnet.com

Abstract - We present results on an optically-controlled, millimeter wave (MMW) scanning antenna. The antenna employs a photo-conducting wafer in which a spatially varying plasma density is photo-injected by a computer controlled light source. The varying plasma density alters the local dielectric constant of the wafer material and allows diffractive control over incident MMW radiation. Operation has been demonstrated from 20 to 100 GHz, with beam scanning of $\pm 30^\circ$ in two-dimensions. Experimental results show that the beam can be scanned (hopped) in arbitrary directions at rates greater than 1000 hops per second with excellent control in software. Beam scanners based on this approach promise to be fast, inexpensive, and easily controlled.

¹ supported under Navy Contract No. N68936-95-C-0101

1. Introduction

Scanning antennas are necessary to form and scan an electromagnetic beam. Mechanically scanned antennas perform scanning by physically moving the antenna. Generally they are slower than desired and the precision hardware is often expensive. Electronically scanned antennas have been based on phased arrays which often employ thousands of phase shifters to individual elements or groups of elements. The phased array approach offers many advantages, but the large numbers of phase shifters make such systems costly. For this reason alternative scanning methods have been of recent interest [1-6]. We have been developing a non-mechanical beam scanner, without phase shifters, which forms and steers a beam of millimeter wave radiation using a light-modulated photoconducting antenna [3-4].

Control of the electronic properties of photoconductors with light has a long history [7]. This capability for optical control of electronic properties is under active investigation in a variety of alternative approaches to beam scanning which employ photoconductors [1-6]. Generally, these alternative approaches are motivated by a desire for higher performance at lower cost. Scanners based on our approach promise to be fast and inexpensive.

The technique described here is based upon a transient Fresnel zone plate approach in which a spatially varying density of charge carriers is created by optical injection of plasma into a semiconductor or photoconductor wafer. The photo-injected charge carriers, electrons and/or holes, alter the index of refraction of the wafer locally, particularly the imaginary part of the index, and thereby attenuate and reflect incident electromagnetic radiation. Conversely, with suitable choice of parameters, the un-illuminated parts of the semiconductor allow the incident electromagnetic waves to be transmitted. The wafer, modified by light in this way, can be made to diffract incident radiation into a beam which can be scanned. Because the wafer responds rapidly to changes in optical injection, it is possible to rapidly change the Fresnel diffractive conditions and thus rapidly change the beam direction.

2. Transient Fresnel Zone Plates

As is well known, Fresnel zone plates work by blocking radiation [8]. Figure 1 shows MMW rays from a source passing through an aperture to a detection point. Rays going through different parts of the aperture add in-phase or out-of-phase at the detector. If those rays which add out of phase are blocked, then there is a large gain in received intensity at the detection point. The aperture with necessary areas blocked is called a Fresnel zone plate.

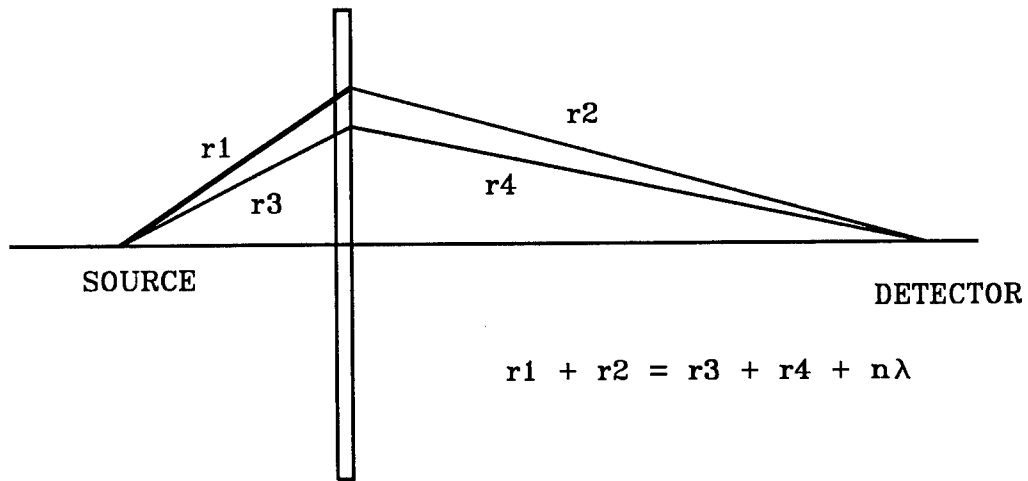
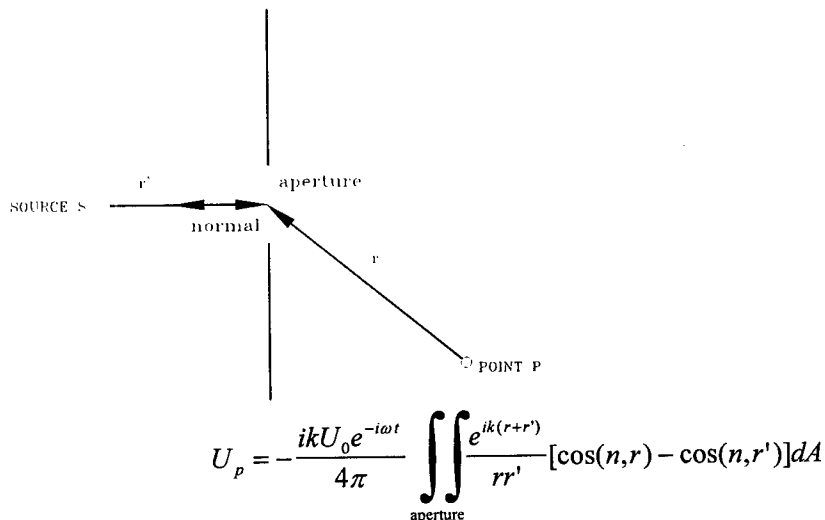


Figure 1. Illustration of path length dependence and condition for constructive interference for rays between a source and a detection point.

The amplitude of the radiation arriving at the detection point P, from a source S, is calculated by solving the Fresnel - Kirchhoff formula in the scalar amplitude approximation [8]. This is shown in Figure 2. Here the radiation from S passes through an aperture in an otherwise opaque screen to arrive at P.



U_p = integrated amplitude at P

Figure 2. Fresnel-Kirchhoff solution for integrated amplitude between source S and detection point P.

In general, rays arriving at P have a relative phase which depends on the point where they went through the aperture. The phase is determined by the exponential in the Fresnel - Kirchhoff relation and depends on the positions of S and of P. Figure 3a shows the relative phase at P of a ray plotted with a gray scale on the plane of the aperture at the point where the ray passed through the aperture. Here S and P have been chosen to be collinear with the aperture.

In Figure 3a, those rays with phase represented from white to gray are taken to be in-phase. Conversely, those rays with phase from gray to black are out-of-phase. If the out-of-phase rays were blocked, then the only rays arriving at S would be in-phase and a large increase in intensity at S would result.

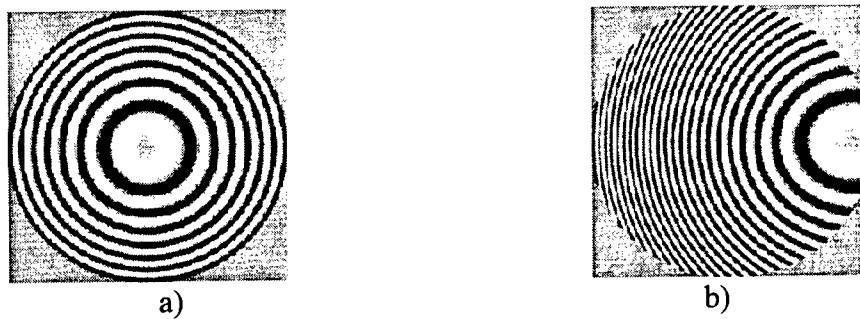


Figure 3. Gray scale plot of phase at detection point plotted on plane of aperture where ray went through aperture; source at 110 mm from 146 mm effective diameter aperture, distant detector, 94 GHz radiation. a) Detector 0° off axis, b) Detector 30° off axis.

It is evident in Figure 3 that the relative phase distribution displays the layout symmetry of S, P, and the aperture. In particular, the relative phase depends on the angle that P makes with the axis of the aperture. If the relative position of P is moved off-axis, then the distribution of relative phase at P is changed. Figure 3b shows the phase distribution when P is moved to 30° off-axis, all other parameters remaining the same. Evidently, to send a beam to this direction requires that a different ray distribution must be blocked.

The two examples of Figure 3 illustrate that to form a MMW beam in a specific direction we wish to inject a plasma selectively in a photoconductor. In order to send the beam in a new direction, we must be able to change the light pattern and thus the spatial distribution of the plasma. We therefore wish to integrate a photoconducting material with a light source having a high degree of controllability.

3. Experimental Details

For the photoconductor we have investigated a variety of materials. Experimental results are given here for Si wafers with dark resistivity in the range 1000 $\Omega\text{-cm}$, diameter of 150 mm, and thickness of 0.7 mm. For photo-injection,

light of wavelength below the band gap is used. In early testing a variable spatial distribution of light intensity was created on the wafer surface by illuminating it through optical masks which were transmissive to MMW [3-4]. Since then programmable arrays of individual lights have been employed.

Figure 4 shows two configurations. In Figure 4a, a MMW feed behind the wafer transmits through the wafer. A programmable light array projects a light pattern onto the wafer to form the Fresnel lens shaped plasma. In Figure 4b, a front feed transmits MMW through the wafer which are reflected by a MMW reflector that is transparent to the light array. The light array projects a light pattern onto the back of the wafer. In this way the MMW make a double pass through the wafer.

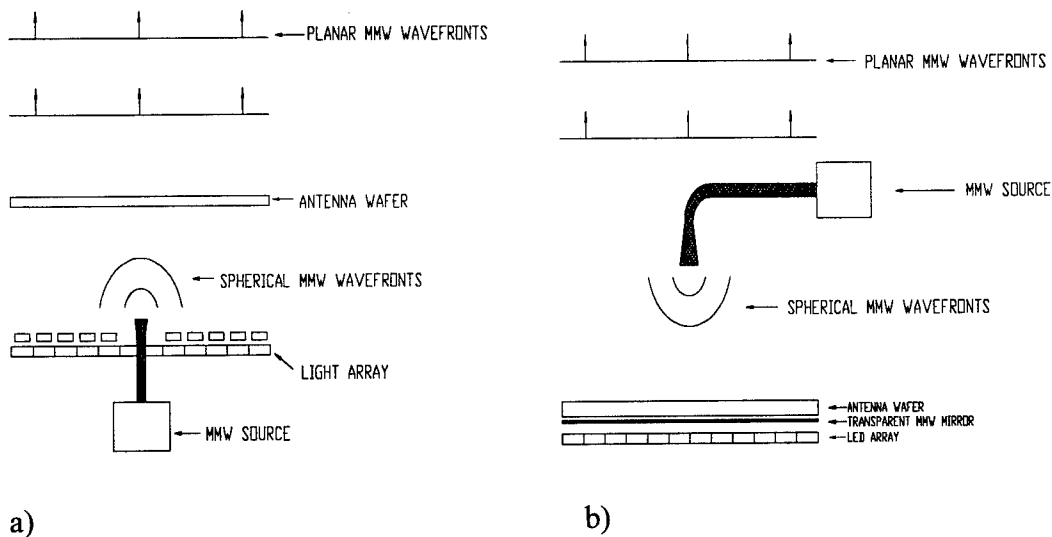


Figure 4. Antenna configurations a) back feed transmissive, b) front feed with transmissive antenna folded around optically transparent MMW mirror.

Here we will give antenna results with two programmable light arrays (PLA) in the geometry of Figure 4b, one containing 1285 LEDs and the other with 2335 LEDs, with a peak LED output at 0.88μ . The light array is controlled by a PC through a custom electronic interface. The system can switch the lights on/off at the maximum rate of 140 MHz (140M lights/sec.) The maximum rate is for the 1285 LED frame is 80K frames per second, however the overall scan rate with either PLA is limited by the properties of the photoconducting material.

4. Experimental Results

The antenna was tested as a *transmitter* with a detector placed about 8 m away and as a *receiver* with the source and detector interchanged. No difference was observed, reciprocity appearing to be obeyed. Figure 5 displays two dimensional scan data at 35 GHz in which the beam is hopped at a rate of 470 hops/second on a $30^\circ \times 30^\circ$ square grid with 1° grid spacing. The detector was collinear with the antenna axis at $(0^\circ, 0^\circ)$. The main lobe is evident when the beam is directed at the detector. Beam width is at the diffraction limit for this wavelength and effective diameter of 146 mm.

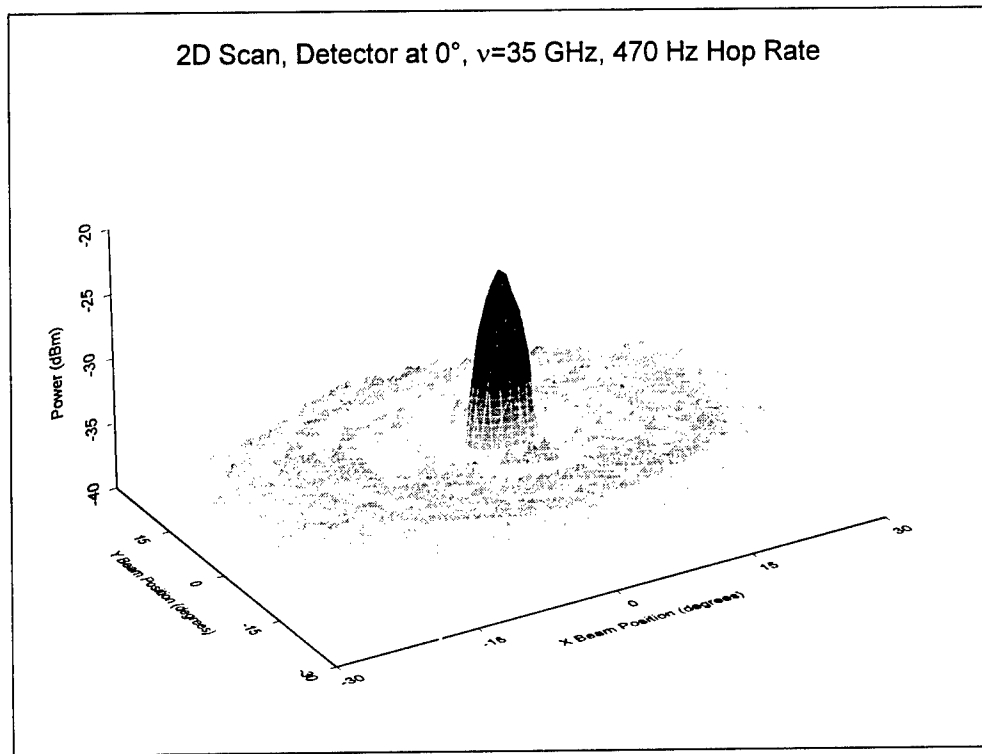


Figure 5. 35 GHz beam scanned on $30^\circ \times 30^\circ$ square grid with 1° grid spacing at 470 Hz with 1285 PLA.

35 GHz beam profile data are shown in Figure 6 where H-plane beam scans were used with the antenna configured as a receiver and the source remote. There are four separate beam scans with the source moved off-axis to 0° , 10° , 20° , and 30° . These scans correspond to scanning the beam in X in Figure 5 with Y=0 $^\circ$ with the source at the designated positions. Main lobe intensity does diminish with off-axis steering. Beam widths, however, are not strongly affected.

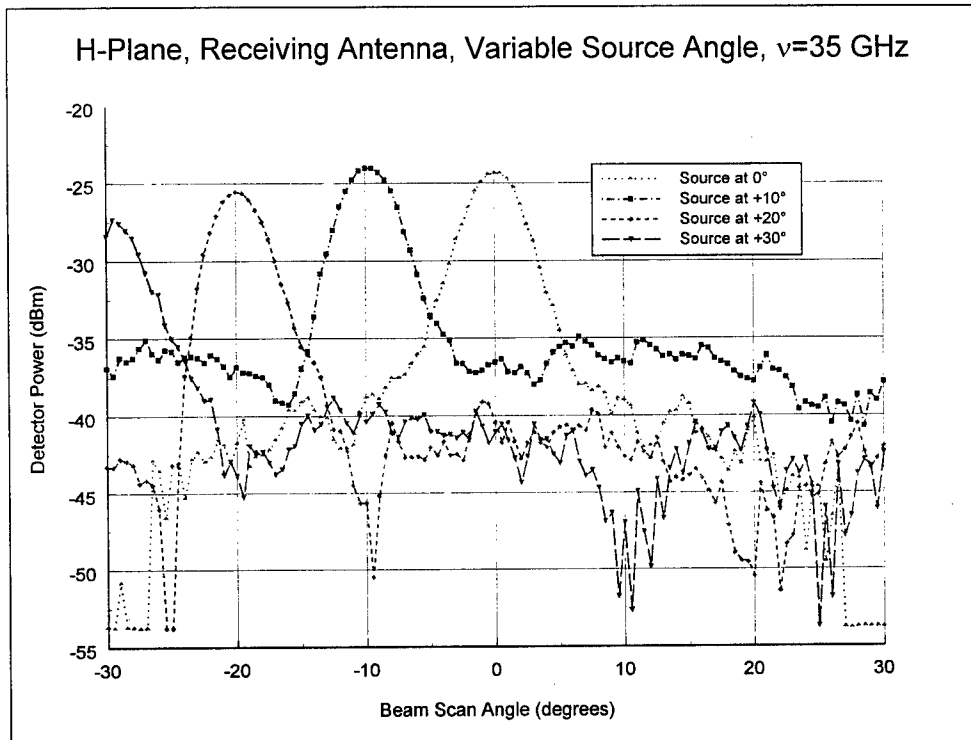


Figure 6. 35 GHz H-plane beam scans from -30° to 30° with the relative angle varied between antenna and source using 1285 PLA.

Two dimensional scan data at 94 GHz are shown in Figure 7. Here the beam was hopped on a $30^{\circ} \times 30^{\circ}$ square grid with a 1° grid spacing at a rate of 1000 hops/second. The detector was again collinear with the antenna axis at $(0^{\circ}, 0^{\circ})$ and the 1285 PLA was used. The main lobe is evident when the beam is directed at the detector, as are the side lobes and nulls when the light pattern is changed to direct the beam off-axis.

The beam width and pointing resolution at 94 GHz are illustrated Figure 8. The beam has been hopped in 0.005° steps. The 3 dB beam width is 1.7° , close to the diffraction limit for 94 GHz and 146 mm effective diameter. It can be seen that successive hops are resolved, but that the resolution limit is being approached. Outside the main lobe, there is asymmetry at low power, possibly due to slight asymmetries in the experimental apparatus

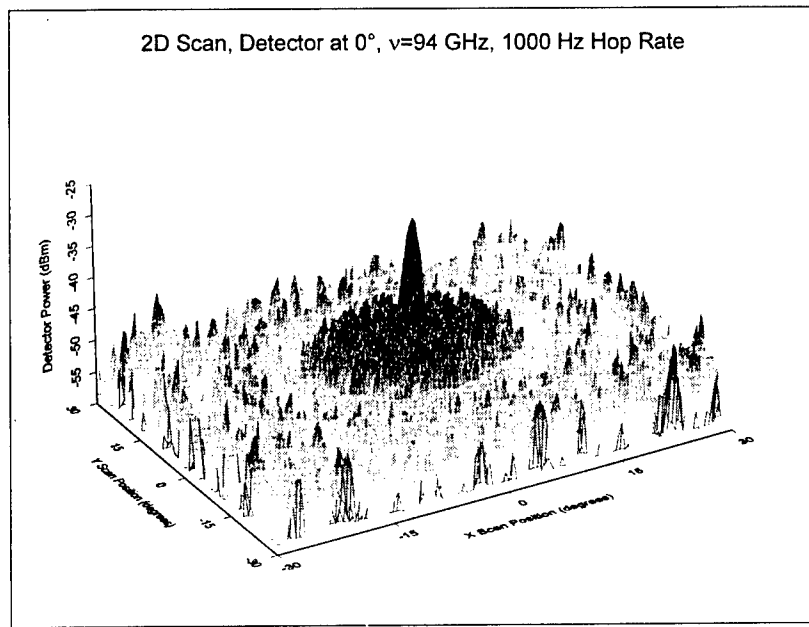


Figure 7. 94 GHz beam scanned on $30^\circ \times 30^\circ$ square grid with 1° grid spacing at 1000 Hz with 1285 PLA.

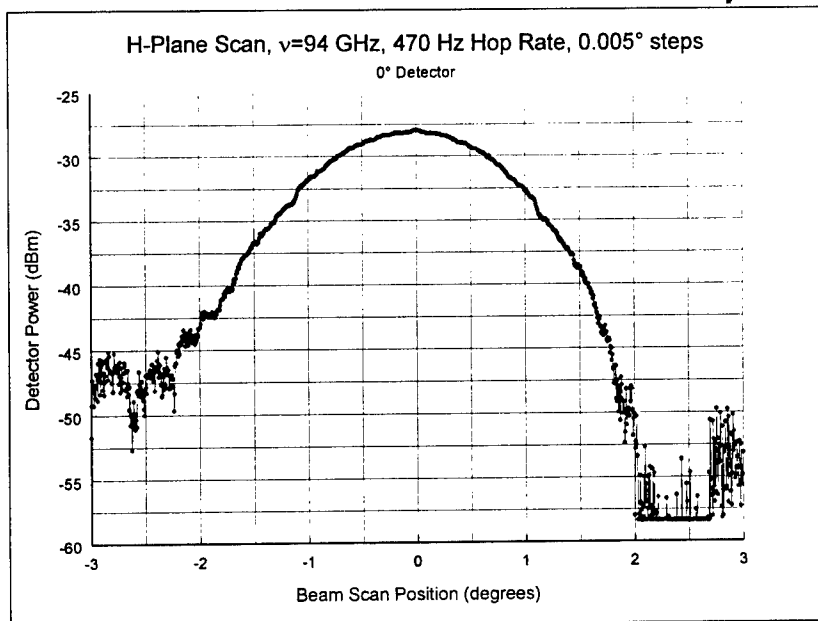


Figure 8. Beam scanned at 200 points per degree illustrating beam width and pointing resolution, 1285 PLA.

A large high angle side lobe was observed at 94 GHz in some directions at about 55° off the main beam when using the 1285 LED PLA. This feature, however, was not observed at lower MMW frequencies. For example, when a 94 GHz beam was scanned to $+30^\circ$ in the H-plane the side lobe could be seen at -25° . It was found that the side lobe was an aliasing effect between the finer zone plate features at 94 GHz and the light spacing of the 1285 LED PLA. Accordingly the light spacing was reduced in the PLA to accommodate a total of 2335 LEDs. This higher light density PLA eliminated the spurious side lobe within the desired scan cone of 30° half angle.

Two dimensional scan data at 94 GHz using the 2335 LED PLA are shown in Figure 9. Here the beam was hopped at a rate of 1000 hops/second on a $30^\circ \times 30^\circ$ square grid with a 1° grid spacing. The detector was collinear with the antenna axis. As with Figure 7, the main lobe is evident when the beam is directed at the detector, as are the side lobes and nulls when the light pattern is changed to direct the beam off-axis.

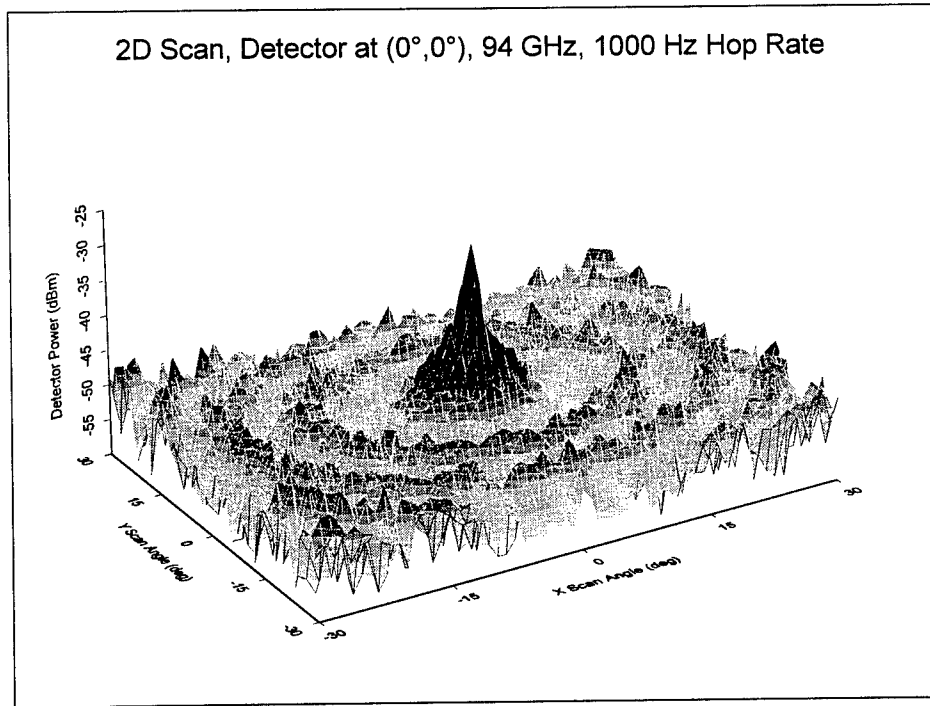


Figure 9. 94 GHz beam scanned on $30^\circ \times 30^\circ$ square grid with 1° grid spacing at 1000 Hz using 2335 PLA. Detector at $(0^\circ, 0^\circ)$.

Beam profile data with 2335 PLA and 94 GHz are shown in Figure 10. H-plane beam scans were used with the antenna configured as a transmitter and a

remote detector. There are four separate beam scans with the detector moved off-axis to 0° , 10° , 20° , and 30° . There is no indication of the spurious side lobe that was seen at 94 GHz with the 1285 PLA. The main lobe intensity does appear to diminish somewhat more strongly with off axis steering at 94 GHz than at 35 GHz, although beam widths are not strongly affected.

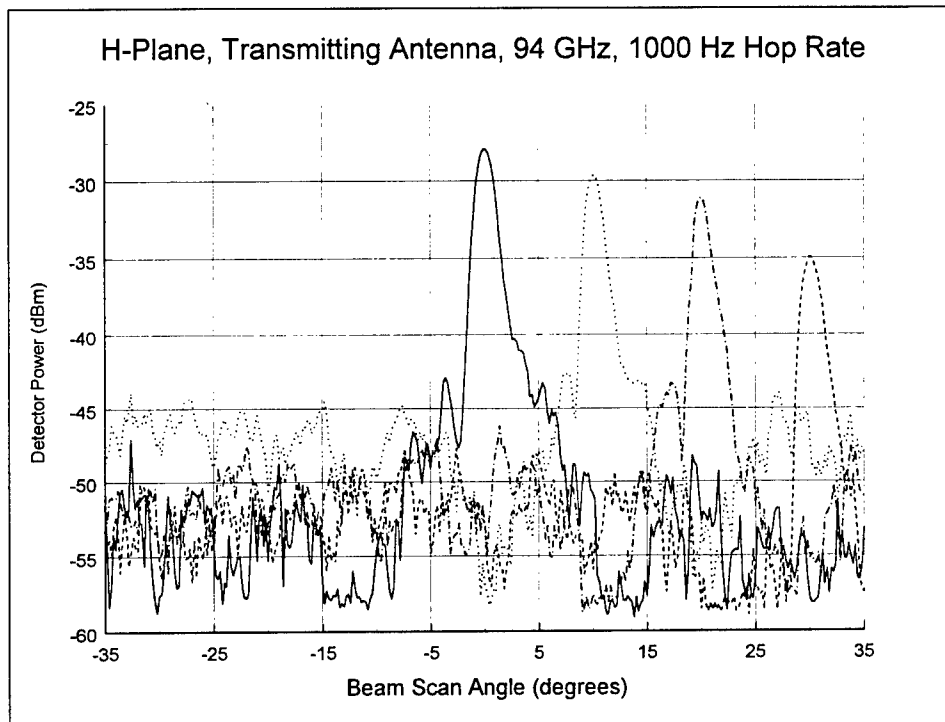


Figure 10. 94 GHz H-plane beam scans from -30° to 30° with the relative angle varied between antenna and detector using the 2335 PLA.

Figure 11 shows the effect of moving the detector off axis to -20° in the E plane. The nulls and expected side lobes are apparent. Moving the detector to 20° in the H plane produces similar results as does moving the detector to $(20^\circ, -20^\circ)$ shown in Figure 12. Here the beam is further off axis than in Figure 11 which results in somewhat less peak beam power.

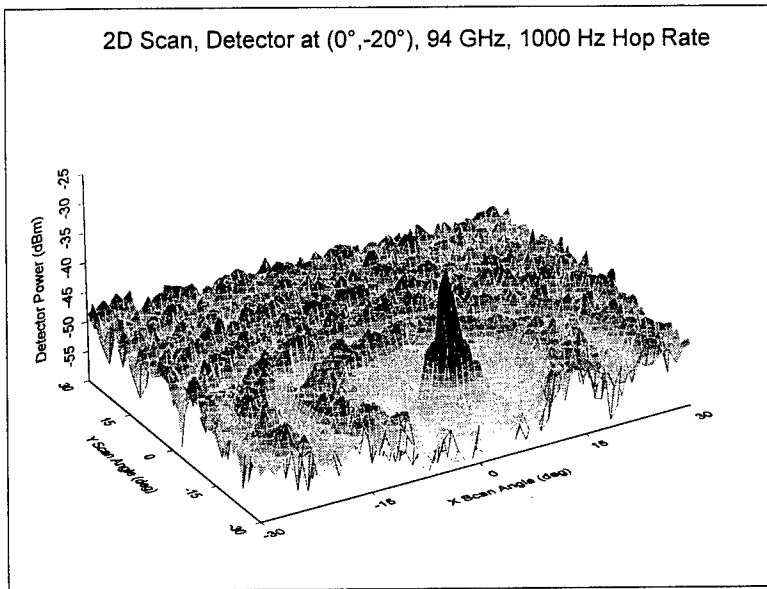


Figure 11. 94 GHz beam scanned on $30^\circ \times 30^\circ$ square grid with 1° grid spacing at 1000 Hz using 2335 PLA. Detector at $(0^\circ, -20^\circ)$.

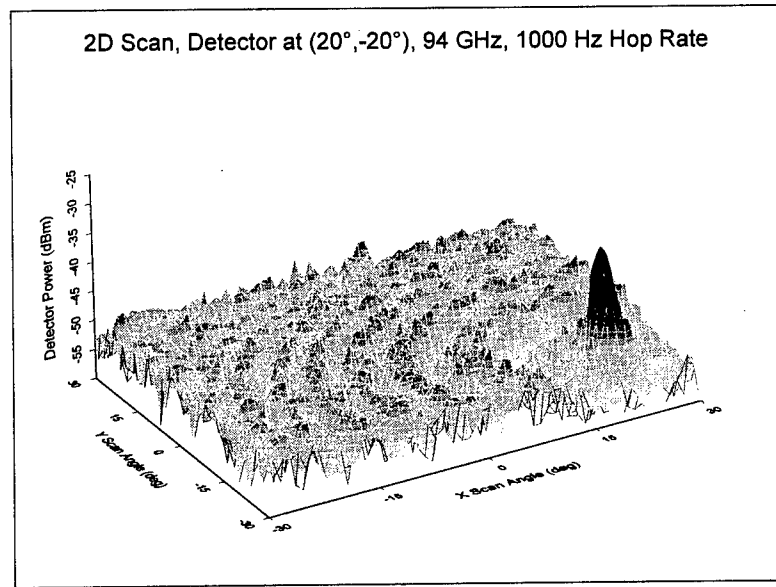


Figure 12. 94 GHz beam scanned on $30^\circ \times 30^\circ$ square grid with 1° grid spacing at 1000 Hz using 2335 PLA. Detector at $(20^\circ, -20^\circ)$.

The maximum hop rate of the antenna depends on the magnitude of the hop. For example Figure 13 shows an H-plane scan at scan rates from 1500 Hz to 4000 Hz. The scan rate is defined as the number of beam hops per second. In Figure 13 there are 10 hops/degree or 0.1° per hop. The measured response does not vary significantly except somewhat at the nulls.

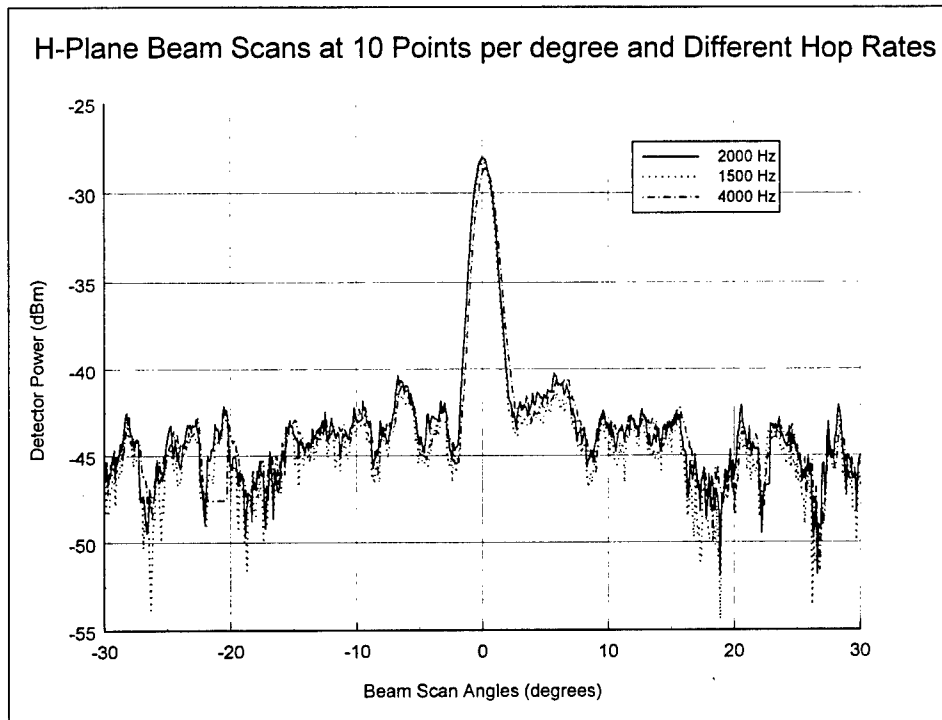


Figure 13. 94 GHz H-plane beam scans at hop rates from 1500 Hz to 4000 Hz and 0.1° per hop. Detector at 0° with 1285 PLA.

As a comparison with the small magnitude hops, Figure 14 shows power data as the beam was hopped back and forth between 0° and -18° with the detector at 0° . Detector power was recorded as the hop rate was varied. Power reaching the detector was maximum when the beam was directed at the detector and as much as 17 dB lower when the beam was at -18° . Figure 14 shows that performance does not change dramatically until the hop rate is larger than 1000 Hz.

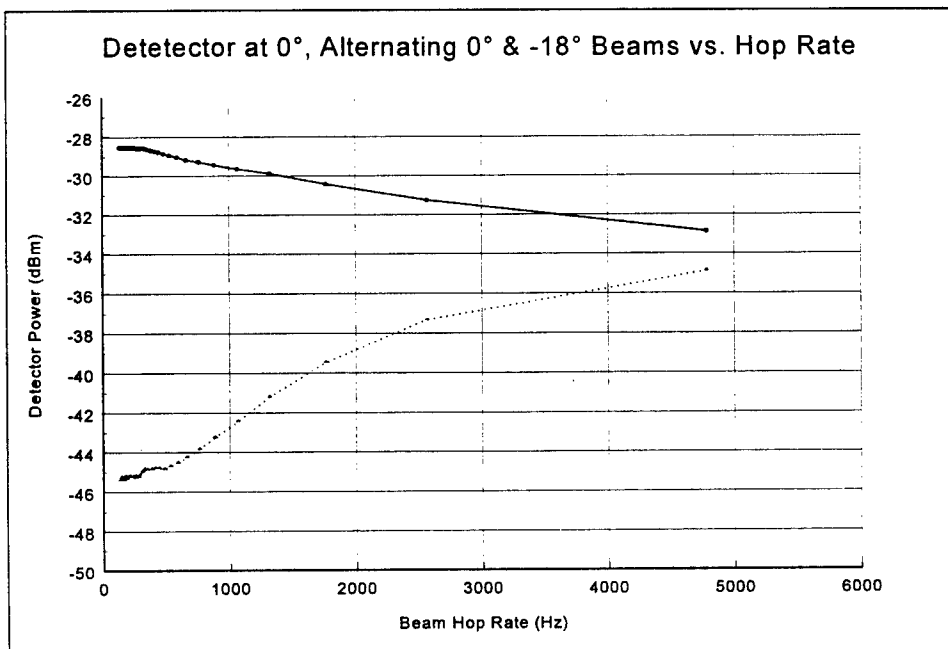


Figure 14. 94 GHz beam hopped between 0° and -18° vs. Hop rate. Detector at 0°, 1285 PLA.

5. DISCUSSION AND CONCLUSIONS

We have demonstrated the ability to form a narrow MMW beam in a solid state scanner by using a photo-injected plasma to block the out-of-phase rays. By controlling which rays are blocked, the beam can be rapidly re-formed in different directions. To estimate maximum efficiency or gain, we note that approximately 50% of the rays are blocked compared to the full aperture. Furthermore, the remaining in-phase rays have a distribution of phases over 180° compared, for example, to a fixed parabolic reflector or a phased array with perfect control over phase. From these considerations, we estimate that the maximum gain or efficiency would be down by approximately 10 dB, as presently configured. The advantage, however, is the ability to rapidly steer the beam over a fixed reflector, and at much lower cost than a phased array.

Programmable light sources have been developed which can produce up to 80×10^3 new plasma patterns per second. However, the fundamental limit on scan rate is limited by the free carrier recombination time in the particular photoconducting material used. Our experiments with this material have shown that we can produce over 1000 independent beams per second, that is to say by hopping in arbitrary direction with hops of arbitrary magnitude. When the beam is hopped in smaller increments, smaller changes are required in successive plasma

distributions. In that case the effective scan rate increases to above 4000 beams per second.

We expect that improved materials and improvements in the configuration will lead to enhanced performance.

ACKNOWLEDGEMENTS

We thank Jennifer Kerns, Ron Skatvold, and Wayne Vernon for discussions and the U.S. Department of the Navy for research support.

REFERENCES

- 1) M. Matsumoto, M. Tsutsumi, and N. Kumagai, "Radiation of millimeter waves from a leaky dielectric waveguide with a light-induced grating layer," IEEE Trans. Microwave Theory Tech. vol. MTT-35, no. 11, pp 1033-1042, 1987.
- 2) P.J. Stabile, A. Rosen, D. Gilbert, R.E. Marx, M.T. Duffy, G. Looney, G. Evans, J.C. Connolly, W. Janton, N. Hughes, and J.K. Butler, "Optically controlled millimeter-wave dielectric waveguides using silicon-on-sapphire technology," CLEO '92, pp.336-338.
- 3) G.W. Webb and L.H. Pinck, "Light-Controlled MMW Beam Scanner", Proc. 1993 SBMO International Microwave Conference, Vol. II, Sao Paolo, Brazil, IEEE Cat. No. 93TH0555-3, p. 417.
- 4) G.W. Webb and L.H. Pinck, "MMW Beam Scanner Controlled by Light", Proc. Workshop on Millimeter-Wave Power Generation and Beam Control, Huntsville, AL, Special Report RD-AS-94-4, U.S. Army Missile Command, p. 333.
- 5) A.R. Rosen, P.J. Stabile, R. Amantea, W.J. Janton, D.B. Gilbert, and J.K. Butler, "Active Millimeter Wave Antenna Array Steered by Optically Induced Gratings," Proc. Workshop on Millimeter-Wave Power Generation and Beam Control, Huntsville, AL, Special Report RD-AS-94-4, U.S. Army Missile Command, p. 341.
- 6) V.A. Manasson, L.S. Sadovnik, V.A. Yepishin, and D. Marker, "An Optically Controlled MMW Beam-Steering Antenna Based on a Novel Architecture," IEEE Trans. On Microwave Theory and Techniques, 45 1497 (1997).
- 7) R.H. Bube, "Photoelectronic Properties of Semiconductors," Cambridge University Press, Cambridge 1992
- 8) G.R. Fowles, Introduction to Modern Optics, 2nd Ed. Dover Publ. New York, 1975.

True Time Delay with Binary Time Delay Control for Large Arrays

Stuart A. Collins Jr., Betty Lise Anderson, Craig Liddle

ElectroScience Laboratory
Department of Electrical Engineering
The Ohio State University
1320 Kinnear Road
Columbus OH 43212

Abstract: In this paper we present a new design for an optical device for producing true time delay. The device, based on the White Cell incorporated with an optical spatial light modulator (SLM). The White cell gives rise to a multiple bounce approach, where the number of bounces is " m ". The SLM allows a large number of independent beams and therefore antenna elements. In previous work we had designs where the number of time delays went as m -squared. Here we present a design where the number of delays goes as two-to-the-power- m . The result is decreased loss and increased antenna array size.

1. Introduction

This paper deals with True Time Delay (TTD) for phased array radars. We present an optical scheme for providing an independent controllable delay for each element of such a radar. This is a free space approach using mirrors and lenses and an optical spatial light modulator. The time delays are generated by switching among paths of different lengths. The scheme has the can easily address hundreds of array elements.

The position of the unit to be discussed in a phased array radar is shown in Fig. 1. The TTD unit is reciprocal and can be used in both transmit and receive modes. The application in the receive mode is shown in Fig. 1a where we see the individual array receive elements at the top. The output of each array element is used to modulate an independent optical beam which is sent through the system

receiving the desired predetermined delay. The optical signal is then detected and the resulting delayed RF signal sent to the processing electronics. In the transmit mode the original signal is modulated, then split into parts, one for each array element. Each beam is delayed the desired amount by the optical unit, detected and applied to the final microwave transmitter.

2. Dual Cell

The basic optical approach uses a set of optical paths of different lengths and a means for switching between them. It is a multiple bounce scheme. This is illustrated conceptually starting with Fig. 2. There we see two spherical mirrors, a polarizing beamsplitter and a lens next to a Spatial Light Modulator (SLM). This is a variation on the White Cell [1] which was originally used to generate long paths to study gaseous absorption.

The SLM operates like a mirror whose reflectivity can be controlled as a function of position. One might think of an array of image elements where the reflectivity of each is controlled independently. In this case it is not the magnitude of the reflectivity that is changed but the polarization of the reflected light at each image element that is changed. The polarizing beamsplitter transmits light polarized in the plane of the figure and reflects light polarized perpendicular to it. At any one point the SLM can either rotate the plane of polarization or leave it unchanged depending on its external control.

In operation an input spot of light comes in from the bottom, reflected from a tiny mirror called the input turning mirror just off the SLM, as shown. The light from the spot is heading to Mirror B. Mirror B is designed to image the light back onto the SLM. Light reflected off the SLM is directed by lens $f/1$ to Mirror C which again images it to a different spot on the SLM. The details of the exact positions of the spots will be considered presently. This multiple bounce process continues with a row of spots on the SLM. The light finally bounces off the SLM at the top and out of the system onto a redirecting mirror called the output turning mirror. If there are m bounces off the SLM, the size and refractive index of the polarizing beamsplitter are d_o and n_o respectively, and the distance from the polarizing beamsplitter to Mirrors B and C is d_1 , then the transit time T after m bounces is

$$T = \frac{1}{c} 2m(n_o d_o + d_1)$$

1

So far we have a single transit time. We need more. We then add in spherical mirrors E and F as shown in Fig. 2b which we will call the Dual Arm Cell. There we see two more spherical mirrors labeled E and F located a distance d_2 from the polarizing beamsplitter. We now have two Siamese White cells joined at the beamsplitter. Mirrors E and F also reimagine the light spots back onto the SLM. Further, lens $f2$ directs from Mirror E to Mirror F after reflection off the SLM. We will call the cell formed by the SLM and Mirrors B and C Cell I and that formed by the SLM and Mirrors E and F Cell II.

Now, if the SLM changes the polarization so that the beam is reflected off the polarizing beamsplitter and travels to mirrors E and F m_2 bounces out of the total m bounces, then the transit time is

$$T = \frac{1}{c} 2((m - m_2)(n_o d_o + d_1) + m_2(n_o d_o + d_2))$$

2

or

$$T = \frac{1}{c} 2(m(n_o d_o + d_1) + m_2(d_2 - d_1))$$

3

In Eq. 3 we see that the transit time has a constant part, T_o ,

$$T_o = \frac{1}{c} 2m(n_o d_o + d_1)$$

4

which is always there, and a variable part, ΔT ,

$$\Delta T = \frac{1}{c} 2m2(d_2 - d_1)$$

5

which depends on m_2 as determined by the addressing of the SLM. ΔT is the desired time delay.

We also note that the minimum delay occurs when the light goes to Mirrors B and C so that $m_2=0$, and the maximum delay is occurs when all the bounces go to Mirrors E and F so that $m_2=m$.

$$\Delta T_{\min} = 0$$

6

Further,

$$\Delta T_{\max} = \frac{2m}{c} (d_2 - d_1)$$

7

The minimum delay increment is

$$\delta T = \Delta T(m_2 + 1) - \Delta Tm_2 = \frac{2}{c} (d_2 - d_1)$$

8

The total number of possible delays is

$$\frac{\Delta T_{\max} - \Delta T_{\min}}{\Delta T} = m$$

9

We note that both the maximum number of delays and the maximum total delay are proportional to m , the number of bounces off the SLM. If we want to improve the capability of the design we want to increase m .

The location of the spots on the SLM are shown in Fig. 3. There we see a view looking towards the SLM from the right in Fig. 2a. We see a row of spots. Next to each spot is a number indicating the bounce number. The zeroth spot is on the input turning mirror next to the bottom of the SLM. The spots then alternate from top to bottom with the last spot on the output turning mirror next to the top of the SLM. Also shown are the centers of curvature of Mirrors B and C. The details of

why this occurs depend on the location of the locations of the centers of curvature of Mirrors B and C and are given elsewhere[2].

The situation shown in Fig. 3a is a special case. The spots are all along a line containing the centers of curvature of Mirrors B and C. If the input spot is not along that line then two columns of spots arise as shown by the circles in Fig. 3b. The spots alternate from one side to the other as well as from top to bottom before being reflected past the top of the SLM. There are vacant spaces formed as the spots alternate from side to side. These can be filled in by another input spot on the input turning mirror as shown in Fig. 3c. We can add many more input spots. Each set of input spots forms a pair of columns on the SLM. The result is a whole array of spots as shown in Fig. 3d. Each input spot has m bounces, each of which can have its polarization changed so that the beam can alternately go to Mirrors E and F. The spots necessarily are made to lie on the SLM pixels.

The design in Fig. 2 has a major advantage. The spots retain their small size independent of the number of bounces because of the reimaging.

3. Design with number of bounces proportional to 2^m

We now want to modify the design of the Dual Arm Cell to improve the number of potential time delays. What we will end up with is a design where the number of delays is proportional to 2^m rather than to m . We will present the modification in two parts. First we will add Auxiliary mirrors in the plane of the SLM and then we will add time delay mechanisms in conjunction with the auxiliary mirrors.

The dual cell with auxiliary mirror is shown in Fig. 4. There we see a three dimensional rendition of the dual cell. Added to it are two mirrors, one over the SLM which we will call Auxiliary Mirror I, and an extra mirror over the edge of the beam-splitting cube. We will call that Auxiliary Mirror II. Lens f_1 has been made larger to cover the SLM and Auxiliary Mirror I. The turning mirrors are at the left of Auxiliary Mirror I and the SLM.

The operation is comparable to that of the Dual Cell with the plane of the SLM enlarged. The light starts on the Input Turning Mirror and goes first to Mirrors B and C. They image the Input Turning Mirror spot onto the SLM. If the SLM does not change the polarization the light is imaged onto Auxiliary Mirror I and again onto the SLM. If the SLM changes the polarization, the light that is reflected off the beam-splitting cube is imaged onto Auxiliary Mirror II. Light leaving Auxiliary Mirror II is similarly reimaged back onto the SLM. Lens f_1 by the

SLM images Mirror B onto Mirror C and lens f2 images Mirror E onto Mirror F, as before.

The spot pattern on the SLM and Auxiliary Mirror I for a single input beam is shown in Fig. 5. There we see the centers of curvature of Mirrors B and C along a horizontal line midway between the two. The spots progress the same as discussed previously in Fig. 3 except that the spots on the SLM and Auxiliary Mirrors now form horizontal lines.

We next choose m , the number of bounces on the SLM, to be equal to the number of bits of time delay required. For example if two hundred different time delays are desired, that would require eight bits, $m=8$, so we require eight bounces on the SLM. We then divide SLM surface into m areas such that each beam falls once into each area. This is shown in Fig. 5.

We then change the length of the path traveled by the beam in Cell II on the traverse in which it strikes each of the different areas. To discuss this approach, suppose we take Mirrors B and C the same distance from the SLM as Mirrors E and F. We next place extra path length in front of or in place of Auxiliary Mirror II. The methods of increasing the path length will be presented shortly. The distance associated with the increase in path length is a binary function of a minimum distance, ΔL ; ΔT is the minimum non-zero time delay. We can write

$$\Delta T = \frac{2}{c} \Delta L$$

10

Thus the incremental time increase associated with first area on Auxiliary Mirror II is ΔT , that with the second area is $2\Delta T$, that with the third area is $4\Delta T$, etc. The general expression for the time delay with this approach is

$$T = 2mD_{BC} + \Delta T(\delta_1 + 2\delta_2 + 4\delta_3 + \dots + 2^{(m-1)}\delta_m) \quad 11$$

where the δ_i describe whether the i -th delay is added in. For example $\delta_i=0$ if the light goes to the Auxiliary Mirror I and $\delta_i=1$ if the light goes to Auxiliary Mirror II.

We notice that Eq. 11 has a constant delay, T_C .

$$T_C = 2mD_{BC}$$

12

The factor of two in front of D_{BC} occurs because the distance from the SLM to Auxiliary Mirror I required for this case is twice the distance from the SLM to Mirror B or Mirror C and back as required for the Dual Arm cell.

There is also an incremental delay, T_I .

$$T_I = 2\Delta T(\delta_1 + 2\delta_2 + 4\delta_3 + \dots + 2^{(m-1)}\delta_m)$$

13

The maximum incremental delay, $T_{I,max}$ is given by

$$T_{I,max} = \Delta T(2^m - 1)$$

14

This is a considerable improvement over Eq. 3 where the time increment is linear in m_2 .

3.1 Incremental time delays using a lens waveguide

One way in which the incremental length, ΔL can be implemented using an optical transmission line. The situation for the lens waveguide is shown in Fig. 6a. There we see in Fig. 6a five groups labeled G1....G5, each group comprising three lenses. The plane on the right is the input or object plane and is intended to be coincident with and replace the plane of Auxiliary mirror II in Fig. 5 so that light which was reflected off Auxiliary Mirror II in Fig. 5 now proceeds to the left into the lens system of Fig. 6a. There are five planes conjugate to the plane of Auxiliary mirror II. They are labeled CP1...CP5 and lie at the junctions of the five optical systems. Fig. 6b shows the plane of Auxiliary Mirror II and the five

conjugate planes in three dimensions. We first consider the unit lens systems and them the images on the conjugate planes.

The first three lenses on the right and Conjugate Plane CP1 form a unit. The lens in the middle with focal length f_{g1} is an imaging lens. It is separated from the plane of Auxiliary Mirror II and from Conjugate Plane CP1 by a distance $2f_{g1}$ so plane of Auxiliary Mirror II is indeed imaged onto Conjugate Plane CP1 with a magnification of -1. The first and third lenses on the right are field lenses. The field lens on the right images the White Cell Mirrors E and F onto lens f_{g1} . The other field lens produces an image of Lens f_{g1} at infinity. If there were a mirror placed at Conjugate Plane CP1, then the third lens with focal length $2f_{g1}$ would image lens f_{g1} back onto itself so that there would be no light lost by passing around the lens.

The next three lenses on the right and the Conjugate Plane CP2 form a similar unit. The lens in the center has focal length f_{g2} and is separated from the two image planes by a distance $2f_{g2}$ so that Conjugate Plane CP3 is an image of Conjugate Plane CP2 with magnification -1. Similarly, the field lens to the left of Conjugate Plane CP1 in conjunction with the lens to the right of Conjugate Plane CP1 images Lens f_{g1} onto Lens f_{g2} . If a mirror were placed in Conjugate Plane II then the lens to the right of Conjugate Plane II would image Lens f_{g2} onto itself. The next three groups of lenses operate in similar fashion. The central lens in each group is an imaging lens and the outside lenses are field lenses. The relative values of focal lengths of the imaging lenses will be considered shortly.

The operation can be observed looking at Fig. 6b. There we see the plane of Auxiliary Mirror II, and the conjugate planes. The lenses are not drawn for clarity. In operation we consider the same areas we did in discussing the glass block method of providing delays. The five areas are shown in the plane of Auxiliary Mirror II at the right, labeled I ... V. These are imaged onto five areas on Conjugate Plane CP1 with the order reversed because of magnification -1. A mirror is placed in the Conjugate Plane CP1 in the strip corresponding to Area I so that light is reflected from that strip. In traveling from the plane of Auxiliary Mirror II to Conjugate Plane CP1 and back the light experiences an additional delay of $8f_{g1}/c$. The remainder of the light passes through Conjugate Plane CP1 and is imaged on Conjugate Plane CP2. The images of the five strips are also shown Conjugate Plane CP2. The image of Strip I is shown in dashed lines indicating that no light gets to it. A mirror is placed in Area II so that light is reflected. The focal length $f_{g2}=f_{g1}$ so that light in Area II takes time $16f_{g1}/c$ to

return to Auxiliary Mirror II, twice as long as light in Area I. In practice adjacent lenses can be combined.

The focal length of the imaging lens in Group G3 is twice as long as that of Groups G1 and G2, $f_{g3}=2f_{g1}$. The result is that the light takes time $32f_{g1}/c$ to travel from the plane of Auxiliary Mirror II to Conjugate Plane CP3 and back, i.e. four times as long as transit time for Area I.

Similarly, a mirror is placed at Area IV in Conjugate Plane CP4 and a mirror is placed in Area V of conjugate plane CP5. The focal length of lenses f_{g4} and f_{g5} are four and eight times the focal length of lens f_{g1} giving transit times of eight and sixteen times the transit time to Conjugate Plane CP1 and back.

The process can be extended if more delays are desired with more unit cells and more areas on Auxiliary Mirror II and its conjugate planes.

3.2 Alternate method of providing delays using glass blocks

A second method of providing the various delays, useful when the delays are small is shown in Fig. 7. There we see a set of glass blocks of various lengths. They are placed across the plane of Auxiliary mirror II. There should be one block for each slit of Auxiliary Mirror II shown in Fig. 5. The left hand surface of each block has a reflective coating. The light coming in from the right is reflected off these coatings and returns to the right. The planes of the reflective coatings are actually somewhat behind the plane of Auxiliary Mirror II because of the refocusing effect of the refractive indices of the blocks. A detailed analysis of the optical design will be presented elsewhere.

4. Summary

In this paper we have presented a free space optical technique for producing True Time Delays for a phased array radar. We first described the general approach showing that the time delays are produced by changing optical paths using a spatial light modulator. In the general approach the number of different delays was proportional to the m , the number of light bounces off the spatial light modulator. Then we presented a more sophisticated scheme using either an optical transmission line or glass blocks in which the delay was proportional 2^m .

References

- [1] J. White, "Long optical paths of large aperture," Journal of the Optical Society of America, vol. 32, pp. 285-288, 1942.
- [2] B. L. Anderson, J. Stuart A. Collins, C. A. Klein, E. A. Beecher, and S. B. Brown, "Photonically Produced True-Time Delays for Phased Antenna Arrays," Applied Optics, vol. 36, pp. 8493-8503, 1997.

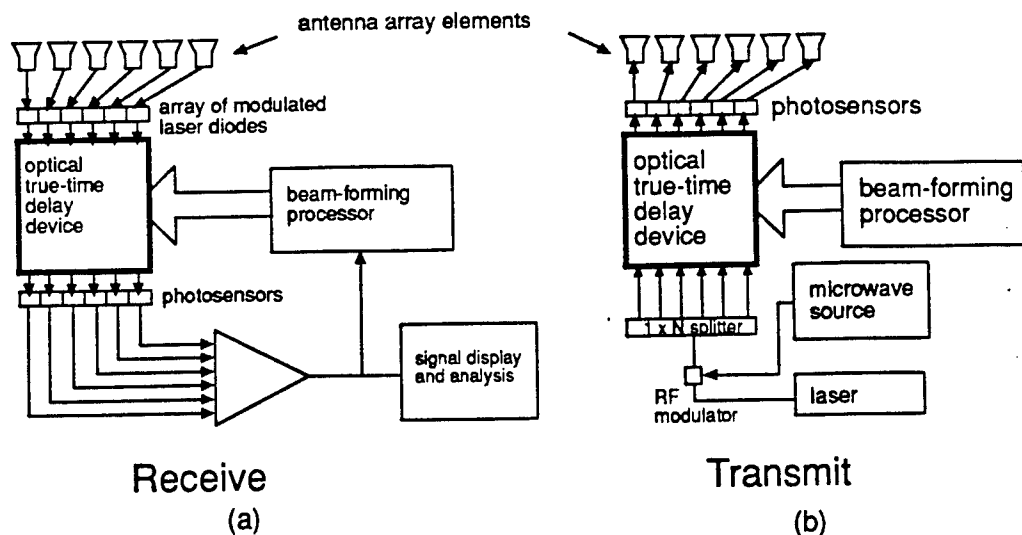


Figure 1. Position of true-time delay unit in a typical phased array radar.
 a) receive mode; b) transmit mode.

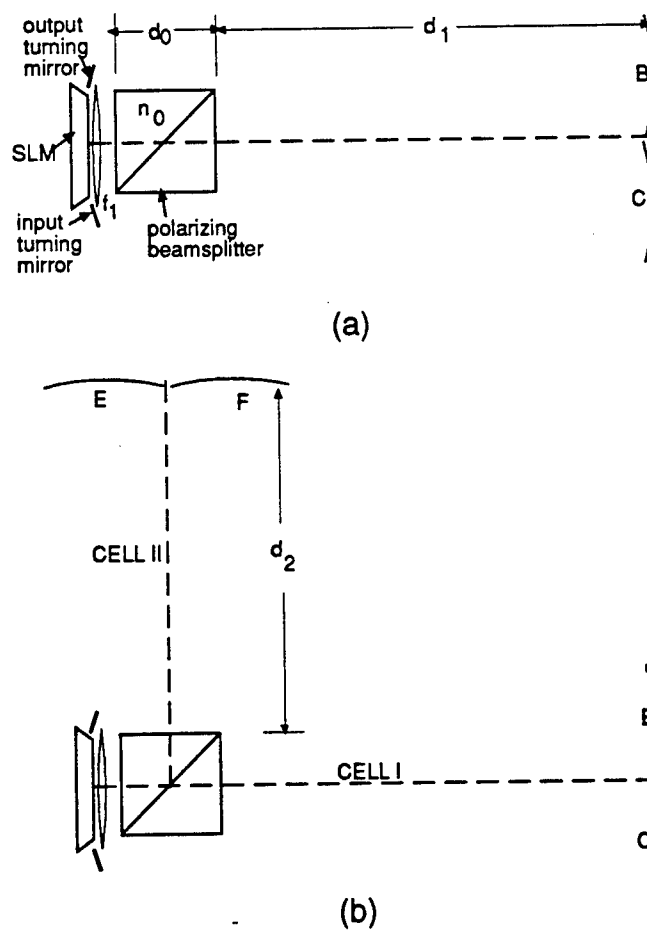
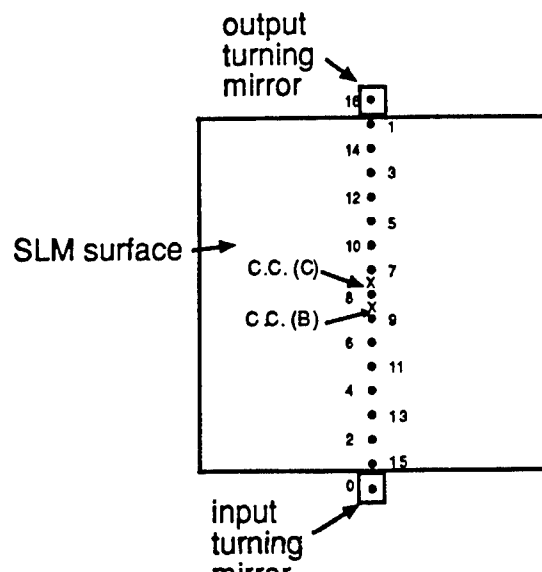
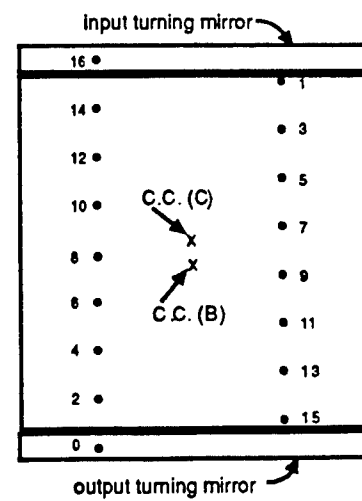


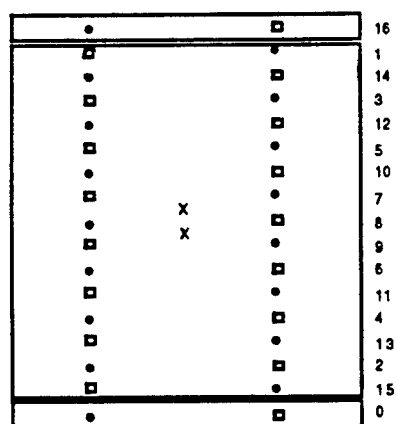
Figure 2. Conceptual TTD Configuration. a) Single cell; b) dual cell.



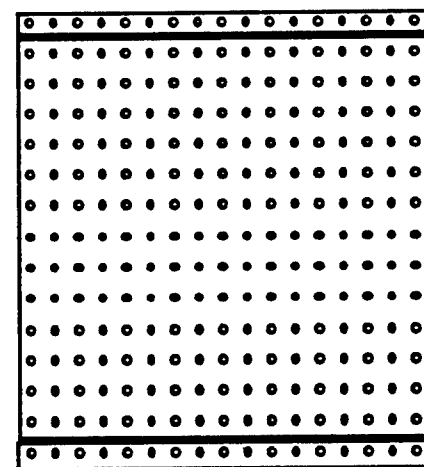
(a)



(b)



(c)



(d)

Figure 3. Spot locations on the SLM. a) a single input spot on axis produces a column of spots; b) a single spot off axis produces two columns of spots; c) another spot is introduced and interleaves with the first; d) an entire row of input spots produces this pattern of bounces on the SLM and each has its own output spot.

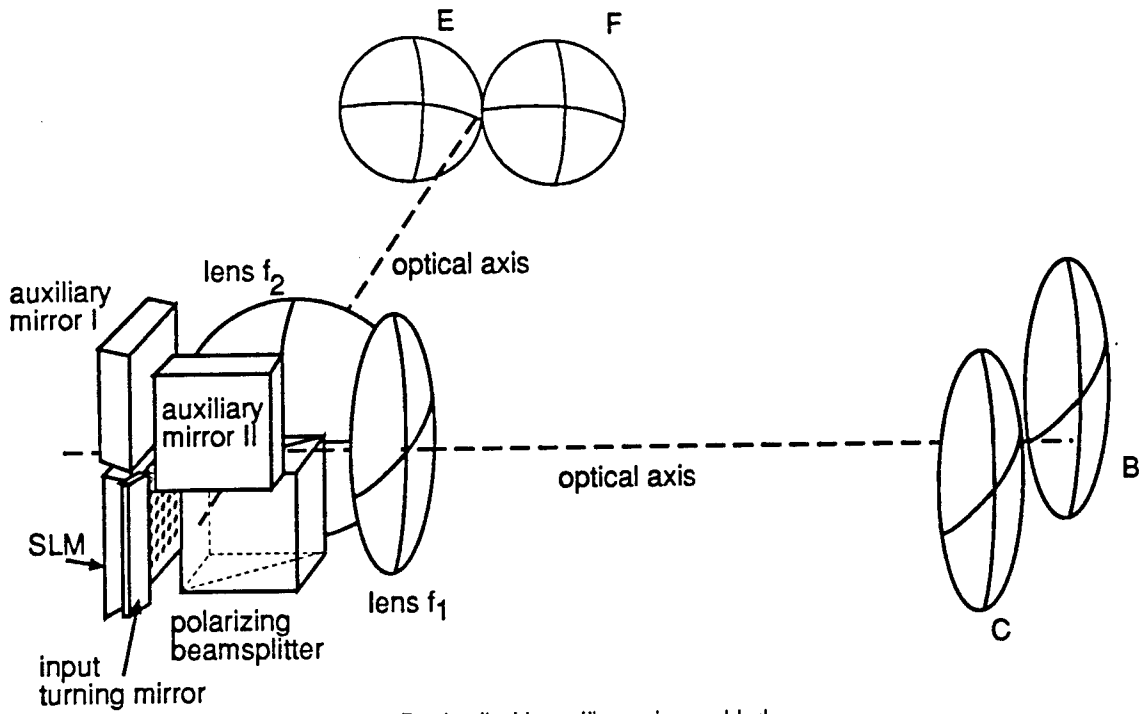


Figure 4. Dual cell with auxiliary mirror added.

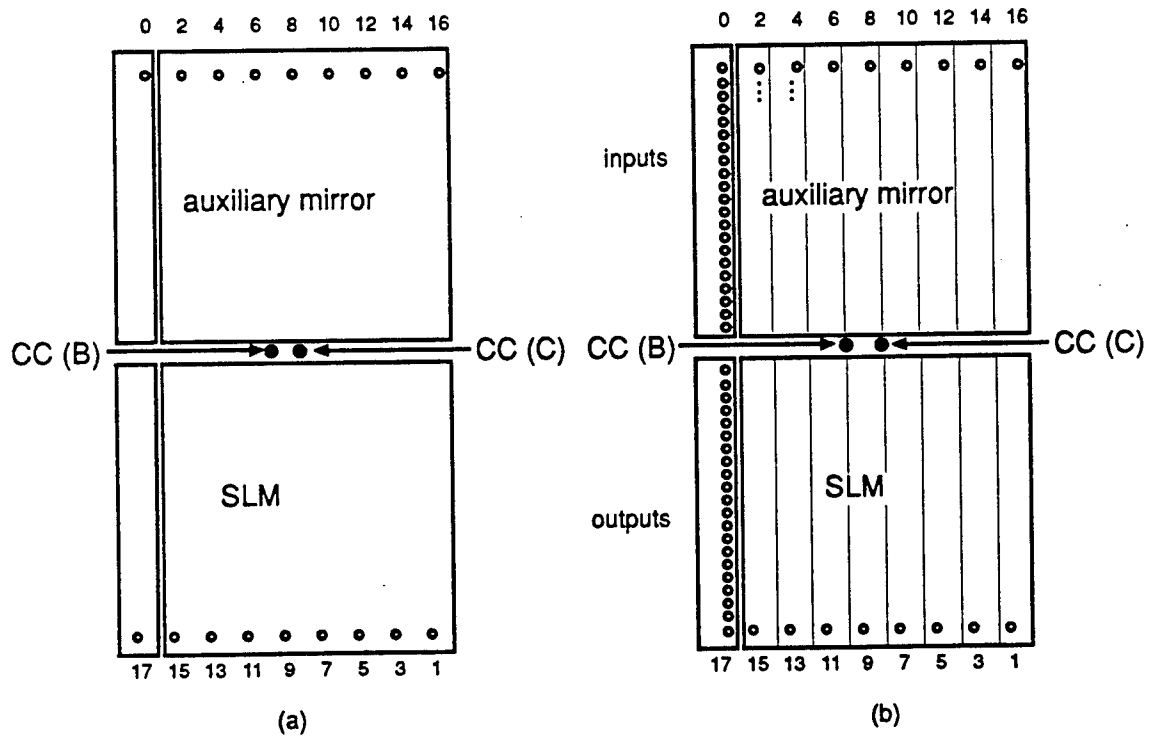


Figure 5. Views showing a) spots on the SLM and Auxiliary mirror I, and b) division into areas.

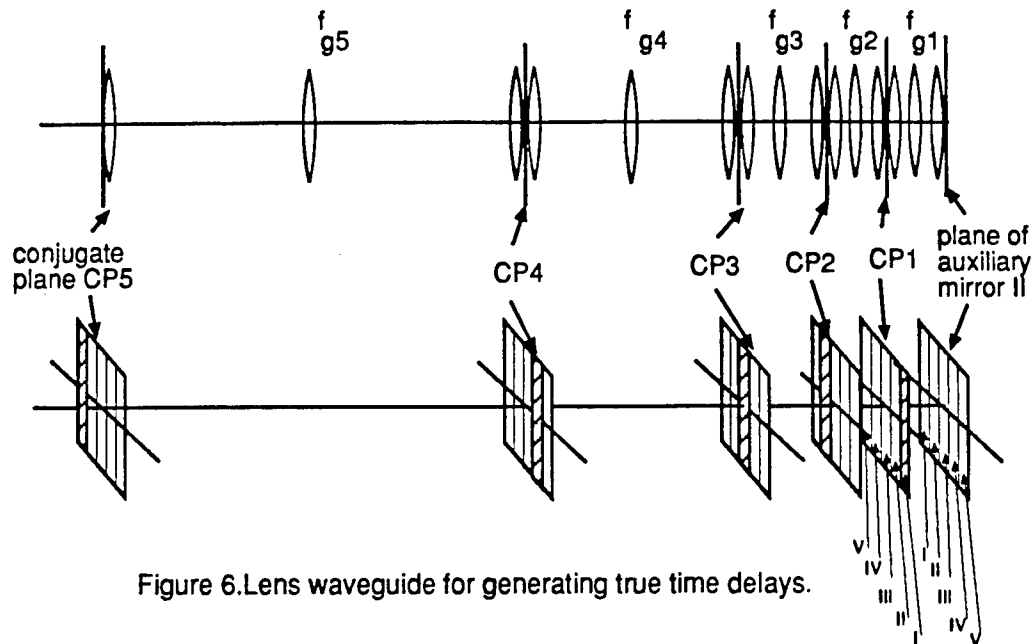


Figure 6. Lens waveguide for generating true time delays.

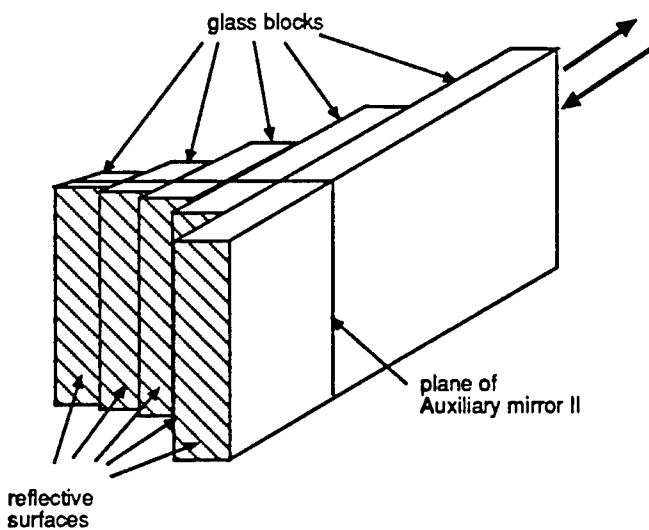


Figure 7. Glass blocks for producing various time delays.

EHF OPTICAL NULLER

R. A. Brown, P. A. Schulz, and S. R. Henion
MIT Lincoln Laboratory
244 Wood Street
Lexington, MA 02140
(781)981-3255
E-mail: brownra@ll.mit.edu

Abstract

Adaptive nulling antennas are used to spatially suppress unwanted interference in microwave communication links. In order to achieve deep broadband nulls, the components that comprise a multi-channel nulling system must track in amplitude and in phase over the entire frequency band of interest. Because of this frequency tracking requirement, all-RF nulling systems operating in the 43.5-45.5 GHz band are limited to null depths in the 25-30 dB range. The EHF optical nuller developed at MIT Lincoln Laboratory is for a seven channel adaptive antenna system, and has achieved null depths of 40 dB as demonstrated in the laboratory. These deep nulls are attributable to optical upconversion since the percentage of occupied bandwidth over which components must track becomes negligible at optical frequencies. The presented technique for applying complex weights to received antenna signals can be applied to frequency bands other than the EHF band. The major subsystems and the measured laboratory performance of the EHF optical nuller are discussed here.

1. Introduction

Future satellite communications will require increased data rates and lower cost. The higher data rates will make communication systems more susceptible to interference. To overcome this, better interference protection such as a strong spatial nulling capability could be designed into future satellite communications.

The optical nuller described here can achieve ~15 dB more interference suppression than a nuller using all RF technology. This performance improvement results from the use of photonics, namely, the improved channel tracking as a consequence of microwave-to-optical conversion and the very small fractional

bandwidth of the 43.5-45.5 GHz communication band relative to the 200 THz optical carrier. Thus, nulls of 40 dB across the 2 GHz EHF band are routinely obtained instead of ~25 dB nulls using all RF processing.

The use of optics can also result in reduced satellite cost due to its low overall weight. Low-weight optical fiber is used to connect electronics, protected within the satellite body, to the antenna, which is exposed to the space environment. Because the microwave signal carried on optical fiber is only weakly affected by changes in the fiber environment, this remoting function is robust. In addition, the optical fiber is nearly lossless for typical intrasatellite distances under 100 m. This is in contrast to the use of RF transmission lines or waveguides which are considerably more bulky and incur higher loss than a functionally equivalent amount of optical fiber.

2. System Description

MIT Lincoln Laboratory has developed optical nuller technology that processes received signals to form a spatial null in the direction of an interferor (see Fig. 1). The outputs of a multi-port receive antenna provide one signal to each channel of the optical nuller. Each channel has a low-noise amplifier followed by a Mach-Zehnder electro-optic modulator to upconvert the millimeter-wave signals to optical frequencies. Each channel has a second modulator to appropriately weight each of the signals in amplitude and phase in order to suppress interference. Phase is controlled using ferrite phase shifters. Amplitude is controlled with the bias voltage on the electro-optic modulator. A channel signal combiner using polarization combiners and 3-dB couplers sums the signals prior to conversion from the optical to the microwave domain.

2.1 LNAs

The LNAs used in the demonstration nuller are Lockheed-Martin devices that use an InP pHEMT for a first stage and GaAs MMICs for second and third stages of amplification. InP pHEMT amplifiers with noise figures below 3 dB have recently become available. By using the InP pHEMT as the first stage, the three-stage LNA has a low noise figure, only slightly larger than the noise figure of the initial InP pHEMT stage. The GaAs MMIC stages have relatively high third-order intercepts so these are used in the final stages. A 6 dB attenuator is included between these two MMICs to further raise the third-order intercept and increase the dynamic range.

The front-end LNAs meet a variety of requirements. First, they have high gain which more than offsets the losses incurred in the RF-to-optical conversion process. The measured average gain of the LNAs is 54 dB. Second, the LNAs have low noise figures and are the dominant source of noise in the system (aside from antenna noise). As measured on a HP8970B noise figure meter, the LNAs have an average noise figure of 2.7 dB. Third, the LNAs possess excellent

frequency tracking to enable the formation of very deep broadband nulls. The LNAs have measured frequency tracking statistics of <0.3 dB in amplitude and <2.0 degrees in phase (both peak-to-peak). These statistics are adequate for 40 dB nulls across the EHF band. Finally, the LNAs are very linear. Utilizing the noise figure measurements of the LNAs and measuring the third-order intercept points of the amplifiers (average ~19 dBm) it was determined that the spur-free dynamic range of the system is 90 dB-Hz^{2/3}.

2.2 EHF-Optical Conversion

Optical modulators for the EHF frequency band have only been commercially available since 1995. These modulators use lithium niobate as the electro-optical material. Optical waveguide in the material splits the incoming optical beam, propagates the optical beams in close proximity to coplanar RF waveguide, and recombines the beams. This popular geometry for modulating the intensity of optical beams is called a Mach-Zehnder interferometer. The coplanar RF waveguide carrying the EHF signal has a microwave signal velocity equal to the optical beam group velocity and, thus, the device forms a traveling wave modulator. The velocity matching enables intensity modulation of the optical beam at RF frequencies up to 50 GHz.

One figure of merit used for this modulator is its voltage sensitivity, which is often measured as V_π . The value of V_π is the voltage required to cause a relative optical phase shift of π radians between the two arms of the Mach-Zehnder interferometer. At 44 GHz, the modulators' measured values for V_π are between 9.4 V and 11.1 V. Optical losses from the input fiber to the output fiber are measured to be between 3.6 dB and 4.9 dB. The optical losses are caused by coupling loss at the fiber optic-to-lithium niobate interface and by waveguide losses such as material losses and losses associated with the bending of the optical waveguides.

Measurement of the modulators' nonlinearities shows that the LNAs limit the dynamic range of the nulling system. The third-order intercept of the modulators is at an input power level of 29.2 dBm. This input power level is 10 dB higher than the third-order intercept for the LNAs. The third-order intercept is related to the value of V_π for modulators with a sinusoidal transfer function, which is the case for Mach-Zehnder modulators. The relationship between V_π and the third-order intercept, T , is:

$$V_\pi = \frac{\pi}{2} \sqrt{TR} \quad (1)$$

where R is the RF input impedance (approximately 50 Ω) of the electro-optic modulator. For a third-order intercept of 29.2 dBm, $V_\pi=10.1$ V, which is in good agreement with the laboratory measurements of V_π .

Frequency tracking measurements indicate that the modulators track over the EHF frequency band to within 0.14 dB in amplitude and 0.9 degrees in phase, adequate for 40 dB cancellation.

Distributed feedback (DFB) diode lasers operating in the 1.55 μm band are used as the optical sources for the electro-optic modulators. These lasers produce 20 mW of average optical power. Since the beamformer combines optical signals, the narrowband light in different channels has different wavelengths in order to avoid optical interference at the photodetector. The optical wavelengths in the various channels have been adjusted by tuning the operating temperature of the individual lasers. The lasers also have low intensity noise (\sim 153 dB/Hz) which keeps system noise low.

2.3 Signal Weighting and Summing

Complex weighting (amplitude and phase shifting) is accomplished by using electro-optic modulators. The amplitudes of the signals in each of the seven channels are directly controlled via the DC bias point of the weighting modulators. This determines output intensity of the exiting light and therefore amplitude of the RF signal that is carried by this light. The phases of the signals are controlled by the phases of 37 GHz CW tones that are modulated onto the channel signals. Modulating the optical signals that carry the EHF signals with phase-shifted CW tones results in optical signals that are intensity modulated at a down-converted frequency of $[(43.5-45.5) - 37]$ GHz = 6.5-8.5 GHz. The RF phases of these down-converted, intensity modulated optical signals are equal to the phases of the applied 37 GHz CW tones. Thus, by controlling the phases of the 37 GHz tones, the phases of the EHF signals in the seven channels can be set as desired.

To accomplish this functionality, the components in the Amplitude and Phase Control block of Figure 1 include a 37 GHz CW source, a splitter to distribute the 37 GHz tone to the seven channels, and seven ferrite phase shifters (one in each channel).

The 37 GHz source is generated from a 10 MHz reference. A 10x multiplier generates a 100 MHz signal. A dielectric resonant oscillator oscillating near 18.5 GHz is locked to the 185th harmonic of the 100 MHz signal. This 18.5 GHz signal is then frequency doubled using a diode to generate a 37-GHz tone, which is then amplified to 21 dBm before distribution to the seven phase shifters.

Although the 1:7 divider for the 37 GHz tone circuit could be constructed of commercially available broadband 1:2 dividers, these have high losses and are heavy. Therefore, a compact and low-loss (2.3 dB excess loss) 1:8 power divider was fabricated at Lincoln Laboratory for the distribution of the 37-GHz phase weighting signal.

After splitting the 37 GHz, seven ferrite phase shifters provide phase control. The phase shifters contain a piece of ferrite in waveguide whose

permeability can be controlled with applied electrical currents. As a result, the phase of the output can be electronically controlled. The phase shifters have a loss of 0.6 - 0.7 dB at 37 GHz. Computer control of the phase shifters allows a phase resolution of better than 0.15°.

The phase-shifted 37 GHz signals are amplified to power levels above 100 mW, then directly connected to the coaxial input of the electro-optic modulators. The coaxial output of the electro-optic modulators is connected to a bias tee with a $50\ \Omega$ termination on the RF port and the bias voltage for amplitude control connected to the dc port.

After complex weighting, the optical signals are combined so that all seven signals are carried on a single fiber. This combining is accomplished in three stages. The first stage combines pairs of channels using polarization-maintaining fibers in conjunction with polarization-sensitive couplers. This combining is accomplished with only 0.5 dB loss. The next two stages of combining is done using polarization-insensitive 3 dB couplers which have 3.2 dB of loss (0.2 dB excess loss). The total optical combining loss for the seven signals is 7 dB.

2.4 Optical-Microwave Conversion

In order to compensate for optical losses, a low noise fiber amplifier (3.2 dB noise figure) is included as a preamplifier prior to photodetection. The fiber amplifier has large gain with a saturated optical output power rating of 20 mW (13 dBm). For the optical input power of 200 μ W, the optical gain is about 20 dB. The resulting microwave gain is 40 dB.

Photodetection is accomplished using an Ortel 2518A photodetector. This is an InGaAs *p-i-n* photodiode that is sensitive to optical wavelengths in the 1.1-1.6 μ m range. The Ortel photodiode has a responsivity of 0.7 A/W, a bandwidth of approximately 15 GHz, and a return loss that is greater than 9.6 dB for frequencies up to 15 GHz.

3. Measured Nulling Performance

Several nulling scenarios demonstrating 40 dB suppression of a simulated interfering signal were performed. In these scenarios, the interfering source location was simulated using an antenna emulator.

The antenna emulator simulates a seven-beam multiple-beam antenna (MBA). The emulator consists of a variety of waveguide components that feed directly into the LNA inputs. The antenna emulator combines two sets of channels which served as inputs to the optical nullder: the user set and the interferor set. The user set allows signals to be injected into any combination of nullder channels by selectively closing or opening appropriate waveguide switches. There is no provision for relative amplitude control in the user input channels. The

interference input can be injected into four channels with amplitude control provided by variable attenuators. By applying the appropriate attenuation, a specific angle-of-arrival for a simulated interferor can be established.

The procedure for measuring achievable null depth began by adjusting the variable attenuators of the antenna emulator to simulate the presence of the interferor. Next, two measurements were made to determine null depth. First, the nullder's complex weights were set to their quiescent values (those values that produced a desired beampattern) and the interference power at the output of the nullder was recorded. Second, the complex weights were set to values calculated to result in cancellation of the interference and the output of the nullder was recorded. The ratio of the two responses gave the measured cancellation depth. Since the complex weights that provide interference suppression were calculated using ideal channel assumptions, and since the channel responses of the nullder tend to drift slightly in time, a closed-loop nulling processor algorithm (see Figure 1) was implemented. This closed-loop algorithm iteratively adjusted the amplitude and phase of the complex weights while monitoring null depth. In the laboratory, this closed-loop search for the deepest null was performed using a desktop computer capable of controlling the complex weights as well as the network analyzer used to measure cancellation depth.

Figure 2 shows the measured cancellation depth achieved for one of the scenarios examined in the laboratory. The average cancellation achieved for this scenario is 45 dB rms. Three additional scenarios, each with a different simulated interferor location, resulted in null depths of 43 dB, 45 dB, and 39 dB (rms).

4. Conclusion

A laboratory demonstration of an optically implemented broadband nulling system typically suppressed simulated interference by 40 dB. This performance is \sim 15 dB better than conventionally implemented millimeter wave systems and provides significantly more margin against interference. The optical nullder provides improved nulling performance because processing in the optical domain results in better channel tracking. This improved channel tracking is a consequence of the very small fractional bandwidth of the 2 GHz communication band relative to the 200 THz optical carrier.

Finally, it is worthwhile to note that the EHF nullder architecture can be applied to other frequency bands. In this case, the optical components need not be replaced because these devices are extremely broadband. Implementing a different frequency band would only require changes in the microwave/RF components that are used in the nulling system.

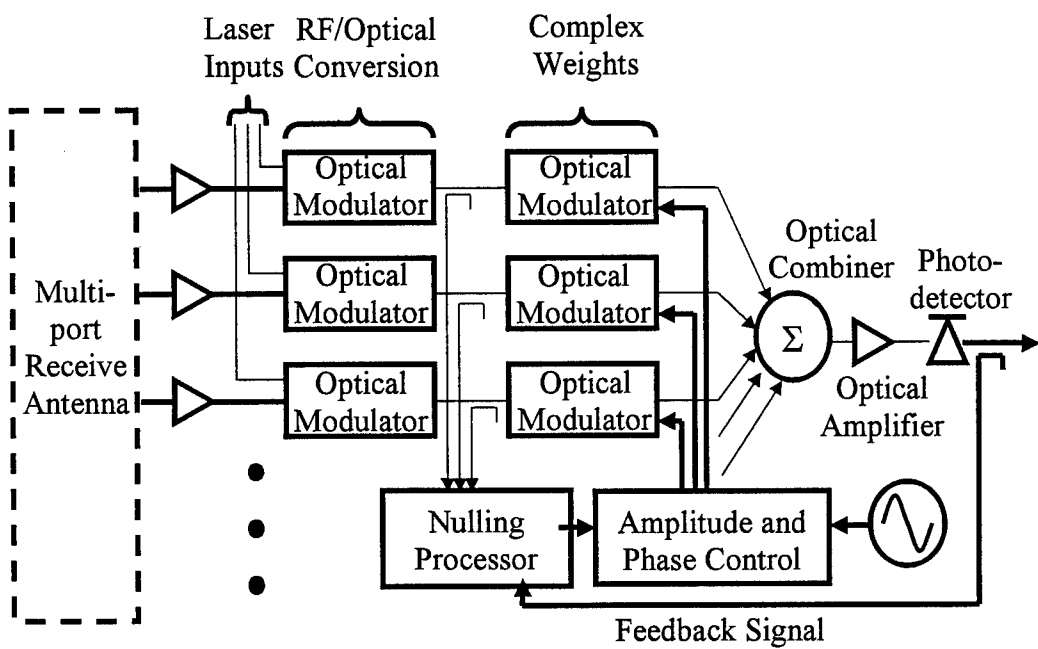


Figure 1. Optical nullder schematic. In the laboratory demonstration, a total of seven channels were implemented, and an antenna emulator was used in place of the antenna. Heavier lines represent RF signal paths, while thinner lines represent optical signal paths.

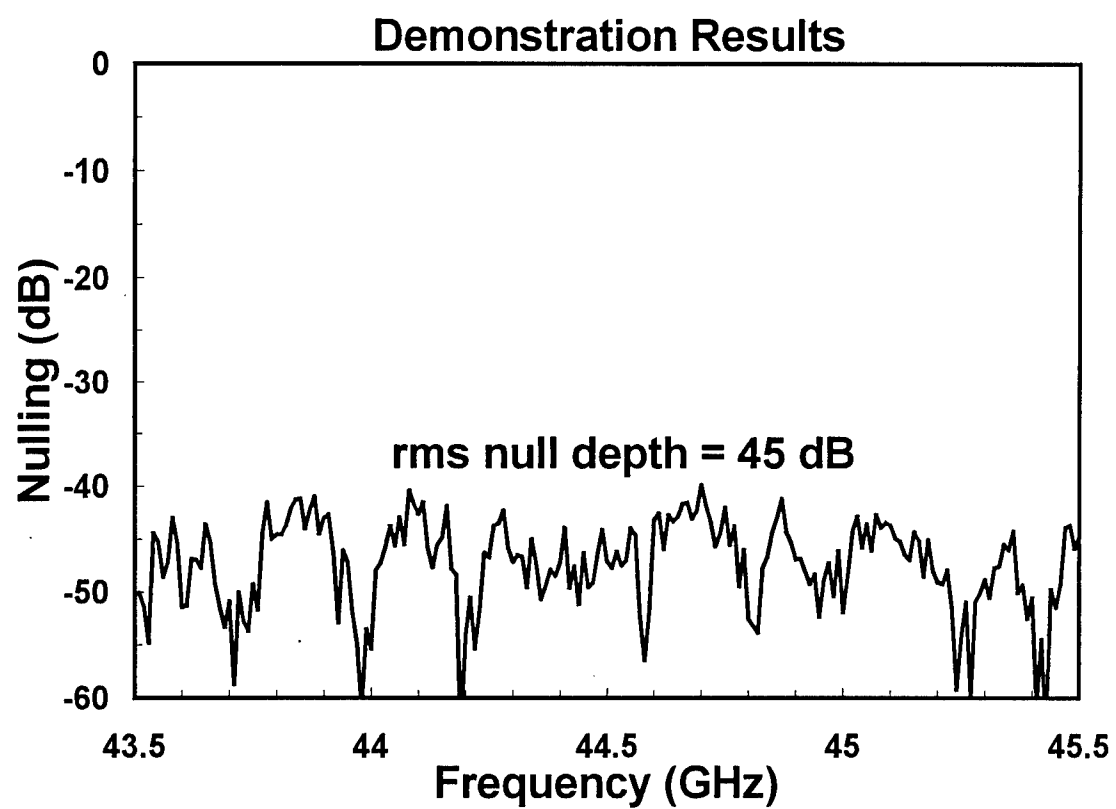


Figure 2. Optical nuller demonstration results. A broadband interfering source was suppressed by more than 40 dB over the 2-GHz band.

SAC-C SATELLITE ANTENNAS

Valentin Trainotti, Norberto Dalmas Di Giovanni,
Juan Skora, Diego A. Schweitzer
CITEFA
Antennas & Propagation Division
Buenos Aires, Argentina

ABSTRACT.

Argentine Scientific Satellite (SAC-C) antennas have been developed in order to fulfill the satellite-ground link requirements for a satellite polar orbit without the on board antenna steering necessity. This task was achieved with a modified Kilgus circular polarized antenna where wide bandwidth and wide beamwidth were necessary so to use one antenna in each band for transmission and reception at the same time. UHF, "S" and "X" band antennas were developed for telemetry, data and control link services. Input impedance, radiation and polarization patterns for each antenna were measured in an anechoic chamber in order to verify if the antenna fulfills link requirements. Radiation patterns and gain were obtained with a satellite mockup installed on an outdoor antenna range turntable so to fulfill the far field requirements and to verify the mechanical satellite structure and all the platform accessories on the antenna characteristics.

UHF patch antenna characteristics are included because this antenna has a low profile and could be used in order not to produce shadows on the observation cameras as in the case of the modified UHF Kilgus antenna. Impedance, radiation and polarization characteristics are presented here and the required task is considered to be fulfilling completely and so the future space links requirements.

INTRODUCTION.

SAC-C satellite is Argentina's first Earth Observation Satellite and the third in a series of science-oriented space missions within Argentina's Space Program. This mission is headed by CONAE the Argentinean Space Commission, with an international agreement of collaboration with NASA and the space agencies of Denmark, Italy, Spain, France and Brazil.

INVAP is the prime contractor for the design and construction of the SAC-C spacecraft and its main payload, a Multispectral Medium Resolution Scanner as well as a High Sensitivity Medium Resolution Camera.

CITEFA through the Antenna and Propagation Division is responsible to develop the spacecraft antennas for data, telemetry and control and scientific experiments link requirements in each operational band.

SAC-C will provide data for the study of terrestrial and marine ecosystems, atmospheric temperature and water vapor monitoring.

SAC-C will determine variability in the ionospheric structure, providing space observatory quality measurements of the geomagnetic field and measurements of the long wavelength components of the gravitational field. The satellite will also update low orbit space radiation environment models.

1.1 SAC-C SATELLITE INSTRUMENTATION:

- Multispectral Medium Resolution Scanner (MMRS), a five band spectral scanner (three bands in the visible, one in the near infrared spectrum and one Short Wave Infrared Band). These bands were selected for study of both terrestrial and coastal marine ecosystems, agricultural and forestry management, desertification, pollution, coastal zone management and fisheries.

- Magnetic Mapper Probe and a Scalar Helium Magnetometer (MMP/SHM) to provide a set of space observatory quality geomagnetic field data, which in combination with that of the ÖRSTED and other Geomagnetic or Gravity future NASA Mission to Planet Earth, will span a decade of data. This contribution will have an impact on a number of areas, including decade

variations in angular momentum, the nature of earth mantle and long-term magnetic field modeling. CRI from Denmark and JPL from USA are to build the MMP and the SHM.

- TurboRogue GPS receiver payload, to be supplied by JPL/NASA. Its measurements will help determine the ionospheric structure, valuable to a number of studies including that of the nature of electrical currents in the ionosphere and magnetosphere, which constitute a significant component of error in geomagnetic field measurements. It will also help to improve the estimates of ionosphere delay, which degrade altimeter radar such as ERS-1, ERS-2, and Geosat-B. SAC-C will carry an array of GPS antennae to perform atmospheric profiling as an extension of the NSF and NASA GPS/MET experiment. Finally, a high sensitivity nadir GPS antenna will test the concept of the use of GPS signals reflecting off the ocean surface to provide high-resolution altimeter.

- High Resolution Technology Demonstration Camera (HRTC) is passed on a 200 mm refractive optics and a similar electronics to a single MMRS channel, covering from 40 to 750 nm, with a ground resolution of 30 m. Resampling studies are possible with this camera in connection with the MMRS images.

- Component and Radiation (COMRAD) French payload that will update low orbit space radiation environment models, monitoring three energy bands, namely, electrons spectrum (50 KeV - 5 MeV). It will also conduct on board tests of a selection of electronic components, in the demanding environment of the so-called South Atlantic Anomaly Area.

- Receiver and data handling electronics for tracking the whales migration about the South Atlantic Ocean.

Figure 1, shows the SAC-C satellite drawing with the solar panels deployed

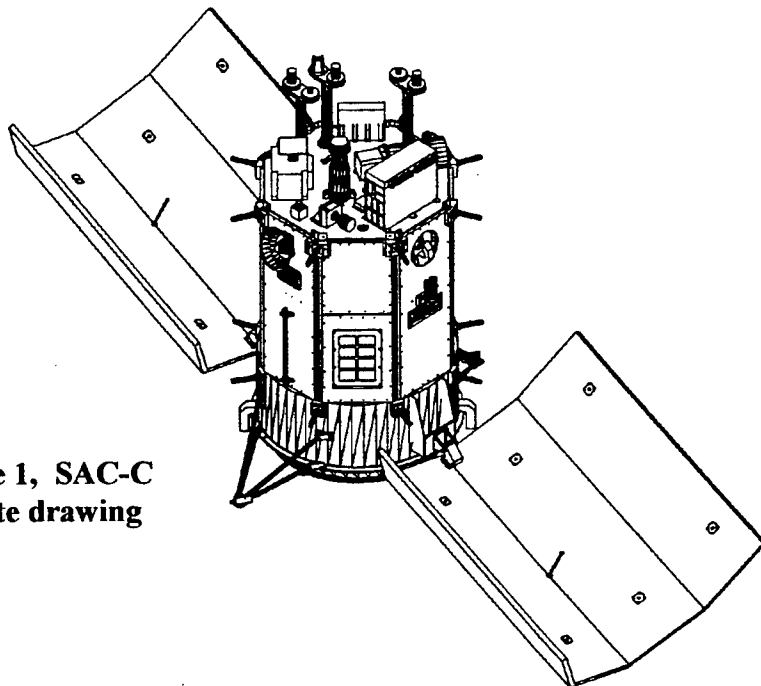


Figure 1, SAC-C satellite drawing

1.2 SAC-C SATELLITE MISSION PROFILE.

General:

Design Life;	4 years
Satellite Mass;	425 Kg
Spacecraft Power	370 W (BOL)

Spacecraft Attitude Control:

Accuracy;	1.5 degrees
Knowledge;	0.2 degrees (Post Facto)

Orbit:

Type;	Circular Sun Synchronous Orbit
Altitude;	702 Km (Stable for lifetime)
Inclination;	98.2 Degrees
Local Hour;	10.15 +/- 5 min (descending node) (stable for lifetime)
Revisit Time;	9 days/subcycles 2 and 7 days
Ground Track Error;	+/- 10 Km (EOL)
Eccentricity;	< 0.05
Payload;	Earth Observation Instruments

1.3. SAC-C SATELLITE ANTENNAS.

SAC-C Mission will use several operating bands.

UHF band with the frequency of 401.75 MHz for South Atlantic WhaleTracking System and low-resolution data downlink transmission.

“L” band for GPS signal reception.

“S” band with three frequencies:

2076 MHz and 2255 MHz for on board telemetry and control reception and transmission up and down link.

2244 MHz for low-resolution data down link transmission.

“X”band with the frequency of 8386 MHz for high resolution data down link transmission.

Antennas have been designed by CITEFA for each operating band with the exception of L band antennas, which are supplied by Jet Propulsion Laboratory (JPL).

1.4. ANTENNA MEASUREMENT SYSTEMS.

During the antenna development and design, antenna parameters were continually measured in order to determine if the antenna model fulfils the design requirements.

Antenna input impedance has been measured using an 8410 Hewlett Packard Network Analyzer in an anechoic chamber. Antenna installed on the satellite mockup in the outdoor range, has been tested by a VSWR Wilttron Autotester so to check the antenna return loss with a small device and with a minimum perturbation on the under test system.

Radiation and polarization patterns have been measured in the anechoic chamber for every band antenna during the development procedure. Radiation patterns have been measured using a model 1780 phase-amplitude receiver and a model 2150 signal generator by Scientific Atlanta.

Antenna gain and polarization pattern have been measured in the anechoic chamber using a swept signal generator model 83623B and a two channel power meter model 438 by Hewlett Packard.

Figure 2 shows the principal satellite platform and antenna positions and the reference axis.

Antennas installed on the satellite mockup have been measured in the CITEFA antenna outdoor range. SAC-C satellite mockup can be seen in the figure 3 during the installation over the outdoor range turntable by means of a plastic-supporting tower.

2. MODIFIED KILGUS ANTENNA FOR UHF BAND.

Several modified Kilgus antennas have been designed due to their wide beamwidth and circular polarization characteristics that fulfill the link requirements. One of them is a half turn modified Kilgus antenna.

This antenna is installed over a small metallic ground plane and is fed through a piece of solid coaxial line. Balance is obtained through a two slots classical balun and impedance matching by a proper central coaxial conductor modification. Right circular polarization is obtained left winding the two-helix arms. Optimum axial ratio within the operating band is obtained when the helix arm length is very close to half wavelength. Nevertheless this modified Kilgus antenna is quite big enough so to produce some shadow over the observation systems and for this reason a quarter turn antenna was develop in order to reduce the mechanical dimensions.

Antenna input impedance can be seen in the figure 4, were more than 20 MHz bandwidth was obtained for a VSWR less than 2, and around 10 MHz for a VSWR less than 1.5.

Antenna absolute gain was measured like a power balance with three-antenna method and right circular polarization. Results can be seen in the figure 5.

Radiation patterns have been measured for all polarization and only for right circular polarization can be seen in figures 6 to 9. These patterns have been

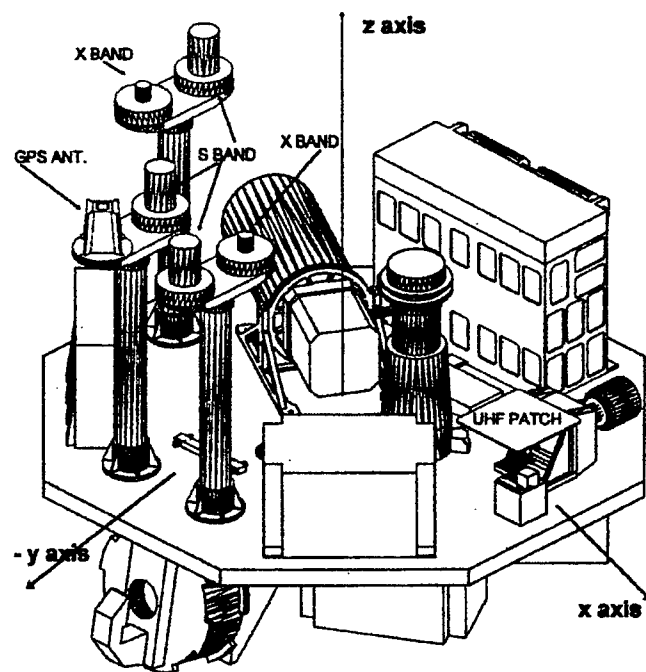


Fig. 2. SAC - C Principal Platform with the antennas installed

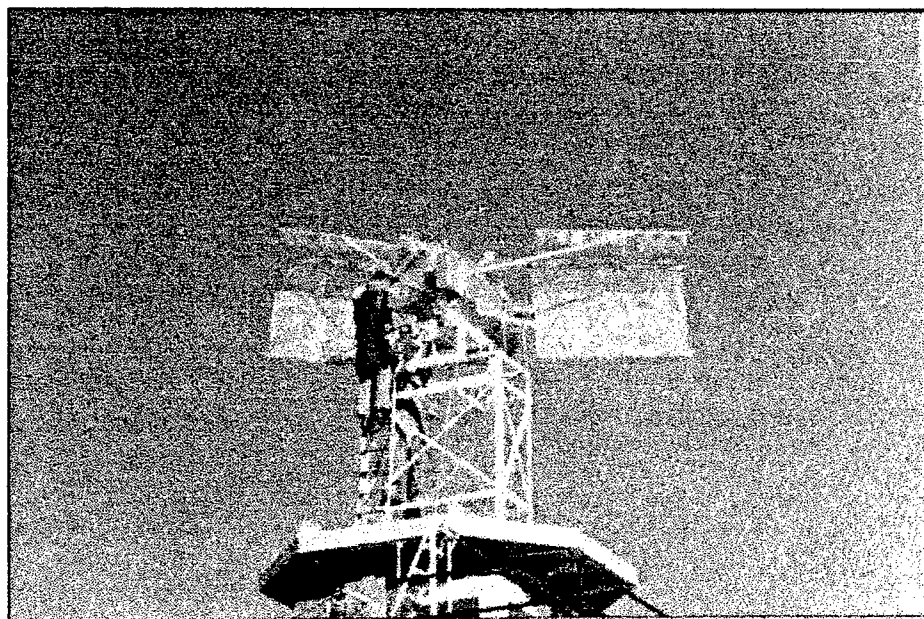
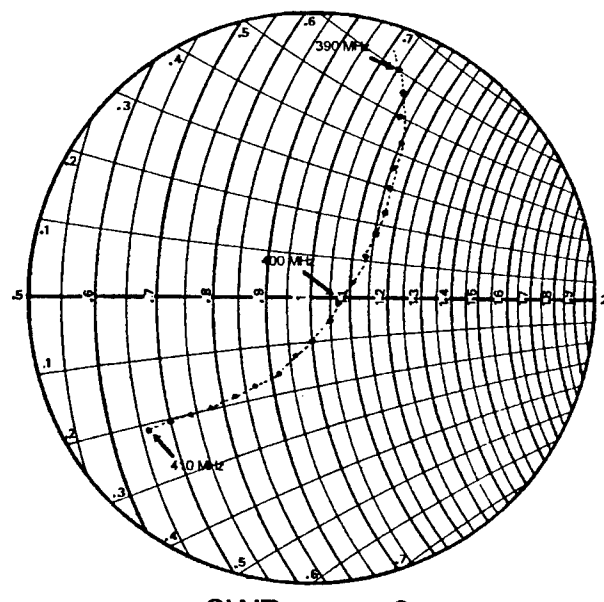


Fig. 3. SAC - C Mockup installed in CITEFA's outdoor antenna range



SWR max = 2

Fig. 4 UHF Modified Kilgus Antenna

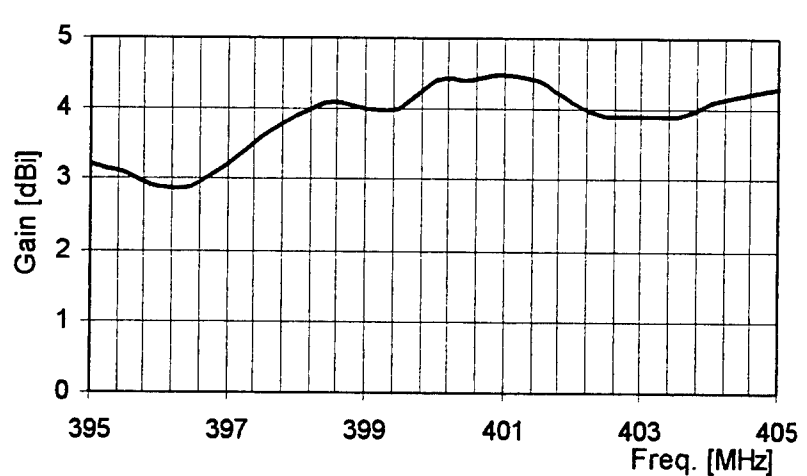


Fig. 5 UHF Band Modified Kilgus Antenna Gain

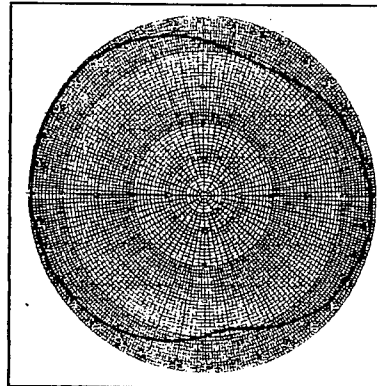


Fig. 6 . Radiation Pattern
F= 400 MHz, Pos.: HORIZ.

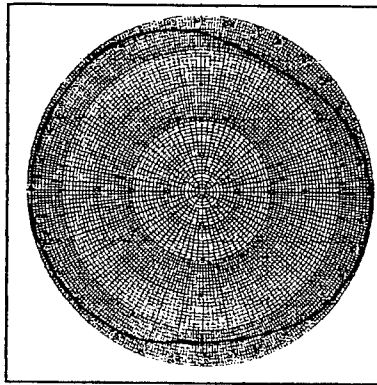


Fig. 7 . Radiation Pattern
F= 405 MHz, Pos.: HORIZ.

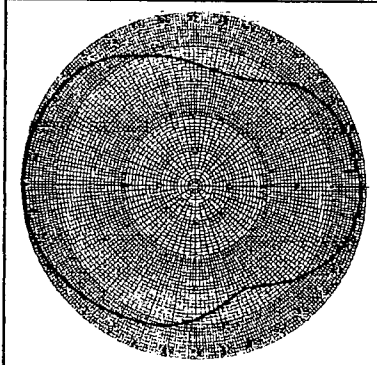


Fig. 8 . Radiation Pattern
F= 400 MHz, Pos.: VERT.

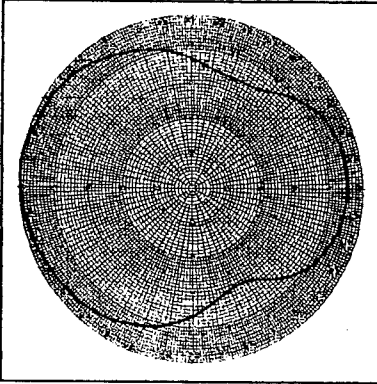


Fig. 9 . Radiation Pattern
F= 405 MHz, Pos.: VERT.

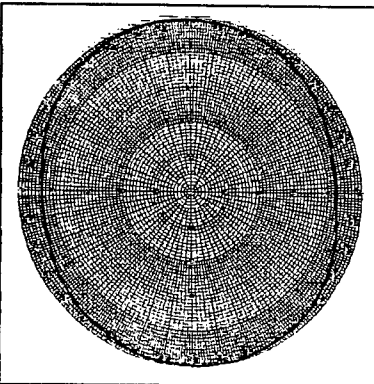
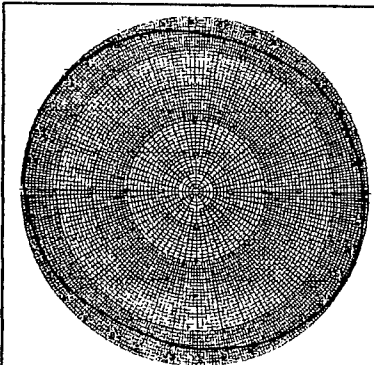
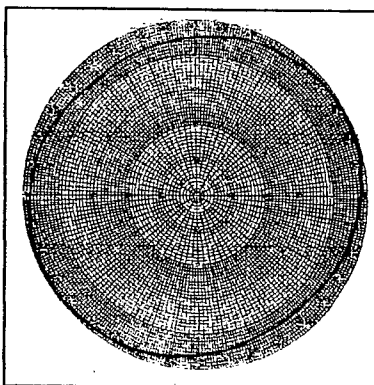
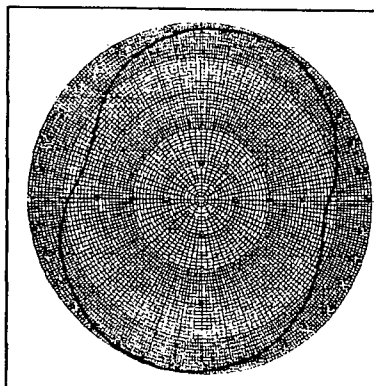


Fig. 13 Polarization Pattern
F= 405 MHz, Pos.: VERT.

Fig. 12 Polarization Pattern
F= 400 MHz, Pos.: VERT.

Fig. 11 Polarization Pattern
F= 405 MHz, Pos.: HORIZ.

Fig. 10 Polarization Pattern
F= 400 MHz, Pos.: HORIZ.

Modified Kilgus Antenna - UHF Band (DYNAMIC RANGE 25 dB)

measured for two position of the helix feeding point, i.e. horizontal or vertical according to the helix connection at the coaxial line.

Polarization patterns can be seen in the figures 10 to 13, were the good axial can be seen. Axial ratio as a function of frequency is shown in the figure 14.

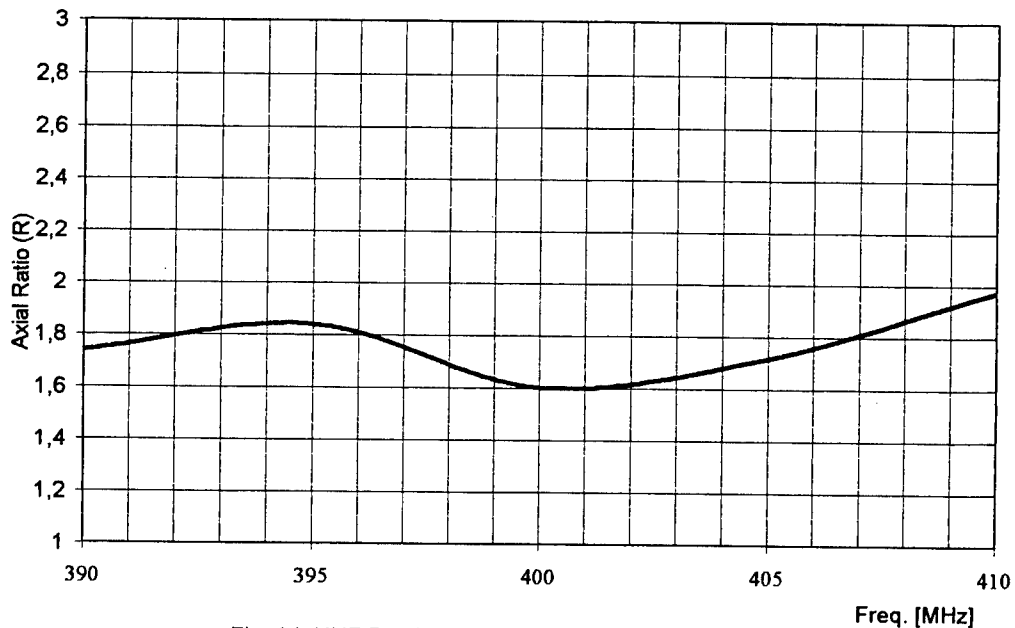
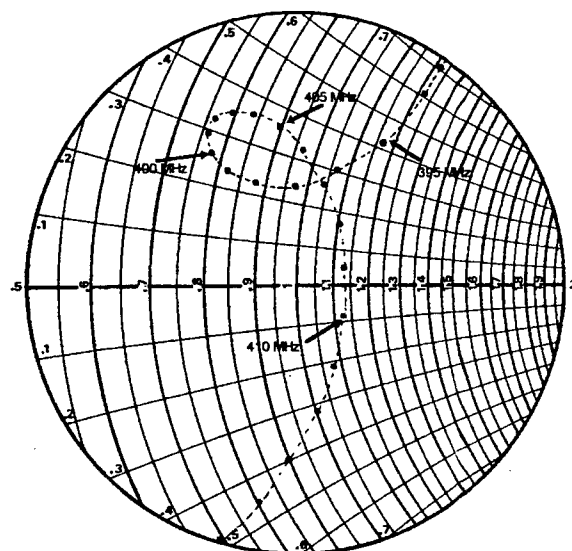


Fig. 14 UHF Band Modified Kilgus Antenna Axial Ratio

3. PATCH ANTENNA FOR UHF BAND.

Circular UHF patch antenna was designed due to its low mechanical profile and for this reason patch antenna doesn't produce any shadow over the observation cameras and sensors. A simple UHF whip antenna array was thought to be installed on board during the preliminary satellite design but this antenna was discarded during the previous antenna design and measurements because of a multi lobe radiation pattern, not permitting to fulfill the link requirements.

Several patch antenna models were constructed, building reinforced polyester dielectric thick sheets to be installed between the ground plane and the metallic



SWR_{max}=2

Fig.:15 UHF Patch Antenna

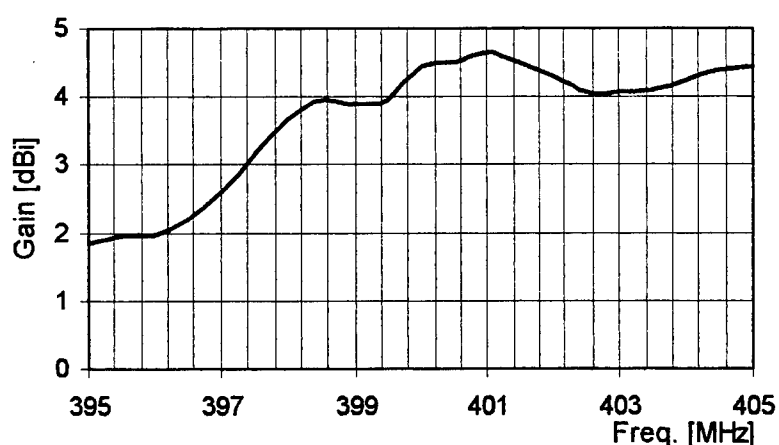
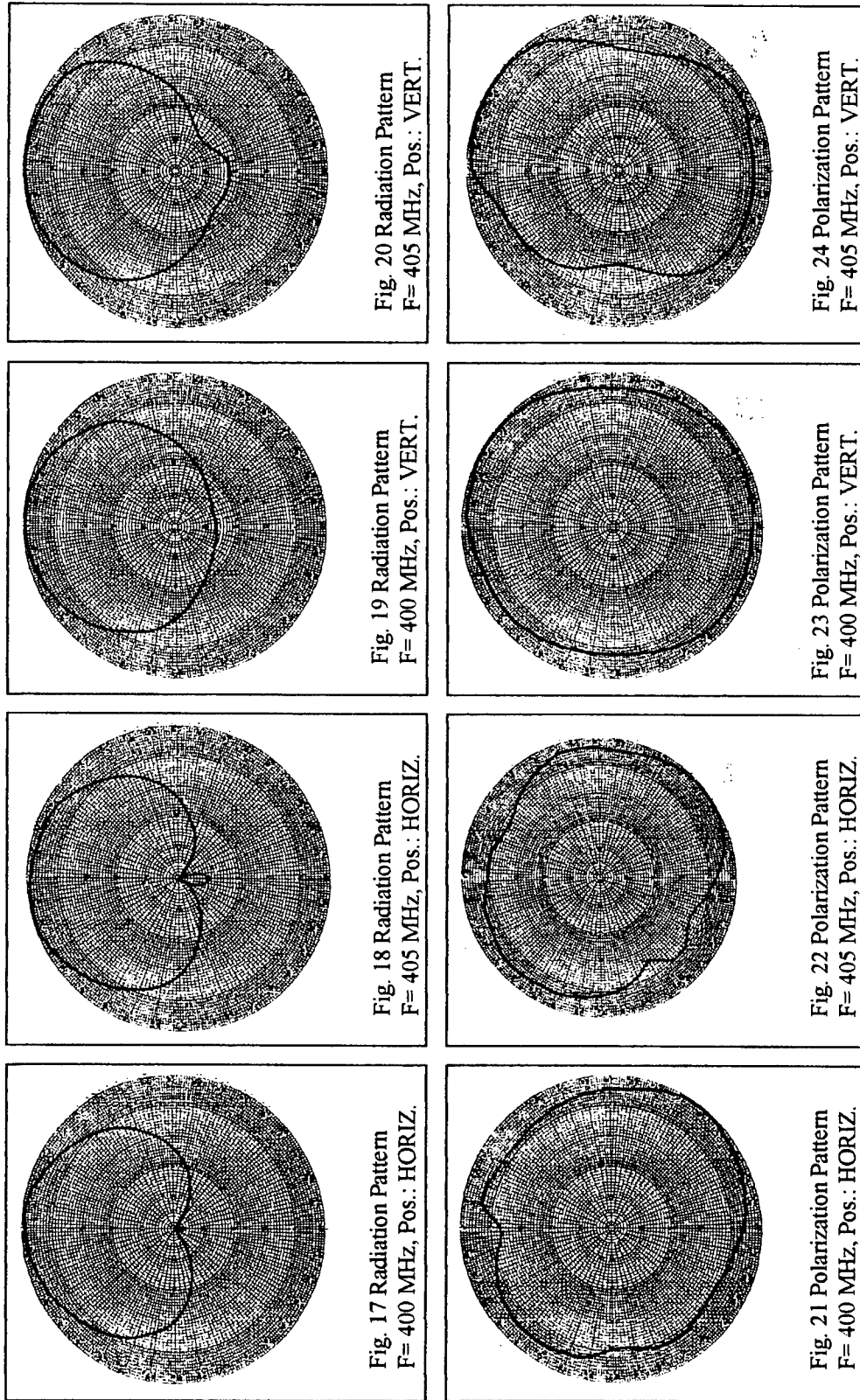


Fig. 16 UHF Patch Antenna Gain



Patch Antenna - UHF Band - (DYNAMIC RANGE 25 dB)

patch. Due to the size restrictions a 0.25x0.25 meter metallic ground plane patch antenna was "prima facie" adopted.

Antenna input impedance as a function of frequency can be seen in the figure 15 and antenna gain in figure 16.

Figures 17 to 24, show some radiation and polarization patterns obtained during the measurements in the antenna anechoic chamber for a right circular polarized reference antenna.

Wide beamwidth lobe is obtained that almost fulfill the pattern requirements and a good axial relationship within the operational band.

Axial ratio as a function of frequency can be seen in figure 25

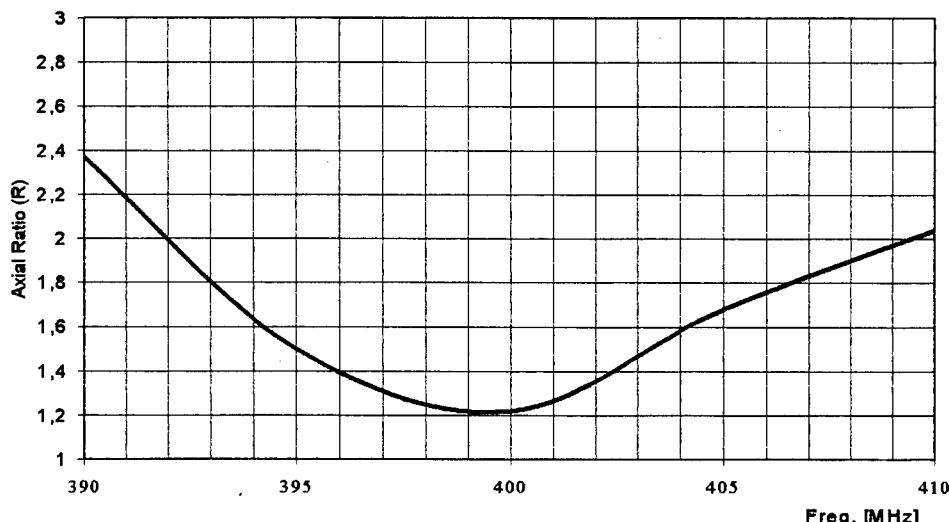


Fig. 25 UHF Patch Antenna Axial Ratio

4. MODIFIED KILGUS ANTENNA FOR "S" BAND.

Modified Kilgus "S" band antenna was designed to fulfill the link requirements for telemetry, control and low resolution data transmission. It will be installed on a small metallic platform over a composite material pole. Three of these poles will be installed on the principal satellite platform. On each of these poles one "S" band antenna will be installed and another one will be installed in the rear satellite part. This last antenna is installed in order to get more control possibilities during the satellite stabilization process after acquiring its orbital

position and will work with one of the front antennas. Both antennas will permit to get an entirely spherical coverage very important during the first part of the orbital flight.

Figure 26, shows the antenna input impedance and figure 27 shows the antenna true gain within the operational "S" band. Antenna gain obtained is around 3.5 dBic +/- 0.5 dB within the operational band from 2 to 2.4 GHz.

Some of the radiation patterns for right circular polarization can be seen in figure 28 to 31. Radiation patterns have been measured for any polarization but only right circular polarization is shown here. Polarization pattern has been measured in order to evaluate the circular radiation properties and these patterns can be seen in figure 32 to 35.

Axial ratio within the operating band can be seen in figure 36.

Very good circular polarization properties have been achieved in the specific working frequencies and these optimum results are obtained adjusting the helical arm lengths at the operational frequency.

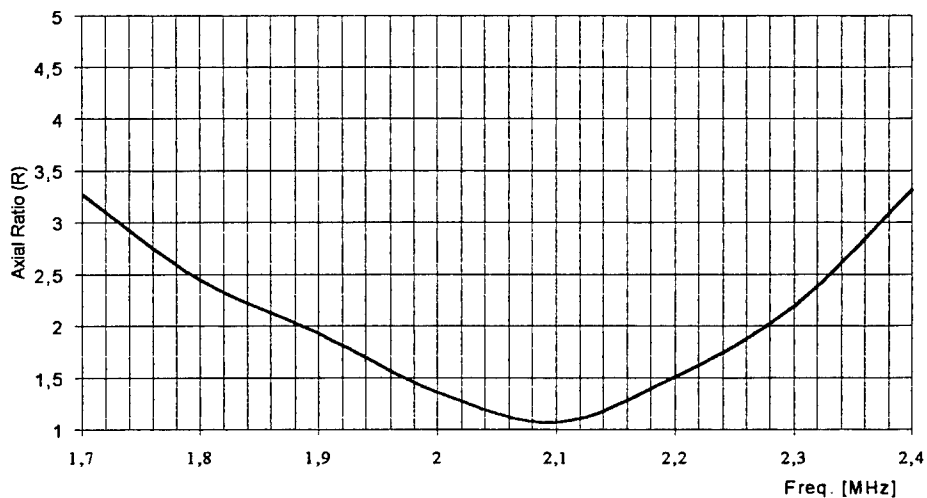


Fig. 36 S Band Modified Kilgus Antenna Axial Ratio

5. MODIFIED KILGUS "X" BAND ANTENNA.

Modified Kilgus antenna for "X" band has been designed for high-resolution image data transmission within the satellite images transmission band (8 to 8.5

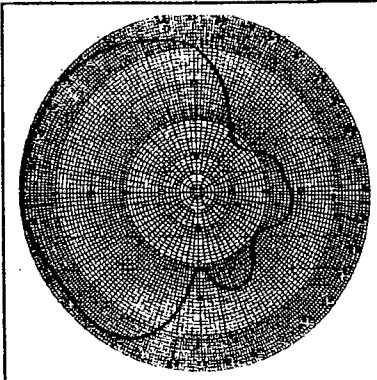


Fig. 28 Radiation Pattern
F= 2075 MHz, Pos.: HORIZ.

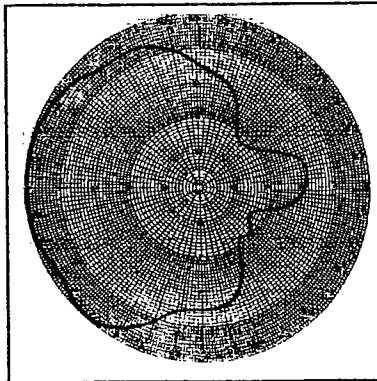


Fig. 29 Radiation Pattern
F= 2250 MHz, Pos.: HORIZ.

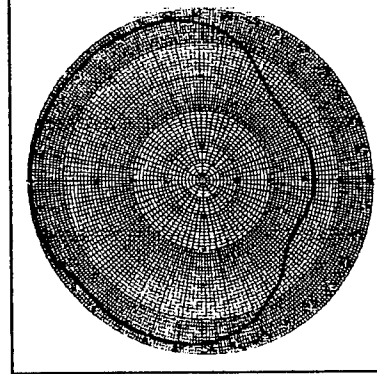


Fig. 30 Radiation Pattern
F= 2075 MHz, Pos.: VERT.

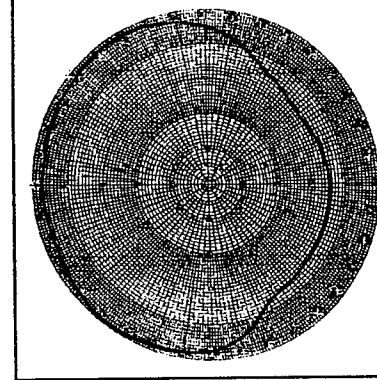


Fig. 31 Radiation Pattern
F= 2250 MHz, Pos.: VERT.

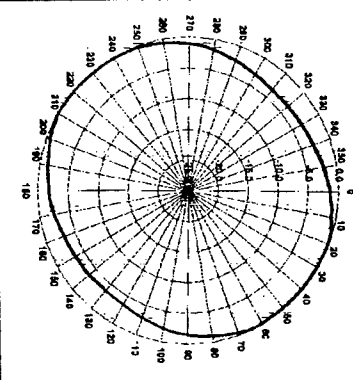


Fig. 32 Polarization Pattern
F= 2075 MHz, Pos.: HORIZ.

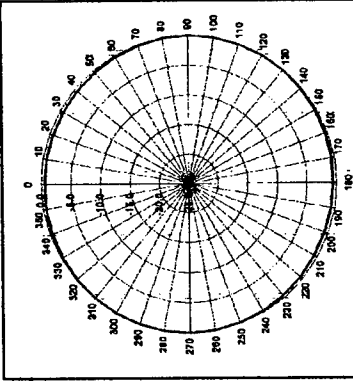


Fig. 33 Polarization Pattern
F= 2250 MHz, Pos.: HORIZ.

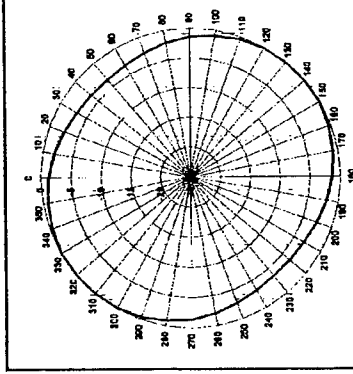


Fig. 34 Polarization Pattern
F= 2075 MHz, Pos.: VERT.

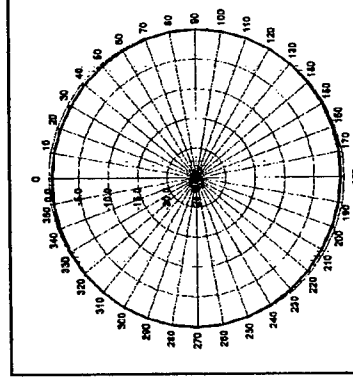


Fig. 35 Polarization Pattern
F= 2250 MHz, Pos.: VERT.

Modified Kilgus Antenna - S Band - (DYNAMIC RANGE 25 dB)

GHz). Design concepts are similar than in the previous "S" band case and installation will be on the small platform very close to the "S" band antenna. Antennas input impedance has been measured in the anechoic chamber by means of a network analyzer and figure 37 shows the impedance results within the operational band.

Means of power meters and the three-antenna method has measured antenna true gain in the anechoic chamber too. These results can be seen in figure 38, where an almost constant gain along the band was achieved and near 4 dBic \pm 0.5 dB within the operational band from 8 to 9 GHz. It can be seen that the antenna gain is surpassing the bandwidth specifications of 8 to 8.5 GHz, but this specification must be compared with the axial ratio specifications in order to determine the real antenna behavior. In this specific case a small increment in gain with respect to the "S" band antenna is due to a wider antenna ground plane in wavelengths.

Figures 39 to 42, show the antenna radiation patterns for right circular polarization measured in the anechoic chamber where polarization patterns have been measured at the same time. Polarization patterns can be seen in figures 43 to 46. From these figures specified beamwidth has been achieved and an almost perfect circularity is obtained between 8.0 and 9.0 GHz. Figure 47 shows the resulting axial ratio.

These results confirm an increase in the antenna specifications in beamwidth, gain and axial ratio compared to the necessary antenna bandwidth.

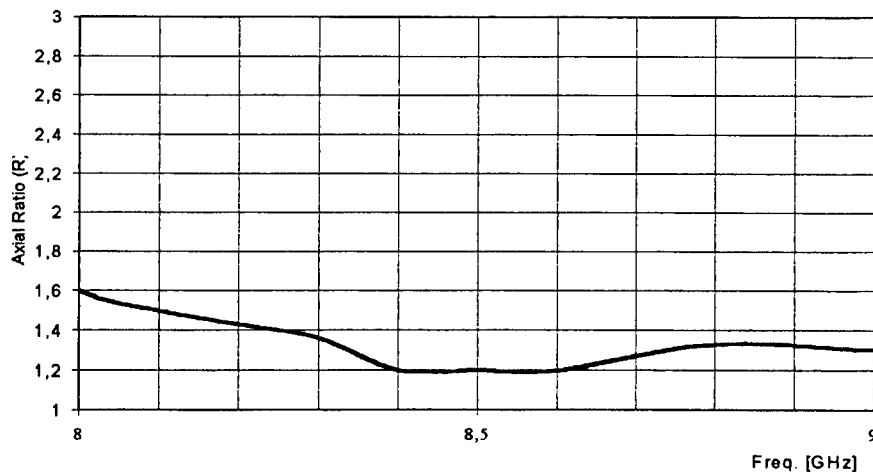


Fig. 47 X Band Modified Kilgus Antenna Axial Ratio

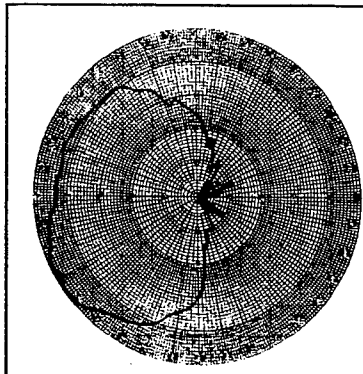


Fig. 39 Radiation Pattern
F= 8300 MHz, Pos.: HORIZ.

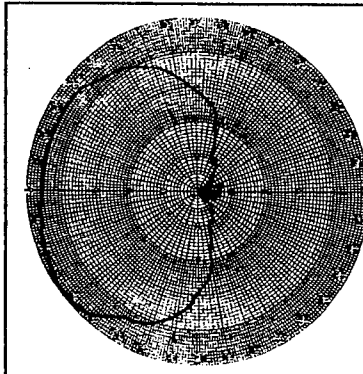


Fig. 40 Radiation Pattern
F= 8400 MHz, Pos.: HORIZ.

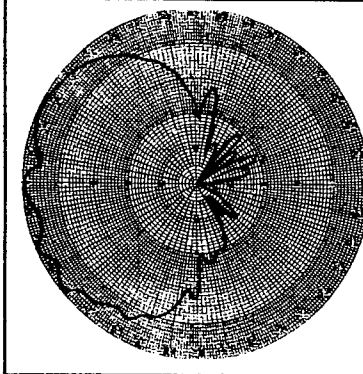


Fig. 41 Radiation Pattern
F= 8300 MHz, Pos.: VERT.

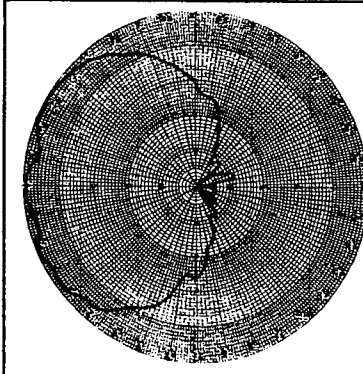


Fig. 42 Radiation Pattern
F= 8400 MHz, Pos.: VERT.

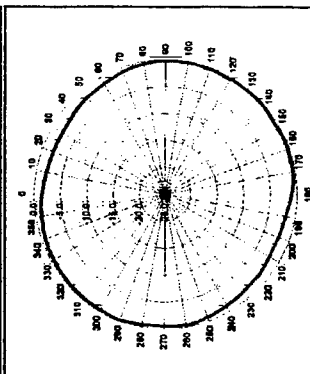


Fig. 43 Polarization Pattern
F= 8300 MHz, Pos.: HORIZ.

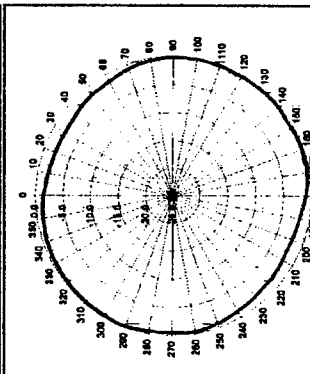


Fig. 44 Polarization Pattern
F= 8400 MHz, Pos.: HORIZ.

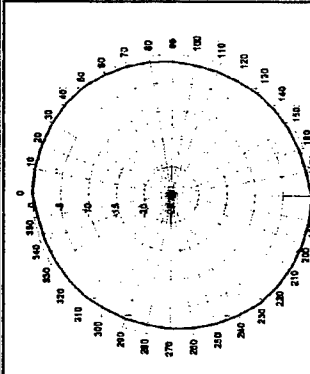


Fig. 45 Polarization Pattern
F= 8300 MHz, Pos.: VERT.

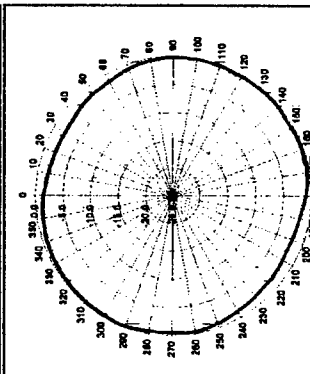


Fig. 46 Polarization Pattern
F= 8400 MHz, Pos.: VERT.

Modified Klgus Antenna - X Band - (DYNAMIC RANGE 25 dB)

6. MOCKUP ANTENNA MEASUREMENTS.

All the previous antenna models designed in each band were installed in the appropriate place on the satellite mockup. This mockup was installed over the CITEFA antenna outdoor range turntable. The resulting VSWR of each antenna have been obtained by means of a VSWR microwave bridge. The small size of this device doesn't disturb the radiating field around the antenna and can determine the VSWR of each system with good accuracy.

Figures 48 to 51 show the VSWR of the UHF modified Kilgus antenna, the UHF patch antenna and the modified Kilgus "S" and "X" antennas.

In each band, SWR is less than 2 within the operation frequencies for these preliminary antenna models. Improvement will be made in the final versions.

Figure 52 show a satellite platform diagram where the system reference axis, in order to analyze the radiation patterns is indicated.

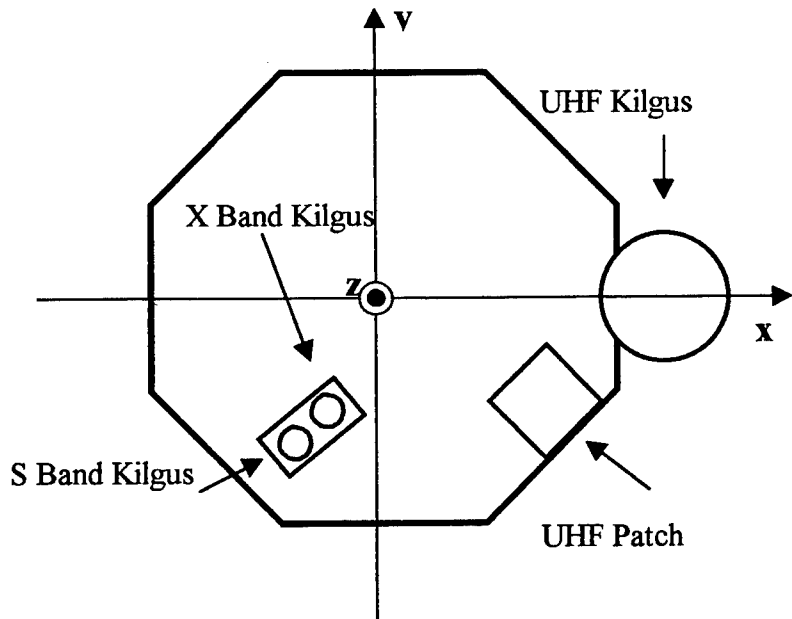


Fig. 52 Antenna locations on the Mockup principal platform

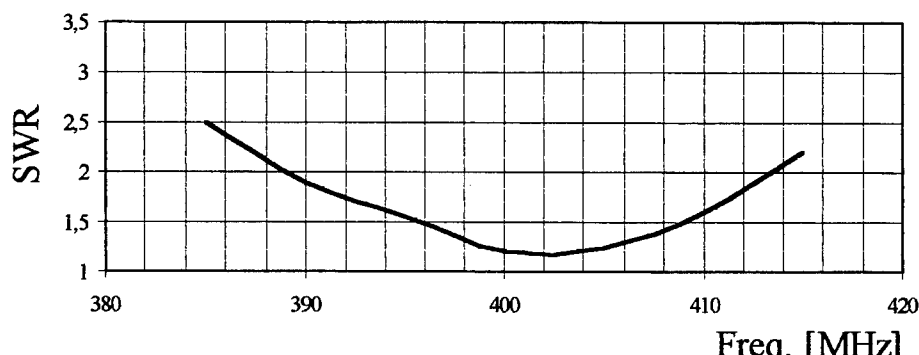


Fig. 48 UHF Modified Kilgus Antenna SWR,
Installed on the Satellite Mockup

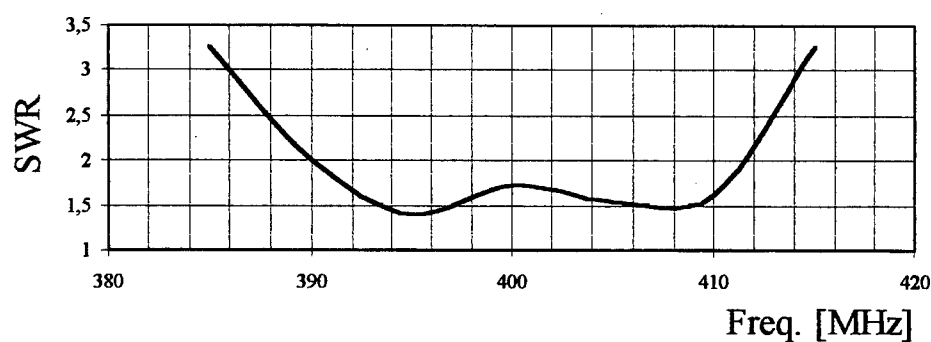


Fig. 49 UHF Patch Antenna SWR, Installed on the
Satellite Mockup

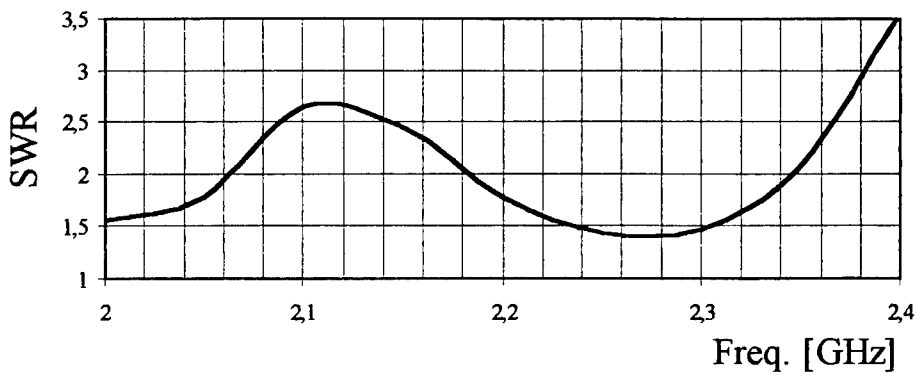


Fig. 50 S Band Modified Kilgus Antenna SWR,
Installed on the Satellite Mockup

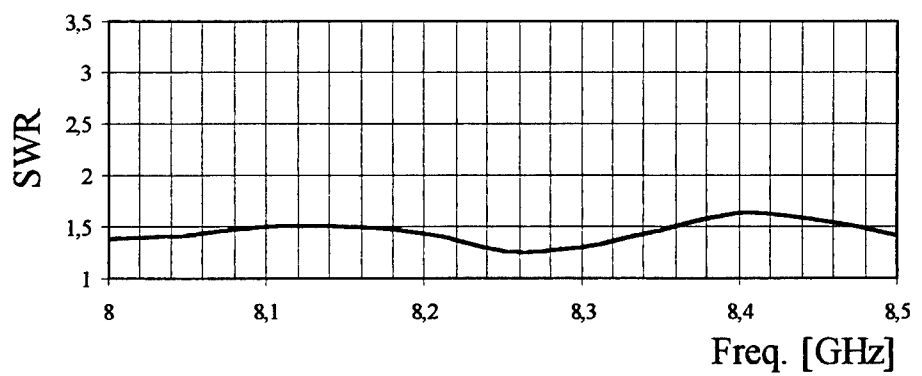


Fig. 51 X Band Modified Kilgus Antenna SWR,
Installed on the Satellite Mockup

Figures 53 to 68 show the radiation patterns that have been determined in the outdoor antenna range for the antennas installed on the satellite mockup. In each radiation pattern, the letter in brackets indicates the axis toward the antenna range turntable, during the measurements.

According to UHF pattern antenna measurements a big difference in the radiation pattern symmetry can be seen.

This is due to the satellite mockup shadow over the antenna radiated energy and more radiated power in the rear of the antennas due to a very small ground plane referred to the wavelength. This effect occurs in both cases, modified Kilgus and Patch antenna installed on the satellite mockup.

In the UHF specific case, is very difficult to find an ideal antenna place, due to the small available places for these antenna physical sizes.

Good symmetry is achieved in S and X bands, because in these cases the antennas ground plane are bigger referred to the wavelength, avoiding back radiation. At the same time, they are located on small platforms over booms putting the antennas in the free space over the principal platform and avoiding the satellite shadow effects.

7. ACKNOWLEDGEMENTS

The authors express their gratitude to the CONAE and CITEFA authorities, permitting the publication of these results, and especially to CONAE engineers Hugo Mascialino, Carlos Alonso and Marcelo Cerocchi.

Also thanks to CITEFA mechanical department and especially to Technician Pablo Perez who made the antennas prototypes.

8. BIBLIOGRAPHY

- 8.1 C. C. Kilgus, "Resonant Quadrifilar Helix Design", The Microwave Journal, December 1970.
- 8.2 J. D. Krauss, "Antennas", Chap 7, 2nd Edition, 1988, Mc. Graw Hill
- 8.3 I.J.Bahl and P.Bhartia, "Microstrip Antennas", 1980, Aertech House
- 8.4 Y.T.Lo, S.W. Lee, "Antenna Handbook", Chapter 10, 1988, Van Nostrand Rainhold, Co. NY.

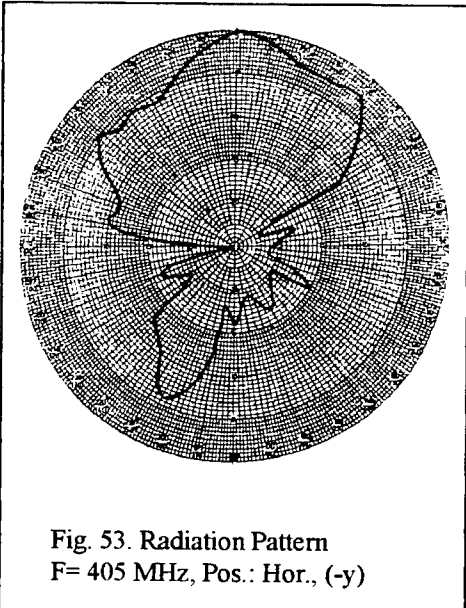


Fig. 53. Radiation Pattern
F= 405 MHz, Pos.: Hor., (-y)

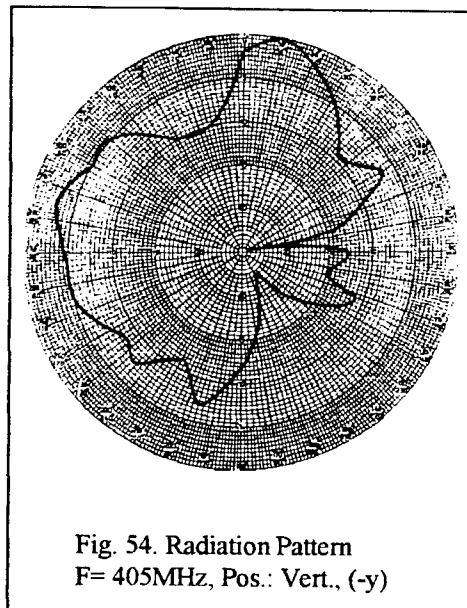


Fig. 54. Radiation Pattern
F= 405MHz, Pos.: Vert., (-y)

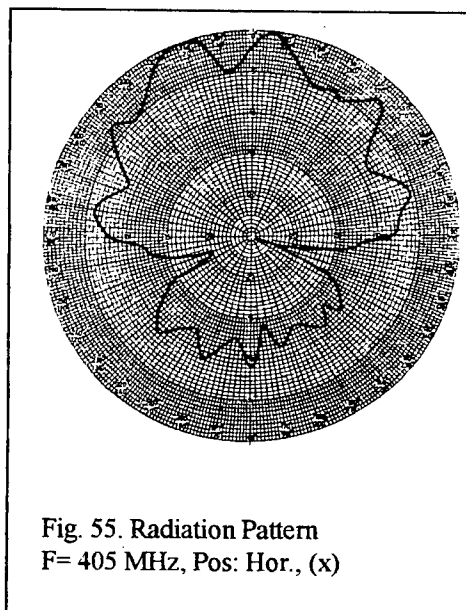


Fig. 55. Radiation Pattern
F= 405 MHz, Pos: Hor., (x)

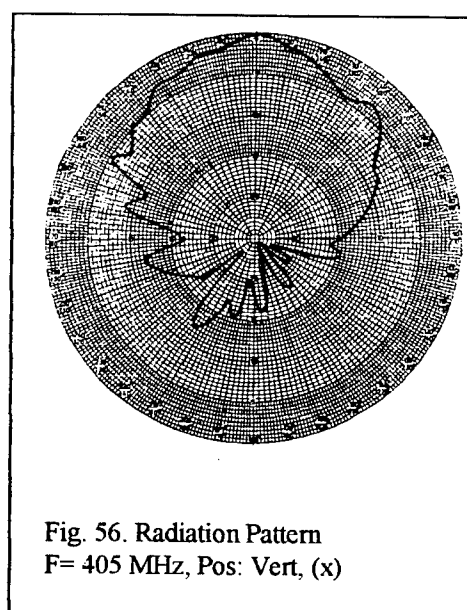


Fig. 56. Radiation Pattern
F= 405 MHz, Pos: Vert, (x)

Modified Kilgus Antenna Installed on the Satellite Mockup - UHF Band
(DINAMIC RANGE 25 dB)

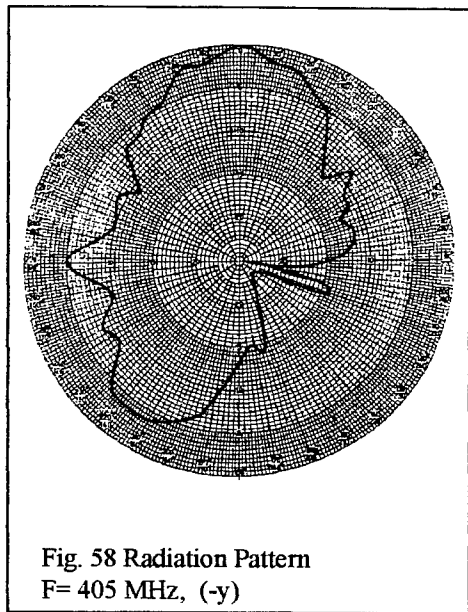
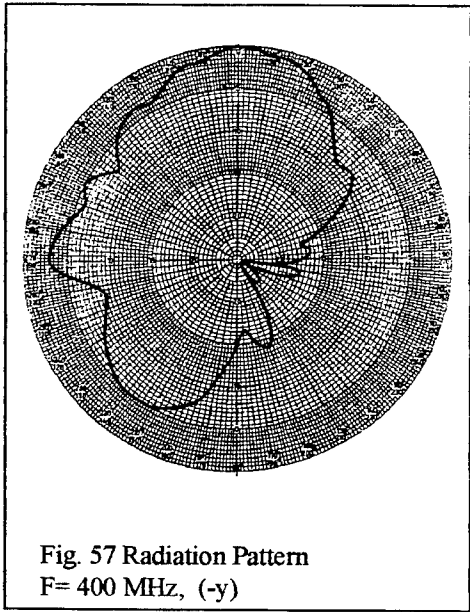


Fig. 57 Radiation Pattern
F= 400 MHz, (-y)

Fig. 58 Radiation Pattern
F= 405 MHz, (-y)

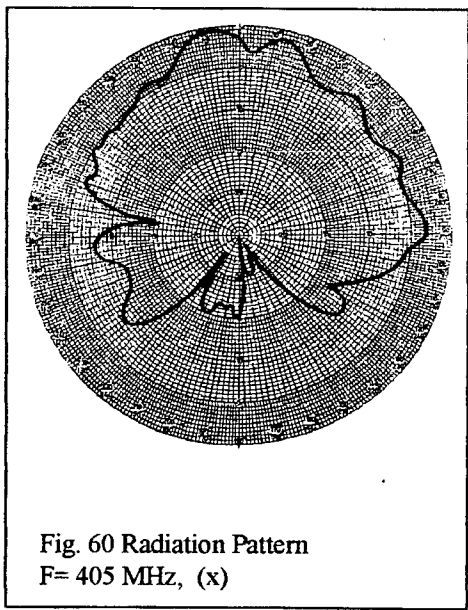
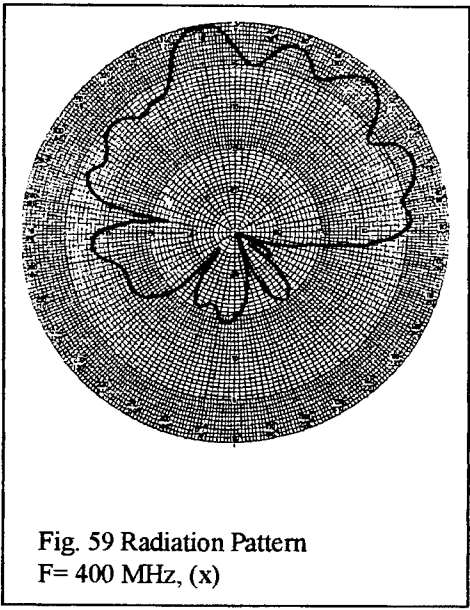


Fig. 59 Radiation Pattern
F= 400 MHz, (x)

Fig. 60 Radiation Pattern
F= 405 MHz, (x)

Patch Antenna Installed on the Satellite Mockup - UHF Band
(DYNAMIC RANGE 25 dB)

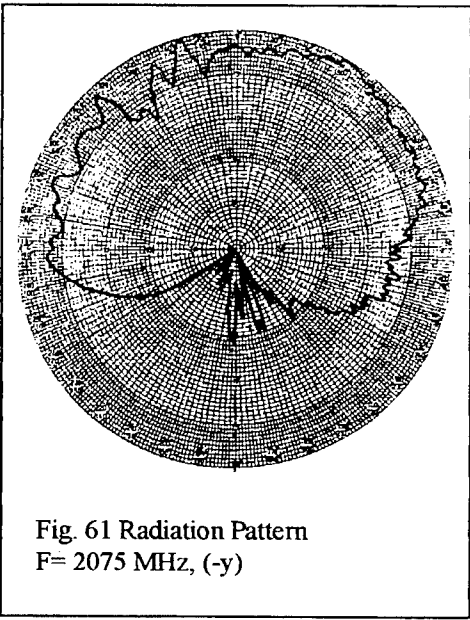


Fig. 61 Radiation Pattern
F= 2075 MHz, (-y)

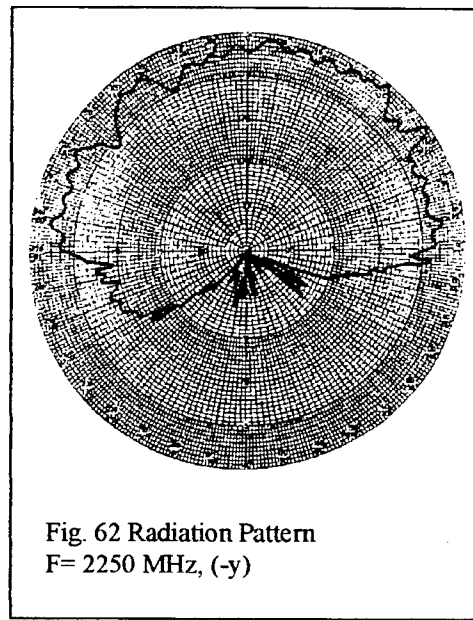


Fig. 62 Radiation Pattern
F= 2250 MHz, (-y)

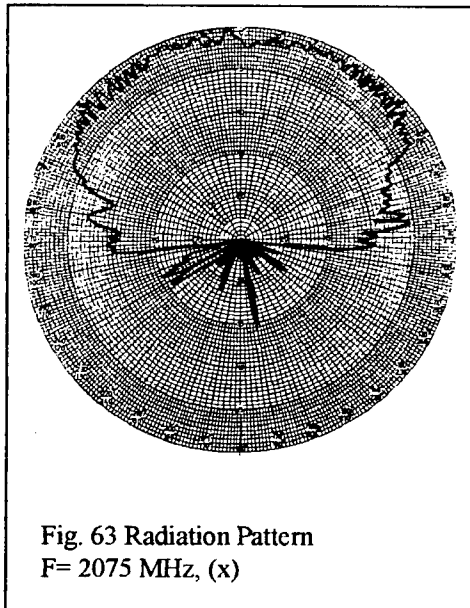


Fig. 63 Radiation Pattern
F= 2075 MHz, (x)

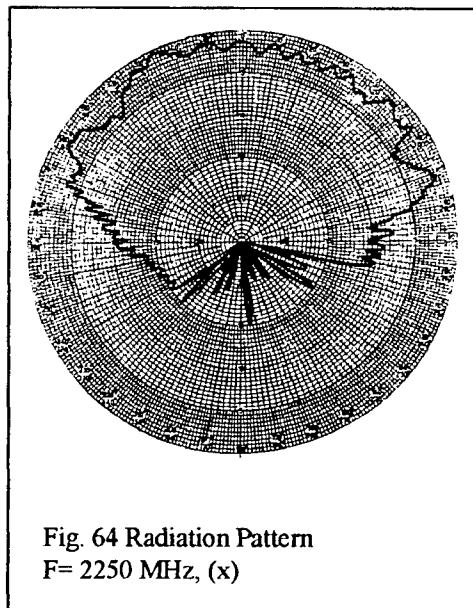


Fig. 64 Radiation Pattern
F= 2250 MHz, (x)

Modified Kilgus Antenna Installed on the Satellite Mockup - S Band
(DYNAMIC RANGE 25 dB)

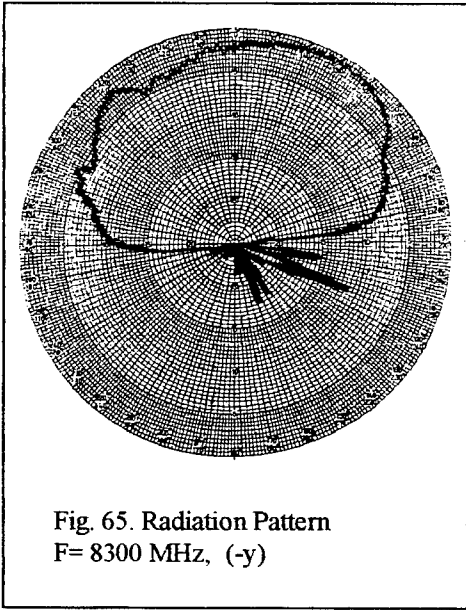


Fig. 65. Radiation Pattern
 $F = 8300$ MHz, (-y)

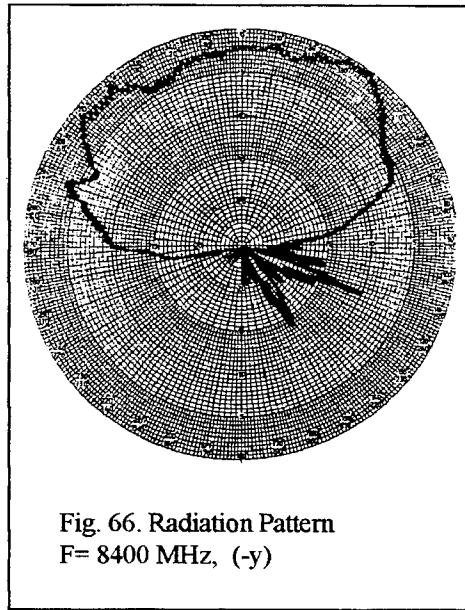


Fig. 66. Radiation Pattern
 $F = 8400$ MHz, (-y)

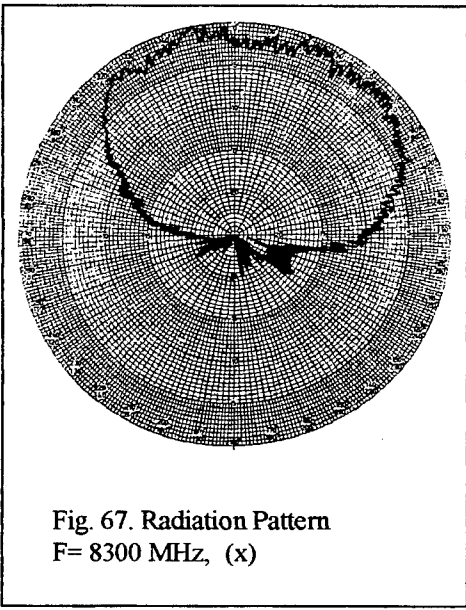


Fig. 67. Radiation Pattern
 $F = 8300$ MHz, (x)

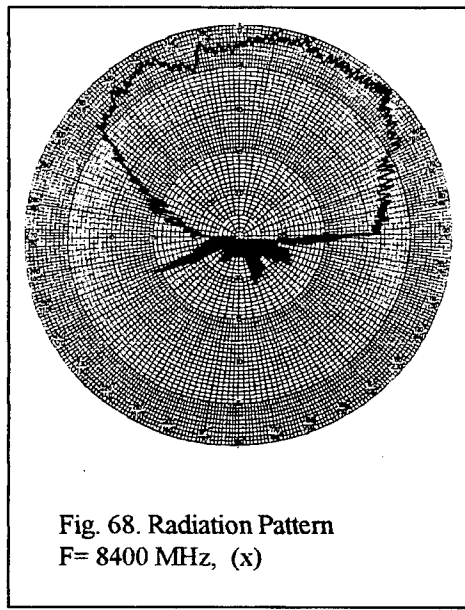


Fig. 68. Radiation Pattern
 $F = 8400$ MHz, (x)

Modified Kilgus Antenna Installed on the Satellite Mockup - X Band -
(DYNAMIC RANGE 25 dB)

An Array Antenna Space Experiment Using Transmit/Receive Antenna Module (TRAM) Technology

Hugh Southall¹ (AFRL/SNHA), William Kornrumpf (GE Corporate R&D), Jim Staggs and Fred Jonas (Nichols Research) and Yolanda King (AFRL/VSS)

ABSTRACT We describe the design, fabrication and ground test of an X-band array antenna using TRAM technology for a satellite experiment with the goal of demonstrating the survivability of an ultra-lightweight, active array in a space radiation environment. TRAM technology uses MHDI (Microwave High Density Interconnect) flex circuits for the RF, control and DC manifolds. MMICS and control ICs are secured in an inexpensive, thin plastic layer directly on the face of the aperture to meet the ultra-lightweight goal of $< 6 \text{ kg/m}^2$ for space based radar (SBR). The demonstration array is receive only. We present measured a theoretical antenna patterns for: scanned beams; a difference beam; and a beam with a null placed deterministically in the sidelobe region.

BACKGROUND An SBR requires very large radiating apertures to provide the necessary power-aperture product for the R^4 monostatic radar problem. Subapertures are required for implementing separate phase centers for clutter cancellation using displaced phase center antenna (DPCA) or for space-time adaptive processing (STAP). One SBR concept has an aperture area of about 130 m^2 . The proposed constellation is low earth orbit (LEO), about 900 km altitude, and the proposed launch vehicle is a Delta III or the Evolved Expendable Launch Vehicle (EELV). Obviously mass is of concern in a space system of this magnitude for launch on boosters smaller than Titan. The goal is $< 6 \text{ kg/m}^2$ for the aperture, including support structure. Also, for LEO constellations, the antenna must have a 10+ year maintenance-free life, must be power efficient and survive the harsh space radiation environment.

Such ultra-lightweight, very large apertures require a radically different approach to integrate the radar transmit and receive hardware with the array radiating elements. For the SBR concept mentioned above, the aperture is $6 \times 22 \text{ m}$, which at X-band ($\lambda=.03 \text{ m}$) gives a $200\lambda \times 734\lambda$ aperture. For a rectangular grid with $\lambda/2$ spacing, 587,200 elements (phase controls) are required. Since the azimuth scan (along the long dimension) is $+- 52^\circ$, the spacing can be increased slightly to $.56\lambda$ and the elevation scan is $+- 36^\circ$, which means elements can be spaced by $.63\lambda$ for 415,587 controls. The Stangel limit (Ref. 1) states that phase controls can be located at most a distance D/λ apart, where

$$\frac{D}{\lambda} = \frac{1}{2 \sin \theta_{\max}} \quad (\text{Equation 1})$$

¹ Currently with ARINC Incorporated

Using this equation with $\theta_{\max} = 36^\circ$ and 52° gives $D/\lambda = .85$ and $.63$ respectively, and results in about 273,700 phase controls. Even using the minimum number of phase controls, there is an incredibly large number of phase shifters. The number of receiver, transmitter and time delay MMICs can be reduced using subarray architectures if phase shifters with sufficiently low loss can be developed.

If each module were individually packaged in the traditional T/R module sense, the weight penalty would be great. A different approach is the Transmit/Receive Antenna Module (TRAM) technology sponsored by the Air Force Research Laboratory Space Vehicles Directorate (AFRL/VSS) at Kirtland AFB, NM, which uses the General Electric microwave high density interconnect (MHDI) technology with MMICs mounted directly on the array aperture. TRAM technology is not a discrete module technology, but a distributed module technology whose focus is ultra-lightweight, active apertures.

The survivability of TRAM will be addressed by placing a TRAM-based array on a British satellite (Scientific Test Research Vehicle, STRV-1d) and conducting a space flight experiment. The STRV-1d mission is a joint US (BMDO) and UK (DERA) scientific mission. The TRAM space experiment is a joint program between the AFRL Space Vehicles Directorate, the AFRL Sensors Directorate (AFRL/SNHA) at Hanscom AFB, MA, and the General Electric Corporate R&D (CRD) Center in Schenectady, NY. The Space Vehicles Directorate was responsible for the experiment interface with the satellite; overall system control including signal detection, data storage, satellite interface and the Data Handling System; and power conditioning. The Sensors Directorate was responsible for the array architecture design; dipole element testing; antenna pattern synthesis and analysis; and pattern measurements at the Ipswich Measurement Site. General Electric CRD, under sponsorship by the Space Vehicles Directorate, was responsible for the detailed engineering design of the array including the RF, DC and control manifolds using their MHDI process; fabrication of the array; test and integration of MMICs; overall technical project leadership and documentation.

The TRAM space experiment is described in detail in Reference 2. It is one of several experiments on the satellite, whose main purpose is to expose the experiments to the harsh radiation environment of space through an elliptical (eccentricity=0.73) geo-transfer orbit. There are 10 experiments on the satellite. They are primarily radiation experiments such as focal plane arrays, charge coupled devices, particle detectors, advanced structures, and, of course, the phased array antenna which is the subject of this paper. The satellite is approximately a two foot cube. The apogee is 36,000 km, the perigee is 620 km and the inclination is 7° , which will take the satellite through the Van Allen radiation belts, exposing the experiments to a severe radiation environment (1 to 3 Mrad/yr Si) during its one year mission life. We have measured the array antenna patterns on a ground range and will compare them with measured patterns obtained when the array is in space. The patterns will be measured by illuminating the satellite with an X-band source (the operational frequency is 10.2 GHz) as it rotates at 5 RPM on a spin axis which is normal to the orbit plane. Received signal strength data will be stored and

downlinked to a ground station. The array is scheduled for launch on an Ariane 5 booster in 1999.

We will now describe the demonstration array architecture and the radiating elements. Then, we will describe the MHDI design, the receiver design and conclude with measurements of antenna gain and the antenna beam patterns.

1 ARRAY ARCHITECTURE As shown in Figure 1, the array architecture consists of a linear array of four subarrays. Each subarray (receive module) has a 6 bit phase shifter and a low noise amplifier (LNA). The original goal was a two dimensional scanning array, which would have required more area on the satellite. More importantly, it would have required more power to operate the LNAs and, of course, more weight. The weight goal for the array (including structure and RF output cable) was only 75 grams. The actual weight of the array, including the RF connector and control pigtails, is 50.8 grams. A photograph of the flight array is shown in Figure 2. Since a one dimensional scanning linear array can also demonstrate performance deterioration, we decided to use a linear array. Subarrays were used to minimize the number of LNAs and phase shifters, and therefore conserve power. Also, the design of a "quad" module of four radiating elements was an existing design at General Electric CRD.

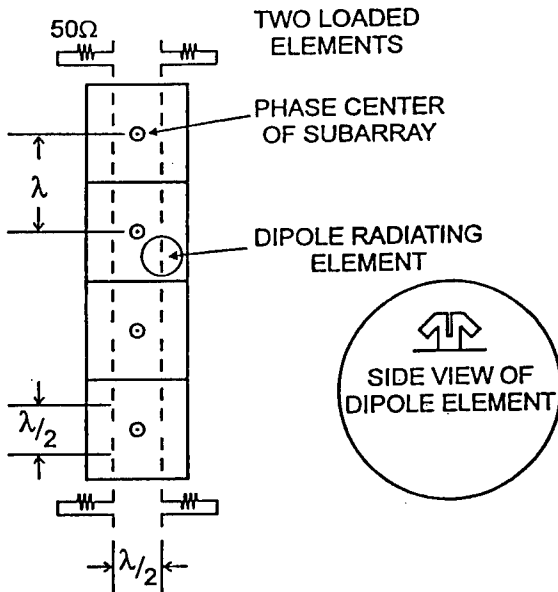


Figure 1 TRAM array architecture.

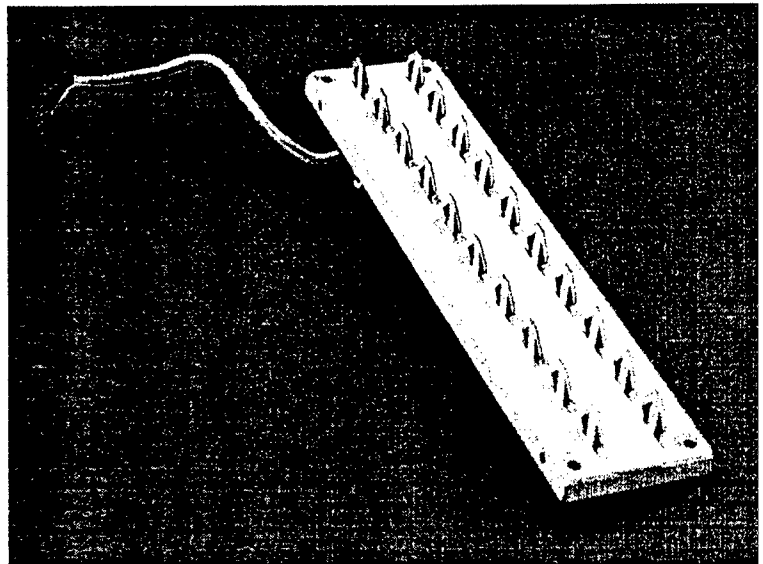


Figure 2 TRAM array flight hardware. Dimensions are 150 X 35 X 5 mm. Mass is 50.8 grams. The control pigtail and the RF GPO connector are at the upper left (underside) of the array.

The dipole radiating elements are spaced by $\lambda/2$ and are oriented such that the array scans in the E-plane of the dipoles. The two elements at either end of the array are terminated

dummy elements. Dummy elements are used to reduce edge effects on this small array by providing a more uniform electromagnetic environment for the few active elements. Even though the elements are spaced by $\lambda/2$, the phase centers of the subarrays, which control the scanning properties, are spaced by λ . We scan the array to 30° , therefore, we expect to see grating lobe effects. Since the gain of the array is not a critical issue, we simply recognize the fact that grating lobes will be present and use that pattern, as well as others, to determine any deterioration in array performance due to the harsh space environment.

As shown in Figure 3, the ideal antenna pattern will be broad in the H-plane (where $\phi=\pi/2$), and will be a sinc function pattern in the E-plane (where $\phi=0$) with a 3 dB beamwidth of about 12.5° . Note that $u=\sin\theta\cos\phi$ and $v=\sin\theta\sin\phi$. The pattern in the H-plane is that of two dipoles over a ground plane spaced by $\lambda/2$. The beam is scanned in the E-plane by adjusting the phase shift between the subarrays using phase shifters. In addition to scanning, we synthesize other antenna patterns by adjusting the phase shifters as described in Section 6.

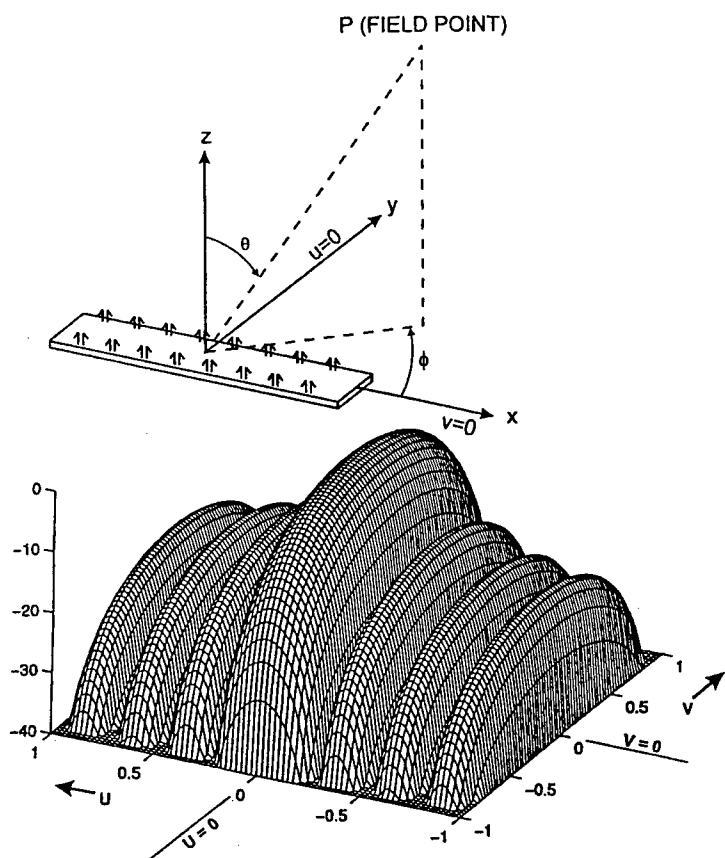


Figure 3 Predicted antenna pattern (broadside scan) for the TRAM array. Inset shows the geometry.

2. RADIATING ELEMENTS The radiating elements selected for the array are bent dipoles as shown in Figure 4. The design of this element was reported in Reference 3 for implementation in microstrip. Our implementation is stripline. The elements are printed circuit dipoles fabricated on a flex circuit with a KAPTON™ polyimide substrate (KAPTON is a trademark of DuPont Co.). Although the MHDI layers connecting the MMICs are parallel to the array face, the dipoles are curved using the flex circuit to be perpendicular to the face of the array and extend through narrow slots in the face of the array to a height of about $\lambda/4$ above the ground plane.

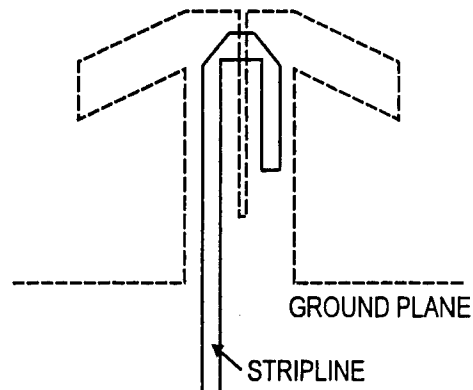


Figure 4 Stripline realization of balun structure with integrated dipole. The ground plane is above and below the stripline center conductor.

The dipole is fed with a 50 ohm stripline which couples to the dipole arms through a balun structure consisting of a length of transmission line parallel to the slot and an open circuited length of transmission line on the other side of the slot. The line crossing the slot generates a voltage across the gap which drives current in the dipole arms (or vice versa on receive). The measured return loss at 10.2 GHz is less than -20 dB and the bandwidth is approximately 1 GHz (at -10 dB return loss) or about 10 %.

3 ARRAY MODULE FABRICATION AND PACKAGING

The TRAM demonstration array (Reference 4) mechanical structure was designed to house the space experiment and is approximately 5 mm thick. A cross section of the structure is shown in Figure 5. Composite Optics Incorporated (COI), an established supplier of space qualified carbon fiber/epoxy composite structures, provided the mechanical housing using materials similar to those which would be used in a deployed SBR. The mass of the 35 X 150 X 5 mm array is 50.8 grams including the RF

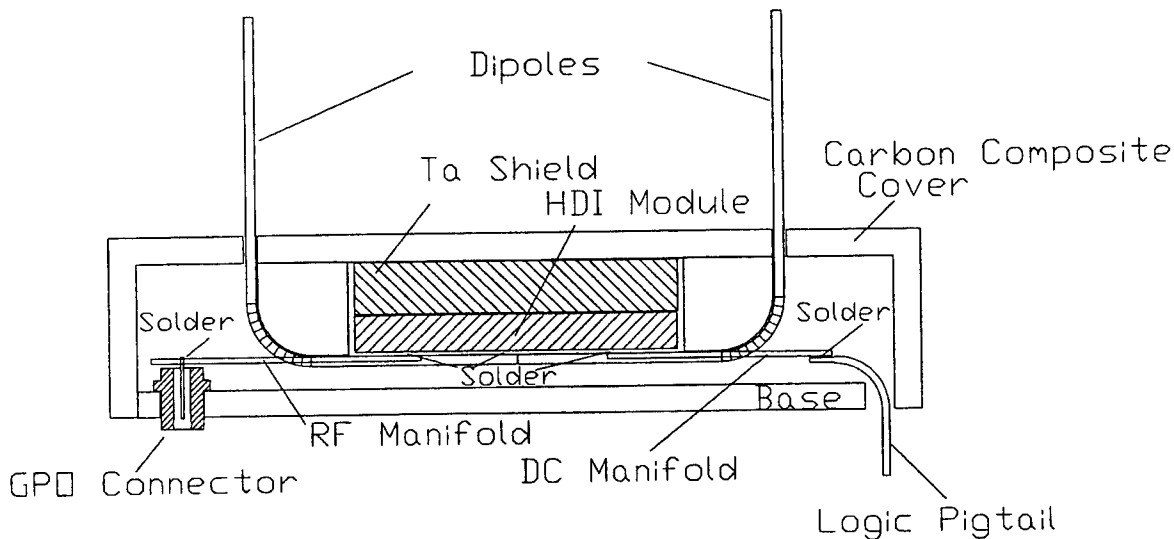


Figure 5 TRAM array cross section. Features: Carbon/epoxy composite cover and base; 4 mil thick polyimide RF and DC manifolds; 10 mil thick polyimide dipole dielectric; Reflow solder joints; GPO connector for RF connection to the spacecraft; Tantalum spot shielding

connector and the dc/logic pigtail. If radiation hardened die were used in the digital section instead of tantalum spot shielding, a mass per unit area of 6.3 kg/m^2 could have been attained.

The power budget for our experiment was 2 watts, including both the spacecraft interface and the TRAM array. The achieved power consumption was 1.7 watts. The TRAM array power budget was 600 milliwatts. Each receive module contains a GaAs LNA, a 6 bit GaAs phase shifter MMIC fabricated by M/A Com, two CMOS control ICs (an 8 bit serial to parallel converter and a hex inverter) and a capacitor for the LNA drain supply.

Each module was designed for fabrication using the low mass, Lockheed Martin/General Electric plastic encapsulated Microwave High Density Interconnect (MHDI) process. In this process, the die are attached to the underside of a pre-patterned flex circuit. A plastic encapsulation is provided and two additional connection layers are written on top of the

flex circuit. KAPTON™ (polyimide sheet) is used as the dielectric, and the interconnect lines are fabricated with copper and gold plated copper traces. The RF signals are connected using stripline transmission lines and are completely shielded from the DC and digital control signals. This packaging approach has proven very flexible in previous programs with applications including: 5 and 35 watt C-band radar T/R modules; 10, 15 and 44 GHz beamformers; and 60 GHz LNAs.

The individual receive modules for the TRAM application are very compact, having dimensions of 9 X 18 X .75 mm and a mass of only 1.08 grams. There are four receive modules in the TRAM demonstration array. The receive modules were processed in the General Electric HDI facility on 6 inch square carriers. While each HDI carrier contains only nine TRAM receive modules, three RF test modules and three reliability test structures, 72 of the 9 X 18 mm modules could have been processed on a single carrier.

The demonstration array requires one manifold structure to supply DC and control signals to each receive module and an RF manifold to combine the module RF outputs. The DC and control manifold was fabricated using the General Electric precision flex circuit process (two mil lines and spaces) with a row of eight 20 mil wide pads on 30 mil centers for solder connection to the four HDI receive modules. The RF manifold has four co-planar waveguide input connections and three Wilkinson combiners to sum the signals from the four receive module RF outputs. The Wilkinson combiners contain integral isolation resistors fabricated on the same layer as the internal stripline transmission lines. The manifold attaches to the receive modules by soldering the ground backed co-planar waveguide with conventional 63/37 solder for ease of assembly and system reliability. The sum port (single output spigot) of the manifold solders to the center pin and ground ring of a full detent Gilbert GPO connector mounted on the back of the TRAM mechanical housing. The detection, processing and storage of the received signal at this port is described in the next section.

4 SIGNAL DETECTION AND STORAGE

As the STRV-1d satellite rotates at 5 RPM, the array antenna pattern mechanically scans past the earth. The data taken from the antenna is the amplitude response of the mechanically scanned pattern. The spacecraft interface (SC IF) will step the antenna through a sequence of antenna patterns as described in Section 6. Experiment scheduling is under control of the onboard Data Handling System (DHS). Specific orbital profiles are defined preflight with the option to alter them during the mission. The experiment will measure the antenna amplitude response within and outside the Van Allen radiation belts. The STRV-1d will download data to a ground site every third orbit, and we define this time as an “experiment period.” During each “experiment period”, data will be taken twice within the belts and once outside the belts. The experiment will have no knowledge of its exact location. As the electronics deteriorate, the effects are measured, studied and duplicated via ground radiation tests. Measured trend information will aid future space based communications and radar system design and development.

The SC IF consists of two functional blocks: a DC coupled AM receiver and a digital interface. The SC IF controller is an 80C31 microcontroller with a small amount of external RAM and ROM. The microcontroller loads a serial 32-bit word to the array phase shifters; takes amplitude data from the A/D converter; processes the data and uploads it to the electronics test bed (ETB) for future download. The 32-bit word consists of four 8-bit bytes with two “don’t care” bits. Six bits in each of the four bytes are used to command the four phase shifters. The experiment will take data at a 30 Hz rate, process the data and prepare it for upload to the DHS. There are seven preloaded antenna beams for data taking. These beams are described in Section 6. Uploads to the DHS may occur once each minute.

The data processing function is the most complicated and has the most involved software. This function performs the following tasks:

- Initialize the four phase shifters by loading a 32-bit serial word. Each minute, the experiment will load one of seven phaser settings corresponding to one of the seven beams described in Section 6.
- Read a data block (360 samples) from the A/D converter. The sample rate is 30 Hz, which corresponds to one degree steps in the amplitude measurement since the satellite rotates at 30 degrees per second.
- Determine “good” data by peak detection.
- Truncate and store the “good” data sets. Truncation consists of selecting 42 data points about the peak as a truncated data set (84 samples). This is equivalent to keeping +/- 42° of data about the antenna beam peak.
- Repeat these steps until usable RAM is full of “good” data. Full means three data sets per DHS poll.

Data analysis is done off line. Data from the satellite will be telemetered to a ground site every third day and made available to experimenters on the internet. Once analysis is concluded, operational flight profiles of interest can be rescheduled and during the next experiment period.

5 ARRAY GAIN MEASUREMENTS The directivity of both a subarray and the entire array can be calculated from the effective area, A_e . Since each subarray is an array of $\lambda/2$ spaced radiating elements, the effective area is λ^2 . For the entire array, the effective area is $4\lambda^2$. We calculated the directivity by integrating the power radiation patterns and obtained the same value for the theoretical directivity calculated from the following equation

$$D = \frac{4\pi}{\lambda^2} A_e . \quad (\text{Equation 2})$$

From this equation, we calculate D=11 dBi for a subarray and D=17 dBi for the entire array, where dBi is the directivity relative to an isotropic radiator. The gain of an antenna is the directivity less any losses (ohmic and mismatch). For an active antenna, the LNA active gain must be added to the directivity to obtain the net antenna gain. The antenna gain can be measured by comparing the gain of the antenna under test with the gain of an antenna with a known gain (standard gain horn). This was done for a quad subarray, the full active array, and an array fabricated without LNAs and phase shifters, which we refer to as the passive array. The measured gain for each configuration is shown in the following table.

<u>Antenna Configuration</u>	<u>Measured Gain (dBi)</u>
Quad subarray	10.6
Active array	10.9
Passive array	6.4

The net module gain is 4.1 dB (the LNA gain is about 14 dB and the phase shifter loss is about 10 dB), and is reflected in the 4.5 dB difference between the active and passive array measurements. The 0.4 dB difference between the net module gain and the measured difference between the active and passive array gains is within measurement error. Since the array directivity is 17 dBi and the measured gain is 10.9 dBi, the antenna loss is -6.1 dB. The loss budget is summarized in the following table.

<u>Loss (or Gain) Component</u>	<u>Loss (or Gain) (dB)</u>
Calculated Dipole Loss	-0.8
Net Module Gain	+4.1
Calculated RF Manifold Loss	-7.3
Measured RF Cable Loss	-1.5

From the above Table, the predicted array loss is -5.5 dB, which is within 0.6 dB of the measured loss. The largest loss component is the loss in the RF manifold. The large loss in the RF manifold is due to the design of the stripline used to implement the manifold. The manifold is a four to one power combiner using stripline and three Wilkinson combiners. The selected substrate thickness was so thin that it resulted in a very narrow stripline center conductor and consequently large ohmic losses. This design can be modified to reduce RF loss significantly with very small weight penalty.

6 ARRAY ANTENNA PATTERN MEASUREMENTS

To demonstrate the performance of the TRAM array, seven beams were synthesized. The beams will be tested sequentially, with the phase shifters set to produce a single beam at any given time. A summary of the seven beams is shown in the following table.

Beam # 1	Broadside beam (all phasers set to 0°)
Beam # 2	15° Left scan beam
Beam # 3	30° Scan beam
Beam # 4	15° Right scan beam
Beam # 5	Difference beam
Beam # 6	20° Null beam
Beam # 7	Broadside beam (all phasers set to 180°)

Since there is no amplitude control in the modules, our synthesis techniques were limited to phase adjustment only. For the first five beams (and Beam # 7), this is a simple matter. To generate the broadside beam, we simply set all of the phase shifters to state zero since the RF combiner is an equal phase combiner. Therefore, all of the subarrays have the same relative phase and a broadside beam is produced. The same discussion applies for Beam # 7. For the difference beam, we set the two left phase shifters to zero state and the two right phase shifters to a state corresponding to 180°. The state corresponding to the desired phase shift is determined from a table of measured insertion phase of a typical module as the phase shifter state is rotated through all 64 states.

For scanned beams, the phase difference between subarray phase centers is equal to $\pi \sin \theta$ since the separation between centers is equal to λ . Referencing an end element to zero state (zero phase), we can calculate phase shifter settings assuming a linear phase taper across the array. For the 30° scanned beam, we note that the grating lobe condition ($\sin \theta = \sin \theta_0 - \lambda/D$) for $\theta_0 = 30^\circ$ and $D = \lambda$ gives a grating lobe at $\theta = -30^\circ$. Therefore, there is no need to scan the 30° beam right *and* left since the patterns are identical.

To deterministically synthesize a null at 20°, we physically align an X-band source 20° from array boresight and use a genetic algorithm technique described in Reference 5 to **minimize** the array received power by adjusting all four phase shifters using the algorithm. A single chromosome corresponds to the four six bit words which set the phase shifter digital states. We use an initial population of 16, and discard the eight lowest performers (chromosomes resulting in higher measured power). The top eight performers are mated pair-wise to produce eight new children. We mutate (negate) one bit in the entire population (except for the top performer) and measure the received power for the children and rank the new population. The end result is a null in the pattern at 20°. For the 15° scanned beams, we performed a similar procedure to calibrate the array (by **maximizing** the received signal at the desired angle of 15°). We calibrated since the table-determined phase settings using a linear phase taper resulted in a poor pattern with high sidelobes for the 15° scanned beams.

Antenna pattern measurements were made at the US Air Force Research Laboratory Ipswich Measurement Site in Ipswich, Massachusetts. The range transmitter is located across a deep valley a quarter of a mile from the bay in which the test antenna is located. The antenna patterns obtained from these measurements will be used as a baseline to compare with patterns obtained during the space experiment. Any degradation due to the space environment can be determined by noting changes from the baseline patterns. Six

measured beam patterns are shown as the solid curves in Figure 6. The 20° null in Beam #6 occurs at -20°, since we intentionally reversed the order of the elements in setting the phase shifters (for both theory and measurement) to check symmetry. Theoretical predictions are shown dotted and are in general good agreement with measured patterns.

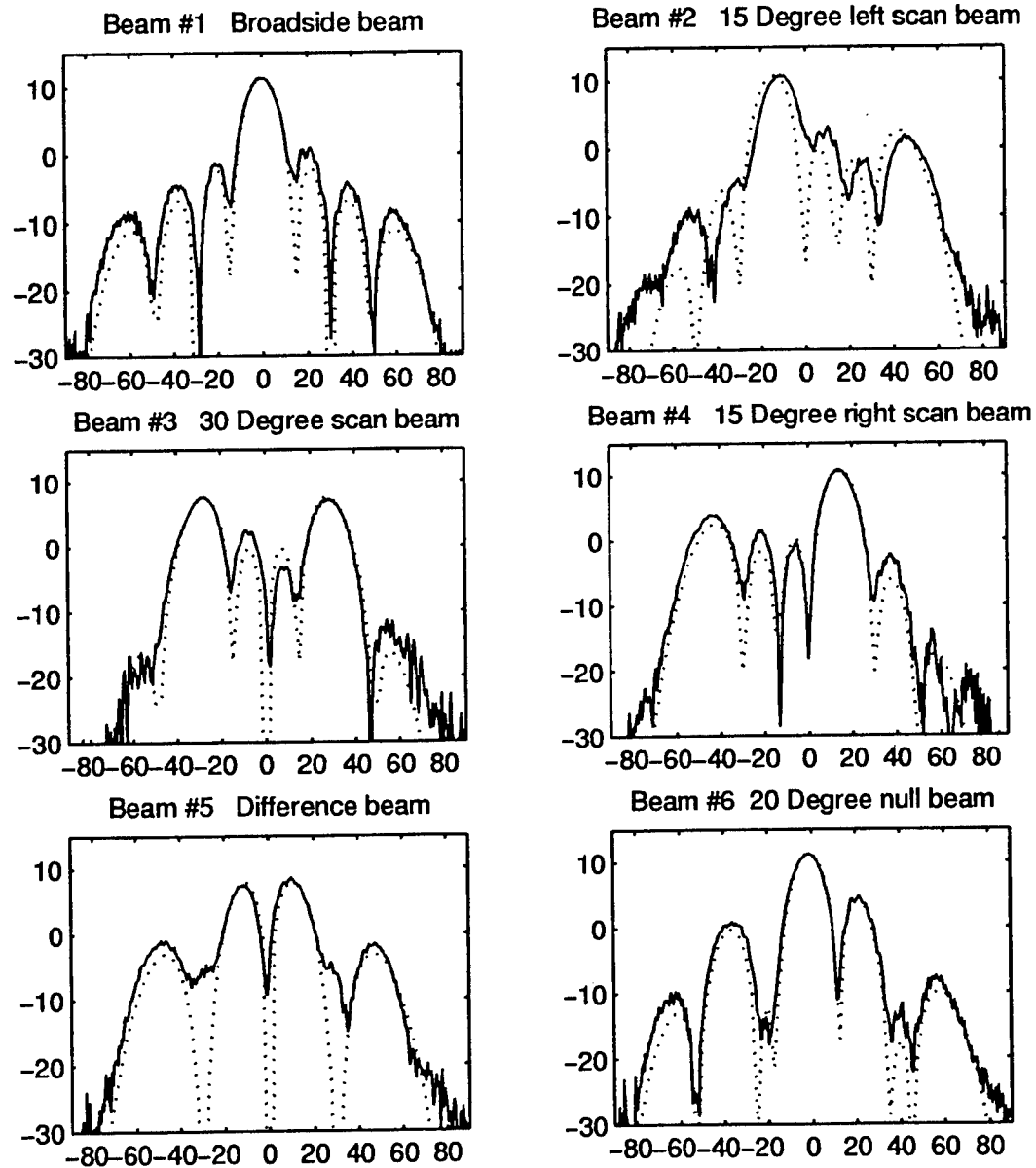


Figure 6 Measured (solid) and theoretical (dotted) TRAM array beams.

CONCLUSIONS

We described the design and ground testing of a small X-band active phased array antenna for a space experiment. The goal of the experiment is to demonstrate the survivability of ultra-lightweight, active arrays in space. Measured antenna patterns indicate that the array is ready for the space experiment.

ACKNOWLEDGEMENTS

We would like to acknowledge the measurement support of Jim Kenney and Ed Martin, and the machining support of Erhard Wisniewski at the Ipswich Measurement Site of AFRL/SNHA. We appreciate the advice and consultation of Bob Mailloux and Peter Franchi of AFRL/SNHA and the help of Terry O'Donnell from Arcon Corp. Thanks to Mr. Joe Perez, AFRL/VSDI (Jackson & Tull) and Mr. Jim Hanson, AFRL/VSDI (Nichols Research) for their support in constructing and testing the RAM receiver and controller board. Thanks to Dr. John Stubstad of the Ballistic Missile Defense Organization (BMDO) for his support of the STRV-1d experiments. At General Electric Corporate R&D Center, we acknowledge the help of Mr. Lou Petrucco, Ms. Lillian Sprinceanu, Ms. Elizabeth Burke and Dr. Nicole Krishnamurthy.

REFERENCES

1. Mailloux, R.J., *Phased Array Antenna Handbook*, Artech House, 1994, page 448.
2. Jonas, Fred; Staggs, Jim; King, Yolanda; Southall, Hugh; and Kornrumpf, Bill; "Transmit/Receive Antenna Module (TRAM) Technology," Government Microcircuit Applications Conference (GOMAC 98), Arlington, VA, 16-19 March 1998.
3. Rees, D. E. and Edward, B. J., "Printed Dipole Radiating Elements for Monolithic Millimeter Wave Phased Arrays," 1986 Antenna Applications Symposium, University of Illinois Allerton House.
4. Final Report: 1997 Transmit/Receive Antenna Module (TRAM) Demonstration Array contract F29601-92-C-0137 (STAR), Work Area 3: Highly Integrated Processing and Packaging, Funding Agency: US Air Force/ Air Force Research Laboratory/Space Vehicles Directorate.
5. Haupt, R. L., "An Introduction to Genetic Algorithms for Electromagnetics," IEEE Antennas and Propagation Magazine, Vol. 37, No. 2, April 1995, page 7.

Design of an Active Antenna Using the Series Feedback Oscillator

Byoung woo Park, Jeong se Han, Kyung soo Jin,
Bierng Chearl Ahn, Young chang Cho*

Dept. of Electrical & Electronics Engineering
Chungbuk National University, KOREA
* ACE Electronic Technology Co.
(E-mail: bwpark@cbucc.chungbuk.ac.kr)

Abstract: In this paper, the series feedback oscillator loaded with a microstrip patch is designed at 1.8GHz by using a HEMT and distributed elements such as the rampart line inductor and the interdigital capacitor.

The 3-port scattering parameter of the HEMT, the inductance, the capacitance and the length of microstrip line used in the active antenna are calculated to satisfy the oscillation condition and to get the maximum output power. Those are optimized by using Touchstone simulator.

Experimental results of the oscillator show -30dBm output at 1.79GHz with the bias voltage of 1V. In order to act as an active antenna, this network must be in the pre-oscillation state which means that the drain bias voltage is some lower than that of starting oscillation.

At 1.68-1.78GHz, the gain of the active antenna biased at the pre-oscillation state show 5-7dBm higher than that of zero-biased antenna.

The radiation pattern of the active antenna has a half power beamwidth of $\pm 30^\circ$.

1. INTRODUCTION

Active antennas which can be used in PCS, cellular phone, wireless LAN are being spotlighted due to the fact that it can easily get installed in the communication equipment because of small-size and low-price.

H. J. Thomas realized an active antenna by using a GUNN diode and microstrip patch antenna[1]. T. O. Perkins used IMPATT diode and microstrip circular patch antenna[2]. These active antennas have 5-10dB antenna gain but their noise figures are somewhat large because diodes are used as active device. K. Chang realized an active antenna by using a parallel feed-back oscillator where an microstrip patch antenna (MPA) is loaded at the parallel feed-back loop[3]. In this case, the microstrip lines have to be longer because of the large size of the MPA in L band and the mutual coupling between the microstrip lines and the MPA will deteriorate the performance of the active

antenna.

In this paper, we propose a series feed-back oscillator as an active circuit to design an active antenna operating at 1.8GHz. The MPA is used as a load of a series feed-back oscillator.

The simulation result of the oscillator optimized by Touchstone simulator shows 35dBm output at 1.8GHz. Experimental results of the oscillator show -30dBm output at 1.79GHz with the bias voltage of 1V.

In order to operate as an active antenna, the oscillator should be in the pre-oscillation state which means the circuit is slightly lower biased than that of starting oscillation. With the injection signal whose frequency is within the locking range (resonance bandwidth of MPA) of this circuit, the circuit impedance($Z_c(\omega)$) moves along the circuit locus. When it meets with the device impedance ($Z_D(A)$), the oscillation is started at the same frequency as an injection signal.

The experimental results of the active antenna show a -49.39dBm output at the 1.755GHz with the drain bias voltage of 0.8V.

The locking range of the active antenna is extended from 1.68GHz to 1.78GHz and 5-7dB antenna gain can be achieved in the locking bandwidth.

2. OSCILLATOR

2.1 Oscillation Condition

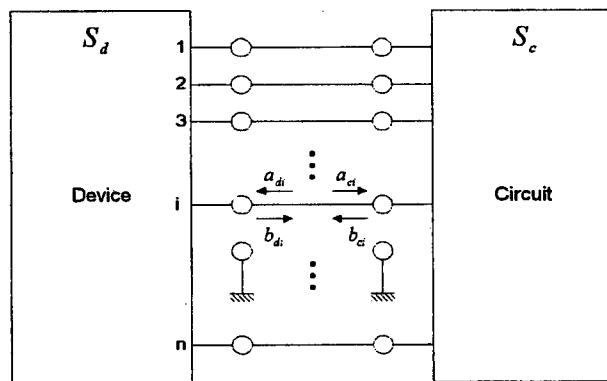


Fig.2-1 Scattering parameters of an N-port device and circuit.

The oscillation condition of an N-port device and circuit can be easily derived as a scattering matrix form.

At the i -th port, the reflected waves are expressed as follows.

$$\mathbf{b}_d = \mathbf{S}_d \mathbf{a}_d, \quad \mathbf{b}_c = \mathbf{S}_c \mathbf{a}_c \quad (2-1)$$

The reflected waves and the incident waves are same because the ports are connected to each other.

$$\mathbf{b}_d = \mathbf{a}_d, \quad \mathbf{b}_c = \mathbf{a}_c \quad (2-2)$$

We can combine these equations,

$$(\mathbf{S}_d \mathbf{S}_c - \mathbf{U}) \mathbf{a}_c = \mathbf{0} \quad (2-3)$$

The oscillation condition is as follows:

$$|\mathbf{S}_d \mathbf{S}_c - \mathbf{U}| = 0 \quad (2-4)$$

The oscillation condition is expressed from the scattering matrix (\mathbf{S}_d) of the HEMT and the reflection coefficients (\mathbf{S}_c) of the 3-port.

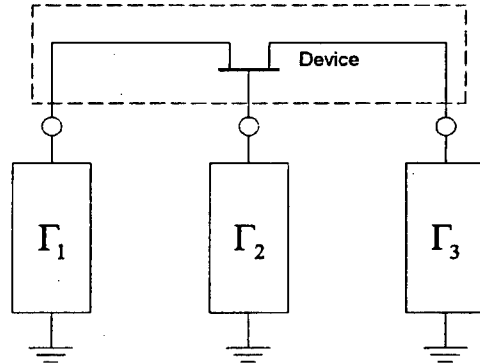


Fig.2-2 Three-port oscillator.

$$\mathbf{S}_d = \begin{pmatrix} S_{11} & S_{12} & S_{13} \\ S_{21} & S_{22} & S_{23} \\ S_{31} & S_{32} & S_{33} \end{pmatrix} \quad (2-5)$$

$$\mathbf{S}_c = \begin{pmatrix} \Gamma_1 & 0 & 0 \\ 0 & \Gamma_2 & 0 \\ 0 & 0 & \Gamma_3 \end{pmatrix} \quad (2-6)$$

The oscillation condition is as follows.

$$\begin{vmatrix} S_{11}\Gamma_1 - 1 & S_{12}\Gamma_2 & S_{13}\Gamma_3 \\ S_{21}\Gamma_1 & S_{22}\Gamma_2 - 1 & S_{23}\Gamma_3 \\ S_{31}\Gamma_1 & S_{32}\Gamma_2 & S_{33}\Gamma_3 - 1 \end{vmatrix} = 0 \quad (2-7)$$

The block diagram of the 3-port oscillator is shown in Fig.2-2.

2.2 Injection-Locked oscillator

When an external RF signal is applied to the input of free running oscillator, the oscillation frequency will be locked to the external signal. We call it injection-locking phenomenon.

The block diagram of the injection-locked oscillator is shown in Fig. 2-3. [4]

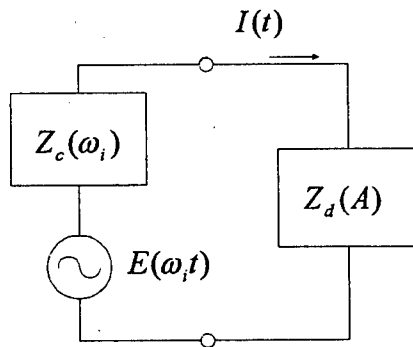


Fig.2-3 Block diagram of the injection-locked oscillator.

The current $I(t)$, injection voltage $E(t)$, and loop equation are as follows.

$$\begin{aligned} I(t) &= A(t)e^{j[\omega_i t + \phi(t)]} \\ E(t) &= |E|e^{j\omega_i t} \\ [Z_c(\omega_i) + Z_d(A)]I(t) &= E(t) \end{aligned} \quad (2-8)$$

When an external signal is small, the amplitude of the RF current (A) can be approximated by free- running amplitude A_0 .

$$Z_c(\omega_i) + Z_d(A) = \frac{|E|}{A_0} e^{-j\phi} \quad (2-9)$$

Herein, ϕ is the phase difference between I and E .

Graphically, the impedance relationship of equation (2-9) is represented as

shown in Fig. 2-4.

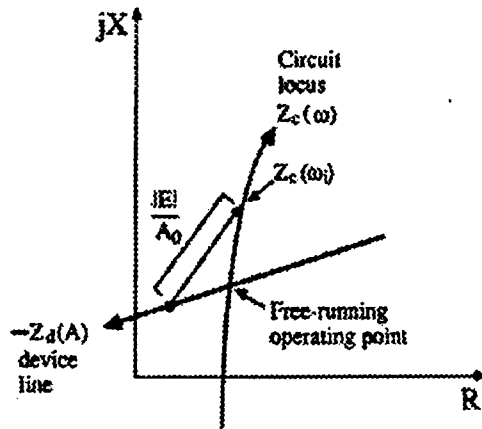


Fig.2-4 Relationship between the injection, device line, and circuit locus.

3. Active Antenna

3.1 Microstrip Patch Antenna (MPA)

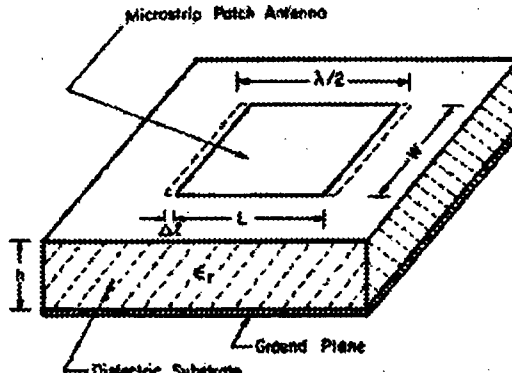


Fig.3-1 Microstrip patch antenna

The width (W) and the length (L) of MPA can be calculated with a following equation [5], [6].

$$W = \frac{\lambda_0}{2} \left(\frac{\epsilon_r + 1}{2} \right)^{-1/2} \quad (3-1)$$

$$L = \frac{c}{2f_r \sqrt{\epsilon_r}} - 2\Delta L \quad (3-2)$$

The characteristic impedance of the antenna Z_c is as follows.

$$Z_c = \frac{\eta_0}{\sqrt{\epsilon_{re}}} \frac{h}{W_e} \quad (3-3)$$

The self-admittance of the antenna can be calculated as follows.

$$\begin{aligned} Y_s &= G_s + jB_s \\ &= \frac{1}{\pi\eta_0} \left[\left(wSi(w) + \frac{\sin w}{w} \cos w - 2 \right) \left(1 - \frac{s^2}{24} \right) + \frac{s^2}{12} \left(\frac{1}{3} + \frac{\cos w}{w^2} - \frac{\sin w}{w^3} \right) \right] \quad (3-4) \\ &\quad + jY_c \tan(\beta\Delta l) \end{aligned}$$

The mutual admittance between radiating slots of MPA can be calculated by following equation.

$$Y_m = G_m + jB_m = G_s F_g K_g + jB_s F_b K_b \quad (3-5)$$

Therefore, the input impedance Z_{Pin} of MPA could be calculated as follows.

$$Z_{Pin} = \frac{Y_s + Y_c \coth(\gamma L)}{Y_c^2 + Y_s^2 - Y_m^2 + 2Y_s + Y_c \coth(\gamma L) - 2Y_m + Y_c \operatorname{csch}(\gamma L)} \quad (3-6)$$

The value of Z_{Pin} at 1.8GHz is $Z_{Pin} = 100.8 - j51.7$.

3.2 Design of Active Antenna

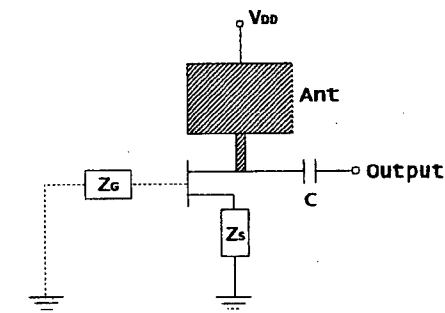


Fig.3-2 Geometry of an active antenna

The active antenna is consisted of an active network and antenna.

In general, either an amplifier or an oscillator is used as an active source and the microstrip patch antenna (MPA) or the microstrip slot antenna (MSA) is

used as an radiating element.

In this paper, an active antenna which can be used at 1.8GHz is designed. It is consisted of a series feed-back oscillator and an MPA.

Z_D , Z_G , Z_s in Fig.3-2 should be calculated to design a series feed-back oscillator.

The oscillation condition can be derived in terms of the 3×3 scattering parameters of the HEMT and the reflection coefficients of each ports. Then, we can calculate the gate impedance (Z_G) and the source impedance (Z_s) by using the reflection coefficients which satisfy the oscillation condition. The drain impedance (Z_D) is same as the input impedance of the MPA.

The drain impedance can be calculated

$$Z_{DD} = \frac{1 + S_{22}^T}{1 - S_{22}^T} \cdot Z_0 \quad (3-7)$$

Herein, the superscript 'T' is the measured S-parameter of HEMT. Therefore, the reflection coefficient of the drain (Γ_D) can be calculated by a following equation.

$$\Gamma_D = \frac{Z_{Pin} - Z_{DD}}{Z_{Pin} + Z_{DD}} \quad (3-8)$$

The S_{11}^T can be calculated by using the signal flow graph.

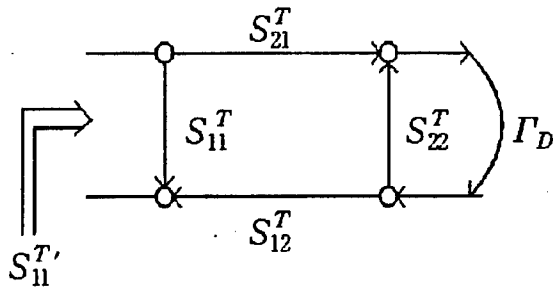


Fig.3-3 Signal flow graph

$$S_{11}^T = S_{11}^T + \frac{S_{21}^T S_{12}^T \Gamma_D}{1 - \Gamma_D S_{22}^T} \quad (3-9)$$

Due to $S_{11}^T = \Gamma_G$, the input impedance Z_{Gin} of the gate can be calculated by the following equation.

$$Z_{Gin} = \frac{1+\Gamma_G}{1-\Gamma_G} \cdot Z_0 \quad (3-10)$$

Consequently, Z_G satisfying an oscillation condition can be calculated by using Γ_G and Z_{Gin} .

$$Z_G = \frac{1+\Gamma_G}{1-\Gamma_G} \cdot Z_{Gin} \quad (3-11)$$

At 1.8GHz, $Z_G = 1291.35 - j294.1248$.

Converting the measured 2×2 S-parameters into the 3×3 S-parameter, following equations are used. [7],[8]

$$\begin{aligned} S_{33} &= \frac{S_{11}^T + S_{12}^T + S_{21}^T + S_{22}^T}{4 - (S_{11}^T + S_{12}^T + S_{21}^T + S_{22}^T)} \\ S_{32} &= \frac{1 + S_{33}}{2} (1 - S_{12}^T - S_{22}^T) \\ S_{23} &= \frac{1 + S_{33}}{2} (1 - S_{21}^T - S_{22}^T) \\ S_{22} &= S_{22}^T + \frac{S_{23}S_{32}}{1 + S_{33}} \\ S_{13} &= 1 - S_{23} - S_{33} \\ S_{31} &= 1 - S_{33} - S_{32} \\ S_{21} &= 1 - S_{22} - S_{23} \\ S_{12} &= 1 - S_{22} - S_{32} \\ S_{11} &= 1 - S_{21} - S_{31} \end{aligned}$$

The reflection coefficients of the source (Γ_s) can be calculated by substituting Γ_G and Γ_D into the oscillation condition.

$$\begin{bmatrix} S_{33}\Gamma_s - 1 & S_{31}\Gamma_G & S_{32}\Gamma_D \\ S_{13}\Gamma_s & S_{11}\Gamma_G - 1 & S_{12}\Gamma_D \\ S_{23}\Gamma_s & S_{21}\Gamma_G & S_{22}\Gamma_D - 1 \end{bmatrix} = 0 \quad (3-12)$$

The input impedance of the source can be calculated by the following

equation.

$$Z_{Sin} = \frac{1+\Gamma_s}{1-\Gamma_s} \cdot Z_0 \quad (3-13)$$

Consequently, Z_s satisfying oscillator term is as follows.

$$Z_s = \frac{1+\Gamma_s}{1-\Gamma_s} \cdot Z_{Sin} \quad (3-14)$$

At 1.8GHz, $Z_s = j45 \times 10^{-9}$.

4. Simulation

Touchstone program is used for the optimization of the circuit elements. The calculated and optimized values are shown in Table-1.

Table 1. The values of elements

	Z_{Pin}		Z_G		Z_s
	R	C	R	C	L
Calculated value	100.8	1.17	1291.35	88.982	3.98×10^{-18}
Optimized value	100.8	1.17	890.58	57.265	3.98×10^{-18}

The simulated result is shown in Fig.4-1.

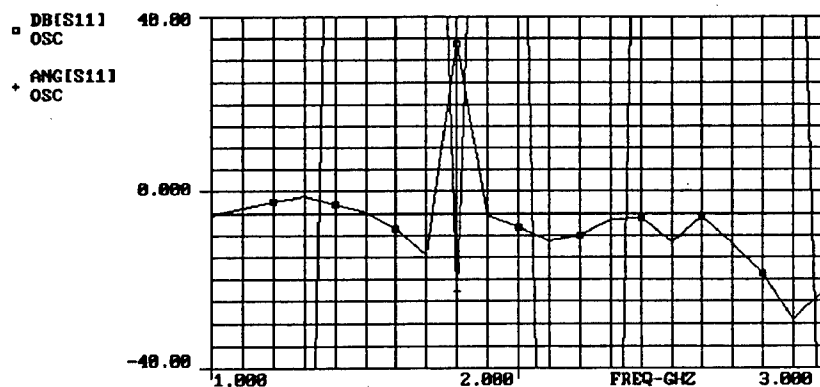


Fig.4-1 Characteristic of the active antenna(simulation)

5. Experiments

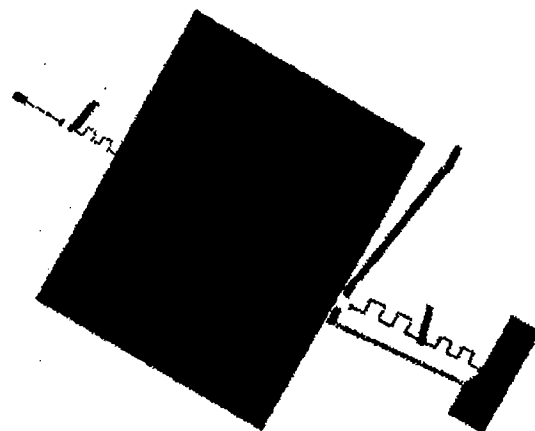


Fig.5-1 Pattern of the designed active antenna.

The circuit is built on Rogers substrate whose relative dielectric constant is 3.38 and 0.5mm thickness.

The pattern of the active antenna designed at 1.8GHz is shown in Fig. 5-1.

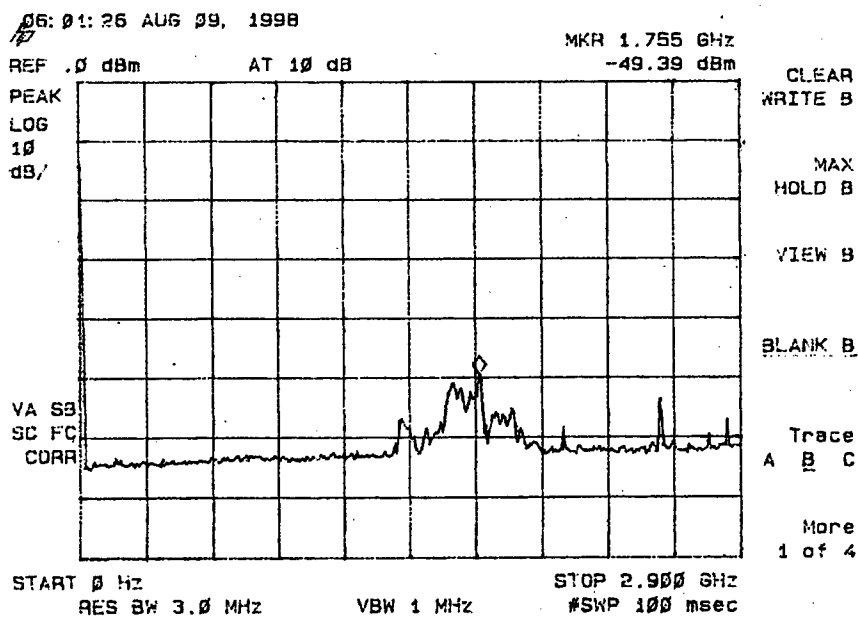


Fig.5-2a Characteristic of active antenna at 0.8V drain bias

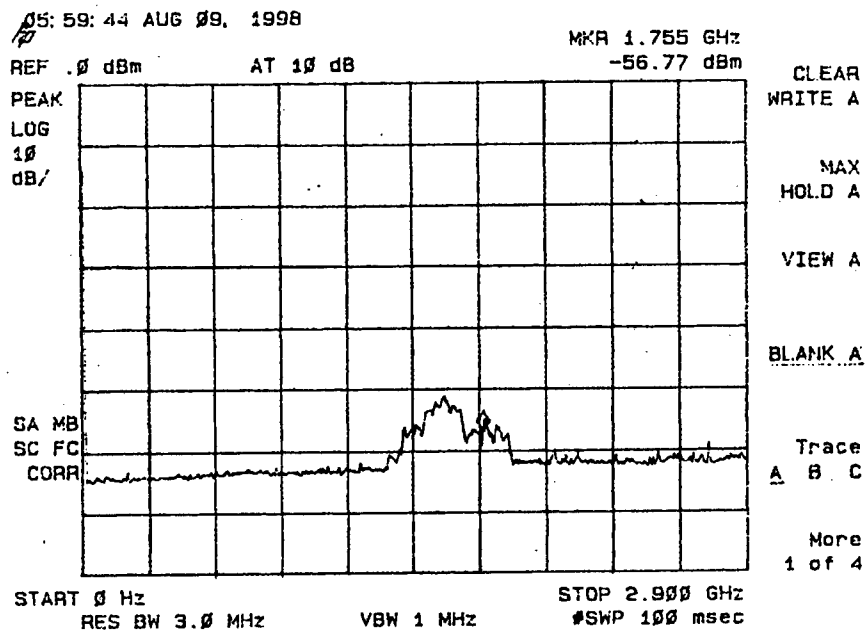


Fig.5-2b Characteristic of active antenna at 0V drain bias

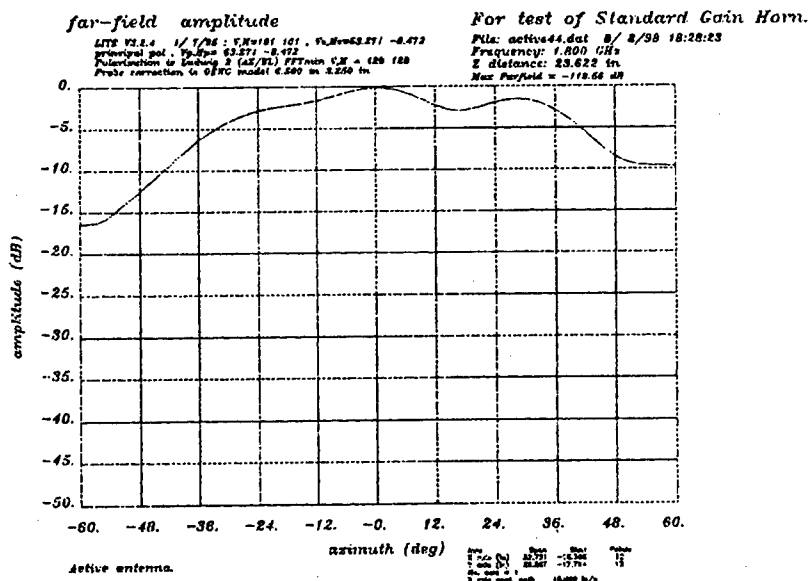


Fig.5-3 Radiation pattern of active antenna at 0.8V drain bias

The receive gain characteristics of the active antenna at 1m away from the transmitting antenna are measured by the spectrum analyzer when a dipole antenna is radiating a 0dBm power at the frequency band of 1.0-2.6GHz.

The experimental results of the active antenna at 0.8V and 0V drain bias voltage are shown in Fig.5-2a and Fig.5-2b.

At 1.755GHz, the received level shows -49.39dBm in Fig.5-2a and

-56.77dBm in Fig.5-2b. Fig.5-2a shows that the active antenna biased at the pre-oscillation state has a large gain for the external signal in the locking range.

The gain of the 0.8V biased active antenna is 5-7dB higher than that of zero-biased antenna in the frequency range of 1.68-1.78GHz.

Fig.5-3 shows the radiation pattern of the 0.8V biased active antenna. The HPBW is approximately $\pm 30^\circ$.

6. Conclusion

In this paper, we realized an active antenna which is a series feed-back oscillator loaded with a MPA at the drain port.

In order to act as an active antenna, this network must be in the pre-oscillation state which means that the drain bias voltage is some lower than that of starting oscillation.

At 1.68-1.78GHz, the gain of the active antenna biased at the pre-oscillation state show 5-7dBm higher than that of zero-biased antenna.

The radiation pattern of the active antenna has a half power beamwidth of $\pm 30^\circ$.

7. References

- [1] H.J.Thmoas, D.L.Fudge, G.Morris, "Gunn, Source intergrated with Microstrip Patch". *Microwave & RF*, pp.87-89, 1985
- [2] T.O.Perkins, "Active microstrip circuit patch antenna" *Microw.J.*, pp110-117, 1987
- [3] K.Chang, K.A.Hummer, G.K.Gopalakrishnan, "Active radiating elements using FET source integrated with microstrip pacth antenna," *Electron Lett.*,24, (21), pp.1347-1348, 1988
- [4] R.Adler., "A study of locking phenomena in oscillators," *Proc. IRE*, Vol.34, No.6, pp.351-357, June 1946
- [5] H. Pues and A. Van de Capelle, "Accurate transmission line model for the Rectangular microstrip antenna," *Proc. IEE*, Vol. 131,pt. H, no.6,pp.334-340, Dec. 1984
- [6] I. J.Bahl,"Design of microstrip antennas covered with a dielectric layer" *IEEE Trans on Antenna & Propagation*, March 1982.
- [7] A. S. Khanna "Three-port S-parameters ease GaAs FET designing," *Microwave&RF.*, pp.81-84, November 1985
- [8] G. E. Bodway, "Circuit design and characterization of transtors by means of 3-port scattering parameters," *Microwave J.*, Vol.11,No.5, pp.55-63, May 1968

Characteristics of Dielectric Multilayer Filters Incorporating a Resonant Grating

***T. R. Holzheimer, **S. Tibuleac, **P. P. Young,
and **R. Magnusson**

***Raytheon Systems Company, P.O. Box 6056, Greenville, Texas 75403
**University of Texas at Arlington, Department of Electrical Engineering,
Arlington, Texas 76019**

Abstract

Dielectric multilayer structures containing one or more waveguide-grating layers exhibit rapid variations in the spectral response of the reflected and transmitted intensities due to resonant coupling of the external propagating waves to the leaky modes of the waveguide. These resonances can be utilized to generate narrow-band transmission (or reflection) filter characteristics by selecting the materials and geometrical parameters of the device to produce a low response at frequencies outside the filter linewidth while maintaining a high transmission (or reflection) resonance peak at the desired frequency. Resonance grating devices with 5 layers containing a grating in the center layer have been fabricated and tested in the 4-20 GHz region. The experimental transmission spectra indicate a good agreement with the theoretical predictions and illustrate narrow-band filter characteristics generated by the grating-induced waveguide-mode resonances.

These filter techniques can be applied to realize narrowband filters, in addition to standard notch, lowpass, and highpass filter designs. Examples are discussed as applied to phased array antennas. All-dielectric frequency selective surfaces can be designed. This technique can yield a diagnostic tool in order to measure the variation in the field of an object such as the verification of the quiet zone in an anechoic chamber.

1. Introduction

Guided-mode resonance effects in waveguide gratings are attracting increasing interest recently due to their potential of generating high-efficiency, narrow-band reflection and transmission filters with unique properties. Theoretical and experimental studies of the guided-mode resonance (GMR) phenomenon have concentrated on the design, fabrication, properties, and applications of reflection filters [1-7]. In the optical region, a filter with narrow linewidth, high reflectance peaks (exceeding 98%) and low reflectance sidebands outside the grating resonance region (central wavelength $\lambda = 860$ nm) has been recently demonstrated experimentally [6]. In the microwave region, Magnusson et al. have reported on a GMR reflection filter with a transmission notch reaching ~ -34 dB [7]. The possibility of using GMR effects to generate transmission filters has been demonstrated theoretically by Magnusson and Wang utilizing structures with two gratings enclosing a number of homogeneous layers in a high-reflectance design [8]. Tibuleac and Magnusson have shown that a GMR transmission filter can be realized with a simpler structure with a single grating inserted in the center of a high-reflective stack of homogeneous layers [9]. The purpose of the present work is to design, build, and test waveguide-grating devices that exhibit transmission resonances in the 4 -20 GHz frequency range.

2. The guided-mode resonance effect

Guided-mode resonance effects in waveguide gratings generate sharp variations in the intensity of the observable propagating waves [1-3]. This resonance results from the coupling of the incident wave to the leaky waveguide modes supportable by the structure and the rapid variation of the phases of re-radiated waves as the wavelength or angle of incidence is varied. The re-radiated waves interfere with the directly reflected and transmitted fields to generate a rapid variation in the intensity of the externally observable electromagnetic fields. To obtain high-efficiency resonance effects, the grating can be designed to admit only zero-order forward- and backward propagating waves with primary contributions from the +1 and/or -1 order evanescent-wave resonances.

A structure with multiple layers containing one or more gratings in separate layers can be used to obtain high efficiency reflection or transmission filters depending on whether the thicknesses and dielectric constants are chosen to yield antireflection (AR) or high reflection (HR) conditions, respectively. The filter characteristics are tailored by adjusting the parameters of the device. Thus, the center frequency of the filter is determined principally by the grating period and

influenced by the dielectric constants of the grating and the layer thicknesses [4]. The sidebands can be made arbitrarily low and extended over a large frequency range by adding layers with dielectric constants and thicknesses obeying AR/HR conditions [5,8]. The linewidth of the filter is determined by the modulation of the grating, the difference between the average dielectric constant in the grating region and the dielectric constant of the surrounding medium, and the grating filling factor [4].

To characterize waveguide-grating resonance filters, rigorous coupled-wave analysis [10] is used. In all calculations presented here, incident plane waves and infinite lateral extent of the waveguide gratings are assumed. Unless otherwise stated, the wave is incident perpendicular to the structure. Approximate values for the resonance wavelength location and the free spectral range of the filters can be obtained with considerably less computation by solving the eigenvalue equation of the equivalent unmodulated slab waveguide corresponding to the waveguide grating [4,5]. A filter design is polarization dependent; the TE and TM polarization states have different resonance locations and free spectral ranges. However, the principles and properties of the microwave waveguide filters presented in this paper are fundamentally similar regardless of polarization.

3. Guided-mode resonance reflection filters

An example of a simple GMR reflection filter is a single-layer grating consisting of plexiglas rectangular bars (dielectric constant $\epsilon = 2.59$ at 10 GHz) in air with a spectral response for a TE-polarized incident wave illustrated in Fig.1. The waveguide grating has a peak in reflection (Fig. 1 (a)), and a corresponding notch in transmission (Fig. 1 (b)) at the resonance frequency $\nu = 9.567$ GHz and low reflectance outside the peak region with linewidth [FWHM], $\Delta\nu = 0.586$ GHz, when excited by a normally-incident, TE-polarized wave. The period, fill factor (i.e., fraction of period occupied by plexiglas), and thickness of the grating are 2.9 cm, 0.5, and 0.635 cm, respectively.

To evaluate and calibrate the measurement system, measurements were performed at the Raytheon Systems Company anechoic chamber (Garland) using the above mentioned filter. Figure 2 indicates the measurement setup with the GMR filter placed between the emitter and receiver antennas. The transmittance was measured in the spectral range 2-18 GHz in increments of 2.5 MHz, thus acquiring 6400 data points. The results presented in Fig. 3 (a) are similar to the previously measured data of reference 7. The split transmittance notch occurring in the data of reference 7 at the resonance frequency ~ 9.5 GHz is also found in the

data of Fig. 3 (a) at the same frequency location. The splitting of the guided-mode resonance visible in Fig. 3 is explained as follows. At normal incidence, the resonances due to the +1 and -1 evanescent diffracted waves coupling to a leaky mode of the waveguide occur at the same frequency. A slight deviation from normal incidence causes an asymmetry of the wave-coupling phenomenon leading to different resonance frequencies for the +1 and -1 diffraction orders. A theoretical plot for the case of an incidence angle $\theta = 1^\circ$ indicating the occurrence of the double notch in the transmittance spectrum is presented in Fig. 3 (b). A GMR reflection filter with a single-layer can be sensitive to angular misalignments and fabrication tolerances.

Adding homogeneous layers in AR design yields devices that are more robust parametrically than the single-layer waveguide grating, since a slight change in one grating parameter has a reduced effect on the filter response. The filter central frequency can be set to the desired value by selecting an appropriate grating period. For multilayer structures, a change in grating period shifts the resonance location linearly within the low-reflectance spectral region with insignificant changes in the filter lineshape or sideband reflectance. Multiple-layer filters also allow for a greater flexibility in the choice of dielectric constants to achieve desired filter parameters as well as an increased control over the pass-band and the angular aperture of the filter.

4. Guided-mode resonance transmission filters

The waveguide-grating resonances that are used to generate reflection filters can be used to produce transmission filters if one or more gratings are embedded in a stack of homogeneous layers with HR (instead of AR) properties [8]. A single-grating transmission filter can be obtained by superimposing the high-efficiency resonance transmittance peak over the low transmittance region achieved by alternating homogeneous layers of high and low dielectric constant materials with quarter-wavelength thicknesses [9]. The design of GMR transmission filters typically requires materials with higher dielectric constants than GMR reflection filters to obtain the required low sideband transmittance over the filter spectral range. The sideband transmittance can be reduced by selecting materials with a higher difference between the dielectric constants of the adjacent layers or by adding more high/low dielectric constant layers. The second approach has the disadvantage of increasing the thickness of the structure which adds volume and weight to the device and also increases the number of leaky modes that can be excited by the incident wave, thereby adding GMR peaks in the vicinity of the desired transmission maxima, and thus, decreasing the filter free spectral range.

Materials possessing a larger dielectric constant utilized with a low-dielectric-constant material (e.g., air and plexiglas) to form a highly-modulated resonance grating can increase the linewidth and angular aperture of GMR filters.

5. Transmission filter with water/plexiglas waveguide grating

5.1 Waveguide grating fabrication

To demonstrate the principles underlying guided-mode resonance transmission filters, a grating with water as the high-dielectric-constant material of the grating was built. The choice of water is justified by the high value of its dielectric constant, significantly higher than other practical, inexpensive materials. Such a high dielectric constant enables the design of a guided-mode resonance transmission filter with just one layer. The water/plexiglas structure under study is shown schematically in Fig. 4. Parallel rectangular grooves 5 mm wide and 1 mm deep were cut with 5 mm spacing between adjacent grooves into a sheet of plexiglas of 3 mm thickness. A flat plexiglas sheet 3 mm thick was glued on top. The sandwich structure has a surface area 2x3 feet with the grooves parallel to the shorter side. The air channels in the plexiglas structure were filled with deionized (DI) water to realize the water/plexiglas grating. The theoretical transmittance of the 3-layer (plexiglas and DI water grating bounded by homogeneous plexiglas layers) device is presented in Fig. 5 for two cases: no losses (Fig. 5 (a)) and with realistic losses (Fig. 5 (b)). The calculated results of Fig. 5 take into account the dispersion of the real and imaginary parts of the dielectric constant of water as given by the experimental data of Fig. 6 [11]. The high modulation of the resulting waveguide grating leads, for a lossless waveguide grating, to a resonance peak at the frequency 12.04 GHz with high transmittance (95%) and broad linewidth (2.62 GHz). The loss grating superimposes over the refractive index grating and increases the reflectance of the device at the resonance frequency thereby reducing the transmittance to approximately 10%.

5.2 Experimental setup and results

Measurements were made with a configuration (Fig. 7) that includes two microwave lenses. The spherical wavefront emitted by the transmitter horn antenna is collimated by a plano-convex teflon lens placed with the flat side facing the source, at a distance from the transmitter equal to the lens focal length, $f = 48$ in. The diameter of the lens is $D = 14$ in, and the refractive index is $n = 2.07$ at 10 GHz. Thus, a planar wavefront incident on the GMR filter is obtained. The zero-order forward-diffracted wave is focused towards the receiver horn

antenna by a second teflon lens identical to the first, located at its focal length away from the receiver. The transmittance of the device is calculated by normalizing the amplitude of the field acquired with this setup to the amplitude measured in the chamber without the waveguide grating. The transmittance of the water grating is illustrated in Fig. 8. Compared to the obtained with no lenses, the spectral response of the device measured with the lenses in the path of the beam has a lower overall transmittance and reduced oscillations and noise, thus, approaching the theoretical data plotted in Fig. 5.

6. Transmission filters with G10 fiberglass waveguide grating

6.1 Design and fabrication

As the results obtained with the water waveguide grating demonstrate, losses due to absorption in the grating material do not significantly affect the transmittance outside the resonance region. However, near the resonance frequency such loss has a much greater effect on the GMR transmittance. Therefore, materials with lower losses were considered in a different type of GMR transmission filter design that uses more layers with lower dielectric constant materials than the water grating which employed effectively only one quarter-wave layer. Such a design was implemented with G10 fiberglass and air as high and low dielectric constant materials, respectively, for both the homogeneous layers as well as for the grating layer. G10 has a dielectric constant $\epsilon \sim 4.5$ and a loss tangent $\tan\delta \sim 0.002$ [12] and is commercially available in large sheets at low cost with good thickness uniformity. The cross-section of the 5-layer waveguide-grating device, presented schematically in Fig. 9, consists of the grating formed with strips of G10 fiberglass in air and homogeneous G10 sheets placed on each side of the grating leaving an air gap between the grating and the external layers. To achieve a low transmittance over the filter spectral range, the thicknesses of the layers must be chosen to be equal to quarter-wavelength at the central frequency of the filter. Two GMR filters with transmission peaks in the 4-20 GHz spectral range have been designed utilizing G10 fiberglass. The thicknesses of the G10 homogeneous plates representing layers 1 and 5 of the structures were chosen to be equal to 0.3175 cm (0.125 in) for the device no. 1, and 0.236 cm (0.093 in) for device no. 2. For G10 fiberglass which has a refractive index $n \sim 2.12$, these thicknesses are equal to a quarter-wavelength at the frequency $\nu = 11.14$ GHz (wavelength, $\lambda = 2.69$ cm) and $\nu = 14.99$ GHz (wavelength, $\lambda = 2.0$ cm), respectively. The variation in thickness of the layers across the surface of each G10 plate is less than ± 0.03 cm according to manufacturer's specification. The high-reflectance design required for the filter operation with low transmittance sidebands at frequencies

outside the bandwidth is accomplished with the G10 plates placed on either side of the grating, at a distance equal to a quarter-wavelength in air. The grating periods for the two gratings are selected to generate a guided-mode resonance within the high-reflectance spectral range of the structure. The dimensions of the waveguide gratings are approximately $36 \times 30 \text{ in}^2$ containing 45 grating periods for the device with grating period $\Lambda = 2.0 \text{ cm}$, and 60 grating periods for the structure with $\Lambda = 1.5 \text{ cm}$. The grating period has a fabrication error of less than $\pm 0.05 \text{ cm}$ and fill factors are estimated to vary within 10% of the design value.

The theoretical frequency response of the two devices for a TE-polarized incident wave at normal incidence is illustrated in Figs. 10 and 11 for the spectral range 4-20 GHz. Guided-mode resonances with theoretical efficiencies approaching 100% are obtained in the two waveguide gratings at central frequencies $\nu = 10.54 \text{ GHz}$ ($\lambda = 2.84 \text{ cm}$) and $\nu = 14.32 \text{ GHz}$ ($\lambda = 2.09 \text{ cm}$) for device no. 1, and $\nu = 14.09 \text{ GHz}$ ($\lambda = 2.13 \text{ cm}$) for device no. 2. The linewidths (FWHM) of the guided-mode resonance transmittance peaks of the two filters are $\Delta\nu = 44.6 \text{ MHz}$ for the first device resonance peak at $\nu = 10.54 \text{ GHz}$ and $\Delta\nu = 59 \text{ MHz}$ for the resonance peak of the second structure at $\nu = 14.09 \text{ GHz}$. The theoretical calculations (Figs. 10 and 11) have been carried out with values for the thicknesses specified by the manufacturer ($d = 0.3175 \text{ cm}$ for structure no. 1 and $d = 0.236 \text{ cm}$ for structure no. 2), and design grating periods $\Lambda = 2.0 \text{ cm}$ for device no. 1 and $\Lambda = 1.5 \text{ cm}$ for device no. 2, and fill factors $f = 0.5$ for both gratings. The dielectric constant of G10 was chosen as 4.4944 (refractive index $n = 2.12$). The value selected for the dielectric constant of G10 fiberglass is in accord with data found in the literature. Reference 12 indicates the dielectric constant of G10 to be $\epsilon = 4.5$ while reference 13 estimates the value of ϵ to be in the range 4.0 - 4.6 in the microwave region.

6.2 Spectral measurements

Testing of the G10 waveguide gratings was performed with each device placed between the two plano-convex lenses that collimate the wave incident upon the grating as illustrated in Fig. 7. The measured transmittance for a TE-polarized wave at normal incidence on the GMR filters with grating periods $\Lambda = 2.0 \text{ cm}$ and $\Lambda = 1.5 \text{ cm}$ are shown in Figs. 12 and 13, respectively. Guided-mode resonance peaks are found at frequencies $\nu = 10.52 \text{ GHz}$ ($\lambda = 2.85 \text{ cm}$) and $\nu = 14.72 \text{ GHz}$ ($\lambda = 2.04 \text{ cm}$) in Fig. 12, and at $\nu = 14.07 \text{ GHz}$ ($\lambda = 2.13 \text{ cm}$) in Fig. 13. The transmittance values at resonance are $\sim 22.9\%$ and $\sim 60.3\%$ for the device of Fig. 12 and $\sim 20.7\%$ for the device of Fig. 13. The responses of these devices for the case of a TM polarized incident wave indicate the same low-transmittance region

as in the case of TE polarization generated by the quarter-wave thick layers of the devices but no guided-mode resonances appear.

In all measured data there exist oscillations superimposed over the transmittance spectrum of the devices. These oscillations represent interference effects due to multiple reflections between components that are placed in the path of the microwave beam during measurements. In the case of an empty chamber, the frequency and wavelength fringe spacing due to multiple beam interference of waves reflected and diffracted inside the measurement chamber between the transmitter and receiver horn antennas, the lens holders, and grating support structure is given by the relations [14] $\Delta\nu_i = c/2nd\cos(\theta)$, and $\Delta\lambda_i = \lambda^2/2nd\cos(\theta)$, where θ is the angle of the wave propagation with the normal, n is the refractive index of the medium, d is the distance between the reflecting surfaces, and c is the velocity of light in vacuum. Assuming $n = 1$ (air), $\theta = 0$ (propagation of waves normal to the reflecting surfaces), and a distance between the two horn antennas of 18 feet, the calculated fringe spacing is thus $\Delta\nu_i = 27.34$ MHz ($\Delta\lambda_i = 0.0082$ cm at $\nu = 10$ GHz). Figure 14 shows the measured transmittance of the empty anechoic chamber over the frequency range 10-11 GHz. Oscillations visible in this plot have a period $\Delta\nu_i \sim 25$ MHz which is consistent with the calculated value. In the measurements performed with the setup of Fig. 7, additional interference effects appear due to reflections from the lenses. Thus, a distance between antenna and lens of 4 feet, results in a calculated value of the fringe spacing, $\Delta\nu_i = 123$ MHz, reflections between lenses placed 10 feet apart produce fringes with fringe spacing, $\Delta\nu_i = 49$ MHz, and interference caused by the horn antenna and the lens furthest away from it ($d = 14$ feet) lead to a fringe spacing, $\Delta\nu_i = 35$ MHz. These interference patterns have different amplitudes and overlap to produce the complex oscillatory behavior that is seen in the measured transmittance data.

6.3 Comparison between experimental and theoretical data

Spectral measurements of guided-mode resonance filters with G10/air waveguide gratings have clearly established the presence of transmission peaks at frequencies that closely match the values predicted by theory. The transmittance spectra of the structures outside the resonance are in excellent agreement with the calculated data for the entire frequency range of the measurements (4-20 GHz).

The reduced peak transmission in the measured data compared to the theoretical predictions in Figs. 10 and 11 is attributed in part to losses in the G10 fiberglass. Using a value of the loss tangent $\tan\delta = 0.002$ (as specified in reference 12), it is

found that the losses do not significantly affect the response of the devices outside the filter linewidth region but reduce the grating resonance peaks. Further increasing the loss tangent to 0.008, gives the spectral responses of Figs. 15 illustrating the reduction in peak transmittance of the guided-mode resonances to 19.6% and 82.1% for the first grating and to 20.9% for the second grating. The sensitivity of the guided-mode resonance transmittance to losses is indicated by the experimental data of Figs. 12 and 13, where the thin-film interference peaks are much less attenuated than the resonance peaks. Comparing Figs. 10 and 15, it is interesting to note that the reduction in peak transmittance is greater for the resonance peak at 10.54 GHz than the resonance peak at 14.32 GHz. This trend is also confirmed by the experimental data (Fig. 12) that indicates the transmittance of the two guided-mode resonance peaks to be affected differently by the losses present in the waveguide grating.

A comparison between theoretical and experimental data is illustrated in Fig. 16 for the waveguide grating with $\Lambda = 2.0$ cm. A smoother experimental response curve is obtained by replacing each point of Fig. 12 (b) with the average transmittance of the 20 neighboring frequency points. The value of the loss tangent, $\tan\delta = 0.01$ is modified in the theoretical calculations to yield the close fit between the experiment and theory presented in Fig. 16. The theoretical plot of Fig. 16 is generated with a layer thickness $d = 0.31$ cm smaller by 0.0075 cm compared to the values used in Fig. 10 (b) but well within the thickness tolerance of ± 0.03 cm specified by the manufacturer of the G10 plates. The grating period used in the calculation ($\Lambda = 2.03$ cm) is the average value determined through measurement on the waveguide grating after assembly.

6.4 Spectral measurements with different experimental configurations

Experimental peak transmittances are lower than theoretically predicted ones. This can be attributed in part to finite-size effect of the device and the phase curvature of the incident beam.

The sensitivity of the guided-mode resonances to the effective, distributed angle of incidence (corresponding to a phase-curved wave) may contribute to the discrepancy in the resonance peak amplitude between the theoretical predictions and the experimental results. While the theoretical calculations assume plane waves incident on the device, in the experiment the power is distributed over the angular spectrum of the incident wave. Each angular component of the non-planar wave produces a resonance at a slightly different frequency. Therefore, only part of the beam incident on the structure can resonate at the frequency specified by

the design resulting in a lower transmittance than predicted by theory. Although the teflon lenses used in the experiments have achieved a degree of collimation of the microwave beam, the wave incident on the waveguide grating might still have a non-planar wavefront due to incomplete collimation.

7. Fabry-Perot filters

7.1 Design and fabrication

Dielectric Fabry-Perot transmission filters consist of a central layer bounded on both sides by two mirrors obtained with alternating high and low dielectric constant layers. Their design is similar to the GMR filter represented in Fig. 9 with the quarter-wave thick grating replaced by a half-wave thick homogeneous layer. Two such Fabry-Perot filters with 5 layers, with silica glass in one case and G10 fiberglass in the other, were built and tested.

The calculated transmittance plot for the glass Fabry-Perot filter (Fig. 17) exhibits a 98.5% transmittance peak at the frequency $\nu = 13.3$ GHz with a linewidth of $\Delta\nu = 1.5$ GHz for a loss tangent in glass $\tan\delta = 0.001$, and a maximum transmittance of 86.5% at $\nu = 13.28$ GHz with a linewidth of $\Delta\nu = 1.56$ GHz for a loss tangent in glass $\tan\delta = 0.01$. A similar response is obtained with the G10 fiberglass Fabry-Perot filter (Fig. 18). Calculations with a loss tangent $\tan\delta = 0.002$ yielded a maximum transmittance of 96.16% at the center frequency of the filter $\nu = 11.32$ GHz and a linewidth $\Delta\nu = 0.97$ GHz. A higher loss tangent ($\tan\delta = 0.008$) results in a transmittance peak of 85.87%, a central frequency $\nu = 11.31$ GHz and a linewidth $\Delta\nu = 1.02$ GHz. Compared to Fabry-Perot filters, GMR filters with the same number of layers typically have narrower linewidths, similar sideband response, and, for low-loss materials, comparable peak transmittance. A Fabry-Perot device requires significantly more layers to obtain the narrow spectral peak of a GMR filter that uses the same materials [15].

7.2 Experimental results

The spectral response of Fabry-Perot filters for a normally-incident wave, measured in the frequency range 4-20 GHz with microwave lenses for beam collimation is illustrated in Fig. 19 for the glass structure, and in Fig. 20 for the G10 fiberglass device. The glass Fabry-Perot exhibits a transmittance maximum of 75.5% at the frequency $\nu = 13.2$ GHz with a linewidth $\Delta\nu \sim 0.82$ GHz. The frequency location of the maximum transmittance is very close to the theoretically

predicted value. The reduced peak response may be due to the inhomogeneity of the glass and the variation in thickness across the surface of the sheets that form the high-dielectric constant layers of the device.

The G10 fiberglass Fabry-Perot filter possesses a high experimentally measured peak transmittance at the frequency $\nu = 11.43$ GHz with a linewidth $\Delta\nu \sim 1.0$ GHz. The experimental transmittance curve compares very well with the calculated spectral response and the central frequency and linewidth of the filter are in excellent agreement with the theoretical predicted values.

8.0 Applications

The GMR waveguide grating structures can be used for the realization of the basic filter types which are lowpass, highpass and bandpass. This can include hybrid combinations of each filter type in order to vary the operational bandwidth and other desired parameters.

The desired application is to include the filter as part of the antenna aperture. The filter is designed and built into the antenna(s) aperture. This may allow the deletion of the filter that would normally be placed in front of the first stage of amplification and which is typically located at the output of the antenna. This amplification stage could be either for reception or transmission.

This type of filter is similar to a frequency selective surface, but is all dielectric having no metallic components incorporated within the filter structure. The incorporation of this type of filter, covering a phased array aperture or a reflector antenna, could be used for interference reduction. Interfering signals at the same frequency emanating from directions other than the main beam of the antenna and filter combination would not reach the antenna. This could work on both receive and transmit where interference to other antenna systems could be greatly limited. A particular use could be interference reduction, both for reception and emanation, for a ground station pointed towards a satellite.

The use of the GMR for a diagnostic tool is also possible. One use could be to verify the quiet zone in an anechoic chamber. With a very narrow GMR response the variation in transmittance can determine the phase and amplitude variation or quiet zone used for measurements. This would take advantage of the analytic software to determine the absolute phase and amplitude responses based on the known GMR data.

There are numerous other applications which are beyond the scope of this present paper.

9. Conclusions

Resonances in waveguide gratings can be used to implement reflection and transmission filters in the microwave spectral range. By merging concepts of diffraction, waveguides, and thin-film electromagnetics, a wide variety of reflection and transmission filters can be designed with full control over the filter characteristics, i.e., center frequency, linewidth, and sidebands. Reflection and transmission filters with high efficiency and low sidebands can be obtained by embedding a grating in an antireflection or high-reflection design, respectively. Transmission filters with high peak response are demonstrated in multilayer waveguide gratings with a grating in the central layer and adjacent quarter-wave thick homogeneous layers. Generally, transmission filters require more layers than reflection filters to obtain a similar sideband response.

To demonstrate the concept of guided-mode resonance transmission filters, waveguide grating structures using low-cost, commercially-available dielectric materials have been fabricated and tested. Their experimental spectral characteristics have been compared with the theoretical predictions. A close match between theoretical and experimental data has been found over the whole measurement spectral range (2-20 GHz). Several experimental configurations were utilized to match the theoretical assumptions with the experimental conditions used in the measurements. The best results were obtained for a setup in which the structure is placed between two microwave lenses, one at its focal length away from the transmitter antenna to collimate the beam incident on the device, and the other lens at its focal length away from the receiver.

The presence of guided-mode resonances in the transmission spectrum of waveguide gratings with G10 fiberglass has been shown. The frequency locations at which guided-mode resonances occur are in excellent agreement with the theoretical predictions as conclusively shown in experiments with devices made of G10 fiberglass. The experimentally measured GMRs in the low transmittance region of the waveguide grating have transmission peaks ~25%. Higher efficiencies (~70%) were measured for GMR peaks lying on the edge of the low transmission curve determined by multilayer interference effects of the equivalent homogeneous-layer structure.

A key contributor to lowered experimental peak transmittance compared to theoretical calculations was established to be bulk loss. Using low-loss materials with higher dielectric constants can yield GMR filters with larger linewidths, lower sidebands, and improved efficiencies.

All-dielectric Fabry-Perot filters have been fabricated with G10 fiberglass and Silica glass as high dielectric constant materials and air as the low dielectric constant material. Testing of these devices indicated an excellent fit with the theoretical spectral characteristics. The Fabry-Perot filters were built with the same number of layers and the same materials as the GMR filters. A comparison between the two types of devices indicates that using the same materials and the same number of layers as the Fabry-Perot devices, GMR filters can achieve narrower transmission peaks while maintaining comparable efficiency and sideband response but are more sensitive to losses than Fabry-Perot structures.

The narrow linewidth of GMR filters and attendant narrow angular aperture yield highly spectrally-selective devices. It is possible to significantly broaden the spectral and angular linewidths by use of spatially phase-shifted gratings as shown elsewhere [16].

New possibilities in design and fabrication of GMR filters are emerging by application of inverse techniques for filter optimization such as genetic algorithms [17,18]. In particular, it is possible to design efficient transmission filters with only a few layers if the grating fill factor is suitably chosen. Such structures are easily fabricated in the microwave region since the features are large.

Numerous applications of GMR filters exist. These include realization of all the basic filter types in addition to very narrow resonance filters. The incorporation of GMR waveguide filters into antenna apertures, such as antenna arrays and reflectors, can provide interference reduction both from the point of reception and emanation. System component reduction is possible with replacement of the filter in front of the first amplification stage with the proposed aperture filter. The GMR filter can also be used as a diagnostic tool, in concert with the analytic software, for quite zone verification, as an example.

Acknowledgments

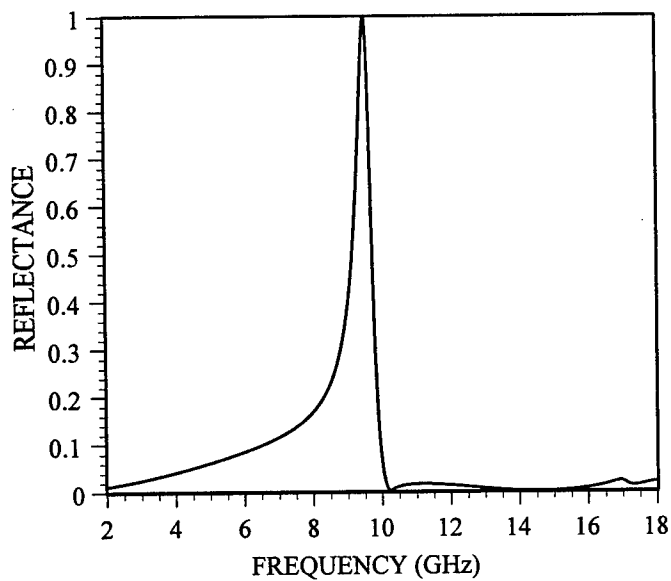
This work was supported in part by Raytheon Systems Company and by the Texas Advanced Technology Program under grant no. 003656-042. Measurement assistance by the Raytheon Systems Company, Garland Antenna Laboratory

personnel is gratefully acknowledged. Technical assistance by Mike I. Jones of Lockheed Martin, Fort Worth, Texas, is gratefully acknowledged.

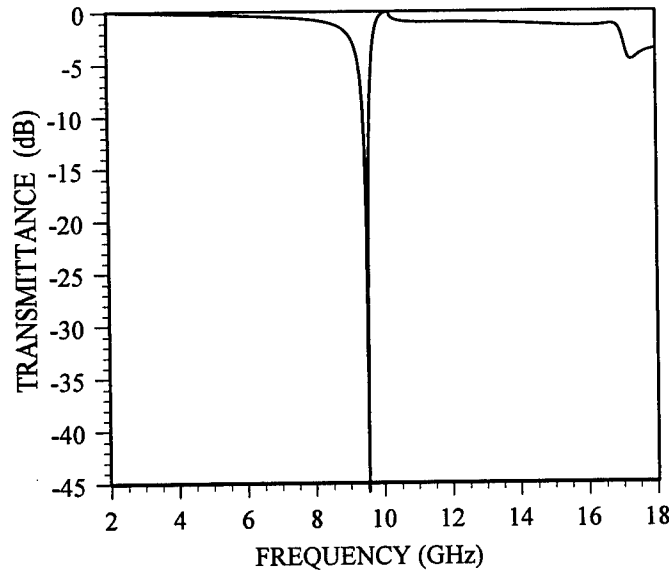
10. References

1. A. Hessel and A. A. Oliner, "A new theory of Wood's anomalies on optical gratings," *Appl. Opt.*, vol. 4, no. 10, pp. 1275-1297, Oct. 1965.
2. S. S. Wang, R. Magnusson, J. S. Bagby, and M. G. Moharam, "Waveguide mode-induced resonances in planar diffraction gratings," Optical Society of America 1989 Annual Meeting Technical Digest, p. 117, 1989.
3. S. S. Wang, R. Magnusson, J.S. Bagby, and M.G. Moharam, "Guided-mode resonances in planar dielectric-layer diffraction gratings," *J. Opt. Soc. Am. A*, vol. 7, no. 8, pp. 1470-1475, Aug. 1990.
4. S. S. Wang and R. Magnusson, "Theory and applications of guided-mode resonance filters," *Appl. Opt.*, vol. 32, no. 14, pp. 2606-2613, May 1993.
5. S. S. Wang and R. Magnusson, "Multilayer waveguide-grating filters," *Appl. Opt.*, vol. 34, no. 14, pp. 2414-2420, May 1995.
6. Z. S. Liu, S. Tibuleac, D. Shin, P. P. Young, and R. Magnusson, "High-efficiency guided-mode resonance laser mirror," postdeadline paper, Proceedings of the Topical Meeting on Diffractive Optics and Micro-Optics, Kailua-Kona, Hawaii, June 8-11, 1998.
7. R. Magnusson, S. S. Wang, T. D. Black, and A. Sohn, "Resonance properties of dielectric waveguide gratings: Theory and experiments at 4-18 GHz," *IEEE Trans. Antennas Propagat.*, vol. 42, no. 4, pp. 567-569, April 1994.
8. R. Magnusson and S. S. Wang, "Transmission bandpass guided-mode resonance filters," *Appl. Opt.*, vol. 34, no. 35, pp. 8106-8109, Dec. 1995.
9. S. Tibuleac and R. Magnusson, "Diffractive narrow-band transmission filters based on guided-mode resonance effects in thin-film multilayers," *Photonics Tech. Lett.*, vol. 9, no. 4, pp. 464-466, April 1997.

10. T. K. Gaylord and M. G. Moharam, "Analysis and applications of optical diffraction by gratings," *Proc. IEEE*, vol. 73, pp. 894-937, May 1985.
11. A. Kraszewsky, Ed., *Microwave Aquametry - Electromagnetic wave interaction with water-containing materials*, IEEE Press, New York, 1996
12. P. Vizmuller, *RF Design Guide Systems, Circuits, and Equations*, Artech House, Boston, 1995.
13. Th. Laverghetta, *Microwave Materials and Fabrication Techniques*, 2nd edition, Artech House, Boston, 1991.
14. M. Born and E. Wolf, *Principles of Optics*, 6th edition, Pergamon Press, Oxford, 1989.
15. S. Tibuleac and R. Magnusson, "Reflection and transmission guided-mode resonance filters," *J. Opt. Soc. of Amer. A*, vol. 14, no. 7, pp. 1617-1626, July 1997.
16. S. Tibuleac, R. Magnusson, S. S. Wang, T. A. Maldonado, and A. E. Oberhofer, "Linewidth broadening mechanisms of guided-mode resonance filters," Optical Society of America Annual Meeting, Portland, Oregon, 1995.
17. C. Zuffada, T. Cwik, and C. Ditchman, "Synthesis of novel all-dielectric grating filters using genetic algorithms," *IEEE Trans. Antennas Propagat.*, vol. 46, no. 5, pp. 657-663, May 1998.
18. S. Tibuleac, R. Magnusson, T. A. Maldonado, D. Shin, and C. Zuffada, "Direct and inverse techniques of guided-mode resonance filter design," 1997 IEEE AP-S Intl. Symposium, Conference Proceedings 4, Montreal, Canada, 2380-2383, 1997.



(a)



(b)

Figure 1. The calculated reflectance (a) and transmittance (b) of a guided-mode resonance filter for TE-polarized, normally-incident plane waves. The single-layer plexiglas/air waveguide grating has a period $\Lambda = 2.93$ cm, fill factor $f = 0.5$, thickness $d = 0.635$ cm. The dielectric constant of plexiglas is $\epsilon = 2.59$.

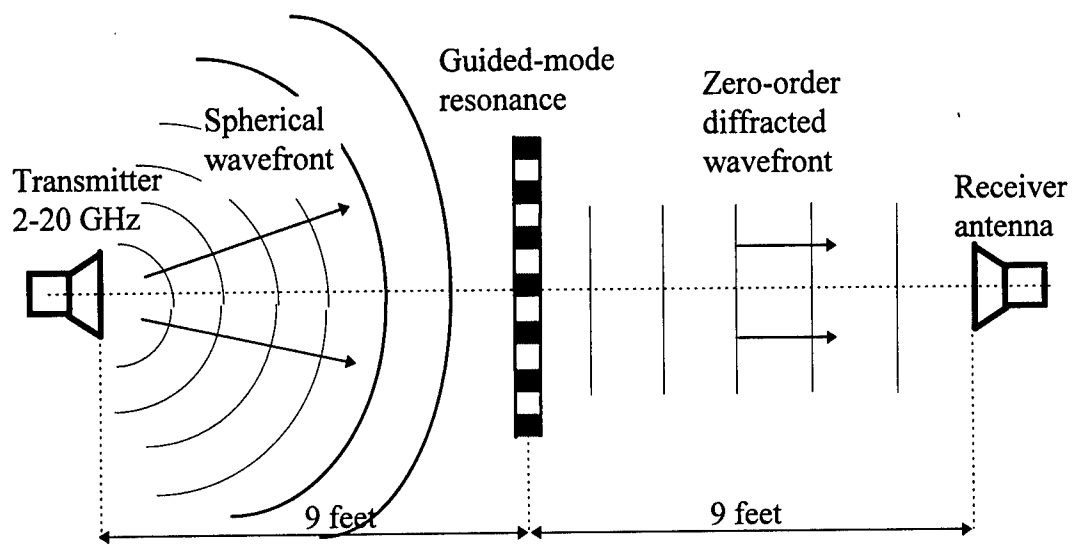
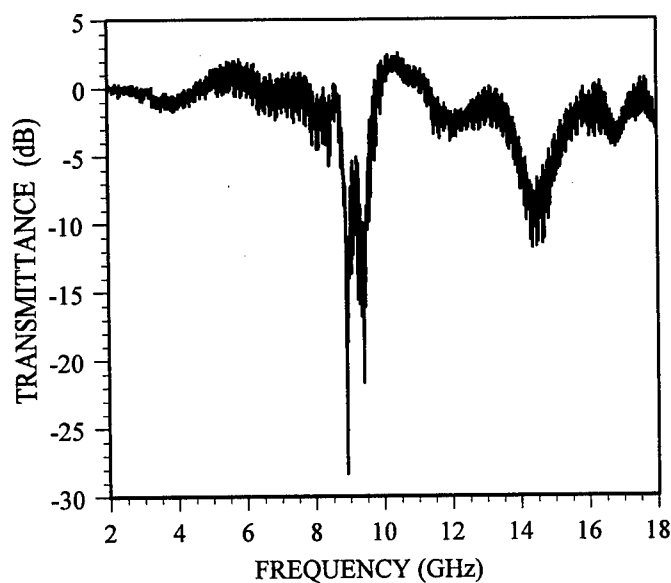
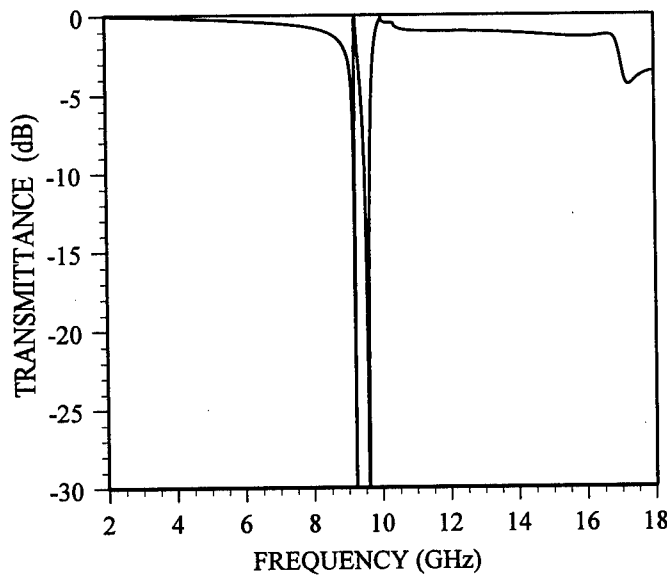


Figure 2. Experimental setup for transmittance measurements of guided-mode resonance filters in an anechoic chamber.



(a)



(b)

Figure 3. Experimental (a) and theoretical (b) transmittance of single-layer plexiglas/air waveguide grating. The parameters are the same as in Fig. 1 except for the angle of incidence $\theta = 1^\circ$.

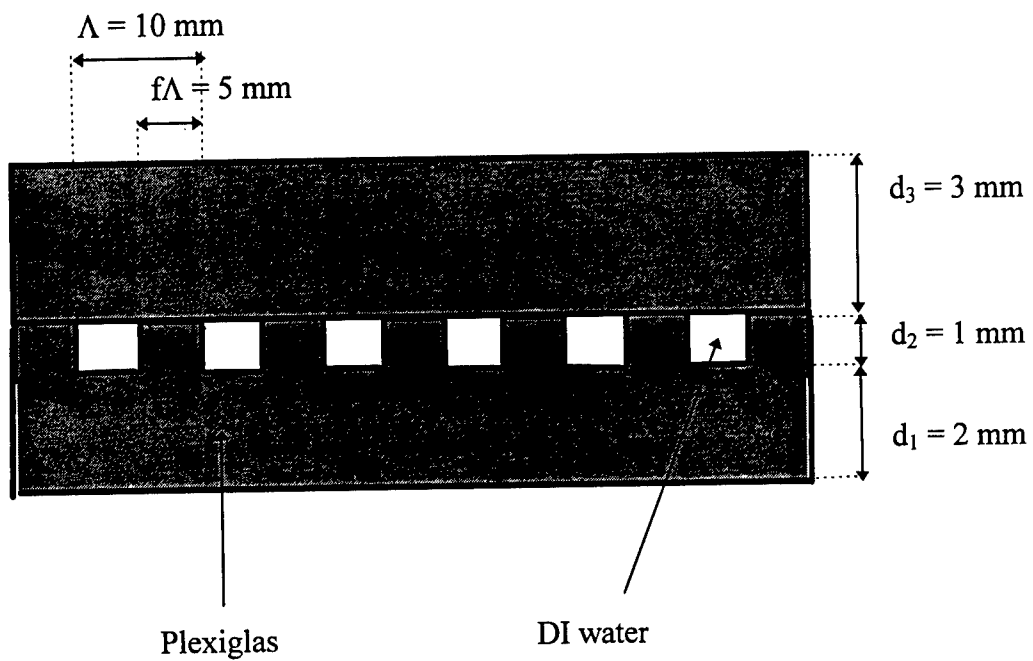


Figure 4. Waveguide grating made with water in rectangular channels cut in a plexiglas sheet with a second plexiglas sheet glued on top. The physical parameters of the device are shown on the figure.

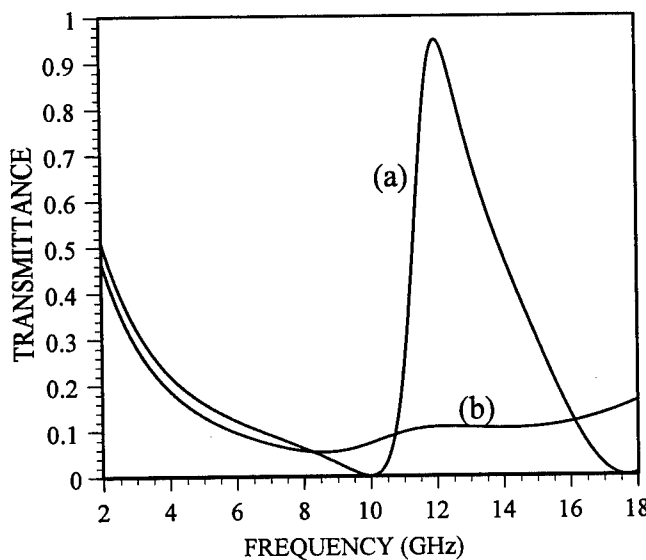


Figure 5. Transmittance of the water/plexiglas waveguide grating shown in Fig. 4. In Fig. 5(a) the imaginary part of the dielectric constant is zero and the dispersion curve of Fig. 6 is used for the real part of the dielectric constant. In Fig. 5(b) the complex dielectric constant of water has values given by the dispersion curve of Fig. 6. The dielectric constant of plexiglas used in the calculation is $\epsilon = 2.59 - j0.01735$. The geometrical parameters of the device are given in Fig. 4(a).

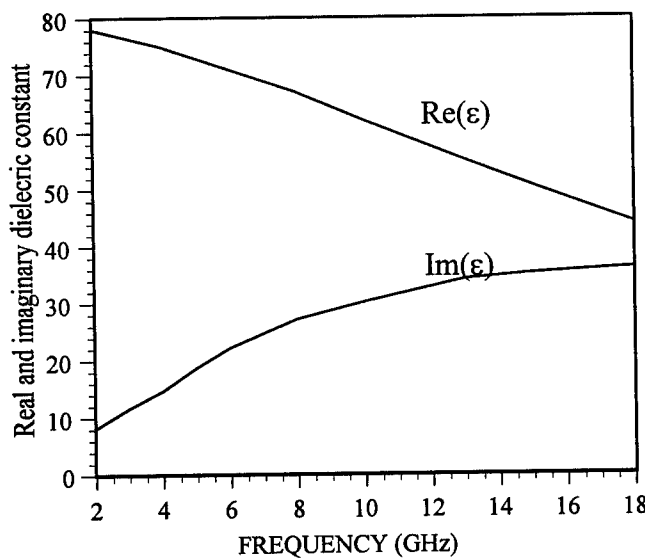


Figure 6. Real and imaginary parts of the dielectric constant of deionized water [Ref. 11].

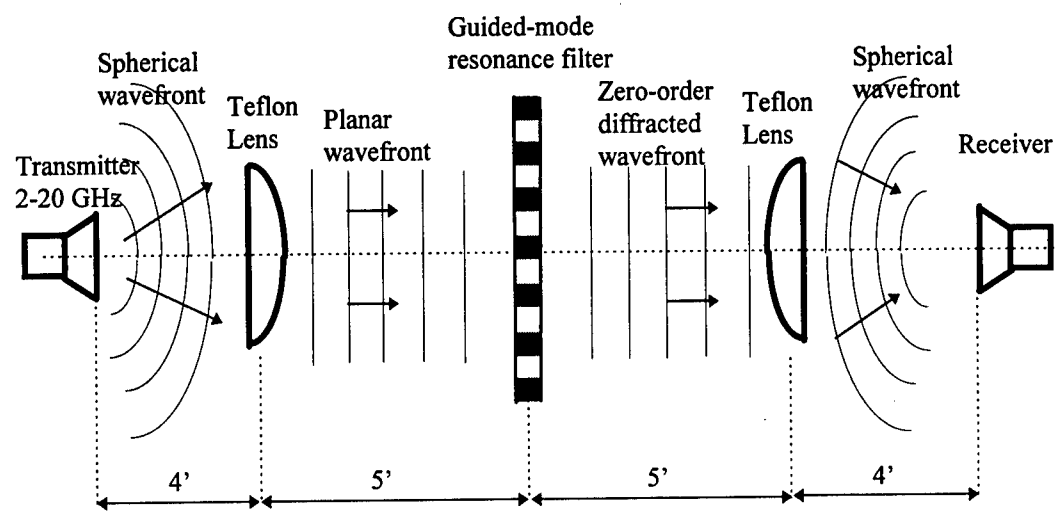
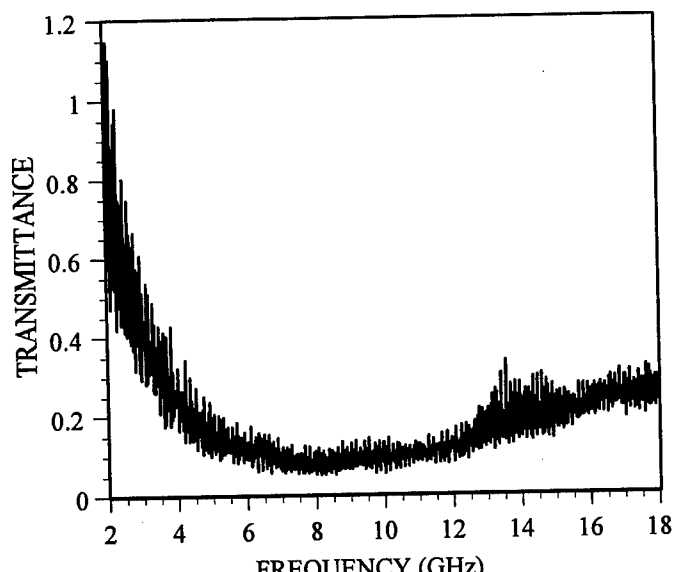
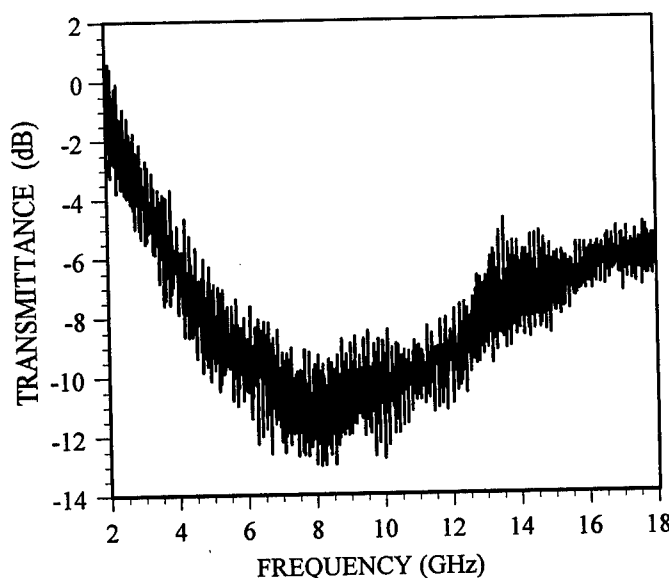


Figure 7. Experimental setup for transmittance measurements of GMR filters with microwave lenses used to collimate the wave incident on the grating structure and to focus the diffracted wave towards the receiver.



(a)



(b)

Figure 8. Experimental transmittance as a fraction (a) and in dB (b) of the water/plexiglass waveguide grating illustrated in Fig. 4. The measurements were performed with the setup described by Fig. 7.

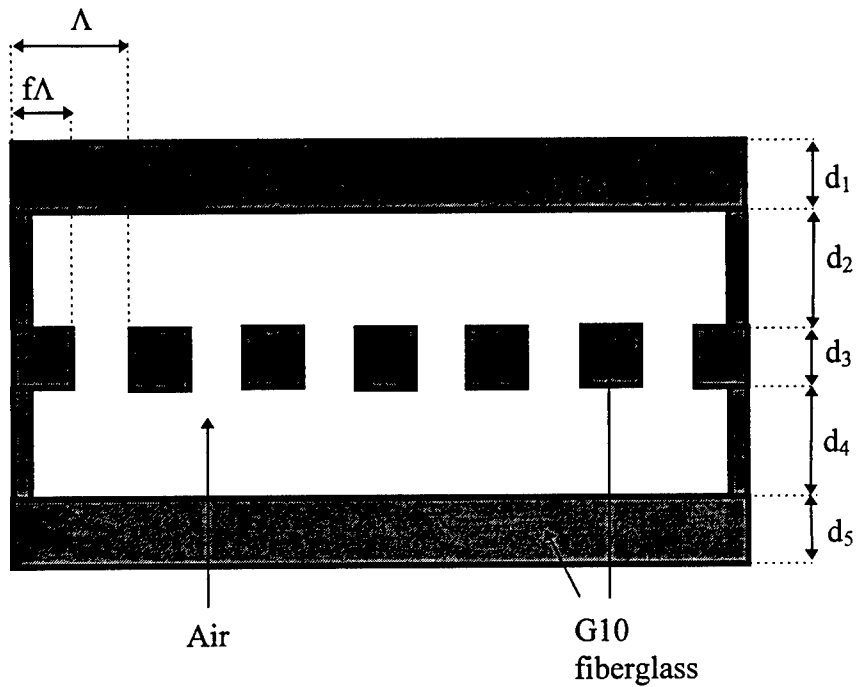


Figure 9. Guided-mode resonance transmission filter with G10 fiberglass and air utilized to form both the grating as well as the high and low homogeneous layers of quarter-wavelength thickness. The parameters for the two fabricated devices are: device no. 1, $\Lambda = 2.0$ cm, $f = 0.5$, $d_1 = d_3 = d_5 = 0.3175$ cm (0.125 in), $d_2 = d_4 = 0.635$ cm (0.25 in); device no. 2, $\Lambda = 1.5$ cm, $f = 0.5$, $d_1 = d_3 = d_5 = 0.236$ cm (0.093 in), $d_2 = d_4 = 0.472$ cm (0.186 in).

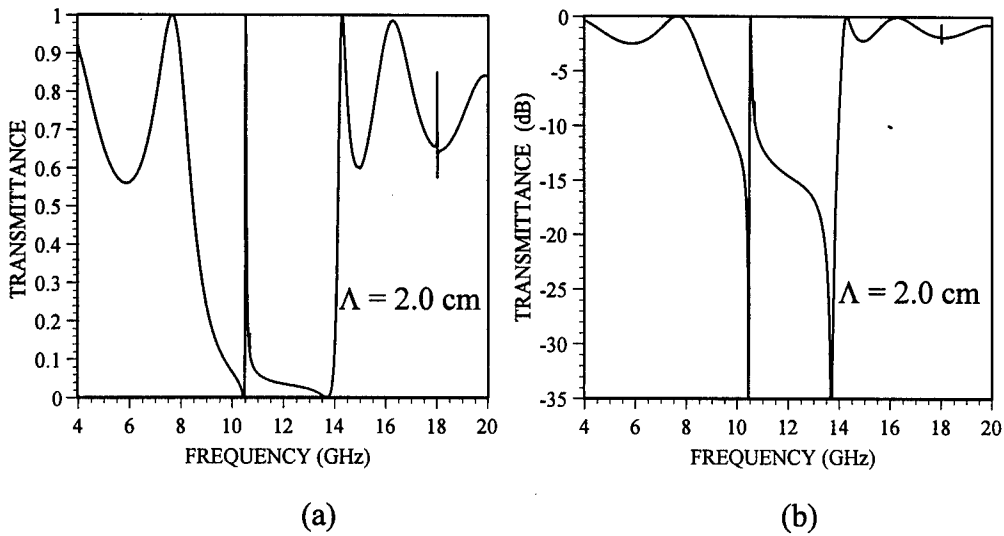


Figure 10. Calculated TE-polarization transmittance as a fraction (a) and in dB (b) of the G10 fiberglass GMR filter with the design represented schematically in Fig. 9. In the notation of Fig. 9, the 5 layer structure has the following parameters: $\Lambda = 2.0$ cm, $f = 0.5$, $d_1 = d_3 = d_5 = 0.3175$ cm, $d_2 = d_4 = 0.635$ cm; the dielectric constant of G10 fiberglass is $\epsilon = 4.4944$ (refractive index, $n = 2.12$).

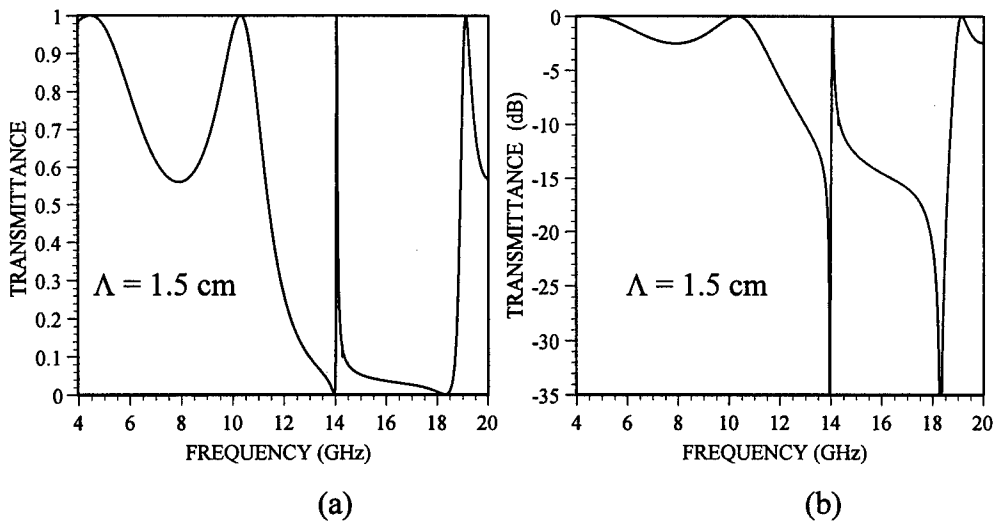


Figure 11. Calculated TE-polarization transmittance as fraction (a) and in dB (b) of the G10 fiberglass GMR filter with the design represented schematically in Fig. 9. In the notation of Fig. 9, the 5 layer structure has the following parameters: $\Lambda = 1.5$ cm, $f = 0.5$, $d_1 = d_3 = d_5 = 0.236$ cm, $d_2 = d_4 = 0.472$ cm; the dielectric constant of G10 fiberglass is $\epsilon = 4.4944$ (refractive index, $n = 2.12$).

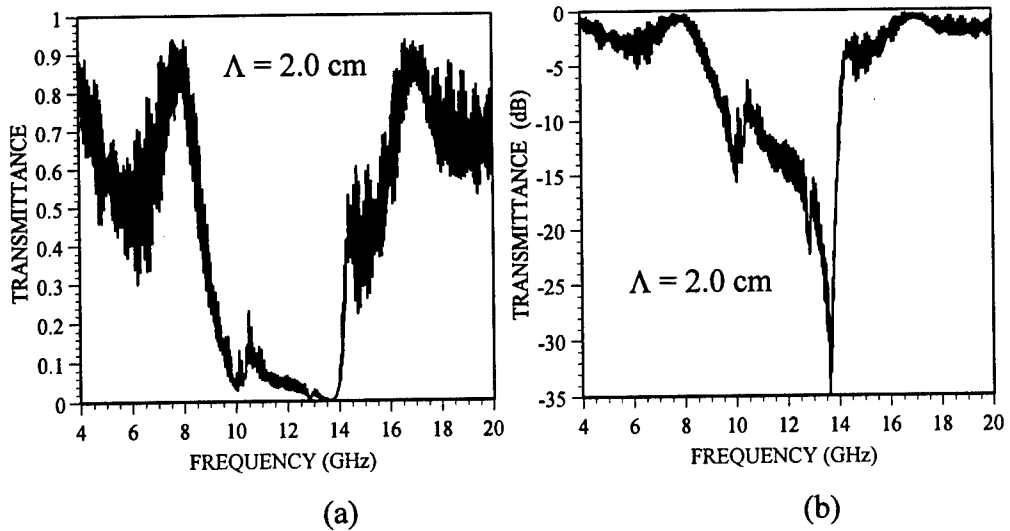


Figure 12. TE-polarized spectral transmittance measurement expressed as a fraction (a) and in dB (b) of the G10 fiberglass GMR filter (period $\Lambda = 2.0 \text{ cm}$) with the theoretical response illustrated in Fig. 10.

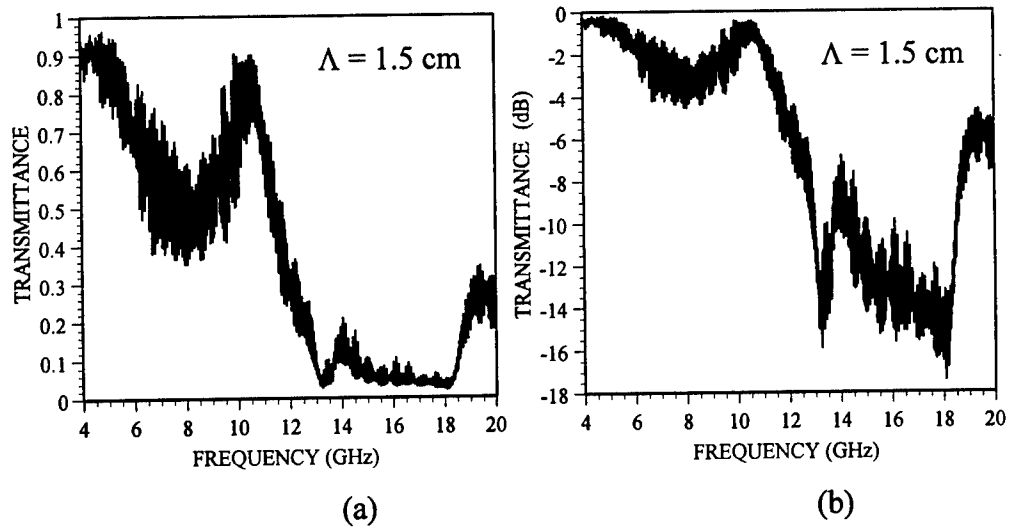


Figure 13. TE-polarized spectral transmittance measurement expressed as a fraction (a) and in dB (b) of the G10 fiberglass GMR filter (period $\Lambda = 1.5 \text{ cm}$) with the theoretical response illustrated in Fig. 11.

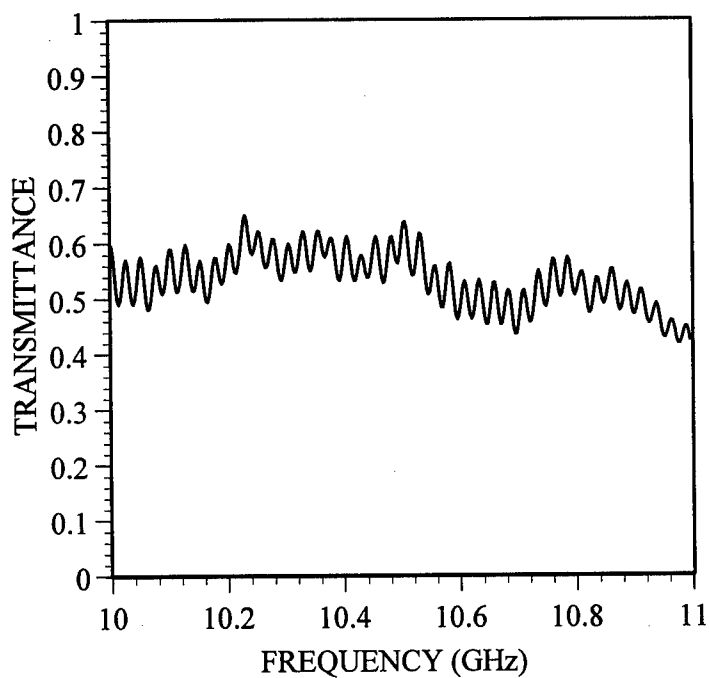
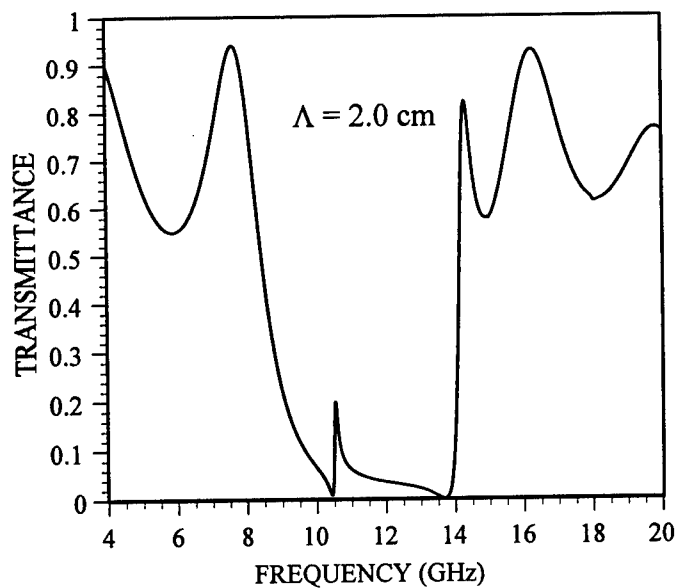
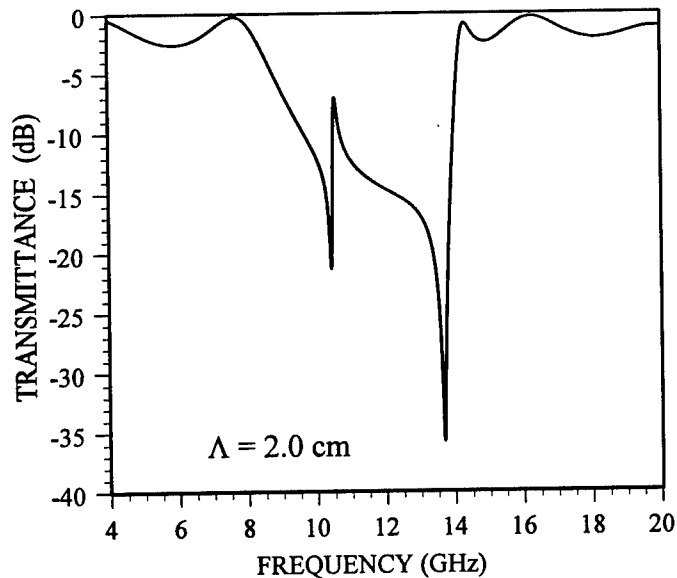


Figure 14. Transmittance of the empty chamber for TE-polarized waves. The oscillations with a periodicity of ~ 25 MHz are caused by interference between waves reflecting between the emitter and receiver horn antennas.



(a)



(b)

Figure 15. Calculated TE-polarization transmittance of a fiberglass GMR filter with a loss tangent of fiberglass, $\tan\delta = 0.008$. All other filter parameters are the same as in the structure with the response of Fig. 10.

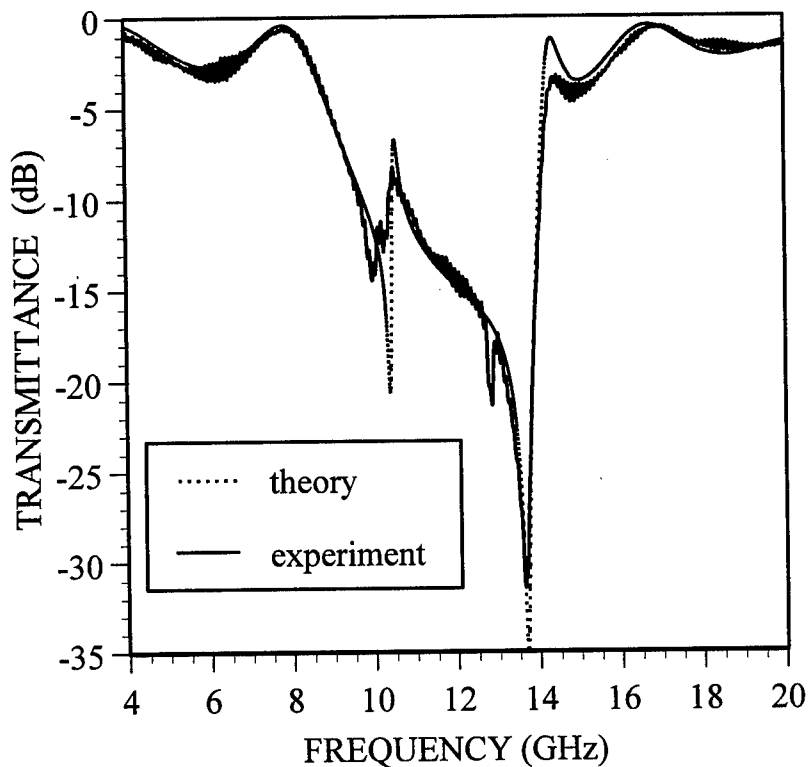


Figure 16. Experimental data of Fig. 12 (a) with transmittance values averaged over 20 frequency points and theoretical response of Fig. 10 with grating period $\Lambda = 2.03$ cm, fill factor $f = 0.5$, thicknesses $d_1 = d_3 = d_5 = 0.31$ cm, $d_2 = d_4 = 0.62$, dielectric constants $\epsilon = 4.4944$ (G10 fiberglass), $\epsilon = 1.0$ (air), and loss tangent $\tan\delta = 0.01$.

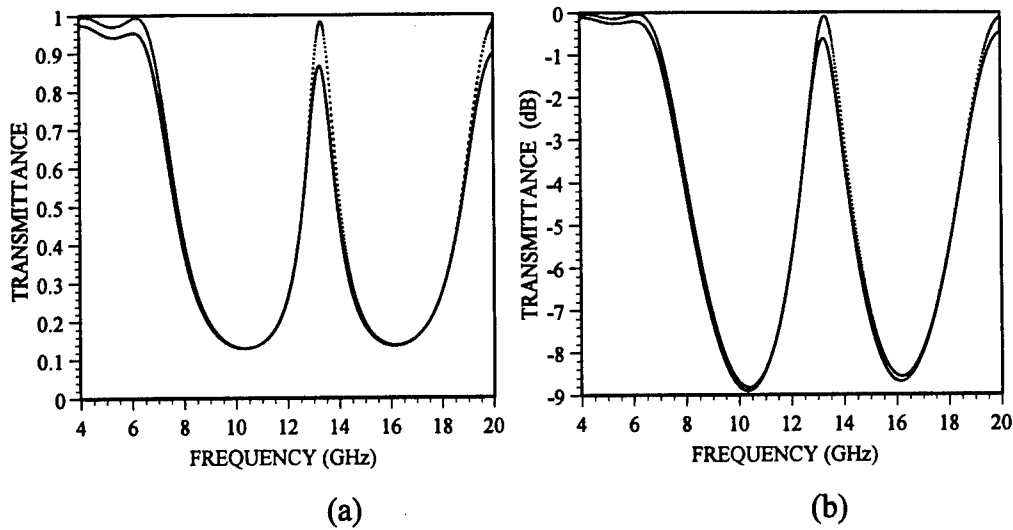


Figure 17. Theoretical transmittance of a 5-layer Fabry-Perot with dielectric constant of the odd layers $\epsilon = 3.7$ (Silica glass), dielectric constant of the even layers $\epsilon = 1.0$ (air), and thicknesses of the layers $d_1 = d_5 = 0.29$ cm, and $d_2 = d_3 = d_4 = 0.58$ cm. The loss tangent is $\tan\delta = 0.001$ (dotted line) and $\tan\delta = 0.01$ (solid line).

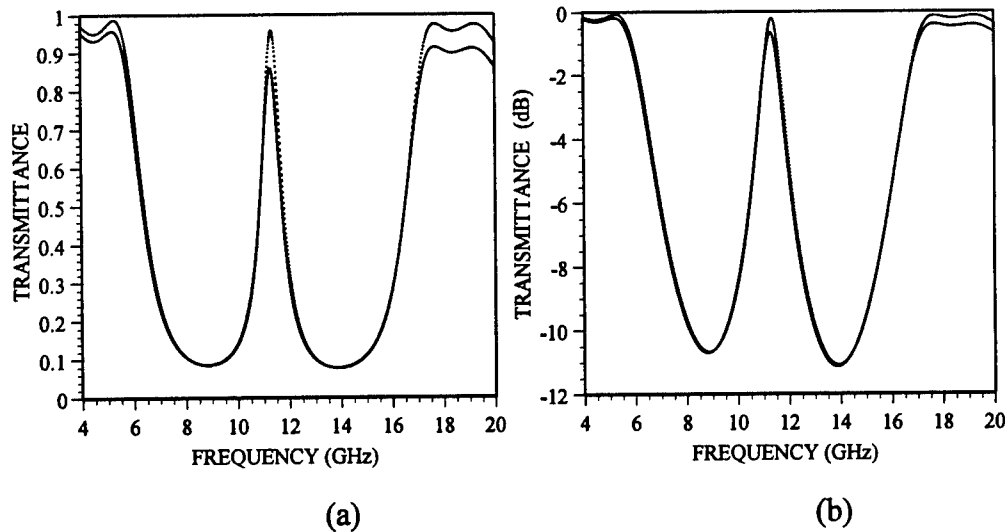


Figure 18. Theoretical transmittance of a 5-layer Fabry-Perot with dielectric constant of the odd layers $\epsilon = 4.5$ (G10 fiberglass), dielectric constant of the even layers $\epsilon = 1.0$ (air), and thicknesses of the layers $d_1 = d_5 = 0.317$ cm, and $d_2 = d_3 = d_4 = 0.635$ cm. The loss tangent is $\tan\delta = 0.002$ (dotted line) and $\tan\delta = 0.008$ (solid line).

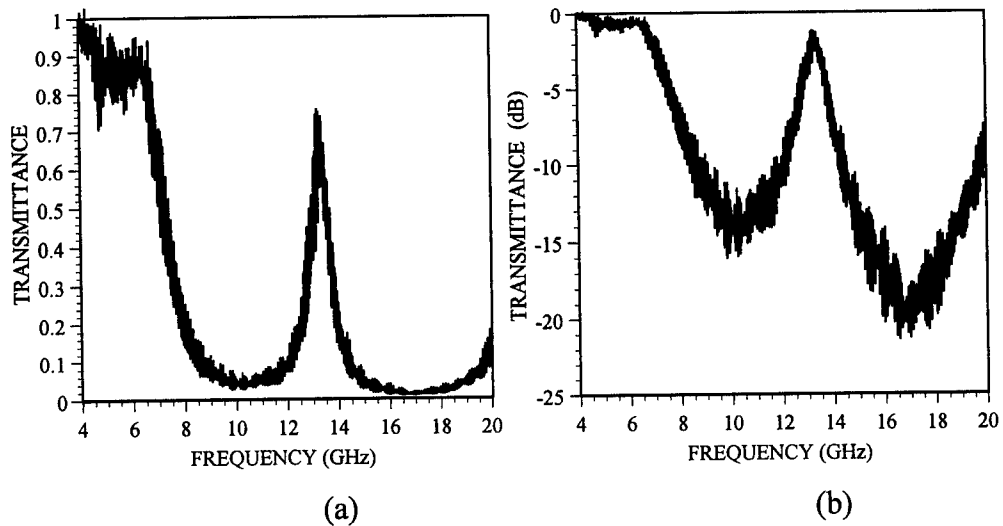


Figure 19. Experimental frequency response of a 5-layer glass/air Fabry-Perot for TE-polarized incident wave. The theoretical plot is shown in Fig. 17.

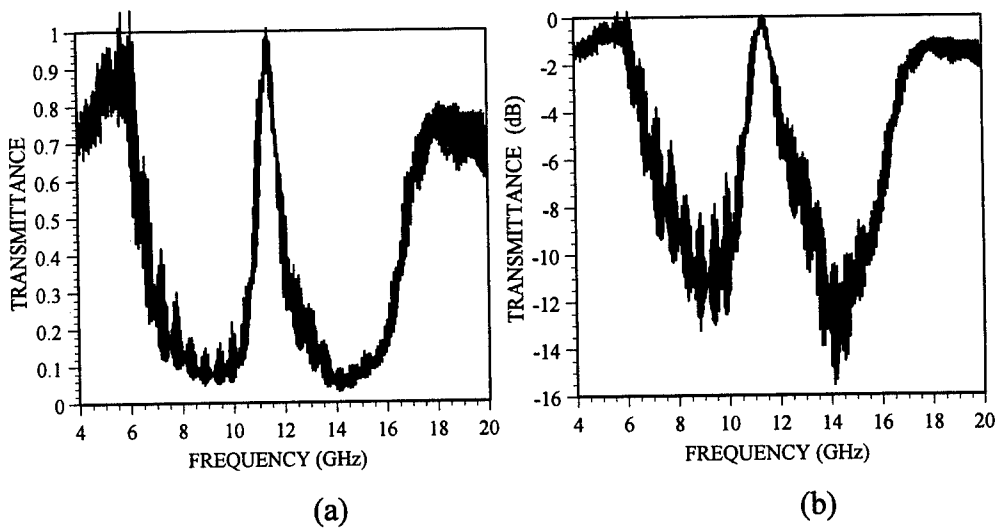


Figure 20. Experimental frequency response of a 5-layer fiberglass/air Fabry-Perot for TE-polarized incident wave. The theoretical plot is shown in Fig. 18.

ELECTRICALLY SMALL, EFFICIENT, WIDE-BAND, LOW-NOISE ANTENNA ELEMENTS

George Skahill, NTL Technologies Inc., 159 Clay Pitts Road,
Greenlawn, New York 11740-2917

Ronald M. Rudish and John Piero, AIL Systems Inc., Commack Road,
Deer Park, New York 11729

Abstract: An investigation was performed to explore a new class of active circuit element for achieving efficient wide-band impedance matching of electrically small antennas. Conventional approaches using passive circuit elements are limited in achievable gain-bandwidth, and previous attempts to overcome this limitation with active circuits were not successful.

Transistor circuits were designed to behave as two terminal impedance elements able to violate the Foster reactance theorem and provide more versatile reactance versus frequency than passive networks. Their utility in matching small antennas was confirmed analytically, resulting, for example, in an estimated VSWR of less than 2:1 for a 100 cm dipole over the frequency range of 30 to 88 megaHertz.

Whether these circuits could actually be realized in low-loss configurations free of microwave instabilities was not known, and most of our effort was devoted to fabricating and testing a working circuit model, nominally a negative inductor, emphasizing its stability at frequencies as high as 25 gigaHertz. The circuit demonstrated non-Foster impedance characteristics from 30 to 88 megaHertz and was free of high frequency instabilities, indicating that the new class of circuits is feasible and can be evolved to enlarge the bandwidth of electrically small antennas many times.

1. Conventional wide-band matching of electrically small antennas.

All electrically small antennas, those which extend less than about 1/3-wavelength are characterized by several features:

- radiation patterns that vary slowly with frequency and exhibit a peak directivity of ~ 1.5 dB,
- small values of radiation resistance that increase as frequency-squared,
- large values of reactance that vary rapidly with frequency,
- limited gain-bandwidth products when matched by orthodox methods.

Small electric dipoles, small magnetic dipoles and combinations of small electric and magnetic dipoles exhibit the same fundamental properties. This discussion focuses on small electric dipoles.

Conventional wide band impedance matching incorporates matching circuits into the antenna with the purpose of obtaining maximum power transfer over a selected range of frequency. The goal is usually constant VSWR over the band. These techniques cannot improve on the antenna's circuit quality. On the other hand, they will not degrade its circuit quality if properly applied. To the extent that total power transfer is achieved over the band, an electrically small antenna can exhibit antenna gain of ~ 1.5 dB.

The input impedance of a thin, short electric dipole is approximated very well over a range of frequencies by an equivalent circuit consisting of the antenna's radiation resistance, its loss resistance, a large capacitive reactance and a small inductive reactance. In most instances, its loss resistance is small enough compared with the radiation resistance that it may be ignored. Figure 1 contains a Smith chart display of the impedance properties of a 100 cm dipole, showing its combination of small resistance and large capacitive reactance over the VHF-FM communications band of 30 to 88 mHz. The first step in matching such an impedance curve is to balance or resonate it by the addition of series inductance (Figure 2) with the result that (Figure 3) the midband of the frequency segment to be matched is on the resistance axis. In this example the midband frequency is 59 mHz. The next step is the addition of a shunt tuned circuit that results in an impedance characteristic (Figure 4) with a VSWR no larger than 7:1 over the range of 57½ to 60½ mHz, corresponding to a matching loss of 3.6 dB over that 3 mHz band. The parameters of the matching circuit were carefully chosen so the 'matched' 3 mHz segment of the curve is centered at Z_0 , eliminating the need for the transformer section included in Figure 2. In general, a transformer will be required.

Even this modest result is obtained with great difficulty. Matching circuit elements must be high Q and their values must be obtained with reasonable accuracy. To achieve these requirements, most practitioners turn to transmission line elements which are able to provide high Q performance and accurate,

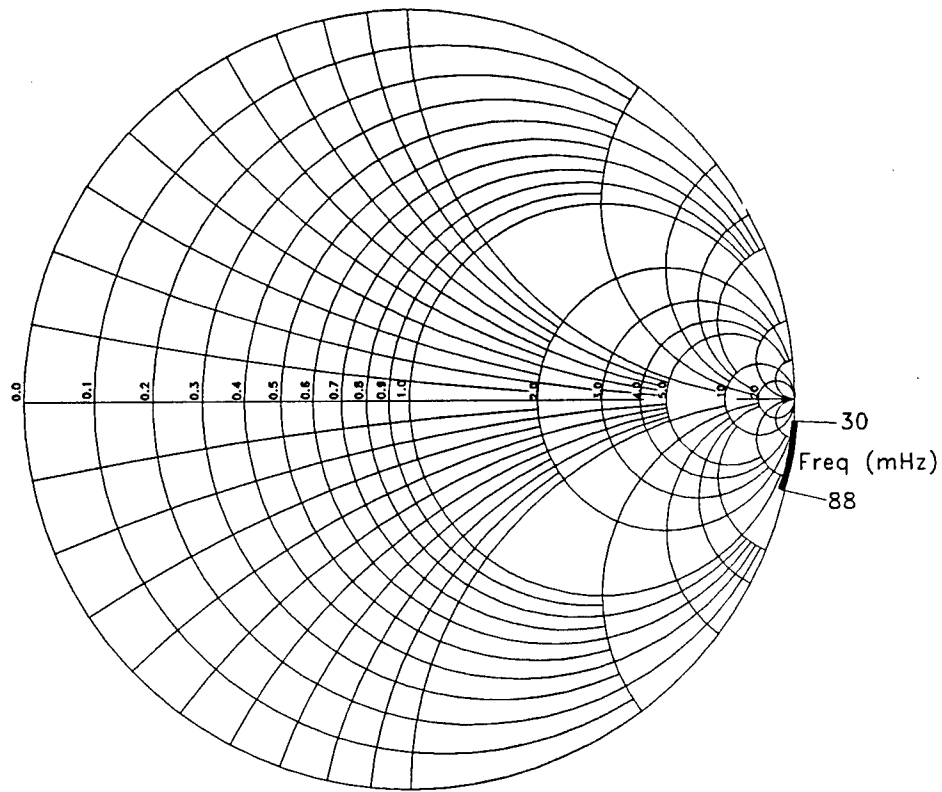


Figure 1. Impedance of a Symmetrical Center-fed Dipole Antenna with Total Length of 100cm. Element Diameters = 0.1 inch
Frequency = 30 to 88mHz
Z-zero = 50 ohms

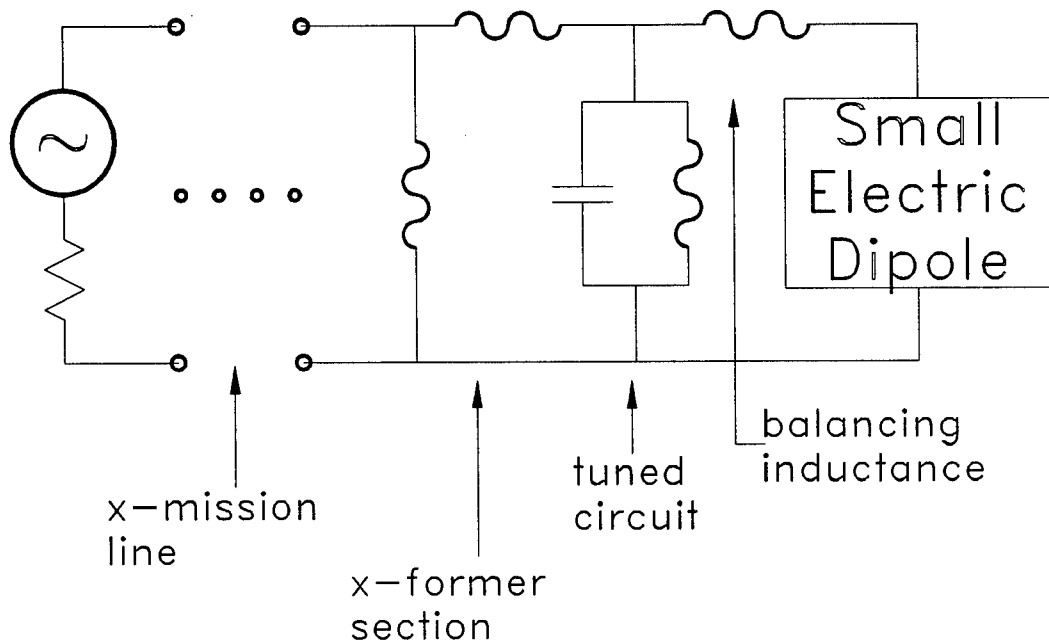


Figure 2. Conventional Matching of Electric Dipole Antenna

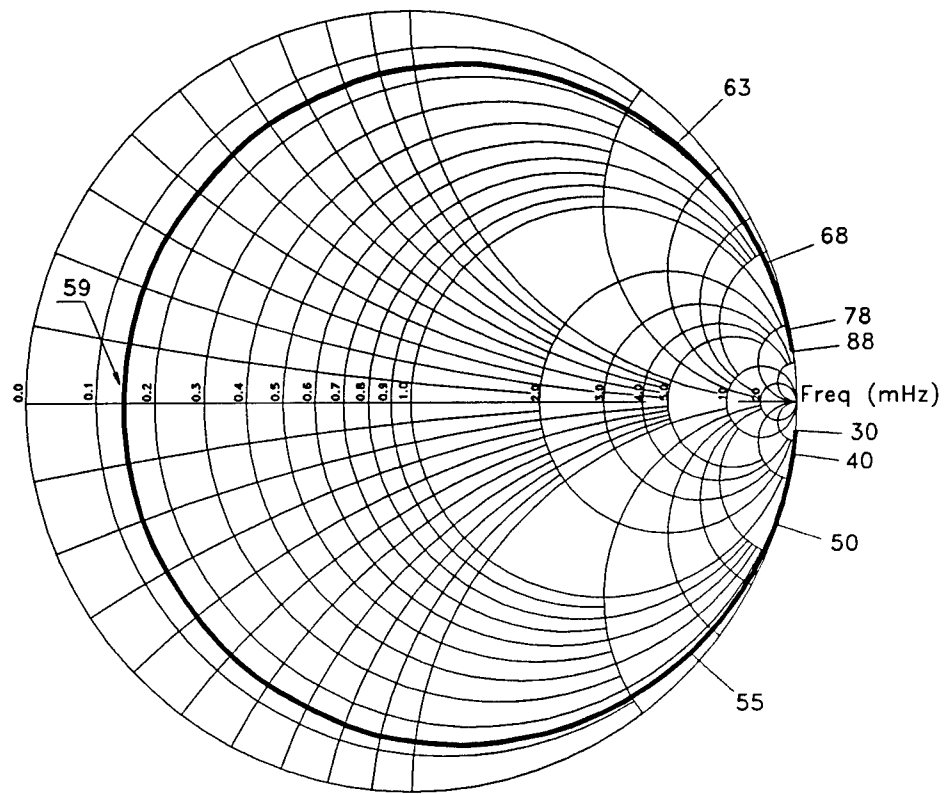


Figure 3. Impedance of a Symmetrical Center-fed Dipole Antenna with Total Length of 100cm. Balancing Series $L = 2.18\mu\text{Henry}$
Element Diameters = 0.1 inch
Frequency = 30 to 88mHz
 Z -zero = 50 ohms

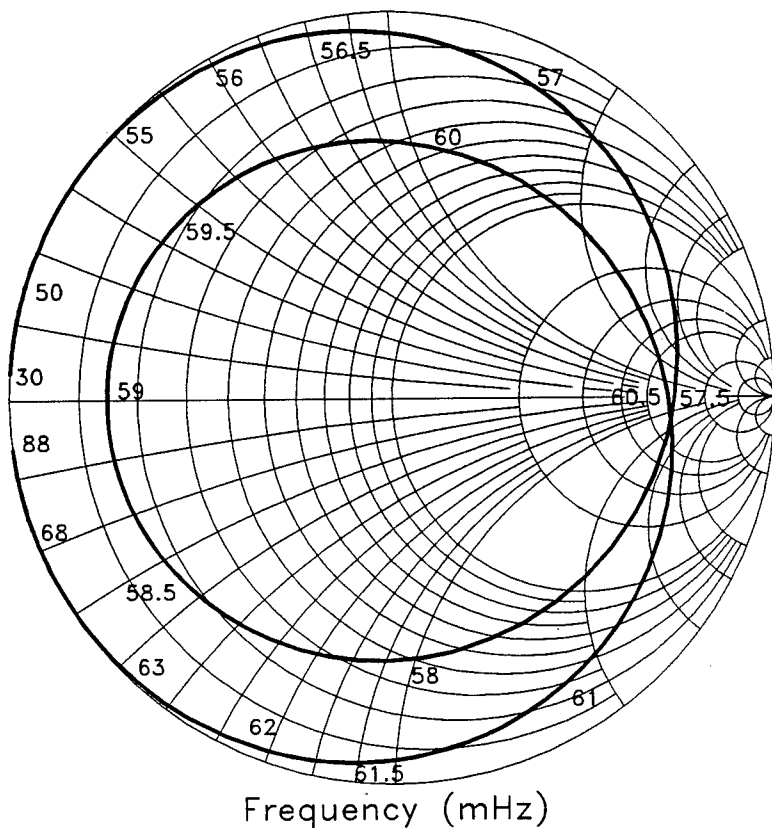


Figure 4. Impedance of a Symmetrical Center-fed Dipole Antenna with Total Length of 100cm. Element Diameters = 0.1 inch.
 Matching with Series L and a Shunt Tuned Circuit
 Frequency = 30 to 88mHz
 Z -zero = 50 ohms

flexible component values, but at the expense of additional dispersions that diminish achievable VSWR. Concepts of switching among matching circuits to cover different band segments are theoretically possible, but their practicality remains an issue in most applications.

2. Non-Foster wide-band matching of electrically small antennas.

The Foster reactance theorem states that the reactance slope of passive circuits is everywhere positive. Circuit elements which could provide negative reactance slopes (non-Foster elements) would improve on the performance achievable using conventional methods many times. Elementary non-Foster components are negative inductances and negative capacitances. Our work indicates that combinations of these elementary non-Foster components can be achieved in a single active circuit, without the need to place several elementary components in tandem.

Using the same electric dipole as before, the non-Foster matching strategy is to compensate the dipole reactance with a non-Foster series circuit element and to transform the resistance level using a transformer in which one of the components is non-Foster (Figure 5). To illustrate some of the details, the antenna impedance model used is more accurate and more complex than that of a simple RLC equivalent circuit while the non-Foster reactances are modelled as purely negative L or negative C. In the first step, a circuit consisting of negative L and negative C is connected in series with the antenna, and the values are chosen so that the end points of the resulting characteristic lie on the resistive axis (Figure 6). Had the antenna impedance been faithfully represented as a simple RLC series circuit, the resulting characteristic would have stayed on the resistive axis across the entire band, reflecting the frequency-squared variation of radiation resistance.

In the second step, an impedance transformer consisting of a series negative inductance and a shunt positive inductance of equal magnitude is employed as indicated in Figure 5 with the resulting impedance characteristic illustrated in Figure 7. This type of transformer has the property of converting a frequency squared resistance to a fixed value, a most fortuitous circumstance for antenna designers. Once again, had the antenna impedance been faithfully represented by a simple RLC circuit, with resistance increasing as frequency squared, the final result would have been a point in the center of the chart. Interchanging the inductors in the transformer leads to a similar result (Figure 8).

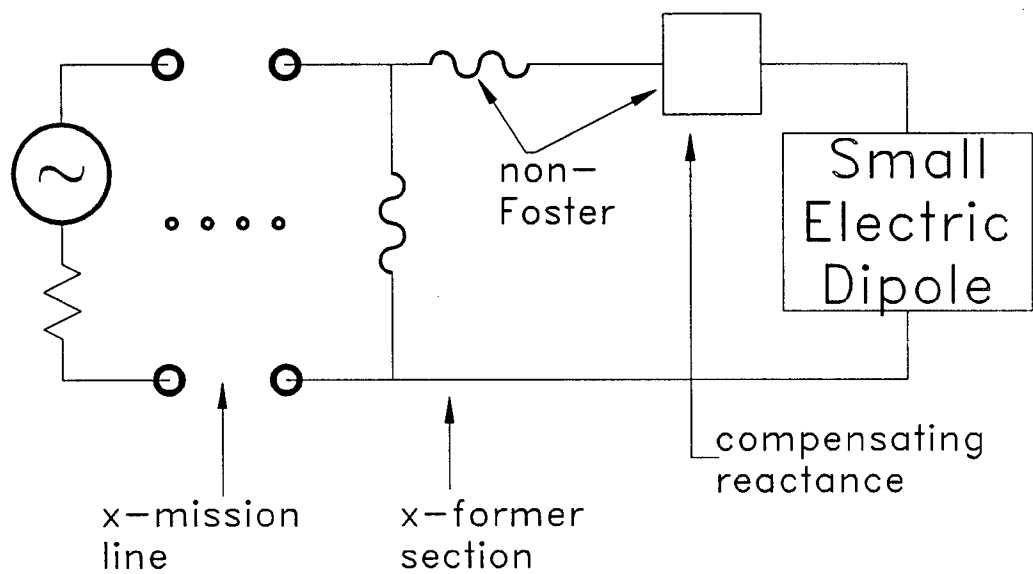


Figure 5. Matching of
Electric Dipole with
non-Foster Reactances

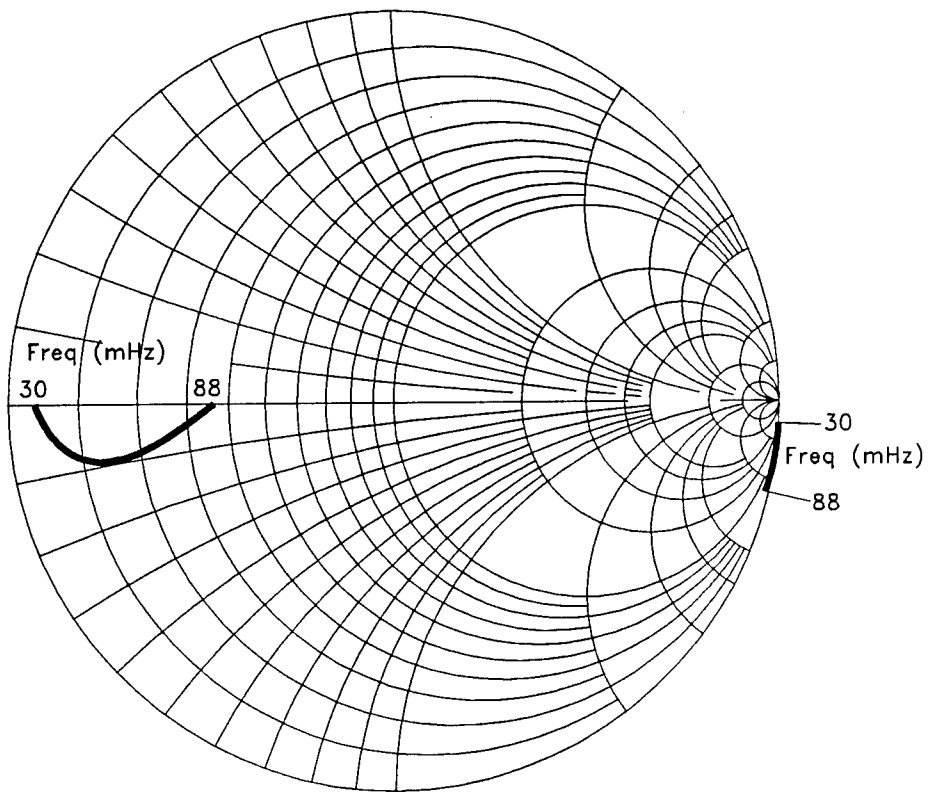


Figure 6. Impedance of a Symmetrical Center-fed Dipole Antenna with Total Length of 100cm. Element Diameters = 0.1 inch
Series L = $-0.370 \mu\text{Henry}$
Series C = -2.861 pFarad
Frequency = 30 to 88mHz
Z-zero = 50 ohms

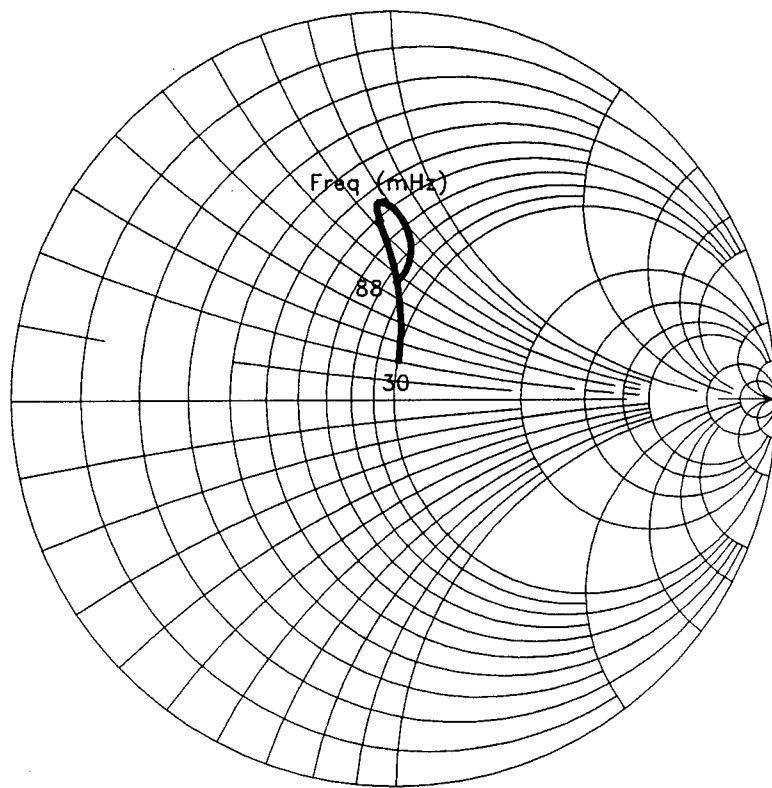


Figure 7. Impedance of the Center-fed Dipole with Series $L = -0.370 \mu\text{Henry}$ Series $C = -2.861 \text{ pFarad}$ and a transformer with Series $L = -50 \mu\text{Henry}$ and Shunt $L = +50 \mu\text{Henry}$ Frequency = 30 to 88mHz $Z\text{-zero} = 50 \text{ ohms}$

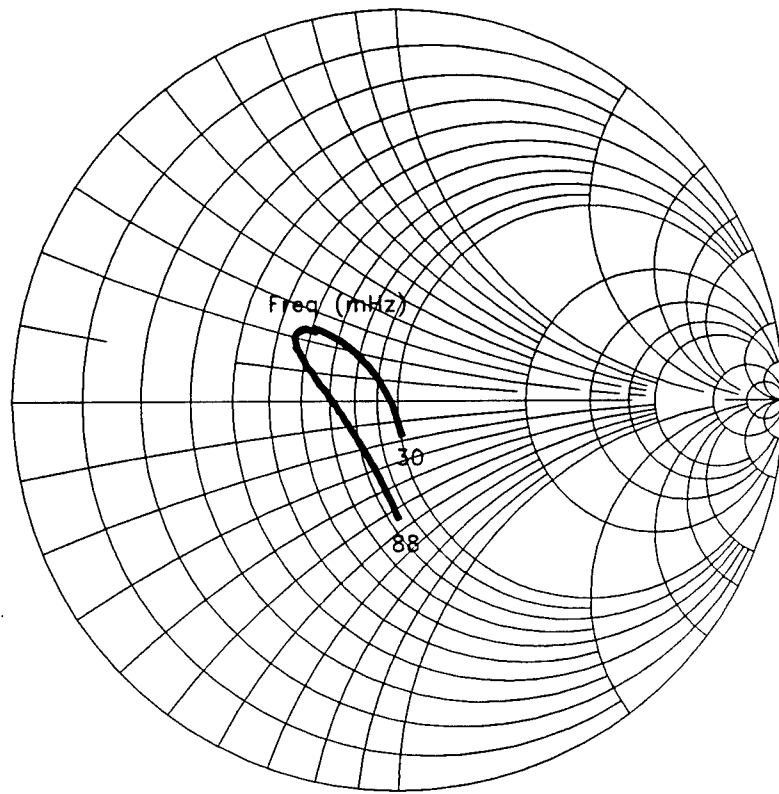


Figure 8. Impedance of the Center-fed Dipole with Series $L = -0.370 \mu\text{Henry}$ Series $C = -2.861 \text{ pFarad}$ and a transformer with Series $L = +50 \mu\text{Henry}$ and Shunt $L = -50 \mu\text{Henry}$ Frequency = 30 to 88MHz $Z\text{-zero} = 50 \text{ ohms}$

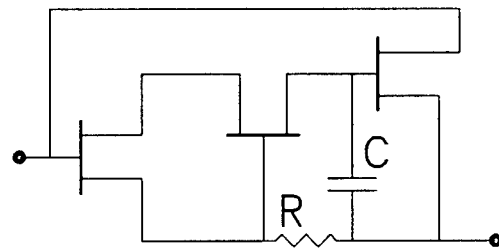
3. Non-Foster Reactance Circuits.

What was not clear at the beginning of our effort was whether, or how well, circuit components able to improve the performance of electrically small antennas could actually be realized. A survey of work in progress turned up a large body of theoretical activity directed at promising configurations of FET amplifiers. All investigators identified wide-band stability as the issue of major concern, and some suggested that monolithic fabrication would be needed to ensure it. Stability problems were clearly the reason for the absence of reports on circuit implementations. We found no evidence of even one working model, excepting for an operational-amplifier based circuit whose designers strongly recommend FET techniques over op-amp approaches.

Our own analyses confirmed that wide band stability was the major issue; circuits designed to provide low-loss reactances at frequencies near 100 mHz required the use of FET devices with positive gain at 25 gHz, and low loss reactive circuit designs were highly susceptible to high frequency oscillation. Substantive progress demanded more information than we could uncover, so we devoted most of our contract effort to achieving a stable non-Foster circuit.

The circuit for this demonstration was selected from a family of circuits proposed by Khouri [1], in which 'current conveyors' are connected to achieve desired terminal properties. The circuit selected for implementation (Figure 9) used three MESFETs. In active network synthesis, three terminal networks called current conveyors have proven to be very useful in synthesizing various functions. The admittance matrix of a current conveyor has the form illustrated in Figure 10. Depending on the connection, it can represent a number of two port devices, including the voltage controlled current source, the voltage controlled voltage source, and the current controlled current source.

Microwave hybrid chip and wire construction was used because it permits tight control of the circuit parasitics able to induce oscillation. The circuit was built on 0.010 inch thick alumina substrate with via holes placed through the substrate to achieve low inductance grounds as needed. A photograph of the circuit is included (Figure 10). Spectrum analyzer measurements from dc to 22 gHz assessed the circuits stability, and vector network analyzer measurements in the 0.5 to 100 mHz range determined its impedance properties. The measurements showed the circuit to be entirely free of microwave oscillations. After a series of adjustments to reduce the level of low frequency oscillations with spectral content up to 21 mHz, it was possible to characterize the circuit's



$$Z_{in} = -sC \frac{1/r_{ds} + g_{m2}}{g_{m1} g_{m2} g_{m3}}$$

Figure 9. Non-Foster
Circuit Based on
Current Conveyor

$$\begin{bmatrix} i_y \\ v_x \\ i_z \end{bmatrix} = \begin{bmatrix} 0 & 1 & 0 \\ 1 & 0 & 0 \\ 0 & \pm 1 & 0 \end{bmatrix} \begin{bmatrix} v_y \\ i_x \\ v_z \end{bmatrix}$$

Figure 10. Admittance
Matrix of Current Conveyor

important performance parameters. Two important results were obtained:

- The sought after, non-Foster, impedance behavior was observed. The measured impedance characteristic (Figure 11) rotated counterclockwise with frequency.
- No microwave instabilities were observed. Microwave oscillations have been the major impediment to realizing circuits of this kind, and demonstration of a working circuit free of microwave instabilities is a very big step in establishing their credibility.

4. Antenna Applications.

Non-Foster techniques can be usefully applied to reduce an antenna's extent whenever the troublesome size is the result of a gain-bandwidth requirement as opposed to a directivity requirement. They can be useful for transmitting sites for all services from ELF to VHF for ground installations, probably through L-band for vehicular installations, particularly on helicopters and stealthy aircraft. For receiving applications they can be applied usefully to expand bandwidth and/or reduce size whenever receiver noise is an important limitation, certainly including frequencies at and above HF.

A few areas where these methods appear to be particularly appropriate include:

- Aircraft and other vehicular installations where the resulting reductions in size of external or subsurface antennas can be very useful. Applications include communications, navigation, signal intercept and countermeasures at HF, VHF, and UHF.
- Global communications and/or navigation system transmissions at and below HF, including AM broadcasting.
- Man portable applications include relatively low frequency field radio service as well as local area telephony, data and entertainment distribution systems. Note that in any free space communications system, if we can elevate the gains of both transmit and receive antennas to near unity, power transfer becomes proportional to frequency-squared. In the example of 900 mHz versus 48 mHz local area data distribution, the lower frequency system enjoys a 13 dB advantage.

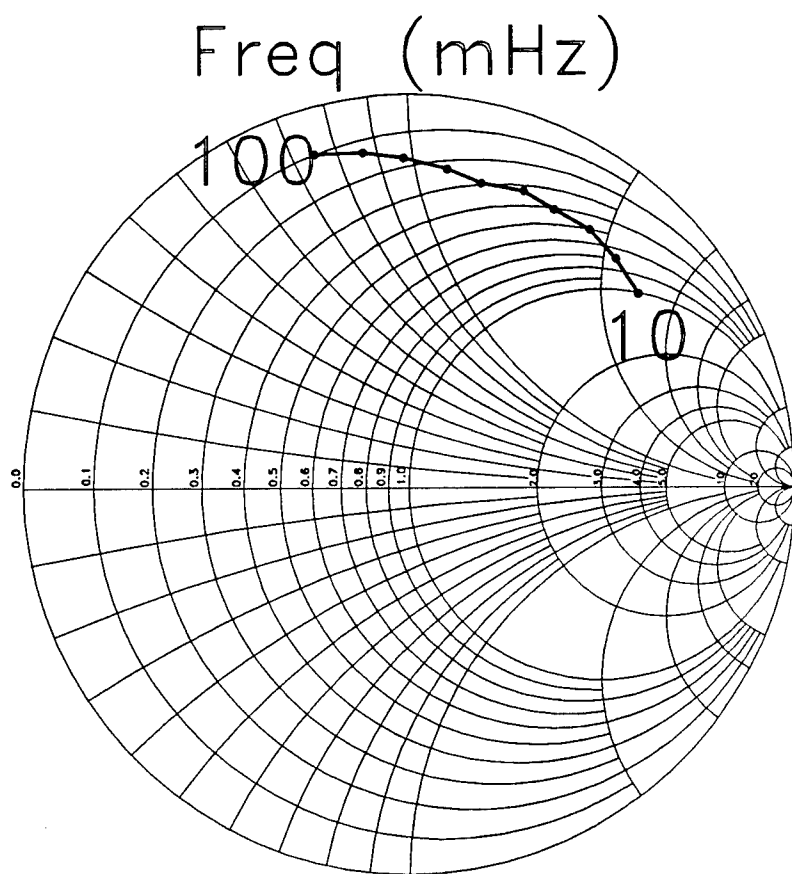


Figure 11. Measured Impedance of Proof of Concept non-Foster Reactance Circuit

Frequency = 10 to 100mHz

Z-zero = 50 ohms

5. Recommended Future Tasks

At the onset of this effort, we uncovered large amounts of literature describing the performances and attributes of current conveyor circuits, and we anticipated rapid progress toward their application to wide-band matching of electricaly small antennas. Instead, we found no evidence of demonstrated performance at radio frequencies, and that these circuits had become a focus for purely theoretical study. We successfully performed a proof of concept experiment and resolved the question of credibility: they do perform in accordance with prediction models, and they can be implemented as radio frequency, low-loss, non-Foster reactances despite their recognized potential for high frequency, parasitic driven, instability. Although an enormously successful proof of concept, it stopped well short of creating enough insight and understanding to support confident design work. That confidence can be built only through additional development tasks.

Some of the parameters that need to be resolved experimentally in evaluating the utility of these circuits, after the big two of STABILITY and LOSS is their noise power generation, their linearity, issues that determine their frequency limits and achievable bandwidth, and power handling.

Rapid growth in understanding the behavior of these circuits can be achieved by designing, fabricating and testing additional circuits based on the thin film, microwave hybrid chip and wire construction method reported here, ensuring control of the parasitics that can cause unforeseen oscillations. The first circuits would be variations of the proof of concept unit, incorporating adjustments: to eliminate entirely its low frequency oscillation; to adjust various bias levels and resistance values to ensure the continued absence of microwave oscillations and to move the impedance trajectory closer to the edge of the Smith chart. Alternative topologies should be designed to demonstrate various combinations of desirable circuit behavior such as, for example, series and shunt negative inductors, negative capacitors, negative L - negative C tuned circuits, and other more general non-Foster reactances.

These hardware developments ought to integrate development and validation of analysis models for characterizing all important performance parameters, including linearity, noise generation and frequency limitations.

While the chip and wire construction method is useful for preliminary circuit evaluation, it is important to generate and evaluate non-Foster circuit elements using fabrication methods more suited to low-cost, high volume production.

An extremely useful task would be to fabricate several fully integrated printed circuits containing the transistor circuit elements, providing for external attachment of sizeable components or other components for which value adjustments via replacement can be useful. This unit would provide for external application of bias voltages and include internal test points.

These steps should be paralleled by evolution, fabrication and testing of surface-mount circuits. With this approach, because the circuits must be more sizeable and they provide for less control of the stray capacitances, the stability issue may be far more difficult to resolve. On the other hand, they are cheaper, more quickly obtained, and more easily modified over and over again, permitting an iterative, more experimental approach to achieving stable, low loss circuits.

Given the availability of the requisite non-Foster component(s) available from earlier tasks, the next task would be to design, fabricate and measure the impedance/efficiency properties of several antennas that have been matched with the aid of non-Foster circuit elements over substantial frequency extents, e.g., 30 to 88 mHz, 2 to 30 mHz, 2 to 88 mHz, etc.

A longer range task is evolution of non-Foster components capable of supporting transmitter power levels. This task may stimulate the evolution of specially tailored high frequency, high power transistors.

6.0 Acknowledgments. The circuit development work described in this paper was sponsored by DARPA under a Phase I SBIR Contract issued to NTL Technologies Inc. by the U.S. Army Missile Command under Contract # DAAH01-96-C-R303. The DARPA Program Manager was Major Daniel Gammon. The MICOM Technical Monitor was Mr. Hugh C. Carson.

7.0 References.

[1] S. El Khoury, "The Design of Active Floating Positive and Negative Inductors in MMIC Technology," *IEEE Microwave Guided Wave Letters*, vol. 5, no. 10, October, 1995

TRAVELING WAVE SLOTTED ARRAY ANTENNA EMPLOYING ASYMMETRIC RIDGE WAVEGUIDE

H. Shnitkin, D. Collier and J. Dickstein

Electronic Sensors and Systems division
Northrop Grumman Corp.
Baltimore, MD

ABSTRACT - A slotted array aperture utilizes asymmetric, single ridge waveguide to achieve low sidelobe performance. A characteristic weakness of current flatplate array designs such as those utilizing offset, broad-wall slotted waveguides, is the creation of unwanted second-order lobes. In the asymmetric approach, the waveguide asymmetry excites *in-line* slots, thereby eliminating the characteristic intercardinal sidelobes, allowing designers to minimize RMS sidelobe levels. This aperture, designed for a shipboard radar application, uses in-line radiating slots arranged in a true rectilinear, planar grid to achieve sidelobes 40 dB below the main beam. The array panel is mast-mounted on a pedestal rotating in azimuth, and scans electronically in elevation. To minimize both cost and weight, the panel consists of 100 horizontal sticks of traveling wave, single ridge waveguides, each containing 68 radiating slots. The sticks are fed in turn with 100 broad-wall couplers through an orthogonally oriented, traveling wave feed guide, which connects through rotary joints to the radar.

Both, analytical and experimental waveguide stick design approaches are presented, and test models, test results and analytical tools are described. An application-sensitive computer program for inexpensively deriving waveguide asymmetry dimensions as a function of waveguide-to-slot coupling values is explained.

1. Introduction

A shipboard search radar antenna is required to provide electronic pitch and roll stabilization while mechanically scanning the horizon for targets. For this reason the aperture is configured into a set of horizontal slotted waveguide arrays

excited by an orthogonal feed with ferrite phase shifters to provide 1-D electronic scan in elevation. It is designed to exhibit -40 dB sidelobes in the azimuth plane. Furthermore, severe cost and weight restraints have been placed upon this new electronically steered aperture.

2. Low Sidelobe Issue

Care must be taken in the design of slotted planar arrays to avoid creation of unwanted second-order lobes caused by small deviations in the orientation or location of successive slots. For instance, if the shunt slot design chosen for this array had utilized the conventional offset approach, either one or two pairs of secondary lobes would have been created, whose magnitudes far exceed values demanded in the specifications [1].

If the configuration illustrated in Figure 1a is chosen, two secondary lobes located on the principal horizontal plane are produced. If the configuration illustrated in Figure 1b is selected, four secondary lobes will appear in intercardinal space.

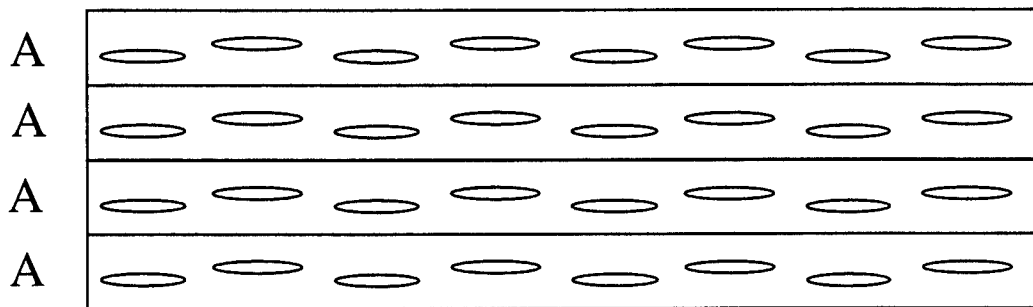


Figure 1a - Linear Arrays of Slots Configured Identically

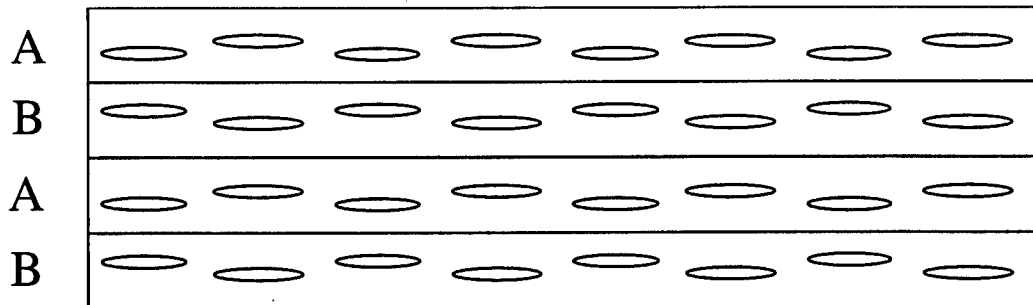


Figure 1b - Linear Arrays of Slots Configured as Mirror Images

To mathematically predict the location of the unwanted secondary lobes, it is necessary to group the radiating slots, such that each group is identical to its neighbor, but at the same time have the minimum number of slots in each group [1]. In the case of the ABAB configuration, this would constrain four slots to each group. The group spacing now becomes twice that of the spacing between slots, and the group element pattern becomes the new element factor.

The radiation pattern of a planar array of grouped slots may now be written as

$$E(\theta, \phi) = F_4(\theta, \phi) \sum_{n=0}^{N/2} A_n e^{jn(k2d_1 \sin \theta \sin \phi - 2\gamma_1)} \cdot \sum_{m=0}^{M/2} A_m e^{jm(k2d_2 \cos \theta - 2\gamma_2)} \quad [\text{eq. 1}]$$

where

$F_4(\theta, \phi)$ = element factor for group of four slots,

A_n, A_m = relative amplitudes of the groups.

$$\gamma = \frac{\text{phase shift}}{\pi}$$

$$d = \frac{\text{slot spacing}}{\lambda}$$

Figure 2, a three-dimensional, Az-El antenna radiation pattern plot of the ABAB configuration, shows these second-order beams. Only two lobes appear in real space, because the main beam is scanned 30° in elevation. Another pair of lobes appears in the upper quadrants with the beam unscanned.

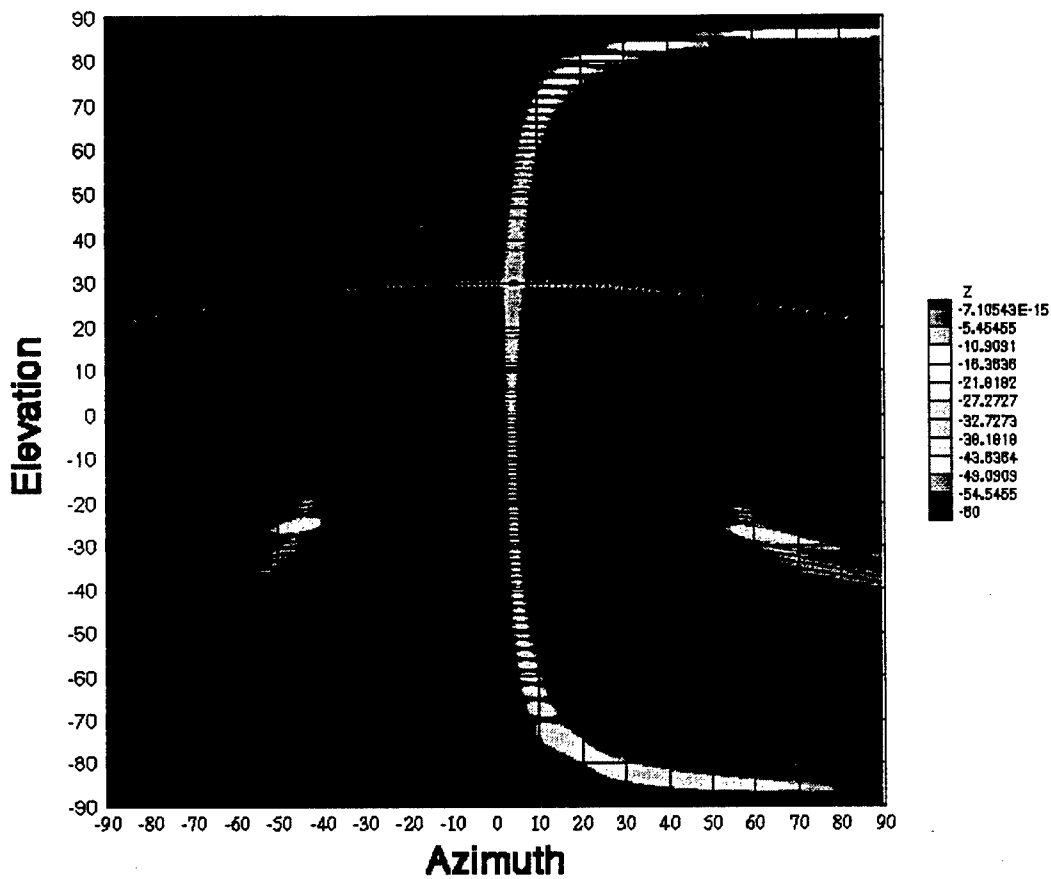


Figure 2 - Three Dimensional Plot of Scanned Beam Showing Second-Order Lobes

Methods of minimizing second-order beams have been dealt with in earlier papers [1,9]. Many require processes that are not cost effective when an array is manufactured in quantity. One obvious means of eliminating these unwanted lobes is by making the slots co-linear and creating a truly rectilinear slot lattice. The corrugated waveguide shown in Figure 3 is one of several possible solutions; however, if an amplitude distribution in elevation is desired, it becomes unfeasible because of the variation in slot-to-slot spacing required in the vertical plane.

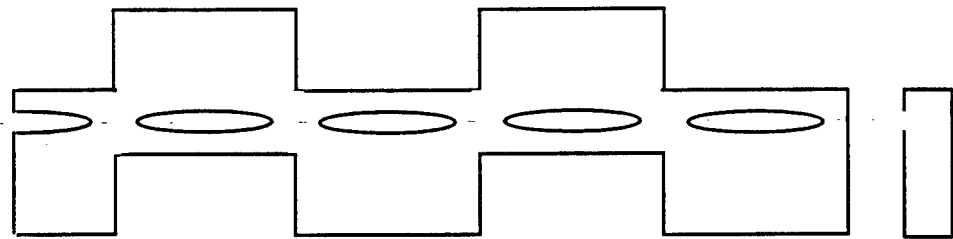


Figure 3 - Corrugated Waveguide Permitting Co-linear Slot Configuration

Norden Systems engineers developed and patented the asymmetric waveguide design shown in Figure 4 for the JointSTARS array [2,3]. The characteristics of this design and its adaptation for this new Navy requirement will be the subject of this paper.

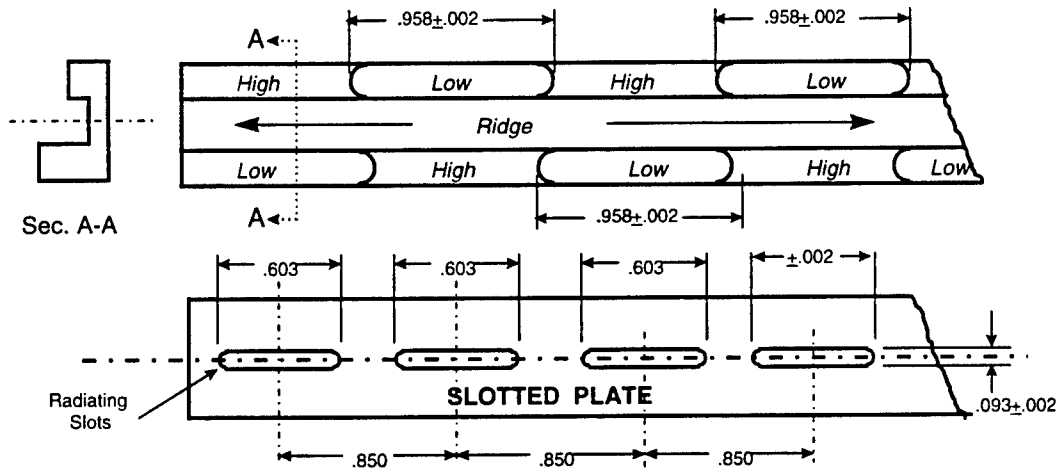


Figure 4 - Asymmetric Single Ridge Waveguide Array Configuration

3. Design Approach

To satisfy all the earlier mentioned requirements, a traveling wave, asymmetric single ridge waveguide array with broad-wall radiating slots has been selected as the horizontal array element, henceforth called a "stick". This chosen configuration avoids the bulky, heavy, and expensive azimuth corporate feed in each and every stick. Furthermore, all radiating slots are positioned co-linearly precisely on the waveguide's centerline to avoid all intercardinal sidelobes, as

discussed in Section 2. These slots are excited via the waveguide's longitudinal H-field, which is generated by making the two legs (or troughs) of the ridge waveguide cross-section un-equal. The amount of asymmetry determines the radiated voltage magnitude while the sense of asymmetry assigns the polarity to the radiated vector.

The specific design values are now determined. By tilting the aperture 10 degree upwards, in order to reduce the horizon splash of RCS, and by allowing ± 30 degrees for maximum ship's roll, a maximum elevation scan angle of 40 degrees from the array normal would be required under conditions of no azimuth scan. However, a small amount of azimuth scan with frequency, such as from 4.3 to 7.6 degrees, must be allowed to avoid excessive VSWR at angles close to zero azimuth scan and to accommodate the frequency sensitive phase delay caused by the traveling wave type of feed. This fact causes the maximum effective scan angle to increase to 41.1 degree, according to equation 2.

$$\text{Effective max. scan angle} = \arcsin \{ \sqrt{[\sin^2(40^\circ) + \sin^2(7.6^\circ)]} \} \quad [\text{eq.2}]$$

In addition, because of the 1.5 degrees elevation beamwidth, a conservative no-grating lobe elevation scan angle of 42.6 degrees was chosen. The resulting maximum elevation array spacing is computed using equation 3.

$$\lambda_{\min} * (1 - 1/N_{\text{eff}}) / (1 + \sin 42.6^\circ) = 0.705 \text{ inches} \quad [\text{eq.3}]$$

where N_{eff} is the effective number of uniformly illuminated vertical elements, namely 80.

The centerline-to-centerline distance between each stick was set at 0.694 inches to allow for clearance, manufacturing and array rigidity tolerances. This spacing minus a 0.060" allowance for waveguide wall thickness resulted in the ridge waveguide's interior cross-section of Figure 5.

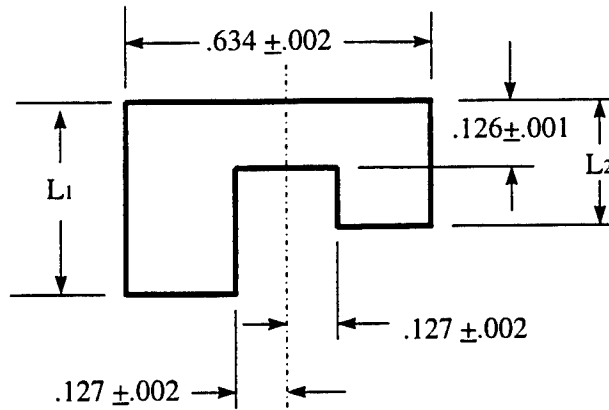


Figure 5 - Ridge Waveguide Array Cross-section

To satisfy the stringent -40 dB azimuth sidelobe requirement, a Taylor illumination of 45n5 was selected. For elevation a Taylor illumination of 25n5 was deemed sufficient. By limiting the maximum slot coupling to 9 dB to assure minimum standing wave error, and by dissipating only 3% of the input power in the load at the end of the stick, a total loss of 0.42 dB in each stick was achieved.

An antenna performance summary table is shown below:

Aperture Gain ($4\pi A/\lambda_{\max}^2$).....	45.1 dB
Azimuth Taper Loss (45n5).....	1.39 dB
Elevation Taper Loss (25n5).....	0.41 dB
Stick Termination Loss (3% into load)	0.13 dB
Stick Waveguide Loss	0.29 dB
Other Circuit Losses	3.4 dB
Net Gain @ F_{\min} & Max. 43° Scan	39.5 dB
Azimuth HPBW	1.53 deg. , MIN.
Elevation HPBW	1.02 deg , MIN.
Elevation Tilt	10 deg.

4. Asymmetric Ridge Design Details

Slotted array designs using slots positioned precisely on the center line of the broad wall of an asymmetric single ridge waveguide have been previously employed as short resonant linear arrays for the JointSTARS phased array

antenna, following the techniques outlined in U.S.Patent No.4,638,323 [2] and in an IEEE paper [3] . The application described here, however, involves a long traveling wave array, radiating in the direction of a few degrees off-normal, and also exhibiting an unavoidable 4.3^0 to 7.6^0 frequency scan. The key to asymmetric ridge waveguide array design is the generation of a function or equation giving the dimensions of the trough asymmetries, shown as L_1 and L_2 in Figure 5, as a function of desired slot coupling.

The preferred starting point for generating this function is a technical paper by Pyle [4] which allows one to determine both, the ridge waveguide's cut-off frequency and the exact location of the null plane of the waveguide's longitudinal H-field. Using a specially prepared computer program based upon the equations presented in reference 4, approximate coupling values were determined. An equivalent rectangular waveguide slotted array with the same cut-off frequency and a height equal to the distance between the ridge and the opposite wall was used together with the computed slot offset from the electrical null plane. To refine the design, several ridge waveguide models, each corresponding to one representative coupling value, but all possessing the same cut-off frequency, were then constructed and measured for coupling, as detailed in Section 6. For the waveguide shown in Figure 4, this procedure was followed using four values of coupling, ranging from -9 dB to -26 dB. Two additional points on the design curve were the "no coupling" point when the ridge waveguide was symmetrical, i.e. $L_1 = L_2$, and a point mid-way between -26 dB and the "no coupling", assuming a linear voltage coupling function for very small values of coupling. Now design curves of trough dimensions vs. coupling can be constructed. A careful examination of this curve disclosed that if coupling were expressed in volts and trough dimensions were referenced to the symmetrical or "no-coupling" trough dimension (when $L_1 = L_2 = 0.3413$ inches) the curves almost resemble straight lines. This makes interpolation for intermediate coupling values both easy and accurate, yielding the curves shown in Figure 6. Subsequently, a regression to a fourth power polynomial was performed for quick and precise computer generation of waveguide dimensions in inches. This yielded the following two equations:

$$L_1 = .3413 -.1386354 z + .2178267 z^2 - 1.73297636 z^3 + 2.8215997219 z^4 \quad [\text{eq.4}]$$

$$L_2 = .3413 + .1509286 z - .3396056 z^2 + 2.40923224 z^3 - 3.6273589134 z^4 \quad [\text{eq.5}]$$

where $z = 10^{-(\text{Cplg. in dB})/20}$

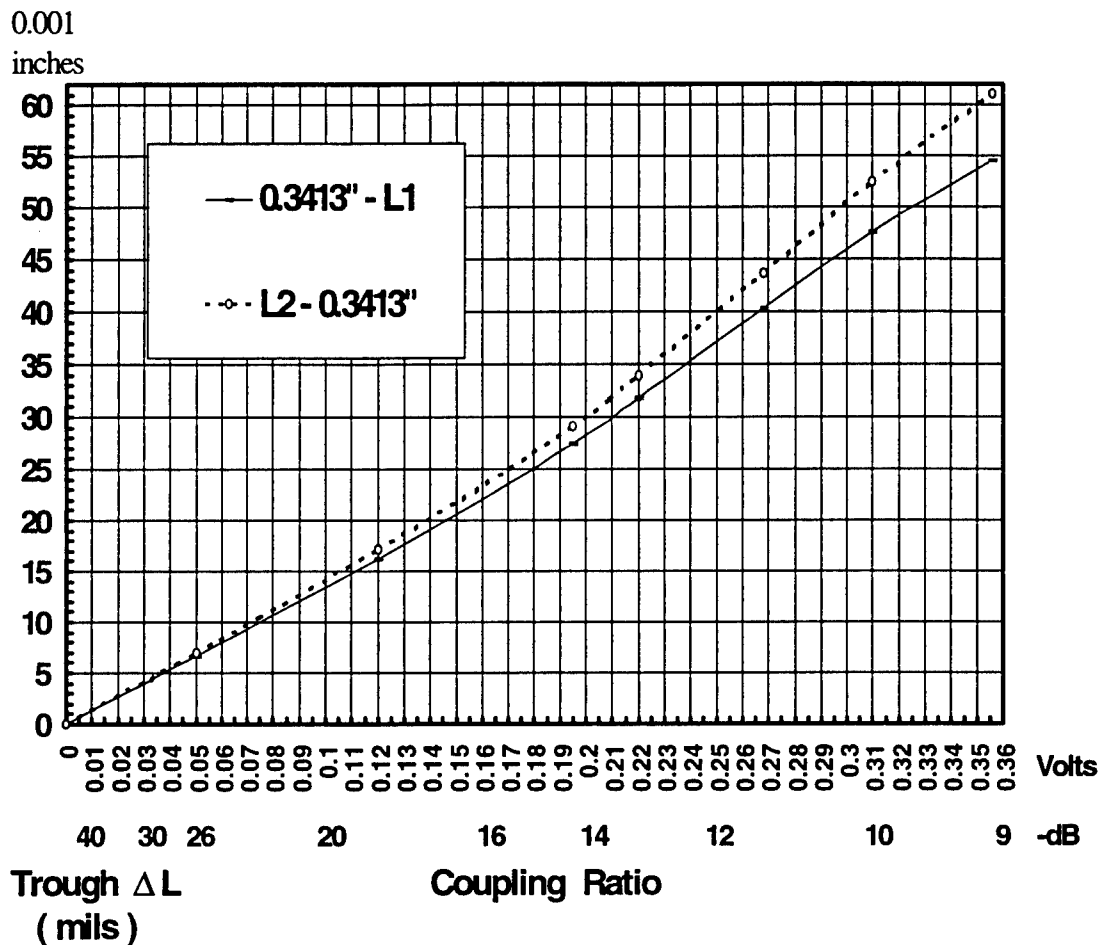


Figure 6 - Ridge Waveguide Trough Dimensions vs. Slot Coupling Volts

A slot separation of 0.850 inches, slightly in excess of a half guide wavelength, was chosen. This represents 0.708 free space wavelengths at the maximum frequency, assuring no grating lobes at the maximum 7.6 degree azimuth scan angle; it also minimizes the number of slots and offers sufficient slot decoupling. Furthermore to achieve very small azimuth scan angles requires alternating the ridge waveguide asymmetry between adjacent slots, as shown in Figure 4.

From this 0.850" slot spacing ("d") , the 5.63 GHz cut-off frequency and the alternating slot voltage polarity, three azimuth scan angles have been computed by equation 6, namely :

	F_{MIN}	F_{CENTER}	F_{MAX}
Frequency	9.50 GHz	9.75 GHz	10.0 GHz
Azimuth Scan Angle	4.29 ⁰	6.00 ⁰	7.60 ⁰

$$\text{Azimuth Scan Angle} = \arcsin \{ (\sqrt{[1 - (F_{co} / F)^2]} - 5.9 / (F * d)) \} \quad [\text{eq.6}]$$

To insure minimum standing wave in the array waveguide the interior step discontinuities due to the 180 degree phase reversal and therefore alternating asymmetry, the interior steps will be staggered by elongating the "bath-tubs" to 0.958 inches and producing an overlap (see Figure 4). This staggering of the discontinuities creates small impedance-matched π -sections consisting of two identical shunt inductances separated by a short section of low impedance waveguide.

A slot width of 0.093 inch was chosen to minimize the Q of the slot without inviting measurable cross-polarization. This limited the total slot coupling variation over the 9.5 GHz to 10 GHz frequency band to 1.9 dB.

A computer circuit model of a set of equally coupled waveguide shunt slots spaced 0.85 inches was generated to ascertain the magnitude of the standing wave created by the non-directional shunt slot conductances. The results for 9 dB coupled slots, the tightest coupling used in this array, produced a VSWR of 1.29, as shown in Figure 7. The resulting rms aperture error is only 0.3 dB. Subsequent antenna pattern tests of a preliminary three foot long, 40 slot array with maximum slot coupling of 9 dB showed that the effect of this standing wave upon sidelobes is negligible.

Loss = .008 dB/slot						G = .11 or 9.6 dB		
F R E Q U E N C Y = 9.500 G H z								
SLOT	NPUT R (ohms)	INPUT X (ohms)	VSWR	FEED VOLTAGE	FEED PHASE	ACTUAL	SLOT dB	dB Error
						SLOT dB	without VSWR	
1	0.908	-0.025	1.11	0.522	-32.7	-15.6	-15.6	0.0
2	0.835	0.005	1.20	0.523	-192.4	-15.6	-15.2	0.4
3	0.800	0.064	1.26	0.536	9.4	-15.4	-14.9	0.5
4	0.804	0.125	1.29	0.566	-148.8	-14.9	-14.5	0.4
5	0.841	0.169	1.29	0.612	52.1	-14.3	-14.1	0.2
6	0.895	0.181	1.25	0.663	-108.5	-13.6	-13.6	0.0
7	0.941	0.157	1.19	0.712	90.0	-12.9	-13.3	0.4
8	0.959	0.111	1.13	0.752	-71.9	-12.5	-12.9	0.4
9	0.944	0.069	1.10	0.782	126.3	-12.1	-12.5	0.4
10	0.909	0.051	1.11	0.805	-34.8	-11.9	-12.1	0.2
11	0.876	0.056	1.16	0.828	-195.0	-11.6	-11.8	0.2
12	0.856	0.079	1.19	0.859	5.3	-11.3	-11.4	0.1

Figure 7 - Twelve-Slot Array Transmission Line Analysis

5. Tolerances and Error Analysis

To predict the expected antenna sidelobes of the one hundred linear array aperture, an error and tolerance analysis must be performed. Three types of error contributors will be considered, namely, dimensional tolerances of the linear array, circuit components, and total assembly tolerances. All errors have been tabulated in Figure 8 together with the resulting computed antenna sidelobes.

	<u>TOPIC</u>	<u>ERROR CONTRIBUTORS</u>	<u>RMS PHASE</u>	<u>RMS AMPL.</u>
1	Cumulative	L_1 & $L_2 \pm .001$ Trough Depth	0.39^0	0.16 dB
2	Slotted Array	$0.634 \pm .002$ Total WG Width	0.62^0	-
3	Phase	$0.126 \pm .001$ Ridge Gap	0.92^0	-
4	Errors	$\pm .002$ Dip-braze	0.96^0	-
5		Step Discontinuity	0.55^0	-
6		RSS , Phase Error between Slots	1.62^0	-
7	Error	Avg. Phase Error , 68-Slot Array	9.3^0	0.16 dB
8	Summation	$\pm .002$ Slot Center Line	-	0.28 dB
9		$0.127 \pm .002$ each edge , Ridge C/L	-	0.26dB
10		$\pm .008$ Aperture Flatness	1.8^0	-
11		Radome	1.5^0	0.2 dB
12		Ferrite Phase Shifter	3.0^0	0.1 dB
13		Phase Shift Quantizing	0.4^0	-
14		Calibration	3.5^0	0.3 dB
15		Temperature Phase Error	1.0^0	
16		Elevation Feed	-	0.4 dB
17		Tracking over Frequency Band	-	0.4 dB
18		VSWR		0.3 dB
19		R S S SUM	10.7^0	0.85 dB
20	Sidelobes	Taylor Sidelobes in Azimuth	-45 dB	
21	68 Slot Array	Random RMS Sidelobes	-30 dB	
22	68 Slot Array	Peak Sidelobe	-20 dB	
23	68 Slot Array	RMS Sidelobe Level	-30 dB	
24	6800 Slot Array	Random RMS Sidelobes	-49 dB	
25	6800 Slot Array	Peak Sidelobe	-36 dB	
26	6800 Slot Array	RMS Sidelobe Level	-44 dB	

Figure 8 - Error and Sidelobe Tabulation

5.1 Linear Array Errors

The various dimensional asymmetric ridge waveguide dimensional

tolerances were entered into the equations given in reference 2 to compute the resulting changes in both, the cut-off frequency and the off-set of the electrical null plane. The former determines the phase delay error between adjacent slots while the latter determines the magnitude of the radiated slot voltage. Both are shown in lines 1 thru 5 & 8 thru 9 of Figure 8 . Since in a traveling wave array all slots are connected in a cascaded fashion, uncorrelated phase errors accumulate as the square root of the slot location number. Thus the RSS phase error of line 6 of Figure 8 must be multiplied by 5.74 to obtain line 7. This was computed by $(1/48) * \text{Sum of } \sqrt{n}$, for $n = 11$ to 58 , in order to obtain the average RMS phase error for the entire linear array of the equivalent number of uniformly illuminated radiators in line 7 .

5.2 Circuit Component Errors

Circuit component errors appear on lines 11, 12, 13, 14, 16 and 18 in Figure 8. Calibration refers to a phase shifter setting versus command procedure using an injected BIT signal, and to measurement of an electronic scan pattern using an injected signal and appropriate phase shifter commands, together with an FFT computation for the purpose of phase-aligning the antenna aperture.

5.3 Assembly Tolerances

This category includes aperture flatness tolerance (line 10) and phase changes due to thermally expanding waveguides (line 15) of Figure 8 .

5.4 Sidelobe Prediction

Azimuth sidelobes arising from the 45n5 aperture illumination together with the aperture phase and amplitude errors can now be predicted. The results for the linear array of 68 slots are given in lines 21 thru 23 and for the total aperture of one hundred 68-slot arrays in lines 24 thru 26 of Figure 8 . The radiation pattern data, given in Section 7, demonstrate that the predicted sidelobes can be achieved.

6. Experimental Array Design Procedure

The purpose of the experimental program is to establish the precise internal dimensions of the asymmetric ridge waveguide and of the radiating slots to satisfy the following four design criteria. These are (1) minimum insertion loss (2) uniform phase velocity (3) low-sidelobe Taylor aperture illumination and (4) minimum performance degradation over the 9.5 to 10 GHz frequency range. The

previously described analytical approach, using reference 4, gives only approximate results because it does not address waveguide step discontinuities due to alternating slot phase, slot wall thickness, and slot coverings.

Five test models, similar to that illustrated in Figure 4, containing twelve identical radiating slots each, were constructed for nominally -9 dB, -12 dB, -14 dB, -26 dB and no coupling. Test data were later interpolated linearly for an additional coupling value of -32 dB. In addition, two matched waveguide adapters from WR-90 to symmetric single ridge waveguide were fabricated. Network analyzer tests of complex S_{11} and S_{21} were subsequently performed from 9.5 to 10 GHz on the four 12-slot test models with waveguide adapters and of the back-to-back adapters themselves.

6.1 Insertion Loss Tests

First the insertion loss of the adapter pair was found from equation 7 and the network analyzer tested magnitudes of S_{11} and S_{21} .

$$\text{Insertion Loss in dB} = 10 \log [S_{21}^2 / (1 - S_{11}^2)] \quad [\text{eq.7}]$$

Then the insertion loss of the "no coupling" or symmetrical model was found via equation 7 and subtraction of the adapters' insertion loss. This was followed by calculating the insertion loss with all radiating slots covered with conducting tape in order to obtain the *ohmic losses*. The measured results for the adapter and the symmetrical ridge waveguide, as shown in the upper portion of Figure 9, compare favorably with expected values.

<u>ADAPTER</u>					
Frequency in GHz :	<u>9.5</u>	<u>9.6</u>	<u>9.75</u>	<u>9.9</u>	<u>10</u>
Insertion Loss in dB	-0.13	-0.11	-0.11	-0.1	-0.09
<u>SYMMETRICAL</u>					
Insertion Loss , dB/1.000 "	-0.004	-0.006	-0.005	-0.007	-0.007
<u>TEST MODEL, SLOTS TAPED</u>					
<u>Insertion Loss in dB</u>					
Embedded	-0.27	-0.28	-0.28	-0.27	-0.29
Model ONLY	-0.14	-0.17	-0.17	-0.17	-0.2
dB per 0.850 in.	-0.011	-0.013	-0.013	-0.013	-0.015
<u>TEST MODEL, 0.604" SLOTS Radiating</u>					
<u>Insertion Loss in dB</u>					
Embedded	-4.79	-6.5	-8.72	-7.31	-5.69
Model ONLY, without Ω	-4.52	-6.22	-8.44	-7.04	-5.4
Single Slot Power Radiated in dB (from Figure 10)	-10.8	-9.5	-8.5	-9.0	-10.0

Figure 9 - Insertion Loss & Slot Coupling Tabulation , 9 dB Slot Test Model

6.2 Radiated Slot Coupling

Finally, the coupled power loss or power radiated for a single slot can be determined by following the five steps, outlined below, resulting in the data of the lower half of Figure 9 for one of the 12-slot test models :

- (1) Using equation 7 on the measured data from the radiating 12-slot model to compute the embedded insertion loss.

- (2) Subtract the adapter loss.
- (3) Subtract the *ohmic loss* to find the coupled power loss of the 12-slot model
- (4) Generate a conversion graph of one-slot versus 12-slot power coupling in dB, from a set of twelve cascaded network computations using equal slot conductances to represent the slot radiated power. (Shown in Figure 10)
- (5) Apply the curve of step (4) to find the single slot power radiated.

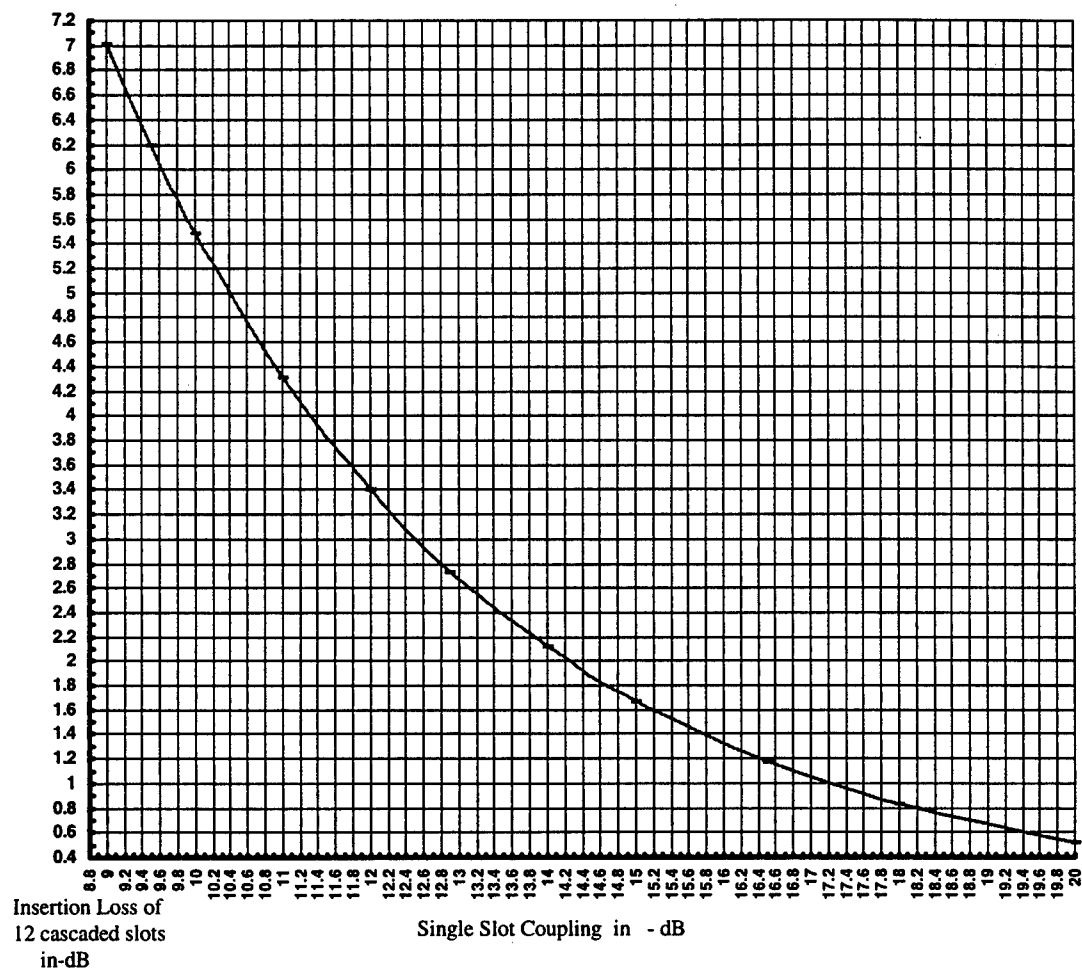


Figure 10 - Conversion Graph from 12-Slot to Single-Slot Coupling

6.3 Slot Dimensions and Bandwidth Effect

The results shown in Figure 10 are typical by showing both an asymmetry about the center frequency of 9.75 GHz and a coupling deviation at the limit

frequencies. To obtain the optimum slot length a plot of the bottom row, the *Single Slot Power Radiated* data, should be made and then centered about the center frequency. Slot length correction and the coupling deviation at the frequency limits can now be determined.

For the 9 dB coupling test model used in Figure 10, the 0.604 inch long slot had to be changed to 0.6055 inches and the coupling will vary from -8.5 dB at band center to -10.4 dB at band edge. Thus, for array design purposes, a nominal coupling value of -9.1 dB was used and design errors of +0.6 and -1.3 dB were accepted.

6.4 Cut-off Frequency and Phase Velocity

In order to justify the equal slot spacing of 0.850", all test models, regardless of slot coupling value, must exhibit the same phase velocity and therefore the same cut-off frequency. Equation 8, derived in Appendix 1, was used to compute the cut-off frequency, F_{co} , from the measured phase of the 12-slot model, i.e., Φ_{S21} .

$$F_{co} = \sqrt{ \{ (\text{Freq. in GHz})^2 - [k (\Phi_{S21} - \Phi_{adapt} + 360n)]^2 \} } \quad [\text{eq.8}]$$

where $k = 11.8 / 360 / L_{\text{inches}}$.

The table below gives the appropriate values for the two required evaluations.

TO SOLVE FOR	Φ_{adapt} (deg)	<u>n</u>	<u>L</u> (inches)
ADAPTER F_{co}	0	3	5.266
12-SLOT MODEL F_{co}	Measured Adapter's Φ_{S21}	8 or 9	12.09

The cut-off frequencies determined for the non-radiating model as well as the 9 dB coupling model, using the above procedure, are tabulated in Figure 11. We were quite pleased with the repeatability of the procedure at the different frequencies, as indicated by the small percentage of deviation.

	<u>Phase</u>	<u>Meas'd</u>				
<u>Freq.</u> (GHz)	<u>Delay of Adapter</u>	<u>Phase of Model</u>	<u>n</u>	<u>Calculated Cut-off Freq</u>		
9.5	120.37 ⁰	-51.6 ⁰	8	5.6585 GHz	SYMMETRICAL	NO SLOTS
9.6	141.27 ⁰	-118.4 ⁰	8	5.6579 GHz	Length >>	12.0473
9.75	172.68 ⁰	142 ⁰	9	5.6577 GHz	AVG. Fco >>	5.6581
9.9	203.89 ⁰	43.2 ⁰	9	5.6577 GHz	Max.Dev >>	0.01%
10	224.29 ⁰	-21.7 ⁰	9	5.6588 GHz		
9.5	120.37 ⁰	-36.6 ⁰	8	5.7292 GHz	METAL TAPE ON	ALL SLOTS
9.6	141.27 ⁰	-104.2 ⁰	8	5.7264 GHz	Length >>	12.0774
9.75	172.68 ⁰	154.7 ⁰	9	5.7214 GHz	AVG. Fco >>	5.7218
9.9	203.89 ⁰	54.5 ⁰	9	5.7168 GHz	Max.Dev >>	0.13%
10	224.29 ⁰	-11.2 ⁰	9	5.7153 GHz		
9.5	120.37 ⁰	-36.7 ⁰	8	5.7288 GHz	RADIATING SLOTS	
9.6	141.27 ⁰	-104.8 ⁰	8	5.7239 GHz		
9.75	172.68 ⁰	155.5 ⁰	9	5.7249 GHz	AVG. Fco >>	5.7273
9.9	203.89 ⁰	56.7 ⁰	9	5.7267 GHz	Max.Dev >>	0.08%
10	224.29 ⁰	-7.5 ⁰	9	5.7321 GHz		

Figure 11 - Results of Typical Test Model Phase Measurements

6.5 Asymmetric Ridge Waveguide Crossection

The experimental program described in sections 6.1 through 6.4 yielded a nominal slot coupling value for each of the four models tested. In addition, a symmetrical single ridge waveguide yielded a fifth data point and linear interpolation a sixth. Each of these data points correspond to the two trough depths, L_1 and L_2 , associated with each model. From this information the data table of Figure 12 was constructed. Columns 2, 4, and 6 of this table then formed the basis for equations 3 and 4 and for the design curves of Figure 6.

COUPLING (DB)	COUPLING (VOLTS)	L ₁ (INCHES)	L _{MEAN} - L ₁ (MILS)	L ₂ (INCHES)	L ₂ - L _{MEAN} (MILS)
8.96	.356	0.4024	61.1	0.2867	54.6
11.45	.268	0.3850	43.7	0.3010	40.3
14.2	.195	0.3704	29.1	0.3138	27.5
26	.050	0.3497	7.0	0.3331	6.6
32 **	.025	0.3448	3.5	0.3380	3.3
NONE	0	0.3413	0	0.3413	0

** Data interpolated from rows No.4 and No.6

Figure 12 - Data Table of Coupling Values and Trough Dimensions

7. Conclusion

The design technique of a low-cost, low weight, and low sidelobe slotted array antenna using asymmetric single ridge waveguide was presented. The described technique was applied to a single forty-slot waveguide test array, whose measured antenna radiation patterns, shown in Figures 13, 14 and 15, demonstrate satisfactory performance over the required 9.5 to 10 GHz frequency band. Sidelobes were typically in the -30 to -40 dB range. When 100 waveguide sticks are joined together in a planar array, the resultant azimuth sidelobes should be far lower, provided the manufacturing errors causing the sidelobes are random in nature.

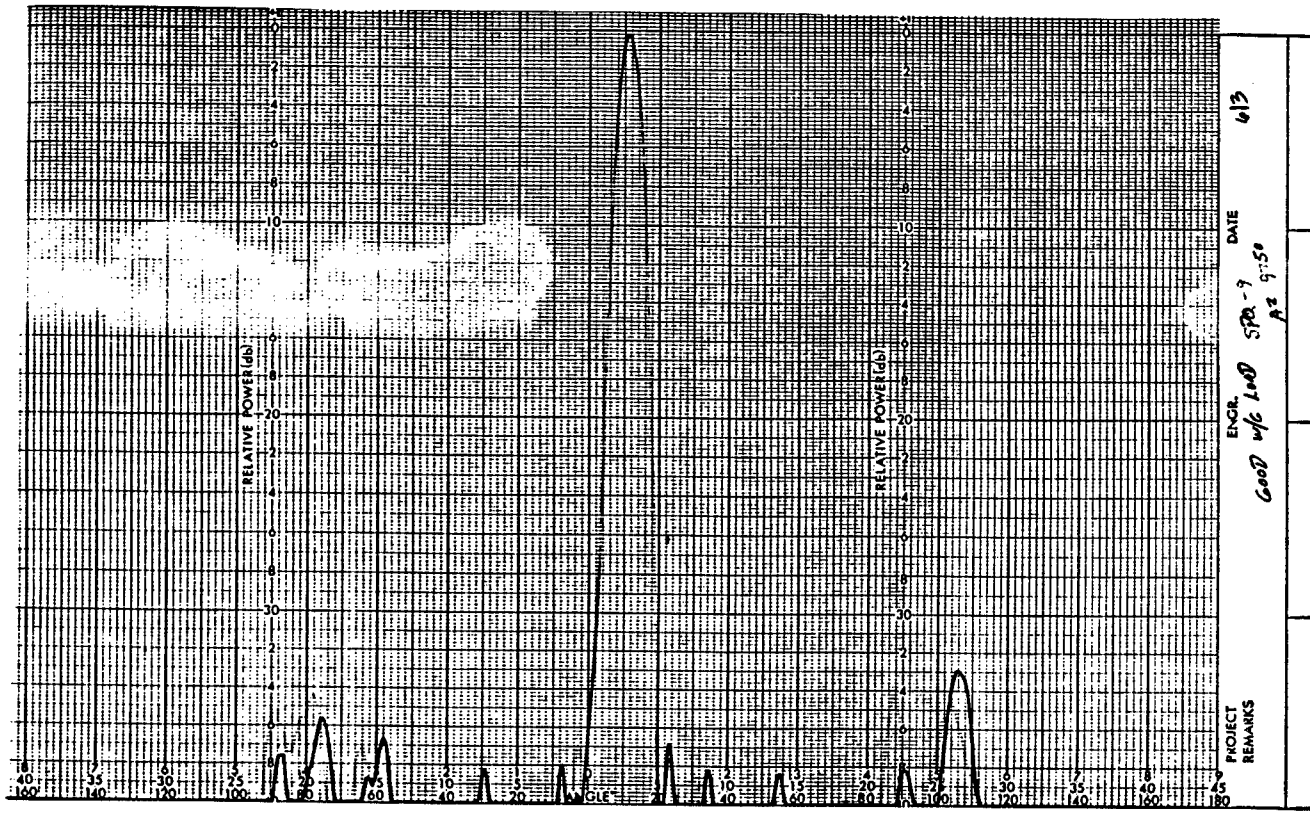


Figure 13 - Azimuth Pattern of 40 Slot Stick at 9.75 GHz

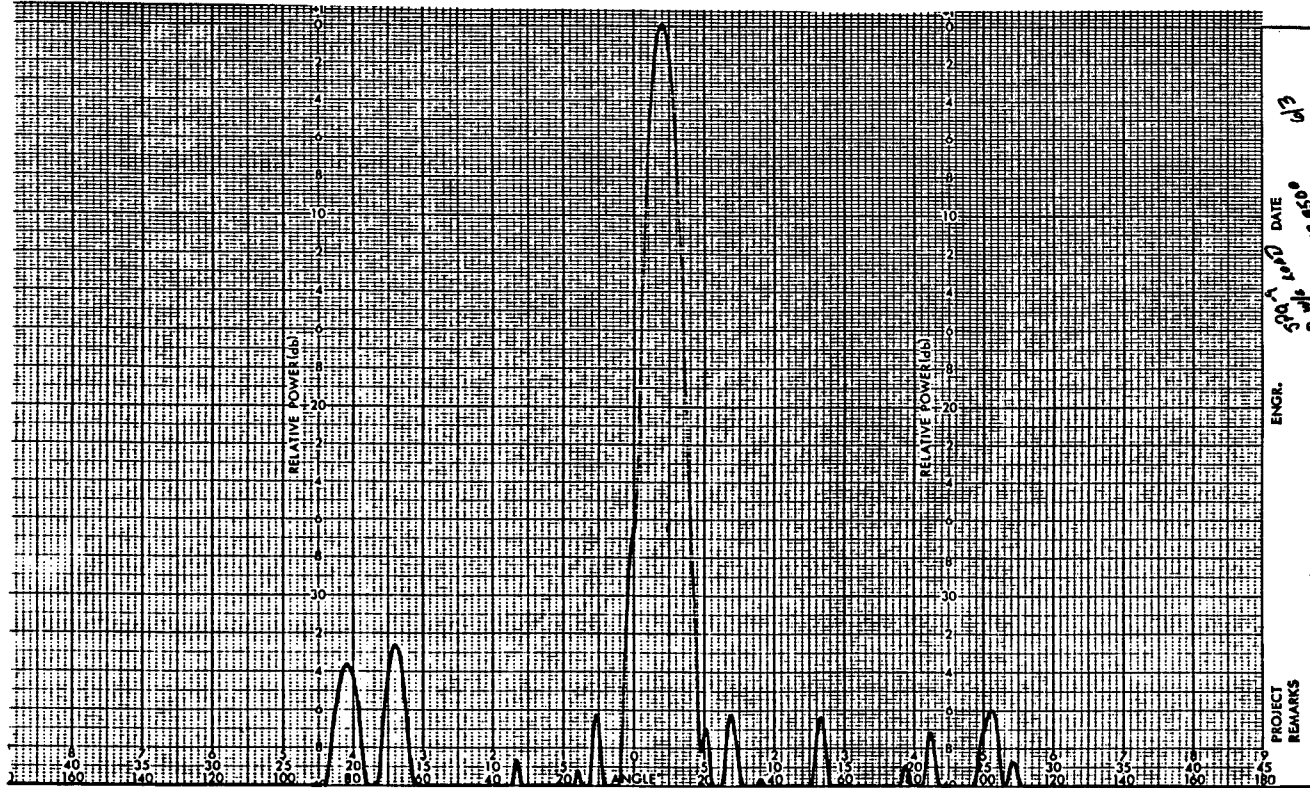


Figure 14 - Azimuth Pattern of 40 Slot Stick at 9.5 GHz

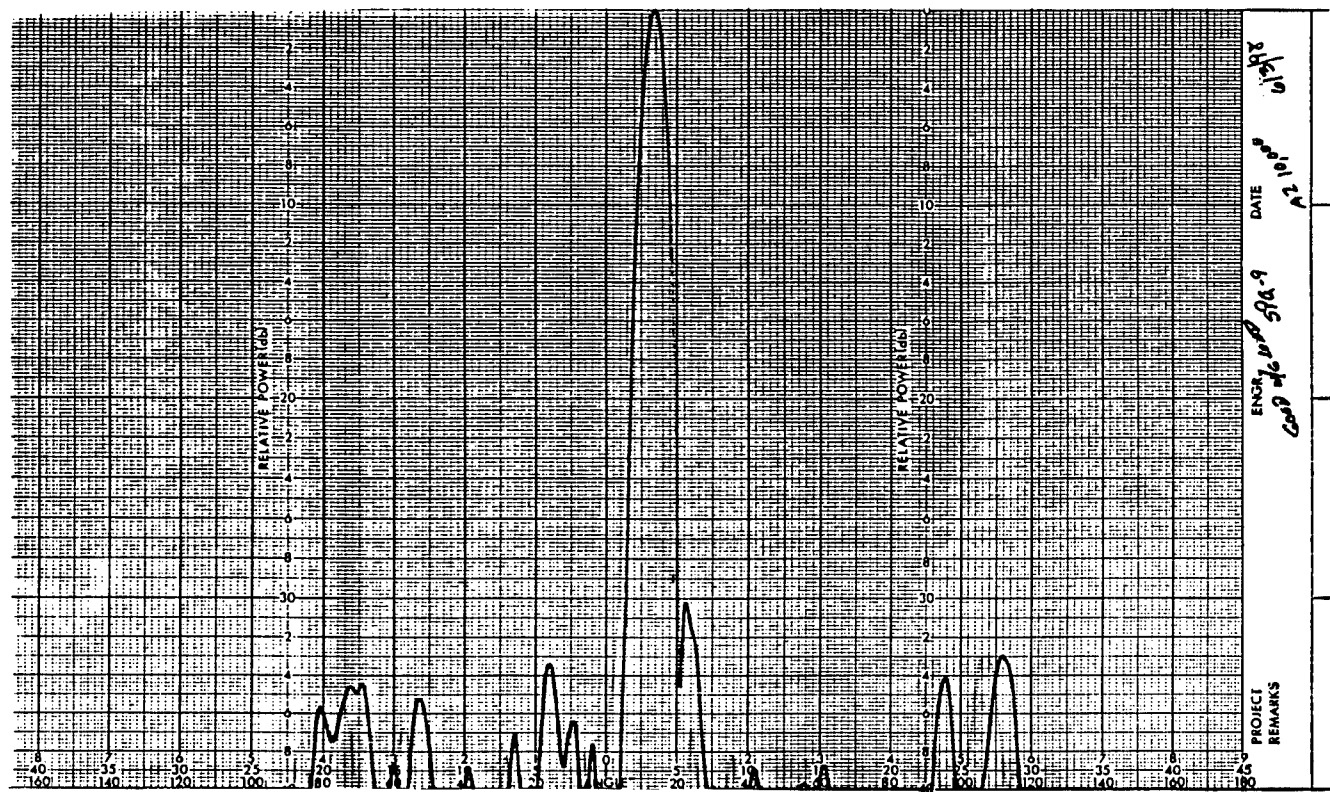


Figure 15 - Azimuth Pattern of 40 Slot Stick at 10.0 GHz

REF E R E N C E S

- [1] L.A. Kurtz and J.S. Yee, "Second order beams of two- dimensional slot arrays", *IRE Trans. Antenna Propagation*, vol.AP-5, pp. 356-362, October 1957.
- [2] H. Shnitkin, J. Green , "Asymmetric Ridge Waveguide Collinear Slot Array Antenna", *U. S. Patent No. 4,638,323* , Jan.. 20, 1987
- [3] J. Green, H. Shnitkin, & P. J. Bertalan "Asymmetric Ridge Waveguide Radiating Element for a Scanned Planar Array" , *IEEE Trans. Antenna and Propagation* , vol. AP-38 , pp.1161-1165 , August 1990
- [4] J. R. Pyle, "The Cut-off Wavelength of the TE_{10} Mode in Ridged Rectangular Waveguide of Any Aspect Ratio", *IEEE Trans. Microwave Theory & Tech*, pp.175-183 , April 1966
- [5] W. J. R. Hoefer, "Closed-Form Expressions for the Parameters of Finned and Ridged Waveguides", *IRE Trans. Microwave Theory & Techniques*, vol. MTT 30, No. 12, December 1982.
- [6] F. Frezza, M. Guglielmi, P. Lamariello, "Millimetre-Wave Leaky-Wave Antennas Based on Slitted Asymmetric Ridge Waveguides", *IEE-Microw. Antennas Propag.*, Vol. 141, No. 3, June 1994.
- [7] F. Frezza, M. Guglielmi, P. Lamariello, " Linear Phase Arrays Based on Slitted Asymmetric Ridge Waveguides", *IEE-Microw. Antennas Propag.*, Vol. 142, No. 1, February 1995.
- [8] D. J. Kim and R. S. Elliott, "A Design Procedure for Slot Arrays Fed by Single- Ridge Waveguide", *IEEE Trans. Ant. Propag.*, vol. 36, pp. 1531-1535, November 1988.
- [9] G.C. McCormick, "The Effect of the Size of a Two-Dimensional Array on Second-Order Beams", *IRE Trans. Antenna Propagation*, pp. 297-299, July 1958.
- [10] G.C. McCormick, "A Two-Dimensional Slotted Array", pp. 26-35, January 1958.

APPENDIX 1

Derivation of Cut-off Frequency , Equation 7

$$\lambda_o / \lambda_g = \sqrt{1 - (F_{co} / F)^2} \quad [\text{eq.A1}]$$

$$F_{co}^2 = F^2 (1 - \lambda_o^2 / \lambda_g^2) = F^2 - c^2 / \lambda_g^2, \quad \text{where } c \text{ is the speed of light} \quad [\text{eq.A2}]$$

Now...

$$\Phi_{S21} - \Phi_{adapt} = 360L / \lambda_g - 360n \quad [\text{eq.A3}]$$

[Note that Φ_{S21} and Φ_{adapt} are expressed in degrees]

$$1 / \lambda_g = (\Phi_{S21} - \Phi_{adapt} + 360n) / 360L \quad [\text{eq.A4}]$$

Substituting in equation A2 ...

$$F_{co}^2 = F^2 - (c / 360L)^2 (\Phi_{S21} - \Phi_{adapt} + 360n)^2 \quad [\text{eq.A5}]$$

$$F_{co} = \sqrt{\{(\text{Freq. in GHz})^2 - [(11.8 / 360L)(\Phi_{S21} - \Phi_{adapt} + 360n)]^2\}} \quad [\text{eq.6}]$$

LIMITED SCAN PHASED ARRAY ANTENNA

Richard R. Kinsey
Sensis Corporation
5793 Widewaters Parkway
DeWitt, NY 13214

Abstract: Applications such as aircraft landing systems, mortar and artillery locators, surface search radars and certain communications systems may require an array antenna with wide angle scanning in azimuth but only limited scan coverage in elevation. To reduce the number of phase controls in a constrained feed array architecture, it is common practice to propose using subarrays of several wavelengths in the limited scan plane together with conventional element spacings in the wide angle scan plane. Overlapped subarray techniques, to suppress grating lobes in the limited scan plane, require a plurality of interconnections between the elements in marked contrast to the simple beamforming network of a conventional phased array antenna. This paper will describe the possible use of high directivity elements (or subarrays) occupying a rectangularly shaped area that is very large in one dimension but very small in the other. By staggering each element column with its neighboring columns, the near-in grating lobes may be suppressed. The required elements are independent and identical to one another so that conventional array beamforming techniques may be utilized. In theory, grating lobe suppression may be as good as or better than the overlapped subarray approach but with greater elevation scan loss.

1. Introduction

Conventional phased arrays, designed for wide angle scanning, require element spacings of approximately one-half wavelength to avoid the undesired formation of grating lobes within visible space. Even for a limited scan in one plane, the grating lobe restriction limits element spacing to less than one wavelength. This design approach is much too expensive for most limited scan applications because of the large number of elements and phase shifters involved. As a result, limited scan architectures have been devised that employ optical (unconstrained) feeds

[1], constrained feeds [2] or a combination of both [3]. Because of the large volume generally required by optical techniques, many potential applications dictate the more compact constrained feed approach.

Constrained feeds often rely on overlapped subarrays to obtain a flatter topped subarray pattern with steep skirts that will maximize the array scan before the nearest grating lobe rises too far out of the first null. However, in order to accomplish this, the individual radiators of the overlapped subarrays may require a plurality of interconnections in marked contrast to the simple beamforming network of a phased array with independent subarrays. The technique to be described in this paper offers a much simpler architecture with high directivity elements that are identical to one another and have no interconnections between the radiators of adjacent elements. In theory, grating lobe suppression may equal or surpass an overlapped subarray approach but scan loss in the limited scan plane is greater because the element pattern is not flat topped.

2. Evolution of the Basic Technique

The evolution of this array architecture will be described assuming a scan requirement of $\pm 60^\circ$ az. and $\pm 7.5^\circ$ el. for an 8 m^2 aperture at 10 GHz. To clarify the semantics used in the following text, array elements refer to entities having separate phase controls. Each element may itself be a small array of equiphased radiators.

Fig. 1 shows a T-plane plot for a rectangular array element grid with dimensions 0.88λ high by 0.53λ wide. The T_x and T_y coordinates represent the direction cosines of points in space, for a right-handed aperture coordinate system, with the z-axis normal. The hemisphere of visible space forward of the aperture is therefore bounded on the T-plane by a unit circle. Transformation from the azimuth (α) and elevation (ε) angles of a point in space to the aperture T-plane is given by the equations

$$T_x = -\cos(\varepsilon) \sin(\alpha) \quad (1)$$

$$T_y = \sin(\varepsilon) \cos(\varepsilon_0) - \cos(\varepsilon) \sin(\varepsilon_0) \cos(\alpha) \quad (2)$$

where ε_0 = the mechanical tiltback of the antenna aperture in elevation.

For a vertical aperture (as in the descriptions that follow), $\epsilon_0 = 0$, and along the principal azimuth and elevation planes, $T_x = -\sin(\alpha)$ and $T_y = \sin(\epsilon)$. The shaded region in Fig. 1 represents the locus of beam scanning to $\pm 7.5^\circ$ elevation and $\pm 60^\circ$ azimuth. Grating lobes and the main beam are indicated by black dots for the main beam at broadside, at the center of the unit circle. All grating lobes scan in concert with the main beam but remain outside visible space for the selected element grid dimensions. However, the rectangular grid, as shown in Fig. 5, has an area of only $0.466\lambda^2$.

Historically, one approach has been to halve the number of elements by doubling the height of the element grid (Fig. 6). With a uniformly tapered element, this results in the T-plane plot of Fig. 2. The nearest grating lobes are centered at the element pattern nulls and therefore suppressed to a low level when the array beam is broadside. However, with array scan in elevation, one grating lobe enters the element pattern main beam while the other enters the first sidelobe and, for a $\pm 7.5^\circ$ scan angle, these are suppressed only about 10-12 dB below the peak of the array main lobe.

If alternate columns of elements are vertically staggered by one-half the element spacing, as shown in Fig. 7, the previous near-in grating lobes are canceled but new grating lobes are formed near the edge of visible space as shown in Fig. 3. This offers little improvement for, with azimuth scan, these grating lobes also enter the element pattern and can reach very high levels.

The technique proposed here, again doubles the element height (from 1.76λ to 3.52λ) and also halves its width (from 0.53λ to 0.265λ) as indicated by the grid in Fig. 8. This retains the same element area as before, but additionally moves the diagonal grating lobes farther outside visible space so that they never enter for the specified scan angles. The larger element spacing doubles the number of elevation grating lobes but they are now located well into the sidelobe region of the element pattern as shown by the T-plane plot in Fig. 4. In fact, there is an excess scan margin for the $\pm 7.5^\circ$ example used to describe this array architecture. This permits increasing the element size, for a further reduction in the number of elements required, and adopting a non-uniform amplitude taper for lower element sidelobes and better grating lobe suppression.

2.1 Element Amplitude Tapers

For conventional array grid spacings, a non-uniform taper of the element amplitude would cause a reduction in aperture efficiency. However, for this limited scan technique, each *pair* of adjacent columns occupy a space close to one-half wavelength and the elements are also staggered by one-half their length. Fig. 9 illustrates an amplitude taper on two adjacent elements and shows that the amplitude for one element diminishes as the amplitude of the adjacent element increases. By an unequal aperture sharing along their length, a uniform aperture power density can be maintained for maximum efficiency. Thus, if the taper in power density along the overlap region of elements 1 and 2 is $P_1(\xi)$ and $P_2(\xi)$, candidate distributions are all those of the form

$$P_1(\xi) = 1 - P_2(\xi) \quad (3)$$

where ξ is the aperture variable normalized to a maximum of unity.

The simplest example of a lossless power taper is given by the expression

$$P(\xi) = 1 - |\xi|, \quad 0 \leq |\xi| \leq 1 \quad (4)$$

This is shown by the plot in Fig. 10. If D designates the length of the element, the continuous power taper given by (4) produces a far-field pattern with -3 dB points at $\pm 0.54\lambda/D$ sines, main beam nulls at $\pm 1.34\lambda/D$ sines and a peak sidelobe level below -22 dB. Since the nearest elevation grating lobes are located at $\pm 2\lambda/D$ sines from broadside, the array may be scanned in elevation at least $\pm(2-1.34)\lambda/D = \pm 0.66\lambda/D$ sines before the grating lobe is no longer suppressed by the first sidelobe but begins to enter the main beam of the element pattern. The maximum practical scan is thus limited more by scan loss than by the grating lobe level.

Another lossless candidate taper is given by the expression

$$P(\xi) = \frac{1 + A \cos(\pi|\xi|)}{2}, \quad 0 \leq |\xi| \leq 1 \quad (5)$$

This is shown in Fig. 11 for $A=0.9$. The resulting far-field pattern has -3 dB points at $\pm 0.55\lambda/D$ sines, main beam nulls at $\pm 1.41\lambda/D$ sines and a peak sidelobe

level of 24.7 dB. Practical scan extent is just slightly greater than before with improved grating lobe suppression.

A more general form of candidate taper can be expressed as

$$P(\xi) = \frac{1 \pm A |\cos(\pi\xi)|^C}{2} \quad (6)$$

where the sign is + for $|\xi| \leq 0.5$ and - for $|\xi| > 0.5$.

This is same as the prior case if $C=1$. However, if $A=0.94$ and $C=0.65$ for example, the element power taper given by (6) is as shown in Fig. 12. This continuous equiphase excitation produces a far-field pattern with -3 dB points at $\pm 0.58\lambda/D$ sines, main beam nulls at $\pm 1.52\lambda/D$ sines and a peak sidelobe level below 26.5 dB. This means the array could be scanned $\pm(2-1.52)\lambda/D = \pm 0.48\lambda/D$ sines before a grating lobe even moves to the main beam null.

2.2 Element Implementation

A practical realization of this “lossless” element taper implies that the effective collecting area of each element must vary along its length in the prescribed manner. However, rather than a continuous taper as indicated in Figs. 10-12, a sampled taper is more attractive from an implementation standpoint. An element consisting of a linear array of radiators becomes a viable candidate, *providing the portion of the incident aperture field not absorbed by each radiator remains available to the neighboring elements*. The practical realization of this is more difficult to visualize on receive than it is on transmit, probably because mutual coupling effects may be more easily visualized in the later mode.

A different type of array antenna that required aperture sharing in a similar manner was previously reported [4]. It consisted of two interleaved edge-slotted waveguide arrays with near $\lambda/4$ spacing between neighboring columns. In spite of their close proximity, each array had entirely different amplitude tapers. Measurements that have since been made show no additional loss in the aperture efficiency of either interleaved array.

Limited scan elements that obtain the desired lossless taper have not yet been experimentally demonstrated. A stripline element consisting of dipoles and combining network is one attractive candidate. Such elements do not need a

separate metallic ground plane because the adjacent element columns form parallel plate waveguides that are cut off to the TE₁ mode and thus provide an electrically solid but mechanically open aperture plane.

3.0 Design Example

Following is an example of a limited scan array designed to meet the coverage requirements stated at the beginning of section 2. Columns of the array are 80λ in height and contain 20 elements that are each 4λ high by 0.265λ wide. This provides an element area of $1.06\lambda^2$ which reduces the number of phase controls to only 44% of the number required for the conventional array described in conjunction with Fig. 1. An 8 m² aperture would therefore require 8400 phase controls rather than 19,090.

Each element has an amplitude (voltage) taper that follows the square root of Eq. (6), with A=0.94 and C=0.65. However, rather than a continuous analytic taper, each element consists of 7 discrete radiators, spaced $4\lambda/7 = 0.57\lambda$ apart, and having effective amplitudes corresponding to impulse samples of the continuous taper. Following a phase shifter at each element port, to scan the array, pairs of adjacent columns may be combined in beamformers to provide an aperture amplitude taper for low array factor elevation sidelobes. For a 30 dB Taylor, the elevation beamwidth will be 0.8°.

The calculated elevation pattern, with the array pointing broadside to the aperture, is shown in Fig. 14. The peak element pattern sidelobes are below -29 dB for the sampled taper. The nearest grating lobes are beyond the center of the element first sidelobes and suppressed over 30 dB relative to the array main lobe peak. Farther out grating lobes are suppressed over 40 dB. With a -7.5° array scan in elevation, the nearest grating lobe is shown in Fig. 15 to have moved into the null region of the element main beam. When the array is scanned within the range of ±7.5° elevation, the grating lobes never exceed the peak element sidelobe level of -29 dB. At ±7.5° elevation scan, array directivity is down 2.44 dB on the element pattern from the level at array broadside.

Fig. 16 illustrates array scan loss more clearly with a T-plane plot of the element contour pattern assuming a projected aperture loss for azimuth scan. This shows contour levels at -1, -2, and -3 dB (darkened line), the nulls and sidelobe structure of the element pattern, and darkened circles which indicate the main lobe and grating lobe positions. The -3 dB elliptical contour reaches to ±8.3° in

elevation and $\pm 60^\circ$ in azimuth. Even at this extended elevation scan, the grating lobe in the element pattern main beam is down 27.8 dB.

A summary of the calculated elevation scan performance is presented in Fig. 17. For scans up to $\pm 7.5^\circ$, the maximum sidelobe remains 27 dB or more below the peak of the scanned main beam and the average elevation sidelobe level remains below -43 dB. Scan loss up to $\pm 5^\circ$ is less than about 1 dB and increases to 2.4 dB at $\pm 7.5^\circ$.

4.0 Conclusions

For limited scan in elevation and wide angle scan in azimuth, high directivity elements that are several wavelengths in one dimension but only half the conventional array spacing in the other ($0.25\text{--}0.3\lambda$), are stacked side-by-side in columns. Adjacent columns are staggered by half the element long dimension which relocates the nearest grating lobes to be outside of visible space.

From the foregoing design example, it can be seen that excellent grating lobe suppression is theoretically possible over a large scan extent with very large array elements. The practical element size may be constrained more by an acceptable array scan loss than by the maximum grating lobe level. The relation between the scan limit (in sines) and the element size for a gain loss of -1, -2, or -3 dB, is approximately $\pm 0.34\lambda/D$, $\pm 0.48\lambda/D$ and $\pm 0.58\lambda/D$ sines respectively.

5.0 References

- [1] L. Diaz, P.K. Kelly, "Lightweight Phased Array Antenna", *Proceedings of the 1997 Antenna Applications Symposium*.
- [2] P. Franchi, et. al., "Constrained Feed for Lightweight, Overlapped Subarray Antennas", *Proceedings of the 1997 Antenna Applications Symposium*.
- [3] V.K. Tripp, et. al., "Light-Weight, Efficient, High-Gain Phased Array", *Proceedings of the 1997 Antenna Applications Symposium*.
- [4] R. Kinsey, "Monopulse Stick Phased Array", *Proceedings of the 1995 Antenna Applications Symposium*.

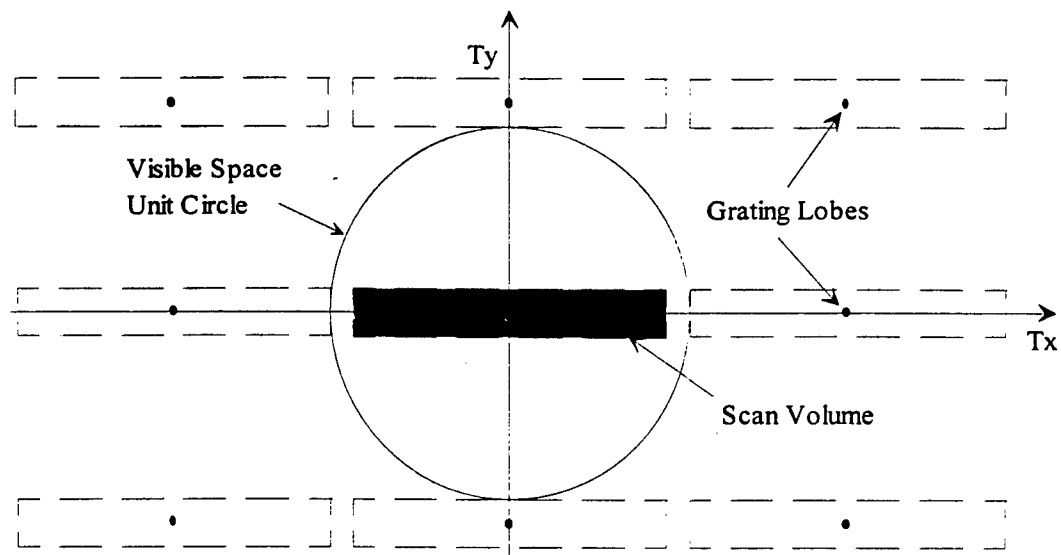


Fig. 1 T-plane Plot for a Rectangular Grid $0.88\lambda \times 0.53\lambda$

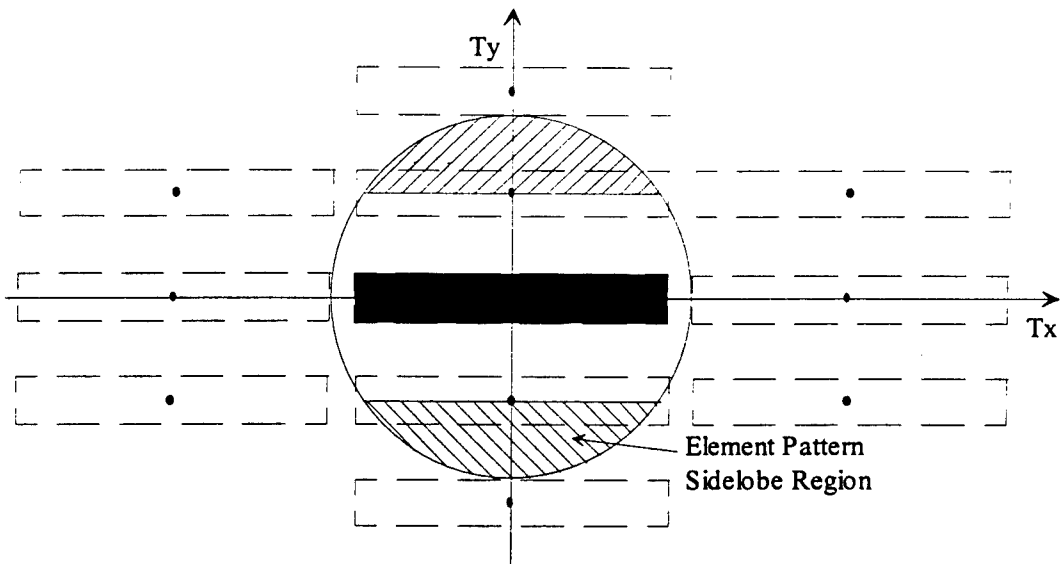


Fig. 2 T-plane Plot for a Rectangular Grid $1.76\lambda \times 0.53\lambda$

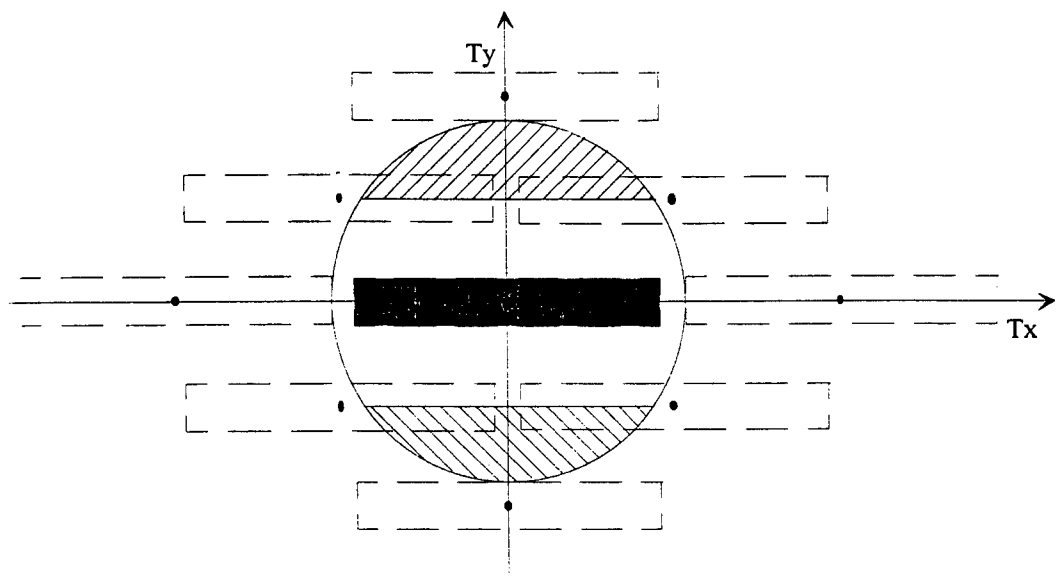


Fig. 3 T-plane Plot as in Fig. 2 With Alternate Columns Staggered

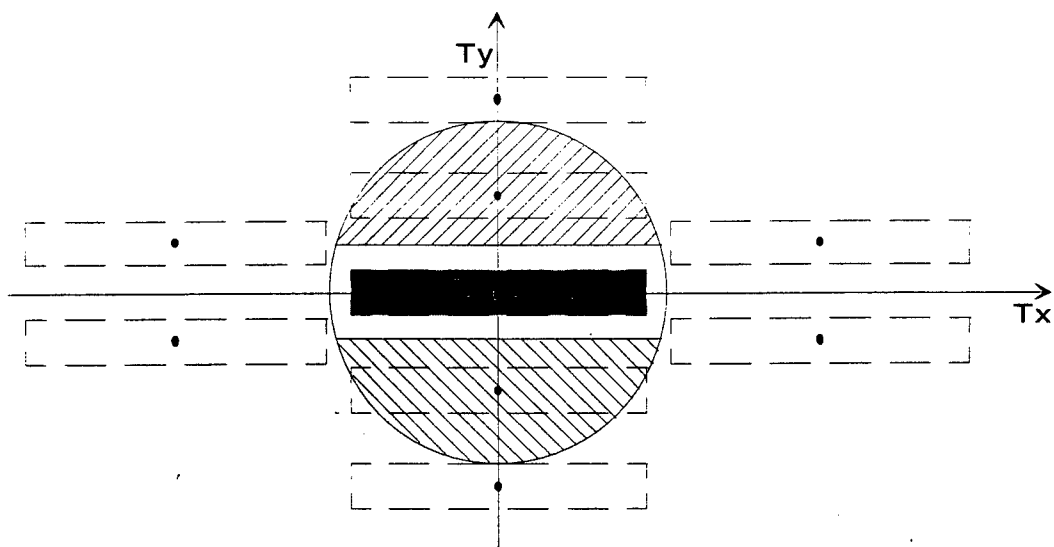


Fig. 4 T-plane Plot for a Rectangular Grid $1.76\lambda \times 0.265\lambda$

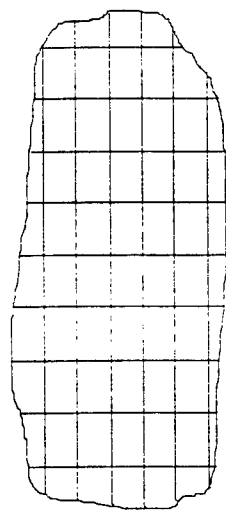


Fig. 5 Element Grid of Fig. 1

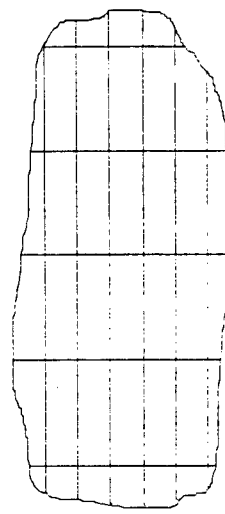


Fig. 6 Element Grid of Fig. 2

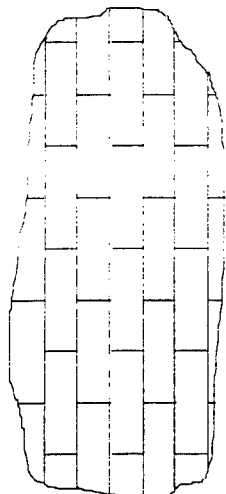


Fig. 7 Element Grid of Fig. 3

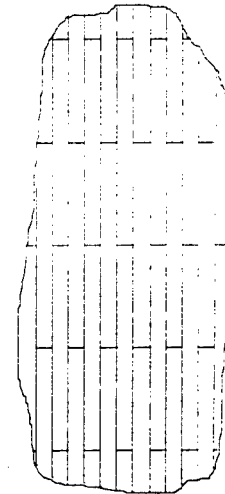


Fig. 8 Element Grid of Fig. 4

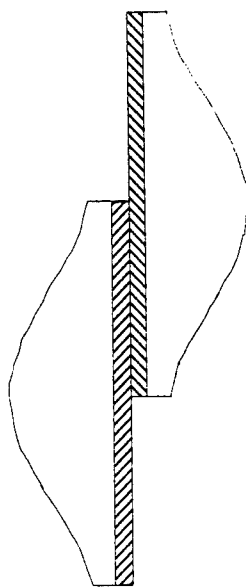


Fig. 9 Amplitude Tapers on Two Adjacent Elements

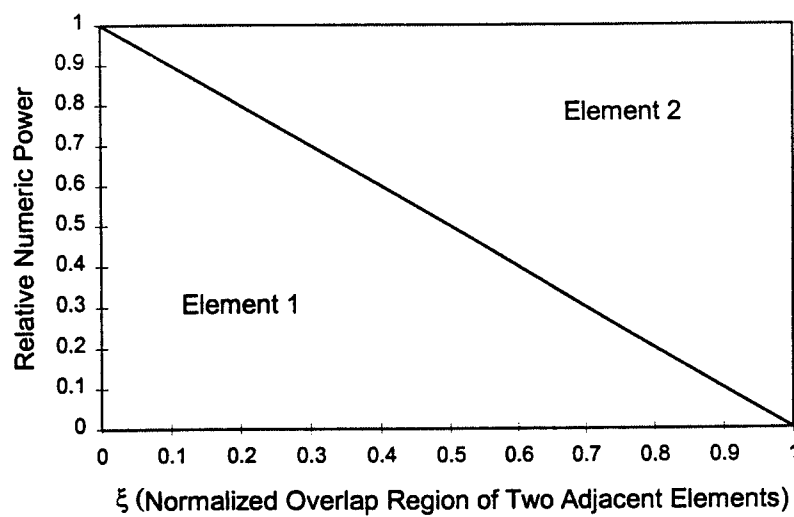


Fig. 10 Lossless Element Power Taper No. 1

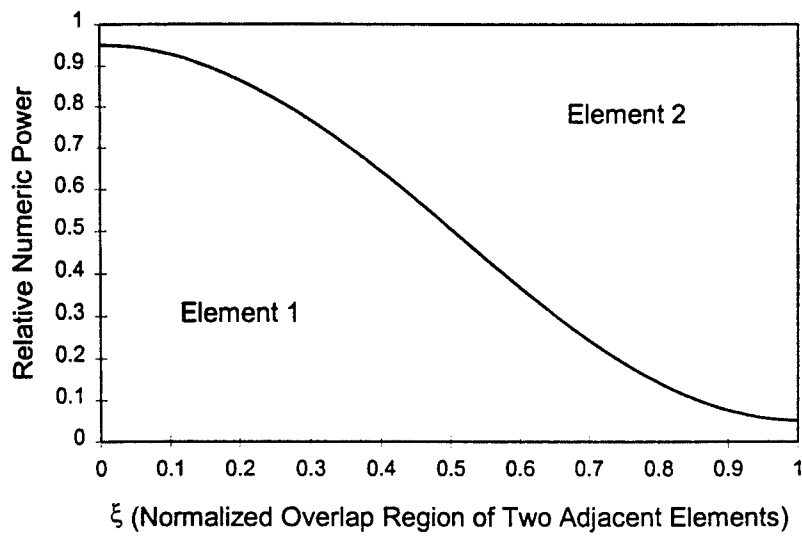


Fig. 11 Lossless Element Power Taper No. 2

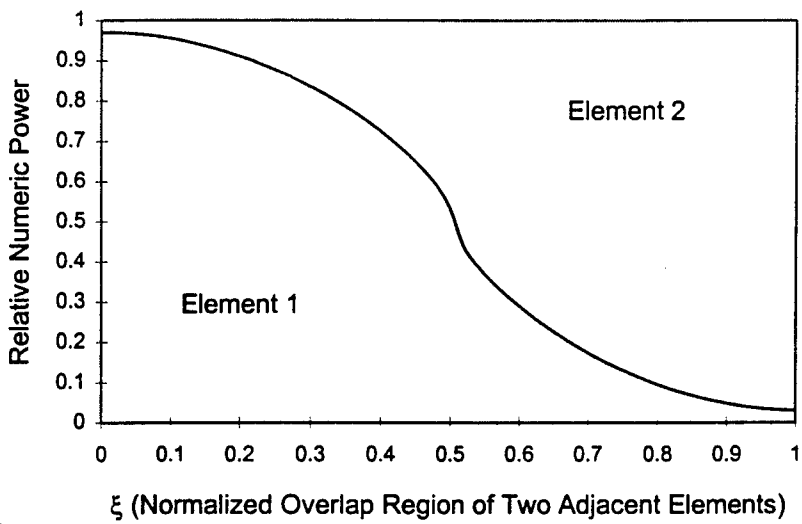


Fig. 12 Lossless Element Power Taper No. 3

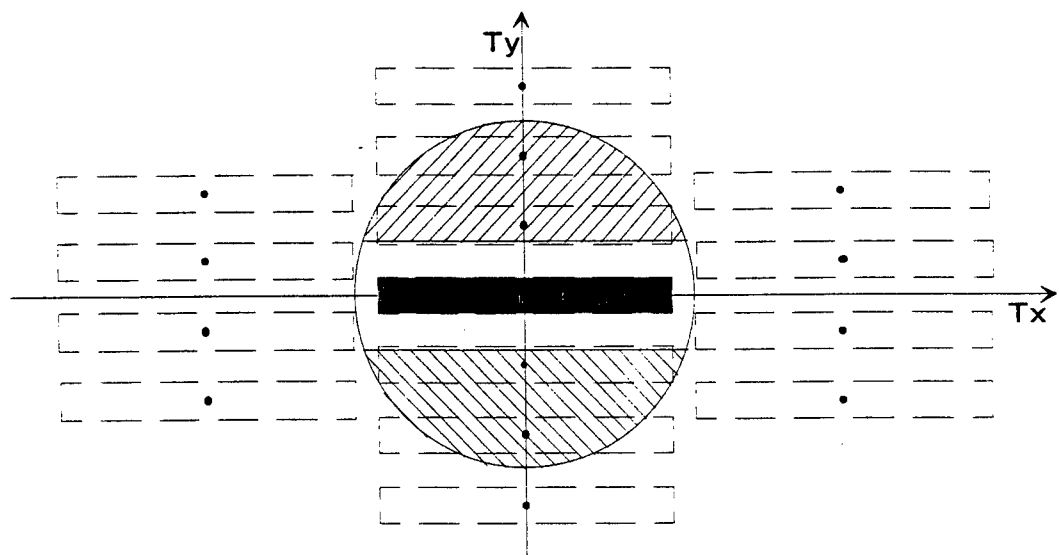


Fig. 13 T-plane Plot for Example Array Design

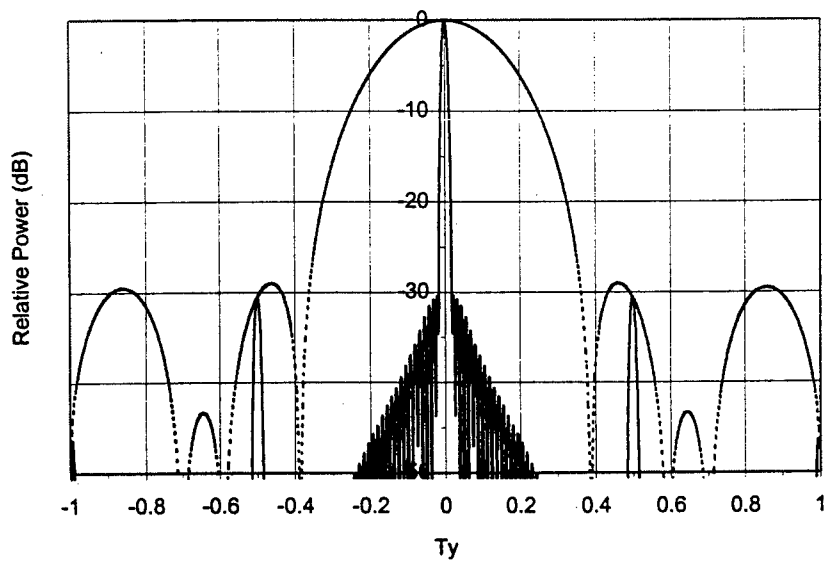


Fig. 14 Superposition of Elevation Element Pattern and Array Pattern

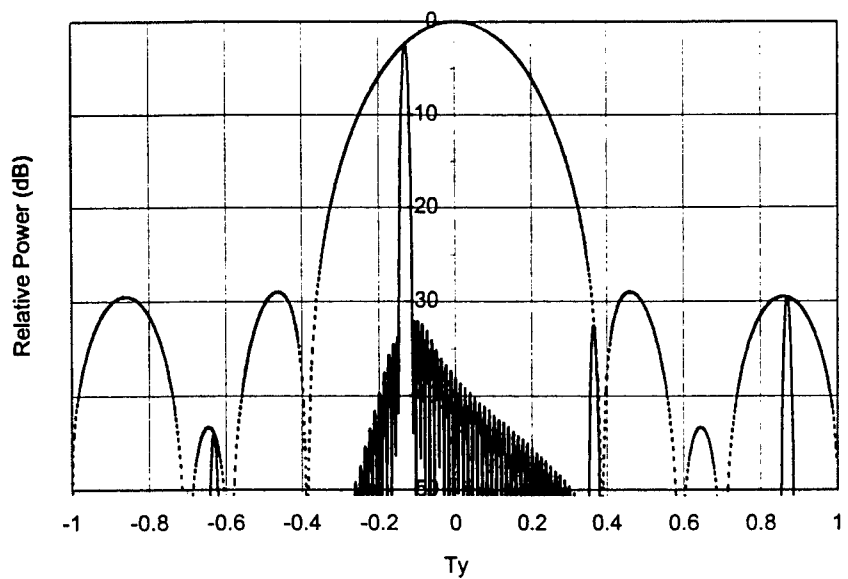


Fig. 15 Repeat of Fig. 14 with -7.5° Elevation Scan

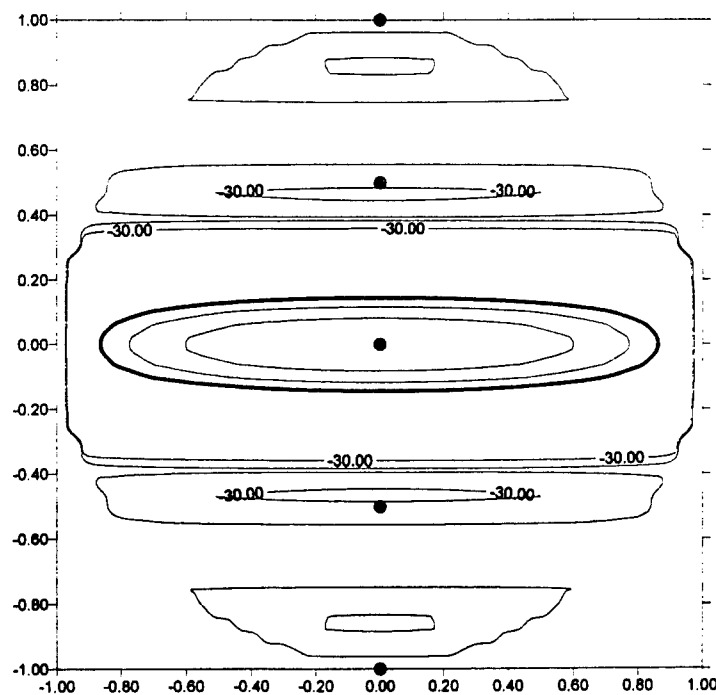


Fig. 16 T-plane Plot Showing Element Contour Pattern

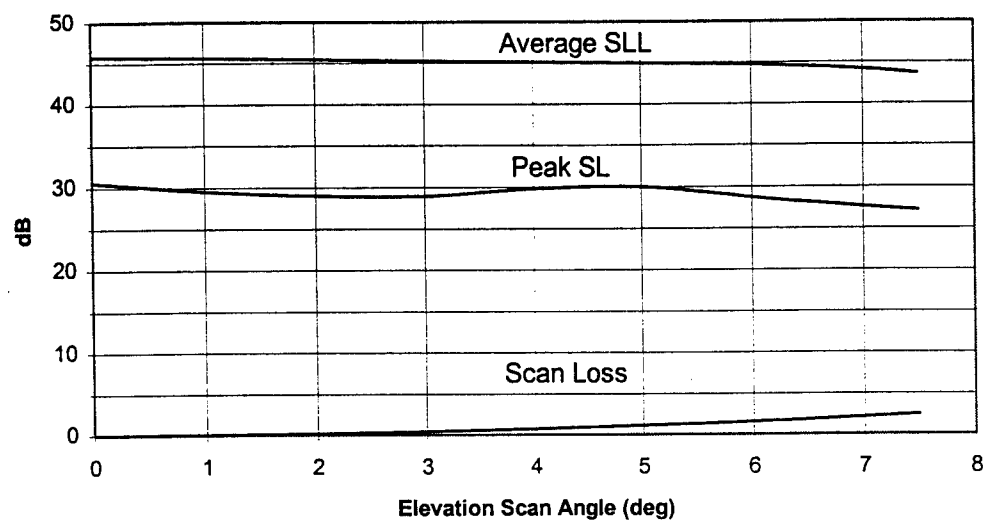


Fig. 17 Summary of Scan Performance

Distributed MEMS True-Time Delay Phase Shifters

N. S. Barker and G. M. Rebeiz

Radiation Laboratory, Department of Electrical Engineering
and Computer Science, University of Michigan, Ann Arbor, MI
48105, USA

sbarker@engin.umich.edu, rebeiz@engin.umich.edu

Abstract

True-time delay (TTD) phase shifters have been developed using distributed microelectromechanical system (MEMS) transmission lines. The design consists of a CPW transmission line ($W=G=100 \mu\text{m}$) fabricated on a $500 \mu\text{m}$ quartz substrate with fixed-fixed beam MEMS bridge capacitors placed periodically over the transmission line, thus creating a slow-wave structure. The measured results demonstrate 0-60 GHz 4.5 psec TTD phase shifters with 2 dB loss/118° phase shift at 60 GHz.

I. INTRODUCTION

Microelectromechanical systems (MEMS) switches have recently been developed for low-loss microwave and millimeter-wave control circuits such as SPST switches and switched-line phase shifters[1][2][3]. The advantage of using MEMS over FETs or PIN diodes is their low-loss performance and lack of measurable intermodulation distortion[4]. MEMS switches have been fabricated in the fixed-fixed beam, cantilever, and diaphragm configurations and the height is typically $3.5-4 \mu\text{m}$ above the transmission line, resulting in an actuation voltage of 25-100 V. This height is necessary in order to reduce the parasitic capacitance of the bridge in the OFF-state (bridge up), and results in a capacitance ratio of $C_{\text{down}}/C_{\text{up}} = 50 - 100$ for capacitive switches.

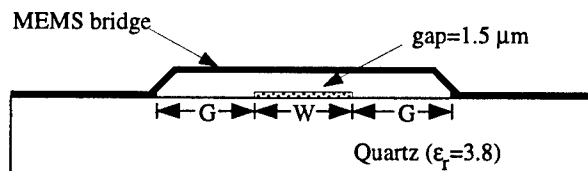


Fig. 1. Fixed-fixed beam MEMS bridge in shunt configuration over a CPW transmission line.

MEMS switch designs have been very similar to standard PIN diode or FET switch networks, with the active device replaced by the MEMS switch. This paper presents a departure from the traditional approach by incorporating the MEMS switches in distributed transmission line designs. In this approach, a CPW transmission line is loaded periodically with the MEMS bridges which act as shunt capacitors/varactors, as shown in Figure 1. The impedance and propagation velocity of this slow-wave transmission line are determined by the size of the MEMS bridges and their periodic spacing. The shunt capacitance associated with the MEMS bridge is in parallel with the distributed capacitance of the transmission line and is included as a design parameter of the loaded line. Thus, the height of the MEMS bridges can be lowered from 3.5-4 μm to 1-1.5 μm . An immediate advantage of the lowered height is that the pull-down voltage of the MEMS bridges is reduced to 10-20 V. By using a single analog control voltage to vary the height of the MEMS bridges, the distributed capacitive loading on the transmission line, and therefore its propagation characteristics, can be varied. This results in an analog control of the transmission line phase velocity and therefore in a true-time delay phase shifter. Furthermore, if the MEMS bridges are pulled down (to form a very large capacitor) the distributed transmission line results in a wideband switch.

II. DESIGN

The per unit-length capacitance, C_t , and inductance, L_t , of the unloaded CPW line, shown in Figure 2a, are given by[5]

$$C_t = \frac{\sqrt{\epsilon_{eff}}}{cZ_o} \quad \text{and} \quad L_t = C_t Z_o^2 \quad (1)$$

where ϵ_{eff} and Z_o are the effective dielectric constant and impedance, respectively, of the unloaded CPW line and c is the free-space velocity. If it is assumed that the MEMS bridge only loads the transmission line with a parallel capacitance, C_b , then the impedance, Z_l , and phase velocity, v_l , of the loaded line, shown in Figure 2b, become

$$Z_l = \sqrt{\frac{L_t}{C_t + C_b/s}} \quad \text{and} \quad v_l = \frac{1}{\sqrt{L_t (C_t + C_b/s)}} \quad (2)$$

where s is the periodic spacing of the MEMS bridges and C_b/s is the distributed MEMS capacitance on the loaded line. Thus, the loaded line can be designed for $Z_l=50 \Omega$ by appropriately choosing an unloaded-line impedance, $Z_o>50 \Omega$, and the periodic spacing, s , for a given MEMS bridge capacitance, C_b .

The periodic structure has an upper frequency limit due to the Bragg re-

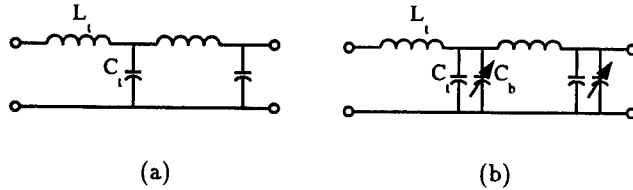


Fig. 2. Ideal (a) unloaded CPW line and (b) loaded distributed MEMS transmission lines.

flection[6] occurring at

$$f_{Bragg} = \frac{1}{\pi s \sqrt{L_t (C_t + C_b/s)}} \quad (3)$$

In order to push the Bragg frequency above the region of interest ($f_{Bragg} \gg 60$ GHz) and maintain the loaded-line impedance at $Z_l = 50 \Omega$, both the periodic spacing and the width of the MEMS bridge should be reduced. Another option is to increase the impedance of the unloaded line, resulting in a decrease in the per-unit length capacitance, C_t . However, changing the unloaded-line impedance also affects the line loss and the pull-down voltage of the MEMS bridge[4]. In this work we have chosen to keep the CPW dimensions constant ($W=G=100 \mu\text{m}$) with $Z_0=96 \Omega$ on a $500 \mu\text{m}$ quartz substrate, and have varied the bridge width and periodic spacing to achieve loaded lines with different Bragg frequencies. Figure 5 shows two designs of the distributed MEMS transmission lines. The top design consists of 8 $60\text{-}\mu\text{m}$ wide bridges spaced at $580 \mu\text{m}$ while the bottom design has 16 $30\text{-}\mu\text{m}$ wide bridges spaced at $306 \mu\text{m}$. Both of these designs have a total length of 5.2 mm.

The force on the MEMS bridge due to an applied bias on the CPW center conductor is given by

$$F = \frac{\epsilon_0 W w}{2g^2} V_{bias}^2 \quad (\text{N}) \quad (4)$$

where ϵ_0 is the free-space permittivity, W is the center conductor width, w is the width of the MEMS bridge, g is the bridge height, and V_{bias} is the applied bias voltage. The spring constant of the bridge is approximated by [7]

$$k = \frac{32Et^3w}{L^3} + \frac{8\sigma(1-\nu)tw}{L} \quad (\text{N/m}) \quad (5)$$

where E is the Young's modulus of the bridge material, t is the bridge thickness, $L=(W+2G)$ is the bridge length, σ is the internal residual stress of the bridge, and ν is Poisson's ratio. The pull-down voltage of the MEMS bridge can be found by setting up a force-balance equation between the electrostatic force

and the restoring force of the bridge. From the solution to this equation, it is found that the MEMS bridge becomes unstable at $2g_o/3$, where g_o is the zero-bias bridge height. The voltage at which this instability occurs is the “pull-down” voltage and is given by

$$V_p = \sqrt{\frac{8k}{27\epsilon_o W w}} g_o^3 \quad (V) \quad (6)$$

Table I gives some example calculations of the pull-down voltage of gold MEMS bridges for varying levels of stress. It is evident from these calculations that to achieve $V_p \leq 20$ V for the given dimensions, the MEMS bridge must have less than 20 MPa of stress.

TABLE I
CALCULATED VALUES OF V_p

σ	V_p ($t=1 \mu\text{m}$)	V_p ($t=0.5 \mu\text{m}$)
0 MPa	10 V	4 V
20 MPa	21 V	14 V
100 MPa	43 V	30 V

The Young's modulus and Poisson's ratio for gold are $E=80$ MPa and $\nu=0.42$, respectively. The bridge dimensions used in the calculation are: $g_o=1.5 \mu\text{m}$, $L=300 \mu\text{m}$, $W=100 \mu\text{m}$.

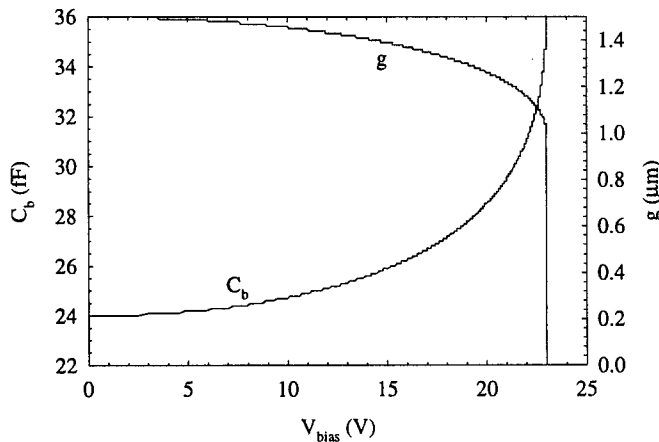


Fig. 3. Variation of the MEMS bridge capacitance and gap height with applied bias voltage for a zero-bias capacitance of 24 fF and a pull-down voltage of 23 V.

Figure 3 shows the MEMS bridge capacitance, C_b , versus applied bias voltage, V_{bias} , for the case of a zero-bias capacitance of 24 fF and a pull-down

voltage of 23 V. It is seen that as the applied bias approaches the pull-down voltage, the MEMS bridge capacitance changes very rapidly and reaches $1.5C_{bo}$ at 23 V, where C_{bo} is the zero-bias bridge capacitance. Because the MEMS bridge cannot be maintained at $2g_o/3$ without becoming unstable, it is not possible in practice to achieve such an increase in the MEMS bridge capacitance. Instead, the applied voltage is limited to 21-22 V which gives a capacitance value of $C_b=29.5-31$ fF, or a 23-30% increase in the zero-bias bridge capacitance.

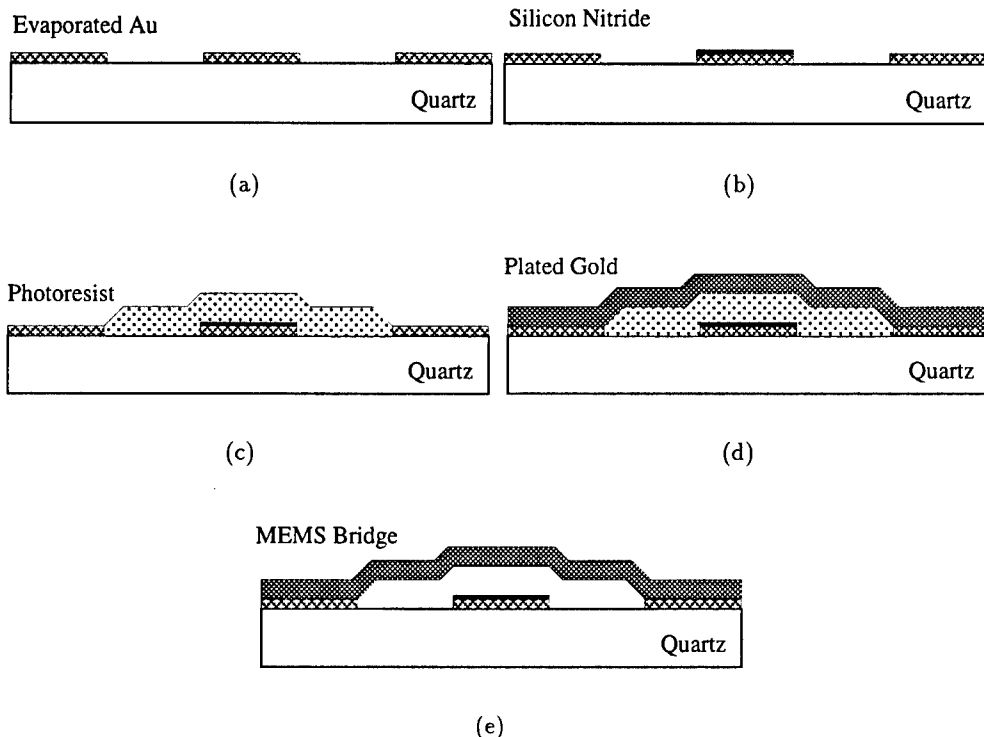


Fig. 4. Details of the fabrication process for the MEMS bridges.

III. Fabrication

The distributed MEMS transmission lines are fabricated on a 500 μm thick quartz substrate ($\epsilon_r=3.8$) using finite-ground plane CPW [8]. The fabrication process is shown in Figure 4. The CPW lines are defined first by evaporating a 500/5000 \AA layer of Ti/Au (Fig. 4a). Next a 500 \AA Cr adhesion layer is sputtered over the wafer, and then a 1000 \AA PECVD Si_xN_y layer is grown on top. The silicon nitride is patterned with photoresist and etched in an RIE such that it is only covering the CPW center conductor (Fig. 4b). Once

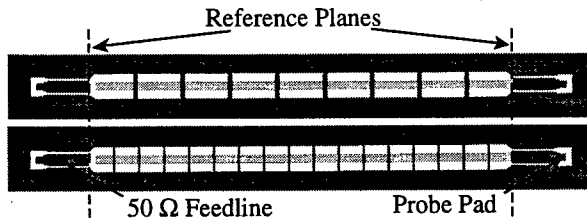


Fig. 5. Picture of fabricated distributed MEMS transmission lines. The CPW dimensions of the loaded lines are $W=G=100\ \mu m$ and of the feedlines are $W=150\ \mu m$ and $G=16\ \mu m$. The width and spacing of the MEMS bridges are $60\ \mu m/580\ \mu m$ and $30\ \mu m/306\ \mu m$, respectively, resulting in a total length of 5.2 mm.

the photoresist masking layer is removed, the exposed Cr is etched. Next the sacrificial photoresist layer, which determines the height of the MEMS bridge, is patterned (Fig. 4c). The nominal height of the air bridges, above the center conductor, is $1.5\ \mu m$. A $500/2000/500\ \text{\AA}$ Ti/Au/Ti seed layer is evaporated and patterned with photoresist to define the width and periodic spacing of the MEMS bridges. Then the MEMS bridges and CPW ground planes are gold electroplated to a thickness of approximately $2.5\ \mu m$, followed by removal of the top photoresist and seed layer (Fig 4d). Thus, the MEMS bridge is a bilayer metal composed of Ti/Au since the titanium is not removed from the bottom of the bridge. The last step is to remove the sacrificial photoresist by soaking the wafer in acetone. At this point, the wafer cannot be air dried because the surface tension of the liquid will pull the MEMS bridges down causing them to stick to the substrate. Therefore, the wafer is placed in denatured ethanol and a critical point drying system is used to release the MEMS bridges (Fig. 4e) [9]. Figure 5 shows a loaded CPW line connected to probe pads via $50\ \Omega$ CPW feedlines ($W=150\ \mu m$, $G=16\ \mu m$) in which the center conductors are also electroplated.

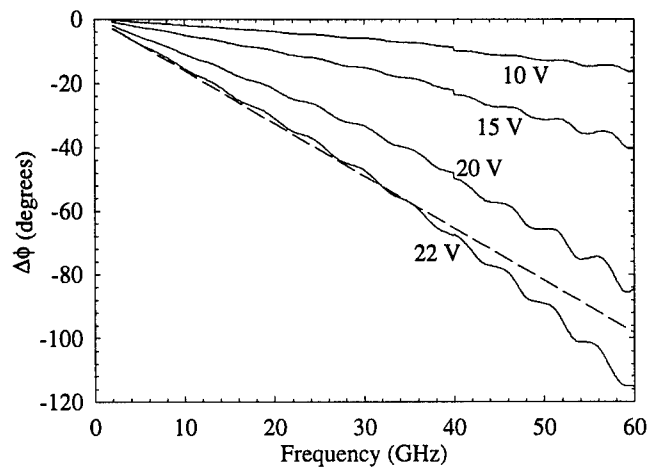
IV. MEASUREMENTS

As mentioned previously, the distributed MEMS transmission line can be used as a true-time delay (TTD) phase shifter. This is done by applying a single bias voltage to the center conductor of the CPW line which causes the height of the MEMS bridges to be decreased, thereby increasing the capacitive loading and decreasing the phase velocity. Although this analog control voltage is susceptible to noise from the power supply, the fact that only one control voltage is required is a major advantage and could be very beneficial in quasi-optical phased arrays.

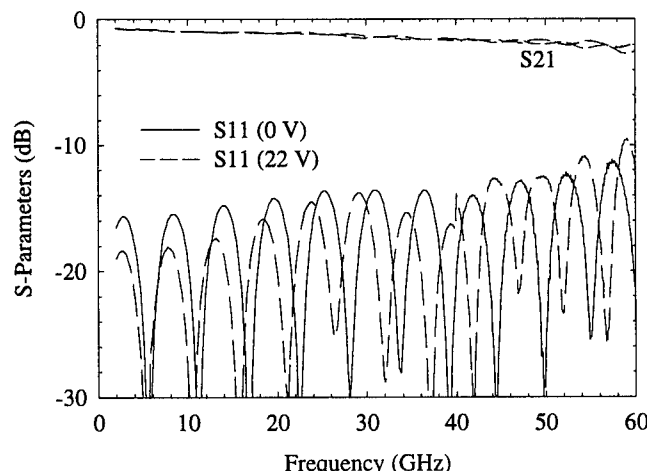
A distributed MEMS line with 32 $30\text{-}\mu m$ bridges spaced at $306\ \mu m$ (total

length=10.1 mm) was tested as a phase shifter. The pull-down voltage for this line was measured to be 23 V so that the maximum voltage that could be applied without the bridges becoming unstable was 22 V. The measured phase shift and insertion loss are shown in Figures 6a and 6b respectively, for varying bias voltages. From these results it is seen that a maximum phase shift of 118° at 60 GHz is achieved with 2.1 dB of loss. Also, it should be noted that the null period of S11 decreases as the bias voltage is increased from 0 V to 22 V. The phase shift is linear with frequency up to 40 GHz, with 1.6 dB loss and -67° phase shift, and then drops at a slightly steeper slope. This is believed to be an effect of approaching the Bragg frequency of the line. In Figure 6b, it is seen that as the bias voltage is increased, the line impedance is lowered from 59 Ω at 0 V to 56 Ω at 22 V due to the increased capacitive loading of the line. The increased loading corresponds to an increase in the bridge capacitance from $C_b=27 \text{ fF}$ at 0 V to $C_b=31 \text{ fF}$ at 22 V. The calculated Bragg frequency for $C_b=31 \text{ fF}$ ($V_{bias}=22 \text{ V}$) is 119 GHz. Also, it is important to note that the insertion loss of the distributed MEMS phase shifter remains nearly constant as the bias voltage (and phase shift) is varied. The phase shift per millimeter is -6.6°/mm at 40 GHz and -11.7°/mm at 60 GHz. Using the linearly extrapolated value of -98° at 60 GHz, as shown in Figure 6a, the time delay is found to be 4.5 psec.

Figure 7 shows measured results for two more examples of distributed MEMS phase shifters with $W=G=100 \text{ } \mu\text{m}$. The results shown in Figure 7a are for a line with 16 60-μm wide bridges spaced at 580 μm (total length=9.8 mm). The insertion loss is 1.7 dB at 40 GHz, the reflection coefficient ranges from -15 dB to -10 dB, and the maximum phase shift is -82° (-8.4°/mm). The time delay at 23 V, calculated from the linear phase shift (0.27 GHz), is 4.5 ps. The line has a zero-bias impedance of 60 Ω and a Bragg frequency of 67 GHz. The measured results shown in Figure 7b are from a line fabricated on a different wafer, where the MEMS bridges are only 1 μm thick, rather than 2.5 μm thick, and do not have a titanium layer on the bottom. The measured pull-down voltage of the MEMS bridges for this line is 6 V (as compared to 23 V). The line is composed of 16 60-μm wide bridges with a periodic spacing of 400 μm (total length=6.74 mm) resulting in a zero-bias impedance of 43 Ω. The maximum phase shift of this line is seen to be -74° (-11°/mm) and has an associated loss of 1.4 dB at 40 GHz with a reflection coefficient ranging from -16 dB to -11 dB. The maximum time delay from the linear phase shift (0.29 GHz) is 4.2 ps. The zero-bias MEMS bridge capacitance is calculated to be 87 fF which is much higher than the simulated value of 42.5 fF. This, together with the low pull-down voltage ($V_p=6 \text{ V}$), indicates the presence of a fairly large compressive stress which may have caused the bridges to buckle down slightly. The calculated Bragg frequency for $C_b=87 \text{ fF}$ is 69 GHz.

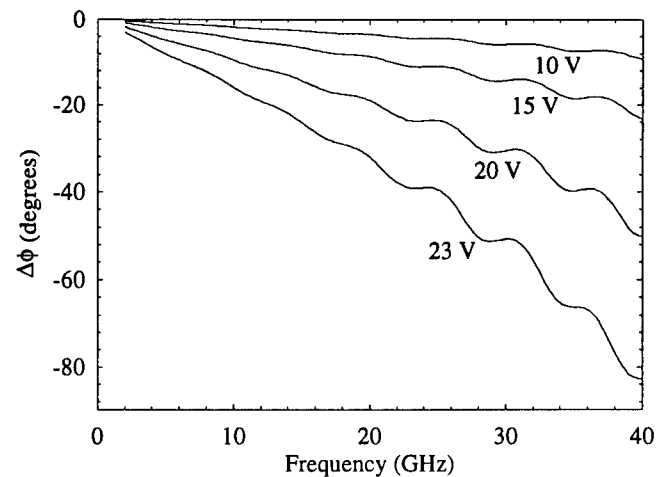


(a)

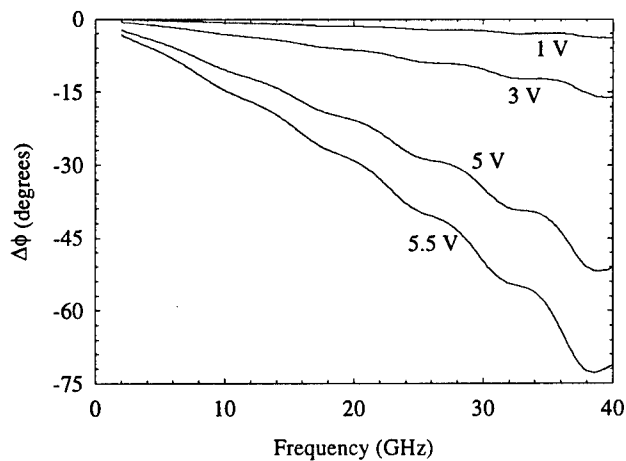


(b)

Fig. 6. Measured (a) phase shift and (b) insertion loss for a distributed MEMS phase shifter with 32 30- μ m wide bridges spaced at 306 μ m (total length = 10.1 mm) for varying bias voltage.



(a)



(b)

Fig. 7. Measured phase shift vs. bias voltage for distributed MEMS phase shifters with (a) 16 60- μ m wide bridges spaced at 580 μ m (total length = 9.8 mm) and (b) 16 60- μ m wide bridges spaced at 400 μ m (total length = 6.7 mm). The phase shifter in (b) has a pull-down voltage of 6 V and a MEMS bridge thickness of 1 μ m.

It is evident from Figure 7, that the lines with lower Bragg frequencies and lower loaded-line impedances (ie, higher C_b/s) result in more phase shift per millimeter in their region of operation. In fact, the line with 60 μm wide bridges spaced at 400 μm ($Z_l=43 \Omega$, $f_{Bragg}=69 \text{ GHz}$) has 67% more phase shift per millimeter at 40 GHz than the line with 30 μm wide bridges spaced at 306 μm ($Z_l=60 \Omega$, $f_{Bragg}=124 \text{ GHz}$). Work is currently being done to design distributed TTD phase shifters for optimal phase shift per millimeter and low insertion loss.

Figure 8 shows the operation of the distributed MEMS transmission lines as phase verniers at 40 GHz. The measurement was done on three lines with identical bridge widths (30 μm) and spacings (306 μm). The number of bridges on each line is labeled in the plot. As can be seen from the measurement, 12°/36°/62° phase shift at 40 GHz can be achieved over a 21 V bias control for the 8/16/32 bridge distributed MEMS lines with an associated insertion loss of 0.51/0.75/1.57 dB. Thus, very fine control of the phase (0°-12°) can be achieved with 0.5 dB insertion loss. This is well suited for applications in which a digital master clock drives several direct digital synthesizers to achieve true time delay over a large array of antenna elements. A phase vernier is needed to fine tune the phase between the antenna elements.

V. CONCLUSIONS

This paper presents, to our knowledge, the first MEMS-based 0-60 GHz TTD phase shifters to-date. The essential idea is to include the capacitance of the MEMS bridge, in the up position, as part of the transmission-line design, rather than treating it as a parasitic capacitance as is done in current MEMS switch designs. An immediate advantage is that the MEMS bridges can be fabricated with a 1.5 μm height above the transmission line, and therefore require a substantially lower pull-down voltage than current designs (10-20 V instead of 25-60 V). The TTD phase shifters offer low-loss performance and are extremely wideband (0-60 GHz), limited only by the Bragg frequency of the loaded transmission line. The associated loss in the TTD phase shifters is state-of-the-art and these distributed MEMS transmission lines have the potential for even further improvement in subsequent designs.

VI. ACKNOWLEDGEMENTS

This work was supported by the US Naval Surface Warfare Center, Dahlgren Division, and the US Army Research Office under contract DAAH04-96-1-0348. The authors would like to thank Andrew Brown of the University of Michigan for his substantial assistance with the fabrication process.

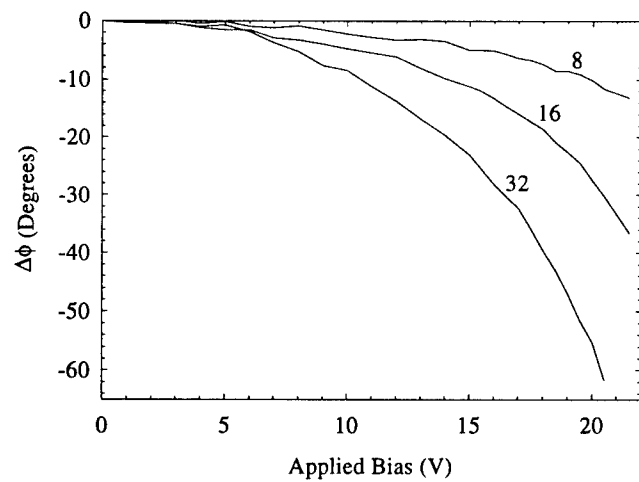


Fig. 8. Distributed MEMS transmission lines measured as phase verniers at 40 GHz. All three lines have 30 μ m wide bridges spaced at 306 μ m with the number of bridges shown in the plot. The insertion loss is 0.51/0.75/1.57 dB for the 8/16/32 bridge distributed MEMS lines.

REFERENCES

- [1] L. E. Larson, R. H. Hackett, M. A. Melendes, and R. F. Lohr, "Micromachined microwave actuator (MIMAC) technology - a new tuning approach for microwave integrated circuits," in *1991 IEEE Microwave and Millimeter-Wave Monolithic Circuits Symposium*, 1991, pp. 27-30.
- [2] C. Goldsmith, T. H. Lin, B. Powers, W. R. Wu, and B. Norvell, "Micromechanical membrane switches for microwave applications," in *1995 IEEE MTT-S Int. Microwave Symp. Dig.*, Orlando, FL, June 1995, pp. 91-94.
- [3] J. J. Yao and M. F. Chang, "A surface micromachined miniature switch for telecommunications applications with signal frequencies from DC up to 4 GHz," in *1995 Int. Conf. on Solid-State Sensors and Actuators Dig.*, Stockholm, Sweden, June 1995, pp. 384-387.
- [4] C. Goldsmith, J. Randall, S. Eshelman, T. H. Lin, D. Dennistor, S. Chen, and B. Norvell, "Characteristics of micromachined switches at microwave frequencies," in *1996 IEEE MTT-S Int. Microwave Symp. Dig.*, San Francisco, CA, June 1996, pp. 1141-1144.
- [5] D. M. Pozar, *Microwave Engineering*, Addison-Wesley Publishing Company, 1990.
- [6] M. J. W. Rodwell, S. T. Allen, R. Y. Yu, M. G. Case, U. Bhattacharya, M. Reddy, E. Carman, M. Kamegawa, Y. Konishi, J. Pusl, and R. Pullela, "Active and nonlinear wave propagation devices in ultrafast electronics and optoelectronics," *Proceedings of the IEEE*, vol. 82, no. 7, pp. 1037-1059, July 1994.
- [7] P. Osterberg, H. Yie, X. Cai, J. White, and S. Senturia, "Self-consistent simulation and modeling of electrostatically deformed diaphragms," in *IEEE Microelectromechanical Systems Conf. Proceedings*, January 1994, pp. 28-32.
- [8] G. E. Ponchak, *Development of Passive Components for Millimeter-Wave Circuits*, Ph.D. thesis, The University of Michigan, Ann Arbor, MI, 1997.
- [9] G. T. Mulhern, D. S. Soane, and R. T. Howe, "Supercritical carbon dioxide drying of microstructures," in *The 7th Int. Conference on Solid-State Sensors and Actuators*, Yokohama, Japan, June 1993, pp. 296-299.

The Multilevel Fast Multipole Algorithm for Analyzing Electromagnetic Radiation from Complex Surfaces-Wire Structures

Hsueh-Yung Chao, Jiming Song, Eric Michielssen, and Weng Cho Chew

Center for Computational Electromagnetics

Department of Electrical and Computer Engineering

University of Illinois at Urbana-Champaign

Urbana, IL 61801-2991

Abstract

In the past, the multilevel fast multipole algorithm (MLFMA) has been successfully applied to the analysis of electromagnetic scattering from large and complex surfaces. Recently, we added a wire and surface-wire junction capability to our existing MLFMA codes, thereby enabling the analysis of radiation problems involving complex surfaces with wire attachments, all within a computational complexity of $O(N \log N)$ per iteration, where N is the number of unknowns. This extension opens the door to several new applications, such as the analysis of antennas mounted on vehicles and the study of electromagnetic compatibility issues. A comparison between the MLFMA and the traditional method of moments (MOM) reveals that the MLFMA requires far less simulation time and memory resources without sacrificing numerical accuracy. As a result, the MLFMA enables the analysis of radiation phenomena involving complex environments using only a small computer.

1. INTRODUCTION

The fast multipole method (FMM) was first developed and applied to acoustic wave scattering problems by Rokhlin [1]. Then, Engheta *et al.*, and Lu and Chew applied the method to two-dimensional TM_Z and TE_Z electromagnetic scattering problems [2,3]. The FMM for three-dimensional Helmholtz equations was discussed by Coifman *et al.* in [4]. Since, the FMM and its more advanced cousin, the multilevel fast multipole algorithm (MLFMA), have been shown to substantially reduce the CPU time and memory requirements of classical MOM solvers in analyzing electromagnetic scattering phenomena [5-9]. Recently, the Center for Computational Electromagnetics and Demaco, Inc. have developed an industrial-strength software tool, the Fast Illinois Solver Code (FISC), which relies on the MLFMA and has enabled the analysis of scattering problems involving very large and complex objects [10].

In this paper, we incorporate wire and surface-wire-junction basis functions into the MLFMA framework. This is achieved by merging SWJ3D, a general purposed MOM program developed by Michielssen and Libbrecht [11], with FISC. By transplanting wire and junction subroutines from SWJ3D into FISC, the latter now accommodates the analysis of scattering and radiation from complex surfaces with wire attachments as well as that of surface-only structures.

This paper discusses the construction of a mixed surface-wire-junction multilevel fast multipole algorithm (MSWJ-MLFMA) through four steps: 1) the formulation of the pertinent integral equation, 2) its discretization and 3) testing by Galerkin's method, and 4) the fast multipole-based acceleration of the iterative solution of the resulting matrix equation. Then, the usefulness of this method will be demonstrated through three different applications.

2. THE ELECTRIC INTEGRAL EQUATION FOR STRUCTURES CONSISTING OF SURFACES, WIRES AND SURFACE-WIRE JUNCTIONS

Consider a perfectly conducting object S that comprises surfaces and wires. These wires are possibly connected to the surfaces; the points of connection will be referred to as surface-wire junctions. Suppose that S is embedded in a homogeneous medium and that an electric field \mathbf{E}^{inc} impinges on S . As a result, a current \mathbf{J} is induced on S . The electric field integral equation (EFIE) that relates \mathbf{J} to \mathbf{E}^{inc} is

$$-i\omega\hat{\mathbf{t}} \cdot \mathbf{A}(\mathbf{J}, \mathbf{r}) + \hat{\mathbf{t}} \cdot \nabla\Phi(\mathbf{J}, \mathbf{r}) = \hat{\mathbf{t}} \cdot \mathbf{E}^{inc} \quad \mathbf{r} \in S, \quad (1)$$

where the vector potential $\mathbf{A}(\mathbf{J}, \mathbf{r})$ is

$$\mathbf{A}(\mathbf{J}, \mathbf{r}) = \frac{\mu}{4\pi} \int_S dS' g(\mathbf{r}, \mathbf{r}') \mathbf{J}(\mathbf{r}'), \quad (2)$$

the scalar potential $\Phi(\mathbf{J}, \mathbf{r})$ is

$$\Phi(\mathbf{J}, \mathbf{r}) = \frac{1}{i\omega 4\pi\epsilon} \int_S dS' g(\mathbf{r}, \mathbf{r}') \nabla' \cdot \mathbf{J}(\mathbf{r}'), \quad (3)$$

and the Green's function is

$$g(\mathbf{r}, \mathbf{r}') = \frac{e^{ikR}}{R}, \quad R = |\mathbf{r} - \mathbf{r}'|. \quad (4)$$

In the above, $\hat{\mathbf{t}}$ denotes an arbitrary unit vector tangent to S .

3. DISCRETIZATION OF INTEGRAL EQUATIONS

All surfaces and wires can be represented in terms of two basic geometric elements, namely triangular patches and linear segments. The current distribution on the conducting surfaces and wires is represented by the basis functions proposed by Rao *et al.* [12, 13], which are schematically illustrated in Figures 1(a) to 1(c). Specifically, the current distribution \mathbf{J} can be expressed as

$$\mathbf{J} = \mathbf{J}^s + \mathbf{J}^w + \mathbf{J}^j = \sum_{n=1}^{N_s} I_n^s \Lambda_n^s + \sum_{n=1}^{N_w} I_n^w \Lambda_n^w + \sum_{n=1}^{N_j} I_n^j \Lambda_n^j, \quad (5)$$

where Λ_n^s , Λ_n^w , and Λ_n^j represent the surface, wire, and junction basis functions, respectively, and N_s , N_w , and N_j are the respective number of basis functions in each category.

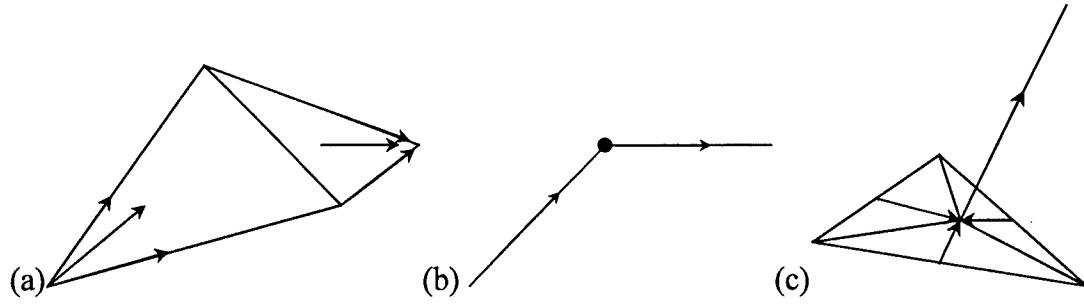


Figure 1. Current flows on (a) a surface, (b) a wire, and (c) a junction.

Because the electric field \mathbf{E} , the magnetic vector potential \mathbf{A} , and the electric scalar potential Φ all linearly depend on the current density \mathbf{J} , each of them can be decomposed into its surface, wire, and junction components. Therefore, the EFIE can be recast in terms of vector and scalar potentials related to surface, wire, and junction basis functions as:

$$\sum_{n=1}^{N_s} [-i\omega \hat{t} \cdot \mathbf{A}_n^s + \hat{t} \cdot \nabla \Phi_n^s] + \sum_{n=1}^{N_w} [-i\omega \hat{t} \cdot \mathbf{A}_n^w + \hat{t} \cdot \nabla \Phi_n^w] + \sum_{n=1}^{N_j} [-i\omega \hat{t} \cdot \mathbf{A}_n^j + \hat{t} \cdot \nabla \Phi_n^j] = \hat{t} \cdot \mathbf{E}^{inc} \quad (6)$$

where \mathbf{A}_n^s , \mathbf{A}_n^w , \mathbf{A}_n^j , Φ_n^s , Φ_n^w , and Φ_n^j denote the vector and scalar potentials associated with each of the surface, wire, and junction basis function.

Techniques for evaluating the vector potentials \mathbf{A} and the scalar potentials Φ associated with surfaces, wires and junction basis functions are described in [11-15].

4. GALERKIN'S METHOD

Next, the integral equation is converted into a matrix equation by taking the inner product of the discretized integral equation (Equation (6)) with the corresponding testing (basis) functions

$$\bar{\mathbf{Z}} \mathbf{I} = \mathbf{V}, \quad (7)$$

Here, $\bar{\mathbf{Z}}$ is an $N \times N$ matrix, and \mathbf{I} and \mathbf{V} are $N \times 1$ vectors with $N = N_s + N_w + N_j$ equal to the total number of basis functions representing the current. The impedance matrix can be subdivided into nine submatrices

$$\bar{\mathbf{Z}} = \begin{bmatrix} \bar{\mathbf{Z}}^{s,s} & \bar{\mathbf{Z}}^{s,w} & \bar{\mathbf{Z}}^{s,j} \\ \bar{\mathbf{Z}}^{w,s} & \bar{\mathbf{Z}}^{w,w} & \bar{\mathbf{Z}}^{w,j} \\ \bar{\mathbf{Z}}^{j,s} & \bar{\mathbf{Z}}^{j,w} & \bar{\mathbf{Z}}^{j,j} \end{bmatrix}, \quad (8)$$

where

$$Z_{mn}^{\alpha,\beta} = -i\omega \langle \mathbf{A}_n^\alpha, \Lambda_m^\beta \rangle + \langle \nabla \Phi_n^\alpha, \Lambda_m^\beta \rangle, \quad (9)$$

where the subscript α and β can be replaced by s , w , and j .

The right hand side \mathbf{V} consists of three sub-vectors

$$\mathbf{V} = (\mathbf{V}^s, \mathbf{V}^w, \mathbf{V}^j)^T, \quad (10)$$

where

$$V_m^s = \langle \mathbf{E}^{inc}, \Lambda_m^s \rangle, \quad (11)$$

$$V_m^w = \langle \mathbf{E}^{inc}, \Lambda_m^w \rangle, \quad (12)$$

and

$$V_m^j = \langle \mathbf{E}^{inc}, \Lambda_m^j \rangle. \quad (13)$$

Similarly, the current vector \mathbf{I} can be decomposed into three subvectors:

$$\mathbf{I} = (\mathbf{I}^s, \mathbf{I}^w, \mathbf{I}^j)^T. \quad (14)$$

5. THE FAST MULTIPOLE METHOD AND ITS MULTILEVEL IMPLEMENTATION

The fast multipole method accelerates the iterative solution of matrix equation (7). First, consider on explicit form of the impedance matrix element describing a surface-surface interaction. A single matrix element can be expressed as

$$Z_{mn} = -\frac{i\omega\mu}{4\pi} \int_S dS \Lambda_m^s(\mathbf{r}) \cdot \int_S dS' \left(\bar{\mathbf{I}} - \frac{\nabla \nabla'}{k^2} \right) \frac{e^{ikR}}{R} \cdot \Lambda_n^s(\mathbf{r}'). \quad (15)$$

During the evaluation of the matrix-vector product, if the m th element is close to the n th element, the above integral is computed directly and its contribution to the matrix-vector product is incorporated classically. But if the two elements are far apart from one another,

then, instead of computing the matrix elements directly, we apply the fast multipole method to accelerate the computation of matrix-vector multiplication.

Let \mathbf{r}_m and \mathbf{r}_n denote the location of the m th element (observer) and the n th element (source). The FMM first divides the volume containing the scatterer into small cubes and groups all elements residing inside these cubes into subscatterers. Assume that the observer resides within a group with center \mathbf{r}_i , and that the source point belongs to a group with center \mathbf{r}_j . If the distance between the group centers is larger than the group size, i.e. if $|\mathbf{r}_{ij}| > |\mathbf{r}_{mi}| + |\mathbf{r}_{nj}|$, we can express the Green's function using the addition theorem in terms of a plane wave basis as

$$\frac{e^{i\mathbf{k}\cdot\mathbf{r}_{mn}}}{|\mathbf{r}_{mn}|} = \frac{ik}{4\pi} \int d^2\hat{k} e^{i\mathbf{k}\cdot(\mathbf{r}_{mi}-\mathbf{r}_{nj})} \sum_{l=0}^{\infty} i^l (2l+1) h_l^{(1)}(k\mathbf{r}_{ij}) P_l(\hat{k} \cdot \hat{r}_{ij}) \quad (16)$$

where $h_l^{(1)}(x)$ is a spherical Hankel function of the first kind and $P_l(x)$ is a Legendre polynomial. Details regarding the truncation of the summation and the evaluation of the integrals can be found in [4,6].

Upon substituting the expansion of the Green's function into Equation (14), we find that

$$Z_{mn} = \frac{\eta k^2}{16\pi^2} \int d^2\hat{k} \mathbf{V}_{f,jn}(\hat{k}) \cdot \alpha_{ji}(\hat{k} \cdot \hat{r}_{ji}) \mathbf{V}_{s,im}^*(\hat{k}) \quad i \neq j, \quad (17)$$

where

$$\mathbf{V}_{f,jn}(\hat{k}) = \int_S dS e^{i\mathbf{k}\cdot\mathbf{r}_{nj}} (\bar{\mathbf{I}} - \hat{k}\hat{k}) \cdot \mathbf{\Lambda}_n^s(\mathbf{r}_{nj}) \quad (18)$$

$$\mathbf{V}_{s,im}(\hat{k}) = \int_S dS e^{i\mathbf{k}\cdot\mathbf{r}_{mi}} (\bar{\mathbf{I}} - \hat{k}\hat{k}) \cdot \mathbf{\Lambda}_m^s(\mathbf{r}_{mi}) \quad (19)$$

$$\alpha_{ji} = \sum_{l=0}^{\infty} i^l (2l+1) h_l^{(1)}(k\mathbf{r}_{ij}) P_l(\hat{k} \cdot \hat{r}_{ij}). \quad (20)$$

The above formulation can be applied to wires and junction basis functions: $\mathbf{V}_f(\hat{k})$ and $\mathbf{V}_s(\hat{k})$ can be thought of as the radiation and receiving patterns of the corresponding basis functions.

A two-level FMM has a computational complexity of $O(N^{3/2})$ per iteration. By extending the above concepts, we can also collect the group centers and aggregate them into larger entities that reside at a higher level. If the electrical size of the object increases, we can apply this procedure recursively to arrive at a multilevel implementation. The complexity of the multilevel fast multipole method has been shown to scale as $O(N \log N)$ per iteration [7]. The multilevel implementation involves a

partitioning of the scatterer into cubes. The larger cubes are partitioned into smaller cubes until the edge length of the finest cube is about a quarter wavelength. Therefore, the larger the object, the more levels will be involved. But if the object is small, we can gain very little from using the MLFMA. The construction of the radiation patterns $V_f(\hat{k})$ has been described in Equation (18). Because the radiation patterns are only directly calculated at the finest level, interpolation and anterpolation are required to relate the radiation patterns between levels that are sampled at different rates to reduce the workload. The reader is referred to Ref. [5,7] for a detailed formulation.

6. APPLICATIONS

We have tested the above algorithm extensively for simple geometries, such as a square plate, a straight wire antenna, and a quarter-wavelength wire antenna mounted on a finite ground plate. All results obtained by the MSWJ-MLFMA were in very good agreement with results obtained by physical optics (Figure 2), the method of moments (Figure 3), and the geometric theory of diffraction (Figure 4). For more complex structures, we adopt the MOM as our base for comparison with the MSWJ-MLFMA.

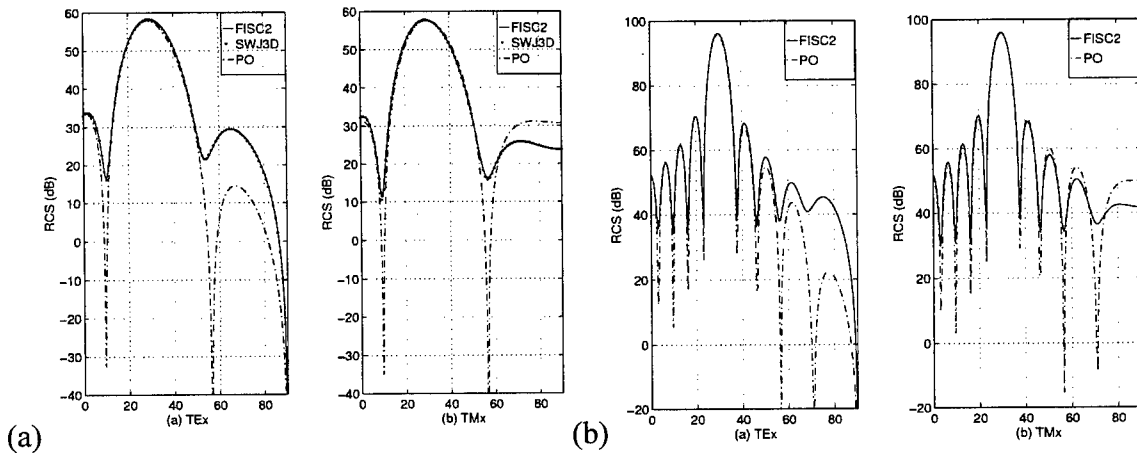


Figure 2. Principal plane bistatic radar cross sections of a square plane. The parameters are $\theta_i = 30^\circ$, $\phi_i = 270^\circ$, $\theta_s = 0^\circ \sim 90^\circ$, and $\phi_s = 90^\circ$ for both TE_x and TM_x wave incidence. (a) $3\lambda \times 3\lambda$ plane (b) $9\lambda \times 9\lambda$ plane [17].

The next example involves a monopole antenna attached to a car. The antenna operating frequency is 88 MHz; at that frequency the car fits inside a box of $2\lambda \times 1\lambda \times 1\lambda$. Even though the electrical size of the object is not very large, we can still gain from using the MSWJ-MLFMA. A delta-gap voltage source is located at the junction between the wire antenna and the trunk. A plot of the current distribution on the car is shown in Figure 5. In Figures 6(a) to 6(c), we compare the H-plane radiation patterns obtained by the MSWJ-MLFMA and the MOM. The small discrepancy between the MOM and the MSWJ-MLFMA based patterns in Figure 6(a) is due to the integration related to junction basis function. If we evaluate the junction integration in double precision, the two patterns exactly overlap with each other.

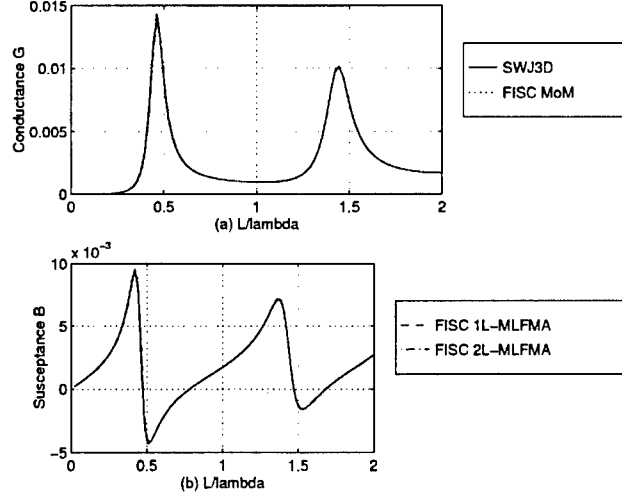


Figure 3. (a) Conductance and (b) susceptance of a center-fed linear antenna. The parameters are $L = 2$ meters, $L/\alpha = 148.4$, and $N = 32$ [18].

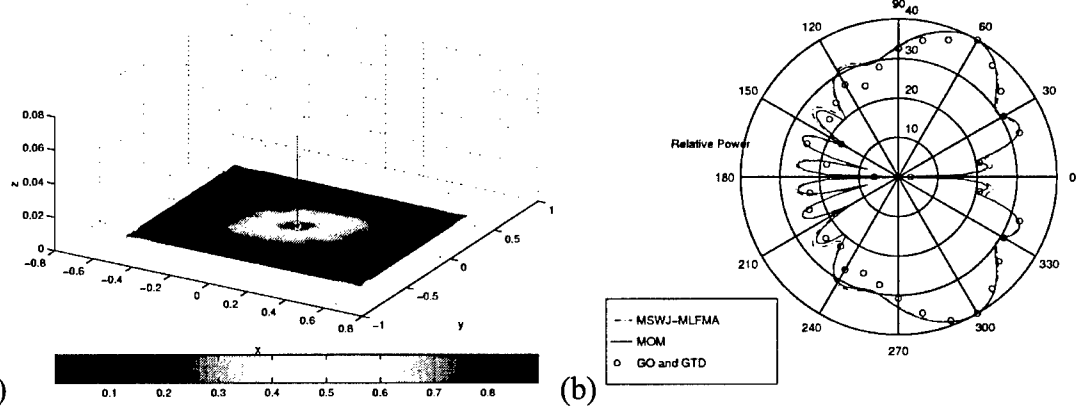


Figure 4. (a) Normalized current distribution of a monopole antenna and its finite ground plane. (b) Principal elevation plane amplitude patterns of a $\lambda/4$ monopole above finite square ground planes ($w \times w$). The parameters are $w = 1.22$ m, $f = 1.0$ GHz, and $l = \lambda/4$ [17].

For this problem which involves 2,451 unknowns, a two-level MSWJ-MLFMA code requires 3.9 minutes on a DIGITAL Personal Workstation. But a straightforward MOM solver requires 33 minutes. Unfortunately, for this problem, the MSWJ-MLFMA does not offer an overwhelming memory advantage over the MOM (46MB for MSWJ-MLFMA compared to 55MB for MOM) because the number of levels is restricted by the size of the object.

Our MSWJ-MLFMA code has also been used to explore the characteristics of a wire antenna array that is attached to an aircraft wing (Figure 7). These wires are fed by transmission lines to form a log-periodic monopole array [19]. The example shown here is for verification purposes only, because the algorithm typically does not offer great advantages over the MOM for problems with fewer than 2,000 unknowns. The simulation by the MOM takes 7.2 minutes and 14 MB of memory for this problem which involves

1,290 unknowns. The simulation by a three-level MLFMA takes more memory (21.5 MB), but offers great savings in execution time (1 minute).

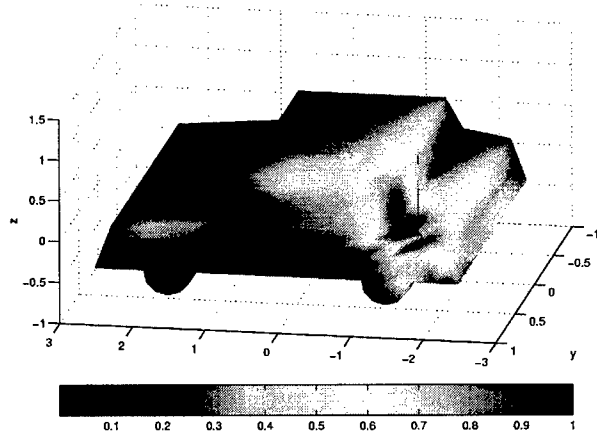


Figure 5. Normalized current distribution on a car and a monopole antenna radiating at 88MHz (FM radio band).

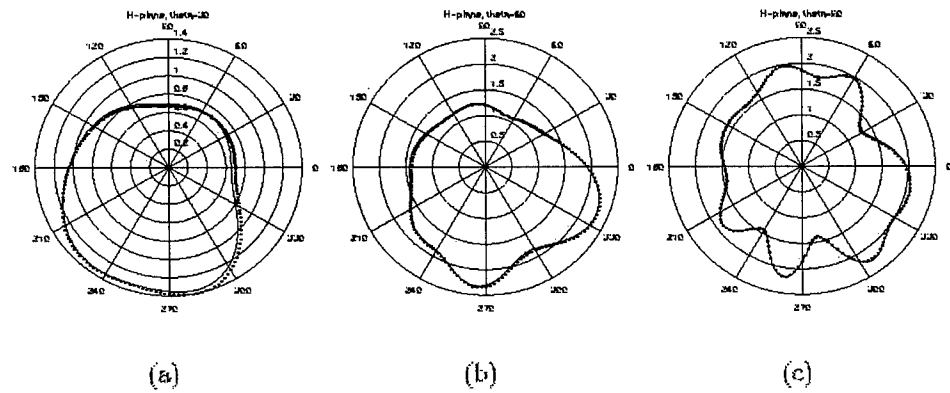


Figure 6. Radiation patterns for the car antenna in several observation planes. Patterns (a), (b), (c) are H-plane patterns ($\phi=0^\circ$ to 360°) for $\theta=30^\circ$, $\theta=60^\circ$, and $\theta=90^\circ$, respectively (MSWJ-MLFMA .., MOM -).

Figures 8 (a) through (c) illustrate the radiation patterns of this antenna in several observation planes. The first two graphs are radiation patterns on the H-plane ($\phi=\text{constant}$, $\theta=0^\circ$ to 360°). From Figure 8(a), we observe that the radiation energy is split into two beams by the wedge-shaped wing and is reflected by the fuselage. Figure 8(b) shows that the two beams point 60° upward and downward to the horizontal plane. Figure 8(c) indicates that radiating energy is reflected by both the wing and the fuselage on the horizontal plane ($\phi=90^\circ$). The discrepancy in Figure 8(b) is again introduced by the finite precision of the junction integration. It deteriorates as the surface patches, which are attached to a wire, form a thin wedge, as shown in Figure 9(a). With double precision computation, we obtain very good agreement between the patterns (Figure 9(b)).

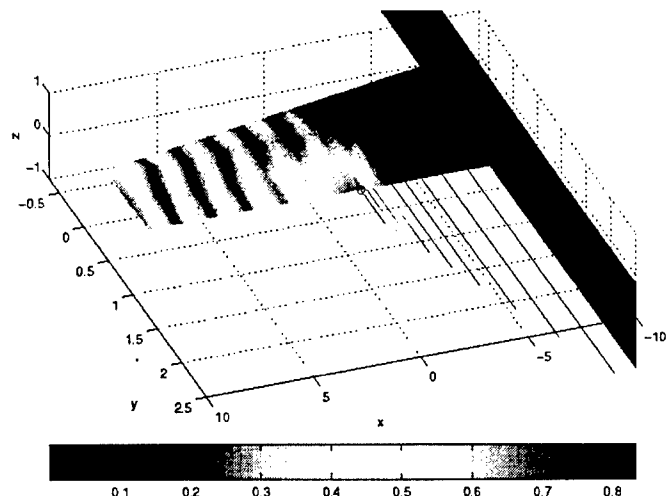


Figure 7. Normalized current distribution on a wing and attached wire antennas at 90MHz (VHF band).

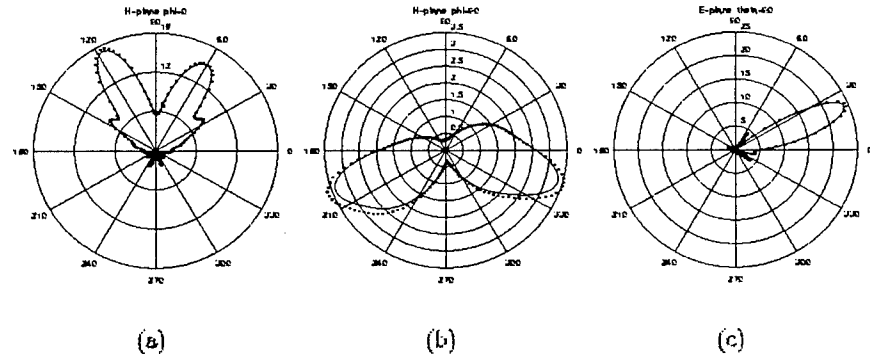


Figure 8. Radiation patterns of the aircraft antenna at several observation planes. Patterns (a) and (b) are H-plane patterns ($\theta=0^\circ$ to 360°) for $\phi=0^\circ$ and $\phi=90^\circ$, respectively. Pattern (c) is an E-plane pattern ($\phi=0^\circ$ to 360° , $\theta=90^\circ$) (MSWJ-MLFMA .., MOM -).

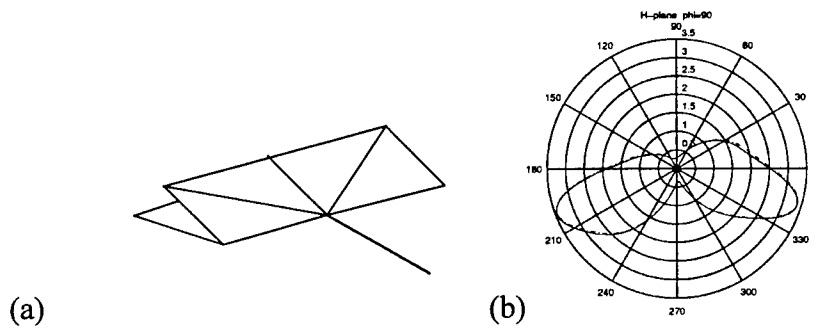
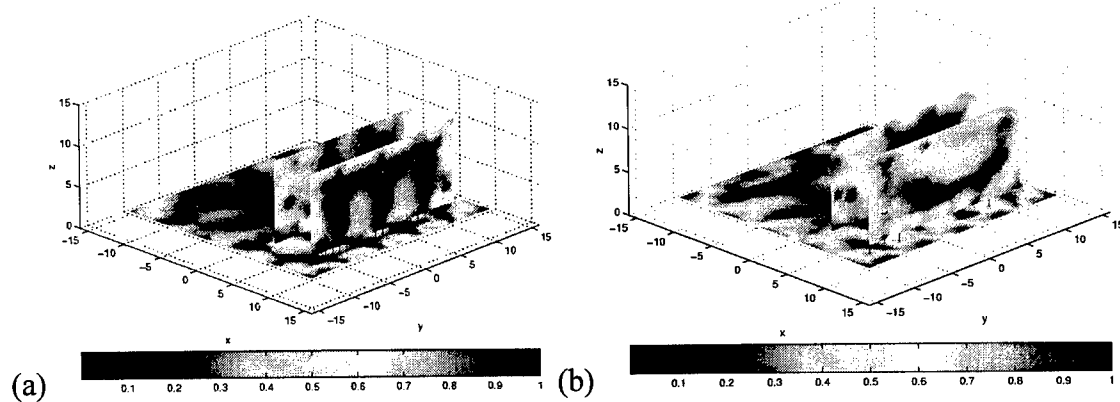


Figure 9. (a) The integration for wires attached to sharp edges can only be evaluated correctly by double precision computation. (b) The discrepancy in Figure 8(b) can be eliminated by performing the MOM and the MSWJ-MLFMA simulation in double precision.

Recently, researchers have started applying the fast multipole method to the analysis of electromagnetic compatibility problems [20-21]. Initially, their formulations were targeted at low frequency applications and only involved surface basis functions. In the low frequency regime, the FMM translation matrix is not diagonalized. As the frequency is raised, the increasing number of multipole required to model the fields radiated by a group necessitates the use of a diagonalized translation operator. In such situations, the MSWJ-MLFMA discussed in this paper offers significant advantages. Its current formulation permits the modeling of printed circuit boards, probes, and chassis, in terms of a combination of surfaces, wires, and interconnections. In the last example, we will study two shielding designs for a desktop computer.

The desktop computer consists of internal structures residing inside a chassis. The internal structures consist of a motherboard, a source card, and a shielding card. In high frequency design, every interface card should have a ground plane for the prevention of interboard interference. We assume that the thickness of the cards is small, i.e. the dielectric layers on these cards can be ignored and all cards can be treated as perfect electric conductors. The ground planes are usually connected to the motherboard through ground pins to ensure signal integrity. In our example, the shielding card is connected to the motherboard through ground pins (16 pins for the first design, 8 pins for the second design). The delta voltage source is located between the source card and the motherboard. The ground pins attached to the shielding card not only stabilize the ground level, but also serve as a shield between the source and the ventilation slot on the chassis.

Figures 10(a) through 10(d) show the normalized current distribution on the internal structures. In Figure 10(a) and 10(b), the similar current distribution on the source card and the shielding card is caused by the coupling effect. The two cards form a parallel plate waveguide and the wave bounces back and forth between them. The more ground pins, the better a ground the shielding card provides. The current magnitude on the shielding card is lower in the first design (Figure 10(a)) than that of the second design (Figure 10(b)). Moreover, because the internal structure is enclosed in a chassis, we can observe the periodic current peaks at the fringe of the motherboard. When the source frequency is 3 GHz, the chassis, which has a dimension of $3\lambda \times 3\lambda \times 1\lambda$, behaves like a cavity resonator. The current plot can serve as a diagnostic tool in circuit board design. In Figures 10(c) and 10(d), the magnitude of the current on the chassis is lower than the magnitude of current in the internal structure. Thus, little energy is radiated to the exterior of the chassis.



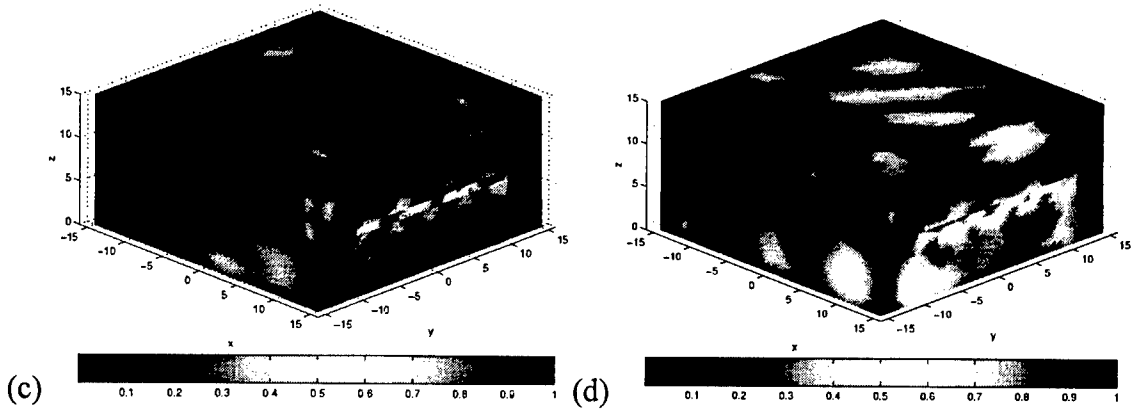


Figure 10. Normalized current distribution for the internal structures and the chassis at 3 GHz. Figures (a) and (c) are for the 16-pin design. Figures (b) and (d) are for the 8-pin design.

The above qualitative analysis can be further supported by the following quantitative results. The radiated powers are compared between 1) the internal cards without a chassis, 2) with a chassis and 8 ground pins, and 3) with a chassis and 16 ground pins for frequencies from 500 MHz to 1.8 GHz. As shown in Figure 11, the chassis effectively provides shielding for all frequencies, even if there is an occasional resonance in the chassis at certain frequencies. But whether the 16-pin design provides better shielding than the 8-pin design depends on the frequency.

A problem of 4,454 unknowns can be solved by two-level MSWJ-MLFMA with only 98 MB of memory and each iteration takes 1.6 second. In the contrast, the MOM requires 160 MB of memory for the same problem.

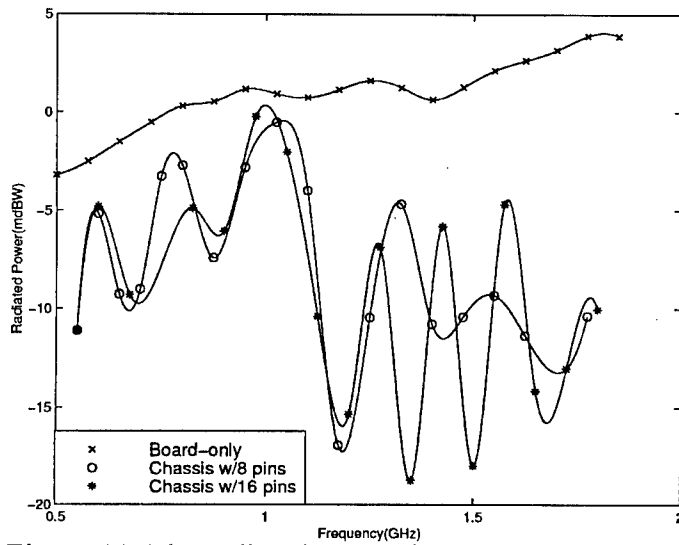


Figure 11. The radiated power for three shielding designs.

7. CONCLUSIONS

The mixed surface-wire-junction multilevel fast multipole algorithm (MSWJ-MLFMA) has demonstrated unprecedented efficiencies in analyzing electromagnetic phenomena involving structures with complex surface-wire interconnections. The MSWJ-MLFMA formulation offer significant time and memory savings over traditional moment methods while retaining their accuracy. The advantages are especially remarkable at high frequencies, when the electrical dimensions of the object are large.

8. ACKNOWLEDGEMENT

The authors appreciate the support from AFOSR under a MURI grant F49620-96-1-0025, from the Office of Naval Research under Grant N00014-95-1-0872, and from the National Science Foundation under Grant NSF ECS 93-02145.

REFERENCES

- [1] V. Rokhlin, "Rapid solution of integral equations of scattering theory in two dimensions", *Journal of Computational Physics*, Vol. 86, No. 2, pp. 414-439, February 1990.
- [2] N. Engheta, W.D. Murphy, V. Roklin, and M.S. Vassiliou, "The fast multipole method for electromagnetic scattering problems," *IEEE Transaction on Antennas and Propagation*, Vol. 40, No. 6, pp. 634-641, June 1992.
- [3] C.C. Lu and W.C. Chew, "Fast algorithm for solving hybrid integral equations," *IEEE Proceedings-H*, Vol. 140, No. 6, pp. 455-460, December 1993.
- [4] R. Coifman, V. Rokhlin, and S. Wandzura, "The fast multipole method for the wave equation: a pedestrian prescription," *IEEE Antennas and Propagation magazine*, Vol. 35, No. 3, pp. 7-12, June 1993.
- [5] C.C. Lu and W.C. Chew, "A multilevel algorithm for solving a boundary integral equation of wave scattering," *Microwave and Optical Technology Letters*, Vol. 7, No. 10, pp. 466-470, July 1994.
- [6] J.M. Song and W.C. Chew, "Fast multipole method solution using parametric geometry," *Microwave and Optical Technology Letters*, Vol. 7, No. 16, pp. 760-765, November 1994.
- [7] J.M. Song and W.C. Chew, "Multilevel fast multipole algorithm for solving combined field integral equations of electromagnetic scattering," *Microwave and Optical Technology Letters*, Vol. 10, No. 1, pp. 14-19, September 1994.
- [8] J.M. Song, C.C. Lu, and W.C. Chew, "Multilevel fast multipole algorithm for electromagnetic scattering by large complex objects," *IEEE Transaction on Antennas and Propagation*, Vol. 45, No. 10, pp. 1488-1493, October 1997.
- [9] W.C. Chew, J.M. Jin, C.C. Lu, E. Michielssen, and J.M. Song, "Fast solution methods in electromagnetics," *IEEE Transaction on Antennas and Propagation*, Vol. 45, No. 3, pp. 533-543, March 1997.
- [10] J.M. Song, C.C. Lu, W.C. Chew, and S.W. Lee, "Fast Illinois Solver Code (FISC)," *IEEE Antennas and Propagation magazine*, Vol. 40, No. 3, June 1998.
- [11] E. Michielssen and K. Libbrecht, "A general purposed electromagnetic moment method algorithm," M.S. thesis, Catholic University of Louvain, Louvain, Belgium, 1987.

- [12] S.M. Rao, "Electromagnetic radiation and scattering from a system of conducting bodies interconnected by wires," Ph.D. dissertation, University of Mississippi, Oxford, MS, 1980.
- [13] S.M. Rao, D.R. Wilton, A.W. Glisson, "Electromagnetic scattering by surfaces of arbitrary shape," *IEEE Transaction on Antennas and Propagation*, Vol. 30, No. 3, pp. 409-418, May 1982.
- [14] D.R. Wilton, S.M. Rao, A.W. Glisson, D.H. Schaubert, O.M. Al-bundak, and C.M. Bulter, "Potential integrals for uniform and linear source distribution on polygonal and polyhedral domains," *IEEE Transaction on Antennas and Propagation*, Vol. 32, No. 3, pp. 276-281, March 1984.
- [15] M.F. Costa and R.F. Harrington, "Electromagnetic radiation and scattering from a system of conducting bodies interconnected by wires," Syracuse University, Syracuse, New York, 1983.
- [16] C.C. Lu and W.C. Chew, "A near-resonance decoupling approach (NRDA) for scattering solution of near-resonance structures," *IEEE Transaction on Antennas and propagation*, Vol. 45, No. 12, pp. 1857-1862, December 1997.
- [17] C.A. Balanis, *Advanced Engineering Electromagnetics*. New York: John Wiley and Sons, 1989.
- [18] R.F. Harrington, *Field Computation by Moment Methods*. New York: IEEE Press, 1993.
- [19] K. Aygun, S.E. Fisher, A. Ergin, B. Shanker, E. Michielssen, "Time Domain Integral Equation Finite Difference Modeling of Complex Antennas and Feed Networks," *IEEE AP-S International Symposium and URSI Science Meeting*, Atlanta, Georgia, June 21-26, 1998.
- [20] G. Hoyler and R. Unbehauen, "The fast multipole method for EMC problems," *Electrical Engineering* 80(1997), pp. 403-411, Springer-Verlag, 1997.
- [21] J. S. Zhao, W. C. Chew, C. C. Lu, E. Michielssen, and J. M. Song, "Thin-stratified medium fast-multipole algorithm for solving microstrip structures," *IEEE Transaction on Microwave Theory and Technology*, Vol. 46, No. 4, pp.395-403, April 1998.

An Electronic “On Aircraft” Boresight Correction Procedure for Single Axis Scanned Phased Array Antennas

**Gary L. Kosanovic
Benjamin R. Meyers
David P. Parrish
Richard S. White
Kurt G. Ramsey**

**Northrop Grumman
Electronic Sensors and Systems Division
Baltimore, MD**

September 18, 1998

Abstract

An electronic “on aircraft” scan plane boresight procedure was recently developed to correct excessive scan plane boresight errors on antennas after they are installed in their respective platform aircraft. These antennas could have been removed from their platform aircraft and sent back to an antenna range for reboresighting; however, this would have resulted in substantial program cost and schedule penalties.

To preclude the aforementioned penalties, a procedure was developed which allowed the antennas to be electronically reboresighted on the platform aircraft using only the operating antenna, a network analyzer and a laptop computer with some application specific code to analyze measured phase data on the antenna. This data was then used to calculate the scan plane boresight error, and then compute phase corrections for the radiating element phase shifters to correct these scan plan beam pointing angle errors.

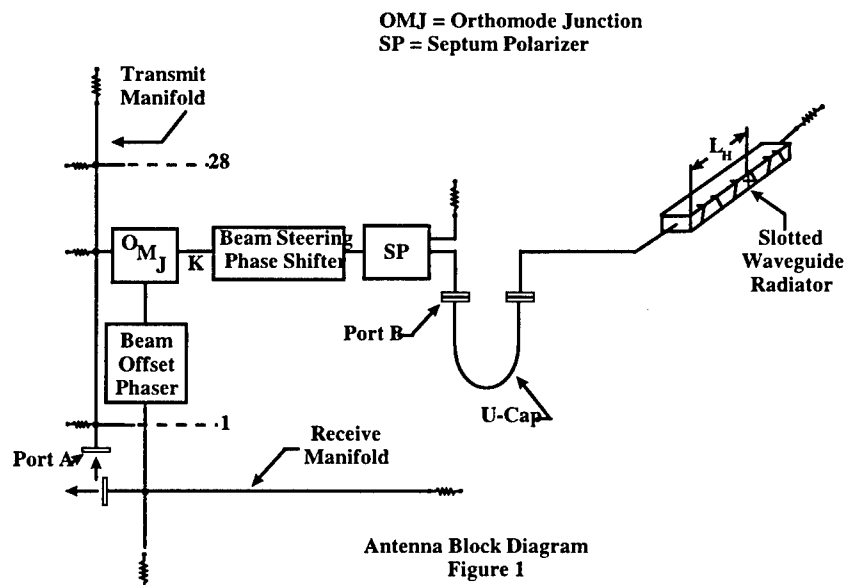
Introduction

It was necessary to reboresight the antennas in question at a number of frequencies across the antenna operating band. Using the procedure described herein, boresight errors at ten or twelve frequencies can easily be corrected in one day.

The procedure in question uses phase measurements on only about one third of the radiating elements to obtain the necessary data. A least squares fit of the measured phase data on these radiators to obtain the phase slopes associated with the predicted boresight errors was found to be sufficient to allow reboresighting of the antennas to the accuracy necessary to meet the associated radar system requirements.

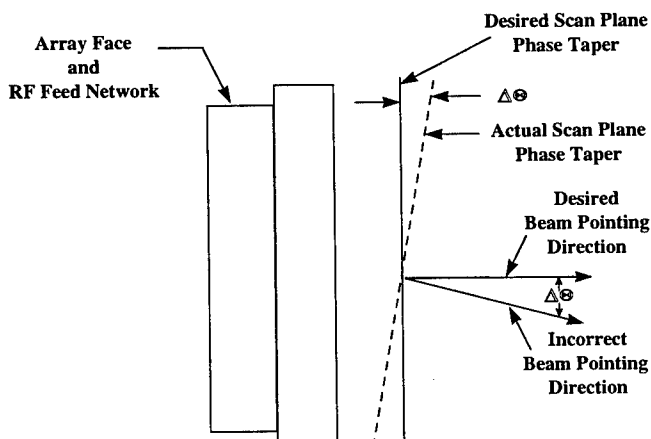
Technical Discussion

A block diagram of the antenna in question is shown in Figure 1. The antenna is comprised of separate transmit and receive manifolds, a common set of beam steering phase shifters, a set of receive only phase shifters and an orthomode junction and septum polarizer RF quarter wave plate, which, in conjunction with the beam steering phase shifters provide duplexing action within the antenna feed network. Also included are the array face and the waveguide transmission lines which connect the array face to the phase shifter and manifold assemblies.



The antenna is non-reciprocal and can have independent, excessive boresight errors on both transmit and receive. Transmit beam pointing errors, if they exist, are corrected by the beam steering phase shifters; receive errors would be corrected by the receive only phase shifters. This paper will deal only with the correction of transmit boresight errors since the antennas on which this procedure was done contained only transmit errors. The beam pointing correction procedure is essentially the same on receive as it is for transmit, with a few minor modifications which will be discussed later.

In order to correct transmit beam pointing errors, the error in the slope of the linear phase taper across the scan plane of the array must be measured and corrected. Figure 2 shows an end view of the array and the scan plane beam pointing error $\Delta\Theta$.



Scan Plane Phase Slope Error
Figure 2

The phases associated with the scan plane elevation pointing error $\Delta\Theta$ are given by:

$$\Phi_k = (k - N/2 - .5) \Delta\phi \quad (1)$$

where: $\Delta\phi = 2\pi s(\sin(\Delta\Theta)/\lambda)$

s = scan plane radiator spacing

λ = free space wavelength

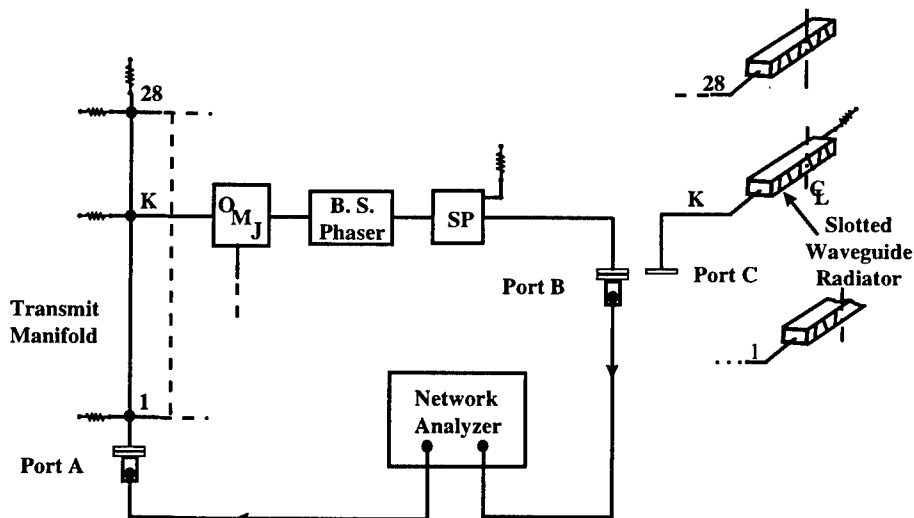
k = the number of the stick

$k = 1, 2, 3, \dots, 27, 28$

and

stick 1 is at the bottom of the array

Using the test setup of Figure 3, the insertion phase of ten of the twenty eight manifold feed lines are measured from port A, at the transmit manifold input, to port B, the input of the slotted waveguide radiating elements (sticks). It was found by experiment that measuring the phase of ten feed lines gives a phase slope measurement that is close enough to that obtained by measuring twenty eight feed lines that the required scan plan boresight error difference is negligible compared to the required beam pointing accuracy. The reason for examining this issue was to limit test and data reduction time since boresight errors at eight operating frequencies were required to be corrected for each antenna requiring scan plane beam pointing correction.



Antenna Feed Network Measurement Setup

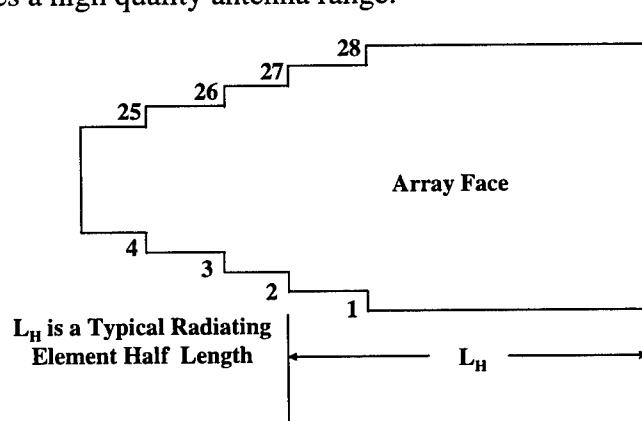
Figure 3

The ten feed lines on the antenna that are measured to obtain the required scan plane phase taper are spread "equally" across the scan plane of the array in

order to achieve the best accuracy in measuring the scan plane phase slope across the array.

Referring again to Figure 3, after the measurement of insertion phases between points A and B, it would normally be necessary to measure the insertion phases from the input to the center of each slotted waveguide radiator in order to account for the effects of this portion of the antenna on scan plane pointing error. It turns out, however, that this is not necessary since the phase velocities of all slotted radiators are matched to within such a small tolerance that equal length radiator paths are matched to within .05 degrees of phase per foot of distance along the slotted radiator. This is done to hold the azimuth beam of each slotted waveguide radiating element to a tight relative tolerance with respect to others in the array in order to control spurious sidelobes.

Thus the phase per unit length, along each of the twenty eight slotted waveguide radiators is held to a very tight tolerance about an unknown value. The fact that the baseline phase per unit length is unknown does not present a problem, however since the errors incurred due to this uncertainty provide an even function systematic error which does not affect the computed scan plane beam pointing angle error. This is demonstrated pictorially in Figure 4. Slotted waveguide radiators which are equidistant from the horizontal centerline of the array have the same physical length, thus ensuring an even function phase error in the unknown insertion phases from to the stick inputs to their center lines. This was a fortunate situation since an accurate insertion phase measurement of the slotted waveguide radiators requires a high quality antenna range.



Radiating Aperture Stick Half Length Profile
Demonstrating an Even Function
Figure 4

In order to obtain the slope of the scan plane phase front, a least squared fit to the measured phase values from each of the ten sticks used in this boresight correction was done and the measured slope obtained. From this, the inter-element scan plane phase differential, $\Delta\phi$, of equation (1) was obtained. Taking the negative of these values for each stick, per equation (1), and correcting the beam steering phase shifters of Figure 1 accordingly corrected the scan plane boresight error. The foregoing is done for each of the operating frequencies of the antenna, since the antenna beam pointing errors differed as a function of frequency.

The procedure was tried experimentally on an antenna which was installed at the Northrop Grumman antenna test range, having a preselected known beam pointing error, and the procedure verified to have accuracy well within the required scan plan beam pointing accuracy.

The procedure works the same for receive as it does for transmit except that the insertion phases which are measured are from the stick outputs to the output of the receive manifold and the errors are corrected in the receive phase shifters rather than in the beam steering phase shifters.

Conclusion

A cost effective solution to reboresighting a large antenna on its operational platform has been described. The aforementioned procedure can be done within a day or two without incurring the tremendous costs of taking the antenna back to a test range to have the scan plane errors corrected. The procedure corrects both transmit and receive at beam pointing errors at multiple frequencies and has the capability of correcting beam pointing errors as a function of scan angle if desired.

LOW-COST PORTABLE NEAR-FIELD ANTENNA MEASUREMENT SYSTEM

David P. Woollen¹, Jeffrey M. Snow¹, Allen R. Tillerson¹, William Slowey², George Leaf¹

¹Naval Surface Warfare Center Crane Division, code 8035, Crane, IN 47522

²Technology Service Corporation, Bloomington, IN 47404

Abstract

The Marine Corps desired a portable test system for the AN/TPS-59 radar antenna (a large, 15.2 feet by 29.1 feet, L-band phased array antenna) to verify on-site performance. The test system was also required to be capable of antenna acceptance testing at the overhaul depot. An innovative mechanical design using commercial off-the-shelf (COTS) products paved the way for the development of this low-cost portable system.

The low-frequency, moderate-sidelobe antenna characteristics allowed for flexibility in mechanical scanner design. The near-field scanner attaches directly to the antenna and is aligned in place. The Hewlett-Packard 8530 Antenna Measurement System is employed for data collection. An interface from the computer to the antenna was designed for beam-steering control (BSC). LabVIEW software controls the HP8530, the near-field scanner, BSC, and other miscellaneous RF hardware. Digital Visual Fortran 5.0 and Matlab are used to run the National Institute of Standards and Technology (NIST) near-field programs.

Keywords: antenna testing, commercial-off-the-shelf, planar near-field, portable, low cost

1.0 Introduction

The AN/TPS-59 radar (figure 1) is an L-band 3-D long range air search radar used by the Marine Corps. The antenna is a large (15.2 feet by 29.1 feet) phased array. The AN/TPS-59 radar is picking up the duty of Theater Ballistic Missile (TBM) defense. This radar is also starting to undergo major overhaul. These two significant events highlighted the need for an overall system test of the radar antenna. The large size of the antenna and its basic structure prevent a complete far-field test of the antenna. A near-field test of the antenna appeared to be the only method to evaluate a complete antenna. The acronym selected for this project was SPACS, representing Special Purpose Antenna Calibration System.



Figure 1. AN/TPS-59 Antenna

2.0 Description of AN/TPS-59

The antenna consists of 54 identical row feeds, each row feed has 24 radiating elements. The outer 6 radiating elements on each end of each row are connected via a rotary coupler to the center 12 elements. This allows the ends of the row feeds to be folded in for transportation, reducing the antenna width from 183 inches to 95 inches. When the row feed ends are folded out, they are supported by tubes that go at an angle from the end of the row feed to the support structure under the center of the row feeds. Row feeds are spaced 6.60 inches apart generating an antenna height of 350 inches. The antenna splits in half for transportation, which breaks the antenna into two 175 inch long halves. Three trailers carry the antenna, one trailer for each antenna half, and one trailer for the base pedestal and azimuth drive. To assemble the antenna the three trailers are fit together forming a rigid three legged structure with the base pedestal at the center of the structure. The lower antenna half is joined to the base pedestal with the antenna facing upward. Next, the upper antenna half is joined to the lower antenna half, still with the antenna facing directly

upward. The antenna is then tilted upward 78° until the antenna is 12° from vertical. The main structural backbone of the antenna is two C-channel beams each 12 inches deep and 4 inches wide.

3.0 Mechanical Scanner Design

3.1 Basic Design

A planar near-field design was selected as the most cost-effective near-field system for this antenna. A linear positioner, located in front of the row feeds, moves the radio frequency (RF) probe parallel to the row feeds. This is called the upper or x-axis positioner. Two coupled linear positioners, located behind the row feeds, move the upper x-axis positioner and its supporting structure perpendicular to the row feeds. These positioners are called the lower or y axis positioners. Figures 2 and 3 show the basic concept. The equipment must be capable of testing an antenna on site, therefore all equipment can be broken down in under 14 foot lengths for ease of shipping. The equipment was designed to be assembled by hand without cranes, forklift, or other load handling equipment. An accuracy of plus or minus 0.10 inches (about 0.01λ) was determined adequate for this low L-band and moderate sidelobe antenna.

3.2 Scanner Orientation and Mounting

There were two key mechanical design decisions. The first design decision was to test the antenna when

it is tilted up (12° from vertical) or tilted down (horizontal). It was decided to test the antenna while it was facing upward (horizontal position). This eliminated the problem of moving and holding a positioner and related structure against gravity. Also it eliminated the problem of erecting a tall structure or mounting structure and weight on an antenna whose top is 36 feet above ground.

The second design decision was to choose between mounting the positioners and related structure directly to the antenna structure or to an independent structure (an exoskeleton). It was decided to mount directly to the antenna structure. The decisive factor against the exoskeleton was the variety of site surfaces (concrete, dirt, asphalt, or sand).

3.3 Linear Positioners

Parker-Hauser linear positioners (figure 4) were selected. Other companies make similar positioners, however, no positioners of the required length (462 inches) were found. The Parker-Hauser linear positioners are hollow extrusions of aluminum with a cruciform interior and a slot to the outside. Carriages with multiple polyamide 12 (nylon 12) wheels ride on the interior surface of the extrusion, the carriages are positioned by a cogged (timing) belt reinforced with steel cords. The belt is moved by a grooved pulley connected to a speed reduction gearbox and bushless servo motor. Upper and lower positioners use the same size of gearbox (25:1) and motor (1 kW and 3,800 rpm).

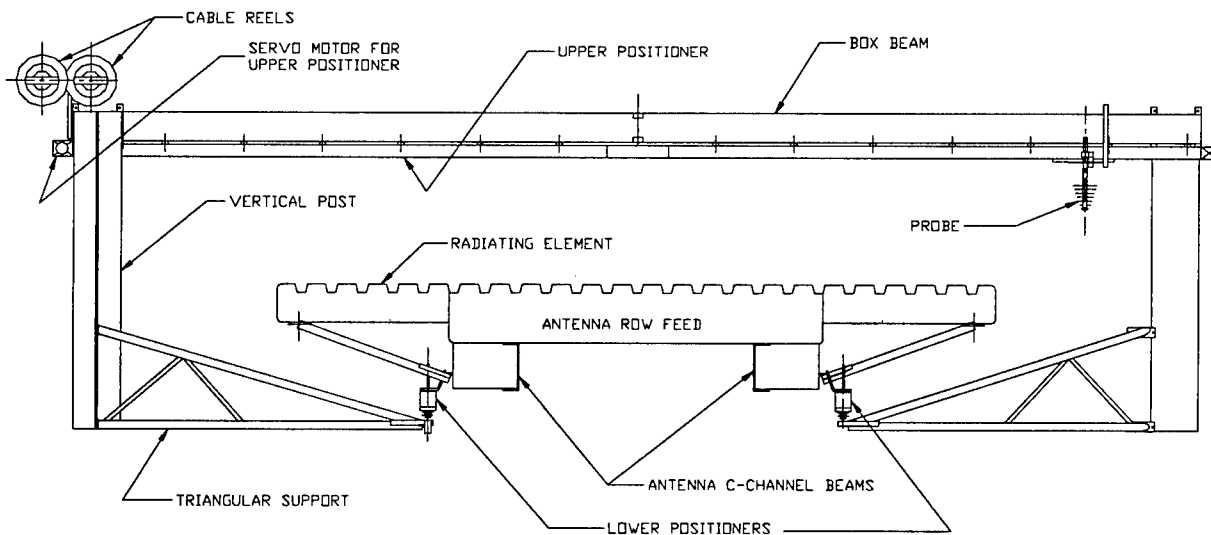


Figure 2. End View of Portable Near-Field System on AN/TPS-59 Antenna (absorber not shown)

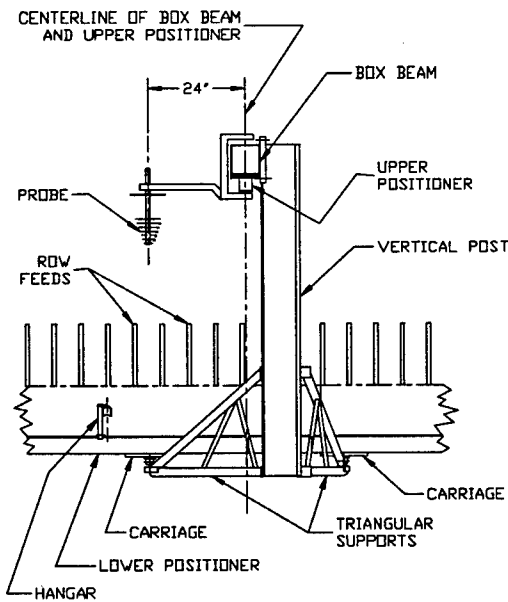


Figure 3. Partial Side View of Portable Near-Field System on AN/TPS-59 Antenna (cable reels and absorber not shown)

Parker-Hauser claimed a repeatability of 0.004 inches. For a short time test (i.e. no thermal movement) measured the same repeatability. If the stop position was approached from the same direction, 0.001 inch repeatability was achieved. While aluminum has a large thermal expansion coefficient the structural backbone of the antenna is also aluminum, therefore differences due to thermal movement will be minimized. The support structure was made from aluminum for the same reason. To minimize solar heating and subsequent thermal expansion effects, the structure was kept unpainted.

3.4 Probe Mounting, Upper Positioner and Related Structure

The upper positioner is supported by an aluminum structure that wraps around the antenna to ride on two lower positioners mounted underneath the antenna. Simple bolted joints were used throughout. These joints are not as quickly assembled as most other joint types, however, shims, spacer plates, or spool pieces can be quickly added to correct alignment problems or make design changes. Given the short project time, low budget, reduced access for prototype integration, and one-time nature of this project, the flexibility of simple bolt joints was very useful. Other joint types are also more expensive due to the tighter tolerances required.

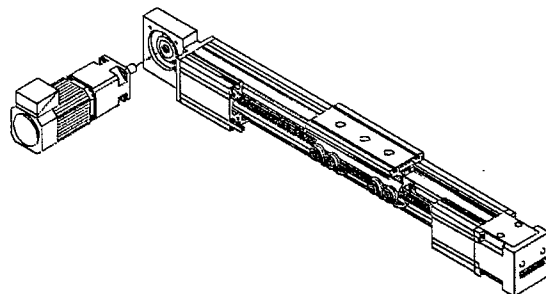


Figure 4. Parker-Hauser Linear Positioner

The probe is attached to a positioner carriage and offset 24 inches to either side of the centerline of the positioner and carriage. The 24 inch probe offset reduces RF reflections from the positioner and related support structure. Also, the 24 inch offset reduces the length of the lower positioners by 48 inches. The reduction in length of the lower positioners greatly reduces the structure required to support the cantilevered ends of the lower positioners. The probe is held at least two wavelengths away from the antenna face.

The upper positioner is approximately 280 inches long and splits in the middle for shipping. A 7 inch by 7 inch box beam supports the positioner and also splits in the middle. The positioner attaches to the box beam at 20 inches intervals. These attachment points are shimmed taking twist out of the positioner and adding deflection, to ensure the probe moves in a straight line. These added deflections account for the deflections due to the shifting weight of the carriage and probe assembly. A vertical post (82 inches long) bolts to each end of the box beam. The post has a triangular cross section for torsional stiffness and reduction of RF reflections. There are two carriages, 48 inches apart, on each lower positioner. A triangular support extends inward from each post to each of these carriages. The separation of 48 inches provides bending stiffness to the upper assembly. The total weight of the upper assembly is 370 pounds.

3.5 Lower Positioners

The two lower positioners are Parker-Hauser HLE 100a (462 inches long) which have a 100mm by 100mm external cross section. They are 104 inches apart and connected through a low speed shaft between the belt pulleys, which is driven by a gearbox and one motor. The positioners are attached to the antenna mostly via hangars on the angle support brackets of the row feeds. The ends of the positioners are supported by end beams and support triangles.

Each positioner breaks into three pieces for shipping. The weight of the two lower positioners is about 560 pounds (not including support structure).

3.6 Assembly and Alignment

The most time consuming activity of installing the equipment is alignment. The hangers and end beams with support triangles are placed and clamped in position. The lower positioner segments are attached to the hangers and triangles, aligned by eye and loosely clamped in place. A transit is used align the segments, plastic shims are used between the hangers and positioner to control the vertical alignment. Segments are joined together with temporary internal alignment plates at each joint. External plates are then clamped over the joint. A force gage is used to move a carriage through the joint. If excessive force is noted the joint is reworked to reduce the misalignment. The cogged drive belt is fed through the positioner drive and tensioning pulleys and attached to the carriages. The belt is then properly tensioned using screws in the tensioning pulley end assembly. Tension is determined by belt deflection and the equation for a catenary curve.

The upper assembly (with the upper positioner) is assembled on the ground. The positioner segments are joined in a similar fashion as the lower positioner except alignment using a transit is not necessary. The upper assembly is lifted by eight people and attached to the four carriages on the lower positioners. Both shims and leveling screws on these four carriages can be used to make the upper rail level with the row feeds. The shaft connecting the two lower positioners has a clutch type joint that allows any relative positioning of the carriages between the two positioners. This allows the upper rail to be made parallel to a row feed.

3.7 Cable Reel

A cable reel controls the RF cable between the probe and upper assembly. To prevent kinking of the cable when it is wound up, a cable drum was designed that is only one cable width wide. A standard industrial spring reel (relatively constant torque) was used to put a constant torque the drum. The minimum flexing bend radius was 5 inches. There are two cable reels, one for each polarization (if required). Movement of the upper carriage pulls the cable off the reel and pulls it along the top of the box beam. A RF rotary joint on the cable reel provides less than .01 VSWR variation with rotation.

3.8 Absorber

RF absorber panels were made to cover the adversely reflective portions of the upper positioner and box beam. The panels were designed to be quickly installed or removed. A 2.25 inch thick flat absorber was used. This gave adequate performance and did not have the thickness of pyramidal absorber. Flat absorber was placed over the portion of the vertical post that might reflect onto the antenna when the probe was at the extreme ends of travel.

4.0 Computer Hardware and Software

Several approaches were considered to accomplish all tasks required by the project. The final design choices were broken into four categories. The categories were scanner motion, data acquisition, beam-steering control and far-field pattern generation. Playing part in the decision, were availability of developed instrument drivers and associated computer hardware. Once all options were considered, National Instruments LabVIEW was selected for use in scanner motion, data acquisition and beam-steering control. Digital Visual Fortran and Matlab were selected for use in running the NIST routines to generate near-field to far-field transformations.

Pre-existing LabVIEW instrument drivers were available, from a secondary source, for use in development of scanner motion profiles. Also, available from the original manufacturer was the computer card for interface to the motor drives and controller. The Hewlett-Packard 8530 was used for data acquisition. LabVIEW drivers were developed for the HP 8530.

All data is collected in the same direction, and saved at the end of the test. Beam-steering control of the AN/TPS-59 is achieved again by use of LabVIEW software and a digital I/O card in conjunction with specific hardware designed and built by NSWC Crane. The beam-steering controller (BSC) is used to set phase shifters for the frequency and the applicable scan angle during the near-field test of the AUT.

The NIST planar near-field software was compiled and linked using the Digital Visual Fortran application. Minimal changes were required, mostly due to input/output issues. Matlab was used to format the measured data into the format required by the NIST programs. Matlab was also used as a graphics package for the graphical output. The analysis programs included a back-transform program for antenna diagnostics. Future plans are to use Matlab to provide a graphical user interface to the NIST software giving a more user-friendly environment.

5.0 Installation, Checkout and Debug Process

SPACS was installed on an AN/TPS-59 antenna for checkout and debugging. All electrical connections were made and the unit was aligned to the antenna. Probe movement, RF switch control, and beam steering were accomplished through the LabVIEW program. Figures 5 and 6 show various views of SPACS during the installation, checkout and debug process.

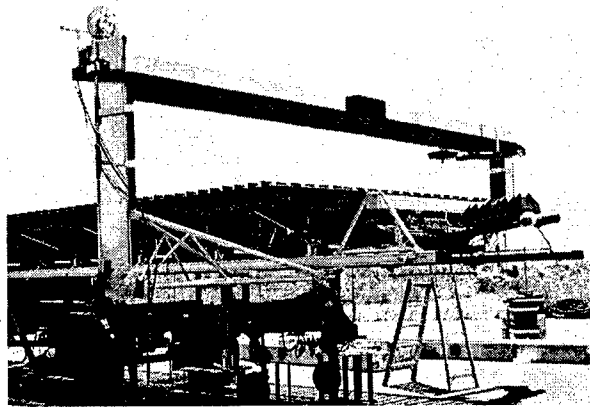


Figure 5. SPACS Installed on AN/TPS-59 Antenna (viewed from below)

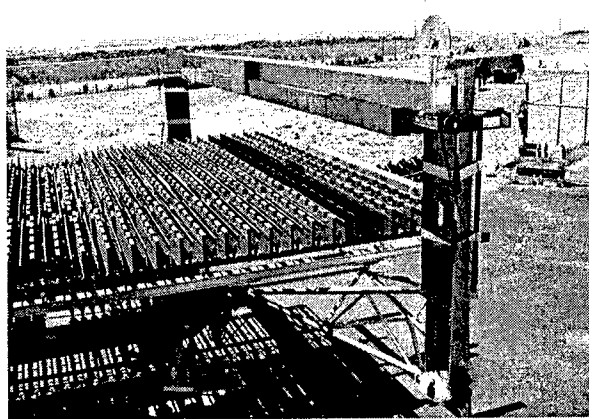


Figure 6. SPACS Installed on AN/TPS-59 Antenna (viewed from above)

An initial diagnostic test was performed to verify beam steering control and to estimate initial phase correction values. These initial phase correction values are required to correct for the unequal path lengths to each row of the antenna. Setting the phase

states to the correction values results in a broadside beam. This broadside beam was set and measured with SPACS. The resulting far-field pattern is shown in figure 7. The initial diagnostic and pattern tests revealed three dead rows on the main antenna. Testing also revealed several dead elements in one of the auxiliary antennas.

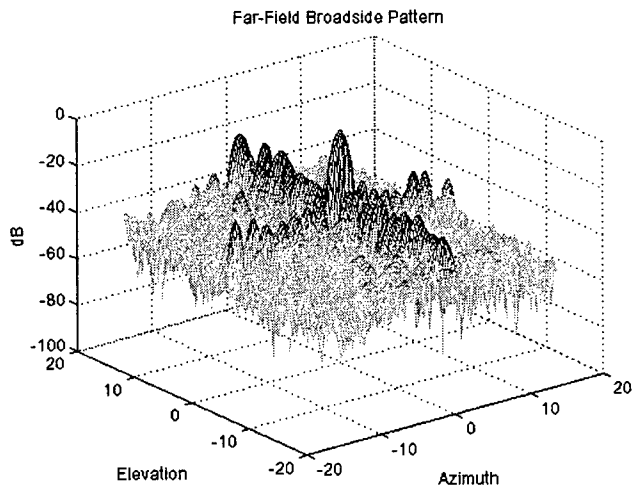


Figure 7. Three-Dimensional Far-Field Pattern of Broadside Beam

6.0 Conclusions

It is possible to design and build a portable near-field measurement system for a low L-band antenna that uses the antenna structure for the measurement systems support structure. It will be more difficult for higher frequency/lower side lobe antennas of the same size. Accurate structural modeling should be done of the combined antenna and near field structure to guard against unexpected deflections. Simple bolt joints offer great flexibility in alignment, low cost, improvement, and modification of one-time systems. Commercially available software facilitates the ease of measurement system development and lends to modification, upgrades and integration to new antenna systems.

Ultra-Wideband Coherent Processing

K.M. Cuomo

J.E. Piou

J.T. Mayhan

Lincoln Laboratory
Massachusetts Institute of Technology
244 Wood Street
Lexington, MA 02173

Abstract

Lincoln Laboratory has developed an approach for estimating a target's ultra-wideband radar signature from sparse sub-band measurements. The approach optimally determines the parameters of an appropriate signal model that best fits the measured data; the fitted signal model is then used to interpolate between and extrapolate outside of the measurement sub-bands. Standard pulse-compression methods are then applied to provide super-resolved range profiles of the target. The algorithm can automatically compensate for lack of mutual coherence between the radar sub-bands, providing the potential for ultra-wideband processing of real-world radar data collected by separate wideband radars. Since the processing preserves the phase distribution across the measured and estimated sub-bands, extended coherent processing can be applied to the ultra-wideband compressed radar pulses to generate super-resolved radar images of the target. Applications to static test range and field data show very promising results.

1. Introduction

Lincoln Laboratory has played a major role in the development of wideband radar systems for many years. The impetus for this development was rooted in the successful application of high power instrumentation radars for research in ballistic missile defense and satellite surveillance. Today's wideband imaging radars provide considerable real-time discrimination and combat identification capability. The

development of advanced signal processing methods have significantly improved the resolution of processed radar return signals, further improving the state-of-the-art in wideband radar technology.

The ability to identify targets and accurately estimate their size and shape is critical to many areas of national defense. The primary goal of a defensive radar system is to find the threat target and provide missile guidance to an interceptor so as to destroy the target with a high probability of success. This can be difficult when there are many objects in the radar's field of view, some purposefully designed to fool radar discrimination algorithms. Decoys, for example, may have radar-cross-section (RCS) levels similar to those of the warhead, making robust target selection based on RCS levels, alone, difficult. Narrowband radars usually lack sufficient range resolution to allow a direct measurement of the target's length, although they are generally useful for tracking and coarse motion estimation. Wideband radars permit a much larger suite of target discrimination algorithms to be employed. Real-time range-Doppler imaging and phase-derived range estimation, for example, are possible with today's wideband radar technology.

In figure 1, we illustrate a typical narrowband radar and wideband radar target response. The narrowband response indicates the position of the target as a whole with the peak RCS corresponding to the 'electromagnetic size' of the target. The wideband response provides resolution within the target's range profile. Individual scattering centers are isolated into small range-resolution cells providing a more direct measurement of the target's size and shape.

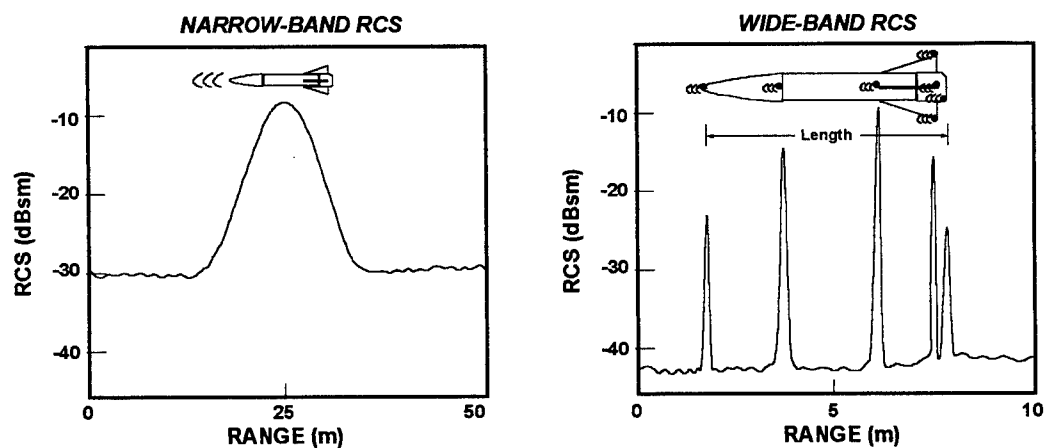


Figure 1. Comparison of a typical narrowband radar and wideband radar target response.

To achieve fine range resolution, field radars utilize coded waveforms with large time-bandwidth products. Wideband “chirp” waveforms are commonly used in practice due to their ease of generation and processing in the radar receiver. By mixing the radar return signals with a replica of the transmitted signal, a baseband signal is produced with frequency components that are proportional to the relative range between scattering centers on the target. The baseband signal is sampled and Fourier-transformed to provide a range-resolved profile of the target. This process is called pulse-compression. Properties of the compressed pulse, such as resolution and sidelobe levels, depend on the extent and shape of the window function applied to the baseband signal samples. The Fourier theory relations define resolution to be inversely proportional to the total signal length. This means that range resolution improves as radar bandwidth increases.

Many field radars operate on these basic wideband principles. As an example, we show in figure 2 an aerial view of the Kiernan Reentry Measurement System (KREMS) facility located on Kwajalein Atoll in the South Pacific. This facility has been the United States' most sophisticated and important wideband radar research center for over thirty years [1]. The photograph provides a clear view of several wideband field radars. The ALCOR C-band radar was developed in 1970 for the purpose of wideband discrimination research. ALCOR utilizes a wideband chirp waveform with a bandwidth of 512 MHz, providing ALCOR with a range resolution capability of about 53 cm. Kwajalein's millimeter-wave radar (MMW) can operate at the Ka- and W-bands and is capable of a transmission bandwidth of 2000 MHz, providing an impressive 14 cm range resolution capability.

The field radars discussed above provide a high degree of range resolution. Because their intended applications are usually very demanding, however, it is often desirable to significantly improve their existing range resolution capabilities: Important target features are often exhibited over a much smaller than conventionally-processed range resolution cell. To improve a radar's range resolution, one can either increase the radar's bandwidth or process the received signals with super-resolution algorithms. Cost and design limitations are major practical drawbacks to increasing a radar's hardware bandwidth. The desire to obtain higher-resolution radar data without incurring tremendous costs motivated us to develop robust super-resolution algorithms that can be applied to a wide range of real-world data sets.

In 1990, Lincoln Laboratory developed a practical super-resolution algorithm that can significantly improve the range resolution of processed radar return signals. The algorithm, which is referred to as bandwidth extrapolation (BWE) [2,3], increases the effective bandwidth of a radar waveform by predicting the

target's response at frequencies that lie outside of the measurement bands. In real-world radar applications, BWE typically improves the range resolution of compressed radar pulses by a factor of two or three. Bandwidth extrapolation often provides striking improvements in the quality of wideband radar images. As an example, we show in figure 3(a) a radar image of a simulated three-point target without BWE processing applied. The resolution is insufficient to clearly resolve the target points. In figure 3(b), we show the same target with BWE processing applied to the compressed radar pulses, first in the range dimension and then in cross-range. The BWE processed image is much more resolved, making it much easier to analyze and identify the target.

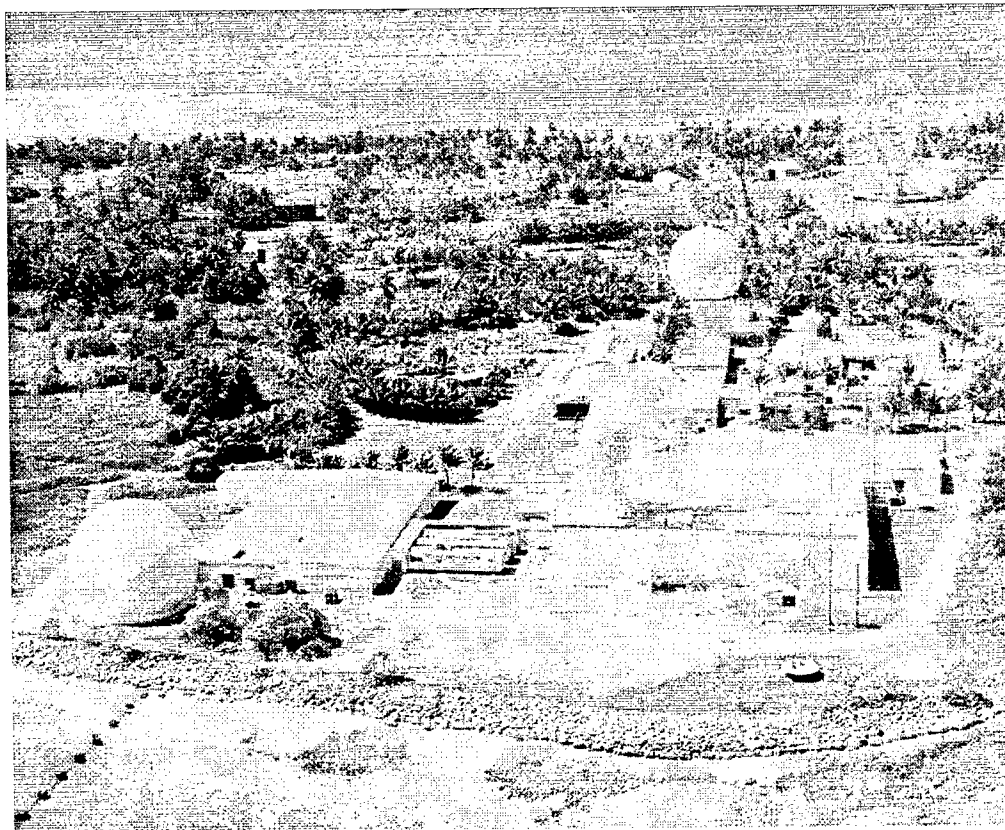


Figure 2. The Kiernan Reentry Measurement System (KREMS) facility located on Kwajalein Atoll in the Central Pacific.

Bandwidth extrapolation improves resolution, but the approach has some inherent limitations. The algorithm is based on signal processing models that characterize a complex target as a collection of point scatterers, each with its own frequency independent scattering amplitude. Such models are often sufficient for

typical wideband signal processing where the waveforms have only a small fractional bandwidth compared to the center frequency. Over ultra-wide bandwidths, i.e. where the radar's bandwidth is comparable to its center frequency, the scattering amplitude of the individual scattering centers can vary significantly with frequency. Spheres, edges, and surface joins are examples of realistic scattering centers that exhibit significant amplitude variations as a function of frequency.

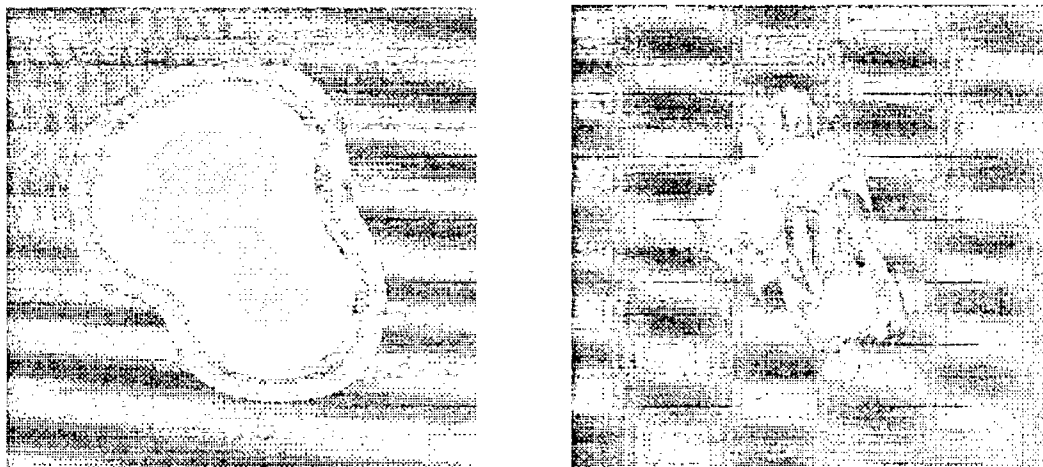


Figure 3. Demonstration of bandwidth extrapolation processing. (a) Three-point target image without bandwidth extrapolation processing; (b) Three-point target image with bandwidth extrapolation processing.

Measuring or estimating a target's ultra-wideband radar signature is very useful from many radar discrimination and target identification viewpoints. Not only would extremely fine range resolution be obtained, but the amplitude variations of isolated scattering centers would help in typing the scattering center. Many canonical scattering centers are known to exhibit f^α -type scattering behavior, e.g. the RCS of flat plates, singly curved surfaces (cone sections), and doubly curved surfaces (sphere) vary as f^2 , f^1 , and f^0 , respectively. The RCS of a curved edge varies as f^{-1} , whereas, a cone vertex may be characterized with an f^{-2} RCS frequency dependence. One of the goals of UWB processing is to detect these frequency dependent terms in the measured data and to exploit them for scattering type identification.

Fielding a true ultra-wideband radar can be very expensive. A more practical approach would be to use conventional wideband radars to sample the target's

response over a set of widely spaced sub-bands as illustrated in figure 4. In this figure, S- and X-band radars are used together to collect coherent target measurements over two widely spaced sub-bands. By coherently processing these sub-bands together, it is possible, in principle, to accurately estimate a target's ultra-wideband radar signature. This concept provides for considerable increases in processing bandwidth with corresponding improvements in range resolution and target characterization capability.

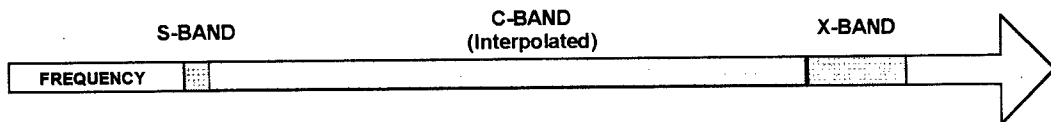


Figure 4. Ultra-wideband processing concept applied to sparse S- and X-band wideband radar measurements.

To perform ultra-wideband processing as illustrated in figure 4, a number of technical issues must be addressed. First, a robust signal processing method needs to be developed to compensate for the potential lack of mutual coherence between the various radar sub-bands. Having accomplished this, we must then fit an appropriate ultra-wideband signal model to the sparse sub-band measurements. The fitted signal model must accurately characterize ultra-wideband target scattering and provide for meaningful interpolations or extrapolations outside of the measurement sub-bands.

This paper discusses each of these concepts and is organized as follows. In Section 2, we discuss our current ultra-wideband processing algorithms. In Section 3, we apply these algorithms to static range data and discuss the results. Section 4 summarizes the main results of this work.

2. Ultra-Wideband Coherent Processing

2.1 Concept

An overview of our approach to ultra-wideband (UWB) coherent processing is illustrated in figure 5. An estimate of the target's ultra-wideband radar signature is obtained by coherently combining sparse sub-band measurements. While the figure illustrates UWB processing for only two sub-bands, it is straightforward to apply this concept to an arbitrary number of sub-bands.

The process illustrated is divided into three major steps:

1. signal processing is used to mutually cohere the radar sub-bands;
2. an ultra-wideband signal model is optimally fit to the mutually coherent sub-bands; the fitted model is used to interpolate between and extrapolate outside of the measurement bands; and
3. standard pulse compression methods are applied to the enlarged band of spectral data to provide a super-resolved range profile of the target.

Step 3 is straightforward; below, we discuss steps 1 and 2 in more detail.

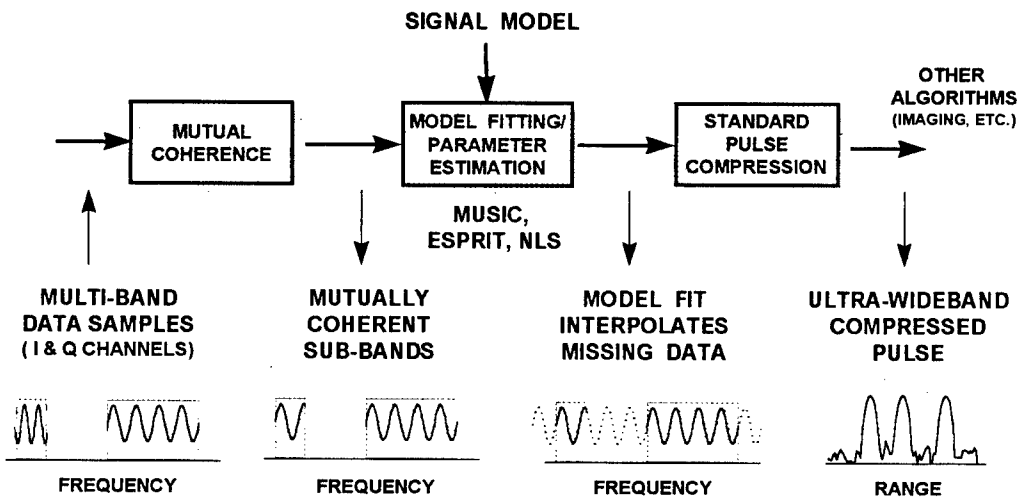


Figure 5. Ultra-wideband processing concept. Sparse sub-band measurements are used to estimate the target's ultra-wideband radar signature.

Step 1 is important when applying UWB processing to field data collected by separate wideband radars. Time delays and phase differences between the radars can make them mutually incoherent. To cohere the sub-bands, we fit an all-pole signal model to the spectral data samples in each sub-band and adjust the models until they optimally match. Corresponding corrections are then applied to the underlying data samples. This approach assumes, of course, that the target can be accurately characterized by a superposition of discrete scattering elements. This is often a valid assumption for targets that are large with respect to a radar's wavelength [4-6]. In section 2.2, we provide a more detailed discussion of mutual coherence processing.

In Step 2, we fit a global all-pole signal model to the mutually coherent sub-bands. We then use the model for interpolation and/or extrapolation purposes. All-pole models are well-suited for UWB processing; they accurately characterize the target by a superposition of discrete scattering centers, each with its own frequency dependent term. While all-pole models are best matched to signals that grow or decay exponentially fast with frequency, they can also be used to accurately characterize scattering behavior over finite bandwidth intervals. This issue is further discussed in Section 2.3 where we develop an algorithm, which uses sparse sub-band measurements to estimate the global all-pole model parameters. Below, we discuss mutual coherence processing and introduce some notation that will be used throughout the article.

2.2 Mutual Coherence Processing

Ultra-wideband processing requires a consistent set of spectral signals in each sub-band, i.e. the all-pole models for each sub-band must be consistent. This is not an issue in multi-band radar systems specifically designed to be mutually coherent. Mutual coherence problems will most likely occur, however, when separate wideband radars operating independently collect the sub-band measurements. This section discusses a straightforward signal processing approach that can compensate for the potential lack of mutual coherence between any number of radar sub-bands. The technique allows us to apply UWB processing across a wider range of radar platforms used in the field.

For illustration purposes, we simulate the radar returns for a hypothetical target consisting of two discrete scattering centers. The scattering center closest to the radar has a scattering amplitude that decays with frequency, whereas the scattering center away from the radar has a scattering amplitude that grows with frequency. The simulated spectral signal samples are given by

$$s_n = 4 \left(\frac{f_n}{f_1} \right)^{-1} e^{i \frac{\pi}{4} n} + \left(\frac{f_n}{f_1} \right)^{+1} e^{i \frac{\pi}{3} n} . \quad (1)$$

The frequency sampled phase terms correspond to a scattering center separation of 15 cm. White Gaussian noise was added to each signal sample; the signal-to-noise ratio is 20 dB.

Let us assume that only two sub-bands are available for coherent processing of the noisy s_n signal as illustrated in figure 6(a). The s_n signal samples in the lower

sub-band have been modulated by the function $e^{-i\frac{\pi}{9}n}$ to simulate the effects of mutual incoherence, i.e. the signal poles for the lower sub-band have been rotated twenty degrees clockwise relative to the upper sub-band signal poles. In figure 6(b), we show the corresponding compressed-pulses; the pulses do not line up because the sub-bands are not mutually coherent. In effect, mutual coherence is seen to be a consequence of uncertainty in position and time sequencing of the separate radars.

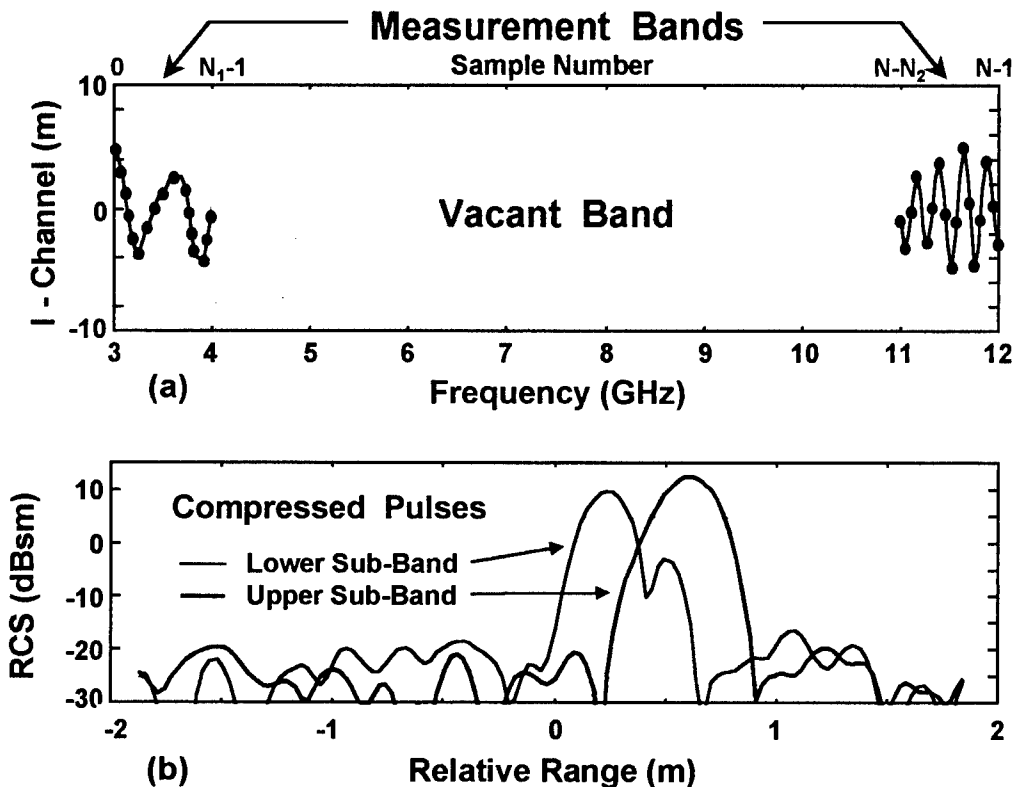


Figure 6. (a) Sparse multi-band measurements of a target consisting of two closely-spaced scattering centers; one scatterer has an amplitude that decays with frequency while the other scatterer's amplitude grows with frequency. The two sub-bands illustrated are not mutually coherent. (b) The corresponding compressed pulses. The pulses do not line up in range because the sub-bands are mutually incoherent.

We begin the mutual cohering process by modeling the spectral signals in each sub-band by a superposition of complex exponential functions. An all-pole signal model of the form

$$M(f_n) = \sum_{k=1}^P a_k p_k^n \quad (2)$$

is used for this purpose. The sample index n ranges from $n=0, \dots, N_I-1$ for the lower sub-band and from $n=N-N_2, \dots, N-1$ for the upper sub-band. Note that the all-pole model parameters are physically meaningful. The number of scattering centers and their complex amplitudes are denoted by P and a_k , respectively. The poles p_k characterize the relative ranges and frequency decay of the individual scattering centers, where the f^α frequency decay model indicated earlier is approximated by an exponential variation over the band of interest. The sub-bands can be mutually cohered by fitting a separate all-pole model to each sub-band and adjusting the models until they are consistent. Below, we discuss the sub-band modeling and mutual coherence process.

Our approach to all-pole modeling utilizes the singular-value-decomposition (SVD) of the forward prediction matrix. Specifically, the forward prediction matrix for the lower sub-band is given by

$$H_I = \begin{bmatrix} s_0 & s_1 & \dots & s_{L-1} \\ s_1 & s_2 & \dots & s_L \\ \vdots & \vdots & \vdots & \vdots \\ s_{N_I-L} & s_{N_I-L+1} & \dots & s_{N_I-1} \end{bmatrix},$$

where L denotes the correlation window length and the s_n are the frequency domain radar measurements. The matrix H_I has a special form; it is a Hankel matrix. Hankel matrices are associated with the transient response of linear-time-invariant (LTI) systems. Subspace decomposition methods exploit the eigenstructure of Hankel matrices to estimate the parameters of LTI signal models [7]. Using a correlation window length $L=N_I/3$ generally provides for robust parameter estimates. Larger values of L can provide better resolution but the estimates may not be as robust to noise. The forward prediction matrix H_2 for the upper sub-band is constructed in a similar way; it is given by

$$H_2 = \begin{bmatrix} s_{N-N_2} & s_{N-N_2+1} & \dots & s_{N-N_2+L-1} \\ s_{N-N_2+1} & s_{N-N_2+2} & \dots & s_{N-N_2+L} \\ \vdots & \vdots & \vdots & \vdots \\ s_{N-L} & s_{N-L+1} & \dots & s_{N-1} \end{bmatrix}.$$

To estimate the all-pole model parameters for the lower and upper sub-bands, we apply the SVD to H_1 and H_2 , respectively. The SVD decomposes H_1 and H_2 into the product of three matrices:

$$H_1 = U_1 S_1 V_1' ,$$

$$H_2 = U_2 S_2 V_2' ,$$

where the symbol “ \prime ” denotes the Hermitian operator. The S matrices are diagonal and positive definite; they contain the “singular values” for the two sub-bands. The U and V matrices contain the corresponding eigenvectors. In particular, the columns of V correspond to the eigenvectors of the sub-band covariance matrices. By decomposing H_1 and H_2 in this way, it is straightforward to estimate the all-pole model parameters for each sub-band. This is done in the four step process listed below.

1. The singular value matrices S_1 and S_2 are used to estimate the model orders P_1 and P_2 for the two sub-bands;
2. P_1 and P_2 are used to partition V_1 and V_2 into orthogonal subspaces – a signal-plus-noise subspace and a noise subspace. A modified root-MUSIC algorithm (discussed below) is applied to estimate the signal poles for each sub-band;
3. The all-pole model amplitude coefficients, a_k , are solved for using a linear least-squares fit to the measured data; and
4. The resulting sub-band signal models are adjusted so that they optimally match.

In Step 1, the singular values in S are used to estimate appropriate model orders for the two sub-bands. The relatively large singular values in S correspond to strong signal components, while the small singular values generally correspond to noise. For low noise levels, there is a sharp transition between the large and small singular values. The transition point can be used as an estimate of the model order. At higher noise levels the transition from large to small singular values is smooth making accurate model order estimation more difficult. The Akaike Information Criterion (AIC) [8,9] and Minimum Description Length (MDL) [10,11] are two model order estimation methods that tend to work well in these cases. In figure 7, we show the singular value spectra for the two sub-band data set in figure 6. The AIC and MDL model order estimates are both correctly equal to two.

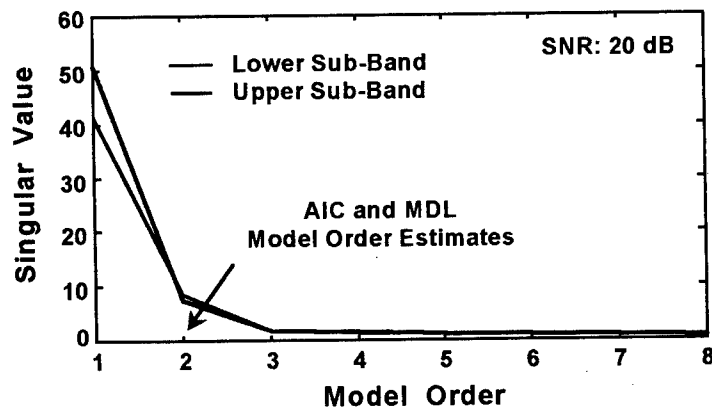


Figure 7. Singular value spectra for the two sub-band data set illustrated in figure 6.

Once the model orders P_1 and P_2 have been estimated, we proceed to step 2 where the subspace decomposition properties of V_1 and V_2 are used to estimate the dominant signal poles for each sub-band. The matrices V_1 and V_2 are partitioned into orthogonal signal-plus-noise and noise subspaces,

$$V_1 = [V_1^{sn} \ V_1^n],$$

$$V_2 = [V_2^{sn} \ V_2^n].$$

The partitioning is performed so that V_1^{sn} and V_2^{sn} have P_1 and P_2 columns, respectively. The noise subspace matrices V_1^n and V_2^n have $L - P_1$ and $L - P_2$ columns, respectively. Pole estimates for each sub-band are obtained by employing a modified root-MUSIC algorithm as described below. Matrices A_1 and A_2 are defined from the noise subspace vectors for each sub-band as follows.

$$A_1 = V_1^n V_1^{n \prime},$$

$$A_2 = V_2^n V_2^{n \prime}$$

Denote by a_{1i} the elements of the first row of A_1 and by b_{1i} the elements of the first row of A_2 . These elements are used to form polynomials $A_1(z)$ and $A_2(z)$ given by

$$A_1(z) = \sum_{i=1}^L a_{1i} z^{(i-1)}$$

$$A_2(z) = \sum_{i=1}^L b_{1i} z^{(i-1)}$$

The roots of $A_1(z)$ and $A_2(z)$ correspond to pole estimates for bands 1 and 2, respectively. This approach can be viewed as a variant of the traditional root-MUSIC algorithm described in [12]. Pole estimates can also be obtained by applying one of the spectral estimation techniques described in [13-19]. Our approach has the important advantage of providing high-resolution pole estimates while eliminating the symmetric pole ambiguities that result from the traditional root-MUSIC approach.

The root-MUSIC approach finds poles corresponding to the signal vectors that are most orthogonal to the noise subspace vectors. In general, the f^α variation of the signal model leads to poles displaced off the unit circle in the complex z -plane. However, over each sub-band, the variation of f^α is small, so that the dominant signals correspond to poles that lie close to the unit circle. Following our model order estimates in Step 1, we use the P_1 poles closest to the unit circle to characterize the dominant lower sub-band signals and the P_2 poles closest to the unit circle to characterize the dominant upper sub-band signals. In figure 8, we show the resulting pole estimates for the two sub-band data set illustrated in figure 6. The poles shown in darker print are considered the dominant signal poles for the lower and upper sub-bands, respectively. Notice that the signal poles in the lower sub-band do not line-up with the signal poles in the upper sub-band. This is due to lack of mutual coherence. Before making the required mutual coherence adjustments, we need to complete the all-pole modeling process as discussed below.

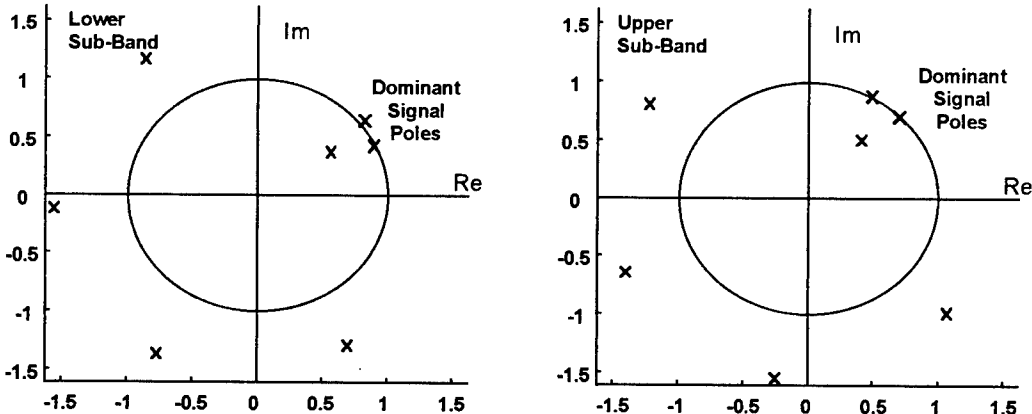


Figure 8. Pole estimates for the two sub-band data set illustrated in figure 6. The dominant signal poles in the lower and upper sub-bands are emphasized.

In Step 3, we estimate the all-pole amplitude coefficients, a_k , for the lower and upper sub-bands. This step is straightforward; an optimal set of amplitude coefficients can be found by solving a standard linear least-squares problem. This step completes the all-pole modeling process for each sub-band. The lower and upper sub-band signal models will be denoted by $M_1(f_n)$ and $M_2(f_n)$, respectively.

In Step 4, the sub-band signal models $M_1(f_n)$ and $M_2(f_n)$, are adjusted until they optimally match. There are many ways to do this. A straightforward method involves modulating and phase aligning the lower sub-band signal model until it closely matches the upper sub-band signal model. For example, the coherence function C ,

$$C = \sum_{n=0}^{N-1} |AM_1(f_n)e^{i\Delta\theta n} - M_2(f_n)|^2, \quad (3)$$

can be minimized with respect to the pole rotation angle $\Delta\theta$ and complex amplitude coefficient A . Another approach for matching the sub-band signal models is to find an appropriate rotation matrix that best aligns the signal subspace vectors contained in V_1 and V_2 . Whichever method is employed, the sub-band model alignment process will tend to promote a strong sense of mutual coherence between the two sub-bands as illustrated below.

In figure 9(a), we show the mutually incoherent sub-band signal models. In figure 9(b), an optimal pole rotation angle $\Delta\theta^*$ and complex amplitude coefficient A^* was applied to the lower sub-band signal model and corresponding data samples, i.e. the lower sub-band data samples were replaced by mutually coherent data samples \tilde{s}_n given by

$$\tilde{s}_n = s_n e^{i(\Delta\theta^* n + \angle A^*)}, \quad \text{for } n=0, \dots, N_1-1. \quad (4)$$

Although the two signal models in figure 9(b) may not entirely agree, it is important to recognize that they have approximately the same signal poles. The corresponding all-pole model coefficients a_k , however, are significantly different. The lower sub-band favors the decaying signal component whereas the upper sub-band favors the growing signal component. Below, we show how to coherently combine the two sub-bands using a single all-pole signal model.

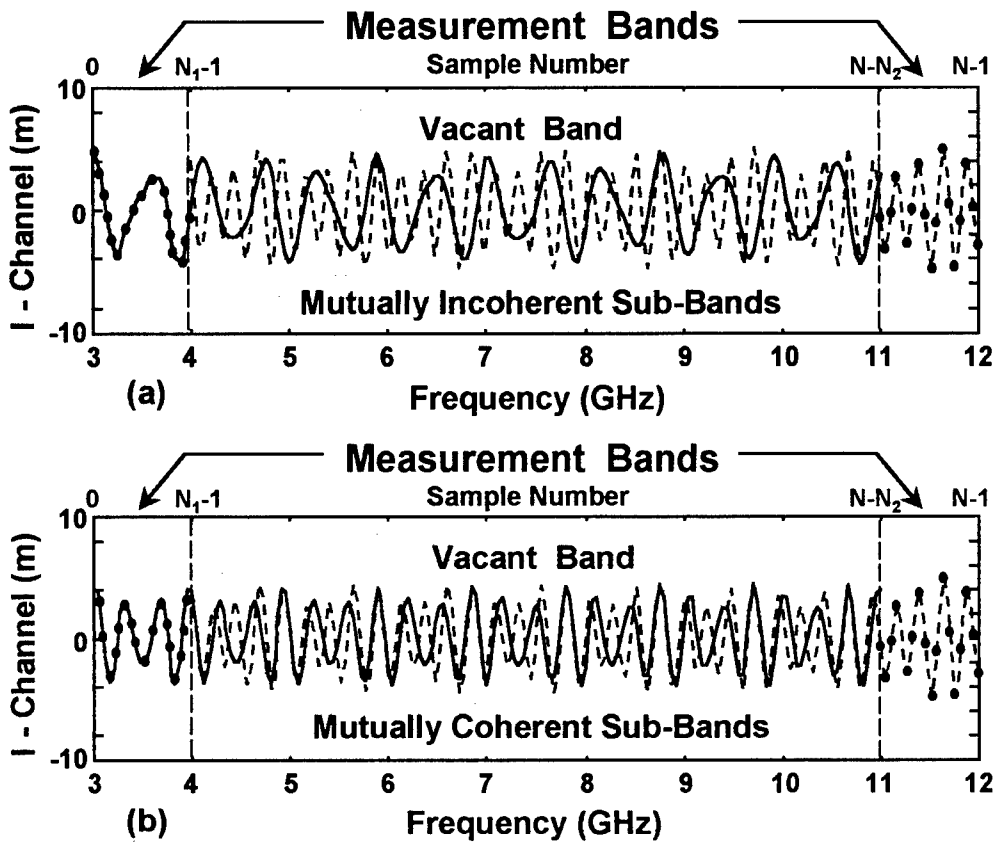


Figure 9. Mutual coherence processing applied to the sparse sub-band data set illustrated in figure 6. (a) Lower (solid line) and upper(dashed line) sub-band models before; and (b) after mutual coherence processing.

2.3 Ultra-Wideband Parameter Estimation and Prediction

Once the radar sub-bands have been mutually cohered, a global all-pole signal model is optimally fit to the measured data. Our approach determines the all-pole model parameters that minimize the function J given by

$$J = \sum_{n} q_n |s_n - M(f_n)|^2. \quad (5)$$

The index n ranges over *all* of the available data samples. The function J measures the total weighted error between the model

$$M(f_n) = \sum_{k=1}^P a_k p_k^n \quad (6)$$

and the mutually coherent data samples in each sub-band. The coefficients q_n are used to weight the measurements appropriately.

Minimizing J with respect to the all-pole model parameters is, unfortunately, a difficult nonlinear problem with no closed-form solution. Brute force numerical solutions are also infeasible due to the potentially large number of signal parameters that need to be estimated. One approach to solving this problem is illustrated in figure 10. Initial estimates of the all-pole model parameters are obtained using the SVD-based technique shown in red. These initial estimates are then iteratively optimized using a Newton-Raphson (NR) nonlinear least-squares algorithm. If the initial parameter estimates are close to optimal, the NR-algorithm will rapidly converge to the all-pole model parameters that minimize J . Below, we further discuss the initial parameter estimation step.

There are many ways to obtain an initial estimate of the global all-pole model parameters. One approach is to construct the multi-band prediction matrix H given by

$$H = \begin{bmatrix} H_1 \\ H_2 \end{bmatrix}$$

The sub-matrices H_1 and H_2 correspond to the forward prediction matrices for the lower and upper sub-bands, respectively. We refer to this approach as sub-aperture processing. The approach combines the data samples from both sub-bands, providing the potential for robust parameters estimates from noisy data. It is also possible to obtain multi-band parameter estimates by allowing for cross-correlation between the sub-bands, i.e. by defining H as

$$H = [H_1 \ H_2]$$

We refer to this method as extended aperture processing. Extended aperture processing provides the potential for true ultra-wideband resolution, although the resulting pole estimates are typically more sensitive to noise. In principle, the two methods, sub-aperture processing and extended aperture processing can be combined to provide robust high-resolution estimates of the dominant signal poles.

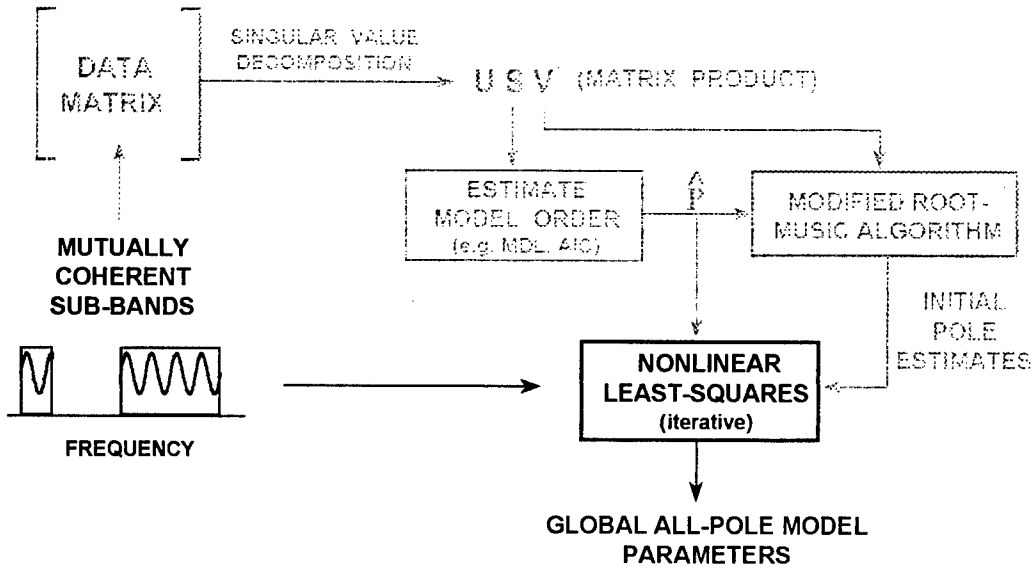


Figure 10. Ultra-wideband parameter estimation. Initial parameter estimates are obtained using a singular-value-decomposition technique (light gray). The initial parameter estimates are iteratively optimized using a Newton-Raphson nonlinear least-squares algorithm.

In either case, multi-band parameter estimates are obtained by decomposing H into the product of three matrices

$$H = USV'$$

An estimate of the model order P is obtained by applying the AIC or MDL techniques to the spectrum of singular values contained in S . For the sparse sub-band data set illustrated in figure 9(b), both the AIC and MDL model order estimates are correctly equal to two. The model order estimate is used to partition V into orthogonal signal-plus-noise and noise subspaces. Initial pole estimates are obtained using the methods of Section 2.2, or any other super-resolution spectral estimation technique.

In figure 11, we show a plot of initial pole estimates for the sparse sub-band data set illustrated in figure 9(b). Note that by including both H_1 and H_2 into the Hankel matrix, both signal poles are correctly identified and associated as f^{+1} and f^{-1} type pole behavior. The two dominant signal poles are used to initialize the Newton-Raphson algorithm as discussed below.

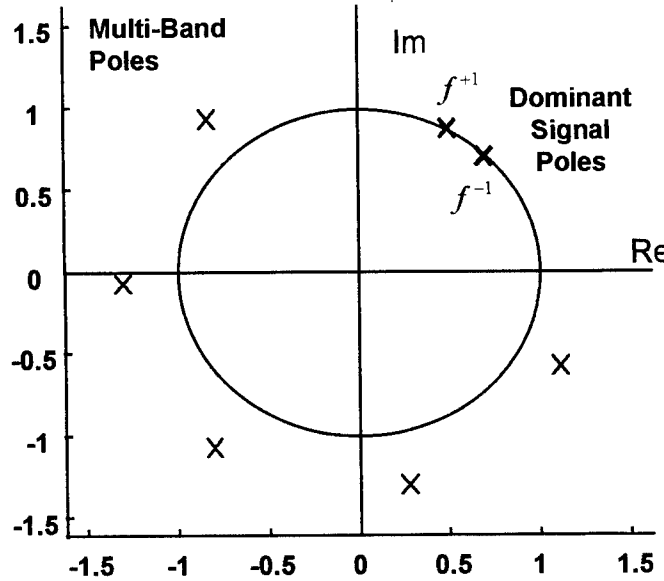


Figure 11. Multi-band pole estimates for the mutually coherent sub-bands illustrated in figure 9(b). The dominant signal pole inside the unit circle corresponds to the f^{-1} scattering center; the dominant signal pole outside the unit circle corresponds to the f^{+1} scattering center.

The NR-algorithm uses the initial parameter estimates to find the global all-pole model parameters, a_k and p_k , that locally minimize the cost function J . The model order P remains fixed during this iterative process. The algorithm typically converges to a local minimum of J in only a few iterations. Details of the NR-algorithm can be found in many standard texts on numerical analysis [20]. Below, we test the approach by optimally fitting a global all-pole signal model to the two sub-bands illustrated in figure 9(b).

In figure 12(a), we show a comparison between the global all-pole signal model and truth. The all-pole model is in excellent agreement with truth over the entire ultra-wideband frequency range. The corresponding compressed pulses are shown in figure 12(b). The sparse sub-band compressed pulse uses the mutually coherent radar measurements within the two sub-bands and the global all-pole model in the vacant band. This approach clearly performs well; the two target points are well-resolved with the estimated ultra-wideband response closely matching truth.

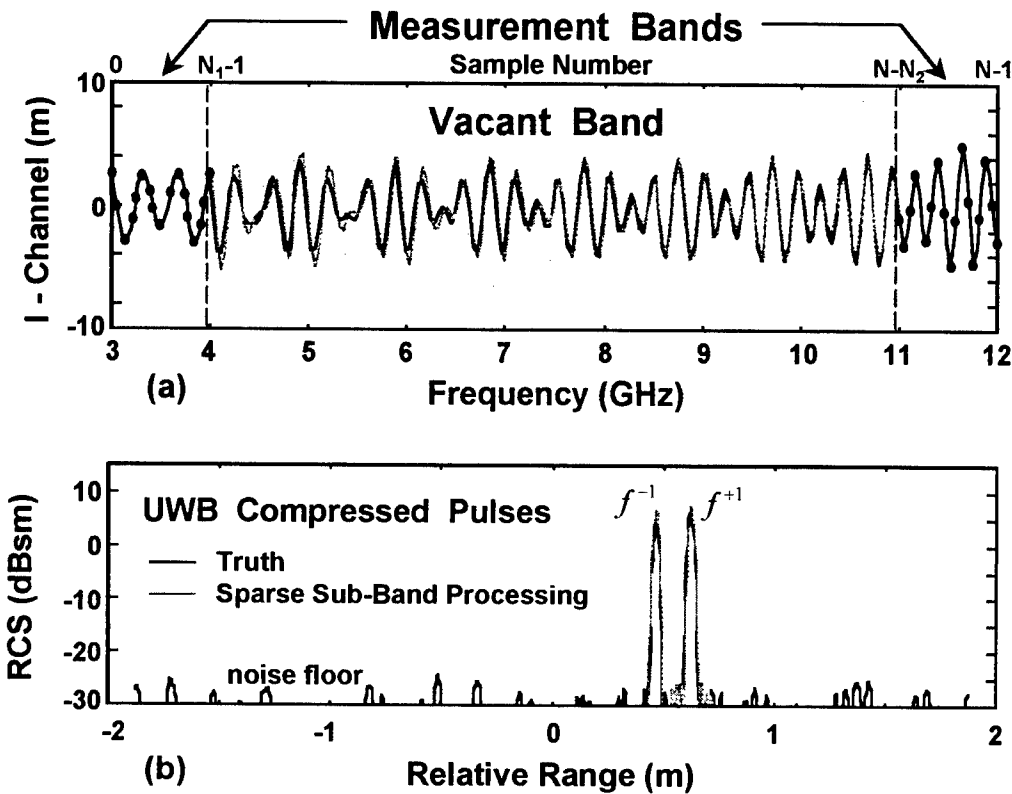


Figure 12. (a) Comparison between the fitted ultra-wideband signal model (light gray line) and truth. (black line). (b) The corresponding compressed pulses. The two scattering centers are well-resolved with the ultra-wideband model closely matching truth.

This example also demonstrates the potential for using all-pole signal models to accurately characterizing f^α -type scattering behavior over ultra-wide bandwidths. In fact, the ultra-wideband pole estimates can be transformed into equivalent estimates of the α coefficients for f^α -type signal models. Clearly, it is always possible to find an f^α function that best matches the exponential behavior of an ultra-wideband signal pole over a given frequency range. One may also derive an approximate analytical relationship between the pole magnitudes and the corresponding α coefficients by matching the functions f^{α_k} and $|p_k|^\alpha$ at the lowest and highest ultra-wideband frequencies. This relationship is given by

$$\alpha_k = \frac{(N-1) \log(|p_k|)}{\log(1 + (N-1) \frac{df}{f_1})} , \quad (7)$$

where df and f_1 denote the spectral sample spacing and lowest ultra-wideband frequency, respectively. The constant N denotes the total number of ultra-wideband frequency samples. In the two scattering center example discussed above, the two dominant signal poles p_1 and p_2 are given by

$$p_1 = 0.992e^{i\pi/4}$$

$$p_2 = 1.005e^{i\pi/3}$$

By substituting these poles into equation (7), one obtains an accurate estimate of the true α coefficients used in the simulation. Thus, the ultra-wideband pole locations provide scatterer-typing information. This information is useful for analyzing the details of targets with the viewpoint of constructing an accurate measurement-based model.

In the next section, we apply these ultra-wideband modeling concepts to radar data collected at a static test range.

3. Static Range Experiments

In section 2, we presented the basic concepts behind our ultra-wideband processing algorithms. In this section, we utilize static range data to demonstrate the applied aspects of ultra-wideband processing.

The target that we will use for the ultra-wideband processing demonstration is shown in figure 13. The target is a monoconic model of a reentry vehicle (RV); the total length is about 1.6 m. The nose-tip of the RV is spherical with a radius of 0.22 cm. The nose section is made from one solid piece of machined aluminum with two grooves and one seam. The first groove is approximately 3 mm deep and 6 mm wide, and is located about 22 cm from the RV's nose-tip. The second groove is approximately 2 mm deep and 4 mm wide, and is located about 44 cm from the RV's nose-tip. The mid-body of the RV is made from a single sheet of rolled aluminum with one groove, one slip-on ring and three seams. The aluminum slip-on ring (not shown in the photo) is approximately 5 mm thick and 10 mm wide, and is placed about 1.4 m from the RV's nose-tip.

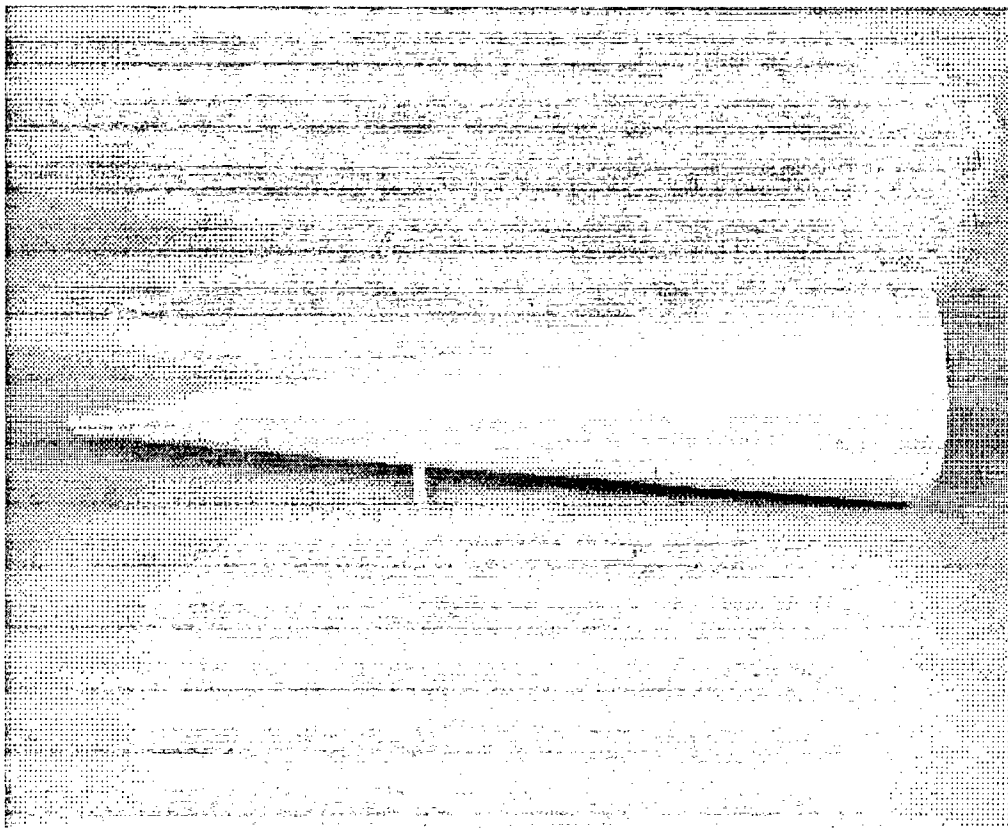


Figure 13. Test target for ultra-wideband processing experiments.

The Lincoln Laboratory static range radar facility was used to collect coherent radar measurements over a wide range of frequencies and viewing aspects of the target. Measurements were taken from 4.64- to 18-GHz in 40 MHz increments. The target viewing angles, relative to nose-on, ranged from -5 deg to 95 deg in 0.25 degree increments. The RV shown in figure 13 is ideal for ultra-wideband processing experiments. The RV has several scattering centers that exhibit significant radar-cross-section variations as a function of frequency. The grooves exhibit the expected f^3 scattering behavior at the low frequency end of the data collection interval.

To demonstrate ultra-wideband processing, we focused on a segment of data collected in the 12- to 18-GHz region. To test our ultra-wideband processing algorithms, we thinned the bandwidth of the uncompressed radar pulses to two 1.0 GHz wide sub-bands – a 13 to 14 GHz sub-band and a 16 to 17 GHz sub-band. The bandwidth of the two sub-bands is insufficient to resolve many of the

scattering centers on the target. We now demonstrate the ability to coherently process the sub-band measurements in a way that allows the target's ultra-wideband response to be accurately estimated.

In figure 14, we show the ultra-wideband pole estimates that were obtained by applying the sparse sub-band spectral estimation technique discussed in section 2. The pole locations are consistent with the physical scattering centers on the target. The pole corresponding to the nose-tip response is close to the unit circle indicating that it has a nearly constant radar cross-section as a function of frequency. The grooves and slip-on ring have non-constant radar cross-sections as a function of frequency, resulting in pole estimates that are either inside or outside the unit circle depending on the functional behavior of the radar scattering.

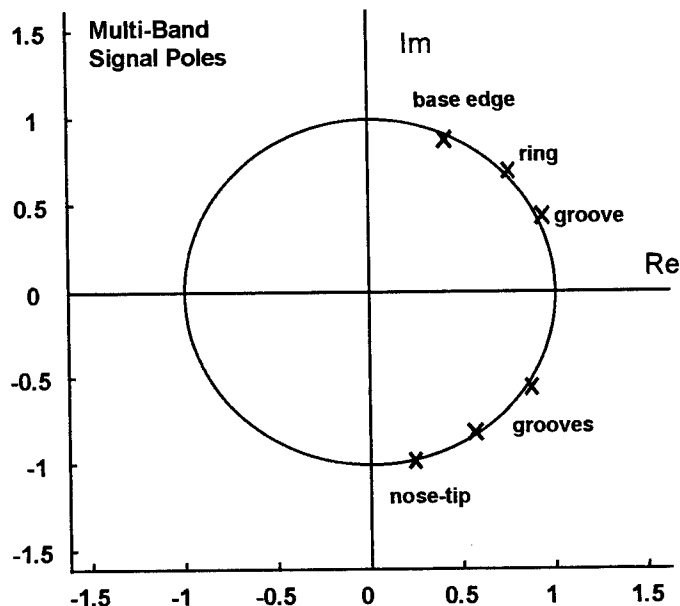


Figure 14. Ultra-wideband pole estimates obtained by coherent ultra-wideband processing of two radar sub-bands -- 13 to 14 GHz and 16 to 17 GHz.

Estimating the corresponding α coefficients for these major scattering centers is straightforward; the magnitude of the signal poles is related to the α coefficients via equation (7). A more accurate relationship can be obtained by solving for the α coefficients that produce the best match between the functions f^{α_k} and $|p_k|''$ over the frequency range of interest, i.e. from 12- to 18 GHz. Using this approach, we estimated the α coefficients for the three major grooves on the RV to be

$$\alpha_1 = -1.1$$

$$\alpha_2 = 2.3$$

$$\alpha_3 = 2.9$$

The coefficients α_1 , α_2 , and α_3 denote the forward, second, and mid-body grooves, respectively. These estimates are consistent with physical optics calculation (not shown in this paper).

In figure 15(a) and (b), we show comparisons between the estimated ultra-wideband target response and the true ultra-wideband radar measurements. The model and the measurements are in excellent agreement. Note that the estimated ultra-wideband target response used measurement data from only two relatively narrow sub-bands as indicated in the figure.

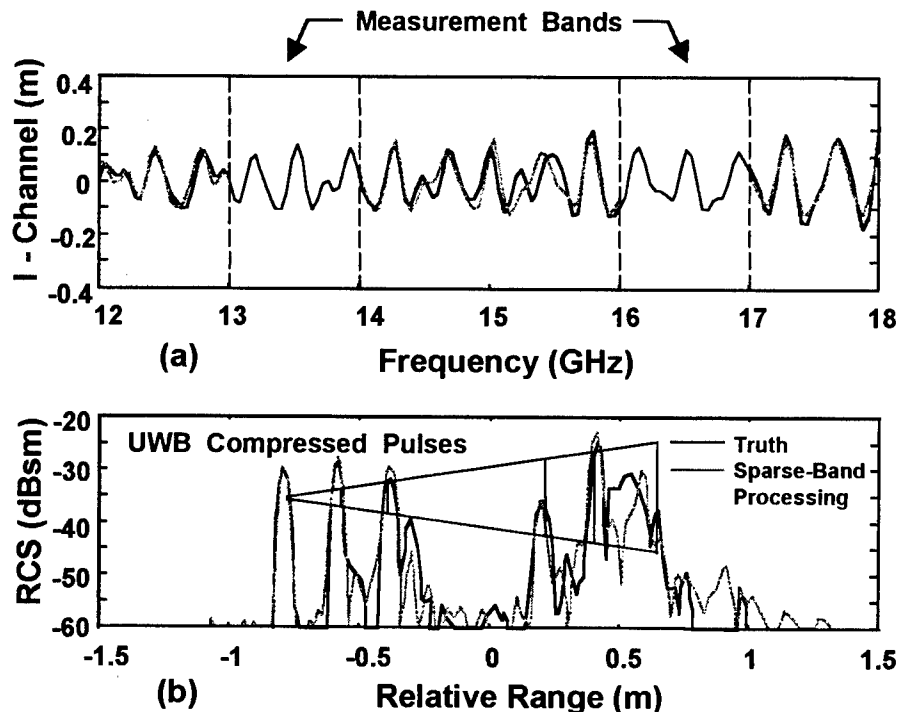


Figure 15. Comparisons between the estimated ultra-wideband target response and the true ultra-wideband radar measurements. (a) Uncompressed radar pulse for the prediction model (light gray line) and the actual radar measurements (black line). (b) The corresponding compressed pulses.

Because radar measurements were taken over a wide range of viewing aspects, we can generate two-dimensional radar images of the target. In figures 16(a) and (b), we show the lower and upper sub-band images, respectively. The resolution is insufficient to resolve many the scattering centers on the target. In figures 16(c) and (d), we show the true and estimated ultra-wideband target images, respectively. All four images were generated by applying extended coherent processing [3] to the corresponding compressed pulse over the full range of available viewing aspects. Target symmetry allowed us to process the data as if we had sampled a range of viewing aspects from -95 degrees to 95 degrees. The ultra-wideband images provide a clear picture of the target and show considerable detail. The sparse sub-band image closely matches the full-band image and provides an accurate estimate of the locations and α coefficients of the many realistic scattering centers on the target.

These experimental results suggest that ultra-wideband processing of sparse sub-band measurements can significantly improve range resolution and provide accurate characterizations of realistic target's over ultra-wide bandwidths. We are currently investigating the fundamental limitations and practical payoffs of ultra-wideband processing.

4. Summary

This article presents an approach for accurately estimating a target's ultra-wideband radar signature from sparse sub-band measurements. Because it is desirable to apply this technology to field data, it was necessary to develop an algorithm that could compensate for the potential lack of mutual coherence between the various radar sub-bands. Robust mutual coherence processing was performed by optimally matching the all-pole signal models for each sub-band. With the radar sub-bands mutually cohered, a single ultra-wideband signal model was optimally fit to the available data. The fitted model was used to interpolate between and extrapolate outside of the measurement bands. Standard pulse compression methods were applied to the enlarged band of spectral data to provide a super-resolved range profile of the target.

These ultra-wideband processing concepts were demonstrated using simulations and static range data. We showed that it was possible to accurately estimate a target's ultra-wideband response when the radar measurements fill only a small fraction of the total processing bandwidth. The practical payoff of this technology is that radar measurements need not be taken over the full ultra-

wideband processing interval; signal processing can be used to a certain extent to compensate for any missing data. Another important benefit of ultra-wideband processing is that the α coefficients of individual scattering centers can be more accurately estimated. This helps us to better identify the scattering centers that make up a target, which significantly benefits our analysis and understanding of the target.

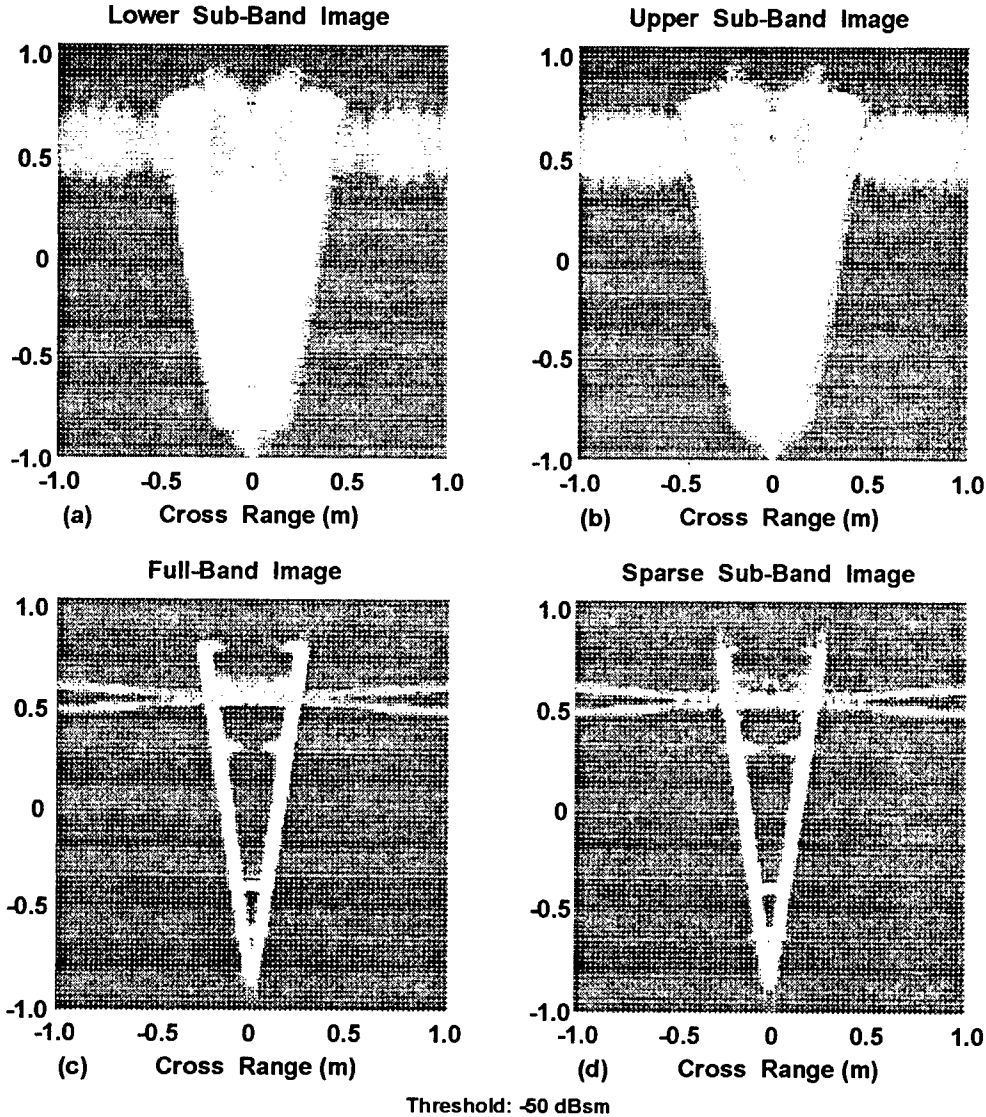


Figure 16. Comparison of two-dimensional radar images. (a) and (b) show the lower and upper sub-band images, respectively. (c) uses actual radar measurements over the full 12- to 18-Ghz frequency range. (d) uses the sparse sub-band measurements with ultra-wideband prediction.

References

- [1] K.R. Roth, M.E. Austin, D.J. Frediani, G.H. Knittel and A.V. Mrstik, "The Kiernan reentry measurements system on Kwajalein Atoll" Lincoln Laboratory Journal, vol. 2, No. 2, pp 247-276, 1989.
- [2] K.M. Cuomo, "A bandwidth extrapolation technique for improved range resolution of coherent radar data" Technical Report CJP-60 Rev.1, Lincoln Laboratory, MIT, 1992.
- [3] S.L. Borison, S.B. Bowling and K.M. Cuomo, "Super-resolution methods for wideband radar" Lincoln Laboratory Journal, vol. 5, No. 3, pp 441-461, 1992.
- [4] J.B. Keller, "Geometrical theory of diffraction" Journal of Optical Society of America, pp 116-130, January 1962.
- [5] W.M. Steedly and R.L. Moses, "High resolution modeling of fully polarized radar returns" IEEE Transactions on Aerospace and Electronic System, vol. AES-27, pp 459-469, May 1991.
- [6] E.F. Knott, J.F. Shaeffer and M.T. Tuley, Radar Cross Section, Artech House, Norwood, MA, pp 178-179, 1985.
- [7] S.Y. Kung, K.S. Arun, and D.V. Bhaskar Rao "State-space and singular-value decomposition-based approximation methods for the harmonic retrieval problem," J. Opt. Soc. Am., Vol. 73, No. 12, Dec. 1983.
- [8] H. Akaike, "A new look at the statistical model identification" IEEE Transactions on Automatic Control, vol. AC-19, pp 716-723, 1974.
- [9] M. Wax and T. Kailath, "Detection of signals by information theoretic criteria" IEEE Transactions on Acoustics, Speech and Signal Processing, vol. ASSP-33, No. 2, pp 387-392, 1985.
- [10] J. Rissanen, "Modeling by shortest data description" Automatica, vol. 14, pp 465-471, 1978.
- [11] M. Wax and I. Ziskind, "Detection of the number of coherent signals by the MDL principle" IEEE Transactions on Acoustics, Speech and Signal Processing, vol. ASSP-37, No. 8, pp 1190-1196, 1989.

[12] A.J. Barabell, "Improving the resolution performance of eigenstructure-based direction finding algorithms", in Proc. ICASSP, Boston, pp 336-339, 1983.

[13] S.W. Lang and J.H. McClellan, "Frequency estimation with maximum entropy spectral estimators" IEEE Transactions on Acoustics, Speech and Signal Processing, vol. ASSP-28, pp 716-724, 1980.

[14] R.O. Schmidt, A Signal Subspace Approach to Multiple Emitter Location and Spectral Estimation Ph.D. dissertation, Stanford University, Stanford, CA, 1981.

[15] T.J. Shan, M. Wax and T. Kailath, "On spatial smoothing for direction of arrival estimation of coherent signals" IEEE Transactions on Acoustics, Speech and Signal Processing, vol. ASSP-33, pp 806-811, 1985.

[16] A. Paulraj, R. Roy and T. Kailath, "Estimation of signal parameters via rotational invariance techniques (ESPRIT)" Proceedings of the 19-th Asilomar Conference Circuits, Syst. Comp., Asilomar, CA, pp 83-89, 1986.

[17] D.W. Tufts and C.D. Melissinos, "Simple, effective computation of principal eigenvectors and their eigenvalues and application to high-resolution estimation frequencies" IEEE Transactions on Acoustics, Speech and Signal Processing, vol. ASSP-34, No. 5, pp 1046-1053, 1986.

[18] A. Moghaddar, Y. Ogawa and E.K. Walton "Estimating the time-delay and frequency decay parameter of scattering components using a modified MUSIC algorithm" IEEE Transactions on Antennas and Propagation, vol. 42, No. 10, pp 1412-1418, 1994.

[19] C.W. Ma and C.C. Teng, "Detection of coherent signals using weighted subspace smoothing" IEEE Transactions on Antennas and Propagation, vol. 44, pp 179-187, 1996.

[20] W.H. Press, S.A. Teukolsky, W.T. Vetterling, and B.P. Flannery "Numerical recipes in C: The art of scientific computing (second edition)," Cambridge University Press, 1992.

IMPACT OF FREQUENCY DEPENDENT MUTUAL COUPLING AND CHANNEL MISMATCH ON CLOSED LOOP DIGITAL ADAPTIVE NULLING ANTENNA PERFORMANCE[†]

K. A. Falcone and Ilir F. Progr
Mayflower Communications Company, Inc.
900 Middlesex Turnpike, Building 8
Billerica, MA 01821

and

P. Olson and K. Beam
Navigation Branch, C2SID
U.S. Army CECOM
Fort Monmouth, NJ 07703

Abstract: This paper presents the results of a computer simulation which models a closed loop digital adaptive nulling antenna for suppression of RF interference. The simulation implements weight adaptation using a modified form of Hooke and Jeeves Optimization to minimize a cost function representing the interference power to satellite power ratio. The adaptive antenna performance is given in terms of the interference power to satellite power statistics with and without frequency dependent mutual coupling and channel mismatch. The results show that closed loop digital adaptive nulling performance is degraded by less than 2 dB in the presence of frequency dependent mutual coupling and channel mismatch, eliminating the need for extensive calibration techniques that are required in an analog adaptive antenna.

[†] This work was supported by Army CECOM under the SAAGA SBIR Contract No. DAAB07-98-C-A501

1. Introduction

As the use of wireless devices increases, the fact that these devices interfere with each other is becoming a serious problem. Interference can be caused by co-channel interference, leakage of LOs, harmonics, or intentional jamming. A number of methods have been devised to remove these undesired interference sources [1]-[3]. This paper will focus on a Global Positioning System (GPS) receiver application with an adaptive spatial filter using a modified form of Hooke and Jeeves Optimization [4] to control the antenna array and mitigate the effects of RF interference.

This work presents the results of a computer simulation that models a closed loop digital adaptive nulling antenna for suppression of RF interference. The complex (I, Q) signals composed of narrow band and/or broad band interference sources (jammers) and GPS signals are corrupted by frequency dependent mutual coupling and channel mismatches. These samples are combined using weights determined by Hooke and Jeeves Optimization, and the resulting average power is measured to give feedback to the algorithm.

Simulation inputs determine the interference and satellite sources' frequency, bandwidth, power, and location. Configurable antenna parameters include antenna element gain, array geometry, and platform location. System parameters such as receiver characteristics and the presence of mutual coupling and channel mismatch can also be controlled. The antenna performance is given in terms of the interference power to satellite power vs. time with and without mutual coupling and channel errors. The results indicate that closed loop digital adaptive nulling performance is not significantly affected by the presence of frequency dependent mutual coupling and channel mismatch, eliminating the need for extensive calibration techniques that are required in an analog adaptive antenna.

The rest of this paper is organized as follows. Section 2 gives an analysis of the impact of frequency independent mutual coupling and channel mismatch. In section 3, the frequency dependent system model is described. The simulation and results are discussed in section 4. Finally, the conclusions of the study are given in section 5.

2. Problem Statement

An Adaptive Spatial Filter (ASF) uses the fact that the signal and interference received by spatially separated antenna elements are correlated. This correlation can be used to minimize the interference power to signal power ratio. The closed loop system modeled here uses direct search Hooke and Jeeves Optimization [4]

to minimize a cost function expressing the interference to signal ratio. A diagram of the algorithm is shown in Figure 1 and a synopsis of the features is given in Table 1. The cost function is formed by measuring the power output from a set of test weights and dividing this by the estimated signal power. This power measurement can be characterized for a generic set of weights by using the correlation matrix of the received electromagnetic signals:

$$P = \mathbf{w}^H \mathbf{R}_{xx} \mathbf{w} \quad (1)$$

Table 1. Hooke-Jeeves Optimization Strategy

Conceptually Simple, Directed Search
Figure of Merit (Cost Function) is External to Optimizer
Vary Parameters (Weights) to Optimize a "Cost" Function
Check Each Parameter Stepping Forward and Backward
After Checking Each Parameter, Scale the Successful "Pattern"
"Best State" is stored for comparison with Subsequent Test States
Increase/Decrease Step Size Depending on Outcome of Previous Attempt

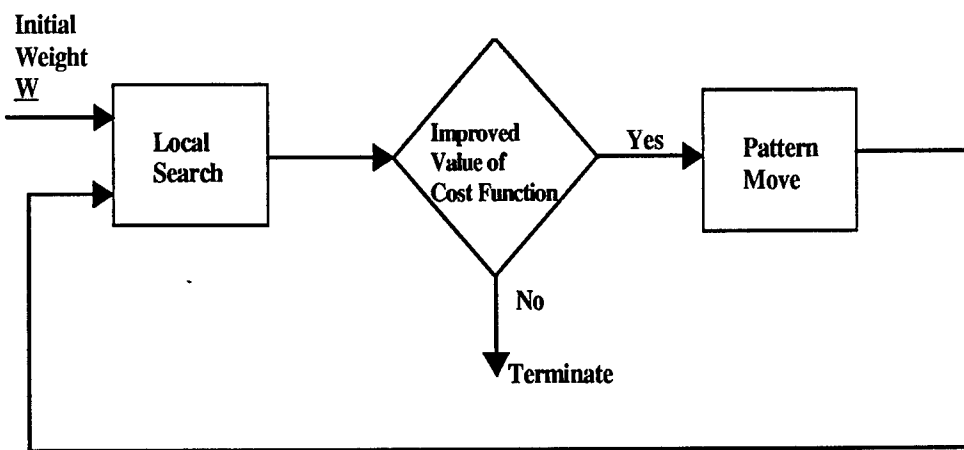


Figure 1. Direct Search Hooke and Jeeves Algorithm Showing the Local Search and Pattern Move used in Weight Optimization.

and the signal power can be estimated from a steering vector:

$$S = \mathbf{w}^H \mathbf{s} \mathbf{s}^H \mathbf{w} \quad (2)$$

to yield a cost function representing the interference to signal power:

$$F = \frac{P}{S} = \frac{\mathbf{w}^H \mathbf{R}_{xx} \mathbf{w}}{\mathbf{w}^H \mathbf{s} \mathbf{s}^H \mathbf{w}} \quad (3)$$

where

\mathbf{w} = the complex column vector representing the test weights

\mathbf{R}_{xx} = the complex matrix representing the cross correlation of the received electromagnetic signals

\mathbf{s} = the complex column vector representing the direction of the desired signal

There are many effects that can reduce the correlation between the different antenna elements or the effectiveness of its use. Some of these include frequency dependence of antenna array gain, signal quantization, weight quantization, thermal noise. These effects have been modeled in a baseline simulation. The two additional effects being studied in this work are mutual coupling of the antenna elements and channel mismatches.

The mutual coupling effect is a cross-coupling of the signals received on different antenna elements. Define:

$\mathbf{x}(t)$ = the complex column vector representing the electromagnetic signals in the environment

$\mathbf{y}(t)$ = the complex column vector representing the electrical signals with mutual coupling in the antenna channels

$$\mathbf{y}(t) = \mathbf{C} \mathbf{x}(t) \quad (4)$$

The mutual coupling matrix, \mathbf{C} , for a two element array can be specified in terms of s parameters:

$$\mathbf{C} = \begin{bmatrix} s_{11} & s_{12} \\ s_{21} & s_{22} \end{bmatrix} \quad (5)$$

A similar procedure is used to find the mutual coupling matrix for a larger number of elements.

Channel mismatch is used to represent the fact that each down converter subsystem has a different gain magnitude and phase. The difference is modeled as an error, where each channel has the same mean gain plus an error offset. Define:

$\mathbf{z}(t)$ = the complex column vector representing the electrical signals with mutual coupling and channel mismatch in the antenna channels

$$\mathbf{E} = \begin{bmatrix} 1 + e_1 & & & 0 \\ & 1 + e_2 & & \\ & & \ddots & \\ 0 & & & 1 + e_n \end{bmatrix} \quad (6)$$

$$\mathbf{z}(t) = \mathbf{E} \mathbf{y}(t) \quad (7)$$

The combined effect of mutual coupling and channel mismatch can be modeled as:

$$\mathbf{z}(t) = \mathbf{E} \mathbf{C} \mathbf{x}(t) = \mathbf{A} \mathbf{x}(t) \quad (8)$$

and if these effects are known, then we can explicitly compensate for them by recovering the original signals from the available ones:

$$\mathbf{x}(t) = \mathbf{A}^{-1} \mathbf{z}(t) \quad (9)$$

We can also compensate implicitly by modifying the weights. If we have the weight vector, w , which produces a good beam when acting on the uncoupled and uncorrupted signals, then we can produce the same beam by applying adjusted weights to the available signals:

$$b(t) = w^H x(t) \quad (10)$$

$$b(t) = w^H A^{-1} z(t) \quad (11)$$

$$b(t) = \tilde{w}^H z(t) \quad (12)$$

$$\tilde{w} = A^{-H} w \quad (13)$$

Evaluating the Hooke and Jeeves Cost Function using the uncoupled and uncorrupted signals and translating to the corrected weights:

$$F = \frac{P}{S} = \frac{w^H R_{xx} w}{w^H S S^H w} \quad (14)$$

$$F = \frac{\tilde{w}^H A R_{xx} A^H \tilde{w}}{\tilde{w}^H A S S^H A^H \tilde{w}} \quad (15)$$

$$F = \frac{\tilde{w}^H R_{zz} \tilde{w}}{\tilde{w}^H A S S^H A^H \tilde{w}} \quad (16)$$

We see from this that a fully digital adaptive antenna system will partially compensate for frequency independent mutual coupling and channel mismatches automatically, as long as they are invertible. The only remaining distortion is in the received signal steering vector.

The impact of mutual coupling and channel mismatch can be more significant than this simple fixed frequency model implies. These effects are frequency dependent, and will have a different matrix representing their combined effect, A , at every frequency. The frequency dependence of these errors can change the

effective structure of the matrix A so that it may not be invertible. Fortunately, the closed loop adaptive antenna system will still attempt to minimize the cost function. Although Hooke and Jeeves Optimization may not be able to completely compensate for frequency dependent errors, it will optimize a solution using the frequency independent parameters (the weight vector, w) it controls.

3. System Model

This system is modeled within the context of the GPS. A receiver will track a number of satellites, and will perform navigation using the signals from multiple satellites. The receiver can perform full navigation when it can demodulate signals from at least four satellites. The simulation uses a modified version of Hooke and Jeeves Optimization [4] to minimize a cost function representing the interference power to satellite power ratio. The power ratio is formed by using a power measurement to represent the interference power and the combination of the antenna weights with a steering matrix to represent the satellite power.

A block diagram of the system model is given in Figure 2. The baseline simulation models frequency dependence of the antenna array gain, thermal noise, quantization of the analog signal, finite precision of the array weights, finite precision of the signal-weight product, and measurement of the output power via a finite number of samples. Other simulations include the effect of frequency dependent mutual coupling, RF and IF filters, and mismatched RF and IF filters.

Figure 3 shows how frequency dependence is implemented in the simulation, by modeling wide band sources as a number of continuous wave (CW) sources. Each CW source has a mean square value equal to the area under the spectrum in the interval associated with that tone. The number of lines used to make a wide band source is found by increasing the number of CW sources in the model until performance has converged. Table 2 below shows baseline performance in terms of Jammer to Satellite power Ratio (JSR) for 1 wide band jammer using 10, 20, and 40 frequencies to model the 20 MHz source. The JSR performance is presented for the fourth best satellite indicating a full four satellite navigation capability. From this analysis, the 20 CW tone representation was judged to be the best compromise for a 20 MHz wideband noise source. Therefore, the remainder of the simulations use 20 frequencies to model the wide band satellites and jammers.

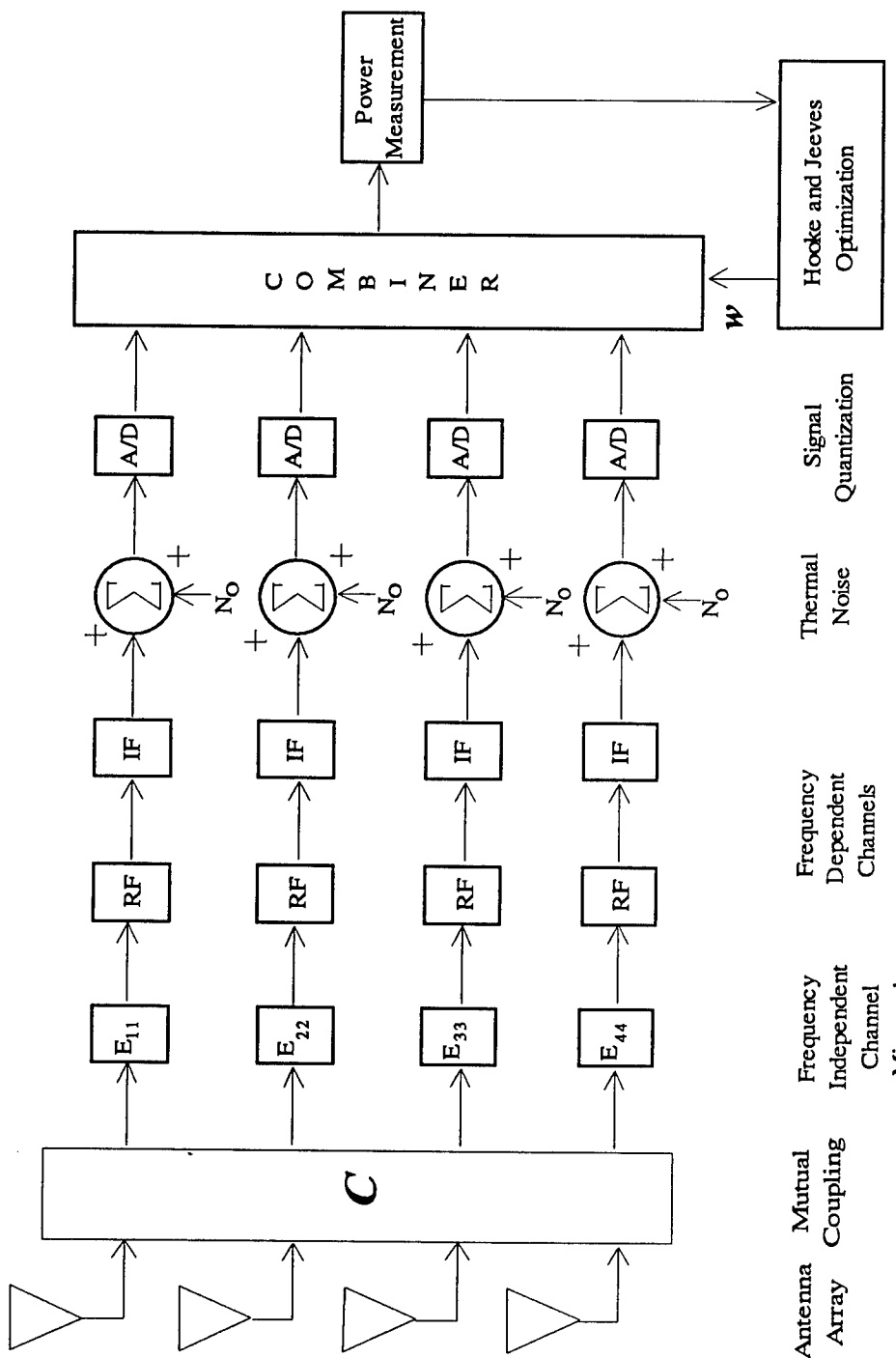


Figure 2. Block Diagram of the Interference Canceller Simulation Model.

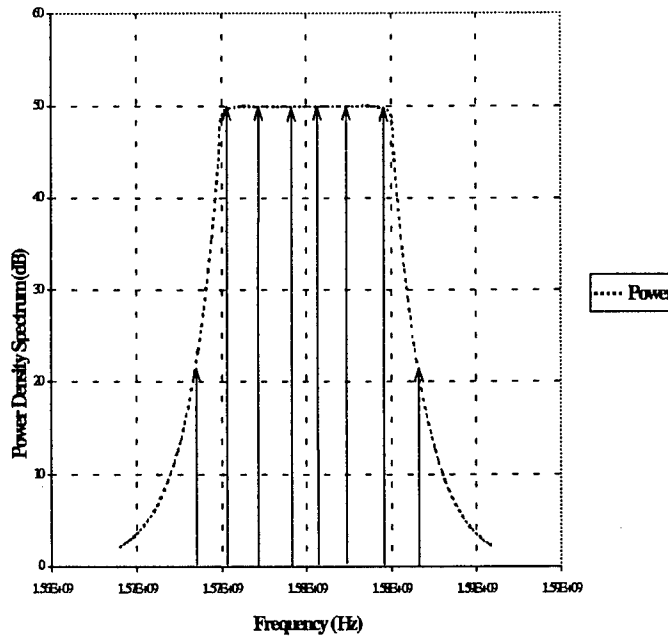


Figure 3. Example of a Wide Band Signal Source Model.

Table 2. JSR for the Fourth Best Satellite for different wide band models.

10 Frequencies/20 MHz	20 Frequencies/20 MHz	40 Frequencies/20 MHz
41.62 dB	39.67 dB	41.00 dB

Frequency dependent mutual coupling is modeled by using a fixed matrix, C , at the center frequency, f_o . The frequency dependent mutual coupling between antenna array elements i and j can be found from the distance between the elements, r_{ij} , and the frequency difference, $f_o - f_k$. The relation between frequency dependent mutual coupling, C_{ij} , and frequency independent mutual coupling, \tilde{C}_{ij}^k , is given as:

$$\tilde{C}_{ij}^k = C_{ij} \exp[j\Delta\phi_{ij}(f_k)] \quad (16)$$

with

$$\Delta\phi_{ij}(f_k) = 2\pi(f_0 - f_k) \tau_{ij} / c \quad (17)$$

The RF and IF filters are modeled as Chebyshev filters of type I. This filter has the property that the magnitude of the frequency response is equiripple in the pass band and monotonic in the stop band. The transfer function is given by [5]:

$$H_c(j\Omega) = \frac{1}{1 - j\epsilon V_N(\Omega / \Omega_c)}. \quad (18)$$

where $V_N(x)$ is the N th-order Chebyshev polynomial defined as:

$$V_N(x) = \cos(N \cos^{-1} x). \quad (19)$$

Three parameters are required to specify the Low Pass Filter (LPF) modeled as Type-I Chebyshev: the ripple tolerance α_{max} , the cutoff radian frequency Ω_c , and the order of filter, N . N determines the number of poles, and the filter drop off rate. The filter's manufacturer usually gives the ripple tolerance in dB, which can be defined as:

$$\epsilon = \sqrt{10^{\alpha_{max}/10} - 1} \quad (20)$$

For the Band Pass Filters (BPF) the center frequency, f_0 , is required in addition to the three parameters needed to specify the LPF. Usually, the filter's manufacturer specifies the filter bandwidth, B , yielding the cutoff radian frequency:

$$\Omega_c = 2\pi B / 2 \quad (21)$$

The models described in this section and the previous one were implemented in C++ simulation code. The simulation uses input files to control the interference and satellite sources frequencies, bandwidths, powers, and locations. The antenna parameters antenna element gain, array geometry, and platform location are also variable. The presence of mutual coupling and channel frequency response and

channel frequency mismatches are turned on selectively in the next section to determine their significance.

4. Simulation and Results

The baseline simulation results use the model described in the previous section. The antenna array is a four element circular array with three elements on the circle and one in the center. Wide band signals are modeled using 20 frequencies to implement the 20 MHz bandwidth, and thermal noise is modeled using a gaussian random variable. The output power is estimated using an average over 100 samples. The received signal is quantized using a 12 bit A/D, the weights are limited to 16 bits of precision, and the output of the combiner is limited to 20 bits. The simulation duration was 3000 power measurements or 17.8 milliseconds.

The simulation implements one wide band satellite, and measures JSR versus time. Because four satellites are needed for full navigation, the simulation post-processor tracks 8 satellites and analytically determines the performance of the fourth best satellite. The positions of 8 satellites were measured at the Mayflower Communications GPS Lab in Billerica, MA at 10 AM EDT on May 8, 1998. Table 3 lists the 8 satellites modeled in the post processor, while the third satellite is implemented in the simulation.

Table 3. Satellite Locations and Signal Strengths.

Satellite	Azimuth (Deg)	Elevation (Deg)	SNR (dB)	Frequency (MHz)
1	50.00	73.00	-24	20 MHz @ L1
2	-116.00	71.00	-31	20 MHz @ L1
3	-56.00	44.00	-25	20 MHz @ L1
4	-52.00	28.00	-31	20 MHz @ L1
5	157.00	26.00	-28	20 MHz @ L1
6	-78.00	25.00	-28	20 MHz @ L1
7	-142.00	14.00	-23	20 MHz @ L1
8	-18.11	4.98	-24	20 MHz @ L1

The simulation implements three wide band jammers, which is the most a four element array can effectively cancel. Table 4 lists the three jammers modeled in the simulation and post-processor. The three jammers have a total signal to noise ratio of 64.77 dB.

Table 4. Jammer Locations and Signal Strengths.

Jammer	Azimuth (Deg)	Elevation (Deg)	SNR (dB)	Frequency (MHz)
1	60.00	-0.31	60	20 MHz @ L1
2	-10.00	12.39	60	20 MHz @ L1
3	-55.00	8.56	60	20 MHz @ L1

Figure 4 shows an example of the measured value of JSR for satellite 3 versus time for the baseline simulation. The JSR performance converges to about 50 dB in about 2 milliseconds, while the algorithm slowly decreases its step size changes until about 6 milliseconds. The final value from the simulation is 50.30 dB. Using the final weights, the analytic value of JSR for satellite 1 is found to be 49.50 dB. The main differences between the two models is that the simulation quantizes the signal and uses 100 samples to estimate the power, while the analytic value is double precision determined from the mean power and final simulation weights. Statistics are given in Table 5. Ten additional simulations were executed, and the mean and variance of their final performance were estimated.

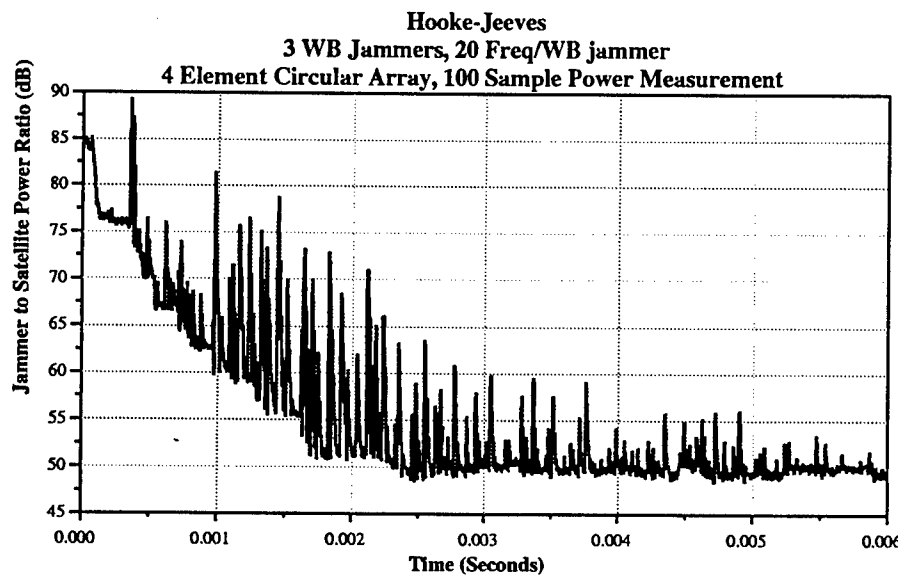


Figure 4. Measured JSR for satellite 3 versus time in the baseline simulation.

Table 5. JSR Statistics for the Fourth Best Satellite for different error models.

Model	FRPA Only (Mean dB / Standard Deviation dB)	ASF (Mean dB / Standard Deviation dB)
Baseline	89.03 / 0	49.11 / 0.33
Mutual Coupling	88.36 / 0	49.30 / 0.26
RF and IF Filters	89.03 / 0	49.36 / 0.54
Mutual Coupling with RF and IF Filters	88.36 / 0	49.08 / 0.24
Mutual Coupling with Mismatched RF and IF Filters	88.36 / 0	51.10 / 0.55

Mutual Coupling was the first frequency dependent error simulated. The Coupling Matrix is given in dB and degrees as:

$$C = \begin{bmatrix} 0\angle 0 & -20\angle 100 & -20\angle 100 & -10\angle -15 \\ -20\angle 100 & 0\angle 0 & -20\angle 100 & -10\angle -15 \\ -20\angle 100 & -20\angle 100 & 0\angle 0 & -10\angle -15 \\ -10\angle -15 & -10\angle -15 & -10\angle -15 & 0\angle 0 \end{bmatrix} \quad (22)$$

where the last antenna element is the center element. Table 5 shows the JSR statistics for 10 different seeds. These values for mutual coupling actually seem to improve performance slightly for the Fixed Reception Pattern Antenna (FRPA), which only uses the center element of the array. The combination of jammer and satellite locations is such that mutual coupling is more detrimental to jammers than to satellites. The difference for the ASF is insignificant.

The RF and IF filter models were simulated next. The same values were used for all four channels, in order to first determine the impact of common mode frequency dependence. The RF and IF filter parameters used are given in Table 6 below. Table 5 above shows the impact on JSR statistics with and without mutual coupling. As with mutual coupling, there is no significant difference in JSR statistics.

Table 6. Channel Frequency Dependence Filter Parameters.

Filter	Center Frequency (Mega-Hertz)	Order	Bandwidth (Mega-Hertz)	Ripple Tolerance α (dB)
RF	1575.42	2	50	0.1
IF	270.09	5	35	0.1

The final simulation considers the case of Mutual Coupling with Mismatched RF and IF Filters. The mismatch is modeled by assuming different tolerances for the filter parameters. Table 7 below lists the tolerances and simulation values. Figure 5 shows an example of the measured value of JSR for satellite 3 versus time for the mismatched filter simulation. The JSR performance converges to about 52 dB in about 3 milliseconds, while the algorithm slowly decreases its step size changes until about 5.5 milliseconds. The final value from the simulation is 51.43 dB. Using the final weights, the analytic value of JSR for satellite 1 is found to be 50.54 dB. The statistics given in Table 5 show that mismatched channels is the only simulation to generate a difference of more than one standard deviation in the mean. The mean penalty associated with all of these frequency dependent errors is found to be 1.99 dB.

Table 7. Channel Mismatch Parameters.

Channel	Filter	Center Frequency (Mega-Hertz)	Order	Bandwidth (Mega-Hertz)	Ripple Tolerance α (dB)
Tolerance (+/-)	RF IF	0.05 B 0.02 B	N/A	0.05 B 0.02 B	0.02 dB 0.02 dB
0	RF IF	1573.9766 270.66883	2 5	49.7 35.6	0.088 0.084
1	RF IF	1576.7002 270.53937	2 5	48.8 34.4	0.107 0.086
2	RF IF	1572.9211 271.31411	2 5	50.7 35.0	0.107 0.113
3	RF IF	1574.5716 270.74006	2 5	49.5 34.7	0.096 0.096

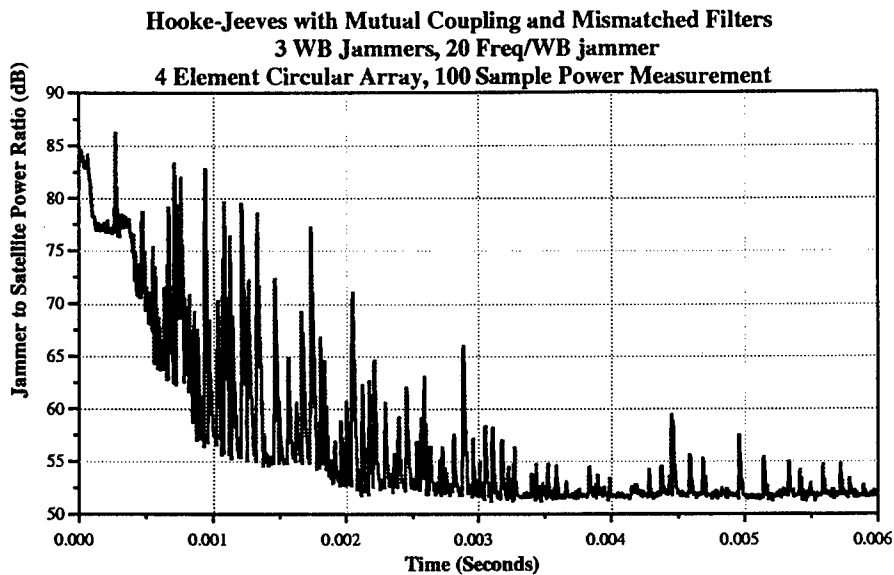


Figure 5. Measured JSR for satellite 3 versus time with Frequency Dependent Mutual Coupling and Mismatched RF and IF Filters.

5. Conclusions

This work studied the antenna performance in terms of the jammer power to satellite power with and without frequency dependent mutual coupling and channel mismatches. The results indicated that closed loop digital adaptive nulling performance is not significantly affected by the presence of frequency dependent mutual coupling and channel filters. A slight penalty, about 2 dB, was seen for channel filter mismatch, with another slight penalty in convergence time. The conclusion is that closed loop digital adaptive nulling eliminates the need for extensive calibration techniques that are required in an analog adaptive antenna.

6. Acknowledgments

The authors would like to thank Dr. Hans Steyskal of the Air Force Rome Laboratory for suggesting the frequency dependent mutual coupling model. They would also like to thank Prof. Wallace Vander Velde of MIT for suggesting the frequency independent mutual coupling and channel mismatch models.

7. References

- [1] J. E. Hudson, Adaptive Array Principles. New York: Peter Peregrinus Ltd., 1981.
- [2] B. Widrow and S. D. Stearns, Adaptive Signal Processing. Englewood Cliffs, NJ: Prentice-Hall, 1985.
- [3] Mayflower Communications Company, Inc., "Digital Beamforming GPS Antenna Architecture Phase I Final Technical Report", Contract No. DAAH0197-97-C-R247, March 1998.
- [4] R. Hooke and T. A. Jeeves, "Direct Search Solution of Numerical and Statistical Problems", J. ACM, Vol. 8, April 1961.
- [5] M. E. Van Valkenburg, Analog Filter Design. New York: Holt, Rinehart and Winston, 1982.